

**ON THE FOUNDATIONS, QUANTIFICATION, AND INTERPRETATION OF
STOCHASTIC COLLISION RISK INDICATORS IN SPACECRAFT
FORMATIONS**

A Dissertation
Presented to
The Academic Faculty

By

Ulises Eduardo Núñez Garzón

In Partial Fulfillment
of the Requirements for the Degree
Doctor of Philosophy in the
Daniel Guggenheim School of Aerospace Engineering
Space Systems Design Lab (SSDL)

Georgia Institute of Technology

May 2023

**ON THE FOUNDATIONS, QUANTIFICATION, AND INTERPRETATION OF
STOCHASTIC COLLISION RISK INDICATORS IN SPACECRAFT
FORMATIONS**

Thesis committee:

Dr. E. Glenn Lightsey, Advisor
Aerospace Engineering
Georgia Institute of Technology

Dr. Brian C. Gunter
Aerospace Engineering
Georgia Institute of Technology

Dr. Mary A. Weitnauer
Electrical Engineering
Georgia Institute of Technology

Dr. J. Russell Carpenter
Space Science Mission Operations
NASA Goddard Space Flight Center

Dr. Cesar Ocampo
Flight Mechanics and Trajectory Design
Odyssey Space Research, LLC

Date approved: April 13, 2023

The heavens declare the glory of God, and the sky above proclaims his handiwork.

Psalm 19:1 (ESV).

To my wife Amanda, my mother Rosa, my brother Daniel, and Papito

ACKNOWLEDGMENTS

In the space allotted for this section, I will not be able to do justice to the many people who have inspired, encouraged, corrected, and shaped me and my journey throughout the years, without whom this dissertation would not exist today. Hence, I apologize for any omissions.

First, I would like to thank Dr. Glenn Lightsey, my academic advisor and mentor since 2016, for having welcomed me into his lab at a time of scarce options for me to obtain space systems-related professional or academic work, and for having encouraged and mentored me in the pursuit of research topics that were mathematically challenging. Through Dr. Lightsey's patient guidance, work that began as handwritten, disconnected scribbles developed into a series of meaningful contributions that are now relevant to members of the astronautics and space systems community. I will always be thankful for the academic freedom and mentorship that I received at Dr. Lightsey's lab.

I would also like to thank the members of the PhD committee which oversaw this dissertation. I appreciate the thoughtfulness and thoroughness of their comments, as well the time and effort they put into their committee tasks. This dissertation has benefited greatly from their insight.

I thank Drs. Bobby Braun, Marcus Holzinger, and Brian Gunter for their instruction in orbital mechanics during my time at the School of Aerospace Engineering at Georgia Tech. In particular, I am appreciative of Dr. Holzinger, whose Advanced Orbital Mechanics course in the Spring 2018 semester sparked my research interest in spacecraft formation flying.

I would also like to thank the editorial leadership and reviewers at the *Journal of Guidance, Control, and Dynamics (JGCD)*. My entire peer-reviewed research corpus thus far has been published by the *JGCD*. I am thankful for all the effort made via *JGCD* towards scrutinizing my work. This process has played an instrumental part in ensuring the quality

of my research contributions in terms of their correctness, understandability, and value to a wide audience.

I am indebted to Dr. Christopher Heil, Professor at the School of Mathematics at Georgia Tech, as he has been a great mentor to me in the topics of Lebesgue and abstract measure theory. It was a formative experience for me to take Undergraduate and Graduate Real Analysis (for Engineers) courses with Dr. Heil. Additionally, Dr. Heil has been very available, and has taken the time to answer my emails about various mathematical conundrums (no matter how ridiculous or irrelevant). Thus, Dr. Heil has helped with making these concepts approachable to someone with otherwise little formal mathematical background.

This discussion would not be complete without recognizing the massively transformational role in my education that was generously played by Mr. Juan Carlos Varela, former President of the Republic of Panama. Mr. Varela fully, personally funded the direct educational costs, as well as corollary costs (room, board, books, and flights), of my bachelor's degree at Georgia Tech (2013-2017). Additionally, Mr. Varela was a significant mentor to me during my undergraduate and early graduate school years. Mr. Varela's strong encouragement for academic excellence during this time became exactly the right background necessary for this investigation to occur. I will forever be grateful to Mr. Varela for being an instrument in the hands of the LORD to bless me and my family.

Additionally, I gratefully acknowledge the support for this work provided by the Georgia Tech Daniel Guggenheim School of Aerospace Engineering, which supported my graduate studies through Graduate Teaching Assistantship (GTA) funding (2017-2019) and an internal Graduate Research Assistantship (GRA) fellowship (2020-2021), as well as the Georgia Tech Research Institute (GTRI), which supported the latter portion of my doctoral studies (2022-2023) via a GRA position at the Formation Flying Radio Astronomy group within GTRI's Precision Aggregated Space Systems (PASS) initiative.

Any views and conclusions contained herein are those of the author, and do not necessarily represent the official positions, express or implied, of the funders.

I would like to thank various other mentors who have shaped my academic journey. First, I thank my high school physics teachers (Mario Rodriguez, Jorge Serrano, and María Him) at the Colegio San Vicente de Paúl school. Through their extended one-on-one interactions with me while preparing for Panamanian Physics Olympics competitions, these teachers inculcated in me a love for physics and a passion for engineering, which would ultimately inform my choice of college major. In particular, María Him was encouraging to me in the decision to move abroad for college in spite of the inherent cultural and language difficulties, and she was the first person to successfully model for me how to be a faithful Christian in a scientific context. I am also indebted to Rodney Wesley, my middle and high school band instructor, for instilling in me the values of persistence, punctuality, discipline, and practice, which are not widely valued in my home culture.

Out of my peer mentors during my time at Georgia Tech, two stand out amongst the rest. For various reasons, the most difficult and time-consuming course I ever took at Georgia Tech was Introduction to Aerospace Engineering, which I took the first semester of my freshman year in college. Dr. Julian Brew from the Johns Hopkins University Applied Physics Lab (JHUAPL), who was a junior undergraduate tutor at the time, took me under his wing, and he patiently and encouragingly spent time with me thinking through that course. Years later, when I joined the SSDL, Julian (who is also an SSDL graduate) was able to consistently clarify the way ahead for me. I am so grateful to Julian for all his help.

I am indebted to Dr. Peter Schulte, formerly with the Charles Stark Draper Laboratory, for being not only a very steadfast friend and spiritual mentor throughout my undergraduate and early graduate years, but for also being an older brother (of sorts) to me when I joined the SSDL. In very real ways, I have been following after Peter's steps: becoming an SSDL grad student in spacecraft guidance, navigation, and controls (GN&C), interning in the same space company that Peter interned for at some point, planning to move to Houston, TX after graduation for a job in a commercial, civilian space company – and most importantly, joining Christ Covenant Church in Atlanta, GA, which Peter helped found. I

am thankful that the LORD placed such a godly man in my life, who modeled faithful Christian living in a scientific context day in and day out, and who has had relevant counsel for me in most of the significant professional decisions I have made for the majority of the past decade.

I seize this opportunity to thank my immediate family in Santiago, Republic of Panama, from whom I have consistently been far away ever since moving to Atlanta, GA for college ten years ago. My mother, Rosa Garzón, who is the very best of moms, was incredibly supportive of my dreams and aspirations from a young age, and she was never willing to curtail them, no matter how far-fetched or counter-cultural they might have been, and no matter how much of a cultural or familial misfit I was at the time. In loving memory, my late father, Regino Saavedra, was the first to instruct me in the fear of the LORD, and to love the LORD first wherever I went, not forgetting where I came from. Rest in peace, Papito, we will see you soon. Possibly the hardest part of leaving home ten years ago to start college was leaving my little brother, Daniel. Even though the past ten years have not exactly been a walk in the park for my family, Daniel has consistently encouraged me in my collegiate and doctoral journey, and he has taken such good care of our parents while I have been away. Without this lifetime of love, support, and encouragement given to me by my immediate family, this dissertation would not exist today.

More than anyone else, I am indebted to my wife Amanda (née Remus) in so many ways, I could write another dissertation on that subject alone. Amanda's companionship has been the greatest gift this life has ever given me. In particular, as it pertains to this investigation: there would be no dissertation to speak of without her encouragement, her companionship, her prayers, her (near-infinite) patience, and the industrial amounts of meal prep she has done all these years. Especially, I thank Amanda for encouraging me to be Christ-like during this time, to not idolize this doctoral investigation, or the accolades that would come as a result of this investigation, but to do it all for the LORD. This has all kept me grounded and hopeful in the most crucial of ways. Writing and finishing this

dissertation is just as much of my doing and achievement as it is Amanda's. I thank Amanda for being patient with me in the midst of so many changes in my level of courage and my emotional state, for pushing me onward with love and care, and for persistently listening to my many irrelevant rants about many a subject about this dissertation. This one's for you, baby.

My brothers and sisters at Christ Covenant Church in Atlanta, GA – specifically, those in the Brooks' community group – have provided such joy, support, encouragement, instruction, and fellowship for the past 2.5 years. For Amanda and I, they have become a community where we could grow and flourish, individually and together. I thank them for steadfastly being there for us, and for seeing this dissertation through to the finish line. I also thank the many believers throughout the world who have participated in my walk with the LORD, including those in the Republic of Panama (La Mata Church, Dos Bocas Church, Roca Eterna Church), Atlanta, GA (Georgia Tech Baptist Collegiate Ministry, Midtown Bridge Baptist Church, Rehoboth Baptist Church), Limerick, Republic of Ireland (Limerick Reformed Fellowship), Charleston, SC (Citadel Square Baptist Church), and Houston, TX (the NASA Intern Bible Study, at the NASA Johnson Space Center). It has been a joy to walk alongside so many brothers and sisters from the global Church.

Last, but not least, I will avail myself of this opportunity to talk about the LORD. “The LORD, the LORD, a God merciful and gracious, slow to anger, and abounding in steadfast love and faithfulness.” [Exodus 34:6b (ESV).] This work would be amiss without acknowledging not only the cosmic and transcendent power and majesty of the Holy God, but also His immanence: that he is aware of all we are and do, and that he is present in the lives of all beings – especially, in the lives of His people. However, all people stand in opposition to this Holy God through sin, which is a disposition and practice of lacking proper reverence, love, gratefulness, and obedience towards God, although God deserves these things from all people as their loving creator and sustainer. In love, God the Father has sent God the Son into our world, as the incarnate man called Jesus, to become the perfect substi-

tute for undeserving sinners through His sinless life and His sacrificial death on behalf of sinful men. Furthermore, Christ Jesus was sent to secure the adoption of such sinners as children of God through His resurrection from the dead (through the power of the Holy Spirit) as the head and victorious forerunner of a new creation. God the Father sent his Son to accomplish these things so that all who believe in Jesus Christ (specifically, as the only acceptable substitute for sinners, and as the only sovereign Lord of the universe) would be declared righteous (or “justified”) before the Holy God. This justification is a work of the grace of God through faith alone in Jesus Christ, made possible by an exchange of His justness for our unjustness, of His holiness for our unholiness, of His righteousness for our unrighteousness, and not through our own perceived goodness or efforts. For all who may read this, my prayer is that they would also believe these things, and that through faith in the Son of God and in the finished work of Jesus Christ (specifically, through faith given via the work of the Holy Spirit), they may receive the gift of eternal life in Christ Jesus our Lord. This eternal life consists of the gift of salvation from the condemnation of sin that all people justly deserve, and the gift of restored fellowship with God alongside the complete body of believers, for the purpose of faithful and loving obedience to God [as a result (and not a cause) of salvation] and for the purpose of grateful enjoyment of His presence (as enabled by the Holy Spirit), in this life and the life to come.

This dissertation has been enabled completely by the LORD, and the honor of its completion is the LORD’s. My LORD, my creator, my savior and redeemer, is the one who has purchased salvation from my sins and fallen nature through the finished work of Jesus Christ. Hence, I am in this world for the purposes of the LORD, and as such, I will aim to do His will on the Earth. If, by my life or writing, I am able to testify about the greatness of God and the redemption that is in Christ Jesus to those who might not otherwise hear about it, I will have fulfilled my life’s purpose: to declare the greatness of the majesty and the purpose of God, to the glory of His holy name.

TABLE OF CONTENTS

Acknowledgments	v
List of Tablesxxiii
List of Figuresxxiv
List of Acronymsxxxii
Thesis Abstractxxxiii
Chapter 1: Introduction	1
1.1 Spacecraft formation flying (SFF) – definition and benefits	1
1.2 Nature of collision risk in spacecraft formation flying (SFF)	2
1.3 Overview of the collision risk management (COLRM) process in spacecraft formation flying (SFF)	4
1.4 Contributions of this investigation	5
1.4.1 Foundational work in spacecraft formation collision risk management	6
1.4.2 Algorithms and methods for SFF collision risk indicator quantification	9
1.4.3 Spacecraft formation collision risk interpretation and decision-making	12
1.4.4 Cylindrical orthogonal norm-based stochastic collision risk measures in SFF	15

1.5	Dissertation outline	17
1.6	Intended audience	19
Chapter 2: Background		21
2.1	Acronyms	21
2.2	Nomenclature	21
2.3	Notation	30
2.4	Definition of collision events	35
2.4.1	Phenomenological notion of collision events	35
2.4.2	Collision events with respect to arbitrary norms	37
2.5	Probabilistic collision risk indicators	40
2.5.1	Instantaneous probability of collision (IPC)	40
2.5.2	Joint-time probability of collision (P_c)	43
2.5.3	A note on the probability dilution of probabilistic collision risk indicators	46
2.6	Distance-based collision risk indicators	46
2.6.1	Expected value of relative position	46
2.6.2	Minimum distance to covariance contour	47
2.6.2.1	Minimum distance to a “geometric” $3-\sigma$ contour	48
2.6.2.2	Minimum distance to a “equivalent” $3-\sigma$ contour	48
2.6.2.3	Formal definition of covariance contours represented by Methodologies 1 and 2	49
2.7	Hybrid collision risk indicators	50
2.7.1	99.73% minimum distance	50

2.7.1.1	99.73% minimum distance ($\rho_{3\sigma}$) – conceptual description	50
2.7.1.2	99.73% minimum distance ($\rho_{3\sigma}$) – formal definition . . .	50
2.8	Computational test cases	51
Chapter 3: Foundational work in spacecraft formation collision risk (Part 1) – Existence of probability density function (pdf) for Euclidean norm of finite-dimensional random vector		
3.1	Introduction	52
3.2	Background	55
3.3	Theory	57
3.3.1	Invertibility of mapping from spherical to Cartesian coordinates . .	57
3.3.2	Absolute continuity of Euclidean norm of absolutely continuous random vector	62
3.4	Applications	64
3.4.1	Properties of cdf of Euclidean norm of absolutely continuous ran- dom vector	64
3.4.2	Sensitivity of Euclidean norm of absolutely continuous relative po- sition random vector	65
3.5	Conclusion	67
Chapter 4: Foundational work in spacecraft formation collision risk (Part 2) – Well-Definedness and Computability of Joint-Time Stochastic Col- lision Risk Measures		
4.1	Introduction	69
4.2	Measurability of a -JTC sets and computability of a - P_c measures	69
4.3	Applicability of a -JTC and a - P_c results in spaceflight mechanics	73
4.4	Equivalence of a - P_c with respect to open vs. closed a -norm collision regions	75

4.5	Conclusion	79
Chapter 5: Adequacy of SFF probabilistic collision risk indicators		80
5.1	Overview of the probability dilution of SFF probabilistic collision risk indicators	80
5.2	On the usability of the IPC for SFF COLRM	82
5.3	Conceptual illustration of IPC/ P_c dilution (one-dimensional relative position)	83
5.4	Asymptotic and transient IPC/ P_c probability dilution behavior (two-dimensional relative position)	86
5.4.1	Asymptotic IPC probability dilution behavior (2D)	86
5.4.2	Transient IPC probability dilution behavior (uncorrelated 2D relative position covariance)	90
5.4.3	Transient IPC probability dilution behavior (effects of 2D relative position expectation nuisance and correlated covariance)	94
5.4.4	Applicability of IPC probability dilution (2D) to short-term P_c probability dilution	97
5.5	On miss distance-based statistical inference models for SFF COLRM	98
5.6	Summary	99
Chapter 6: Spacecraft formation collision risk quantification (Part 1) – Stochastic Convergence of Sobol-based Mahalanobis Shell Sampling (MSS) Collision Probability Computation		100
6.1	Introduction	100
6.2	Background	103
6.2.1	Notation adjustments for this Chapter	103
6.2.2	Motivation for a sampling algorithm for P_c computation	104
6.2.3	Review of Monte Carlo Stochastic Convergence Properties	107

6.3	Theory	108
6.3.1	Probabilistic results on Mahalanobis shells	108
6.3.2	Introducing the Mahalanobis Shell Sampling (MSS) algorithm	110
6.3.3	Theoretical guarantees of the MSS algorithm	112
6.3.4	MSS application to collision probability computation	115
6.3.5	Application of scrambled Sobol nets for MSS sequence generation	116
6.3.5.1	Overview of Sobol low-discrepancy sequence generation	116
6.3.5.2	Introduction to scrambled Sobol sequences	118
6.3.5.3	Application of scrambled Sobol qrn to MSS	119
6.4	Implementation – Test methodology for MSS stochastic convergence properties	120
6.4.1	Clohessy-Wiltshire (CW) vector and matrix norm	120
6.4.2	Estimating sample MSE	121
6.4.3	Regression analysis	123
6.4.3.1	Setting up regression analysis	123
6.4.3.2	Goodness of fit	125
6.5	Results and discussion	127
6.5.1	Test case and sample parameters for MSS stochastic convergence study	127
6.5.1.1	Test case for MSS stochastic convergence study	127
6.5.1.2	Sample parameters for MSS stochastic convergence study	128
6.5.2	Validation of Monte Carlo MSE convergence rate	129
6.5.3	MSS results, adequacy of error fit model	130
6.5.4	Computational results on MSS stochastic convergence properties	132

6.5.4.1	MSS asymptotic convergence rate results, sample mean and covariance	132
6.5.4.2	MSS asymptotic convergence rate results, sample IPC	136
6.6	Conclusion	139
Chapter 7: Spacecraft formation collision risk quantification (Part 2) – Distance-based SFF collision risk indicators		142
7.1	Introduction	142
7.2	Notation adjustments for this Chapter	143
7.3	Minimum Euclidean distance from origin to Mahalanobis contour – Theory	143
7.4	Minimum Euclidean distance from origin to Mahalanobis contour – Computational algorithm in \mathbb{R}^3	152
7.5	Simulation Cases, Results and Discussion	158
7.6	Minimum Euclidean distance from origin to Mahalanobis contour – Effectiveness of \mathbb{R}^3 algorithm	158
7.7	Summary	161
Chapter 8: Spacecraft formation collision risk interpretation and decision making (Part 1) – Relating collision probability and separation indicators in spacecraft formation collision risk analysis		163
8.1	Introduction	163
8.2	Background	166
8.2.1	Notation adjustments for this Chapter	166
8.2.2	Epistemic interpretation of collision probabilities	167
8.2.3	Projection IPCs	167
8.2.4	CW simulation cases	170
8.3	Theory	171

8.3.1	Theoretical results on projection IPCs	171
8.3.1.1	Projection IPCs overestimate true IPCs	172
8.3.1.2	Invariance of Euclidean norm-based projection IPCs	175
8.3.2	Validation of projection IPC theoretical results	179
8.3.3	Motivating distance measures for correlation with true IPC	180
8.3.4	Definition of collision correlation index	183
8.4	Results and discussion	184
8.4.1	Implementation notes	185
8.4.2	Validation of MC sample and projection IPC theoretical results	187
8.4.3	Correlating miss distance and true IPC	190
8.4.4	Comparing the 99.73% minimum distance to the P_c	195
8.5	Conclusion	197

Chapter 9: Spacecraft formation collision risk interpretation and decision making (Part 2) – Sensitivity of separation indicators in spacecraft formation collision risk analysis 199

9.1	Introduction	199
9.2	Background	203
9.2.1	Notation adjustments for this Chapter	203
9.3	Theory	203
9.3.1	Introducing radial probability measures	203
9.3.1.1	Radial probability measures – definition.	203
9.3.1.2	Euclidean norm of the relative position – definition.	204
9.3.2	Radial probability measures for non-singular, normal relative position	206

9.3.2.1	Euclidean norm of non-singular, normal relative position – integral computation.	206
9.3.3	Radial probability measures – approximations	207
9.3.3.1	Radial probability measures – Monte Carlo integration.	207
9.3.4	Characterizing the 99.73% minimum distance ($\rho_{3\sigma}$)	209
9.3.4.1	99.73% minimum distance ($\rho_{3\sigma}$) – definition.	209
9.3.4.2	99.73% minimum distance ($\rho_{3\sigma}$) – sensitivity analysis.	211
9.4	Methodology	212
9.4.1	99.73% minimum distance ($\rho_{3\sigma}$) – numerical computation method- ology	212
9.4.2	99.73% minimum distance ($\rho_{3\sigma}$) – sample computation methodology	214
9.4.3	99.73% minimum distance ($\rho_{3\sigma}$) – derivative computation method- ology	216
9.5	Results and discussion	217
9.5.1	Simulation parameters and CW dynamic cases	217
9.5.2	99.73% minimum distance ($\rho_{3\sigma}$) – sample validation results	218
9.5.3	99.73% minimum distance ($\rho_{3\sigma}$) – sensitivity analysis results	219
9.6	Conclusion	223
Chapter 10: Cylindrical orthogonal norm-based stochastic collision risk mea- sures in spacecraft formation flying		224
10.1	Introduction	224
10.2	Background	230
10.3	Theory	230
10.3.1	Cylindrical Orthogonal (c.o.) collision safety – conceptual results	230

10.3.1.1	Cylindrical-orthogonal collision region (COCR) construction	231
10.3.1.2	Cylindrical-orthogonal (c.o.) vector norm – definition and basic properties	232
10.3.2	Cylindrical Orthogonal (c.o.) collision safety – quantitative results	236
10.3.2.1	Spherical and box collision regions vs. COCR – linear and volumetric comparison	236
10.3.2.2	Spherical and box collision regions vs. COCR – IPC measure comparison	240
10.3.2.3	Spherical and box collision regions vs. COCR – JTC set and P_c measure comparison	243
10.4	Results and discussion	246
10.4.1	Simulation cases and computational methodology	246
10.4.1.1	CW simulation cases	246
10.4.1.2	Description of computational methodology	247
10.4.1.3	Validation of computational methodology	248
10.4.2	Validation of COCR-based probabilistic collision risk inequalities	249
10.4.2.1	Validation of c.o.-IPC inequalities	250
10.4.2.2	Validation of c.o.- P_c inequalities	253
10.4.3	Conservatism of COCR-based probabilistic collision risk inequalities	254
10.4.3.1	Agreement between c.o.- and m -bound-based IPC/ P_c values	254
10.4.3.2	Relative averaged difference between c.o.- and m -bound-based IPC/ P_c values	257
10.5	Conclusion	261
Chapter 11: Status of investigation and future work		263

Chapter 12:Concluding remarks	267
12.1 Dissertation problem statement	267
12.2 Overview of findings and implications of this investigation	268
12.2.1 Foundational SFF COLRM work	268
12.2.1.1 Existence of probability density function (pdf) for Euclidean norm of finite-dimensional random vector	268
12.2.1.2 Well-Definedness and Computability of Joint-Time Stochastic Collision Risk Measures	269
12.2.2 Algorithms and methods for SFF collision risk indicator quantification	270
12.2.2.1 Stochastic Convergence of Sobol-based Mahalanobis Shell Sampling (MSS) Collision Probability Computation	270
12.2.2.2 Quantification of distance-based SFF collision risk indicators	271
12.2.3 Spacecraft formation collision risk interpretation and decision-making	272
12.2.3.1 Relating collision probability and separation indicators in spacecraft formation collision risk analysis	272
12.2.3.2 Sensitivity of separation indicators in spacecraft formation collision risk analysis	273
12.2.4 Cylindrical orthogonal norm-based stochastic collision risk measures in spacecraft formation flying	274
12.3 Final remarks	275
Appendices	277
Chapter A: Clohessy-Wiltshire (CW) dynamics, geometry, and test cases	278
A.1 Clohessy-Wiltshire (CW) dynamics and geometry	278
A.2 CW simulation cases	284

A.3	Effects of two-body relative orbital dynamics on SFF probabilistic collision risk indicators	286
A.3.1	Setting up relative two-body propagation of a prior Hill-frame relative state sample	286
A.3.2	Probabilistic SFF collision risk indicators based on two-body relative orbital dynamics: simulation results	289
Chapter B:	Monte Carlo Stochastic Convergence Properties	292
B.1	Monte Carlo sample estimators of mean and covariance	292
B.2	Monte Carlo errors in sample mean and covariance	293
B.3	Expressions for Monte Carlo mean-square error (MSE) in sample mean	294
B.4	Expressions for Monte Carlo mean-square error (MSE) in sample covariance	295
B.5	Why study in Monte Carlo convergence in the RMSE sense	297
B.6	Probability measure estimators in the Monte Carlo sense	299
B.7	Monte Carlo estimators for the instantaneous probability of collision (IPC)	300
Chapter C:	Monte Carlo Stochastic Large Sample Management	302
C.1	Introduction	302
C.2	Notation adjustments for this Chapter	302
C.3	Monte Carlo (MC) sample requirements	302
C.4	MC sample propagation and data reduction process	308
C.4.1	Step 1: MC sample generation	308
C.4.2	Step 2: intermediate data reduction	310
C.4.2.1	Step 2: conceptual description	310
C.4.2.2	Step 2: algorithmic implementation	311

C.4.3	Step 3: aggregation of final results	313
C.4.3.1	Step 3: conceptual description	313
C.4.3.2	Step 3: algorithmic implementation	314
C.5	Extensions of the current MC sample management framework methodology	317
C.6	Discussion of MC sample methodology application	318
Chapter D: Clohessy-Wiltshire (CW) vector and matrix norm		320
D.1	Introduction	320
D.2	Clohessy-Wiltshire (CW) vector and matrix norm – definition	320
D.3	Clohessy-Wiltshire (CW) vector and matrix norm – deterministic and MSE convergence rates	322
D.4	Discussion on application of the CW vector and matrix norms	324
Chapter E: Proofs related to Foundational work in spacecraft formation colli- sion risk		325
E.1	Measurability of a -JTC sets	325
E.2	Computability of a -PC measures	335
Chapter F: Proofs of Mahalanobis Shell Sampling (MSS) Theoretical Results . .		348
F.1	Preliminaries	348
F.2	Mahalanobis Shell Sampling (MSS) – Asymptotically Unbiased Theoreti- cal Results	349
F.3	Mahalanobis Shell Sampling (MSS) – Unbiased Theoretical Results	376
References		398
Vita		416

LIST OF TABLES

1.1	Outline of contributions from this investigation to the SFF COLRM literature	18
3.1	Reference suggestions for topics in measure and probability theory.	56
6.1	Representative values of p_{exc} as a function of dimension (s) and cutoff Mahalanobis distance (d_{max}).	112
6.2	Peak IPC times, Example 3D.001.	128
6.3	Choice of N_{ss} sequence size for regression analysis.	129
10.1	COCR-based set membership and probabilistic collision risk m -bounds. . .	246
10.2	COCR volumetric (and uniform $\mathbf{R}_{i,j}(t)$ distribution-based IPC) m -reference comparison values.	259
11.1	Publication list for this investigation.	266
A.1	Initial relative state covariance parameters	286
A.2	Initial relative state expectation parameters	286

LIST OF FIGURES

1.1	Classification of SFF COLRM work: foundational, and operational. Note: collision risk is denoted as COLR.	6
1.2	Set (A_t) of initial conditions which, after propagation to time t , indicate an a -norm collision condition. Note: the a -JTC set is constructed via the union of all A_t sets, $t \in [t_0, t_f]$	8
1.3	Initial steps for generating an MSS sample of relative position random variable $\mathbf{R}_{i,j}$ in \mathbb{R}^3 : a) sample of unit square, b) sample of unit 2-sphere, and c) sample of d -Mahalanobis contour, $L_d(\mathbf{R}_{i,j})$ in \mathbb{R}^3	11
1.4	Conceptual (Euclidean) direct and inverse IPC computation through integration of relative position pdf for a system with normally distributed (two-dimensional) relative position. Note: for a joint HBR set to $\rho_{3\sigma}$, the corresponding IPC value is 0.27%.	13
1.5	Conceptual examination of the sensitivity of $\rho_{3\sigma}$ to small changes in the target probability which defines $\rho_{3\sigma}$, i.e., $p_{3\sigma} = 0.27\%$	14
1.6	Construction of the cylindrical orthogonal collision region (COCR) in three-dimensional relative position space.	16
2.1	Agents under the HBR simplification: a) not colliding, and b) colliding. Note: these circles represent Euclidean balls in $\mathbb{R}^{d_{\mathbf{R}}}$ that circumscribe agent bodies, not position pdf's.	36
2.2	Comparison between instantaneous collision regions based on L^2 and L^∞ norms.	39
2.3	Evolution of instantaneous collision sets (in relative state space) for the case of two timesteps, focusing on whether collision at one timestep indicates collision at another timestep. Note: the a -JTC set is the region in relative state space at time t_0 (left) which indicates collision at time t_0 (bright orange region) and at time t_1 (green region).	45

2.4	Conceptual illustration of expected value of relative position for a system with normally distributed (two-dimensional) relative position.	47
2.5	Instantaneous relative position pdf, representative Low-Earth Orbit (LEO) relative orbit in Hill frame, covariance contours: “geometric” $3-\sigma$ and “equivalent” $3-\sigma$	49
2.6	Instantaneous cdf of the Euclidean norm of relative position, representative Low-Earth Orbit (LEO) relative orbit: (top) complete cdf; (bottom) closeup of cdf left-tail, focusing on the 99.73% minimum distance ($\rho_{3\sigma}$).	51
3.1	Conceptual (Euclidean) IPC computation through integration of relative position pdf for a system with normally distributed (two-dimensional) relative position.	67
5.1	IPC as a function of first- and second-order statistics of a one-dimensional (1D) normally distributed relative position.	84
5.2	Covariance growth for a two-dimensional (2D) normally distributed relative position (anti-correlated x - and y -axis $\underline{\mathbf{R}}_{i,j}$ -variances).	87
5.3	Covariance growth for a two-dimensional (2D) normally distributed relative position (uncorrelated x - and y -axis $\underline{\mathbf{R}}_{i,j}$ -variances).	90
5.4	$V_{i,j}$ -radial variance growth for a two-dimensional (2D) normally distributed relative position (uncorrelated x - and y -axis $\underline{\mathbf{R}}_{i,j}$ -variances).	91
5.5	$V_{i,j}$ -orthogonal variance growth for a two-dimensional (2D) normally distributed relative position (uncorrelated x - and y -axis $\underline{\mathbf{R}}_{i,j}$ -variances).	92
5.6	IPC as a function of statistical moments of two-dimensional (2D) normally distributed relative position (uncorrelated x - and y -axis $\underline{\mathbf{R}}_{i,j}$ -variances, relative position expectation along x -axis).	93
5.7	Maximum IPC as a function of the Euclidean norm of the expected value of two-dimensional (2D) normally distributed relative position (uncorrelated x - and y -axis $\underline{\mathbf{R}}_{i,j}$ -variances, relative position expectation along x -axis).	95
5.8	$V_{i,j}$ -orthogonal variance growth for a two-dimensional (2D) normally distributed relative position (correlated x - and y -axis $\underline{\mathbf{R}}_{i,j}$ -variances).	97
6.1	Computation of finite-step approximation to the P_c , two timesteps ($N = 1$).	107

6.2	d -Mahalanobis volume and contour: a) V_d and b) L_d , respectively.	109
6.3	Probability measures of normally distributed random variables over s -hypervolumes whose boundaries are $(s - 1)$ -hypersurfaces (of constant d -Mahalanobis distance).	110
6.4	Conceptual application of MSS to IPC computation for a system with one-dimensional relative position and normally distributed (two-dimensional) relative state.	116
6.5	$4-\sigma$ confidence region on fit parameter space, regression on IPC at Time = 1.222 orbit periods, Monte Carlo sample from CW relative state, Example 3D.001.	126
6.6	Sample, true, and $[x]_H$ - $[y]_H$ projection IPC waveforms, Example 3D.001.	127
6.7	Monte Carlo asymptotic MSE-coefficient of determination results ($N_{\text{rep}} = 1000$), Example 3D.001.	130
6.8	MSS asymptotic MSE-fit coefficient-of-determination (R_{fit}^2) results ($N_{\text{rep}} = 100$), $d_{\text{max}} = 7$, CW relative position, Example 3D.001: blue) 'complete' N_{ss} , and orange) 'incomplete' N_{ss}	131
6.9	MSS asymptotic MSE-fit coefficient-of-determination (R_{fit}^2) results ($N_{\text{rep}} = 100$), $d_{\text{max}} = 7$, CW relative position rate, Example 3D.001: blue) 'complete' N_{ss} , and orange) 'incomplete' N_{ss}	131
6.10	MSS asymptotic MSE-fit coefficient-of-determination (R_{fit}^2) results ($N_{\text{rep}} = 100$), $d_{\text{max}} = 7$, CW relative state, Example 3D.001: blue) 'complete' N_{ss} , and orange) 'incomplete' N_{ss}	132
6.11	MSS asymptotic MSE-fit convergence rate (a) results ($N_{\text{rep}} = 100$), $d_{\text{max}} = 7$, CW relative position, Example 3D.001: blue) 'complete' N_{ss} , and orange) 'incomplete' N_{ss}	133
6.12	MSS asymptotic MSE-fit convergence rate (a) results ($N_{\text{rep}} = 100$), $d_{\text{max}} = 7$, CW relative position rate, Example 3D.001: blue) 'complete' N_{ss} , and orange) 'incomplete' N_{ss}	133
6.13	MSS asymptotic MSE-fit convergence rate (a) results ($N_{\text{rep}} = 100$), $d_{\text{max}} = 7$, CW relative state, Example 3D.001: blue) 'complete' N_{ss} , and orange) 'incomplete' N_{ss}	134

7.1	Illustration of bounds of $L_d(\underline{X})$ (in two-dimensional case) about its expected value.	150
7.2	Process of finding initial conditions in Methodologies 1 & 2 in \mathbb{R}^3 : a) sample of unit 2-square, b) sample of unit 2-sphere, and c) sample of d -Mahalanobis contour, L_d	153
7.3	Distortions introduced by the Lambert transform to pre-images of open balls (relative to \mathbb{S}^2) centered at $\pm[0, 0, 1]^T$: a) unit 2-square space, b) unit 2-sphere space.	156
7.4	Distortions introduced by the Lambert transform to pre-images of open balls (relative to \mathbb{S}^2) centered at $\pm[1, 0, 0]^T$: a) unit 2-square space, b) unit 2-sphere space.	156
7.5	Objective function, min. distance from $L_d(\mathbf{R}_{i,j})$ to origin, unit 2-square space (Eq. 7.55), strictly convex neighborhood around unique global optimal: a) unit 2-square, and b) closeup.	159
7.6	Objective function, min. distance from $L_d(\mathbf{R}_{i,j})$ to origin, unit 2-square space (Eq. 7.55), ill-conditioned neighborhood around global optimal: a) unit 2-square, and b) closeup.	159
7.7	Monte Carlo sample relative position distribution (marginalization of sample relative state distribution) after 0.67 orbits.	161
8.1	Conceptual distinction between true IPC and \widetilde{W} -projection IPC measures for a 3D relative position pdf (expressed in the coordinates of an arbitrary frame \mathcal{J}).	173
8.2	Geometry of W -projection frame with $\Xi_{W,\mathcal{J}} = A_{312}(-Az, El, \gamma)$ parametrization: a) Az, El geometry, b) γ geometry in \widetilde{W} -projection plane. Note: the AER frame is parametrized with $\gamma = 0$	176
8.3	Relative position sample distribution (marginalization of relative state sample distribution), Example 3D.005, time = 0 orbits (3.2×10^8 particles in sample).	179
8.4	True IPC, projection IPCs, and Monte Carlo IPC, Example 3D.005 (projection IPCs are on planes normal to dynamics vectors).	180
8.5	True IPC, projection IPCs, and Monte Carlo IPC, Example 3D.005 (projection IPCs are on coordinate planes).	181

8.6	Relationship between a) unit square, b) unit 2-sphere, and c) $L_d(\mathbf{R}_{i,j})$	187
8.7	Cross-correlation coefficient between sample and true IPC waveforms (over 2 orbit periods), Monte Carlo results (all cases).	188
8.8	Sample-to-true IPC waveform \mathcal{L}^2 -norm ratios (over 2 orbit periods), Monte Carlo results (all cases).	188
8.9	Cross-correlation coefficient between sample and projection IPC waveforms (over 2 orbit periods), Monte Carlo results (all cases, biased waveforms).	189
8.10	Cross-correlation coefficient between sample and true IPC waveforms (over 2 orbit periods), Monte Carlo results (all cases, unbiased waveforms).	190
8.11	Sample, true, and $[x]_H$ - $[y]_H$ projection IPC waveforms, Example 3D.001.	191
8.12	Comparison of IPC and “miss distance”-like waveforms, Methodologies 1, 2, and 3, Example 3D.001 (no $[z]_H$ motion).	191
8.13	Comparison of IPC and “miss distance”-like waveforms, Methodologies 1, 2, and 3, Example 3D.002 ($[x]_H$ and $[z]_H$ motion in phase).	192
8.14	Collision correlation index between sample IPC and “miss distance” waveforms: Methodologies 1-3, and Euclidean norm of expected relative position ($[x]_H$, $[z]_H$ motion out of phase).	192
8.15	Collision correlation index between true IPC and sample $\rho_{3\sigma}$ waveforms (all cases).	195
8.16	Comparison of IPC, P_c , and 99.73% minimum distance waveforms, Example 3D.002.	196
9.1	Numerical computation of the pdf of the Euclidean norm of the relative position using nested implementation of the <code>ode113</code> solver.	212
9.2	Numerical computation of radial probability measures and the 99.73% minimum distance ($\rho_{3\sigma}$) using nested implementation of the <code>ode113</code> solver.	213
9.3	Sample computation of the 99.73% minimum distance ($\rho_{3\sigma}$) through Monte Carlo simulation based on instantaneous relative position statistics.	215
9.4	Example 3D.001, $\rho_{3\sigma}$ waveform results: (upper) numerical and sample results; (lower) absolute difference between numerical and sample results.	220

9.5	Example 3D.001, sample $\rho_{3\sigma}$ waveform results over full horizon.	220
9.6	Example 3D.001, derivative of $\rho_{3\sigma}$ with respect to its target probability $p_{3\sigma}$, $d\rho_{3\sigma}/dp_{3\sigma}$, full horizon time-history.	221
9.7	Example 3D.001, relative sensitivity of $\rho_{3\sigma}$ to a change $\delta p = 0.01\%$ in target probability $p_{3\sigma}$	221
9.8	Examples 3D.001-026, maximum relative sensitivity of $\rho_{3\sigma}$ to a change $\delta p = 0.01\%$ in target probability $p_{3\sigma}$	222
10.1	Construction of the cylindrical orthogonal collision region (COCR; i.e., the A_{co} set) in \mathbb{R}^3	232
10.2	Comparison between instantaneous collision regions based on cylindrical-orthogonal and L^∞ norms.	234
10.3	Comparison between instantaneous collision regions based on cylindrical-orthogonal and L^2 norms.	241
10.4	Cross-correlation coefficient between sample and numerical IPC waveforms (over 2 orbit periods), c.o.- and m -bound-based collision regions.	249
10.5	Sample-to-numerical IPC waveform \mathcal{L}^2 -norm ratios (over 2 orbit periods), c.o.- and m -bound-based collision regions.	249
10.6	Comparison of IPC and Pc waveforms, c.o.- and Euclidean-bound-based collision regions, Example 3D.013.	250
10.7	Comparison of IPC and Pc waveforms, c.o.- and box-bound-based collision regions, Example 3D.013.	251
10.8	Numerical c.o.-to- m -bound IPC waveform \mathcal{L}^2 -based comparison (over 2 orbit periods): (orange) Bound 1, (yellow) Bound 2, (purple) Bound 3, (green) Bound 4.	256
10.9	Sample c.o.-to- m -bound Pc waveform \mathcal{L}^2 -based comparison (over 2 orbit periods): (orange) Bound 1, (yellow) Bound 2, (purple) Bound 3, (green) Bound 4.	257
10.10	Cylindrical orthogonal IPC and Pc m -comparison indices (over 2 orbit periods), Bound 1 (i.e., Euclidean lower bound, $m = 1$).	259

A.1	Geometry of closed CW trajectories, where P is the chief orbit period.	283
A.2	Relative change of maximum Pc based on two-body relative orbital dynamics with respect to maximum Pc based on CW dynamics (Euclidean norm-based relative position space collision regions).	290
A.3	Comparison of IPC and Pc waveforms, two-body- and CW-based dynamics, Euclidean-norm-based collision regions, Example 3D.012.	291
C.1	Notion of sample leftover points, N_{Leftover} (see Eq. C.2) for multivariate normal distributions (in six dimensions): (top) N_{Leftover} , $d \in [0, 8.5]$; (middle) N_{Leftover} , closeup; (bottom) probability of sample points at MHD greater than or equal to d	304
C.2	MC sample processing Step 1 (sample generation).	308
C.3	MC sample processing Steps 2 and 3 (high level logic).	309
C.4	MC sample processing Step 2.	311
C.5	MC sample processing, Step 2, Pre-processing #1 subroutine.	312
C.6	MC sample processing, Step 2, Pre-processing #2 subroutine.	313
C.7	MC sample processing, Step 2, Pre-processing #3 subroutine.	314
F.1	Values of $ G - 1 $ as a function of MSS sample dimension (s) and number of MSS sample shells (N_{sh}): (blue) $G < 1$, (red) $G > 1$	397

LIST OF ACRONYMS

- Pc*** Probability of collision (joint-time)
- 2D** Two-dimensional
- 3D** Three-dimensional
- a.e.** Almost everywhere
- a.s.** Almost surely
- APF** Artificial Potential Function
- c.o.** Cylindrical orthogonal
- CARA** Conjunction analysis and risk assessment
- cdf** Cumulative distribution function
- CI** Confidence interval
- COCR** Cylindrical orthogonal collision region
- COLA** Collision avoidance
- COLRM** Collision risk management
- CR** Confidence region
- CW** Clohessy-Wiltshire
- DCM** Direction Cosine Matrix
- HBR** Hard-body radius
- i.i.d.** independent, and identically distributed
- IPC** Instantaneous probability of collision
- JTC** Joint-time collision set
- LEO** Low-Earth Orbit
- LTI** Linear Time-Invariant

MC Monte Carlo
ME Mean error
MHD Mahalanobis distance
MSE Mean-square error
MSS Mahalanobis Shell Sampling
pdf Probability density function
pmf Probability mass function
QMC Quasi-Monte Carlo
qrns quasi-random number sequence
RMSE Root-mean-square error
RQMC Randomized Quasi-Monte Carlo
RV Random variable
S3AC spherical, three-dimensional (3D) avoidance constraint
SFF Spacecraft formation flying

THESIS ABSTRACT

This dissertation provides an overview of the benefits of spacecraft formation flying (SFF), of the sources of collision risk in SFF, and a discussion on how relative orbital dynamics make the problem of collision risk management (COLRM) in SFF different from the standard obstacle avoidance problem in robotics. Progress in SFF COLRM is classified in terms of foundational work, which consists of the formulation and basic properties of stochastic collision risk indicators, and operational work, which is concerned with SFF collision risk quantification, interpretation and decision-making, and reduction. Except for collision risk reduction, this doctoral investigation contributes to all aspects of the SFF COLRM problem.

First, a sampling method is developed for the computation of probability measures associated with rare event simulation, with the goal of computing instantaneous and joint-time collision probabilities in SFF with comparable performance to Monte Carlo. Second, a methodology is developed for examining the consistency between collision risk insights that may be gleaned from distance-based and probability-based collision risk indicators, with recommendations for certain distance-based collision risk indicators whose relationship to collision probability is in accordance with intuition. Third, a new collision region is introduced which arises from the combination of mutually orthogonal circular constraint violations, and its application to the approximate satisfaction of spherical avoidance constraints is motivated by quantifying the extent of the overestimate of stochastic collision risk measures based on the proposed collision region when compared to their isotropic counterparts. Fourth, for sensitivity analyses of the direct and inverse instantaneous collision probability problems, their soundness is substantiated by proving the absolute continuity of the Euclidean norm of an absolutely continuous finite-dimensional random vector. For instantaneous collision conditions based on balls with respect to arbitrary norms in relative position space, their corresponding joint-time collision probability measures are shown to

be well-defined and computable.

Together, these contributions to an integrated approach to SFF COLRM constitute progress toward the goal of practical implementations of mission concepts based on the spacecraft formation flying paradigm.

CHAPTER 1

INTRODUCTION

1.1 Spacecraft formation flying (SFF) – definition and benefits

Spacecraft formation flying (SFF) is defined as a “set of more than one spacecraft whose dynamic states are coupled through a common control law”. [1] Under this commonly accepted definition, for any spacecraft formation, there exists at least one agent of such formation which tracks a relative state with respect to some other agent of the formation, and the control law of the former must be a function of its relative state with respect to the latter. In other words, SFF is a group of more than one space vehicle, whose members are coupled as follows: the control law of any member is a function of dynamic states relative to other members of the group.

According to this SFF definition, spacecraft in constellations, though related operationally to each other, are not linked from the perspective of control laws; hence, spacecraft constellations are not instances of SFF. Conversely, spacecraft that undergo certain operations that require relative control laws (such as rendezvous, docking, or relative station-keeping, to name a few examples) are instances of SFF. In this dissertation, only instances of SFF will be considered in which the intent is not to completely eliminate inter-agent separation.

As a space mission design paradigm, SFF is attractive for several reasons. Chiefly, spacecraft formations are able to replace failed agents or add new ones, and agents in a spacecraft formation are able to exchange roles and/or tasks. The availability of such mission architecture choices has broad implications. In particular, SFF can enable missions with increased system robustness, as deterioration or failure of an agent in a spacecraft formation may only cause performance degradation in the mission, rather than caus-

ing the end of the mission.[2] Conversely, spacecraft formation missions may also have longer lifetimes, as well as performance improvements over their lifetimes, due to the ability to replace failed agents or add new ones. Hence, SFF schemes are advantageous from a spacecraft systems engineering perspective because spacecraft missions may become more scalable, adaptable, flexible, and/or maintainable as a result of implementing the SFF paradigm.[3] Such performance-enhancing mission architecture capabilities are unavailable to monolithic spacecraft missions.[4]

Additionally, the SFF concept may be employed to carry out high-precision scientific missions, specifically, by distributing a formation over large regions and by using sensor fusion.[5] These techniques may be applied in scientific endeavors such as gravity field recovery, weather forecasting, exoplanet detection, and more.[5, 6, 7, 8, 9, 10, 11]

1.2 Nature of collision risk in spacecraft formation flying (SFF)

Because spacecraft formations are vulnerable to the threat of not only collisions with objects external to the formation, but also internal collisions (i.e., collisions among satellites within the formation), the survivability and success of spacecraft formation missions are intrinsically linked with the effective management of collision risk.[12]

Typically, agents in a spacecraft formation operate in close enough proximity to each other that their individual dynamics can be modeled as small variations near a reference orbit.[2] Yet, unlike in the context of other proximity operations such as rendezvous, agents in an SFF mission must operate without ever colliding or coming dangerously close together.[13] Since orbit navigation, dynamic modeling, and actuation errors, even if reducible, cannot be fully eliminated, some level of inter-agent drift is inherent to spacecraft formations;[2] hence, it is always possible that such drifting (or any maneuvering) might cause collision events. Additionally, geometry maintenance constraints, as well as the possible failure of individual spacecraft, make collision risk assessment and risk reduction a challenging problem in spacecraft formations.[13]

Furthermore, several Earth-orbit regimes have become hosts to surging populations of debris, whose presence is hazardous to current and future missions.[14, 15] Collision with debris is an ever-intensifying concern because the debris population continues to grow through three main modes: cascading random collisions, the introduction of new objects to the environment every time a new mission is launched, and the lack of debris removal implementation.[16, 17, 18, 19, 20, 21] Collisions with debris could do substantial harm to active spacecraft, up to destroying such assets altogether.[17] In order to mitigate the concerns of space debris, several schemes of debris removal have been proposed, although none have been implemented.[20, 21] Thus, collision avoidance maneuvers remain the “single most important technique in managing the risk associated with space object collision”.[22]

Therefore, the most important exogenous kinetic threat to spacecraft formations is external debris, even to a greater extent than to monolithic spacecraft. When in close approach, debris can be conceptualized as non-cooperative agents with high relative velocity with respect to one (or several) agents in the formation. Hence, spacecraft encounters with debris have been traditionally conceptualized as short-term, one-time encounters.[23, 24] Whenever a correction maneuver is undertaken by an endangered agent in a spacecraft formation, its effect is not isolated to said agent, but it necessarily induces changes to the structure of the formation, and such changes may prompt corresponding actions by the remaining agents in order to maintain safety and operational performance.[25, 26] Thus, avoiding an external threat in SFF is a complex process because external debris avoidance maneuvers many induce unintended internal collision risk which must also be avoided.

Consequently, even when considering the short-term risk of debris impact, the primary safety concern to spacecraft formations stems from the long-term risk of potential collisions between pairs of agents in such formations. Since the threat of internal collisions is ever present, methods of internal collision monitoring and avoidance must meet safety constraints while minimizing resource expenditure in order to extend mission lifetime.[2]

Therefore, this dissertation focuses on the risk of internal collisions in spacecraft formations.

1.3 Overview of the collision risk management (COLRM) process in spacecraft formation flying (SFF)

Fundamentally, collision risk management (COLRM) is an inherent operational function in SFF which seeks to reconcile two primary aims: first, to ensure the safe and continued operation of spacecraft formations considering the ongoing threat of collisions; and second, to balance safety requirements in a way that maximizes mission lifetime (which is constrained by onboard propellant).[2, 12]

The ongoing process of spacecraft formation collision risk management involves the following tasks: collision risk quantification, interpretation and decision-making, and reduction.[12] First, collision risk is quantified through some indicator, either a separation metric or a measure of the likelihood of this adverse event.[27, 28] Second, the outcome of this indicator should inform, via a predetermined rule, whether corrective actions are warranted. Third, if necessary, collision avoidance (COLA) maneuvers must achieve the reduction of quantifiable risk to a tolerable level.[13] This process is analogous to the management of debris collision risk for monolithic spacecraft.[29]

Implicit to the ongoing process of SFF COLRM are foundational COLRM tasks, which pertain to the meaning of collision risk, and consequently, the suitable formulation of deterministic and stochastic representations of collision risk. First, collision events must be defined in ways that are physically sensible, tractable, and consistent, and which might be verifiable in the case of highly accurate relative state knowledge. Second, because relative state information is always imperfect in practice,[30] collision risk indicators must be chosen in ways that adequately account for the uncertainty in relative state information. The choice of collision risk indicator type is significant because it leads to different representations of collision risk thresholds, and consequently, different guidance and con-

trol philosophies for collision risk reduction.[28] Therefore, the choice and computation of suitable collision risk indicators is a central concern to the concept of operations for any spacecraft formation mission.

Hence, in the field of SFF COLRM, a distinction may be made between foundational work regarding collision risk indicators, and practical work that employs such collision risk indicators in the context of ongoing operational tasks. As illustrated in Fig. 1.1, on the one hand, foundational work in SFF COLRM includes the formal definition and basic properties of collision risk indicators, specifically, as it pertains to their well-definedness and usability; such work becomes particularly relevant when new collision risk indicators are introduced. On the other hand, operational SFF COLRM tasks are understood in this dissertation as follows. First, SFF collision risk quantification work refers to any algorithms or techniques that may be employed to quantify collision risk indicators. Second, SFF interpretation and decision-making work includes: the relationship among different types of collision risk indicators, the consistency of conclusions gleaned from different indicators, the physical and operational interpretation of collision risk indicators, and any other work that is relevant to the application of collision risk indicators in order to decide whether collision avoidance maneuvers are operationally warranted. Finally, SFF collision risk reduction work encompasses relative trajectory planning algorithms and techniques whose aim is to ensure the sufficient reduction of collision risk.

1.4 Contributions of this investigation

This dissertation focuses on contributions to the process of spacecraft formation COLRM. These contributions rely upon the deterministic formulation of collision events, as well as on the definition of uncertain collision risk indicators, which may be probabilistic, separation-based, or both. These formulations are presented in Chapter 2.

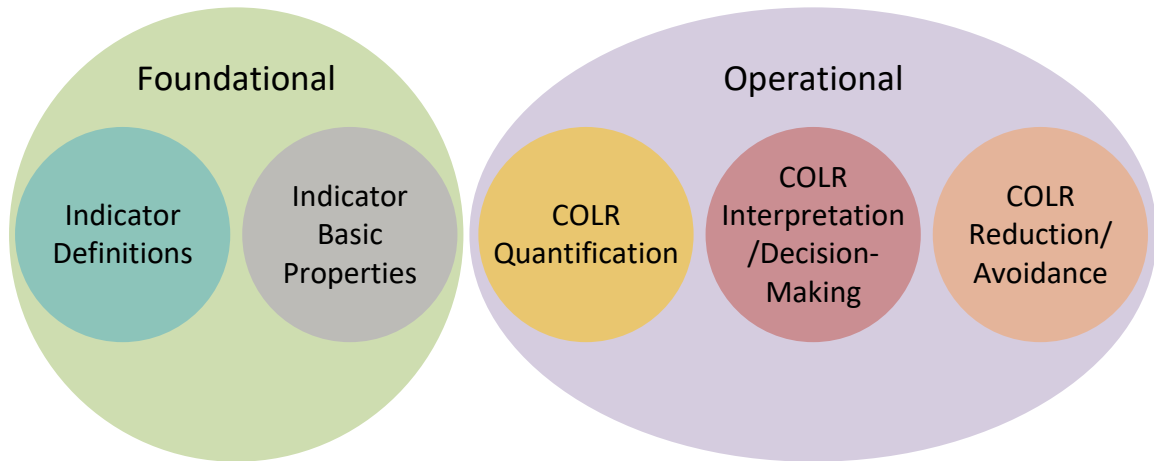


Figure 1.1: Classification of SFF COLRM work: foundational, and operational. Note: collision risk is denoted as COLR.

1.4.1 Foundational work in spacecraft formation collision risk management

Contribution 1: *To substantiate sensitivity studies of instantaneous collision probabilities (with respect to hard-body radii), and to show the computability of joint-time SFF collision risk measures whose corresponding instantaneous collision conditions are based on arbitrary norms in relative position space*

The first part of this contribution addresses the instantaneous probability of collision (IPC), which is employed for spacecraft collision risk quantification, specifically under the hard-body radius (HBR) assumption.[31] When using a probabilistic description of the relative position between two objects, and under the HBR assumption, the IPC can be conceptualized as the probability mass within a Euclidean distance (away from the origin of relative position space) equal to the joint HBR between both objects.[32]

Since the IPC depends on the HBR, it is important to ascertain the effects on the IPC caused by changes in the HBR.[28, 31] Sensitivity analyses of the IPC can be formulated in terms of changes to the cumulative distribution function (cdf) of the Euclidean norm of the instantaneous relative position (denoted as R), which, in the limit of small changes, involve derivatives of this cdf.[33] However, it is not known a priori whether the cdf of

R is equal to the Lebesgue integral of its derivative, i.e., whether the cdf of R is an absolutely continuous function.[34] In measure-theoretic terms, it is not known whether the probability measure associated with R is absolutely continuous.[35] This would be the case under the assumption of normality of the distribution of the relative position.[36] However, there is growing evidence that normality is not an appropriate assumption for probability distributions in space flight mechanics.[37]

In the first part of this contribution, it is proven that, for a finite dimensional random vector with an absolutely continuous probability distribution (that is, if it has a probability density function, or pdf, through which probability measures may be computed via Lebesgue integration), then, its norm also has an absolutely continuous probability distribution (i.e., it has a pdf).[12] This result lays the foundation for sensitivity analyses of the IPC in a Lebesgue integral-derivative sense because, by assuming the existence of a pdf for the relative position, it follows that R also has a pdf.

The second part of this contribution addresses the joint-time probability of collision (P_c), which is the probability that two agents collide at any time within a finite time interval.[31] The P_c is implicitly dependent on the underlying condition which defines an instantaneous collision event. It is a known fact, if the instantaneous collision event is defined via a Euclidean ball in relative position space, that the corresponding P_c is well-defined.[38] However, instantaneous collision conditions may be operationally defined via balls with respect to other norms in relative position space, such as the box norm,[39] ellipsoidal norms,[40] or norms arising from meeting mutually orthogonal circular constraints.[41] Hence, it is not immediately clear whether P_c measures (induced via arbitrary norms in relative position space) are well-defined.

In the second part of this contribution, the well-definedness and computability properties of P_c measures is extended to a - P_c measures, i.e., P_c measures that are induced by instantaneous collision regions that are defined via balls with respect to arbitrary norms (denoted by a) in relative position space. This result is shown under the assumptions of

continuity of the flow function corresponding to the dynamics of relative agent motion, and continuity of the joint HBR time-history. Under these conditions, a - PC measures are well-defined (i.e., they exist) and computable, i.e., finite timestep approximations to the a - PC are able to approximate real a - PC values arbitrarily well in the limit.[41] These results buttress the application of arbitrary a -norms in order to induce stochastic collision risk measures, as well as applications of the measures in a SFF COLRM context. The construction of the a -JTC set, upon which a - PC measures are based, is illustrated in Fig. 1.2.

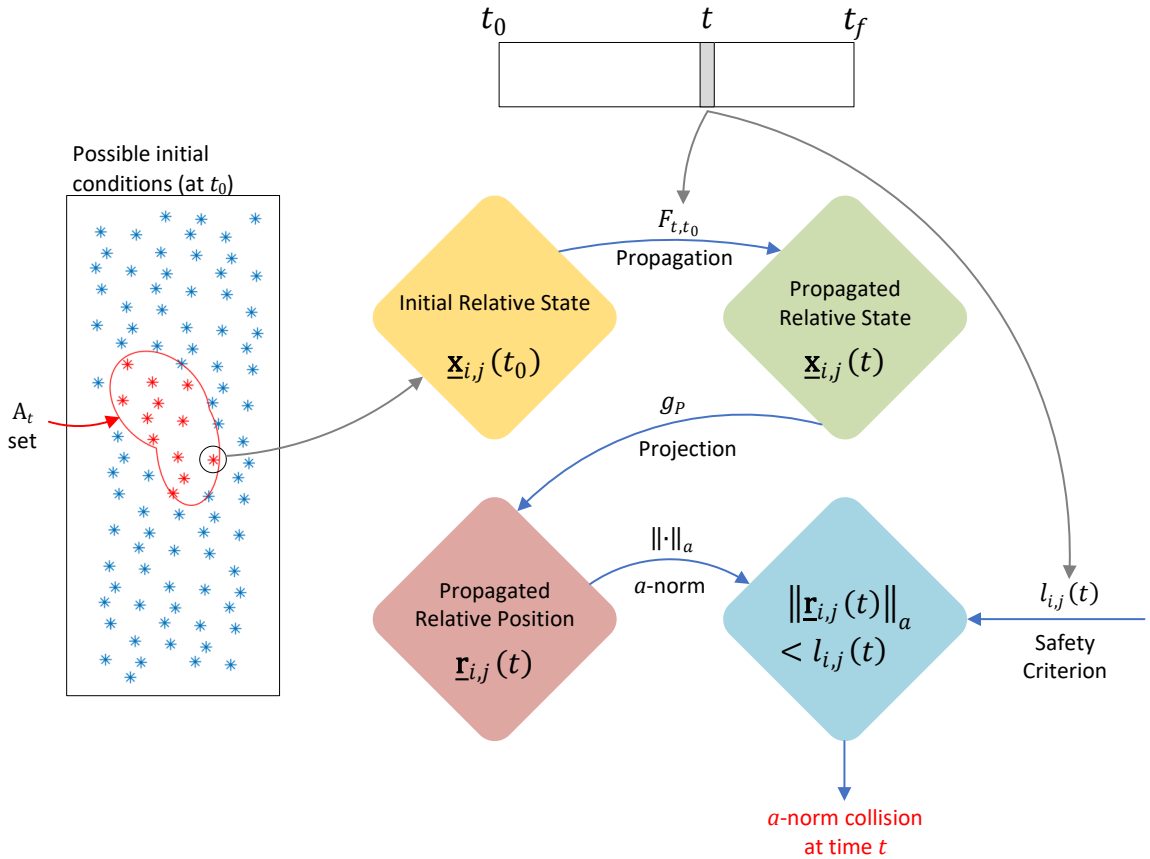


Figure 1.2: Set (A_t) of initial conditions which, after propagation to time t , indicate an a -norm collision condition. Note: the a -JTC set is constructed via the union of all A_t sets, $t \in [t_0, t_f]$.

The first and second parts of this contribution are addressed in Chapters 3 and 4. Both parts of this contribution represent foundational work in SFF COLRM; cf. Section 1.3.

1.4.2 Algorithms and methods for SFF collision risk indicator quantification

Contribution 2: *To motivate and develop sampling methods for probabilistic SFF collision risk indicators, and to formulate practical computational techniques for separation-based collision risk indicators*

The problem of SFF COLRM differs from the standard obstacle avoidance problem in robotics because of the instability of relative orbital dynamics, the lack of spatial restraints in spacecraft motion, and limitations in sensing accuracy and onboard resources.[30] These facts imply the need to quantify uncertain indicators of collision risk, to make decisions based on acceptable risk thresholds, and to plan appropriate corrective actions to reduce quantifiable collision risk accordingly.[29, 27, 28, 13]

Because the relative position between space objects cannot be deterministically known, [42], the first part of this contribution focuses on probability measures associated with the likelihood of collision events which have been explored considerably in SFF research, being employed as probabilistic indicators of collision risk, with particular focus on the P_c , which is the probability of collision over a finite time interval, and the instantaneous probability of collision (IPC).[31, 43, 44] One consequence of the probability dilution phenomenon in relative orbital dynamics is that, operationally, certain practitioners in the spacecraft conjunction assessment community adopt a threshold of significance for P_c values of 1×10^{-7} (that is, P_c values above this threshold are considered significant, and vice versa).[45, 29] Via the construct of projection instantaneous probabilities of collision, it could be argued that this threshold of significance may also be valid for IPC values in an SFF COLRM context [28] – and hence, this threshold may be regarded as valid for P_c values in this context as well. Thus, for sampling algorithms employed to estimate SFF probabilistic collision risk indicators, it would be beneficial to produce samples that allow for accurately reproducing low-valued probability measures – which implies the need to account for probabilistic outliers consistently.[46, 47]

The first part of this contribution motivates the use of sampling algorithms for approximating the probability of joint-time events, i.e., events that involve the application of a single logical condition over a finite time interval (such as the P_c) after propagating an initial distribution through a dynamic process. Under certain conditions, estimating the probability of joint-time events implies the need for computing probabilities over a number of sets that is a combinatorial function of the number of timesteps into which the time interval is subdivided.[38] This motivates the development of a sampling method (which naturally allows for nonlinear sample element propagation) which has unbiased sample mean and covariance over invertible linear transformations, and which has asymptotically unbiased convergence for probability measures over measurable subsets of relative dynamic state space. Specifically, the Mahalanobis Shell Sampling (MSS) algorithm is developed to geometrically sample from non-degenerate multivariate, normal distributions in a way that allows for obtaining an arbitrary amount of sample points that may be regarded as probabilistic outliers in a systematic fashion, and without requiring unmanageably large sample sizes, for the purpose of reproducing the probability of rare events (specifically, those involving probability distribution tails). The MSS algorithm is then validated for application to SFF probabilistic collision risk indicator computation through simulation in a pertinent relative orbital dynamic context.

Some of the basic elements of the MSS algorithm are illustrated in Fig. 1.3 for the case of sampling from an instantaneous relative position random variable $\underline{\mathbf{R}}_{i,j}$ in \mathbb{R}^3 : obtaining a sample of the unit $(s - 1)$ -hypercube, transforming this sample into a sample of the unit $(s - 1)$ -hypersphere, and transforming this sample (via 1st and 2nd order statistics of $\underline{\mathbf{R}}_{i,j}$) into a sample of the d -Mahalanobis contour of $\underline{\mathbf{R}}_{i,j}$. The MSS algorithm, as well as study of its stochastic convergence properties, are discussed in Chapter 6.

The second part of this contribution examines the problem of finding the minimum Euclidean distance from the origin of a finite-dimensional space to a d -Mahalanobis contour of a non-degenerate normal random vector \underline{X} [$L_d(\underline{X})$]; this problem has applications for

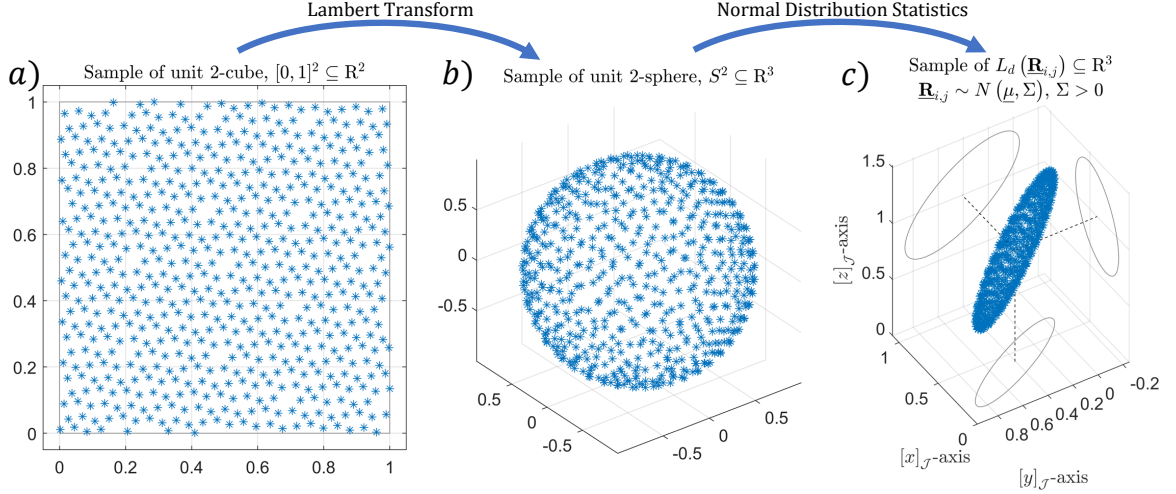


Figure 1.3: Initial steps for generating an MSS sample of relative position random variable $\mathbf{R}_{i,j}$ in \mathbb{R}^3 : a) sample of unit square, b) sample of unit 2-sphere, and c) sample of d -Mahalanobis contour, $L_d(\mathbf{R}_{i,j})$ in \mathbb{R}^3 .

computing certain SFF collision risk indicators whose relationship to instantaneous and joint-time probabilities of collision is consistent with intuition.[27, 28] Chapter 7 of the general, finite-dimensional problem of finding the minimum Euclidean distance to $L_d(\underline{X})$, such as the existence of solutions to this problem, as well as upper and lower bounds to these solutions.

These theoretical results are applied in the context of developing a computational methodology for finding the minimum Euclidean distance from the origin of three-dimensional relative position space to the d -Mahalanobis contour of the relative position $\mathbf{R}_{i,j}$ [$L_d(\mathbf{R}_{i,j})$]; this methodology employs a dimensionality-reducing, area-preserving mapping from the unit square to the unit sphere, and a suitable coordinate transformation, in order to reframe the original problem (a three-dimensional non-convex minimization problem with non-linear constraints) as an unconstrained two-dimensional search over a convex, simply-connected region. This computational methodology is validated for searches which become ill-condition after extended propagation horizons, as shown in Chapter 7.

1.4.3 Spacecraft formation collision risk interpretation and decision-making

Contribution 3: *To develop methodologies for comparison of distance-based and probability-based SFF collision risk indicators, and to characterize properties of proposed indicators which validate their practical use in SFF applications*

With active SFF COLA methods, collision risk is managed through predicting the future motion of agents, determining whether the anticipated collision risk is acceptable, and if it is not, planning and executing COLA-dedicated maneuvers. The existing literature in active SFF COLA can be broadly categorized in terms of which type of collision risk indicator is chosen, whether inter-agent separation (via some function of the stochastic description of the relative position),[48, 49, 50, 51, 52, 26, 53] or probability measures associated with instantaneous or joint-time collision events.[13, 54, 55]

This dichotomy in guidance and control philosophies prompts study of the relationship between separation- and probability-based collision risk indicators, specifically, to understand whether insights on collision risk that may be inferred from each indicator type are mutually consistent in view of the corresponding physical interpretation of each indicator. First, the collision correlation index, which is an unbiased, normalized inner product between two signals, and which can be interpreted as a coefficient of linear correlation between the two signals, is proposed to compare time histories of the instantaneous probability of collision (IPC) and other separation-based indicators. In terms of the collision correlation index, it has been found that the 99.73% minimum distance, denoted by $\rho_{3\sigma}$, has the most consistent relationship with the IPC over a significant propagation horizon, and over a wide range of relative orbit regimes and spacecraft classes. Specifically, the $\rho_{3\sigma}$ is more likely to indicate a close approach between agents while, at the same time, the IPC indicates increased collision risk, and vice versa.

Therefore, the 99.73% minimum distance, $\rho_{3\sigma}$, can be understood as a joint hard-body radius such that, if the isotropic keep-out zone distance requirement between two agents is

$\rho_{3\sigma}$, the instantaneous probability that such agents are collision in 0.27%. Thus, the 99.73% minimum distance is a collision risk boundary in relative position space with probabilistic interpretation. Figure 1.4 illustrates the distinction between instantaneous collision regions that define the IPC and $\rho_{3\sigma}$. On the one hand, the IPC is found by fixing the joint HBR and solving the direct-IPC problem; that is, computing the probability mass inside the Euclidean ball with radius $l_{i,j}$ centered at the origin of instantaneous relative position space. On the other hand, the $\rho_{3\sigma}$ is obtained by letting the joint HBR vary and solving the inverse-IPC problem; that is, finding the minimum joint HBR whose corresponding direct-problem IPC has a predetermined value (in this case, 0.27%).

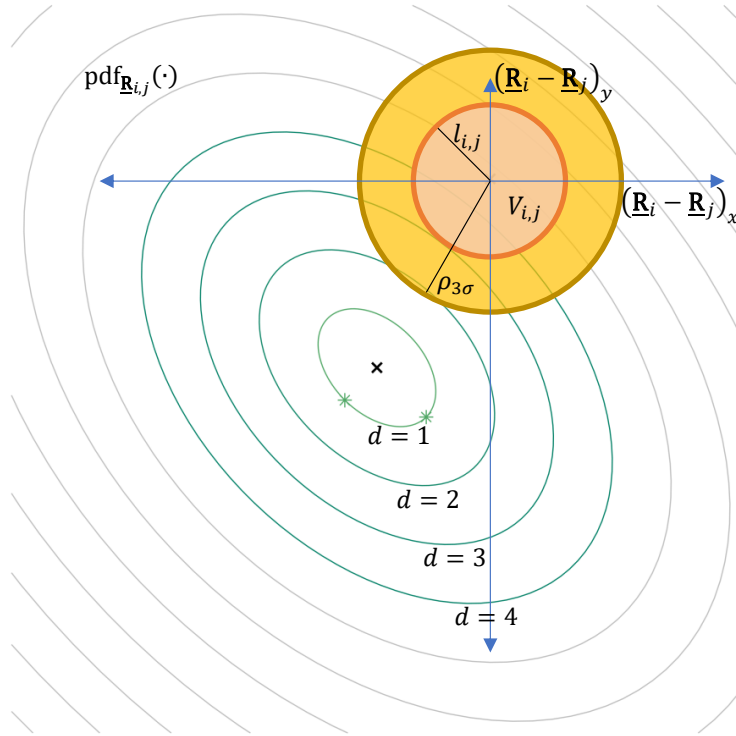


Figure 1.4: Conceptual (Euclidean) direct and inverse IPC computation through integration of relative position pdf for a system with normally distributed (two-dimensional) relative position. Note: for a joint HBR set to $\rho_{3\sigma}$, the corresponding IPC value is 0.27%.

The foregoing interpretation of $\rho_{3\sigma}$ has been validated through a computational investigation that shows, over a wide range of relative orbit regimes, that small changes to the probability value that defines $\rho_{3\sigma}$ (that is, 0.27%) result in correspondingly small changes to $\rho_{3\sigma}$. [33] This result validates the foregoing interpretation of $\rho_{3\sigma}$ in the presence of small

errors in computation or in navigation solutions, which would justify the use of this hybrid collision risk indicator in practical SFF COLRM applications. Figure 1.5 conceptually illustrates an examination of the sensitivity of $\rho_{3\sigma}$ to small changes in the target probability which defines $\rho_{3\sigma}$, i.e., $p_{3\sigma} = 0.27\%$.

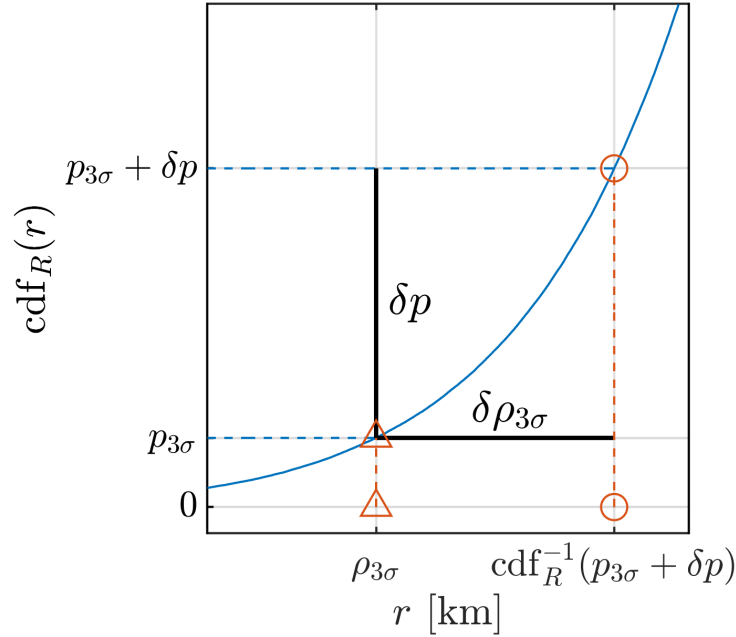


Figure 1.5: Conceptual examination of the sensitivity of $\rho_{3\sigma}$ to small changes in the target probability which defines $\rho_{3\sigma}$, i.e., $p_{3\sigma} = 0.27\%$.

This contribution addresses advances to the field of spacecraft formation collision risk interpretation and decision-making. The first part of this contribution is discussed in Chapter 8, and it comprises a study undertaken to ascertain the extent of internal consistency between conclusions gleaned from probabilistic collision risk indicators when compared to distance-based collision risk indicators. In response to this study, a hybrid collision risk indicator (that is, a distance-based collision risk indicator with probabilistic interpretation) is developed, and it is empirically shown that this hybrid indicator has an appropriate relationship to probabilistic indicators. Consequently, as shown in the second part of this contribution (which is documented in Chapter 9), a sensitivity study of the hybrid indicator is performed in order to verify whether its probabilistic interpretation is plausible.

1.4.4 Cylindrical orthogonal norm-based stochastic collision risk measures in SFF

Contribution 4: *To motivate the development of SFF COLRM frameworks based on the cylindrical orthogonal collision region (COCR), and to show their feasibility by addressing region well-definedness, as well as inequalities and quantitative comparisons between COCR-based stochastic SFF collision risk measures and counterparts in the literature*

The operational aspect of the SFF COLRM process (collision risk quantification, interpretation, and reduction) depends on both the choice and efficient formulation of suitable collision risk indicators.[12] The formulation of collision risk indicators reflects how collision events are defined operationally – in the spaceflight mechanics community, commonly defined as the violation of minimum distance constraint with respect to the Euclidean norm under the HBR assumption.[27, 28, 38, 32, 56, 57]

This contribution motivates the use of new collision regions as alternatives to spherical, three-dimensional (3D) avoidance regions (S3AC) in an SFF COLRM context. In particular, the cylindrical orthogonal collision region (COCR) is constructed as the intersection of three mutually orthogonal 3D cylinders in relative position space, each of which corresponds to a circular collision constraint in a planar, two-dimensional projection of 3D spacecraft relative motion. Hence, the COCR is the 3D region that is avoided when at least one out of three mutually orthogonal planar circular constraints is satisfied at any one time, as illustrated in Fig. 1.6. The COCR construct is advocated for application in an SFF COLRM context because it provides both safety sufficiency and reduced conservatism as compared to other collision regions that approximate spherical, 3D avoidance regions advocated in the literature, such as box collision regions,[39] or infinite cylinders corresponding to the two-dimensional circular avoidance constraints.[27, 28] Additionally, avoiding a COCR may provide computational advantages to spacecraft relative trajectory planning tasks – specifically, by leveraging existing work in the literature regarding planar circular avoidance constraint satisfaction.[58, 53, 59, 60, 61, 62, 63]

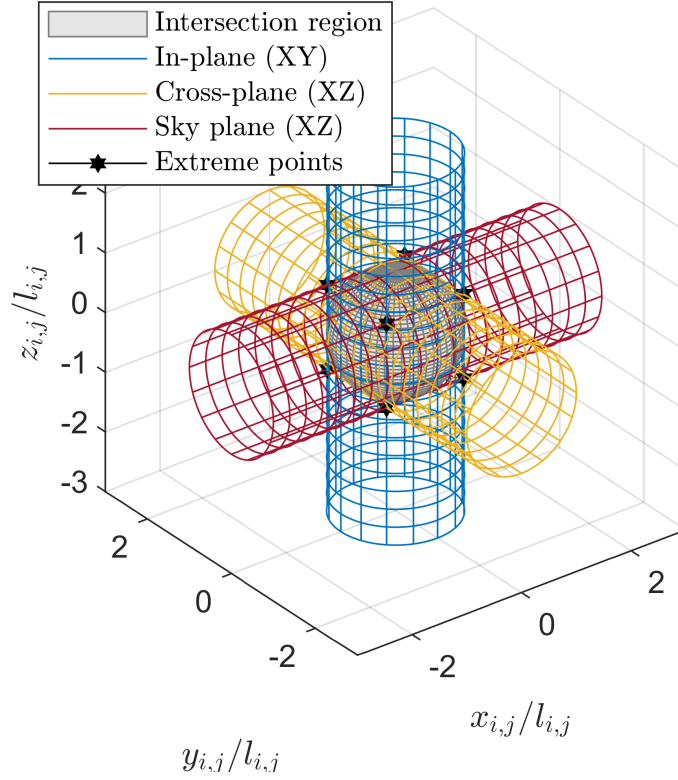


Figure 1.6: Construction of the cylindrical orthogonal collision region (COCR) in three-dimensional relative position space.

The research work pertaining to this contribution motivates implementation of the COCR construct in a SFF COLRM context by showing the feasibility of such an application, specifically, by addressing concerns that arise from the construction of the COCR. First, the COCR is shown to be a well-defined 3D collision region, and the deterministic advantages of employing the COCR over other approximate collision regions are quantified. Second, leveraging the result of well-definedness and computability of stochastic measures of collision risk under certain non-restrictive assumptions on relative dynamics (cf. Chapter 4), it follows that stochastic measures of collision risk whose underlying instantaneous collision conditions in relative position space are based on the COCR are well-defined and computable, in both an instantaneous and a joint-time sense. Third, theoretical inequalities for COCR-based instantaneous and joint-time probabilities of collision are presented in terms of their Euclidean and box-norm, upper and lower bound counterparts. Fourth, these

inequalities are computationally validated through numerical integration and large-sample Monte Carlo simulation in the context of relevant geometric regimes of Clohessy-Wiltshire (CW) relative orbital dynamics. Finally, the extent of the overestimate of stochastic collision risk measures based on the COCR over those based on spherical collision regions is explored computationally.

Since this contribution is concerned with both the definition of new collision risk indicators (specifically, stochastic collision risk measures based on the COCR) and with the relationship between them and other existing collision risk indicators, this contribution may be classified as belonging to both foundational work in SFF COLRM and to SFF collision risk interpretation and decision-making; cf. Section 1.3. This contribution is addressed in Chapter 10.

1.5 Dissertation outline

This dissertation, whose outline is summarized in Table 1.1, is organized as follows.

Contribution 1 comprises advancements in foundational SFF COLRM work, specifically, to ascertain whether the Euclidean norm of an absolutely continuous random vector is also an absolutely continuous random variable (Ch. 3), and to establish whether *a-PC* measures are well-defined and computable (Ch 4).

Contribution 2 addresses SFF collision risk quantification, in particular, to introduce and characterize the stochastic convergence properties of the MSS algorithm (Ch. 6), and to present methodologies for the computation of distance-based collision risk indicators (Ch. 7).

Contribution 3 focuses on SFF collision risk interpretation and decision-making, specifically, to examine the consistency of the correlation relationship between dissimilar (but complementary) types of SFF collision risk indicators (Ch. 8), and to ascertain whether it is appropriate to conceptualize the 99.73% minimum distance ($\rho_{3\sigma}$) indicator as encoding a region in relative position space with a specific interpretation in terms of probabilistic SFF

Table 1.1: Outline of contributions from this investigation to the SFF COLRM literature

SFF COLRM Category	Foundational	Operational	
	Definition/Basic Properties	Quantification	Interpretation/ Decision-Making
Contribution 1.1	Existence of $\ \mathbf{R}\ _2$ pdf (Ch. 3)		
Contribution 1.2	a -JTC measurability/ a -Pc computability (Ch. 4)		
Contribution 2.1		MSS Convergence (Ch. 6)	
Contribution 2.2		Distance-based indicators (Ch. 7)	
Contribution 3.1			Risk Indicator Correlations (Ch. 8)
Contribution 3.2			Sensitivity of $\rho_{3\sigma}$ (Ch. 9)
Contribution 4	COCR-based IPC/Pc well-definedness (Ch. 10)		COCR-based IPC/Pc Inequalities (Ch. 10)

collision risk (Ch. 9).

Finally, Contribution 4 (Ch. 10) represents progress in foundational SFF COLRM work, as well as in SFF collision risk interpretation. First, a new collision region, the COCR, is introduced, and new probabilistic collision risk indicators based on the COCR are shown to be well-defined. Second, inequalities are presented which relate COCR-based collision probability measures to counterparts that are common in the literature; such inequalities are computationally validated.

This dissertation (Ch. 2) also restates the formal definition of SFF collision risk indicators as they are understood in this work, and it outlines concepts in mathematical analysis in order to provide basic background for the unfamiliar reader. Additionally, this dissertation briefly discusses the adequacy of employing probabilistic SFF collision risk indicators

based on stochastic representations of epistemic uncertainty (Ch. 5). Furthermore, this dissertation recapitulates the geometry of closed Clohessy-Wiltshire (CW) relative orbital geometry (Appx. A), as well as the basic properties of the Monte Carlo method (Appx. B). Finally, a methodology for the management of large Monte Carlo samples for SFF collision risk indicator computation and analysis is detailed in Appx. C.

1.6 Intended audience

Therefore, with the exception of SFF collision risk reduction (cf. Fig. 1.1), the contributions and supplementary content laid out in this dissertation (see Section 1.5) constitute a systematic (albeit not comprehensive) treatment of the management of SFF collision risk. This dissertation will be beneficial as a starting point to members of the the spaceflight and astronautics communities who might be interested in a reference work which explores the definition, usability, computation, and interpretation of SFF collision risk indicators, as well as the underlying reasoning for these contributions.

Because of the prevalent nature of SFF collision risk (cf. Section 1.2), this dissertation is thus useful in practical, flight hardware implementations of the SFF concept. Specifically, this dissertation is meant to assist existing or potential SFF practitioners seeking to address questions that are central to the development and execution of any SFF-based space mission concept of operations, such as: is it sensible to employ certain SFF collision risk indicators commonly used in the literature? Is it possible to extract consistent information from dissimilar, yet complementary SFF collision risk indicators? What are some methods to compute such SFF collision risk indicators? Is it advantageous to introduce new ways to conceptualize, quantify, and interpret SFF collision risk? Questions of this nature are relevant to members of the spaceflight communities who might be interested in designing and operating SFF missions, such as: space mission architects, spacecraft systems engineers, space mission operators, command and data handling (CD&H) engineers, flight software (FSW) engineers, trajectory designers, and spacecraft guidance, navigation, and controls

(GN&C) engineers. It is therefore the author's hope that this dissertation will be a valuable resource for its intended audience.

CHAPTER 2

BACKGROUND

This Chapter introduces certain helpful preliminaries to this dissertation. First, the notation utilized in this dissertation is established. Concepts related to mathematical analysis such as norms, measures, and probabilities are expounded. Then, instantaneous collision events are formally, topologically defined. Next, probabilistic risk indicators employed in this dissertation are introduced and discussed. Subsequently, distance-based collision risk indicators examined in this dissertation are listed. Finally, a hybrid collision risk indicator (that is, a distance-based collision risk indicator with probabilistic interpretation) is presented.

2.1 Acronyms

Acronyms employed in this dissertation are listed on page xxxi. The Nomenclature may employ these acronyms without further restating.

2.2 Nomenclature

$A \setminus B$	=	complement of set A relative to set B ; i.e, set of points in A that are not members of set B
$A \subsetneq B$	=	proper subset relationship; i.e., $A \subseteq B$ and $A \neq B$
$[A]^C$	=	complement of A relative to implied reference superset $\Omega \supseteq A$; i.e., $[A]^C = \Omega \setminus A$
A_0, B_0	=	amplitudes of radial and cross-track motion, respectively,

	in closed CW trajectories, km
a_{j_0}, n_{j_0}	= orbit semimajor axis [km] and mean motion [rad/s], respectively, of chief agent j_0
$A_j(\cdot)$	= rotation matrix with rotation angle (\cdot) along j^{th} axis, $j \in \{1, 2, 3\}$
A_{j_1, \dots, j_n}	= composite rotation matrix given by $A_{j_n}(\cdot) \dots A_{j_1}(\cdot)$
$B_{N,k}$	= set of initial conditions $\{\mathbf{x}_{i,j}(t_0)\}$ such that $\mathbf{x}_{i,j}(t) \in C_{i,j}(t; l_{i,j}(t), a), t = h_T(c), c = k/N,$ $k \in \{0, \dots, N\}, N \in \mathbb{N}$
$\mathbb{B}_r^{s a}(\underline{x})$	= open a -norm ball of radius $r \in (0, \infty)$ centered at $\underline{x} \in \mathbb{R}^s$, i.e., the set $\{\underline{y} \in \mathbb{R}^s : \ \underline{x} - \underline{y}\ _a < r\}, s \in \mathbb{N}$
$\mathbb{B}_r^s(\underline{x}), \mathbb{B}_r(\underline{x})$	= $\mathbb{B}_r^{s a}(\underline{x})$ for Euclidean vector norm (i.e., $a = \text{Eu}$, or $a = 2$)
$\overline{\mathbb{B}}_r^{s a}(\underline{x})$	= closed a -norm ball of radius $r \in (0, \infty)$ centered at $\underline{x} \in \mathbb{R}^s$, i.e., the set $\{\underline{y} \in \mathbb{R}^s : \ \underline{x} - \underline{y}\ _a \leq r\}, s \in \mathbb{N}$
$\overline{\mathbb{B}}_r^s(\underline{x}), \overline{\mathbb{B}}_r(\underline{x})$	= $\overline{\mathbb{B}}_r^{s a}(\underline{x})$ for Euclidean vector norm (i.e., $a = \text{Eu}$, or $a = 2$)
$C_b([a_1, a_2])$	= space of continuous, bounded, real-valued functions $f : [a_1, a_2] \rightarrow \mathbb{R}$
cdf_X	= cumulative distribution function (cdf) of univariate, real-valued random variable X
cdf_X^{-1}	= quantile function of univariate, real-valued random variable X ; i.e., generalized inverse function of cdf_X
$C_{i,j}(t; l_{i,j}(t), a)$	= set in \mathbb{R}^{n_x} whose projections onto $\mathbb{R}^{d_{\mathbf{R}}}$ belong to $V_{i,j}(t; l_{i,j}(t), a)$
$C_{i,j}$	= $C_{i,j}(t; l_{i,j}(t), a)$ for $a = \text{Eu}$, time-invariant $l_{i,j}$
$\text{comp}_m\text{-IPC}_{i,j}$	= c.o.-IPC m -comparison index, $m \in \{1, 2, 3, 4\}$
$\text{comp}_m\text{-Pc}_{i,j}$	= c.o.-Pc m -comparison index, $m \in \{1, 2, 3, 4\}$
$\text{comp}_m\text{-vol}_{i,j}$	= COCR m -relative volumetric difference, $m \in \{1, 2, 3, 4\}$

D_{Eu}	= set of spherical coordinates, given by $D_{\text{Eu}} = [0, 2\pi) \times [0, \pi]^{s-2} \times [0, \infty)$
$\text{Cov}(\underline{X})$	= covariance of random variable \underline{X} in \mathbb{R}^s
D_{Eu}^*	= restricted set of spherical coordinates, $D_{\text{Eu}}^* \subsetneq D_{\text{Eu}}$
$\det(\cdot)$	= determinant operator
d_{max}	= cutoff Mahalanobis distance in MSS sample
$d_{\mathbf{R}}$	= dimensionality of deterministic or random position vectors; $d_{\mathbf{R}} \in \{1, 2, 3\}$
$D_{\underline{X}}(\underline{x})$	= Mahalanobis distance of instance $\underline{x} \in \mathbb{R}^s$ of random variable $\underline{X} \in \mathbb{R}^s$
$D_1, G, H, S_1, S_2, S_3, S_4$	= constants related to MSS sample mean and covariance estimators
$D^*(P_n)$	= star discrepancy of set $P_n = \{y_k\}$ in $[0, 1]^s$, $k \in S_n$
$\mathbb{E}[\cdot]$	= expectation operator
$\text{ess sup}_{\underline{x} \in \mathbb{R}^s} f(\underline{x})$	= essential supremum of a measurable function $f : \mathbb{R}^s \rightarrow \mathbb{R}$
f_{Eu}	= mapping (for finite-dimensional vector) from Cartesian to spherical coordinates, $f_{\text{Eu}} : \mathbb{R}^s \rightarrow D_{\text{Eu}}$
f_{Eu}^*	= restriction of Cartesian-to-spherical coordinate mapping f_{Eu} ; i.e., $f_{\text{Eu}}^* : S_{\text{Eu}}^* \rightarrow D_{\text{Eu}}^*$
f_E	= characteristic (or indicator) function of subset E
$F_{t_0}(t, \underline{\mathbf{x}}_0), F_{t, t_0}(\underline{\mathbf{x}}_0)$	= solution (at time t) to dynamic system $\dot{\underline{\mathbf{x}}}(\tau) = f(\tau, \underline{\mathbf{x}}(\tau))$, $t_0 \leq \tau \leq t$, for $\underline{\mathbf{x}}(t_0) = \underline{\mathbf{x}}_0$
g_{Eu}	= mapping (for finite-dimensional vector) from spherical to Cartesian coordinates, $g_{\text{Eu}} : D_{\text{Eu}} \rightarrow \mathbb{R}^s$
g_{Eu}^*	= restriction of spherical-to-Cartesian coordinate mapping g_{Eu} ; i.e., $g_{\text{Eu}}^* : D_{\text{Eu}}^* \rightarrow S_{\text{Eu}}^*$
g_P	= function that projects points in $\mathbb{R}^{n_{\mathbf{X}}}$ onto points in $\mathbb{R}^{d_{\mathbf{R}}}$

$h_{\mathbf{R}}$	=	cdf of Euclidean norm of position random variable \mathbf{R} ; i.e., $h_{\mathbf{R}} = \text{cdf}_R, R = \ \mathbf{R}\ _2$
$\widehat{h}_{\mathbf{R},N}$	=	Monte Carlo (MC) estimator of $h_{\mathbf{R}}$ based on MC sample size N
h_T	=	linear mapping from $[0, 1]$ to $[t_0, t_f]$
H_{Eu}	=	set complement of S_{Eu}^* ; i.e., $H_{\text{Eu}} = \mathbb{R}^s \setminus S_{\text{Eu}}^*$
I_f	=	integral of function f over $[0, 1]^s$
$\inf(\cdot)$	=	infimum operator
$\text{IPC}_{i,j}(t; l_{i,j}(t), a)$	=	instantaneous probability of a -norm collision between agents i and j at time t
$\text{IPC}_{i,j}(t)$	=	$\text{IPC}_{i,j}(t; l_{i,j}(t), a)$ for $a = \text{Eu}$, time-invariant $l_{i,j}$
$\text{IPC}_{i,j}^{\widetilde{W}}(t)$	=	$\text{IPC}_{i,j}(t)$ computed on the \widetilde{W} -projection plane at time t
$\text{IPC}_{i,j}\text{-ratio}_m(t)$	=	c.o.-IPC difference (relative to m -bound) at time t , $m \in \{1, 2, 3, 4\}$
\mathbb{I}_s	=	identity matrix in $\mathbb{R}^{s \times s}$
\mathbf{J}_s	=	Jacobian matrix (in $\mathbb{R}^{s \times s}$) of spherical-to-Cartesian mapping $g_{\text{Eu}} : D_{\text{Eu}} \rightarrow \mathbb{R}^s$
J_s	=	Jacobian of spherical-to-Cartesian mapping g_{Eu} ; i.e., determinant of \mathbf{J}_s
$\text{JTC}_{i,j}([t_0, t_f]; l_{i,j}(\cdot), a)$	=	joint-time i - j a -norm collision event, $t \in [t_0, t_f]$
$\text{JTC}_{i,j}[t_0, t_f]$	=	$\text{JTC}_{i,j}([t_0, t_f]; l_{i,j}(\cdot), a)$ for $a = \text{Eu}$, time-invariant $l_{i,j}$
$\text{JTC}_{i,j}^N([t_0, t_f]; l_{i,j}(\cdot), a)$	=	N -timestep discretization of $\text{JTC}_{i,j}([t_0, t_f]; l_{i,j}(\cdot), a)$, $N \in \mathbb{N}$
$\text{JTC}_{i,j}^N[t_0, t_f]$	=	$\text{JTC}_{i,j}^N([t_0, t_f]; l_{i,j}(\cdot), a)$ for $a = \text{Eu}$, time-invariant $l_{i,j}$
$L_d(\underline{X})$	=	d -Mahalanobis contour of non-degenerate normal random variable $\underline{X} \in \mathbb{R}^s$
l_i	=	characteristic length, or hard-body radius (HBR), of agent

	i, m	
$l_{i,j}$		= i - j joint HBR, i.e., $l_{i,j} \doteq l_i + l_j, m$
$\mathcal{L}(\mathbb{R}^s)$		= set of Lebesgue-measurable subsets of \mathbb{R}^s
$\mathcal{L}^1(\mathbb{R}^s)$		= set of Lebesgue-integrable, measurable real-valued functions $g : \mathbb{R}^s \rightarrow \mathbb{R}$
$\mathcal{L}^\infty(\mathbb{R}^s)$		= set of essentially bounded, measurable real-valued functions $g : \mathbb{R}^s \rightarrow \mathbb{R}$
$\text{mod}(a, n)$		= modulus of a after division by n
$\mathcal{N}(\underline{\mu}, \Sigma)$		= normal distribution with mean $\underline{\mu} \in \mathbb{R}^s$ and covariance matrix $\Sigma \in \mathbb{R}^{s \times s}, \Sigma > 0$
N_{rep}		= number of times a finite random sample is repeated
N_{samples}		= total number of points in MSS sample
N_{sh}		= number of shells in MSS sample
N_{ss}		= number of sample points per shell in MSS sample
$p(\cdot), \mathbb{P}(\cdot)$		= probability of event (\cdot)
p_{comp}		= lower limit on probabilistic collision risk indicators for relative change averaging
$Pc_{i,j}([t_0, t_f]; l_{i,j}(\cdot), a)$		= joint-time probability of i - j a -norm collision event, $t \in [t_0, t_f]$
$Pc_{i,j}[t_0, t_f]$		= $Pc_{i,j}([t_0, t_f]; l_{i,j}(\cdot), a)$ for $a = \text{Eu}$, time-invariant $l_{i,j}$
$Pc_{i,j}^N([t_0, t_f]; l_{i,j}(\cdot), a)$		= N -timestep discretization of $Pc_{i,j}([t_0, t_f]; l_{i,j}(\cdot), a)$, $N \in \mathbb{N}$
$Pc_{i,j}^N[t_0, t_f]$		= $Pc_{i,j}^N([t_0, t_f]; l_{i,j}(\cdot), a)$ for $a = \text{Eu}$, time-invariant $l_{i,j}$
$Pc_{i,j}\text{-ratio}_m(t)$		= c.o.- Pc difference (relative to m -bound) at time t , $m \in \{1, 2, 3, 4\}$
pdf_X		= probability density function (pdf) of absolutely continuous random variable X

p_{exc}	=	probability of points precluded from MSS sample
pmf_X	=	probability mass function (pmf) of discrete random variable X
$P_{\text{req}}, P_{\text{threshold}}$	=	significance threshold for probabilistic collision risk indicators
$p_X(\cdot)$	=	probability measure associated with random vector \underline{X} in probability space (Ω', Σ', p_X) ; i.e., $p_X(E) = p(\underline{X} \in E)$ for event $E \in \Sigma'$
$p_{3\sigma}$	=	constant with value $1 - \text{cdf}_{\chi_1^2}(3^2) \approx 1 - 0.9973 = 0.0027$
$\underline{\mathbf{R}}$	=	position random variable in $\mathbb{R}^{d_{\mathbf{R}}}$, $d_{\mathbf{R}} \in \{1, 2, 3\}$, km
$[\underline{\mathbf{R}}]_{\mathcal{J}}$	=	expression of $\underline{\mathbf{R}} \in \mathbb{R}^{d_{\mathbf{R}}}$ in the coordinates of a reference frame \mathcal{J}
$[\underline{\mathbf{R}}]_H$	=	$[\underline{\mathbf{R}}]_{\mathcal{J}}$ for the Hill reference frame (H)
$\dot{\underline{\mathbf{R}}}(t)$	=	time-rate of instantaneous position random variable at time t , $\underline{\mathbf{R}}(t)$ (in $\mathbb{R}^{d_{\mathbf{R}}}$), km/s
$\tilde{\underline{\mathbf{R}}}$	=	planar projection in \mathbb{R}^2 of position random variable $\underline{\mathbf{R}}$ in \mathbb{R}^3 , km
\mathbb{Q}	=	field of real, rational numbers
$\mathbb{R}^{s \times m}$	=	set of all $s \times m$ real-valued matrices
R_{fit}^2	=	coefficient of determination of stochastic convergence model fit
$\text{sep}_{i,j}^m$	=	m^{th} alternative separation measure between agents i and j , $m \in \{m_1, m_2, m_3\}$, km
S_{Eu}^*	=	restricted set of Cartesian coordinates, $S_{\text{Eu}}^* \subsetneq \mathbb{R}^s$
S_n	=	set $B = \{1, \dots, n\}$, $n \in \mathbb{N}$
$\mathbb{S}_r^{(s-1) a}(\underline{x})$	=	$(s-1)$ -sphere (with respect to the a -norm) of radius $r \in (0, \infty)$ centered at $\underline{x} \in \mathbb{R}^s$, i.e., the set

	$\{\mathbf{y} \in \mathbb{R}^s : \ \mathbf{x} - \mathbf{y}\ _a = r\}$
$\mathbb{S}^{(s-1)}$	= unit $(s - 1)$ -sphere under the Euclidean norm, i.e., the set $\mathbb{S}_1^{(s-1) \text{Eu}}(\mathbf{0}_{s \times 1}) = \{\mathbf{y} \in \mathbb{R}^s : \ \mathbf{y}\ _2 = 1\}$
$\sup(\cdot)$	= supremum operator
$\text{supp}(f)$	= support of the function f , i.e., subset B of the domain of f where $f(x) \neq 0 \forall x \in B$
$T_{\mathbb{S}^2}$	= Lambert area-preserving mapping between the unit square and the unit 2-sphere; i.e., $T_{\mathbb{S}^2} : [0, 1) \times [0, 1] \rightarrow \mathbb{S}^2$
$\mathbb{U}(A)$	= uniform distribution on A
$u_{\text{MC}}, u_{\text{MSS}}$	= exponential rate of stochastic convergence with Monte Carlo and MSS samples, respectively
$\text{Var}(X)$	= variance of univariate random variable X in \mathbb{R}
$V_d(\underline{X})$	= d -Mahalanobis volume of non-degenerate normal random variable $\underline{X} \in \mathbb{R}^s$
$V_{d_1}^{d_2}(\underline{X})$	= d_1, d_2 -Mahalanobis shell of non-degenerate normal random variable $\underline{X} \in \mathbb{R}^s$
$V_{i,j}(t; l_{i,j}(t), a)$	= i - j a -norm intersection volume in $\mathbb{R}^{d_{\mathbb{R}}}$, i.e., the set $\mathbb{B}_{l_{i,j}(t)}^{d_{\mathbb{R}} a}(\mathbf{0}_{d_{\mathbb{R}} \times 1})$
$V_{i,j}$	= $V_{i,j}(t; l_{i,j}(t), a)$ for $a = \text{Eu}$, time-invariant $l_{i,j}$
$V_{i,j}^{\widetilde{W}}$	= i - j \widetilde{W} -projection collision disk in \mathbb{R}^2 , i.e., the set $\mathbb{B}_{l_{i,j}}^{2 \text{Eu}}(\mathbf{0}_{2 \times 1})$
$V_{i,j}^W$	= i - j \widetilde{W} -projection collision cylinder in \mathbb{R}^3
W_l	= collective weight of MSS sample points in l^{th} shell
$w_{l,q}$	= weight of q^{th} MSS sample point in l^{th} shell
\bar{X}	= expected (or “mean”) value of random variable \underline{X} in \mathbb{R}^s , i.e., $\bar{X} \doteq \mathbb{E}[\underline{X}]$
\mathbf{X}	= dynamic state random variable in $\mathbb{R}^{n_{\mathbf{X}}}$, $n_{\mathbf{X}} \in \mathbb{N}$

y_{off}	= steady-state offset of along-track motion in closed CW trajectories, km
α_0, β_0	= phases of radial and cross-track motion, respectively, in closed CW trajectories, rad
$\Gamma(x)$	= complete gamma function evaluated at $x > 0$
$\Gamma_{i,j}$	= i - j collision correlation index over the $[t_0, t_0 + T]$ time interval
$\lambda(\cdot)$	= Lebesgue measure in \mathbb{R}^s
$\underline{\mu}_X$	= expected (or “mean”) value of random variable \underline{X} in \mathbb{R}^s
$\widehat{\underline{\mu}}_{\text{MSS}}, \widehat{\underline{\Sigma}}_{\text{MSS}}, \widehat{p}_{E,\text{MSS}}$	= MSS estimators of sample mean, covariance, and probability measure of subset E
$\Xi_{\mathcal{J}_2, \mathcal{J}_1}$	= coordinate transformation matrix in $\mathbb{R}^{3 \times 3}$ from frame \mathcal{J}_1 to frame \mathcal{J}_2
$\rho_{3\sigma}$	= 99.73% minimum distance, km
$\underline{\Sigma}_X$	= covariance matrix of random variable \underline{X} in \mathbb{R}^s
$\Upsilon(l N, k)$	= l^{th} combination of $\binom{N+1}{k+1}$
χ_s^2	= chi-square distribution with $s \in \mathbb{N}$ degrees of freedom
(Ω', Σ', ν)	= measure space with reference set Ω' , sigma-algebra Σ' on Ω' , and measure ν on Σ'
$\mathbf{0}_{s \times 1}, \mathbf{0}_{s \times m}$	= zero-valued vector (in \mathbb{R}^s) and matrix (in $\mathbb{R}^{s \times m}$), respectively
$\lceil \cdot \rceil$	= ceiling (or round-up) operator
$\lfloor \cdot \rfloor$	= floor (or round-down) operator
$\lceil \cdot \rceil$	= rounding operator
$\widehat{(\cdot)}$	= sample estimate of random variable (\cdot)
$\widetilde{(\cdot)}$	= countable counterpart of uncountable a -norm collision set (or probability based on this countable counterpart)

$\bar{(\cdot)}$	=	expected (or “mean”) value of random variable (\cdot)
$\overline{(\cdot)}$	=	closed counterpart of open a -norm collision set (or probability based on this closed counterpart)
$\langle \cdot, \cdot \rangle$	=	\mathcal{L}^2 -inner product operator of real-valued “waveforms”, “signals”, or functions defined on the closed interval $[a, b]$
$\ \cdot\ _2, \ \cdot\ _{Eu}, \ \cdot\ $	=	L^2 vector norm operator in \mathbb{R}^s (also known as Euclidean norm)
$\ \cdot\ _\infty$	=	L^∞ vector norm operator in \mathbb{R}^s , given by $\max\{ x_i \}$ for $\underline{x} = [x_1, \dots, x_s]^T$ in \mathbb{R}^s
$\ \cdot\ _a, \ \cdot\ _b$	=	Generic vector norm operator in \mathbb{R}^s (denoted as the a - or b -norm, respectively)
$\ \cdot\ _{co}$	=	Cylindrical orthogonal (c.o.) vector norm operator in \mathbb{R}^3
$\ \cdot\ _{CW}$	=	Clohesy-Wiltshire vector (CW) norm operator in \mathbb{R}^s
$\ \cdot\ _{\mathcal{L}^1}$	=	\mathcal{L}^1 -norm of Lebesgue-measurable, Lebesgue-integrable, real-valued functions $g : \mathbb{R}^s \rightarrow \mathbb{R}$
$\ \cdot\ _{\mathcal{L}^2}$	=	\mathcal{L}^2 -norm of Lebesgue-measurable, square-Lebesgue-integrable, real-valued “waveforms”, “signals”, or functions defined on the closed interval $[a, b]$
$\ \cdot\ _{\mathcal{L}^\infty}$	=	\mathcal{L}^∞ -norm of Lebesgue-measurable, essentially bounded, real-valued functions $g : \mathbb{R}^s \rightarrow \mathbb{R}$
$\ \cdot\ _F, \ \cdot\ _{CW,F}$	=	Frobenius and Clohesy-Wiltshire (CW) matrix norm operator in $\mathbb{R}^{s \times s}$, respectively
$\ \cdot\ _u$	=	uniform norm (or sup-norm) for functions $f : X \rightarrow \mathbb{R}$ on metric space X

2.3 Notation

Vectors are underlined, while matrices and functions are not. Although boldface is reserved for multidimensional variables (i.e., vectors and matrices), sometimes boldfacing such variables may be avoided for clarity. For mathematical objects $\{\mathcal{A}, \mathcal{B}, \mathcal{C}\}$ and for expressions LHS and RHS, the statement “ $\mathcal{A} \doteq \text{RHS}$ ” denotes that \mathcal{A} is defined via the expression RHS, whereas the statements “LHS $=: \mathcal{B}$ ” and “ $\mathcal{C} := \text{RHS}$ ” indicate that the expressions LHS and RHS are equal to \mathcal{B} and \mathcal{C} (respectively) by definition.

Let $\underline{\mathbf{X}} \in \mathbb{R}^{n_{\mathbf{X}}}$ and $\underline{\mathbf{R}} \in \mathbb{R}^{d_{\mathbf{R}}}$ denote a dynamic state and position state, respectively, where $n_{\mathbf{X}}$ and $d_{\mathbf{R}}$ respectively denote the dimensions of $\underline{\mathbf{X}}$ and $\underline{\mathbf{R}}$. (Note: since object positions may be physically defined in 1, 2, or 3 dimensions, $d_{\mathbf{R}} \in \{1, 2, 3\}$.) Because regions in both relative position and relative state space are addressed in this dissertation, the dimensions of these spaces are denoted explicitly in order to avoid confusion with one another or with generic finite-dimensional, real vector spaces (denoted by \mathbb{R}^s).

When used with the subscript i , $\underline{\mathbf{X}}_i$ and $\underline{\mathbf{R}}_i$ denote the dynamic state and position of agent i , respectively. It is understood that $\underline{\mathbf{R}}_i$ refers to the position of the center of mass of agent i with respect to the origin of some reference frame. When used with a composite subscript such as “ i - j ”, $\underline{\mathbf{X}}_{i,j}$ and $\underline{\mathbf{R}}_{i,j}$ denote the dynamic state and position of agent i relative to agent j , respectively, i.e., $\underline{\mathbf{X}}_{i,j} \doteq \underline{\mathbf{X}}_i - \underline{\mathbf{X}}_j$ and $\underline{\mathbf{R}}_{i,j} \doteq \underline{\mathbf{R}}_i - \underline{\mathbf{R}}_j$.

When written in uppercase, $\underline{\mathbf{X}}$ and $\underline{\mathbf{R}}$ denote an uncertain dynamic state and uncertain position, respectively. The nature of the initial state uncertainty (at time t_0) is epistemic, i.e., it arises from inaccuracies and errors inherent to measurement and estimation. Furthermore, state uncertainty estimates at times $t \geq t_0$ are Bayesian in the sense that they are dependent on the original uncertainty description at time t_0 , with propagation based on the assumption of some dynamic model. Consequently, for any time t , a dynamic state $\underline{\mathbf{X}}(t)$ and position $\underline{\mathbf{R}}(t)$ are interpreted as random variables (RVs) whose probability distributions reflect epistemic uncertainty. Conversely, when written in lowercase, $\underline{\mathbf{x}}$ and $\underline{\mathbf{r}}$ denote

specific, deterministic “instances” or values that $\underline{\mathbf{X}}$ and $\underline{\mathbf{R}}$ may take on, respectively. The variables $\underline{\mu}$ and $\underline{\Sigma}$ are used to denote the expected value (or “mean”) and covariance of a random variable, e.g., for $\underline{\mathbf{X}}$,

$$\underline{\mu}_{\mathbf{X}} = \mathbb{E} [\underline{\mathbf{X}}] \quad (2.1)$$

$$\underline{\Sigma}_{\mathbf{X}} = \text{Cov} (\underline{\mathbf{X}}) = \mathbb{E} \left[(\underline{\mathbf{X}} - \mathbb{E} [\underline{\mathbf{X}}]) (\underline{\mathbf{X}} - \mathbb{E} [\underline{\mathbf{X}}])^T \right] \quad (2.2)$$

When referring to a square matrix in $\mathbb{R}^{s \times s}$, the notation “ > 0 ” implies that such is a symmetric, positive definite matrix.[64]

Let ψ_1, ψ_2, ψ_3 denote real numbers representing angles. Then, the direction cosine matrices (DCMs; or coordinate transformation matrices) denoted by $A_1(\psi_1)$, $A_2(\psi_2)$, and $A_3(\psi_3)$ are given as follows, in accordance with the notation of Markley and Crassidis:[65]

$$A_1(\psi_1) = \begin{bmatrix} 1 & 0 & 0 \\ 0 & \cos(\psi_1) & \sin(\psi_1) \\ 0 & -\sin(\psi_1) & \cos(\psi_1) \end{bmatrix} \quad (2.3)$$

$$A_2(\psi_2) = \begin{bmatrix} \cos(\psi_2) & 0 & -\sin(\psi_2) \\ 0 & 1 & 0 \\ \sin(\psi_2) & 0 & \cos(\psi_2) \end{bmatrix} \quad (2.4)$$

$$A_3(\psi_3) = \begin{bmatrix} \cos(\psi_3) & \sin(\psi_3) & 0 \\ -\sin(\psi_3) & \cos(\psi_3) & 0 \\ 0 & 0 & 1 \end{bmatrix} \quad (2.5)$$

Coordinate transformation matrices are orthonormal matrices; for further background on orthogonal or orthonormal matrices, see Refs. [64, 65].

When inside a square bracket and with a subscript outside of such bracket, $[\underline{\mathbf{R}}]_{\mathcal{J}} \in \mathbb{R}^{d_{\mathbf{R}}}$ denotes that $\underline{\mathbf{R}} \in \mathbb{R}^{d_{\mathbf{R}}}$ is expressed in the coordinates of a reference frame \mathcal{J} ; similarly,

$[b]_{\mathcal{J}} \in \mathbb{R}$ denotes the b^{th} component of $\underline{\mathbf{R}}$ in the \mathcal{J} -frame ($b \in \{x, y, z\}$). When $\underline{\mathbf{R}} \in \mathbb{R}^3$ can be expressed in the coordinates of a W -frame as

$$[\underline{\mathbf{R}}]_W^T = \begin{bmatrix} [x]_W & [y]_W & [z]_W \end{bmatrix} \quad (2.6)$$

and when overlaid by a tilde symbol, $[\tilde{\underline{\mathbf{R}}}]_{\tilde{W}} \in \mathbb{R}^2$ denotes the projection of $\underline{\mathbf{R}}$ onto the \tilde{W} -projection plane (or simply \tilde{W}), where \tilde{W} denotes the $[x]_W$ - $[z]_W$ plane frame. Thus, $[\tilde{\underline{\mathbf{R}}}]_{\tilde{W}}$ is related to $[\underline{\mathbf{R}}]_W$ through the mapping $[\tilde{\underline{\mathbf{R}}}]_{\tilde{W}} = \mathbf{M}_p[\underline{\mathbf{R}}]_W$, where

$$\mathbf{M}_p \doteq \begin{bmatrix} 1 & 0 & 0 \\ 0 & 0 & 1 \end{bmatrix} \quad (2.7)$$

For example, given a coordinate frame \mathcal{J} , if the \tilde{W} -projection plane of interest is the $[y]_{\mathcal{J}}$ - $[z]_{\mathcal{J}}$ plane, then one possibility for the coordinate transformation matrix (also known as a direction cosine matrix, or DCM) from frame \mathcal{J} to the projection frame W , $\Xi_{W,\mathcal{J}}$, is given by

$$\Xi_{W,\mathcal{J}} \doteq \begin{bmatrix} 0 & 1 & 0 \\ -1 & 0 & 0 \\ 0 & 0 & 1 \end{bmatrix} \quad (2.8)$$

In the context of a measure space (Ω', Σ', ν) , where Ω' denotes a reference set (for a probability measure, Ω' is referred to as an “outcome” or “sample” space), Σ' is a sigma-algebra in Ω' , and $\nu : \Sigma' \rightarrow [0, \infty]$ is a measure,[34] the statement “ ν is defined in Σ' ” means that the sets for which ν has defined values belong to the sigma-algebra Σ' , as reflected in the definition $\nu : \Sigma' \rightarrow [0, \infty]$. In this dissertation, only measure spaces of the kind $(\mathbb{R}^s, \mathcal{L}(\mathbb{R}^s), \nu)$ will be considered, where $\mathcal{L}(\mathbb{R}^s)$ is the set of Lebesgue-measurable subsets of \mathbb{R}^s . [34] Note: probability spaces (or probability measure spaces) are measure spaces.

This dissertation employs heavily the concepts of direct and inverse images of sets

under functions. Consider a function $g : A \rightarrow B$, and the sets $A_1 \subseteq A$ and $B_1 \subseteq B$. Then, the direct image of A_1 under g , denoted by $g(A_1) \subseteq B$, is the set of all values of $g(\underline{x})$ for which $\underline{x} \in A_1$. Similarly, the inverse image (or pre-image) of B_1 , denoted by $g^{-1}(B_1) \subseteq A$, is the set of all points \underline{x} such that $g(\underline{x}) \in B_1$. Explicitly,[34]

$$g(A_1) = \{g(\underline{x}) : \underline{x} \in A_1\} \quad (2.9)$$

$$g^{-1}(B_1) = \{\underline{x} \in A : g(\underline{x}) \in B_1\} \quad (2.10)$$

In any space, a set is open if and only if it can be expressed as a union of open balls; the topology of a space is the set of all open subsets in such space.[34] In this dissertation, the underlying topology of \mathbb{R}^s is assumed to be based on the Euclidean norm, $\|\cdot\|_2$; that is, the statement “ $A \in \mathbb{R}^s$ is an open set” implicitly means that A is open with respect to the $\|\cdot\|_2$ norm in \mathbb{R}^s . [66] Additionally, vector norms ($\|\cdot\|$) refer to the Euclidean norm ($\|\cdot\|_2$) unless indicated otherwise. For two vector norms $\|\cdot\|_a$ and $\|\cdot\|_b$ in \mathbb{R}^s to be equivalent means that there exist real-valued, scalar constants $0 < C_1 \leq C_2 < \infty$ such that, for every $\underline{x} \in \mathbb{R}^s$, [66]

$$C_1 \|\underline{x}\|_a \leq \|\underline{x}\|_b \leq C_2 \|\underline{x}\|_a \quad (2.11)$$

In the context of the probability space $(\mathbb{R}^s, \mathcal{L}(\mathbb{R}^s), \mathbb{P})$, for the probability measure $\mathbb{P} : \mathcal{L}(\mathbb{R}^s) \rightarrow [0, 1]$ to be “absolutely continuous” may be characterized by the existence of a function pdf : $\mathbb{R}^s \rightarrow [0, \infty)$ [defined almost everywhere (a.e.) in \mathbb{R}^s] such that for every $A \in \mathcal{L}(\mathbb{R}^s)$, $\mathbb{P}(A)$ may be computed in terms of the Lebesgue integral, as given by

$$\mathbb{P}(A) = \int_{\underline{\mathbf{x}} \in A} \text{pdf}(\underline{\mathbf{x}}) d\underline{\mathbf{x}} \quad (2.12)$$

It is assumed that $\underline{\mathbf{X}}(t)$ and $\underline{\mathbf{R}}(t)$ are absolutely continuous for any time t ; that is, probability measures of $\underline{\mathbf{X}}(t)$ and $\underline{\mathbf{R}}(t)$ are zero-valued on sets of zero measure in their respective sample spaces.[67] Consequently, probability density functions (pdfs) for $\underline{\mathbf{X}}(t)$ and $\underline{\mathbf{R}}(t)$

exist almost everywhere (a.e.) in their respective sample spaces, and probability measures on $\underline{\mathbf{X}}(t)$ and $\underline{\mathbf{R}}(t)$ can be computed as integrals of their pdfs.[35]

Given $\underline{\mu} \in \mathbb{R}^s$, $\underline{\Sigma} \in \mathbb{R}^{s \times s}$, $\underline{\Sigma} > 0$, the notation $\underline{X} \sim \mathcal{N}(\underline{\mu}, \underline{\Sigma})$ entails that \underline{X} is a non-degenerate, normal RV, and that, for \underline{x} in \mathbb{R}^s , it follows that pdf $f_{\underline{X}}(\underline{x})$ is given by

$$f_{\underline{X}}(\underline{x}) = [(2\pi)^s \det \underline{\Sigma}]^{-1/2} \exp\left(-\frac{1}{2} D_{\underline{X}}^2(\underline{x})\right) \quad (2.13)$$

where the Mahalanobis distance of \underline{x} (with respect to \underline{X}), denoted by $D_{\underline{X}}(\underline{x})$, is defined as[68]

$$D_{\underline{X}}(\underline{x}) \doteq \sqrt{(\underline{x} - \underline{\mu})^T \underline{\Sigma}^{-1} (\underline{x} - \underline{\mu})} \quad (2.14)$$

For $d \in (0, \infty)$, the d -Mahalanobis contour and volume of \underline{X} , denoted by $L_d(\underline{X})$ and $V_d(\underline{X})$, are defined as the sets

$$L_d(\underline{X}) \doteq \{\underline{x} \in \mathbb{R}^s : D_{\underline{X}}(\underline{x}) = d\} \quad (2.15)$$

$$V_d(\underline{X}) \doteq \{\underline{x} \in \mathbb{R}^s : D_{\underline{X}}(\underline{x}) \leq d\} \quad (2.16)$$

Clearly, $L_d(\underline{X})$ is the boundary of $V_d(\underline{X})$. A known analytical result is that[46]

$$p(\underline{X} \in V_d(\underline{X})) = \text{cdf}_{\chi_s^2}(d^2) \quad (2.17)$$

Consider the constant $p_{3\sigma} \doteq 1 - \text{cdf}_{\chi_1^2}(3^2) \approx 1 - 0.9973 = 0.0027$. Via Eq. 2.17, for $X \sim \mathcal{N}(\mu, \sigma^2)$ for some μ in \mathbb{R} and $\sigma > 0$, $p_{3\sigma}$ coincides with the probability that X takes on a value that is further than 3σ away from the mean μ .

2.4 Definition of collision events

2.4.1 Phenomenological notion of collision events

A collision between two agents is defined to occur whenever their respective physical, nonempty volumes in $d_{\mathbf{R}}$ -dimensional space have a nonempty intersection, i.e., in a collision event, two agents may occupy portions of the same volume of space at the same time. The notion of a hard-body radius (HBR; or characteristic length) is used to simplify the definition of collision events, and consequently, the computation of probabilistic collision risk indicators.

Definition 1 (s -ball and $(s - 1)$ -sphere [69, 34]). Let $r > 0$. The ball (with respect to the a -norm in \mathbb{R}^s) of radius r , centered at $\underline{x} \in \mathbb{R}^s$, denoted by $\mathbb{B}_r^{s|a}(\underline{x})$, is defined as the set

$$\mathbb{B}_r^{s|a}(\underline{x}) \doteq \{\underline{y} \in \mathbb{R}^s : \|\underline{x} - \underline{y}\|_a < r\} \quad (2.18)$$

The closed ball (with respect to the a -norm in \mathbb{R}^s) of radius r , centered at $\underline{x} \in \mathbb{R}^s$, denoted by $\overline{\mathbb{B}}_r^{s|a}(\underline{x})$, is defined as the set

$$\overline{\mathbb{B}}_r^{s|a}(\underline{x}) \doteq \{\underline{y} \in \mathbb{R}^s : \|\underline{x} - \underline{y}\|_a \leq r\} \quad (2.19)$$

The sphere (with respect to the a -norm) of radius r , centered at $\underline{x} \in \mathbb{R}^s$, denoted by $\mathbb{S}_r^{(s-1)|a}(\underline{x})$, is defined as the set

$$\mathbb{S}_r^{(s-1)|a}(\underline{x}) \doteq \{\underline{y} \in \mathbb{R}^s : \|\underline{x} - \underline{y}\|_a = r\} \quad (2.20)$$

Note: for the L^2 and L^∞ vector norms, a is denoted as “Eu” and “ ∞ ”, respectively. \diamond

Notation 2 (Characteristic length). Let the “body of agent i ”, B_i , be defined as the set

$$B_i \doteq \{\underline{x} \in \mathbb{R}^{d_{\mathbf{R}}} : \underline{x} \text{ is in the body of agent } i\} \quad (2.21)$$

Then, the i^{th} characteristic length, $l_i \in (0, \infty)$, is defined as

$$l_i \doteq \sup_{\underline{x} \in B_i} \|\underline{x} - \underline{\mathbf{r}}_i\|_2 \quad (2.22)$$

Note: the body of agent i is circumscribed within $\mathbb{B}_{l_i}^{d_{\mathbf{R}}|\text{Eu}}(\underline{\mathbf{r}}_i)$, i.e., $B_i \subseteq \mathbb{B}_{l_i}^{d_{\mathbf{R}}|\text{Eu}}(\underline{\mathbf{r}}_i)$. \diamond

Definition 3 (HBR simplification). The body of agent i , B_i , satisfies $B_i = \mathbb{B}_{l_i}^{d_{\mathbf{R}}|\text{Eu}}(\underline{\mathbf{r}}_i)$ by assumption.

Note: The (HBR) simplification is illustrated in Figure 2.1. \diamond

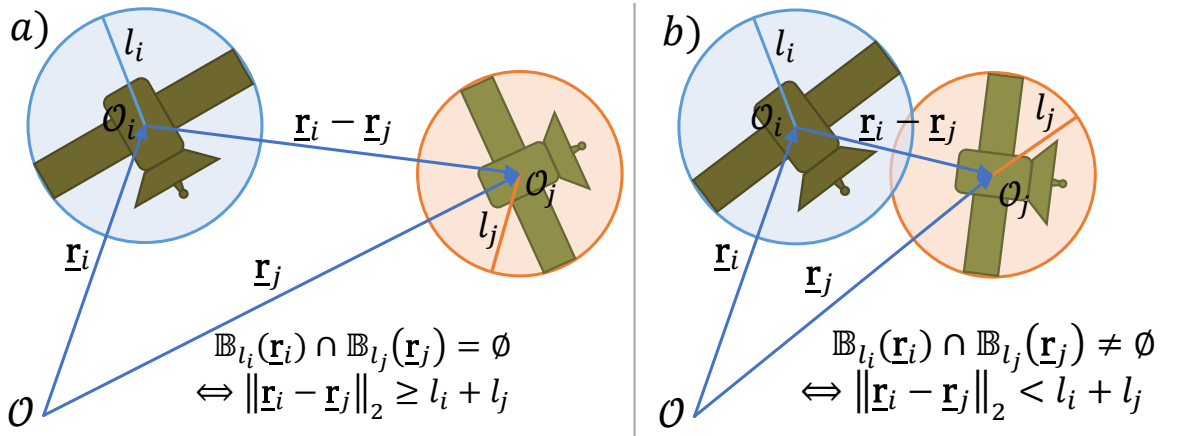


Figure 2.1: Agents under the HBR simplification: a) not colliding, and b) colliding. Note: these circles represent Euclidean balls in $\mathbb{R}^{d_{\mathbf{R}}}$ that circumscribe agent bodies, not position pdf's.

Let i and j refer to two agents in proximity. Through the HBR simplification, l_i encodes a no-contact zone for agent i . Specifically, agent i does not collide with any other agent j ($i \neq j$) if no point belonging to the body of agent j becomes closer to the i^{th} center of mass than an isotropic distance l_i . Thus, in order to avoid a collision with agent i , it is sufficient for agent j to be at least an isotropic distance l_i away from agent i , and vice versa. Using this insight, the i - j collision event is now formally defined in terms of the Euclidean norm.

Definition 4 (Collision event). Assume the HBR simplification holds (see Definition 3).

Then, a collision event between agents i and j occurs when there is a nonempty intersection

between the “volumes spanned” by agent i [$\mathbb{B}_{l_i}^{d_{\mathbf{R}}|\text{Eu}}(\mathbf{r}_i)$] and agent j [$\mathbb{B}_{l_j}^{d_{\mathbf{R}}|\text{Eu}}(\mathbf{r}_j)$], i.e., a collision occurs whenever

$$\mathbb{B}_{l_i}^{d_{\mathbf{R}}|\text{Eu}}(\mathbf{r}_i) \cap \mathbb{B}_{l_j}^{d_{\mathbf{R}}|\text{Eu}}(\mathbf{r}_j) \neq \emptyset \quad \diamond \quad (2.23)$$

Since the Euclidean norm is rotation-invariant for any $d_{\mathbf{R}}$, stating the HBR simplification in terms of the Euclidean norm allows for formulating the defined i - j collision event without regard to relative object geometry (and hence, avoiding a definition of collision events that depends on relative attitude).

A simpler way to infer that a collision is occurring is by observing that, whenever the i^{th} and j^{th} (Euclidean ball-) volumes intersect, the Euclidean, isotropic distance between the respective centers of mass is less than the sum of their respective hard-body radii, as seen in Figure 2.1. This characterization may also be utilized to infer when a collision event might be occurring.

2.4.2 Collision events with respect to arbitrary norms

Let $l_{i,j}$ denote the i - j joint HBR; i.e., $l_{i,j} \doteq l_i + l_j$ (see the Nomenclature). Although collision events in this dissertation are defined with respect to the Euclidean norm in $\mathbb{R}^{d_{\mathbf{R}}}$ (for the reasons aforementioned), there may be operational or computational reasons to employ other norms in $\mathbb{R}^{d_{\mathbf{R}}}$ for this purpose. For example, in [39] (Eq. 13), a collision constraint is violated if $\mathbf{r}_{i,j} = \begin{bmatrix} x_{i,j} & y_{i,j} & z_{i,j} \end{bmatrix}^T$ satisfies

$$|x_{i,j}| < l_{i,j} \bigwedge |y_{i,j}| < l_{i,j} \bigwedge |z_{i,j}| < l_{i,j} \quad (2.24)$$

This condition is equivalent to defining a collision in terms of the L^∞ norm; that is,

$$\text{Eq. 2.24 holds} \quad \iff \quad \|\mathbf{r}_{i,j}\|_\infty < l_{i,j} \quad (2.25)$$

Therefore, this dissertation also considers collision events that are defined with respect to norms in $\mathbb{R}^{d_{\mathbf{R}}}$ other than the Euclidean norm.

Notation 5 (a -norm intersection volumes). For $l_{i,j}(t) > 0$, the i - j intersection volume (under the a -norm in $\mathbb{R}^{d_{\mathbf{R}}}$) at time t , denoted by $V_{i,j}(t; l_{i,j}(t), a)$, is defined as the set

$$V_{i,j}(t; l_{i,j}(t), a) \doteq \mathbb{B}_{l_{i,j}(t)}^{d_{\mathbf{R}}|a}(\mathbf{0}_{d_{\mathbf{R}} \times 1}) = \{\underline{\mathbf{r}} \in \mathbb{R}^{d_{\mathbf{R}}} : \|\underline{\mathbf{r}}\|_a < l_{i,j}(t)\} \quad (2.26)$$

where $\mathbf{0}_{s \times 1}$ denotes the zero-valued vector in \mathbb{R}^s . Note: for any a -norm in $\mathbb{R}^{d_{\mathbf{R}}}$, any of its open balls is an open set in $\mathbb{R}^{d_{\mathbf{R}}}$. [66] Therefore, $V_{i,j}(t; l_{i,j}(t), a)$ is an open set; hence, it is a measurable subset of $\mathbb{R}^{d_{\mathbf{R}}}$. \diamond

In other words, $V_{i,j}(t; l_{i,j}(t), a)$ is the open ball (with respect to the a -norm in $\mathbb{R}^{d_{\mathbf{R}}}$) centered at the origin of relative position space (i.e., at $\mathbf{0}_{d_{\mathbf{R}} \times 1}$) with radius equal to the joint-HBR $l_{i,j}(t)$.

Proposition 6 (a -norm collision condition equivalencies). Let $\underline{\mathbf{r}}_i, \underline{\mathbf{r}}_j \in \mathbb{R}^{d_{\mathbf{R}}}$, and let $l_i(t), l_j(t) > 0$. Let $\|\cdot\|_a$ be a norm in $\mathbb{R}^{d_{\mathbf{R}}}$. Then, the following statements are equivalent:

1. $\mathbb{B}_{l_i(t)}^{d_{\mathbf{R}}|a}(\underline{\mathbf{r}}_i) \cap \mathbb{B}_{l_j(t)}^{d_{\mathbf{R}}|a}(\underline{\mathbf{r}}_j) \neq \emptyset$
2. $\|\underline{\mathbf{r}}_i - \underline{\mathbf{r}}_j\|_a < l_{i,j}(t)$
3. $(\underline{\mathbf{r}}_i - \underline{\mathbf{r}}_j) \in V_{i,j}(t; l_{i,j}(t), a)$

Note: this result holds in \mathbb{R}^s for any $s \in \mathbb{N}$. \diamond

While the intersection of two a -norm balls in absolute position space (which represent the physical extent of two agents) is not itself generally an a -norm ball, Proposition 6 implies that the region in relative position space which represents the instantaneous a -norm collision event is an a -norm ball – specifically, the a -norm ball whose center is the center of mass of either agent, and whose radius is equal to the joint-HBR.

Because all finite-dimensional vector norms are equivalent (in the sense of Eq. 2.11; see [66]), inclusion relationships (among collision events defined via different norms in $\mathbb{R}^{d_{\mathbf{R}}}$) may always be found. For example, since for $\mathbf{r} \in \mathbb{R}^{d_{\mathbf{R}}}$,

$$0 \leq \|\mathbf{r}\|_{\infty} \leq \|\mathbf{r}\|_{\text{Eu}} \leq \sqrt{d_{\mathbf{R}}} \|\mathbf{r}\|_{\infty} < \infty \quad (2.27)$$

which implies that, for $\mathbf{r} \in \mathbb{R}^{d_{\mathbf{R}}}$, $c > 0$,

$$\mathbb{B}_{c/\sqrt{d_{\mathbf{R}}}}^{d_{\mathbf{R}}|\infty}(\mathbf{r}) \subseteq \mathbb{B}_c^{d_{\mathbf{R}}|\text{Eu}}(\mathbf{r}) \subseteq \mathbb{B}_c^{d_{\mathbf{R}}|\infty}(\mathbf{r}) \quad (2.28)$$

it follows that, for $l_{i,j}(t) > 0$,

$$V_{i,j} \left(t; \frac{l_{i,j}(t)}{\sqrt{d_{\mathbf{R}}}}, \infty \right) \subseteq V_{i,j} (t; l_{i,j}(t), \text{Eu}) \subseteq V_{i,j} (t; l_{i,j}(t), \infty) \quad (2.29)$$

The inclusion relationships listed in Eq. 2.29 are illustrated in Figure 2.2 for the \mathbb{R}^3 case (i.e., if $d_{\mathbf{R}} = 3$).

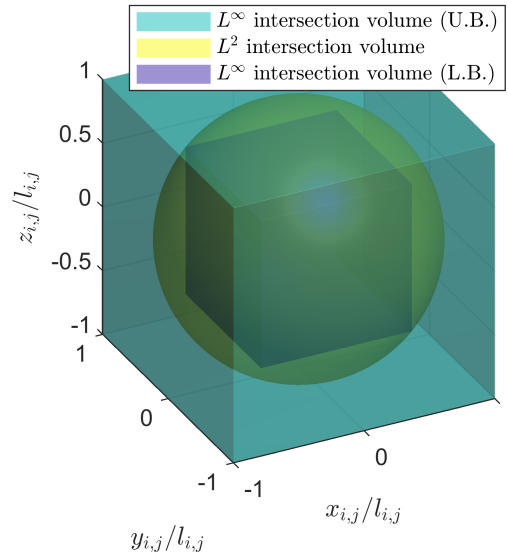


Figure 2.2: Comparison between instantaneous collision regions based on L^2 and L^∞ norms.

2.5 Probabilistic collision risk indicators

Within Subsections 2.4.1 and 2.4.2, collision events have been topologically defined without any notion of the positions of colliding agents being random variables at the time of collision. Thus, if the relative positions of agents are known deterministically, the question of whether or not agents are colliding – in the sense that the conditions in Proposition 6 are met, which may or may not imply a physical collision – can be answered as either true or false, but not both.

However, the primary aim of this dissertation is to examine collision events when the relative position between agents is not deterministically known. In such cases, whether or not an object is colliding at any given time with another object is a question that can only be strictly answered in a probabilistic sense. Thus, inter-agent relative position and relative state vectors are henceforth treated as random variables.

2.5.1 Instantaneous probability of collision (IPC)

Let $g_P : \mathbb{R}^{n_{\mathbf{x}}} \rightarrow \mathbb{R}^{d_{\mathbf{x}}}$ be a function that projects points in relative state space into points in relative position space. Let $C_{i,j}(t; l_{i,j}(t), a)$ denote the set of points in relative state space whose projection onto relative position space lies inside the instantaneous i - j a -norm intersection volume, $V_{i,j}(t; l_{i,j}(t), a)$. Hence, by definition, $C_{i,j}(t; l_{i,j}(t), a)$ is the inverse image of $V_{i,j}(t; l_{i,j}(t), a)$ under g_P ; that is,

$$\begin{aligned} C_{i,j}(t; l_{i,j}(t), a) &\doteq \{\mathbf{x} \in \mathbb{R}^{n_{\mathbf{x}}} : g_P(\mathbf{x}) \in V_{i,j}(t; l_{i,j}(t), a)\} \\ &= g_P^{-1}(V_{i,j}(t; l_{i,j}(t), a)) \quad (2.30) \end{aligned}$$

Without any assumption on the surjectivity of g_P , $C_{i,j}(t; l_{i,j}(t), a)$ would only generally satisfy the condition $g_P(C_{i,j}(t; l_{i,j}(t), a)) \subseteq V_{i,j}(t; l_{i,j}(t), a)$. [66] Therefore, in this dissertation, g_P is assumed to be surjective (that is, g_P is an onto function), which implies that

the direct image of $C_{i,j}(t; l_{i,j}(t), a)$ under g_P , denoted by $g_P(C_{i,j}(t; l_{i,j}(t), a))$, satisfies

$$g_P(C_{i,j}(t; l_{i,j}(t), a)) = V_{i,j}(t; l_{i,j}(t), a) \quad (2.31)$$

Additionally, g_P is assumed to be continuous. It should be noted that, since $V_{i,j}(t; l_{i,j}(t), a)$ is an open subset of $\mathbb{R}^{d_{\mathbf{R}}}$ (see Notation 5), continuity of g_P is sufficient for $C_{i,j}(t; l_{i,j}(t), a)$ to be an open subset of $\mathbb{R}^{n_{\mathbf{x}}}$ (with respect to the Euclidean norm; see Section 2.3). Because open sets are measurable,[34] $C_{i,j}(t; l_{i,j}(t), a)$ is a measurable subset of $\mathbb{R}^{n_{\mathbf{x}}}$. For the specific case of a relative orbital dynamic state expressed in Hill-frame coordinates,[5] $g_P : \mathbb{R}^6 \rightarrow \mathbb{R}^3$ is given by

$$g_P(\mathbf{x}) = \begin{bmatrix} \mathbb{I}_3 & \mathbf{0}_{3 \times 3} \end{bmatrix} \mathbf{x} \quad (2.32)$$

for any \mathbf{x} in \mathbb{R}^6 . Note: for this example, g_P is both surjective and continuous.

Although the instantaneous collision set in relative position space $V_{i,j}(t; l_{i,j}(t), a)$ is an open a -norm ball (see Notation 5), and even though the set of relative state points whose projections onto relative position space denote an a -norm collision condition [i.e., $C_{i,j}(t; l_{i,j}(t), a)$] is an open set [specifically, the pre-image (under the continuous function g_P) of an open a -norm ball], the $C_{i,j}(t; l_{i,j}(t), a)$ set is not generally an open ball with respect to any norm in relative state space. Under the assumption of continuity of g_P , it is only known that $C_{i,j}(t; l_{i,j}(t), a)$ is an open set in relative state space, which implies that this set may be expressed as a union of open balls (in particular, with respect to the Euclidean norm in $\mathbb{R}^{n_{\mathbf{x}}}$; cf. Section 2.3).

It must be stressed that, because $V_{i,j}(t; l_{i,j}(t), a)$ and $C_{i,j}(t; l_{i,j}(t), a)$ are subsets of different spaces (i.e., relative position and relative state, respectively), openness of each set is determined with respect to norms defined within the corresponding superset space of each set. This is significant because a -norms in relative position space (upon which instantaneous collision conditions are defined) may or may not have counterparts in relative state space.

Definition 7 (Instantaneous probability of collision under a -norm (a -IPC)). The instantaneous probability of collision between agents i and j at time t (under the a -norm), denoted by $\text{IPC}_{i,j}(t; l_{i,j}(t), a)$, is defined as the probability of the event that agents i and j are colliding at time t (as indicated under the a -norm). Under a -norm collision condition equivalencies (see Proposition 6), $\text{IPC}_{i,j}(t; l_{i,j}(t), a)$ may be expressed as

$$\text{IPC}_{i,j}(t; l_{i,j}(t), a) = p(\underline{\mathbf{R}}_{i,j}(t) \in V_{i,j}(t; l_{i,j}(t), a)) = p(\|\underline{\mathbf{R}}_{i,j}(t)\|_a < l_{i,j}(t)) \quad (2.33)$$

$$\begin{aligned} \text{IPC}_{i,j}(t; l_{i,j}(t), a) &= p(\underline{\mathbf{X}}_{i,j}(t) \in C_{i,j}(t; l_{i,j}(t), a)) \\ &= p(\|g_P(\underline{\mathbf{X}}_{i,j}(t))\|_a < l_{i,j}(t)) \end{aligned} \quad (2.34)$$

If $\underline{\mathbf{R}}_{i,j}(t)$ and $\underline{\mathbf{X}}_{i,j}(t)$ are absolutely continuous random variables, $\text{IPC}_{i,j}(t; l_{i,j}(t), a)$ may be computed as an integral of the pdf of either $\underline{\mathbf{R}}_{i,j}(t)$ or $\underline{\mathbf{X}}_{i,j}(t)$, as given by

$$\text{IPC}_{i,j}(t; l_{i,j}(t), a) = \int_{\underline{\mathbf{r}} \in V_{i,j}(t; l_{i,j}(t), a)} \text{pdf}_{\underline{\mathbf{R}}_{i,j}(t)}(\underline{\mathbf{r}}) d\underline{\mathbf{r}} \quad (2.35)$$

$$\text{IPC}_{i,j}(t; l_{i,j}(t), a) = \int_{\underline{\mathbf{x}} \in C_{i,j}(t; l_{i,j}(t), a)} \text{pdf}_{\underline{\mathbf{X}}_{i,j}(t)}(\underline{\mathbf{x}}) d\underline{\mathbf{x}} \quad (2.36)$$

where $d\underline{\mathbf{r}}$ and $d\underline{\mathbf{x}}$ denote the Lebesgue measure in $\mathbb{R}^{d\underline{\mathbf{r}}}$ and $\mathbb{R}^{n\underline{\mathbf{x}}}$, respectively. \diamond

Relative position-based a -IPC computation (see Eq. 2.35) is illustrated with a two-dimensional example where the relative position is normally distributed, as shown in Figure 3.1, where the d -contours represent contours of constant Mahalanobis distance.[46] Although the collision regions $V_{i,j}$ and $C_{i,j}$ are specified as time-invariant for the current computational test cases, it is helpful to define these regions as time-dependent for the sake of generality of the a -IPC formulation.

2.5.2 Joint-time probability of collision (PC)

Remark 8 (Assumptions on relative dynamics). Let $t_0, t_f \in \mathbb{R}$ such that $t_0 < t_f$. Let $f : [t_0, t_f] \times \mathbb{R}^{n_{\mathbf{x}}} \rightarrow \mathbb{R}^{n_{\mathbf{x}}}$ be the differential equation that defines the relative dynamic system given by

$$\dot{\mathbf{x}}(t) = f(t, \mathbf{x}(t)) \quad (2.37)$$

for $t \in [t_0, t_f]$, $\mathbf{x}(t) \in \mathbb{R}^{n_{\mathbf{x}}}$. For this dynamic system, let solutions for the initial condition $\mathbf{x}(t_0) = \mathbf{x}_0$ exist and be unique for every $\mathbf{x}_0 \in \mathbb{R}^{n_{\mathbf{x}}}$, and let solutions be given by the function $F_{t_0} : [t_0, t_f] \times \mathbb{R}^{n_{\mathbf{x}}} \rightarrow \mathbb{R}^{n_{\mathbf{x}}}$ such that

$$\mathbf{x}(t) = F_{t_0}(t, \mathbf{x}_0) \quad (2.38)$$

for $t \in [t_0, t_f]$, $\mathbf{x}_0 \in \mathbb{R}^{n_{\mathbf{x}}}$. ◇

For deterministic dynamic systems, examples of sufficient conditions for Remark 8 to hold include: 1) f is piecewise continuous in t , and f is Lipschitz in \mathbf{x} ; or 2) f is piecewise continuous in t , and f is locally Lipschitz in \mathbf{x} , and for every initial condition within some compact set W , solutions to the system lie in W . [70] For stochastic dynamic systems, similar sufficient conditions exist, such as f being bounded in t for fixed \mathbf{x} , and f being Lipschitz in \mathbf{x} . [71]

Definition 9 (Joint-time collision set under a -norm (a -JTC)). Let Remark 8 hold. Let the i - j joint HBR be strictly positive during its time-history; i.e., let $l_{i,j} : [t_0, t_f] \rightarrow (0, \infty)$. Fix $t \in [t_0, t_f]$. Let $F_{t,t_0} : \mathbb{R}^{n_{\mathbf{x}}} \rightarrow \mathbb{R}^{n_{\mathbf{x}}}$ be defined as

$$F_{t,t_0}(\mathbf{x}_0) \doteq F_{t_0}(t, \mathbf{x}_0) \quad (2.39)$$

for $\mathbf{x}_0 \in \mathbb{R}^{n_{\mathbf{x}}}$. Then, the joint-time i - j collision set (under the a -norm), denoted by

$\text{JTC}_{i,j}([t_0, t_f]; l_{i,j}(\cdot), a)$, is given by

$$\text{JTC}_{i,j}([t_0, t_f]; l_{i,j}(\cdot), a) = \bigcup_{t \in [t_0, t_f]} [F_{t,t_0}]^{-1} [C_{i,j}(t; l_{i,j}(t), a)] \quad \diamond \quad (2.40)$$

The joint-time a -collision set under the a -norm (a -JTC) may be interpreted as a set of initial conditions such that, after propagation to some time t , their projections onto relative position space lie in the a -collision region at time t . In other words, the a -JTC is a set of initial conditions such that there exists an a -norm collision condition after propagation to some time t in $[t_0, t_f]$. The a -JTC set depends on the joint-HBR time history over the $[t_0, t_f]$ interval, and not just at any specific time t in $[t_0, t_f]$; this is reflected by the notation $l_{i,j}(\cdot)$ in $\text{JTC}_{i,j}([t_0, t_f]; l_{i,j}(\cdot), a)$.

Even though the instantaneous a -norm collision condition encoded in $V_{i,j}(t; l_{i,j}(t), a)$ is based on open a -norm balls (see Notation 5), because the a -JTC set is a union of sets [specifically, pre-images (over the flow function F_{t,t_0}) of pre-images (over the projection function g_P) of the $V_{i,j}(t; l_{i,j}(t), a)$ sets] which are generally not open balls in relative state space, the a -JTC set is generally not an open ball in relative state space. Because the $\text{JTC}_{i,j}([t_0, t_f]; l_{i,j}(\cdot), a)$ set is defined via an uncountable union of sets, it is unclear whether the $\text{JTC}_{i,j}([t_0, t_f]; l_{i,j}(\cdot), a)$ set is measurable, even if each individual $(F_{t,t_0})^{-1}(C_{i,j}(t; l_{i,j}(t), a))$ set is measurable.

Figure 2.3 illustrates the a -JTC set for the case of a relative state pdf with compact support (i.e., which is zero-valued outside a compact set) for the case of two discrete timesteps without regard for the times in between. In this example, the a -JTC set can be conceptually understood as those regions of the initial relative state pdf (on the left) that indicate collision at either timestep.

Definition 10 (Probability of a -norm collision (a -Pc)). Let Remark 8 hold. Let $l_{i,j} : [t_0, t_f] \rightarrow (0, \infty)$. Assume that $\text{JTC}_{i,j}([t_0, t_f]; l_{i,j}(\cdot), a)$ (see Definition 9) is a measurable subset of $\mathbb{R}^{n_{\mathbf{x}}}$. Then, the $[t_0, t_f]$ -probability of a -norm collision between agents i and

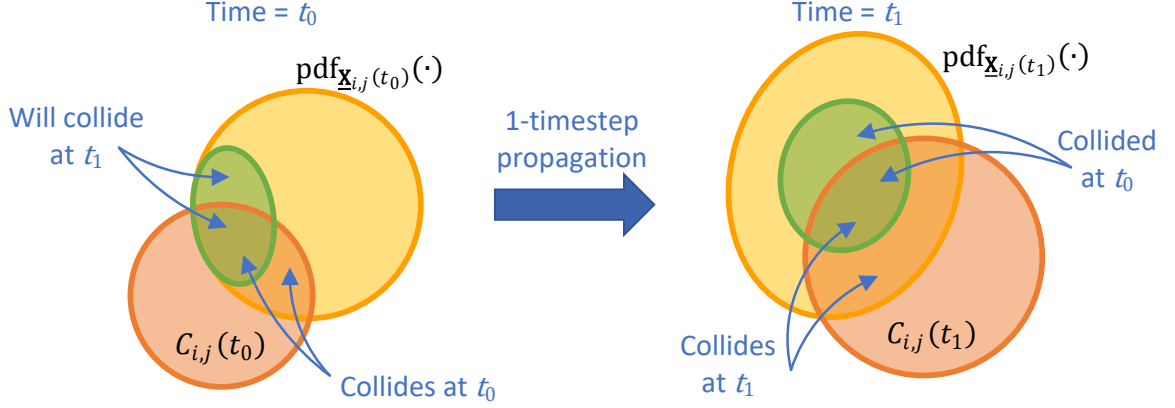


Figure 2.3: Evolution of instantaneous collision sets (in relative state space) for the case of two timesteps, focusing on whether collision at one timestep indicates collision at another timestep. Note: the a -JTC set is the region in relative state space at time t_0 (left) which indicates collision at time t_0 (bright orange region) and at time t_1 (green region).

j , denoted by $P_{C_{i,j}}([t_0, t_f]; l_{i,j}(\cdot), a)$, is defined as the probability of the event that agents i and j collide (as indicated under the a -norm in $\mathbb{R}^{d_{\mathbf{R}}}$) at any time t in $[t_0, t_f]$. Under a -norm collision condition equivalencies (see Proposition 6), $P_{C_{i,j}}([t_0, t_f]; l_{i,j}(\cdot), a)$ may be expressed as

$$P_{C_{i,j}}([t_0, t_f]; l_{i,j}(\cdot), a) = p(\underline{\mathbf{X}}_{i,j}(t_0) \in \text{JTC}_{i,j}([t_0, t_f]; l_{i,j}(\cdot), a)) \quad (2.41)$$

If $\underline{\mathbf{X}}_{i,j}(t_0)$ is an absolutely continuous random variable, $P_{C_{i,j}}([t_0, t_f]; l_{i,j}(\cdot), a)$ may be computed as an integral of the pdf of $\underline{\mathbf{X}}_{i,j}(t_0)$, as given by

$$P_{C_{i,j}}([t_0, t_f]; l_{i,j}(\cdot), a) = \int_{\underline{\mathbf{x}} \in \text{JTC}_{i,j}([t_0, t_f]; l_{i,j}(\cdot), a)} \text{pdf}_{\underline{\mathbf{X}}_{i,j}(t_0)}(\underline{\mathbf{x}}) d\underline{\mathbf{x}} \quad \diamond \quad (2.42)$$

Unlike the a -IPC, which can be computed solely in terms of regions in relative position space, the a -PC may only be defined in terms of regions in relative state space. This holds even though the instantaneous a -norm collision condition is a criterion based only on instantaneous relative position information. In general, an a -norm collision event at one timestep may or may not indicate an a -norm collision at a future timestep, as this propaga-

tion depends not only on the specific region of relative state space that defines the a -norm collision event, but also on the relative dynamic process f and the timestep length. Similarly to the a -JTC set, the a - Pc depends on the joint-HBR time history over the $[t_0, t_f]$ interval, and not just at any specific time t in $[t_0, t_f]$; this is reflected by the notation $l_{i,j}(\cdot)$ in $Pc_{i,j}([t_0, t_f]; l_{i,j}(\cdot), a)$.

2.5.3 A note on the probability dilution of probabilistic collision risk indicators

The question of whether it is adequate to employ probabilistic collision risk indicators that are based on stochastic distributions which reflect an epistemic representation of uncertainty has been previously addressed in the literature. A discussion of this topic is undertaken in Chapter 5, including remarks on the probability dilution phenomenon displayed by the probability of collision between spacecraft in a relative orbital dynamic context.[72]

2.6 Distance-based collision risk indicators

2.6.1 Expected value of relative position

The expected value is one of the most basic statistical parameters in the characterization of probability distributions. In particular, one of the goals of spacecraft state estimation is to estimate the expected value of the spacecraft dynamic state, as well as the dispersion about the expected value, assuming certain dynamic propagation and noise models. Hence, it is natural to account for expected relative position information when ascertaining whether the collision condition in relative position space (see Proposition 6) has been violated. Figure 2.4, for a two-dimensional example where the relative position is normally distributed, illustrates the use of the Euclidean norm of relative position in ascertaining collision safety.

For an extended discussion on the expected values of general random variables, the reader is encouraged to consult Ref. [73], Appendix A.

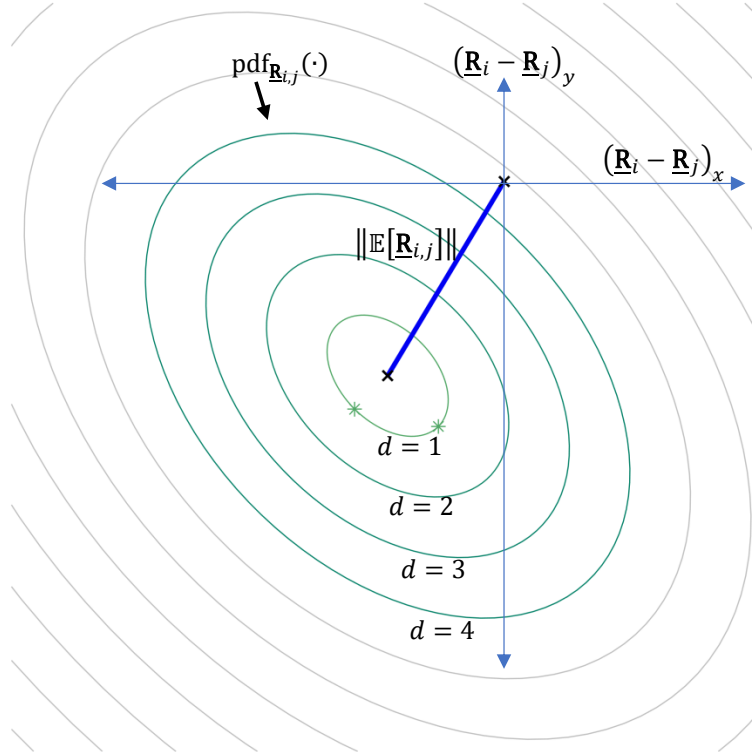


Figure 2.4: Conceptual illustration of expected value of relative position for a system with normally distributed (two-dimensional) relative position.

2.6.2 Minimum distance to covariance contour

For $X \sim \mathcal{N}(\mu, \sigma^2)$ for some μ in \mathbb{R} and $\sigma > 0$, colloquially, a $3\text{-}\sigma$ set (in this case, the points $\{\mu \pm 3\sigma\}$) is considered a boundary between extreme events and non-extreme events. That is, events between $\mu - 3\sigma$ and $\mu + 3\sigma$ are typically not considered extreme, and events outside of that interval are colloquially considered extreme. In particular, the value of the constant $p_{3\sigma}$, defined as

$$p_{3\sigma} \doteq 1 - \text{cdf}_{\chi_1^2}(3^2) \approx 1 - 0.9973 = 0.0027 \quad (2.43)$$

coincides with the probability that X takes on a value that is further than 3σ away from the mean μ . Ideally, probabilistic collision risk would have low values, in a way that allows for collision events to also be deemed as extreme events. Therefore, it is desirable for any proposed separation indicators to represent extreme events in some sense as well.

Based on analogous extensions of the univariate normal $3-\sigma$ concept to higher dimensions, “miss distance”-like indicators may be devised with the goal of more properly accounting for relative position uncertainty than is achieved by the Euclidean norm of expected relative position, specifically, in ways that have a consistent relationship with probabilistic collision risk indicators.

2.6.2.1 *Minimum distance to a “geometric” $3-\sigma$ contour*

The minimum distance from the origin to a “geometric” $3-\sigma$ contour, which is denoted by $\text{sep}_{\text{geo}|i,j}(t)$, is the Euclidean norm of the point closest to the origin within a covariance contour (of the relative position pdf) at a Mahalanobis distance (MHD) of 3 away from the mean.[46] This contour is a “ $3-\sigma$ ” boundary in the following sense: events that are further than 3 standard deviations away from the mean occur past this boundary away from the mean. Hence, the current separation measure is the smallest distance from the origin to any point on this boundary between extreme and non-extreme events. In this dissertation, the prior relative state statistics are normally distributed, and since CW dynamics are linear, the distribution retains normality over time. Since the relative position pdf is three-dimensional, 97.07% of cases are within $\text{MHD} = 3$ from the mean of the pdf.

2.6.2.2 *Minimum distance to a “equivalent” $3-\sigma$ contour*

The minimum distance from the origin to an “equivalent” $3-\sigma$ contour, which is denoted by $\text{sep}_{\text{eq}|i,j}(t)$, is the Euclidean norm of the point closest to the origin within a covariance contour (of the relative position pdf) at a Mahalanobis distance (MHD) such that 99.73% cases are within the corresponding MHD. Since the relative position pdf is three-dimensional, $\text{MHD} = 3.7625$ in this case. This contour is a “ $3-\sigma$ ” boundary in the following sense: the probability of events occurring past this boundary away from the mean is $p_{3\sigma}$. Therefore, this “miss distance”-like indicator is the shortest distance from the origin to any point on this boundary between extreme and non-extreme events.

The “geometric” and “equivalent” $3\text{-}\sigma$ contours, as well as points in such contours that are closest to the origin, are illustrated in Figure 2.5.

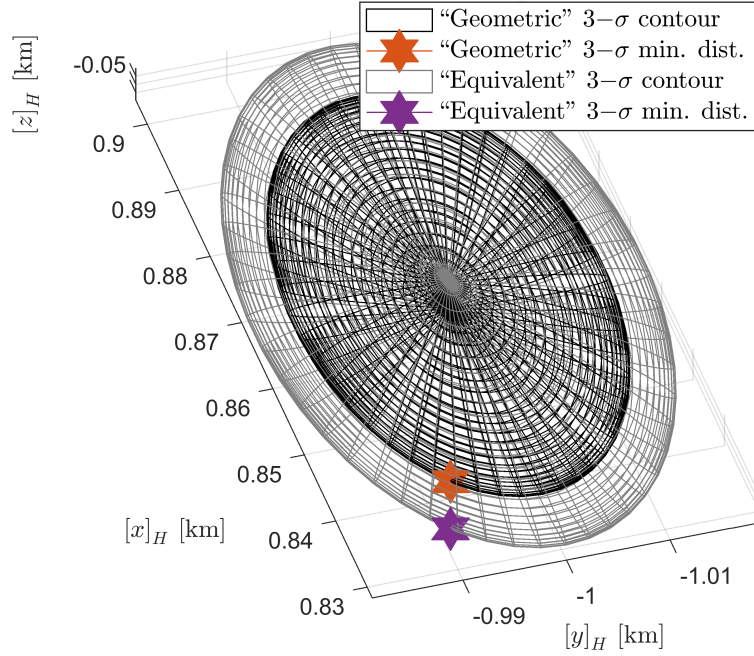


Figure 2.5: Instantaneous relative position pdf, representative Low-Earth Orbit (LEO) relative orbit in Hill frame, covariance contours: “geometric” $3\text{-}\sigma$ and “equivalent” $3\text{-}\sigma$.

2.6.2.3 Formal definition of covariance contours represented by Methodologies 1 and 2

Definition 11 (Methodologies 1 and 2). The measure of separation between agents i and j denoted by Methodologies 1 and 2 (m_1 and m_2 , respectively), $\text{sep}_{i,j}^m$, $m \in \{m_1, m_2\}$, is defined as $\text{sep}_{i,j}^m(t) \doteq \|\underline{\mathbf{r}}_m^*\|_2$, where $\underline{\mathbf{r}}_m^*$ is a solution to the constrained optimization problem (COP)

$$\begin{aligned} \min_{\underline{\mathbf{r}} \in \mathbb{R}^{d_{\mathbf{R}}}} \quad & \underline{\mathbf{r}}^T \underline{\mathbf{r}} \\ \text{s.t.} \quad & \underline{\mathbf{r}} \in L_{d_m}(\underline{\mathbf{R}}_{i,j}(t)) \subseteq \mathbb{R}^{d_{\mathbf{R}}} \end{aligned} \quad (2.44)$$

The MHD of Methodology 1 is $d_{m_1} = 3$, while d_{m_2} satisfies $\text{cdf}_{\chi_3^2}(d_{m_2}^2) = \text{cdf}_{\chi_1^2}(3^2) \approx 99.73\%$. Thus, $d_{m_2} \approx 3.7625$. Note: it can be shown that a solution exists to the COP posed in Eq. 2.44. \diamond

2.7 Hybrid collision risk indicators

2.7.1 99.73% minimum distance

2.7.1.1 99.73% minimum distance ($\rho_{3\sigma}$) – conceptual description

This 99.73% minimum distance, denoted by $\rho_{3\sigma}$, is the effective hard-body radius (HBR) such that the IPC is equal to $\text{IPC}_{i,j}(t) = p_{3\sigma}$. Alternatively, $\rho_{3\sigma}$ can be interpreted as the $p_{3\sigma}$ -percentile in the cumulative distribution function (cdf) of the inter-agent distance, i.e., the cdf of the Euclidean norm of the relative position. Probabilistically, $\rho_{3\sigma}$ coincides with colloquial understanding of a “3- σ ” event. That is, $\rho_{3\sigma}$ is a true 3- σ boundary because 100 $p_{3\sigma}$ % of events have a distance from the origin lower than $\rho_{3\sigma}$, whereas 100(1 - $p_{3\sigma}$)% of events have a distance from the origin higher than $\rho_{3\sigma}$.

The 99.73% minimum distance introduces the concept of the distance cumulative distribution function (cdf), which is induced through the transformation defined by the Euclidean norm of relative position.[67] That is, conceptually, a new cdf is created by taking the Euclidean norm of the relative position of every point in the relative state distribution, and then sorting the values from such set according to the norms found. Because of the point where $\rho_{3\sigma}$ fits in the distance cdf, i.e., a boundary between colloquially extreme and non-extreme cases, $\rho_{3\sigma}$ can be thought of as a “probabilistic” worst case miss distance.

The 99.73% minimum distance measure (i.e., $\rho_{3\sigma}$) is illustrated in Figure 2.6.

2.7.1.2 99.73% minimum distance ($\rho_{3\sigma}$) – formal definition

Definition 12 (Methodology 3). The measure of separation between agents i and j denoted by Methodology 3, $\text{sep}_{i,j}^{m_3}$, is defined as $\text{sep}_{i,j}^{m_3}(t) \doteq \rho_{3\sigma}$, where, for $R \doteq \|\underline{\mathbf{R}}_{i,j}(t)\|_2$ (i.e., for R denoting the Euclidean norm of the relative position),

$$\rho_{3\sigma} \doteq \min \{r \in [0, \infty) : \text{cdf}_R(r) = p_{3\sigma}\} \quad (2.45)$$

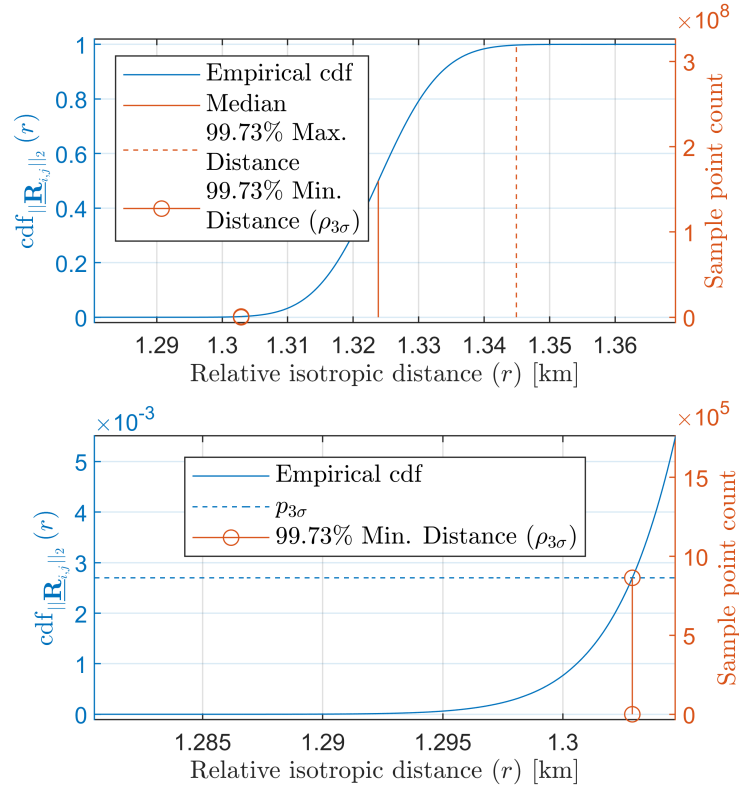


Figure 2.6: Instantaneous cdf of the Euclidean norm of relative position, representative Low-Earth Orbit (LEO) relative orbit: (top) complete cdf; (bottom) closeup of cdf left-tail, focusing on the 99.73% minimum distance ($\rho_{3\sigma}$).

Since $\text{cdf}_R(\cdot)$ is non-decreasing, when $\text{cdf}_R(\cdot)$ is strictly increasing, $\rho_{3\sigma}$ uniquely satisfies $\text{cdf}_R(\rho_{3\sigma}) = p_{3\sigma}$. Note: for a given $l_{i,j}(t)$, it follows that $\text{IPC}_{i,j}(t) = \text{cdf}_R(l_{i,j}(t))$. \diamond

2.8 Computational test cases

Computational test cases in this dissertation are assumed to be subject to Clohessy-Wiltshire (CW) relative orbital dynamics. Appendix A includes an overview of CW dynamics and geometry, as well as a description of the assumed probability distribution of the relative dynamic state for each computational test case.

CHAPTER 3

FOUNDATIONAL WORK IN SPACECRAFT FORMATION COLLISION RISK (PART 1) – EXISTENCE OF PROBABILITY DENSITY FUNCTION (PDF) FOR EUCLIDEAN NORM OF FINITE-DIMENSIONAL RANDOM VECTOR

In the context of an absolutely continuous random vector [that is, a random vector with a probability density function (pdf)], this Chapter shows that the Euclidean norm of such a random vector is also an absolutely continuous random variable. Such a result justifies studying the effects of hard-body radius (HBR) local changes on the Euclidean-norm-based instantaneous probability of collision (IPC), and vice-versa.

3.1 Introduction

Collision risk management is an inherent operational function of spacecraft missions, and it involves collision risk quantification, interpretation and decision-making, and reduction.[29] First, collision risk is quantified through some indicator, either a separation metric or a measure of the likelihood of this adverse event.[27, 28] Second, the outcome of this indicator should inform, via a predetermined rule, whether corrective actions are warranted. Third, if necessary, collision avoidance must achieve the reduction of quantifiable risk to a tolerable level.[13] Thus, the choice and computation of suitable collision risk indicators is a central concern to any space mission concept of operations.

In practice, the relative position between space objects cannot be deterministically known, so examining whether or not an object is colliding at any given time with another object is a question that can only be strictly answered in a probabilistic sense.[42] Hence, within the space flight mechanics community, there has been extensive examina-

tion of probability measures of the distribution of the relative state between two agents to be employed as collision risk quantifiers, with particular focus on two such measures: the P_c , which is the probability of collision over a finite time interval, and the IPC, which is the instantaneous probability of collision.[31, 43, 44] Typically, these measures are examined through the assumption of approximating each object by a ball with radius set to the object's hard-body radius (HBR).[74, 32, 75] This assumption allows defining collision events solely in terms of relative translational states, which simplifies the computation of collision probabilities by avoiding a relative attitude formulation; this would be computationally challenging, and not implementable if object geometry and attitude information were not available.[56]

Both the P_c and IPC are instances of the direct collision probability problem, which, under the HBR assumption, typically entails computing a collision probability measure for a fixed HBR. This is contrasted with the inverse collision probability problem, which entails finding the HBR for which the corresponding collision probability achieves a fixed, predetermined value. This has been studied by Chan for the inverse- P_c HBR problem,[31] and by Núñez Garzón and Lightsey for the inverse-IPC HBR problem.[27, 28]

This Chapter focuses on the direct IPC problem and the inverse-IPC HBR problem; hence, only instantaneous relative position information is needed. Implicitly, these problems treat the Euclidean norm of the relative position (R) as a random variable (RV) in its own right. This is not obvious for the direct IPC problem, as it only involves computing a measure over a ball centered at the origin of relative position space, and thus is well defined.[33] However, it is necessary to treat R as its own RV when studying direct IPC sensitivity, i.e., when examining how changes in HBR affect IPC, or when considering inverse IPC sensitivity, i.e., when observing the effects on HBR from changes in fixed-value IPC.[33]

In both cases, such sensitivities can be formulated in terms of changes to the cumulative distribution function (cdf) of R , which, in the limit of small changes, involve derivatives of

the cdf of R . It would be useful if such a derivative were equal to the probability density function (pdf) of R . However, this would be true if and only if the cdf of R is an absolutely continuous function, i.e., if the derivative of the cdf of R exists almost everywhere (a.e.) and is integrable, and if the cdf of R is equal to the integral of this derivative.[34] Absolute continuity of the cdf of R in this sense, i.e., satisfying the fundamental theorem of calculus, is a stronger condition than continuity, as there exist continuous random variables (i.e., random variables with a continuous cdf) whose cdf is not equal to the integral of its derivative, e.g., the Cantor function, or the devil's staircase.[76] In measure-theoretic terms, the issue is whether R satisfies the following conditions, which are equivalent through the Radon-Nikodym theorem: a) probability measures in R are absolutely continuous (i.e., they are zero-valued in sets of zero measure); and b) there exists a density function (unique a.e.) such that probability measures in R are equal to the integral of this density function.[35]

Hence, the question of whether R is an absolutely continuous random variable (i.e., whether the pdf of R exists) is crucial for spacecraft collision risk management, as the latter presupposes the former. If the instantaneous relative position has a non-degenerate, normal (i.e., Gaussian) distribution, it can be shown that R is the square root of a strictly convex combination of scaled, non-central chi-square random variates;[36] hence, R is absolutely continuous. However, there is a growing body of evidence that points to the general unsuitability of normal pdfs to describe relative state information in space flight mechanics, e.g., for uncertainty propagation, filtering, data association, orbit determination, and the direct collision probability problem.[37, 77, 78, 79, 80, 81, 82] Since these non-normal uncertainty descriptions may depict relative states more accurately, employing them in collision risk management is a natural choice, so the existence of the pdf of R must be guaranteed under these conditions in order to buttress this generalization.

The foregoing discussion of the existence of the pdf of R may also have limited application to P_c -related problems since, under the short-encounter assumptions, a P_c is mathematically equivalent to a two-dimensional IPC computed on a plane normal to the

relative velocity vector at the instant of closest approach between objects.[28] For instance, Alfano performed an HBR-sensitivity analysis for the direct and inverse Pc problems under the short encounter assumptions.[56]

This Chapter proves that, for a finite-dimensional, absolutely continuous random variable, the Euclidean norm of this random vector is also absolutely continuous. This result is shown by identifying a suitable mapping from spherical to Cartesian coordinates, and demonstrating where this mapping is invertible. Then, it can be shown, via the inverse of the mapping at hand, that a finite-dimensional random vector with a pdf is transformed into another finite-dimensional random vector with a pdf, from which the Euclidean norm of the original random vector is obtained through marginalization. By applying this result to a relative position vector with a pdf, the desired conclusion follows.

3.2 Background

This Chapter relies heavily on several concepts from measure and probability theory whose exposition and discussion are beyond the scope of this doctoral dissertation. Some of these topics include the following:

1. The term “measure” refers to the Lebesgue measure in \mathbb{R}^s .
2. Properties that hold almost everywhere (a.e.) refer to properties that apply everywhere in a set, except possibly within a set of measure zero.
3. The term “integral” refers to the Lebesgue integral of Lebesgue-measurable functions.
4. To state that a measure is absolutely continuous with respect to the Lebesgue measure means the following: that the measure at hand is zero-valued on any set of zero measure.
5. For a measure to have a density function with respect to the Lebesgue measure means

the following: that such a measure can be computed as an integral of this density function with respect to the Lebesgue measure, and that such a density function exists and is unique a.e.

6. The following statements are equivalent:

- (a) A measure is absolutely continuous (with respect to the Lebesgue measure).
- (b) A measure has a density function with respect to the Lebesgue measure.

Note: Statement (a) implies statement (b) via properties of Lebesgue integrals, and statement (b) implies statement (a) via the Radon-Nikodym theorem.

7. For a random variable X , the notation “ X is an absolutely continuous random variable” (or, equivalently, “ X is absolutely continuous”) implies that the probability measure associated with X is absolutely continuous with respect to the Lebesgue measure, which itself implies that X has a probability density function (pdf) in the sense of Item 5, i.e., which can be used to compute the probability measure associated with X via integration.

Table 3.1 gives reference suggestions for the reader to become familiar with such topics.

Table 3.1: Reference suggestions for topics in measure and probability theory.

Concept	Reference
Lebesgue measure	[34], Chapter 2
Measurable functions, and a.e. properties	[34], Chapter 3
Lebesgue integral	[34], Chapter 4
Density functions	[35], Chapter 3
Absolute continuity vs. existence of density functions	[35], Chapter 6
Random variables	[35], Chapter 4

3.3 Theory

In this Section, it will be proven that finite-dimensional random vectors with a pdf, when mapped through the Euclidean norm, produce random variables that also have a pdf. This will be accomplished by presenting a continuously differentiable mapping from spherical to Cartesian coordinates in finite dimensions, and by identifying a suitable subset where this mapping is invertible. Then, the inverse of this mapping will be used to produce a representation of the original random vector as another random vector in spherical coordinates. The result is then obtained by extending the definition of the mapped random vector to the entire space of spherical coordinates, and finally, by obtaining the Euclidean norm of the original random vector through marginalization.

3.3.1 Invertibility of mapping from spherical to Cartesian coordinates

Fix $s \in \mathbb{N}$. Let D_{Eu} be the Cartesian product defined by $D_{\text{Eu}} = [0, 2\pi) \times [0, \pi]^{s-2} \times [0, \infty)$.

Consider the mapping $g_{\text{Eu}} : D_{\text{Eu}} \rightarrow \mathbb{R}^s$ given by

$$g_{\text{Eu}}(\underline{w}) = [x_1, \dots, x_s]^T \quad (3.1)$$

for every $\underline{w} \in D_{\text{Eu}}$ such that

$$\underline{w} = [\theta_1, \theta_2, \dots, \theta_{s-1}, r]^T \quad (3.2)$$

where $\theta_1 \in [0, 2\pi)$, $\theta_j \in [0, \pi]$ for $j \in \{2, \dots, s-1\}$ and $r \in [0, \infty)$, such that the components of $g_{\text{Eu}}(\underline{w})$ satisfy

$$\begin{aligned}
x_1 &= r \sin(\theta_1) \sin(\theta_2) \dots \sin(\theta_{s-1}) \\
x_2 &= r \cos(\theta_1) \sin(\theta_2) \dots \sin(\theta_{s-1}) \\
x_3 &= r \cos(\theta_2) \sin(\theta_3) \dots \sin(\theta_{s-1}) \\
&\vdots \\
x_{s-1} &= r \cos(\theta_{s-2}) \sin(\theta_{s-1}) \\
x_s &= r \cos(\theta_{s-1})
\end{aligned} \tag{3.3}$$

Hence, g_{Eu} maps the spherical coordinate representation of points in \mathbb{R}^s to their Cartesian counterparts.[83] Additionally, it should be noted that, given $\underline{x} = g_{\text{Eu}}(\underline{w})$ for $\underline{w} \in D_{\text{Eu}}$, the Euclidean norm of \underline{x} satisfies $\|\underline{x}\|_2 = r = [\mathbf{0}_{1 \times (s-1)}, 1] \underline{w}$.

The determinant $\det(\mathbf{J}_s)$ of the Jacobian matrix of $g_{\text{Eu}}(\mathbf{J}_s)$, or simply the Jacobian of $g_{\text{Eu}}(J_s)$, is given by

$$J_s = \det(\mathbf{J}_s) = \det \left(\frac{\partial g_{\text{Eu}}}{\partial \underline{w}} \right) = (-1)^{s-1} r^{s-1} \prod_{j=2}^{s-1} [\sin(\theta_j)]^{(j-1)} \tag{3.4}$$

for $\underline{w} \in D_{\text{Eu}}$ as parameterized previously.[83] The mapping g_{Eu} from spherical to Cartesian coordinates was chosen because the expression for its Jacobian is concise and will be helpful to make the proof more succinct later on.

It should be noted that g_{Eu} is continuously differentiable in D_{Eu} , since all its partial derivatives exist and are continuous in D_{Eu} (as each is the product of continuous functions). Since $J_s = 0$ when either $r = 0$ or $\theta_j \in \{0, \pi\}$ for $j \in \{2, \dots, s-1\}$, g_{Eu} is not an invertible mapping into \mathbb{R}^s . Lemma 13 presents a set where g_{Eu} is invertible.

Lemma 13 (Restricted invertibility of g_{Eu}). For $\underline{w} \in D_{\text{Eu}}^* \subseteq D_{\text{Eu}}$, let $g_{\text{Eu}}^* : D_{\text{Eu}}^* \rightarrow S_{\text{Eu}}^*$

satisfy

$$g_{\text{Eu}}^*(\underline{w}) = g_{\text{Eu}}(\underline{w}) \quad (3.5)$$

where $D_{\text{Eu}}^* = \Theta_1 \times (\Theta_2)^{s-2} \times (0, \infty)$ and $S_{\text{Eu}}^* = \mathbb{R}^s \setminus H_{\text{Eu}}$, where

$$\Theta_1 = \left(0, \frac{\pi}{2}\right) \cup \left(\frac{\pi}{2}, \pi\right) \cup \left(\pi, \frac{3\pi}{2}\right) \cup \left(\frac{3\pi}{2}, 2\pi\right) \quad (3.6)$$

$$\Theta_2 = \left(0, \frac{\pi}{2}\right) \cup \left(\frac{\pi}{2}, \pi\right) \quad (3.7)$$

$$H_{\text{Eu}} = \{\underline{x} \in \mathbb{R}^s : \exists k \in \{1, \dots, s\} \text{ such that } [\underline{x}]_k = 0\} \quad (3.8)$$

Then, g_{Eu} is invertible, and there exists a function $f_{\text{Eu}}^* : S_{\text{Eu}}^* \rightarrow D_{\text{Eu}}^*$ such that $f_{\text{Eu}}^* = (g_{\text{Eu}}^*)^{-1}$, and which is also an invertible, continuously differentiable mapping. \diamond

Proof. Take $\underline{w} \in D_{\text{Eu}}^*$. Then, $r \neq 0$, $\theta_1 \notin \{0, \frac{\pi}{2}, \pi, \frac{3\pi}{2}\}$, and $\theta_j \notin \{0, \frac{\pi}{2}, \pi\}$ for j in $\{2, \dots, s-1\}$. This implies, for j in $\{1, \dots, s-1\}$, that $\cos(\theta_j), \sin(\theta_j) \neq 0$. Since, for k in $\{1, \dots, s\}$, $[g_{\text{Eu}}(\underline{w})]_k$ is a product of r and $\cos(\theta_j), \sin(\theta_j)$ for j in $\{1, \dots, s-1\}$, it follows that $\underline{x} = g_{\text{Eu}}(\underline{w})$ is a point in \mathbb{R}^s with all non-zero components. That is, $g_{\text{Eu}}(\underline{w}) \in S_{\text{Eu}}^*$, where

$$S_{\text{Eu}}^* = \{\underline{x} \in \mathbb{R}^s : [\underline{x}]_k \neq 0 \text{ for all } k \in \{1, \dots, s\}\} \quad (3.9)$$

Clearly, $S_{\text{Eu}}^* = \mathbb{R}^s \setminus H_{\text{Eu}}$, where

$$H_{\text{Eu}} = \{\underline{x} \in \mathbb{R}^s : \exists k \in \{1, \dots, s\} \text{ such that } [\underline{x}]_k = 0\} \quad (3.10)$$

Therefore, the direct image of D_{Eu}^* under g_{Eu} , $g_{\text{Eu}}(D_{\text{Eu}}^*)$, satisfies $g_{\text{Eu}}(D_{\text{Eu}}^*) \subseteq S_{\text{Eu}}^*$.

Take $\underline{x} \in S_{\text{Eu}}^*$. Then, $[\underline{x}]_k \neq 0$ for all $k \in \{1, \dots, s\}$. Hence,

$$r = \|\underline{x}\|_2 \geq |[\underline{x}]_k| > 0 \quad (3.11)$$

for $k \in \{1, \dots, s\}$, so $r \neq 0$. Consider

$$\frac{[\underline{x}]_1}{r} = \sin(\theta_1) \sin(\theta_2) \dots \sin(\theta_{s-1}) \neq 0 \quad (3.12)$$

Then, $\theta_j \notin \{0, \pi\}$ for j in $\{1, \dots, s-1\}$. Consider

$$\frac{[\underline{x}]_2}{r} = \cos(\theta_1) \sin(\theta_2) \dots \sin(\theta_{s-1}) \neq 0 \quad (3.13)$$

Then, $\theta_1 \notin \{\frac{\pi}{2}, \frac{3\pi}{2}\}$. Consider, for j in $\{3, \dots, s-1\}$,

$$\frac{[\underline{x}]_j}{r} = \cos(\theta_{j-1}) \sin(\theta_j) \dots \sin(\theta_{s-1}) \neq 0 \quad (3.14)$$

Then, $\theta_j \neq \frac{\pi}{2}$ for j in $\{2, \dots, s-2\}$. Finally, consider

$$\frac{[\underline{x}]_s}{r} = \cos(\theta_{s-1}) \neq 0 \quad (3.15)$$

Then, $\theta_{s-1} \neq \frac{\pi}{2}$. It follows that $r \neq 0$, $\theta_1 \notin \{0, \frac{\pi}{2}, \pi, \frac{3\pi}{2}\}$, and $\theta_j \notin \{0, \frac{\pi}{2}, \pi\}$ for j in $\{2, \dots, s-1\}$. Hence, there exists a representation of \underline{x} in g_{Eu} coordinates such that $x = g_{\text{Eu}}(\underline{w})$ for some \underline{w} in D_{Eu}^* . Thus, $\underline{x} \in g_{\text{Eu}}(D_{\text{Eu}}^*)$, which implies that $S_{\text{Eu}}^* \subseteq g_{\text{Eu}}(D_{\text{Eu}}^*)$. It follows that $S_{\text{Eu}}^* = g_{\text{Eu}}(D_{\text{Eu}}^*)$.

The set D_{Eu}^* is open, since it is a Cartesian product of open sets. Additionally, for $\underline{w} \in D_{\text{Eu}}^*$, $J_s \neq 0$, which implies that the Jacobian matrix of g_{Eu} is invertible (via the characterization of invertible matrices) everywhere in D_{Eu}^* . Therefore, via the inverse function theorem, for each $\underline{w} \in D_{\text{Eu}}^*$, there exists an inverse mapping f_{Eu} into an open neighborhood of \underline{w} in D_{Eu}^* , and f_{Eu} is continuously differentiable in this open neighborhood.[84]

Let $f_{\text{Eu}}^* : S_{\text{Eu}}^* \rightarrow D_{\text{Eu}}^*$ denote the restriction of f_{Eu} to the S_{Eu}^* domain. It can be shown that $f_{\text{Eu}}^*(S_{\text{Eu}}^*) = D_{\text{Eu}}^*$. This fact implies that $f_{\text{Eu}}^*(g_{\text{Eu}}^*(D_{\text{Eu}}^*)) = D_{\text{Eu}}^*$, and that $g_{\text{Eu}}^*(f_{\text{Eu}}^*(S_{\text{Eu}}^*)) = S_{\text{Eu}}^*$. Hence, f_{Eu}^* satisfies $f_{\text{Eu}}^* = (g_{\text{Eu}}^*)^{-1}$, i.e., f_{Eu}^* is the inverse of g_{Eu}^* in

its domain. Furthermore, f_{Eu}^* is continuously differentiable. \square

Considering the D_{Eu}^* and S_{Eu}^* sets discussed in Lemma 13, then, Lemma 14 indicates the measure of the relative complements $D_{\text{Eu}} \setminus D_{\text{Eu}}^*$ and $\mathbb{R}^s \setminus S_{\text{Eu}}^*$.

Lemma 14 (Measure outside restricted invertibility of g_{Eu}). Let D_{Eu}^* and S_{Eu}^* be as defined in Lemma 13. Then, $D_{\text{Eu}} \setminus D_{\text{Eu}}^*$ and $\mathbb{R}^s \setminus S_{\text{Eu}}^*$ have zero measure. \diamond

Proof. Take j in $\{1, \dots, s\}$. Take a in \mathbb{R} , and restrict it such that

$$a = \begin{cases} b \in [0, 2\pi) & \text{if } j = 1 \\ b \in [0, \pi] & \text{if } j \in \{2, \dots, s-1\} \\ b \in [0, \infty) & \text{if } j = s \end{cases} \quad (3.16)$$

Let $B_{a,j}$ be defined as

$$B_{a,j} = \left\{ \underline{w} \in D_{\text{Eu}} : [\underline{w}]_j = a \right\} \quad (3.17)$$

Specifically, $B_{0,j}$ is a subset of the proper subspace $\{\underline{w} \in \mathbb{R}^s : [\underline{w}]_j = 0\}$ in \mathbb{R}^s . Any proper subspace in \mathbb{R}^s has zero measure; hence, by monotonicity of measures, $B_{0,j}$ has zero measure as well. Let $\underline{y}_{a,j} \in \mathbb{R}^s$ satisfy

$$[\underline{y}_{a,j}]_k = \begin{cases} a & \text{if } k = j \\ 0 & \text{if } k \neq j \end{cases} \quad (3.18)$$

Then, it is clear that $B_{a,j} = B_{0,j} + \underline{y}_{a,j}$; that is,

$$B_{a,j} = \left\{ \underline{w}' \in D_{\text{Eu}} : [\underline{w}']_j = a \right\} = \left\{ \underline{w}' \in D_{\text{Eu}} : \underline{w}' = \underline{w} + \underline{y}_{a,j}, \underline{w} \in B_{0,j} \right\} = B_{0,j} + \underline{y}_{a,j} \quad (3.19)$$

Since the Lebesgue measure is translation invariant, $B_{a,j}$ has zero measure as well. The set

$D_{\text{Eu}} \setminus D_{\text{Eu}}^*$ can be expressed as

$$D_{\text{Eu}} \setminus D_{\text{Eu}}^* = B_{\frac{3\pi}{2},1} \cup \left[\bigcup_{j=1}^{s-1} (B_{0,j} \cup B_{\frac{\pi}{2},j} \cup B_{\pi,j}) \right] \cup B_{0,s} \quad (3.20)$$

Since $D_{\text{Eu}} \setminus D_{\text{Eu}}^*$ is the finite union of sets of zero measure, $D_{\text{Eu}} \setminus D_{\text{Eu}}^*$ has zero measure as well.

Take j in $\{1, \dots, s\}$. Let A_j be the proper subspace of \mathbb{R}^s defined by

$$A_j = \{\underline{x} \in \mathbb{R}^s : [\underline{x}]_j = 0\} \quad (3.21)$$

Hence, A_j has zero measure. The set $\mathbb{R}^s \setminus S_{\text{Eu}}^*$ can be expressed as

$$\mathbb{R}^s \setminus S_{\text{Eu}}^* = \bigcup_{j=1}^s A_j \quad (3.22)$$

Since $\mathbb{R}^s \setminus S_{\text{Eu}}^*$ is the finite union of sets of zero measure, $\mathbb{R}^s \setminus S_{\text{Eu}}^*$ has zero measure as well. □

3.3.2 Absolute continuity of Euclidean norm of absolutely continuous random vector

Lemma 13 shows the existence, albeit restricted, of a continuously differentiable, invertible mapping from Cartesian to spherical coordinates (namely, f_{Eu}^*). When a random variable with a pdf is mapped through f_{Eu}^* , via the change of variables formula,[35] the invertibility property of f_{Eu}^* guarantees existence of a pdf for the mapped random variable, whose domain can then be extended to include the entire space of spherical coordinates via Lemma 14. Finally, the pdf of the Euclidean norm of the original random vector can be extracted through marginalization.

Proposition 15 (Pdf existence for random vector in spherical coordinates). Let \underline{X} be a random variable in \mathbb{R}^s . Let \underline{Y} be the expression of \underline{X} in spherical coordinates (in the sense of Subsection 3.3.1). Then, the following statements are equivalent:

(a) \underline{X} is absolutely continuous.

(b) \underline{Y} is absolutely continuous. ◇

Proof. (a) \implies (b). Let \underline{X} be an absolutely continuous random variable in \mathbb{R}^s , which implies that $\text{pdf}_{\underline{X}}$ exists a.e. in \mathbb{R}^s . Let \underline{X}^* be a restriction of \underline{X} to $S_{\text{Eu}}^* = \mathbb{R}^s \setminus H_{\text{Eu}}$, where H_{Eu} is as defined in Lemma 13. Since H_{Eu} has zero measure in \mathbb{R}^s , $\text{pdf}_{\underline{X}}$ exists a.e. in S_{Eu}^* as well. Hence, \underline{X}^* is an absolutely continuous random variable in S_{Eu}^* , and $\text{pdf}_{\underline{X}^*} = \text{pdf}_{\underline{X}}$ in S_{Eu}^* .

Let $\underline{Y} = f_{\text{Eu}}^*(\underline{X}^*)$. Via Lemma 13, f_{Eu}^* is invertible; additionally, the Jacobian of its inverse, g_{Eu}^* , never vanishes in D_{Eu}^* , as can be verified through Eq. 3.4. Via the change-of-variables formula,[35] \underline{Y} is an absolutely continuous random variable in S_{Eu}^* , i.e., its pdf exists a.e. in D_{Eu}^* (as defined in Lemma 13), and probability measures on \underline{Y} may be computed as integrals of this pdf. Now, it remains to be seen if the a.e. existence of the pdf of \underline{Y} can be extended to all of D_{Eu} .

However, via Lemma 14, $D_{\text{Eu}} \setminus D_{\text{Eu}}^*$ has zero measure in \mathbb{R}^s . Hence, setting

$$\text{pdf}_{\underline{Y}}(\underline{y}) = 0 \quad \forall \underline{y} \in D_{\text{Eu}} \setminus D_{\text{Eu}}^* \tag{3.23}$$

does not change the a.e. existence of $\text{pdf}_{\underline{Y}}$, nor does it change any measures in \underline{Y} as defined in D_{Eu}^* . Hence, it is concluded that \underline{Y} is an absolutely continuous random variable in D_{Eu} .

(b) \implies (a). Let \underline{Y} be an absolutely continuous random variable in D_{Eu} . The proof is similar to that for (a) \implies (b), while restricting \underline{Y} (as \underline{Y}^*) to be defined in D_{Eu}^* , defining $\underline{X} = g_{\text{Eu}}^*(\underline{Y}^*)$, and extending the definition of \underline{X} from $\mathbb{R}^s \setminus H_{\text{Eu}}$ to all of \mathbb{R}^s , via Lemma 13, Lemma 14, and the change-of-variables formula.[35] □

Although it is likely that Proposition 15 would also hold for other spherical coordinate transformations into \mathbb{R}^s other than g_{Eu} , such a result is not implied by this Chapter.

Corollary 16 (Pdf existence for Euclidean norm of random vector with pdf). Let \underline{X} be an absolutely continuous random variable in \mathbb{R}^s . Define $X \doteq \|\underline{X}\|_2 = (\underline{X}^T \underline{X})^{1/2}$. Then, X is an absolutely continuous random variable as well. \diamond

Proof. Let \underline{X} be an absolutely continuous random variable in \mathbb{R}^s . Let \underline{Y} be the expression of \underline{X} in spherical coordinates (in the sense of Subsection 3.3.1).

Via Proposition 15, \underline{Y} is an absolutely continuous random variable in D_{Eu} . Defining $X = \|\underline{X}\|_2$ and $\underline{\Theta} = [\mathbb{I}_{s-1}, \mathbf{0}_{(s-1) \times 1}] \underline{Y}$, then \underline{Y} may be expressed as $\underline{Y} = [\underline{\Theta}^T, X]^T$. It follows that X is an absolutely continuous random variable in $[0, \infty)$, and its pdf may be obtained through marginalization of $\underline{\Theta}$ from \underline{Y} . \square

3.4 Applications

The focus of this section is on practical implications of the theoretical results presented in the Theory section. First, it is shown that for norms of finite-dimensional, absolutely continuous random variables, their cumulative distribution functions (cdfs) are absolutely continuous functions, i.e., they satisfy the Fundamental Theorem of Calculus for Lebesgue integrals. Second, when applying these results to a random vector that represents the instantaneous relative position between two objects, it follows that the assumption of absolute continuity of the relative position is necessary and sufficient for sensitivity analyses of the instantaneous probability of collision (IPC) to be grounded in a Lebesgue integral-derivative sense.

3.4.1 Properties of cdf of Euclidean norm of absolutely continuous random vector

Let \underline{X} be an absolutely continuous random variable in \mathbb{R}^s . Let X be the Euclidean norm of \underline{X} , and let $p_X : \mathcal{L}([0, \infty)) \rightarrow [0, 1]$ be the probability measure associated with X , where $\mathcal{L}([0, \infty))$ is the set of all measurable subsets of $[0, \infty)$. Then, via Corollary 16, there exists

a function $\text{pdf}_X : [0, \infty) \rightarrow [0, \infty)$ such that, for $A \in \mathcal{L}([0, \infty))$,

$$p_X(A) = \int_A \text{pdf}_X(x) dx \quad (3.24)$$

and where $d\lambda$ denotes the Lebesgue measure in $[0, \infty)$. Then, the cumulative distribution function (cdf) of X , $\text{cdf}_X : \mathbb{R} \rightarrow [0, 1]$, satisfies, for $a \in \mathbb{R}$,

$$\text{cdf}_X(a) = p_X((-\infty, a]) = \int_{-\infty}^a \text{pdf}_X(x) dx \quad (3.25)$$

Since the expression on the right-hand side is a Lebesgue integral, it follows through the Fundamental Theorem of Calculus for Lebesgue integrals that cdf_X is an absolutely continuous function.[34] That is, the derivative of cdf_X exists a.e. and is equal to pdf_X a.e., pdf_X is integrable, and cdf_X is equal to the integral of its derivative.

These observations have the very practical implication that pdf_X may be estimated through differentiation of cdf_X – if such information were available. However, if X is only known to be absolutely continuous and no further information about pdf_X is available, then, only the integrability and a.e. existence of pdf_X can be guaranteed, which is all that can be gleaned from the Fundamental Theorem of Calculus in the Lebesgue integral sense. That is, it cannot be concluded (without further information) that pdf_X is continuous a.e., which is a necessary condition for the Fundamental Theorem of Calculus for Riemann integrals; if this condition is met, then the integral in Eq. 3.25 would be a Riemann integral.

3.4.2 Sensitivity of Euclidean norm of absolutely continuous relative position random vector

Let \mathbf{R} be a random variable in $\mathbb{R}^{d_{\mathbf{R}}}$ that represents the instantaneous relative position between two agents in one-, two- or three-dimensions (i.e., $d_{\mathbf{R}} \in \{1, 2, 3\}$) at some time t . Let $l_{i,j}(t) > 0$ represent the instantaneous joint hard-body radius (HBR), i.e., the minimum separation distance required to avoid a collision between the agents. Then, the instanta-

neous probability of collision (with respect to the Euclidean norm) at time t , $\text{IPC}_{i,j}(t)$, is defined as

$$\begin{aligned} \text{IPC}_{i,j}(t) &= \text{IPC}_{i,j}(t; l_{i,j}(t), \text{Eu}) = p_{\mathbf{R}} \left(\mathbb{B}_{l_{i,j}(t)}^{d_{\mathbf{R}}|\text{Eu}} \left(\mathbf{0}_{d_{\mathbf{R}} \times 1} \right) \right) \\ &= p_{\mathbf{R}} (\{\|\mathbf{R}\|_2 < l_{i,j}(t)\}) \end{aligned} \quad (3.26)$$

Since \mathbf{R} is absolutely continuous, $\text{IPC}_{i,j}(t)$ may be computed as an integral of the pdf of \mathbf{R} , as given by

$$\text{IPC}_{i,j}(t) = \int_{\{\|\mathbf{R}\|_2 < l_{i,j}(t)\}} \text{pdf}_{\mathbf{R}}(\mathbf{r}) \, d\mathbf{r} \quad (3.27)$$

and where $d\mathbf{r}$ indicates the Lebesgue measure in $\mathbb{R}^{d_{\mathbf{R}}}$. Eq. 3.27 is illustrated with two-dimensional example where the relative position is normally distributed, as shown in Figure 3.1, where the d -contours represent contours of constant Mahalanobis distance,[46] where the i, j subscripts are added to emphasize that Figure 3.1 illustrates the relative position between two arbitrary agents i and j , and where $V_{i,j} = V_{i,j}(t; l_{i,j}(t), a)$.

Let R denote the Euclidean norm of \mathbf{R} . Via Corollary 16, R itself has a pdf; hence, $\text{IPC}_{i,j}(t)$ can be computed in terms of the pdf of R as given by

$$\text{IPC}_{i,j}(t) = \int_{\{R < l_{i,j}(t)\}} \text{pdf}_R(r) \, dr = p_R(\{R < l_{i,j}(t)\}) \quad (3.28)$$

Since R is absolutely continuous, the set $\{R = l_{i,j}(t)\}$ (which has zero measure) also has zero probability in R . Hence,

$$\text{IPC}_{i,j}(t) = p_R(\{R \leq l_{i,j}(t)\}) = \text{cdf}_R(l_{i,j}(t)) \quad (3.29)$$

The duality presented by Eqns. 3.28 and 3.29 lays the foundation for sensitivity analyses of $\text{IPC}_{i,j}(t)$. That is, changes to $\text{IPC}_{i,j}(t)$ can be formulated in terms of changes in cdf_R , which in the limit of small changes (i.e., derivatives of cdf_R) can be quantified

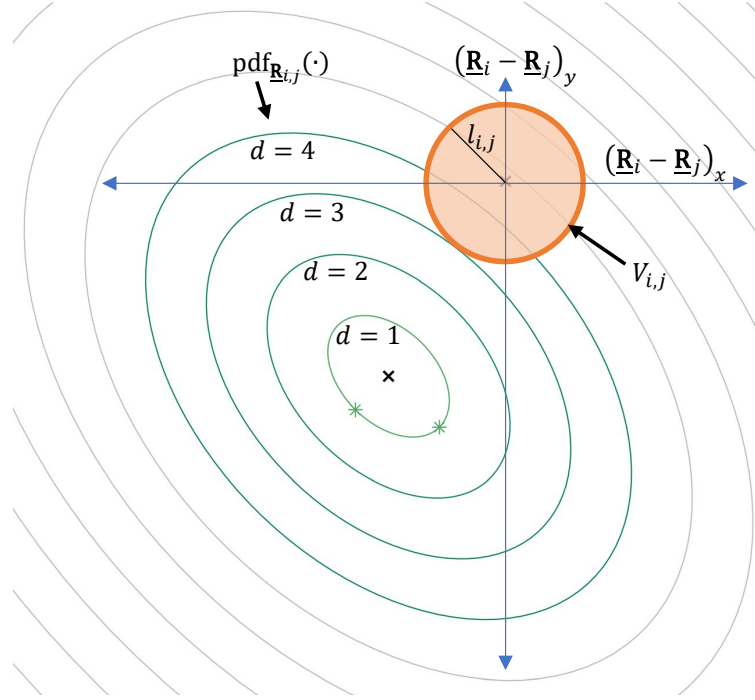


Figure 3.1: Conceptual (Euclidean) IPC computation through integration of relative position pdf for a system with normally distributed (two-dimensional) relative position.

through $\text{pdf}_{\mathbf{R}}$, which exists and is unique a.e., and which is integrable. Therefore, the absolute continuity of \mathbf{R} is a necessary and sufficient condition for sensitivity analyses of the $\text{IPC}_{i,j}(t)$ to be sound in a Lebesgue integral-derivative sense. As discussed in Subsection 3.4.1, more restrictions in $\text{pdf}_{\mathbf{R}}$ are needed in order for the sensitivity analyses to also be sound in a Riemann integral-derivative sense (namely, for $\text{pdf}_{\mathbf{R}}$ to be continuous a.e.).

3.5 Conclusion

In this Chapter, several results regarding finite-dimensional random vectors are presented. First, a random vector in finite-dimensional Cartesian coordinates has a probability density function (pdf) if and only if a certain spherical coordinate representation of the original random vector also has a pdf. Second, by implication, for any random vector in finite-dimensions with a pdf, it follows that the Euclidean norm of such random vector also has a pdf. These results are applied to the problem of computing the instantaneous probability of collision (IPC) between two arbitrary objects. In particular, sensitivity analyses of the

Euclidean norm-based IPC can be formulated in terms of changes to the cumulative distribution function (cdf) of the Euclidean norm of the relative position, which, in the limit of small changes, can be quantified through the pdf of the Euclidean norm of relative position, which is shown to exist and be unique almost everywhere (a.e.; that is, except possibly within a set of zero measure), to be integrable, and to be equal a.e. to the derivative of the cdf of the Euclidean norm of relative position. These findings show that the assumption of absolute continuity of the relative position between objects is a necessary and sufficient condition for sensitivity analyses of the Euclidean norm-based IPC to be meaningful in a Lebesgue integral-derivative sense. However, this Chapter does not present conditions for the pdf of the Euclidean norm of the relative position to be continuous a.e. Hence, this Chapter provides no conditions for sensitivity analyses of the Euclidean norm-based IPC to also be meaningful in a Riemann integral-derivative sense.

CHAPTER 4

FOUNDATIONAL WORK IN SPACECRAFT FORMATION COLLISION RISK (PART 2) – WELL-DEFINEDNESS AND COMPUTABILITY OF JOINT-TIME STOCHASTIC COLLISION RISK MEASURES

Sufficient conditions are established for the measurability of JTC sets and the computability of Pc measures whose underlying instantaneous collision events (in relative position space) are defined through balls with respect to arbitrary norms (specifically, in \mathbb{R}^3). Then, the applicability of these sufficient conditions in a spaceflight mechanics context is discussed. Finally, the extent to which it might be probabilistically equivalent to define collision events via closed or open balls is examined.

4.1 Introduction

General results concerning stochastic collision risk measures (where collision events are defined through balls with respect to some a -norm in $\mathbb{R}^{d_{\mathbb{R}}}$) are presented.

4.2 Measurability of a -JTC sets and computability of a - Pc measures

Let the countable a -JTC set, denoted by $\widetilde{\text{JTC}}_{i,j}([t_0, t_f]; l_{i,j}(\cdot), a)$, be defined as

$$\widetilde{\text{JTC}}_{i,j}([t_0, t_f]; l_{i,j}(\cdot), a) = \bigcup_{c \in \mathbb{Q} \cap [0,1]} [F_{h_T(c), t_0}]^{-1} [C_{i,j}(h_T(c); l_{i,j}(h_T(c)), a)] \quad (4.1)$$

where $F_{t,t_0} : \mathbb{R}^{n_{\mathbb{X}}} \rightarrow \mathbb{R}^{n_{\mathbb{X}}}$ is as defined in Eq. 2.39, and where, for c in $[0, 1]$, $h_T : [0, 1] \rightarrow [t_0, t_f]$ is defined as

$$h_T(c) = t_0 + (t_f - t_0)c \quad (4.2)$$

The countable a -JTC set is defined via the union of initial conditions in relative state space (at time t_0) that meet an a -norm collision condition at any time t in $[t_0, t_f]$ which is linearly mapped from the set of rational numbers between 0 and 1. In other words, every rational fraction between 0 and 1 (of which there only exist countably infinitely many) is mapped via h_T to obtain times t between $[t_0, t_f]$, and the collection of all relative state space initial conditions (at time t_0) that cause a -norm collision conditions at such times t is collected in the countable a -JTC set.

Correspondingly, the countable a - PC measure, denoted by $\tilde{P}_{C_{i,j}}([t_0, t_f]; l_{i,j}(\cdot), a)$, is defined as

$$\tilde{P}_{C_{i,j}}([t_0, t_f]; l_{i,j}(\cdot), a) = p\left(\mathbf{X}_{i,j}(t_0) \in \widetilde{\text{JTC}}_{i,j}([t_0, t_f]; l_{i,j}(\cdot), a)\right) \quad (4.3)$$

Proposition 17 (Measurability of a -JTC). Let Remark 8 hold. Let $l_{i,j} : [t_0, t_f] \rightarrow (0, \infty)$. Let $\|\cdot\|_a$ be any norm in $\mathbb{R}^{d_{\mathbf{R}}}$. Assume the function $F_{t_0}(t, \mathbf{x})$ (see Eq. 2.38) is continuous in t and \mathbf{x} . Then, the $\text{JTC}_{i,j}([t_0, t_f]; l_{i,j}(\cdot), a)$ set (see Definition 9) is an open set (and hence, it is a measurable subset of $\mathbb{R}^{n_{\mathbf{X}}}$). Consequently, the $P_{C_{i,j}}([t_0, t_f]; l_{i,j}(\cdot), a)$ measure is well-defined.

Assume the joint-HBR time history, $l_{i,j} : [t_0, t_f] \rightarrow (0, \infty)$, is continuous. Then, the $\text{JTC}_{i,j}([t_0, t_f]; l_{i,j}(\cdot), a)$ set can be computed as a countable union of sets; specifically, as given by

$$\text{JTC}_{i,j}([t_0, t_f]; l_{i,j}(\cdot), a) = \widetilde{\text{JTC}}_{i,j}([t_0, t_f]; l_{i,j}(\cdot), a) \quad (4.4)$$

Consequently, under these assumptions, the a - PC and the countable a - PC are equivalent; that is,

$$P_{C_{i,j}}([t_0, t_f]; l_{i,j}(\cdot), a) = \tilde{P}_{C_{i,j}}([t_0, t_f]; l_{i,j}(\cdot), a) \quad \diamond \quad (4.5)$$

Proof. See the proof of Proposition 61, which is listed in Chapter E, Section E.1. This Proposition is a consequence of the continuity of $l_{i,j}(\cdot)$ and F_{t,t_0} , of Proposition 17, and of the Lebesgue Dominated Convergence Theorem (DCT) (as applied to integrals with respect

to the abstract measure \mathbb{P}).[85] □

Proposition 17 is a foundational result in the study of joint-time a -norm collision probabilities, from both theoretical and practical standpoints. First, Proposition 17 shows that, under certain assumptions on the relative dynamic process f , that the a -JTC set is measurable, and therefore, a - PC measures are defined. This implies that it is sensible to study the properties of a - PC measures as defined via any a -norm in $\mathbb{R}^{d_{\mathbf{R}}}$ (at the very least under the current assumptions, as well as with any relaxation that may be shown thereafter).

Second, for continuously varying HBR time histories $l_{i,j} : [t_0, t_f] \rightarrow (0, \infty)$, Proposition 17 gives justification for discrete-time approximations to the a -JTC set, specifically, by characterizing the a -JTC set as given by

$$\text{JTC}_{i,j}([t_0, t_f]; l_{i,j}(\cdot), a) = \bigcup_{N \in \mathbb{N}} \text{JTC}_{i,j}^N([t_0, t_f]; l_{i,j}(\cdot), a) \quad (4.6)$$

where the $\text{JTC}_{i,j}^N([t_0, t_f]; l_{i,j}(\cdot), a)$ set is an equal-timestep discretization of the a -JTC set, as given by

$$\text{JTC}_{i,j}^N([t_0, t_f]; l_{i,j}(\cdot), a) = \bigcup_{k=0}^N B_{N,k} \quad (4.7)$$

$$B_{N,k} = [F_{h_T(c), t_0}]^{-1} [C_{i,j}(h_T(c); l_{i,j}(h_T(c))), a] \quad (4.8)$$

for $c = k/N$, $k \in \{0, \dots, N\}$. In other words, under the assumptions of Proposition 17, the a -JTC set is equivalent to the union of every discrete, equal-timestep approximation to the a -JTC set. Even though there may be other characterizations of the a -JTC set besides the one stated in Eq. 4.6, such a characterization implies that the actual a -JTC set may be reproduced by aggregating the successive refinements of an equal-timestep a -JTC set approximation; such approximations arise naturally, e.g., by performing GN&C tasks on a predetermined temporal frequency, as commanded by a flight computer.

Note: the $B_{N,k}$ sets are generally not open balls in initial relative state space (with re-

spect to the Euclidean norm; cf. Section 2.3), even though they are pre-images (over the flow function F_{t,t_0}) of pre-images (over the projection function g_P) of the $V_{i,j}(t; l_{i,j}(t), a)$ sets, which are open balls in relative position space (with respect to the a -norm); cf. Subsubsection 2.5.2. However, under the current assumptions on g_P and F_{t,t_0} , the $B_{N,k}$ sets are open sets in initial relative state space.

In turn, the N -discrete timestep approximation to the a -PC (also known as the finite a -PC), denoted by $Pc_{i,j}^N([t_0, t_f]; l_{i,j}(\cdot), a)$, may be defined as

$$Pc_{i,j}^N([t_0, t_f]; l_{i,j}(\cdot), a) = p(\underline{\mathbf{X}}_{i,j}(t_0) \in \text{JTC}_{i,j}^N([t_0, t_f]; l_{i,j}(\cdot), a)) \quad (4.9)$$

Proposition 18 (Convergence of discrete-timestep a -JTC/ a -PC approximations). Let Remark 8 hold. Let $\|\cdot\|_a$ be any norm in $\mathbb{R}^{d_{\mathbf{x}}}$. Assume the function $F_{t_0}(t, \underline{\mathbf{x}})$ (see Eq. 2.38) is continuous in t and $\underline{\mathbf{x}}$. Assume the joint HBR time history, $l_{i,j} : [t_0, t_f] \rightarrow (0, \infty)$, is continuous. Let A, D_N denote the sets

$$A = \text{JTC}_{i,j}([t_0, t_f]; l_{i,j}(\cdot), a) \quad (4.10)$$

$$D_N = \text{JTC}_{i,j}^N([t_0, t_f]; l_{i,j}(\cdot), a) \quad (4.11)$$

for $N \in \mathbb{N}$. Let \mathbb{P} denote the probability measure associated with $\underline{\mathbf{X}}_{i,j}(t_0)$. Then,

$$\lim_{N \rightarrow \infty} \mathbb{P}(A \setminus D_N) = 0 \quad (4.12)$$

$$\lim_{N \rightarrow \infty} \mathbb{P}(D_N) = \mathbb{P}(A) \quad (4.13)$$

In terms of the current notation, the preceding equations may be expressed as

$$\lim_{N \rightarrow \infty} p(\underline{\mathbf{X}}_{i,j}(t_0) \in [\text{JTC}_{i,j}([t_0, t_f]; l_{i,j}(\cdot), a)] \setminus [\text{JTC}_{i,j}^N([t_0, t_f]; l_{i,j}(\cdot), a)]) = 0 \quad (4.14)$$

$$\lim_{N \rightarrow \infty} Pc_{i,j}^N([t_0, t_f]; l_{i,j}(\cdot), a) = Pc_{i,j}([t_0, t_f]; l_{i,j}(\cdot), a) \quad \diamond \quad (4.15)$$

Proof. See the proof of Proposition 62, which is listed in Chapter E, Section E.2. \square

Discretizations of the a -JTC may be employed to construct discrete-time approximations to the a - Pc that are computable via numerical methods, e.g., direct integration, sampling, or geometric approximations of the a -JTC. This practice is supported by Proposition 18 in two ways. First, via Eq. 4.12, in the limit of vanishingly small timesteps, discrete-time a -JTC set approximations are able to approximate the true a -JTC set arbitrarily well [from the perspective of the probability measure associated with the random variable $\underline{\mathbf{X}}_{i,j}(t_0)$]. Specifically, the complement of the a -JTC set relative to the finite a -JTC approximation set (i.e., the set of points in the a -JTC set that are not also included in the finite a -JTC approximation set) has zero probabilistic size in the limit. Second, via Eq. 4.13, in the limit of vanishingly small timesteps, discrete-time a - Pc approximations are able to approximate real a - Pc values arbitrarily well – and hence, such a - Pc approximations can be considered to be accurate estimators of the real a - Pc for small enough timesteps.

Therefore, Proposition 17 is a crucial result for the interpretation, accuracy, and validity of numerical approaches to a - Pc computation. Proposition 17 is a stronger statement than the analogous result presented in Ref. [38] because in that work, the Pc measures considered have collision events defined only with respect to the Euclidean norm (in $\mathbb{R}^{d_{\mathbf{R}}}$), and because only time-invariant $V_{i,j}$ regions are considered.

4.3 Applicability of a -JTC and a - Pc results in spaceflight mechanics

It has been assumed that $\underline{\mathbf{R}}_{i,j}(t)$ and $\underline{\mathbf{X}}_{i,j}(t)$ have pdfs for $t \in [t_0, t_f]$. Besides the assumption of $\underline{\mathbf{R}}_{i,j}(t_0)$ and $\underline{\mathbf{X}}_{i,j}(t_0)$ having pdfs (which has already been imposed), existence of pdfs for $\underline{\mathbf{R}}_{i,j}(t)$ and $\underline{\mathbf{X}}_{i,j}(t)$ relies on the implicit assumption that $F_{t,t_0} : \mathbb{R}^{n_{\mathbf{x}}} \rightarrow \mathbb{R}^{n_{\mathbf{x}}}$ (known in the literature as the flow function of the dynamic process f , [86] see Remark 8) meets the following criteria: [35]

1. F_{t,t_0} is smooth (i.e., continuously differentiable),

2. F_{t,t_0} is injective (i.e, one-to-one), and
3. F_{t,t_0} has a non-vanishing Jacobian

These assumptions are applicable in several cases of spacecraft relative motion. For example, whenever spacecraft relative dynamics may be modeled as a linear system (e.g., Clohessy-Wiltshire (CW),[5] Tschauner-Hempel (TH),[87] Inhallan et al.,[88] and Gim et al.;[89] for a review of linear models of SFF motion, see [90]), then F_{t,t_0} meets conditions 1, 2, and 3 automatically.

More generally, in the context of a flow function $\phi_t : \mathbb{R}^{n_{\mathbf{x}}} \rightarrow \mathbb{R}^{n_{\mathbf{x}}}$, $t \in [t_0, t_f]$ (with vector field $g : [t_0, t_f] \times \mathbb{R}^{n_{\mathbf{x}}} \rightarrow \mathbb{R}^{n_{\mathbf{x}}}$ which satisfies $\dot{\phi}_t(\mathbf{x}) = g(t, \mathbf{x})$ for $\mathbf{x} \in \mathbb{R}^{n_{\mathbf{x}}}$), if g is differentiable and has locally bounded derivative g' (which implies that g is locally Lipschitz[91]), then the Picard-Lindelöf theorem implies that $\phi_t(\mathbf{x})$ exists and is unique.[92] Since g' being locally bounded implies that the solution of the reverse flow ϕ_{-t} also exists and is unique, local boundedness of g' is sufficient for ϕ_t to be invertible (and hence, for 2. ϕ_t to be one-to-one, and for 3. ϕ_t to have non-vanishing Jacobian). Additionally, if g has continuous derivatives up to order k , so does ϕ_t . [86] Clearly, if g is smooth (that is, if g' is continuous), then 1. ϕ_t is smooth, and g' is locally bounded,[66] which implies that: 2. ϕ_t is one-to-one, and 3. ϕ_t has non-vanishing Jacobian.

In the context of the Restricted Three-Body Problem (RTBP) these conditions are often met for some agent i with vector field $f_i : [t_0, t_f] \times \mathbb{R}^{n_{\mathbf{x}}} \rightarrow \mathbb{R}^{n_{\mathbf{x}}}$ satisfying $\dot{\mathbf{x}}_i(t) = f_i(t, \mathbf{x}_i(t))$. First, for the RTBP, f_i is often directly assumed to be smooth.[93] Second, more generally, for typical RTBP vector fields f_i , [94, 95] f_i meets bounded differentiability conditions, except: a) at points where the spacecraft is exactly colliding with either gravitational mass – where (f'_i) is not defined; and b) at near-binary-collision regions (i.e., at points in the immediate vicinity of spacecraft collision with either gravitational mass) – where (f'_i) is not bounded. Many RTBP trajectory families of interest avoid near-binary-collision regions altogether.[96] When it is of interest to study RTBP trajectories in near-binary-collision regions,[97, 98, 99] schemes based on the Levi-Civita regularization are

employed to ensure existence, uniqueness, and smoothness of trajectory solutions in these regions.[100]

Hence, in a wide range of RTBP cases, and for the case of linear relative orbital dynamics (as well as other cases of interest not addressed here), and unless $\underline{\mathbf{X}}_i(t) = \underline{\mathbf{X}}_j(t)$ with probability 1 (which is a trivial case), $\underline{\mathbf{X}}_{i,j}(t)$ has a pdf – and therefore, so does $\underline{\mathbf{R}}_{i,j}(t)$.

4.4 Equivalence of a -Pc with respect to open vs. closed a -norm collision regions

Consider the following sets in $\mathbb{R}^{d_{\mathbf{R}}}$:

$$a\text{-UNSAFE}_{i,j}(t) \doteq \{\underline{\mathbf{r}} \in \mathbb{R}^{d_{\mathbf{R}}} : \|\underline{\mathbf{r}}\|_a < l_{i,j}(t)\} = \mathbb{B}_{l_{i,j}(t)}^{d_{\mathbf{R}}|a} \left(\underline{\mathbf{0}}_{d_{\mathbf{R}} \times 1} \right) \quad (4.16)$$

$$a\text{-M.SAFE}_{i,j}(t) \doteq \{\underline{\mathbf{r}} \in \mathbb{R}^{d_{\mathbf{R}}} : \|\underline{\mathbf{r}}\|_a = l_{i,j}(t)\} = \mathbb{S}_{l_{i,j}(t)}^{(d_{\mathbf{R}}-1)|a} \left(\underline{\mathbf{0}}_{d_{\mathbf{R}} \times 1} \right) \quad (4.17)$$

$$a\text{-SAFE}_{i,j}(t) \doteq \{\underline{\mathbf{r}} \in \mathbb{R}^{d_{\mathbf{R}}} : \|\underline{\mathbf{r}}\|_a > l_{i,j}(t)\} = \left[\mathbb{B}_{l_{i,j}(t)}^{d_{\mathbf{R}}|a} \left(\underline{\mathbf{0}}_{d_{\mathbf{R}} \times 1} \right) \right]^C \quad (4.18)$$

Hence, $\mathcal{C}_a = \{a\text{-UNSAFE}_{i,j}(t), a\text{-M.SAFE}_{i,j}(t), a\text{-SAFE}_{i,j}(t)\}$ is a partition of $\mathbb{R}^{d_{\mathbf{R}}}$; i.e., any point $\underline{\mathbf{r}}_{i,j}$ in $\mathbb{R}^{d_{\mathbf{R}}}$ belongs to exactly one of these sets. This partition \mathcal{C}_a corresponds exactly to any possible classification of points $\underline{\mathbf{r}}_{i,j}$ in $\mathbb{R}^{d_{\mathbf{R}}}$ that arise from the instantaneous a -collision condition:

1. $\underline{\mathbf{r}}_{i,j}$ meets an (instantaneous) a -collision condition $\iff \underline{\mathbf{r}}_{i,j} \in a\text{-UNSAFE}_{i,j}(t)$
2. $\underline{\mathbf{r}}_{i,j}$ is (instantaneously) a -collision-safe $\iff \underline{\mathbf{r}}_{i,j} \in a\text{-SAFE}_{i,j}(t)$
3. $\underline{\mathbf{r}}_{i,j}$ is (instantaneously) neither a -collision-safe nor a -collision-unsafe $\iff \underline{\mathbf{r}}_{i,j} \in a\text{-M.SAFE}_{i,j}(t)$

The $\mathbb{S}_{l_{i,j}(t)}^{(d_{\mathbf{R}}-1)|a} \left(\underline{\mathbf{0}}_{d_{\mathbf{R}} \times 1} \right)$ set is not included as part of either the $a\text{-SAFE}_{i,j}(t)$ set or the $a\text{-UNSAFE}_{i,j}(t)$ set because the former region is the boundary of the two latter regions. Thus, by definition, any open ball centered at a point in $\mathbb{S}_{l_{i,j}(t)}^{(d_{\mathbf{R}}-1)|a} \left(\underline{\mathbf{0}}_{d_{\mathbf{R}} \times 1} \right)$ will contain a -safe and a -unsafe points.[66] Hence, it is not meaningful to consider $\mathbb{S}_{l_{i,j}(t)}^{(d_{\mathbf{R}}-1)|a} \left(\underline{\mathbf{0}}_{d_{\mathbf{R}} \times 1} \right)$ as either a -safe or a -unsafe; instead, it may be regarded as a marginally a -safe region.

Because the $\mathbb{S}_{l_{i,j}(t)}^{(d_{\mathbf{R}}-1)|a} \left(\mathbf{0}_{d_{\mathbf{R}} \times 1} \right)$ set is the boundary of both the a -SAFE $_{i,j}(t)$ set and the a -UNSAFE $_{i,j}(t)$ set, study of the marginally a -safe region a -M.SAFE $_{i,j}(t)$ is a useful endeavor in SFF COLRM, for example, by providing a starting point for identifying the corresponding boundary of deterministic relative orbital dynamic state values (whether Cartesian, or expressed via relative geometric parameters or relative orbital elements) whose ensuing spatial trajectories in $\mathbb{R}^{d_{\mathbf{R}}}$ may transition from being a -safe to being a -unsafe.

Additionally, $\mathbb{S}_{l_{i,j}(t)}^{(d_{\mathbf{R}}-1)|a} \left(\mathbf{0}_{d_{\mathbf{R}} \times 1} \right)$ has zero measure in $\mathbb{R}^{d_{\mathbf{R}}}$. If the instantaneous relative position $\mathbf{R}_{i,j}(t)$ has a stochastic description through a probability density function (pdf), which would entail that probabilities of events in that space may be computed as integrals of the pdf,[35] the zero measure of $\mathbb{S}_{l_{i,j}(t)}^{(d_{\mathbf{R}}-1)|a} \left(\mathbf{0}_{d_{\mathbf{R}} \times 1} \right)$ implies that there is zero $\mathbf{R}_{i,j}(t)$ -probability mass contained within that set.[67] In other words, under these assumptions, the probability measure associated with $\mathbf{R}_{i,j}(t)$ is absolutely continuous with respect to the Lebesgue measure in relative position space. Hence, from a stochastic (instantaneous) perspective, excluding $\mathbb{S}_{l_{i,j}(t)}^{(d_{\mathbf{R}}-1)|a} \left(\mathbf{0}_{d_{\mathbf{R}} \times 1} \right)$ from the definition of the a -SAFE $_{i,j}(t)$ and a -UNSAFE $_{i,j}(t)$ sets does not affect them in any practical way.

These observations remain true in a stochastic (joint-time) sense for a large class of spacecraft collision risk management applications.

Remark 19. Let the closed a -intersection volume, denoted by $\overline{V}_{i,j}(t; l_{i,j}(t), a)$, be defined as

$$\overline{V}_{i,j}(t; l_{i,j}(t), a) \doteq \overline{\mathbb{B}}_{l_{i,j}(t)}^{d_{\mathbf{R}}|a} \left(\mathbf{0}_{d_{\mathbf{R}} \times 1} \right) = \{ \mathbf{r} \in \mathbb{R}^{d_{\mathbf{R}}} : \|\mathbf{r}\|_a \leq l_{i,j}(t) \} \quad (4.19)$$

Then, the definition of certain “open” objects (denoted without an overbar) can be made into the definition of their corresponding “closed” object counterparts (denoted with an overbar) by *mutatis mutandis*, specifically:

- $\overline{C}_{i,j}(t; l_{i,j}(t), a)$, and $\overline{\text{IPC}}_{i,j}(t; l_{i,j}(t), a)$: by replacing “ $V_{i,j}$ ” with “ $\overline{V}_{i,j}$ ” (in Eqns. 2.30, and 2.33, respectively)
- $\overline{\text{IPC}}_{i,j}(t; l_{i,j}(t), a)$, $\overline{\text{JTC}}_{i,j}([t_0, t_f]; l_{i,j}(\cdot), a)$, $\widetilde{\overline{\text{JTC}}}_{i,j}([t_0, t_f]; l_{i,j}(\cdot), a)$, and

$\overline{\text{JTC}}_{i,j}^N([t_0, t_f]; l_{i,j}(\cdot), a)$: by replacing “ $C_{i,j}$ ” with “ $\overline{C}_{i,j}$ ” (in Eqns. 2.34, 2.40, 4.1, and 4.7-4.8, respectively)

- $\overline{P}c_{i,j}([t_0, t_f]; l_{i,j}(\cdot), a)$, $\widetilde{P}c_{i,j}([t_0, t_f]; l_{i,j}(\cdot), a)$, $\overline{P}c_{i,j}^N([t_0, t_f]; l_{i,j}(\cdot), a)$: by replacing “JTC” with “ $\overline{\text{JTC}}$ ” (in Eqns. 2.41, 4.3, and 4.9 respectively)

Note: the closed a -JTC sets are related to their open a -JTC counterparts via the following unions of sets (not necessarily disjoint) in $\mathbb{R}^{n_{\mathbf{x}}}$:

$$\overline{\text{JTC}}_{i,j}([t_0, t_f]; l_{i,j}(\cdot), a) = \text{JTC}_{i,j}([t_0, t_f]; l_{i,j}(\cdot), a) \cup A_1 \quad (4.20)$$

$$\widetilde{\overline{\text{JTC}}}_{i,j}([t_0, t_f]; l_{i,j}(\cdot), a) = \widetilde{\text{JTC}}_{i,j}([t_0, t_f]; l_{i,j}(\cdot), a) \cup A_2 \quad (4.21)$$

$$\overline{\text{JTC}}_{i,j}^N([t_0, t_f]; l_{i,j}(\cdot), a) = \text{JTC}_{i,j}^N([t_0, t_f]; l_{i,j}(\cdot), a) \cup A_3 \quad (4.22)$$

where the sets A_1 , A_2 , and A_3 in $\mathbb{R}^{n_{\mathbf{x}}}$ are given by

$$A_1 = \bigcup_{t \in [t_0, t_f]} [F_{t, t_0}]^{-1} \left[g_P^{-1} \left(\mathbb{S}_{l_{i,j}(t)}^{(d_{\mathbf{R}}-1)|a} \left(\mathbf{0}_{d_{\mathbf{R}} \times 1} \right) \right) \right] \quad (4.23)$$

$$A_2 = \bigcup_{c \in \mathbb{Q} \cap [0, 1]} [F_{h_T(c), t_0}]^{-1} \left[g_P^{-1} \left(\mathbb{S}_{l_{i,j}(h_T(c))}^{(d_{\mathbf{R}}-1)|a} \left(\mathbf{0}_{d_{\mathbf{R}} \times 1} \right) \right) \right] \quad (4.24)$$

$$A_3 = \bigcup_{k=0}^N [F_{h_T(\frac{k}{N}), t_0}]^{-1} \left[g_P^{-1} \left(\mathbb{S}_{l_{i,j}(h_T(\frac{k}{N}))}^{(d_{\mathbf{R}}-1)|a} \left(\mathbf{0}_{d_{\mathbf{R}} \times 1} \right) \right) \right] \quad (4.25)$$

While A_2 and A_3 are measurable sets in $\mathbb{R}^{n_{\mathbf{x}}}$, it is not clear whether A_1 is a measurable set in $\mathbb{R}^{n_{\mathbf{x}}}$. Hence, while the countable and finite closed a -JTC sets are measurable in $\mathbb{R}^{n_{\mathbf{x}}}$, the closed a -JTC set, $\overline{\text{JTC}}_{i,j}([t_0, t_f]; l_{i,j}(\cdot), a)$, may or not be measurable in $\mathbb{R}^{n_{\mathbf{x}}}$. \diamond

Proposition 20 (Equivalence between open and closed a - Pc measures (countable and finite)). Let $\underline{\mathbf{X}}_{i,j}(t)$ have a pdf for $t \in [t_0, t_f]$. Then, the open and closed countable a - Pc measures, as well as the open and closed finite a - Pc measures, are respectively equivalent.

That is,

$$\widetilde{P}c_{i,j}([t_0, t_f]; l_{i,j}(\cdot), a) = \widetilde{P}c_{i,j}([t_0, t_f]; l_{i,j}(\cdot), a) \quad (4.26)$$

$$\overline{P}c_{i,j}^N([t_0, t_f]; l_{i,j}(\cdot), a) = Pc_{i,j}^N([t_0, t_f]; l_{i,j}(\cdot), a) \quad (4.27)$$

In particular, for $t \in [t_0, t_f]$,

$$\overline{\text{IPC}}_{i,j}(t; l_{i,j}(t), a) = \text{IPC}_{i,j}(t; l_{i,j}(t), a) \quad \diamond \quad (4.28)$$

Proof. Let \mathbb{P} denote the probability measure of $\underline{\mathbf{X}}_{i,j}(t_0)$. By monotonicity and countable subadditivity, Eq. 4.21 implies that

$$0 \leq \mathbb{P} \left(\widetilde{\text{JTC}}_{i,j}([t_0, t_f]; l_{i,j}(\cdot), a) \right) - \mathbb{P} \left(\widetilde{\text{JTC}}_{i,j}([t_0, t_f]; l_{i,j}(\cdot), a) \right) \leq \mathbb{P}(A_2) \quad (4.29)$$

By countable subadditivity (on Eq. 4.24),

$$\begin{aligned} 0 \leq \mathbb{P}(A_2) &\leq \sum_{c \in \mathbb{Q} \cap [0,1]} \mathbb{P} \left([F_{h_T(c), t_0}]^{-1} \left[g_P^{-1} \left(\mathbb{S}_{l_{i,j}(h_T(c))}^{(d_{\mathbf{R}}-1)|a} \left(\mathbf{0}_{d_{\mathbf{R}} \times 1} \right) \right) \right] \right) \\ &= \sum_{c \in \mathbb{Q} \cap [0,1]} p \left(\underline{\mathbf{X}}_{i,j}(h_T(c)) \in g_P^{-1} \left[\mathbb{S}_{l_{i,j}(h_T(c))}^{(d_{\mathbf{R}}-1)|a} \left(\mathbf{0}_{d_{\mathbf{R}} \times 1} \right) \right] \right) \\ &= \sum_{c \in \mathbb{Q} \cap [0,1]} p \left(\underline{\mathbf{R}}_{i,j}(h_T(c)) \in \mathbb{S}_{l_{i,j}(h_T(c))}^{(d_{\mathbf{R}}-1)|a} \left(\mathbf{0}_{d_{\mathbf{R}} \times 1} \right) \right) \end{aligned} \quad (4.30)$$

Any $(d_{\mathbf{R}} - 1)$ -sphere (with respect to the a -norm) is a set of zero measure in $\mathbb{R}^{d_{\mathbf{R}}}$. Note: $\underline{\mathbf{R}}_{i,j}(t)$ is an absolutely continuous random variable [that is, sets of zero measure have zero probability in $\underline{\mathbf{R}}_{i,j}(t)$]. Since, Eq. 4.30 denotes a countable sum, it follows that $\mathbb{P}(A_2) = 0$.

Hence, Eq. 4.29 implies that

$$\widetilde{P}c_{i,j}([t_0, t_f]; l_{i,j}(\cdot), a) = \widetilde{P}c_{i,j}([t_0, t_f]; l_{i,j}(\cdot), a) \quad (4.31)$$

A similar argument is used to prove Eq. 4.27. Finally, Eq. 4.28 follows from applying either Eq. 4.26 or Eq. 4.27 over the degenerate interval $[t, t]$ for t in $[t_0, t_f]$. \square

In other words, Proposition 20, implies that, under the condition that $\underline{\mathbf{X}}_{i,j}(t)$ has a pdf for $t \in [t_0, t_f]$, then whether instantaneous a -norm collisions are defined via either open or closed a -norm balls has no effect on the value of countable and finite a - PC measures. Since, A_1 is defined via an uncountable union of measurable sets, it is unclear whether A_1 is measurable; therefore, it is unclear whether the closed a -JTC set is measurable, or what the relationship of the closed a - PC (if defined) is to the open a - PC value (besides the former being bounded below by the latter). However, if the closed a -JTC set can be characterized via the countable closed a -JTC set as can be done for the open a -JTC set (see Eq. 4.4), which must be true in any practical applications (cf. the discussion of the implications of Proposition 17), it follows that, via Proposition 20, defining instantaneous a -norm collision events via either closed or open a -norm balls in relative position space is stochastically equivalent in an instantaneous and joint-time sense for most practical purposes.

4.5 Conclusion

In this Chapter, it is shown that joint-time probabilities of collision between a pair of agents in a spacecraft formation are both well-defined and computable if the underlying instantaneous collision condition is defined through a ball with respect to some norm in relative position space, and under certain assumptions on the flow function, which are often met in spaceflight mechanics applications.

CHAPTER 5

ADEQUACY OF SFF PROBABILISTIC COLLISION RISK INDICATORS

The probability dilution phenomenon generally displayed by probabilistic spacecraft collision risk indicators based on epistemic representations of relative state uncertainty has motivated debate in the literature concerning the suitability of employing these indicators for the purposes of spacecraft collision risk assessment. This Chapter provides a brief overview of these concerns in the context of this dissertation. Asymptotic and transient probability dilution behaviors are illustrated for probabilistic SFF collision risk indicators in the context of simplified, reduced-dimensionality relative dynamic state examples. The applicability of epistemic-probabilistic SFF collision risk indicators for SFF collision risk assessment purposes is argued from the perspective of how such indicators may be interpreted as statistical estimators of deterministic SFF collision indicators. Finally, although this dissertation does not formally define, characterize, or implement statistical inference models that employ miss distance-based likelihood functions for collision safety-related hypothesis testing, such models are briefly discussed.

5.1 Overview of the probability dilution of SFF probabilistic collision risk indicators

In the current SFF COLRM framework, the IPC and P_c SFF collision risk indicators are based on the treatment of the initial relative state as a random variable with a pdf, and with subsequent assumptions that ensure that the propagated relative state and its associated

functions (such as the instantaneous relative position) may also be regarded as random variables with a pdf. (For further discussion, see Sections 2.3 and 4.3.) Then, the IPC and P_c are defined as probability measures arising from the instantaneous or joint-time violation of minimum norm constraints in relative position space with respect to some norm in relative position space. (For IPC/ P_c formal definitions, see Section 2.5.)

Because $IPC_{i,j}(t)$ and $P_{c_{i,j}}[t_0, t_f]$ are measures based on probability distributions that reflect epistemic uncertainty, it follows that $IPC_{i,j}(t)$ and $P_{c_{i,j}}[t_0, t_f]$ may be regarded as epistemic probabilities as well. As discussed in [28], a criticism of quantifying collision risk in spaceflight mechanics via epistemic probabilities is the concept of probability dilution, which posits that, for a fixed inter-agent geometry and keep-out distance, increasing uncertainty about relative state knowledge eventually decreases collision probability; [45] this is an inevitable consequence of the probability mass being spread more sparsely over its sample space (i.e., relative state space) due to increased uncertainty. [72] Furthermore, because relative state covariances are open-loop divergent in relative orbital dynamics (at least to within CW dynamics), any probability measure over a bounded set in relative state space will inexorably become diluted over time in this sense.

These observations raise three important research questions. First, which initial uncertainty profiles and restrictions on the propagation horizon might be needed in order to make statistically significant inferences of collision risk (e.g., through epistemic collision probability measures)? Second, is it appropriate in any way to use epistemic collision probability measures as indicators of collision risk, either by themselves or in combination with other criteria? And third, are there more suitable probabilistic collision risk indicators (for SFF COLRM purposes) than epistemic collision probability measures? Although these questions are the subject of past and active research efforts in the community, [101, 102, 103, 104, 56, 105, 106] such questions lie outside of the scope of this dissertation.

However, epistemic probability measures are used in this work for several reasons. First, this dissertation defines, characterizes, quantifies, and compares SFF collision risk

criteria that have distinct philosophical meaning and physical interpretation (namely, probability, separation, or both), but since they are all based on the same underlying epistemic uncertainty, separation and hybrid SFF collision risk indicators will be epistemic as well. Second, even though epistemic probabilities might not be the most suitable SFF collision risk indicators, they are a good starting point for collision risk assessment because of how a collision event is topologically defined, and how a probability may be assigned to measure such an event — hence, computing epistemic collision probabilities is widely practiced in spaceflight mechanics.[105] Third, although it is expected that lower uncertainties might generally lead to more statistically significant inferences of collision risk, fundamentally, assessment of risk must be performed with respect to some uncertainty description, and it makes sense to employ a representation that arises from the outcome of relative state estimation – that is, an epistemic representation of uncertainty.

5.2 On the usability of the IPC for SFF COLRM

The IPC construct has been introduced in the literature by Chan, under the assumption of a normally distributed relative position pdf.[31] It is noteworthy that, even though the initial relative velocity uncertainty affects the relative position uncertainty through propagation, the relative velocity uncertainty itself does not directly affect the formulation of $IPC_{i,j}(t)$; that is, in Eq. 2.35, there are no terms inside the integrand that depend on relative velocity, and apart from possible marginalization, integration is not performed with respect to relative velocity. Such terms would appear in analytical formulations of the “probability of collision” (Pc), i.e., the probability that two agents might collide at any time within a time period $[t_0, t_0 + T]$ for some $T > 0$.[44] The IPC is advocated as complementary to the Pc notion. First, by definition, the IPC is less than or equal to the Pc , so any values of the former become lower bounds for the latter, as shown by Alfano.[43] Second, if the IPC is null or insignificant over an interval, by implication, changes to the Pc must be null or insignificant as well. Third, in SFF, frequent state knowledge updates are needed. However, since

the estimation process entails that an initial state pdf is superseded by an updated pdf, the P_c can only be computed between state knowledge updates, as it would not be meaningful to relate portions of the initial state pdf (which, during its validity period, might indicate collision events) to portions of the updated state pdf. In the limit of vanishing time between knowledge updates, a constantly restarting P_c and the IPC would be in agreement.

5.3 Conceptual illustration of IPC/ P_c dilution (one-dimensional relative position)

The IPC probability dilution phenomenon is illustrated in this Section in the context of a simplified, low-dimensionality model. Let $R_{i,j} \sim \mathcal{N}(\mu, \sigma^2)$, where $\mu \in \mathbb{R}$, $\sigma > 0$. Hence,

$$\text{IPC}_{i,j}(t) = p(|R_{i,j}(t)| < l_{i,j}) \quad (5.1)$$

After some manipulation, and letting $Z \sim \mathcal{N}(0, 1)$, Eq. 5.1 may be explicitly expressed as

$$\text{IPC}_{i,j}(t) = \text{cdf}_Z\left(\frac{1 - \mu/l_{i,j}}{\sigma/l_{i,j}}\right) - \text{cdf}_Z\left(\frac{-1 - \mu/l_{i,j}}{\sigma/l_{i,j}}\right) \quad (5.2)$$

Fig. 5.1 illustrates Eq. 5.2.

In this context, let μ be interpreted as a current best estimate of inter-agent relative position, and let $\sigma > 0$ be interpreted as encoding relative position confidence information (specifically, with lower σ values representing greater confidence on the μ estimate). As shown in Fig. 5.1 and Eq. 5.2, when $\sigma \rightarrow 0$, $\text{IPC}_{i,j} \rightarrow K'_{i,j}$, where

$$K'_{i,j} = \begin{cases} 1 & \text{if } \left|\frac{\mu}{l_{i,j}}\right| < 1 \\ 0.5 & \text{if } \left|\frac{\mu}{l_{i,j}}\right| = 1 \\ 0 & \text{if } \left|\frac{\mu}{l_{i,j}}\right| > 1 \end{cases} \quad (5.3)$$

However, for the unique, deterministic relative position $r_{i,j}$, its corresponding deterministic

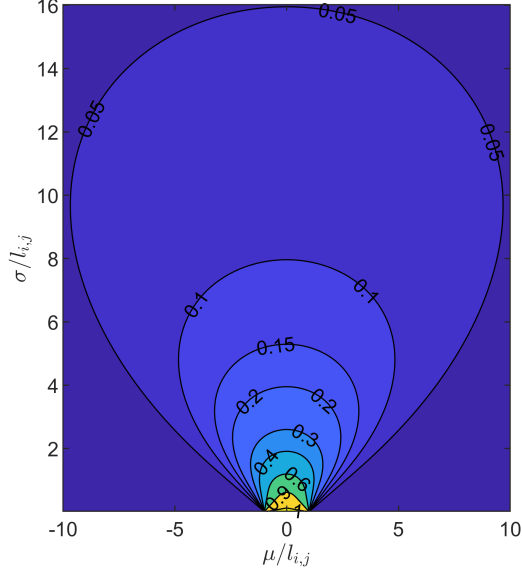


Figure 5.1: IPC as a function of first- and second-order statistics of a one-dimensional (1D) normally distributed relative position.

collision indicator $K_{i,j}$ is given by

$$K_{i,j} = \begin{cases} 1 & \text{if } |r_{i,j}| < l_{i,j} \\ c_{\text{marginal}} & \text{if } |r_{i,j}| = l_{i,j} \\ 0 & \text{if } |r_{i,j}| > l_{i,j} \end{cases} \quad (5.4)$$

where c_{marginal} is a user-defined constant in $[0, 1]$ for two reasons. First, whether or not a deterministic collision is indicated for $|r_{i,j}| = l_{i,j}$ depends on the interpretation of the practitioner. Second, since the set $\{\pm l_{i,j}\}$ is a set of zero Lebesgue measure in \mathbb{R} , for any stochastic description of the relative position via a pdf, the event set $\{x \in \mathbb{R} : |x| = l_{i,j}\}$ has zero probability mass; therefore, the value of c_{marginal} is not practically relevant for SFF collision risk assessments. In the view of this dissertation, the event set $\{x \in \mathbb{R} : |x| = l_{i,j}\}$ represents a marginally collision-safe condition (i.e., such a condition is neither collision-safe nor collision-unsafe; cf. Section 4.4). Hence, in this Chapter, $c_{\text{marginal}} = 0.5$.

Therefore, in the limit of full confidence in a relative position knowledge estimate, the $\text{IPC}_{i,j}$ may be interpreted as an estimator of the deterministic i, j collision indicator $K_{i,j}$.

On the other hand, Fig. 5.1 also illustrates the probability dilution phenomenon as it pertains to the IPC. First, for any $\mu \neq 0$ and IPC values $p' \in (0, 1)$, the same $\text{IPC}_{i,j} = p'$ value is obtained for two scalar values $\sigma_L, \sigma_U > 0$ of σ such that $0 < \sigma_L < \sigma_U$. In other words, for a fixed μ , the $\text{IPC}_{i,j}$ has the same value for a high and a low variance.

Second, via Eq. 5.2 it can be seen that for a fixed $\mu \in \mathbb{R}$, the IPC has strictly monotonically decreasing values with decreasing confidence in relative position knowledge; in the limit of no confidence in relative position knowledge, the IPC estimator is zero-valued, i.e.,

$$\lim_{\sigma \rightarrow \infty} \text{IPC}_{i,j}(t; \sigma) = 0 \quad (5.5)$$

The foregoing insights concerning IPC probability dilution in the aforementioned simplified model apply more generally to IPC measures based on two-dimensional (2D) relative position information (cf. Section 5.4), as well as to the joint-time probability of collision (Pc) for short-term encounters,[72, 56] from the perspectives of: a) achieving the same IPC/Pc values for different relative state-based covariance magnitudes, and b) resulting in zero-valued IPC/Pc measures in the limit of increased covariance magnitude.

It has been proposed that the seemingly paradoxical IPC/Pc behavior observed should entail the general discontinuance of the application of IPC/Pc constructs in spacecraft conjunction assessment contexts [45] – and hence, in an SFF COLRM context also. However, it is the view of this dissertation that: 1) IPC/Pc measures have applicability in spaceflight mechanics because their high-confidence behaviors are consistent with their interpretation as estimators of deterministic (yet unknown) instantaneous/joint-time collision indicators; and 2) IPC/Pc probability dilution arises from changes in the variability of the underlying relative state measurement observation data, and not from inherent probability paradoxes.

[106]

5.4 Asymptotic and transient IPC/PC probability dilution behavior (two-dimensional relative position)

5.4.1 Asymptotic IPC probability dilution behavior (2D)

Let the $\underline{\mathbf{R}}_{i,j}^c(t) = [X, Y]$ denote a non-degenerate normal random variable in \mathbb{R}^2 with distribution

$$\underline{\mathbf{R}}_{i,j}^c(t) \sim \mathcal{N}(\underline{\mu}, \Sigma_c) \quad (5.6)$$

where $\underline{\mu} = [\mu_X, \mu_Y] \in \mathbb{R}^2$, $\Sigma_c = B_c \Sigma B_c^T$, where Σ is a positive-definite covariance matrix, given by

$$\Sigma = \begin{bmatrix} \sigma_X^2 & \rho\sigma_X\sigma_Y \\ \rho\sigma_X\sigma_Y & \sigma_Y^2 \end{bmatrix} \quad (5.7)$$

where $\sigma_X, \sigma_Y > 0$, $-1 < \rho < 1$. (Note: $\underline{\mathbf{R}}_{i,j}^c(t) = \underline{\mathbf{R}}_{i,j}^1(t)$.) In this context, for $c \geq 1$, B_c represents a scaling matrix such that

$$B_1 = \mathbb{I}_2 = \begin{bmatrix} 1 & 0 \\ 0 & 1 \end{bmatrix} \quad (5.8)$$

and where the magnitude of Σ_c under some norm is expected to grow in some sense for $c > 1$. Common patterns of covariance growth include the following: along x -axis, along y -axis, and isotropic growth. (These patterns are illustrated in Fig. 5.2.)

Covariance growth along the x -coordinate only is given by

$$B_c^x = \begin{bmatrix} c & 0 \\ 0 & 1 \end{bmatrix} \quad (5.9)$$

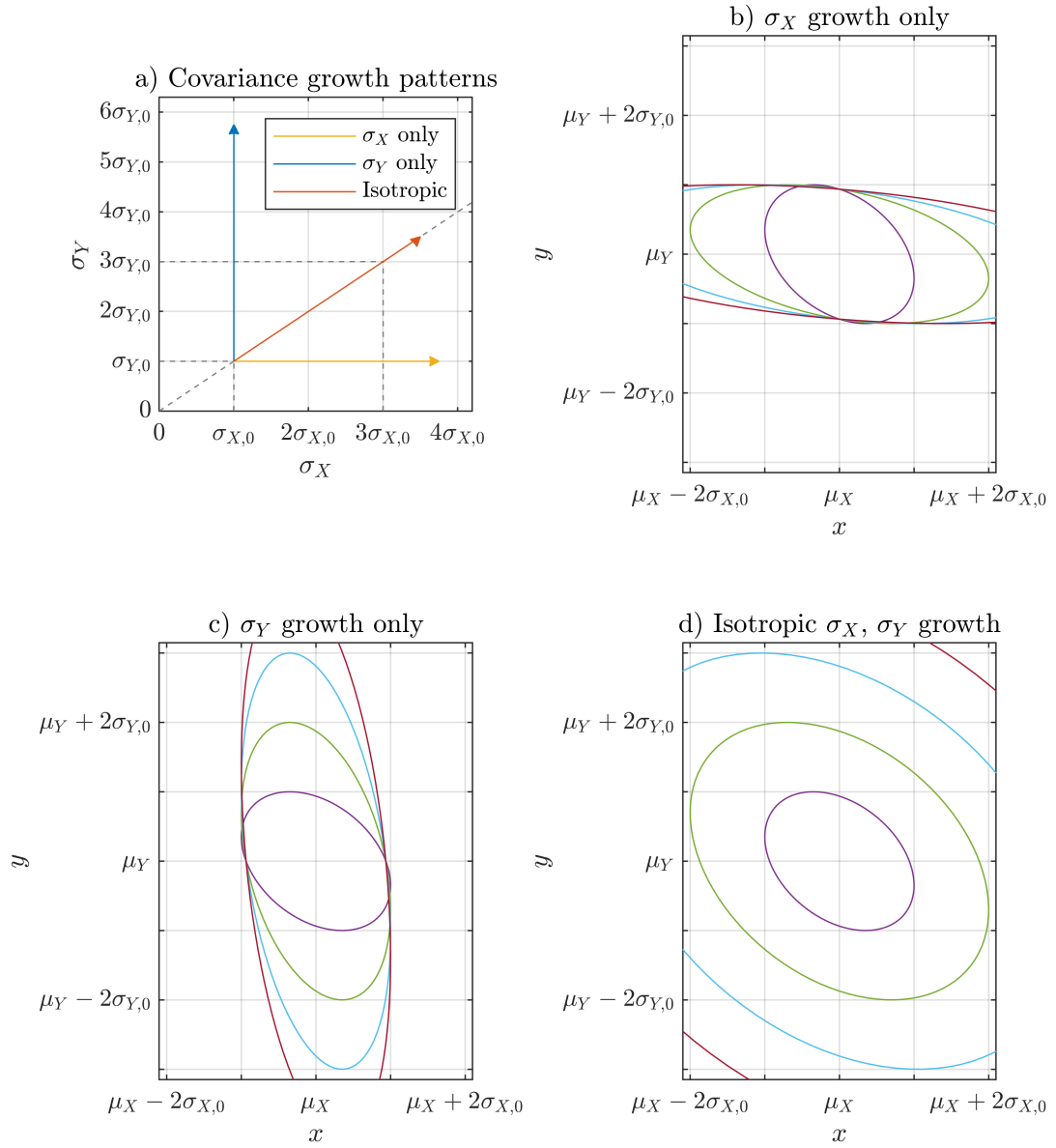


Figure 5.2: Covariance growth for a two-dimensional (2D) normally distributed relative position (anti-correlated x - and y -axis $\mathbf{R}_{i,j}$ -variances).

whereas covariance growth along the y -coordinate only is given by

$$B_c^y = \begin{bmatrix} 1 & 0 \\ 0 & c \end{bmatrix} \quad (5.10)$$

Finally, isotropic covariance growth is given by

$$B_c^{\text{iso}} = \begin{bmatrix} c & 0 \\ 0 & c \end{bmatrix} \quad (5.11)$$

Via the definition of Mahalanobis contours (see Eq. 6.10), isotropic covariance growth entails a uniform scaling of covariance contours in all directions, as shown by

$$\begin{aligned} L_d(\mathbf{R}_{i,j}^c(t)) &= \left\{ \underline{x} \in \mathbb{R}^2 : \sqrt{(\underline{x} - \underline{\mu})^T \Sigma_c^{-1} (\underline{x} - \underline{\mu})} = d \right\} \\ &= \left\{ \underline{x} \in \mathbb{R}^2 : \sqrt{(\underline{x} - \underline{\mu})^T \frac{1}{c^2} \Sigma^{-1} (\underline{x} - \underline{\mu})} = d \right\} \\ &= \left\{ \underline{x} \in \mathbb{R}^2 : \sqrt{(\underline{x} - \underline{\mu})^T \Sigma^{-1} (\underline{x} - \underline{\mu})} = dc \right\} = L_{dc}(\mathbf{R}_{i,j}(t)) \end{aligned} \quad (5.12)$$

Isotropic covariance growth implies a quadratic scaling of the covariance magnitude as quantified by any matrix norm $\|\cdot\|_M$ in $\mathbb{R}^{2 \times 2}$, i.e.,

$$\|\Sigma_c\|_M = \|B_c \Sigma B_c^T\|_M = |c^2| \|\Sigma\|_M \quad (5.13)$$

(This observation is a consequence of the homogeneity property of $\|\cdot\|_M$.)

Let $\text{IPC}_{i,j}(t; c)$ denote the IPC based on $\mathbf{R}_{i,j}^c(t)$. Under the current framework, it can be shown easily that

$$\lim_{c \rightarrow \infty} \text{IPC}_{i,j}(t; c) = 0 \quad (5.14)$$

The following argument holds for x -axis and isotropic growth directly, and for y -axis growth via *mutatis mutandis* (specifically, by replacing x with y).

The event $\{\underline{\mathbf{r}} \in \mathbb{R}^2 : \|\underline{\mathbf{r}}\|_2 < l_{i,j}\}$ is a subset of the event $\{[x, y]^T \in \mathbb{R}^2 : |x| < l_{i,j}\}$. Letting $\mathbf{R}_{i,j}^c(t)$ be expressed as $\mathbf{R}_{i,j}^c(t) = [[R_{i,j}^c]_X(t), [R_{i,j}^c]_Y(t)]$, it follows from the mono-

tonicity of probability measures that

$$\text{IPC}_{i,j}(t; c) = p\left(\|\mathbf{R}_{i,j}^c(t)\|_2 < l_{i,j}\right) \leq p\left(|[R_{i,j}^c]_X(t)| < l_{i,j}\right) \quad (5.15)$$

Letting $Z \sim \mathcal{N}(0, 1)$ and after some manipulation, it follows that $\text{IPC}_{i,j}(t; c)$ is bounded above in terms of the cdf of Z as given by

$$\text{IPC}_{i,j}(t; c) \leq \text{cdf}_Z\left(\frac{1 - \mu_X/l_{i,j}}{(c\sigma_X)/l_{i,j}}\right) - \text{cdf}_Z\left(\frac{-1 - \mu_X/l_{i,j}}{(c\sigma_X)/l_{i,j}}\right) \quad (5.16)$$

Hence, by the non-negativity of probability measures, it follows that IPC measures based on balls with respect to the Euclidean norm are subject to probability dilution in the sense of Eq. 5.17 under the x -axis, y -axis, and isotropic covariance growth patterns.

$$\lim_{c \rightarrow \infty} \text{IPC}_{i,j}(t; c) = 0 \quad (5.17)$$

Although asymptotic IPC probability dilution was only demonstrated for simple covariance growth patterns (cf. Figure 5.2), the foregoing analysis applies also to uncountably many covariance growth patterns, namely, for patterns that fit the following description: for continuous functions $f_x, f_y : [1, \infty) \rightarrow [1, \infty) \times [1, \infty)$ such that there exists an orthonormal matrix \mathbf{U} in \mathbb{R}^2 , and a strictly increasing sequence $\{c_k\}_{k \in \mathbb{N}}$ of scalars in $[1, \infty)$ such that the sequence $\{\sigma_k\}_{k \in \mathbb{N}}$ defined (for $k \in \mathbb{N}$) by

$$\sigma_k^2 = \begin{bmatrix} 1 & 0 \end{bmatrix} \mathbf{U} \begin{bmatrix} f_x(c_k) & 0 \\ 0 & f_y(c_k) \end{bmatrix} \Sigma \begin{bmatrix} f_x(c_k) & 0 \\ 0 & f_y(c_k) \end{bmatrix} \mathbf{U}^T \begin{bmatrix} 1 \\ 0 \end{bmatrix} \quad (5.18)$$

is also a strictly increasing sequence. Practically, this condition implies that the IPC probability dilution results of this Subsection are applicable to any covariance growth pattern such that there exists some unit vector along which there is consistent variance growth.

5.4.2 Transient IPC probability dilution behavior (uncorrelated 2D relative position covariance)

Within this Subsection, the transient behavior of IPC probability dilution is examined in the context of non-degenerate normal 2D relative position distributions for the case of uncorrelatedness between x -axis and y -axis relative position variances (i.e., by setting $\rho = 0$ in Eq. 5.7), as illustrated in Fig. 5.3.

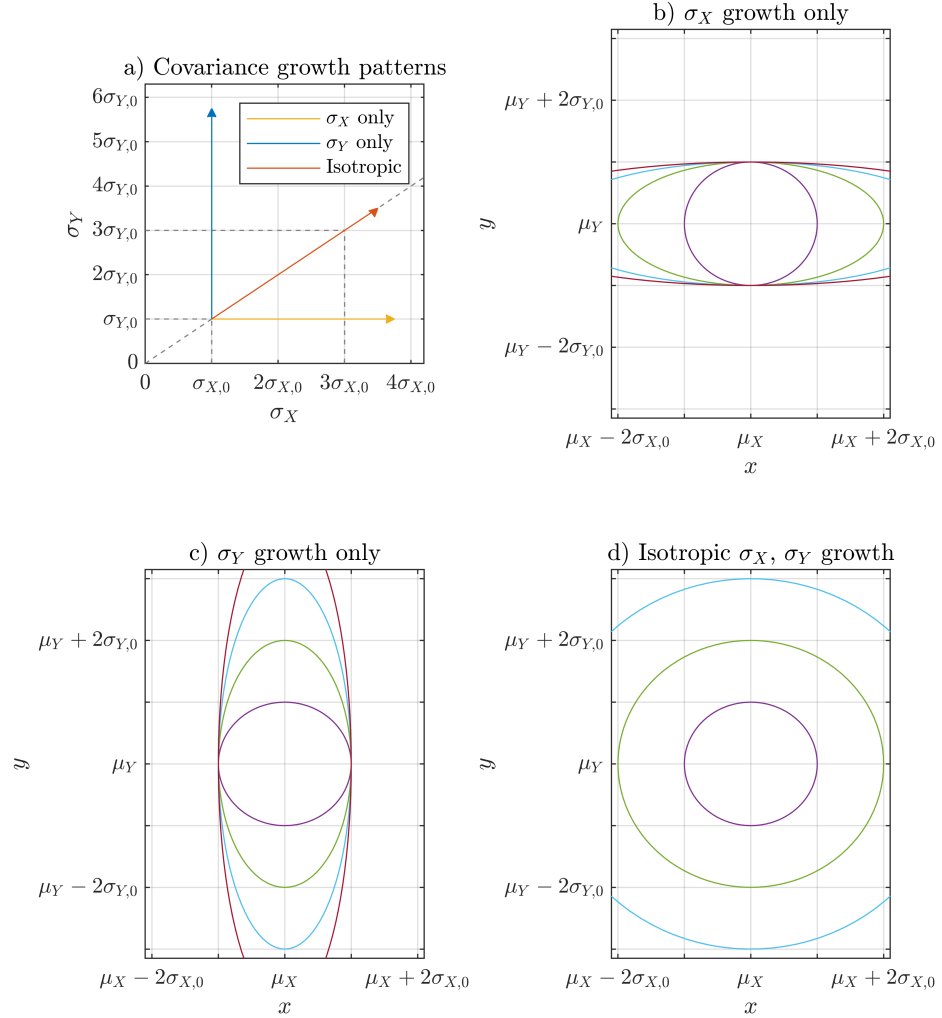


Figure 5.3: Covariance growth for a two-dimensional (2D) normally distributed relative position (uncorrelated x - and y -axis $\mathbf{R}_{i,j}$ -variances).

For simplicity, changes in σ_X and σ_Y are addressed directly (i.e., without intermediate scaling constants).

The expected value of the of the relative position, $\underline{\mu}$, is assumed to be located along

the x -axis, i.e., $\mu_Y = 0$ (cf. Eq. 5.6). Hence, changes in σ_X may be understood as uncertainty changes in the direction of the expected relative position and the collision region (denoted as the $V_{i,j}$ -“radial” direction), and σ_Y changes may be interpreted as uncertainty changes in the direction perpendicular to the expected relative position (referred to as the $V_{i,j}$ -“orthogonal” direction). Uncertainty growth along the $V_{i,j}$ -radial and $V_{i,j}$ -orthogonal directions is illustrated in Figs. 5.4 and 5.5.

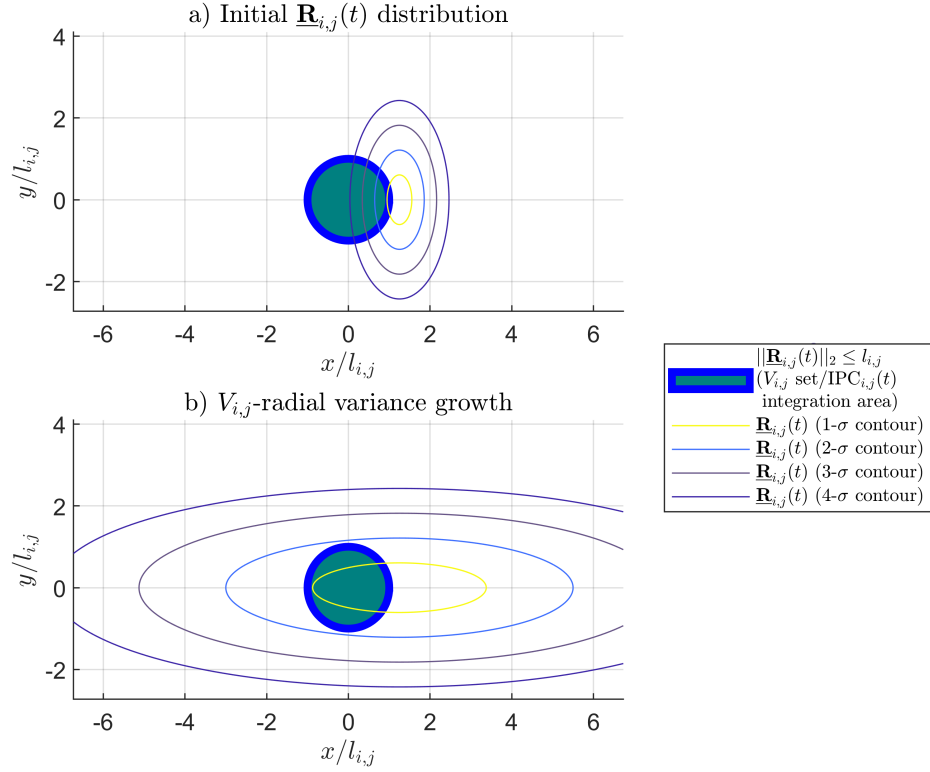


Figure 5.4: $V_{i,j}$ -radial variance growth for a two-dimensional (2D) normally distributed relative position (uncorrelated x - and y -axis $\underline{\mathbf{R}}_{i,j}$ -variances).

The transient IPC probability dilution behavior under the current simplified model is studied by computing IPC values for $\sigma_X, \sigma_Y \in (0, 16l_{i,j}]$ and $\mu_X \in [0, 10l_{i,j}]$. (Practically, $\sigma_X, \sigma_Y \in [0.01l_{i,j}, 16l_{i,j}]$.) Such IPC values have been computed in MATLAB R2018b through brute force quadrature via the `integral2` function.[107] These results are summarized in Fig. 5.6.

First, low-covariance-magnitude IPC behavior (i.e., for $\sigma_X, \sigma_Y \rightarrow 0$) is discussed.

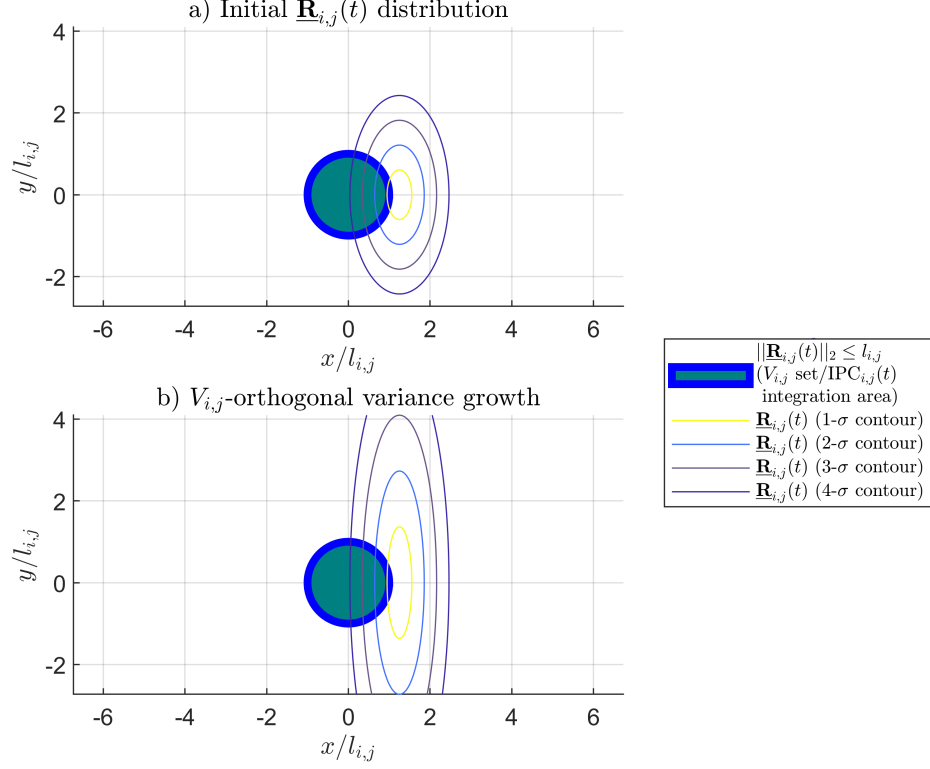


Figure 5.5: $V_{i,j}$ -orthogonal variance growth for a two-dimensional (2D) normally distributed relative position (uncorrelated x - and y -axis $\mathbf{R}_{i,j}$ -variances).

Numerical IPC results show that when $\sigma_X, \sigma_Y \rightarrow 0$, $\text{IPC}_{i,j} \rightarrow K'_{i,j}$, where

$$K'_{i,j} = \begin{cases} 1 & \text{if } \|\underline{\mu}\|_2 < l_{i,j} \\ 0.5 & \text{if } \|\underline{\mu}\|_2 = l_{i,j} \\ 0 & \text{if } \|\underline{\mu}\|_2 > l_{i,j} \end{cases} \quad (5.19)$$

These low- $\mathbf{R}_{i,j}$ -covariance-magnitude IPC results are consistent with the 1D relative position-based IPC interpretation as an estimate of the deterministic i, j -collision indicator. Specifically, since low σ_X, σ_Y values entail a low magnitude of the relative position covariance, which corresponds to high confidence in $\underline{\mu}$ as an estimator of the deterministic relative position ($\mathbf{r}_{i,j}$), it follows that: $\|\underline{\mu}\|_2 < l_{i,j}$ corresponds to an expected collision, $\|\underline{\mu}\|_2 > l_{i,j}$ corresponds to a collision not being expected, and $\|\underline{\mu}\|_2 = l_{i,j}$ corresponds to the transition between a collision-safe and a collision-unsafe condition. Hence, in the limit of low rela-

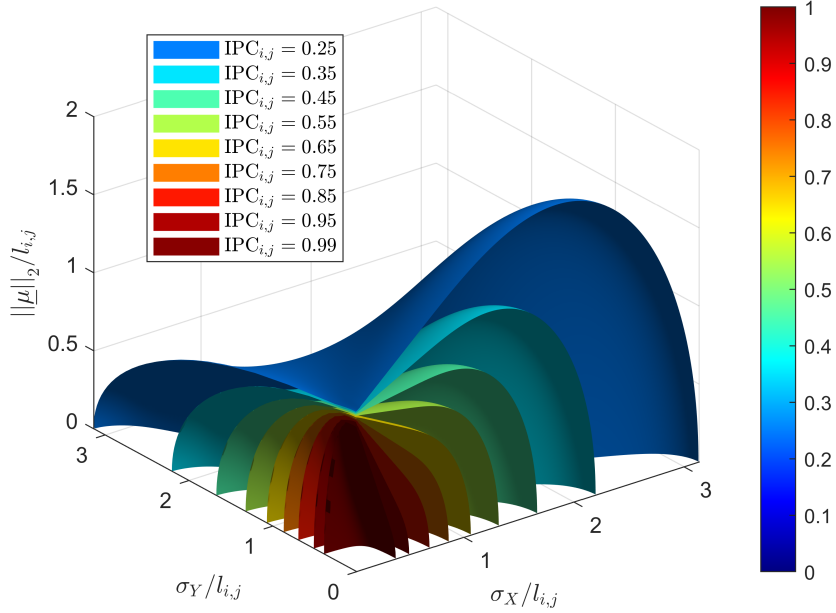


Figure 5.6: IPC as a function of statistical moments of two-dimensional (2D) normally distributed relative position (uncorrelated x - and y -axis $\underline{\mathbf{R}}_{i,j}$ -variances, relative position expectation along x -axis).

tive position covariance magnitude, the current simplified IPC model is a valid estimator of the deterministic i, j -collision indicator, $K_{i,j}$, which is given by Eq. 5.20.

$$K_{i,j} = \begin{cases} 1 & \text{if } \|\underline{\mathbf{r}}_{i,j}\|_2 < l_{i,j} \\ c_{\text{marginal}} & \text{if } \|\underline{\mathbf{r}}_{i,j}\|_2 = l_{i,j} \\ 0 & \text{if } \|\underline{\mathbf{r}}_{i,j}\|_2 > l_{i,j} \end{cases} \quad (5.20)$$

(Note: in this Chapter, $c_{\text{marginal}} = 0.5$; cf. Section 5.3.)

Second, the IPC probability dilution behavior for the case of high $\underline{\mathbf{R}}_{i,j}$ covariance magnitude (i.e., for $\sigma_X, \sigma_Y \rightarrow \infty$) is discussed. For $\|\underline{\boldsymbol{\mu}}\|_2 < l_{i,j}$, increasing either σ_X and σ_Y leads to IPC reduction-only probability dilution. The explanation for this behavior is that, while most of the $\underline{\mathbf{R}}_{i,j}$ -probability mass is contained within $V_{i,j}$ for low $\underline{\mathbf{R}}_{i,j}$ covariance magnitude, increasing the $\underline{\mathbf{R}}_{i,j}$ covariance magnitude causes the $\underline{\mathbf{R}}_{i,j}$ -probability mass to

become more sparsely spread over \mathbb{R}^2 (and hence, consistently away from $V_{i,j}$).

For $\|\underline{\mu}\|_2 > l_{i,j}$, increasing σ_X causes IPC growth first and then IPC reduction, whereas σ_Y causes IPC reduction; hence, IPC probability dilution is anisotropic for this expected relative position case. The explanation for the observed IPC decay anisotropy in response to $\underline{\mathbf{R}}_{i,j}$ covariance growth is evident from Figs. 5.4 and 5.5: for $\|\underline{\mu}\|_2 > l_{i,j}$, $\underline{\mathbf{R}}_{i,j}$ variance growth in the $V_{i,j}$ -radial direction introduces $\underline{\mathbf{R}}_{i,j}$ -probability mass into $V_{i,j}$ before such probability mass becomes inexorably diluted, whereas $\underline{\mathbf{R}}_{i,j}$ variance growth in the $V_{i,j}$ -orthogonal direction only dilutes the $\underline{\mathbf{R}}_{i,j}$ -probability mass already contained in $V_{i,j}$.

Although $\underline{\mathbf{R}}_{i,j}$ covariance magnitude is the primary factor in ascertaining transient IPC probability dilution behavior, the Euclidean norm of expected relative position ($\|\underline{\mu}\|_2$) sets an upper bound for the IPC values that may be observed over a wide range of relevant $\underline{\mathbf{R}}_{i,j}$ moment statistics, as summarized in Fig 5.7. This behavior is consistent with the interpretation of the IPC as an estimator of the deterministic i, j collision indicator $K_{i,j}$ (see Eq. 5.20), where the IPC converges to $K_{i,j}$ almost everywhere for $\|\underline{\mu}\|_2 \in [0, \infty)$ (see Eq. 5.19) in the limit of low $\underline{\mathbf{R}}_{i,j}$ covariance magnitude.

5.4.3 Transient IPC probability dilution behavior (effects of 2D relative position expectation nuisance and correlated covariance)

Within this Subsection, the effects of $\underline{\mathbf{R}}_{i,j}$ expectation nuisance and covariance correlation on transient IPC probability dilution are studied. For the short term Pc problem, the nuisance parameter $\underline{\lambda}$ encodes relative position unit vector direction information, as well as relative position rate information.[106] Since this Section is only concerned with IPC probability dilution, relative position rate information is ignored.

Given that the current simplified $\underline{\mathbf{R}}_{i,j}$ model is two-dimensional, relative position expectation nuisance information may be encoded by the angle λ , which represents a right-handed rotation (i.e., a z -axis rotation) of the x -axis-aligned expected relative position ($\underline{\mu}$). Hence, the nuisance parameter λ affects the relative position distribution (under the current

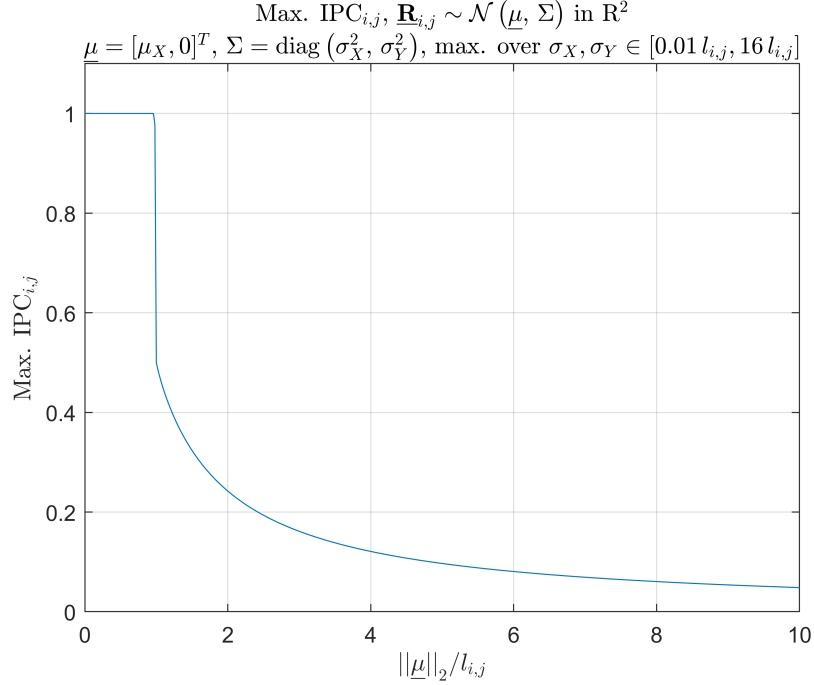


Figure 5.7: Maximum IPC as a function of the Euclidean norm of the expected value of two-dimensional (2D) normally distributed relative position (uncorrelated x - and y -axis $\mathbf{R}_{i,j}$ -variances, relative position expectation along x -axis).

simplified model) as given by $\mathbf{R}'_{i,j} \sim \mathcal{N}(\underline{\mu}'_\lambda, \Sigma)$, where

$$\underline{\mu}'_\lambda = \begin{bmatrix} \cos \lambda & -\sin \lambda \\ \sin \lambda & \cos \lambda \end{bmatrix} \underline{\mu} \quad (5.21)$$

where $\underline{\mu} = [\mu_X, 0]^T$ for some μ_X in \mathbb{R} , and where Σ is as given by Eq. 5.7.

Let $\mathbf{R}'_{i,j}$ have uncorrelated x - and y -axis variances (i.e., let $\rho = 0$ in Eq. 5.7). Then, due to the isotropy of the Euclidean norm, the $\mathbf{R}'_{i,j}$ -based IPC, $\text{IPC}'_{i,j}$ is equivalent to the IPC based on a modified relative position under nuisance ($\mathbf{R}''_{i,j}$), whose distribution is given by $\mathbf{R}''_{i,j} \sim \mathcal{N}(\underline{\mu}, \Sigma''_\lambda)$, where

$$\Sigma''_\lambda = \begin{bmatrix} (\sigma_{X,\lambda})^2 & \rho_\lambda \sigma_{X,\lambda} \sigma_{Y,\lambda} \\ \rho_\lambda \sigma_{X,\lambda} \sigma_{Y,\lambda} & (\sigma_{Y,\lambda})^2 \end{bmatrix} \quad (5.22)$$

$$\sigma_{X,\lambda} = \sqrt{\sigma_X^2 \cos^2 \lambda + \sigma_Y^2 \sin^2 \lambda} \quad (5.23)$$

$$\sigma_{Y,\lambda} = \sqrt{\sigma_X^2 \sin^2 \lambda + \sigma_Y^2 \cos^2 \lambda} \quad (5.24)$$

$$\rho_\lambda = \frac{(\sigma_Y^2 - \sigma_X^2) \sin(2\lambda)}{\sqrt{[(\sigma_Y^2 - \sigma_X^2) \sin(2\lambda)]^2 + 4\sigma_X^2 \sigma_Y^2}} \quad (5.25)$$

In other words, via Eq. 5.25, the nuisance parameter λ introduces $\underline{\mathbf{R}}_{i,j}$ -covariance correlation to the $\underline{\mathbf{R}}_{i,j}$ distribution which was formulated as uncorrelated in Subsection 5.4.1. Therefore, without loss of generality, the effects of the $\underline{\mu}$ -affecting nuisance parameter λ on transient IPC probability dilution are subsumed into the effects of $\underline{\mathbf{R}}_{i,j}$ -covariance correlation on transient IPC probability dilution.

As illustrated in Fig 5.8, the same anisotropy in the transient IPC probability dilution behavior which has previously been observed for uncorrelated $\underline{\mathbf{R}}_{i,j}$ -covariances is also expected for correlated $\underline{\mathbf{R}}_{i,j}$ -covariances because, even for the case of correlated $\underline{\mathbf{R}}_{i,j}$ -covariances, IPC decay-after-growth dilution is only possible if there is $\underline{\mathbf{R}}_{i,j}$ -variance growth in the $V_{i,j}$ -radial direction. In particular, it can be shown that for fixed $\underline{\mu}$, increasing $\underline{\mathbf{R}}_{i,j}$ -variance in the $V_{i,j}$ -orthogonal direction by a factor of $c^2 > 1$ is equivalent (from a Euclidean norm-based IPC perspective) to reducing the extent of the $V_{i,j}$ region in the y -axis direction, specifically, by replacing the collision region $V_{i,j}$ [an $(l_{i,j}): (l_{i,j})$ open circular disk] with an $(l_{i,j}): \left(\frac{l_{i,j}}{c}\right)$ open elliptical disk. Hence, increasing $\underline{\mathbf{R}}_{i,j}$ -variance in the $V_{i,j}$ -orthogonal direction causes monotonic IPC reduction (which is strictly monotonic if the support of the pdf of $\underline{\mathbf{R}}_{i,j}$ is \mathbb{R}^2).

The foregoing observations also imply that, for a correlated $\underline{\mathbf{R}}_{i,j}$ -covariance, $\underline{\mathbf{R}}_{i,j}$ -variance growth along either $\underline{\mathbf{R}}_{i,j}$ -covariance principal axis is also expected to cause IPC decay-after-growth dilution for the following reason: $\underline{\mathbf{R}}_{i,j}$ -variance growth along either $\underline{\mathbf{R}}_{i,j}$ -covariance principal axis (for a correlated $\underline{\mathbf{R}}_{i,j}$ -covariance) also induces $\underline{\mathbf{R}}_{i,j}$ -variance growth along the $V_{i,j}$ -radial direction.

Therefore, for a non-degenerate normal relative position ($\underline{\mathbf{R}}_{i,j}$) distribution, letting $\underline{\mu}$

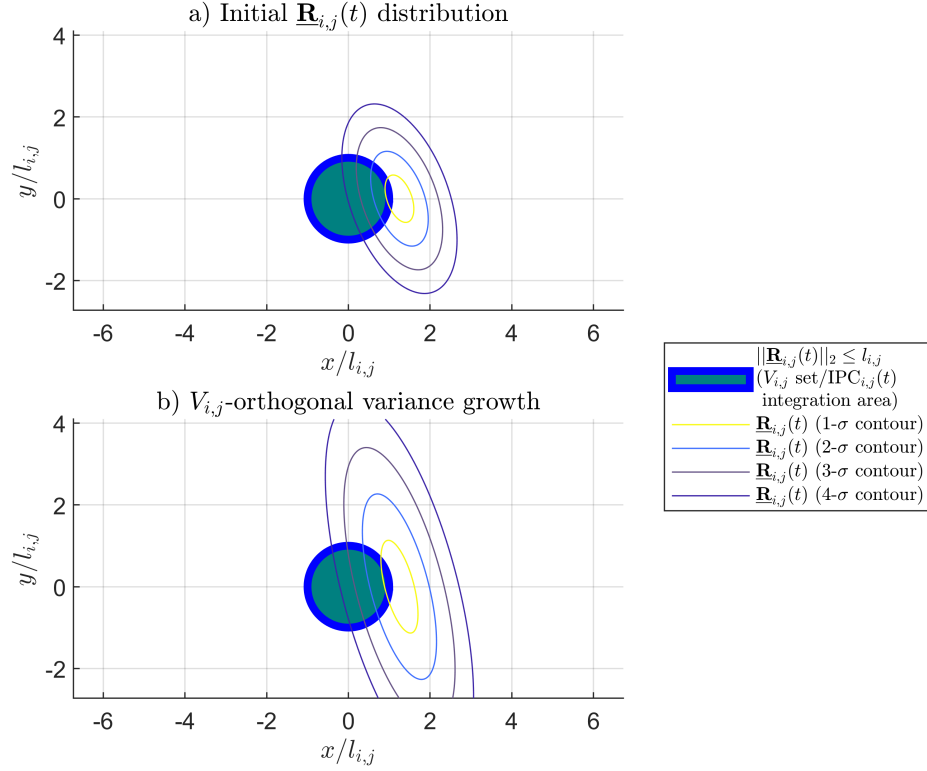


Figure 5.8: $V_{i,j}$ -orthogonal variance growth for a two-dimensional (2D) normally distributed relative position (correlated x - and y -axis $\mathbf{R}_{i,j}$ -variances).

denote the expected value of $\mathbf{R}_{i,j}$, transient IPC probability dilution behavior may be summarized as follows: IPC decay-only dilution occurs either when a collision is expected (as indicated by $\underline{\mu}$), or when 1) a collision is not $\underline{\mu}$ -expected, and 2) when there is no $\mathbf{R}_{i,j}$ -variance growth along the $V_{i,j}$ -radial direction; and IPC decay-after-growth dilution occurs when 1) a collision is not $\underline{\mu}$ -indicated, and 2) when there is $\mathbf{R}_{i,j}$ -variance growth along the $V_{i,j}$ -radial direction.

5.4.4 Applicability of IPC probability dilution (2D) to short-term Pc probability dilution

The short-term Pc formulation is mathematically equivalent to a specific realization of the $IPC_{i,j}$ paradigm laid out in this Section – specifically, the short-term Pc is a probability measure (over a Euclidean ball) of the projection of the relative position onto the conjunction plane at the instant of closest approach between two space objects.[23, 28, 106]

Therefore, short-term Pc measures are subject to asymptotic probability dilution be-

havior in the sense of Eq. 5.17.[72] Furthermore, short-term P_c measures are subject to anisotropy in transient P_c probability dilution behavior which is analogous to the anisotropy in transient IPC probability dilution behavior discussed in Subsections 5.4.2 and 5.4.3.

5.5 On miss distance-based statistical inference models for SFF COLRM

It has been proposed that statistical inference models that test hypotheses on inter-agent separation or miss distance (specifically, the violation of minimum inter-agent Euclidean distance constraints) are preferable and more informative for spacecraft collision risk assessment purposes than IPC/ P_c constructs,[105, 106] which may be regarded as models for statistical inference on deterministic collision risk indicators themselves,[104] as discussed in Sections 5.3 and 5.4. Miss distance-based statistical inference models utilize likelihood functions based on relative state observation data, as well as methods for calibrating such likelihood functions (e.g., Bayesian inference,[108] or modified likelihood roots [106]) in order to obtain estimates of inter-agent miss distance upon which collision safety-related hypotheses may be tested.

The outcome of miss distance-based statistical inference (i.e., significance probabilities with an interpretation akin to that of IPC/ P_c constructs [106]) may be employed in the development of actionable thresholds for deciding whether to execute spacecraft collision avoidance maneuvers, for example: by minimizing the expected cost of maneuver execution,[106, 108] or by employing the Wald Sequential Probability Ratio Test (WSPRT).[109, 110] These techniques have been employed in spacecraft collision assessment scenarios,[111, 112, 113, 114] although the ability to find reliable a priori statistics on miss distance (upon which to construct statistical models for collision safety hypothesis testing) is restricted except in limited contexts.[104]

Nevertheless, study of the formulation, applicability, or implementation of miss distance-based statistical inference models for SFF COLRM purposes is outside of the scope of this dissertation.

5.6 Summary

An overview of objections to employing probabilistic SFF collision risk indicators (derived from epistemic uncertainty representations) is provided. Such objections arise primarily from the probability dilution phenomenon, which is generally displayed by these indicators.

Hence, asymptotic and transient IPC probability dilution behavior is studied in a simplified, reduced-dimensionality context. The applicability of this study extends to short-term P_c measures because of the equivalence of their mathematical formulation to that utilized by the aforementioned IPC study.

The legitimacy of employing probabilistic SFF collision risk indicators is argued from the relative covariance low-magnitude limiting behavior displayed by these indicators, under which deterministic SFF collision indicators are adequately approximated by probabilistic SFF collision risk indicators.

Nevertheless, although not employed in this dissertation, because statistical inference models for spacecraft collision safety-related that employ miss distance-based likelihood functions may improve the quality and extent of safety-related insights over those provided by IPC/ P_c constructs, such statistical inference models are briefly discussed.

CHAPTER 6
SPACECRAFT FORMATION COLLISION RISK QUANTIFICATION (PART 1) –
STOCHASTIC CONVERGENCE OF SOBOL-BASED MAHALANOBIS SHELL
SAMPLING (MSS) COLLISION PROBABILITY COMPUTATION

Sample-based computation of the joint-time probability of collision (P_c) motivates developing the Mahalanobis Shell Sampling (MSS) algorithm, which samples non-degenerate normal random variables, enabling rare event simulation without unduly penalizing sample size. The MSS method has unbiased estimators in sample mean and covariance, and it may achieve arbitrary precision when approximating probability measures. For Clohessy-Wiltshire relative orbital dynamics, computational MSS exponential rates of error convergence (in the mean-square-error (MSE) sense) are shown to improve by one order of magnitude (for sample mean and covariance) over Monte Carlo; when reproducing the instantaneous probability of collision (IPC), MSS has a comparable MSE convergence rate performance to Monte Carlo.

6.1 Introduction

The problem of spacecraft formation flying (SFF) collision risk management (COLRM) differs from the standard obstacle avoidance problem in robotics because of the instability of relative orbital dynamics, the lack of spatial restraints in spacecraft motion (in essence, six degrees of freedom), and the limitations in sensing accuracy and onboard resources.[30] These facts imply the need to quantify uncertain indicators of collision risk, to make decisions based on acceptable risk thresholds, and to plan appropriate corrective actions to

reduce quantifiable collision risk accordingly.[29, 27, 28, 13] Hence, the process of SFF COLRM (i.e., collision risk quantification, interpretation and decision-making, and reduction) hinges not only on the choice of suitable collision risk indicators, but also on their efficient computation.[12]

Since the relative position between space objects cannot be deterministically known, whether two such objects are colliding is a question that may only be ascertained probabilistically.[42] Hence, probability measures associated with the likelihood of collision events have been explored considerably in SFF research, with the purpose of employing these measures as probabilistic indicators of collision risk, with particular focus on the P_c , which is the probability of collision over a finite time interval, and the instantaneous probability of collision (IPC). [31, 43, 44]

This Chapter focuses on the computation of probabilistic collision risk indicators via quasi-random sampling. One consequence of the probability dilution phenomenon in relative orbital dynamics is that, operationally, certain practitioners in the spacecraft conjunction assessment community adopt a threshold of significance for P_c values of 1×10^{-7} (that is, P_c values above this threshold are considered significant, and vice versa).[45, 29] Via the construct of projection instantaneous probabilities of collision, it could be argued that this threshold of significance may also be valid for IPC values in an SFF COLRM context [28] – and hence, this threshold may be regarded as valid for P_c values in this context as well.

Thus, for sampling algorithms employed to estimate SFF probabilistic collision risk indicators, it would be beneficial to produce samples that allow for accurately reproducing low-valued probability measures – which implies the need to account for probabilistic outliers consistently.[46, 47] In particular, it would be helpful if such algorithms achieve this result in a systematic fashion, and without requiring unmanageably large sample sizes. However, the Monte Carlo method does not meet these criteria because, in order to reproduce low probability values, this method is expected to require samples whose sizes have an

inversely proportional relationship to the probability values in question.[28] Additionally, there are no deterministic guarantees that a specific fixed-size Monte Carlo sample realization will contain any elements within an arbitrary Mahalanobis distance of the sample mean.

Therefore, the main goal of this Chapter is twofold: first, to develop a sample algorithm suitable for probabilistic collision risk computation, which may be achieved in three steps: 1) through a judicious choice of boundary between significant and ignorable sample points, 2) by stratifying the significant sample space, and 3) by sampling within each stratum in an efficient, space-filling manner; and second, to validate practical use of such sampling algorithm by characterization of its computational convergence properties. Because there may exist multiple probability measures of interest in the same sample space (e.g., any IPC or P_c), it is that such outcome samples would reflect the original distribution as accurately as possible. Hence, a secondary goal of this Chapter is to develop unbiased estimators for sample mean and covariance, which may be used not only to validate the quality of specific realizations of finite samples, but also as building blocks in the development of sample-based filtering schemes for spacecraft relative navigation. This result would create natural efficiencies in the integration of SFF guidance, navigation, and control (GN&C) and COLRM tasks, as collision risk quantification requires an uncertain description of relative dynamic state knowledge, which operationally would be based on the outcome of relative state estimation.

This Chapter is organized as follows. First, this Chapter will motivate the use of sampling algorithms for approximating the probability of joint-time events, i.e., events that involve the application of a single logical condition over a finite time interval (such as the P_c) after propagating an initial distribution through a dynamic process. Under certain conditions, it will be shown that estimating the probability of joint-time events implies the need for computing probabilities over a number of sets that is a combinatorial function of the number of timesteps into which the time interval is subdivided. Second, the

Mahalanobis Shell Sampling (MSS) algorithm is developed to geometrically sample from non-degenerate multivariate, normal distributions in a way that allows for obtaining an arbitrary amount of sample points that may be regarded as probabilistic outliers without unduly penalizing sample size, for the purpose of reproducing the probability of rare events (specifically, those involving probability distribution tails). Third, MSS estimators for the sample mean and covariance are presented which are unbiased over invertible linear transformations, and MSS estimators for probability measures (over measurable subsets) are presented which have asymptotically unbiased convergence. In particular, MSS probability measure estimators are applied to samples in relative dynamic state space for approximating probabilistic collision risk indicators. Fourth, a computational investigation of MSS stochastic convergence properties is undertaken for reproducing the sample mean, covariance, and IPC, in order to validate application of the MSS method in an SFF collision risk quantification example. Together, these contributions make the MSS algorithm an attractive methodology in the contexts of SFF COLRM and SFF GN&C.

6.2 Background

6.2.1 Notation adjustments for this Chapter

The Notation and Nomenclature used in this Chapter, as well as the deterministic definition of collision events (derived from relative-attitude abstraction, and induced by arbitrary a -norm balls in relative position space), and the definition of stochastic collision risk measures (in both an instantaneous and joint-time sense), are addressed in Chapter 2.

Such general Notation and Nomenclature are made more specific for this Chapter as follows. First, the balls and spheres used are only those with respect to the Euclidean norm; additionally, only open balls are employed. (See Definition 1.) Hence, implicitly $a = 2$ or $a = \text{Eu}$; consequently, the a -norm symbol is omitted throughout this Chapter. (See Section 2.2.) Note: when the dimension of elements in $\mathbb{B}_r^s(\underline{x})$ is implicit, it is referred to as $\mathbb{B}_r(\underline{x})$ for simplicity. Additionally, the symbol “ $\mathbb{S}^{(s-1)}$ ” denotes $\mathbb{S}_1^{(s-1)}(\mathbf{0}_{s \times 1})$, i.e.,

the unit $(s - 1)$ -sphere centered at the origin. From the aforementioned, it follows that collision sets and probabilities are induced from instantaneous collision conditions based on open balls with respect to the Euclidean norm in relative position space.

Second, the formulation for collision sets and stochastic collision risk measures, whether instantaneous or joint-time, are based on time-invariant joint-hard body radii. In other words, within this Chapter, formulations of instantaneous collision sets and the IPC, as well as JTC set and the Pc measure, implicitly assume that the corresponding joint HBR is constant throughout the propagation horizon.

The foregoing assumptions are reflected in the notation adjustments concerning the following sets and probabilities:

- Instantaneous collision set in relative position space, denoted as $V_{i,j}$ (see Notation 5)
- Instantaneous collision set in relative state space, denoted as $C_{i,j}$ (see Eq. 2.30)
- Instantaneous probability of collision, $IPC_{i,j}(t)$ (see Definition 7)
- Joint-time collision set, $JTC_{i,j}[t_0, t_f]$ (see Definition 9)
- Joint-time probability of collision, $Pc_{i,j}[t_0, t_f]$ (see Definition 10)

6.2.2 Motivation for a sampling algorithm for Pc computation

Proposition 21 (Measurability of JTC[38]). Let Remark 8 hold. Assume the function $F_{t_0}(t, \mathbf{x})$ (see Eq. 2.38) is continuous in t and \mathbf{x} . Then, the $JTC_{i,j}[t_0, t_f]$ set (see Definition 9) is an open set (and hence, it is a measurable subset of $\mathbb{R}^{n\mathbf{x}}$). Furthermore, the $JTC_{i,j}[t_0, t_f]$ set can be computed as a countable union of sets, as given by

$$JTC_{i,j}[t_0, t_f] = \bigcup_{c \in \mathbb{Q} \cap [0,1]} [F_{h_T(c), t_0}]^{-1} [C_{i,j}(h_T(c))] \quad (6.1)$$

where $F_{t,t_0} : \mathbb{R}^{n_{\mathbf{x}}} \rightarrow \mathbb{R}^{n_{\mathbf{x}}}$ is as defined in Eq. 2.39, and $h_T : [0, 1] \rightarrow [t_0, t_f]$ is defined as

$$h_T(c) = t_0 + (t_f - t_0)c \quad (6.2)$$

for c in $[0, 1]$. ◇

Proof. This result follows from Proposition 17, by letting the a -norm be given by the Euclidean norm (i.e., $a = \text{Eu}$, or $a = 2$), and by letting the joint-HBR time history be constant.

That is, $l_{i,j} : [t_0, t_f] \rightarrow (0, \infty)$ is given by

$$l_{i,j}(t) = L$$

for some scalar constant $L > 0$, for $t \in [t_0, t_f]$. □

Proposition 21 gives justification for a discrete-time approximation to the JTC, specifically, as given by

$$\text{JTC}_{i,j}[t_0, t_f] = \bigcup_{N \in \mathbb{N}} \text{JTC}_{i,j}^N[t_0, t_f] \quad (6.3)$$

where the set $\text{JTC}_{i,j}^N[t_0, t_f]$ is an equal-step discretization of $\text{JTC}_{i,j}[t_0, t_f]$ given by

$$\text{JTC}_{i,j}^N[t_0, t_f] = \bigcup_{k=0}^N B_{N,k} \quad (6.4)$$

$$B_{N,k} = \left[F_{h_T(\frac{k}{N}), t_0} \right]^{-1} \left[C_{i,j} \left(h_T \left(\frac{k}{N} \right) \right) \right] \quad (6.5)$$

for $k \in \{0, \dots, N\}$. It should be noted that, for such a k ,

$$\begin{aligned} \text{IPC}_{i,j} \left(h_T \left(\frac{k}{N} \right) \right) &= p \left(\underline{\mathbf{x}}_{i,j}(t) \in C_{i,j} \left(h_T \left(\frac{k}{N} \right) \right) \right) \\ &= p \left(\underline{\mathbf{x}}_{i,j}(t_0) \in \left[F_{h_T(\frac{k}{N}), t_0} \right]^{-1} \left[C_{i,j} \left(h_T \left(\frac{k}{N} \right) \right) \right] \right) \\ &= p \left(\underline{\mathbf{x}}_{i,j}(t_0) \in B_{N,k} \right) \end{aligned} \quad (6.6)$$

It follows that the N -discrete timestep approximation to the Pc , denoted by $Pc_{i,j}^N[t_0, t_f]$, may be computed as

$$\begin{aligned}
Pc_{i,j}^N[t_0, t_f] &= p(\underline{\mathbf{x}}_{i,j}(t_0) \in \text{JTC}_{i,j}^N[t_0, t_f]) \\
&= \sum_{k=0}^N \text{IPC}_{i,j} \left(h_T \left(\frac{k}{N} \right) \right) + \sum_{k=1}^N (-1)^k \sum_{l=1}^{\binom{N+1}{k+1}} p \left(\underline{\mathbf{x}}_{i,j}(t_0) \in \bigcap_{n \in \Upsilon(l|N,k)} B_{N,n-1} \right) \quad (6.7)
\end{aligned}$$

where $\Upsilon(l|N, k)$ is the l^{th} combination of $\binom{N+1}{k+1}$. For example, for $N = 3$, after temporarily denoting $p(\underline{\mathbf{x}}_{i,j}(t_0) \in B_{N,k})$ as $p(B_{N,k})$, the expression in Eq. 6.7 becomes

$$\begin{aligned}
Pc_{i,j}^N[t_0, t_f] &= \left[\text{IPC}_{i,j}(t_0) + \text{IPC}_{i,j} \left(\frac{2t_0 + t_f}{3} \right) + \text{IPC}_{i,j} \left(\frac{t_0 + 2t_f}{3} \right) + \text{IPC}_{i,j}(t_f) \right] \\
&\quad - [p(B_{N,0} \cap B_{N,1}) + p(B_{N,0} \cap B_{N,2}) + p(B_{N,0} \cap B_{N,3}) \\
&\quad + p(B_{N,1} \cap B_{N,2}) + p(B_{N,1} \cap B_{N,3}) + p(B_{N,2} \cap B_{N,3})] \\
&\quad + [p(B_{N,0} \cap B_{N,1} \cap B_{N,2}) + p(B_{N,0} \cap B_{N,1} \cap B_{N,3}) \\
&\quad + p(B_{N,0} \cap B_{N,2} \cap B_{N,3}) + p(B_{N,1} \cap B_{N,2} \cap B_{N,3})] \\
&\quad - p(B_{N,0} \cap B_{N,1} \cap B_{N,2} \cap B_{N,3}) \quad (6.8)
\end{aligned}$$

This example illustrates that, even for a finite-timestep Pc approximation, whose computation scheme relies on propagation of relative state statistics over an equal-step discretization of the propagation horizon, the number of distinct sets whose probability must be computed (for an unbiased estimate) is a combinatorial function of the number of timesteps. This process is illustrated for the case of two timesteps in Figure 6.1, which follows the same example listed on Figure 2.3, specifically, focusing on the regions of the support of the initial relative state pdf which indicate collision at either timestep, as well as the corresponding probability measures associated with each subset.

These observations motivate use of sampling schemes, from relative orbital dynamic state probability distributions, with application to finite-timestep Pc computation. For a

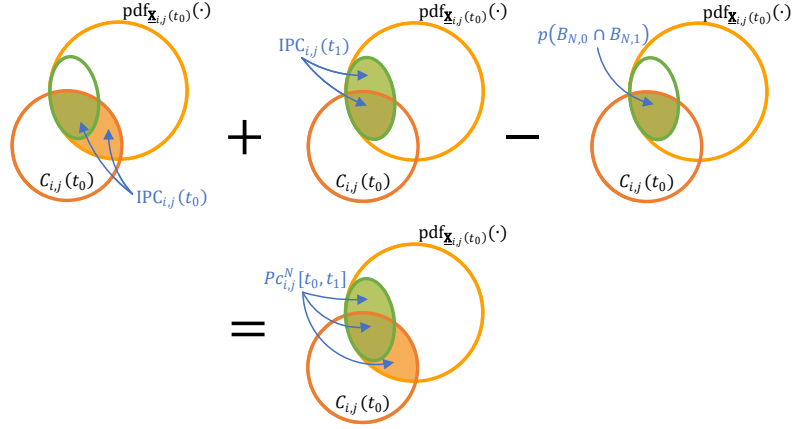


Figure 6.1: Computation of finite-step approximation to the P_C , two timesteps ($N = 1$).

fixed timestep length, and for a given logical condition, sampling schemes enable sequential computation of joint-time probabilities via the following process: a) performing logical checks via sequential OR operations on each element of the sample as it is propagated over time, and b) approximating the corresponding probability of the joint-time logical condition as a function of the weights of those points which have been flagged at any previous timestep. Hence, for $PC_{i,j}^N[t_0, t_f]$ approximations, employing sampling schemes is preferable to direct numerical integration, because the former method only requires sequentially checking a single logical condition over time, while the latter method requires ascertaining the locations of combinatorially-many regions in initial relative state space, as well as computing the corresponding probability masses within each region. Furthermore, sample schemes allow adjusting timestep length arbitrarily, which allows for easily increasing the resolution of joint-time probabilities.

6.2.3 Review of Monte Carlo Stochastic Convergence Properties

A review of the definition of Monte Carlo (MC) sample estimators of random variable mean and covariance, of MC finite and asymptotic error properties for these estimators, and of probability measure estimators, is discussed in Appendix B. This review is undertaken in order to provide a theoretical baseline upon which to quantitatively compare the

performance of the MSS algorithm.

6.3 Theory

In the context of random variables with non-degenerate, normal distributions, the Mahalanobis Shell Sampling (MSS) algorithm is designed to produce weighted samples that have a spatially and statistically “uniform” distribution within compact, simply connected sets whose boundaries consist of points with constant Mahalanobis distance. The purpose of this process is to “directly” sample points which may be regarded as probabilistic outliers. This allows for studying the properties of rare events (that is, events with low probability) without unduly penalizing sample size.

6.3.1 Probabilistic results on Mahalanobis shells

Within this subsection, let $\underline{X} \sim \mathcal{N}(\underline{\mu}, \Sigma)$, where $\underline{\mu} \in \mathbb{R}^s$, $\Sigma \in \mathbb{R}^{s \times s}$, $\Sigma > 0$. The Mahalanobis distance in \underline{X} , $D_{\underline{X}} : \mathbb{R}^s \rightarrow [0, \infty)$, is defined as[68, 115, 116]

$$D_{\underline{X}}(\underline{x}) \doteq \sqrt{(\underline{x} - \underline{\mu})^T \Sigma^{-1} (\underline{x} - \underline{\mu})} \quad (6.9)$$

for $\underline{x} \in \mathbb{R}^s$. Note: it is meaningful to define the Mahalanobis distance for general probability distributions, and this is often done to evaluate the presence of outlier points for empirical, sample distributions of arbitrary phenomena.[115, 116, 117, 118] However, use of the Mahalanobis distance in this work is restricted to non-degenerate normal distributions.

Let $0 \leq d < \infty$. Then, the d -Mahalanobis contour and volume of \underline{X} , $L_d(\underline{X})$ and $V_d(\underline{X})$, respectively, are the sets defined as

$$L_d(\underline{X}) = \{\underline{x} \in \mathbb{R}^s : D_{\underline{X}}(\underline{x}) = d\} \quad (6.10)$$

$$V_d(\underline{X}) = \{\underline{x} \in \mathbb{R}^s : D_{\underline{X}}(\underline{x}) \leq d\} \quad (6.11)$$

Figure 6.2 illustrates the notions of Mahalanobis contour and volume for a non-degenerate, normally distributed (finite-dimensional) random variable \underline{X} . The d -Mahalanobis volumes $V_d(\underline{X})$ are hypervolumes (specifically, hyperellipsoids) while the d -Mahalanobis contours $L_d(\underline{X})$ are hypersurfaces (specifically, hyperellipses) in s -dimensions.

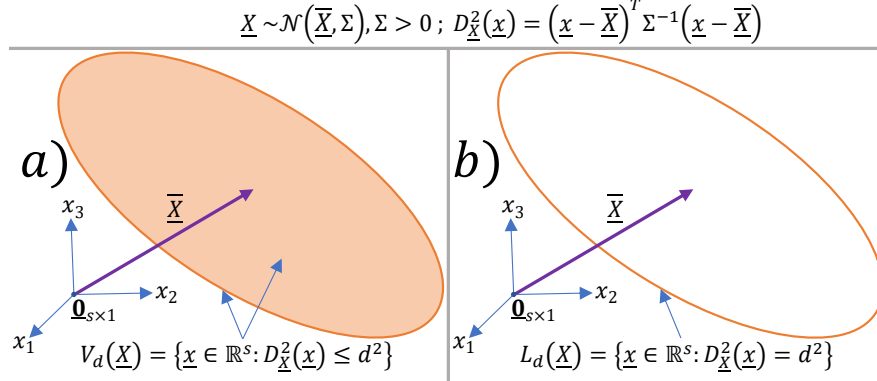


Figure 6.2: d -Mahalanobis volume and contour: a) V_d and b) L_d , respectively.

Let $0 \leq d_1 < d_2 < \infty$. Then, the d_1, d_2 -Mahalanobis shell of \underline{X} , $V_{d_1}^{d_2}(\underline{X})$, is defined as

$$V_{d_1}^{d_2}(\underline{X}) = \{\underline{x} \in \mathbb{R}^s : d_1 \leq D_{\underline{X}}(\underline{x}) \leq d_2\} \quad (6.12)$$

In the context of multivariate normal probability distributions, it is a known theoretical result that[46]

$$p_{\underline{X}}(V_{d_1}^{d_2}(\underline{X})) = p(\underline{X} \in V_{d_1}^{d_2}(\underline{X})) = \text{cdf}_{\chi_s^2}((d_2)^2) - \text{cdf}_{\chi_s^2}((d_1)^2) \geq 0 \quad (6.13)$$

For nondegenerate, normal random variables, as illustrated in Figure 6.3, probability measures over s -hypervolumes whose boundaries are $(s - 1)$ -hypersurfaces of constant Mahalanobis distances (say, d_1 and d_2) can be found analytically as functions that depend only on d_1 and d_2 (through chi-square cdfs), regardless of the statistics and dimension of the random variable.

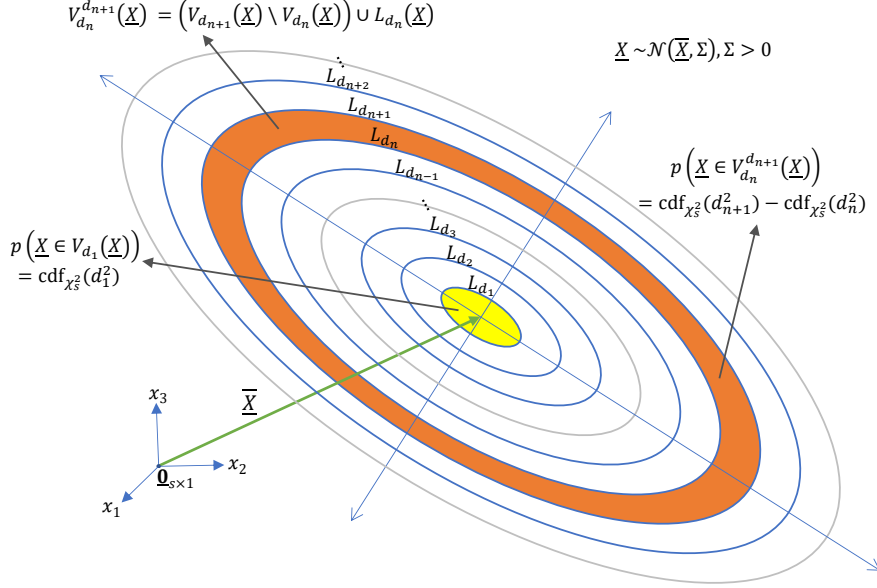


Figure 6.3: Probability measures of normally distributed random variables over s -hypervolumes whose boundaries are $(s - 1)$ -hypersurfaces (of constant d -Mahalanobis distance).

6.3.2 Introducing the Mahalanobis Shell Sampling (MSS) algorithm

Eq. 6.13 is the theoretical basis for the MSS algorithm, which considers a collection of evenly spaced Mahalanobis shells $\{V_{d_{l-1}}^{d_l}(\underline{X})\}$, $l \in S_{N_{\text{sh}}}$, where $N_{\text{sh}} \in \mathbb{N}$, $d_{\text{max}} > 0$, and

$$d_l = d_{\text{max}} \left(\frac{l}{N_{\text{sh}}} \right) \text{ for } l \in \{0, \dots, N_{\text{sh}}\} \quad (6.14)$$

From a measure-theoretic perspective, these shells are non-overlapping in the sense that, for $l \in S_{(N_{\text{sh}}-1)}$,

$$V_{d_l}^{d_{l+1}}(\underline{X}) \cap V_{d_{l-1}}^{d_l}(\underline{X}) = L_{d_l}(\underline{X}) \quad (6.15)$$

and, since non-degenerate normal random variables in \mathbb{R}^s have probability measures that are absolutely continuous with respect to the Lebesgue measure in \mathbb{R}^s , the fact that any d -Mahalanobis contour has zero measure in \mathbb{R}^s implies that

$$p_{\underline{X}} \left(V_{d_l}^{d_{l+1}}(\underline{X}) \cap V_{d_{l-1}}^{d_l}(\underline{X}) \right) = p_{\underline{X}}(L_{d_l}(\underline{X})) = 0 \quad (6.16)$$

Then, as shown in Algorithm 1, for $l \in S_{N_{\text{sh}}}$, a uniform, i.i.d. sample of the unit $(s - 1)$ -sphere, $\mathbb{S}^{(s-1)}$, is transformed into a sample of $V_{d_{l+1/2}}^{d_l}(\underline{X})$, which is then distributed more uniformly over $V_{d_{l-1}}^{d_l}(\underline{X})$ through use of a uniform, i.i.d. sample of the unit interval $[0, 1]$ that is also independent of the $\mathbb{S}^{(s-1)}$ sample. Then, the collective weight of each shell is assigned in accordance with Eq. 6.13, and weights within each shell are evenly distributed amongst its respective points.

```

Input:  $N_{\text{sh}}, N_{\text{ss}}, s \in \mathbb{N}; 0 < d_{\text{max}} < \infty$ 
Output: MSS sample  $\{\tilde{x}_{l,q}\}$ , MSS sample weights  $\{w_{l,q}\}, \{W_l\}; l \in S_{N_{\text{sh}}},$ 
            $q \in S_{N_{\text{ss}}}$ 
Data:  $\underline{\mu} \in \mathbb{R}^s, \Sigma \in \mathbb{R}^{s \times s} > 0$ ; assumption that  $\underline{X} \sim \mathcal{N}(\underline{\mu}, \Sigma)$ 
1  $N_{\text{samples}} \leftarrow N_{\text{sh}} N_{\text{ss}}$ 
2  $\{\underline{z}_k\}_{k \in \{1, \dots, N_{\text{samples}}\}} \leftarrow$  output of unit  $(s - 1)$ -sphere uniform, i.i.d. sampling
   algorithm
3  $\{u_k\}_{k \in \{1, \dots, N_{\text{samples}}\}} \leftarrow$  output of uniform, i.i.d. sample on  $[0, 1]$  that is independent
   from  $\{\underline{z}_k\}_{k \in \{1, \dots, N_{\text{samples}}\}}$ 
4  $\delta_d \leftarrow d_{\text{max}}/N_{\text{sh}}$ 
5  $\mathbf{U}, \mathbf{Q} \in \mathbb{R}^{s \times s} \leftarrow$  such that  $\Sigma = \mathbf{U}\mathbf{Q}\mathbf{U}^T$  // output of singular value
   decomposition
6  $\Sigma^{1/2} \leftarrow \mathbf{U}\mathbf{Q}^{1/2}\mathbf{U}^T$ 
7 for  $l \leftarrow 1$  to  $N_{\text{sh}}$  do
8    $d_l \leftarrow (l - 1)\delta_d$ 
9    $W_l \leftarrow \text{cdf}_{\chi_s^2}((d_l + \delta_d)^2) - \text{cdf}_{\chi_s^2}((d_l)^2)$  // probability mass in  $l^{\text{th}}$ 
   ( $s$ -dimensional) Mahalanobis shell
10  for  $q \leftarrow 1$  to  $N_{\text{ss}}$  do
11     $k \leftarrow (l - 1)N_{\text{ss}} + q$ 
12     $\tilde{x}_{l,q} \leftarrow \underline{\mu} + (d_l + u_k\delta_d) [\Sigma^{1/2}] \underline{z}_k$  // point in  $l^{\text{th}}$  Mahalanobis shell
13     $w_{l,q} \leftarrow W_l/N_{\text{ss}}$  // same weight for points in the same
   Mahalanobis shell
14 return  $\{\tilde{x}_{l,q}\}, \{w_{l,q}\}, \{W_l\}; l \in S_{N_{\text{sh}}}, q \in S_{N_{\text{ss}}}$ 

```

Algorithm 1: Generation of MSS sample, general s -dimensional, non-degenerate normal random vector.

The cutoff Mahalanobis distance, $0 < d_{\text{max}} < \infty$, is used to determine the probabilistic extent of the points that are preemptively excluded from an MSS sample. Noting that

$$\bigcup_{l=1}^{N_{\text{sh}}} V_{d_{l-1}}^{d_l}(\underline{X}) = V_{d_{\text{max}}}(\underline{X}) \quad (6.17)$$

then, the constant $p_{\text{exc}} \in (0, 1)$ is defined as

$$p_{\text{exc}} = p_{\underline{X}} \left([V_{d_{\text{max}}}(\underline{X})]^C \right) = 1 - p_{\underline{X}}(V_{d_{\text{max}}}(\underline{X})) = 1 - \text{cdf}_{\chi_s^2}((d_{\text{max}})^2) \quad (6.18)$$

and it represents the collective probability of all the points that are precluded from entering an MSS sample. Hence, a suitable value of d_{max} depends on the dimension s and the needs of the user at hand. Table 6.1 shows values of p_{exc} as function of some representative dimensions and values of d_{max} .

Table 6.1: Representative values of p_{exc} as a function of dimension (s) and cutoff Mahalanobis distance (d_{max}).

p_{exc}	$s = 1$	$s = 3$	$s = 6$	$s = 12$
$d_{\text{max}} = 1$	0.3173	0.8013	0.9856	1.0000
$d_{\text{max}} = 3$	0.0027	0.0293	0.1736	0.7029
$d_{\text{max}} = 4$	6.3342×10^{-5}	0.0011	0.0138	0.1912
$d_{\text{max}} = 7$	2.5596×10^{-12}	1.3045×10^{-10}	7.4559×10^{-9}	2.0917×10^{-6}

6.3.3 Theoretical guarantees of the MSS algorithm

In this Subsection, unbiased estimators for the sample mean, covariance, and probability measures that may be obtained through an MSS sample are presented. Such unbiased estimators require introducing the following constants:

$$S_1 = \sum_{l=1}^{N_{\text{sh}}} W_l = \text{cdf}_{\chi_s^2}((d_{\text{max}})^2) \quad (6.19)$$

$$S_2 = \sum_{l=1}^{N_{\text{sh}}} W_l^2 \quad (6.20)$$

$$S_3 = \frac{1}{s} \left(\frac{d_{\text{max}}}{N_{\text{sh}}} \right)^2 \sum_{l=1}^{N_{\text{sh}}} W_l \left(l - \frac{1}{2} \right)^2 \quad (6.21)$$

$$S_4 = \frac{1}{s} \left(\frac{d_{\text{max}}}{N_{\text{sh}}} \right)^2 \sum_{l=1}^{N_{\text{sh}}} W_l^2 \left(l - \frac{1}{2} \right)^2 \quad (6.22)$$

$$D_1 = \frac{1}{12s} \left(\frac{d_{\text{max}}}{N_{\text{sh}}} \right)^2 \quad (6.23)$$

Proposition 22 (Unbiased MSS estimators in sample mean, covariance, and probability).

Let $s, N_{\text{sh}}, N_{\text{ss}} \in \mathbb{N}$, and let $0 < d_{\text{max}} < \infty$. Let $\underline{X} \sim \mathcal{N}(\underline{\mu}, \Sigma)$, where $\underline{\mu} \in \mathbb{R}^s$, $\Sigma \in \mathbb{R}^{s \times s}$, $\Sigma > 0$. Let $\{\tilde{\underline{x}}_{l,q}\}$, $l \in S_{N_{\text{sh}}}$, $q \in S_{N_{\text{ss}}}$ be an MSS sample drawn in accordance with Algorithm 1, with sample weights $\{w_{l,q}\}$ and $\{W_l\}$. Let the constants H and G be defined as

$$H = \frac{1}{S_1} = \frac{1}{\text{cdf}_{\chi_s^2}((d_{\text{max}})^2)} \quad (6.24)$$

$$G = \left[1 + \frac{H^2 S_2}{N_{\text{ss}}}\right] S_3 - \frac{2(HS_4)}{N_{\text{ss}}} + D_1 \left(S_1 - \frac{HS_2}{N_{\text{ss}}}\right) \quad (6.25)$$

Let $\hat{\underline{\mu}}_{\text{MSS}}$ and $\hat{\Sigma}_{\text{MSS}}$ be defined as

$$\hat{\underline{\mu}}_{\text{MSS}} = H \sum_{l=1}^{N_{\text{sh}}} \left(\frac{W_l}{N_{\text{ss}}}\right) \sum_{q=1}^{N_{\text{ss}}} \tilde{\underline{x}}_{l,q} \quad (6.26)$$

$$\hat{\Sigma}_{\text{MSS}} = \frac{1}{G} \sum_{l=1}^{N_{\text{sh}}} \left(\frac{W_l}{N_{\text{ss}}}\right) \sum_{q=1}^{N_{\text{ss}}} (\tilde{\underline{x}}_{l,q} - \hat{\underline{\mu}}_{\text{MSS}}) (\tilde{\underline{x}}_{l,q} - \hat{\underline{\mu}}_{\text{MSS}})^T \quad (6.27)$$

Then, $\hat{\underline{\mu}}_{\text{MSS}}$ and $\hat{\Sigma}_{\text{MSS}}$ are unbiased estimators of $\underline{\mu}$ and Σ ; that is,

$$\mathbb{E}[\hat{\underline{\mu}}_{\text{MSS}}] = \underline{\mu} \quad (6.28)$$

$$\mathbb{E}[\hat{\Sigma}_{\text{MSS}}] = \Sigma \quad (6.29)$$

Furthermore, let $E \subseteq \mathbb{R}^s$ be a measurable subset of \mathbb{R}^s , and let $f_E : \mathbb{R}^s \rightarrow \{0, 1\}$ be the characteristic function of E . Let $p_E = p_{\underline{X}}(E) = p(\underline{X} \in E)$. Let $\hat{p}_{E,\text{MSS}}$ be defined as

$$\hat{p}_{E,\text{MSS}} = \sum_{l=1}^{N_{\text{sh}}} \left(\frac{W_l}{N_{\text{ss}}}\right) \sum_{q=1}^{N_{\text{ss}}} f_E(\tilde{\underline{x}}_{l,q}) \quad (6.30)$$

Assume $E \subseteq V_{d_{\text{max}}}(\underline{X})$. Then, in the limit, $\hat{p}_{E,\text{MSS}}$ is an unbiased estimator of p_E ; that is,

$$\lim_{N_{\text{sh}} \rightarrow \infty} \mathbb{E}[\hat{p}_{E,\text{MSS}}] = p_E \quad (6.31)$$

If $E \not\subseteq V_{d_{\max}}(\underline{X})$, then, the error between p_E and $\mathbb{E}[\widehat{p}_{E,\text{MSS}}]$, in the limit, is bounded above by

$$\left| p_E - \lim_{N_{\text{sh}} \rightarrow \infty} \mathbb{E}[\widehat{p}_{E,\text{MSS}}] \right| = p_E - \lim_{N_{\text{sh}} \rightarrow \infty} \mathbb{E}[\widehat{p}_{E,\text{MSS}}] \leq p_{\text{exc}} \quad \diamond \quad (6.32)$$

Proof. This result is an aggregation of the results listed in Propositions 72 and 72 (for unbiased MSS sample mean and covariance estimators, respectively), as well as in Proposition 70 (for asymptotically unbiased MSS estimators of probability measures). Such intermediate results are described in Chapter F. \square

It must be noted that the sample mean and covariance estimators proposed in Proposition 22 hold under invertible linear transformations; hence, they are applicable to initial distributions that are propagated through linear dynamics. However, these estimators are not generally applicable as estimators for sample mean and covariance after propagation through arbitrary nonlinear processes. This is the subject of future work.

In general, it cannot be guaranteed that an arbitrary measurable subset (e.g., $E \subseteq \mathbb{R}^s$) of interest will be contained in $V_{d_{\max}}(\underline{X})$, especially if the MSS sample points in question are propagated through arbitrary dynamic processes. However, Proposition 22 implies that if p_{exc} is “sufficiently” low, then, in the limit, $\widehat{p}_{E,\text{MSS}}$ is approximately an unbiased estimator for p_E . That is, for “sufficiently” high d_{\max} ,

$$\lim_{N_{\text{sh}} \rightarrow \infty} \mathbb{E}[\widehat{p}_{E,\text{MSS}}] \approx p_E \quad (6.33)$$

Computational formulae for these unbiased MSS sample estimators are presented subsequently. Let $\widehat{\underline{\mu}}_l$ and $\widehat{\underline{\Sigma}}_l$ denote the sample mean and covariance (see Eqns. B.3 and B.4) of the MSS sample points in the l^{th} shell, i.e., $\{\widetilde{\underline{x}}_{l,q}\}$, $q \in S_{N_{\text{ss}}}$. Then, the $\widehat{\underline{\mu}}_{\text{MSS}}$ estimator may be computed as the sample mean of $\{\underline{a}_l\}$, $l \in S_{N_{\text{sh}}}$, where

$$\underline{a}_l = (N_{\text{sh}} HW_l) \widehat{\underline{\mu}}_l \quad (6.34)$$

Additionally, the $\widehat{\Sigma}_{\text{MSS}}$ estimator may be computed as

$$\widehat{\Sigma}_{\text{MSS}} = (-1) \left(\frac{S_1}{G} \right) (\widehat{\underline{\mu}}_{\text{MSS}}) (\widehat{\underline{\mu}}_{\text{MSS}})^T + \left(\frac{1}{G} \right) \sum_{l=1}^{N_{\text{sh}}} W_l \left(\left[1 - \frac{1}{N_{\text{ss}}} \right] \widehat{\Sigma}_l + (\widehat{\underline{\mu}}_l) (\widehat{\underline{\mu}}_l)^T \right) \quad (6.35)$$

Finally, the $\widehat{p}_{E,\text{MSS}}$ estimator may be computed as the sample mean of $\{\underline{b}_l\}$, $l \in S_{N_{\text{sh}}}$, where

$$\underline{b}_l = (N_{\text{sh}} W_l) \widehat{\underline{\mu}}_{E,l} \quad (6.36)$$

and where $\widehat{\underline{\mu}}_{E,l}$ denotes the sample mean of the f_E -transformed MSS sample points in the l^{th} shell; that is, $\{f_E(\tilde{\underline{x}}_{l,q})\}$, $q \in S_{N_{\text{ss}}}$.

6.3.4 MSS application to collision probability computation

The MSS algorithm may be applied to collision probability computation as illustrated in Figure 6.4, which shows a notional picture of a relative state space, with the relative position on one axis and relative position rate on the other axis, as well as an MSS sample of a normally distributed instantaneous relative state distribution on this relative state space. For the case of IPC computation, the entire MSS sample is passed through the characteristic function of the instantaneous collision set, which identifies MSS particles that indicate an instantaneous collision event.

For the case of P_c computation, an MSS sample is made of the initial distribution of a relative dynamic state, and after propagating the MSS sample through an arbitrary dynamic process, the instantaneous collision condition is checked sequentially for each particle, and the JTC set is approximated via logical OR operations (on the instantaneous collision condition) applied to each sample particle. In both cases, these collision probabilities are computed by adding the MSS weights that meet the respective collision condition, whether instantaneous or joint-time, as listed in Eq. 6.30.

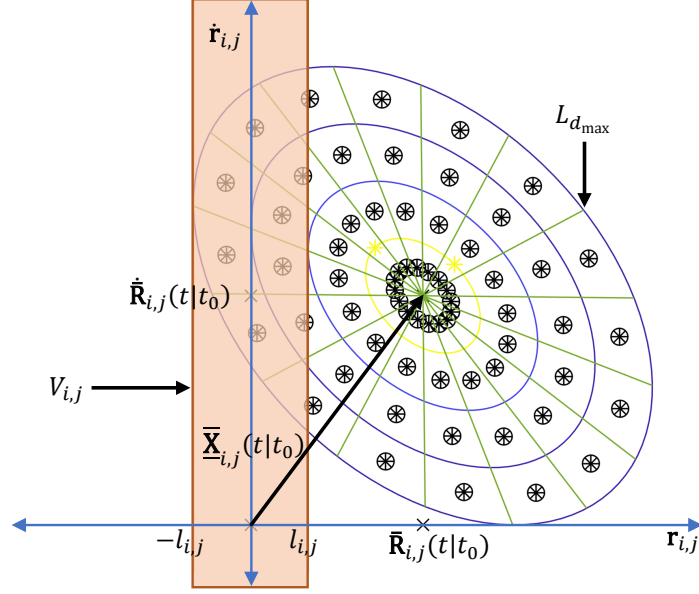


Figure 6.4: Conceptual application of MSS to IPC computation for a system with one-dimensional relative position and normally distributed (two-dimensional) relative state.

6.3.5 Application of scrambled Sobol nets for MSS sequence generation

The MSS algorithm requires the use of random, independent, uniformly distributed samples on the unit $(s - 1)$ -sphere, $\mathbb{S}^{(s-1)}$, and on the unit interval, $[0, 1]$. In this Chapter, computational investigations of MSS asymptotic convergence in the MSE sense are undertaken by utilizing linearly scrambled Sobol sequences on the unit hypercube, which are then transformed into samples of the unit hypersphere via the Lambert area-preserving transform.[119]

6.3.5.1 Overview of Sobol low-discrepancy sequence generation

The Sobol method is an instance of low-discrepancy sequence generation methods, which aim to produce a finite point set in the unit s -hypercube $([0, 1]^s)$ that minimizes the discrepancy function of the point set, which measures the quality of the spacing between points.[120] By so doing, low-discrepancy sequences, also known as quasi-random number sequences (qrns), produce points are uniformly spaced in $[0, 1]^s$ (in a spatial sense), and whose application as quadrature rules for the estimation of integrals over $[0, 1]^s$ (also known

as quasi Monte Carlo (QMC) quadrature rules) have beneficial error properties compared to Monte Carlo because the former fill the unit hypercube in a much more regular way than the latter.[73]

Let $P_n = \{y_k\}$, $k \in S_n$ denote any point set in $[0, 1]^s$. A foundational result of the study of low discrepancy sequences is the Hoksma-Hlawka inequality, which states that, for a function $f : [0, 1]^s \rightarrow \mathbb{R}$ with bounded variation $V(f)$ in the sense of Hardy and Krause, for the integral I_f given by

$$I_f = \int_{[0,1]^s} f(y) dy \quad (6.37)$$

and, if the corresponding point set estimate for the integral I_f , \hat{I}_f , is given by

$$\hat{I}_f = \frac{1}{n} \sum_{k=1}^n f(y_k) \quad (6.38)$$

then, the \hat{I}_f -error satisfies

$$\hat{I}_f\text{-error} = \left| \hat{I}_f - I_f \right| \leq V(f)D^*(P_n) \quad (6.39)$$

where $D^*(P_n)$ is the star discrepancy of the point set P_n . [121, 122] On one hand, the bounded variation $V(f)$ is independent of the point set P_n ; on the other hand, the star discrepancy $D^*(P_n)$ does not depend on the function f to be integrated. Hence, the goal of low discrepancy sequence generation is to minimize $D^*(P_n)$, and the asymptotic rate of deterministic convergence of the \hat{I}_f -error is the same as that of $D^*(P_n)$. [73]

Definition 23 ((t, m, s) -nets and (t, s) -sequences [120]). Let b be a positive integer greater than or equal to 2. Let $q_1, \dots, q_s \in \mathbb{N}$, and let $q = q_1 + \dots + q_s$. A point set P_n in $[0, 1]^s$ with $n = b^m$ points is (q_1, \dots, q_s) -equidistributed in base b if every cell (or elementary

interval) of the form

$$J(r_1, \dots, r_s) = \prod_{j=1}^s \left[\frac{r_j}{b^{q_j}}, \frac{r_j + 1}{b^{q_j}} \right)$$

for $0 \leq r_j < b^{q_j}$, r_j integer, $j \in \{1, \dots, s\}$, contains b^{m-q} points from P_n .

Then, the point set P_n is a (t, m, s) -net in base b if it is (q_1, \dots, q_n) -equidistributed in base b whenever $q \leq m - t$ for some integer $t \geq 0$. A (t, s) -sequence is a sequence $\{y_k\}_{k \in \mathbb{N}}$ of points in $[0, 1]^s$ for which every b -ary finite subsequence of the form $\{y_k\}$, $k \in \{lb^m + 1, \dots, (l+1)b^m\}$ (with $m \geq t$ and some integer $l \geq 0$) is a (t, m, s) -net in base b . The smallest value for which P_n is a (t, m, s) -net is called the t -value of P_n , and similarly for (t, s) -sequences. \diamond

The Sobol qrn method employs XOR bitwise, modulo 2 arithmetic to produce direction numbers, which are used to generate (t, s) -sequences via recurrence relations, and these direction numbers are chosen such that the corresponding sequences satisfy certain uniformity features known as Property A and Property A'. [123] For functions f of bounded variation in the sense of Hardy and Krause, Sobol (t, m, s) -nets achieve \widehat{I}_f -error = $\mathcal{O}\left(n^{-1} [\log n]^{(s-1)}\right)$, and Sobol (t, s) -sequences achieve \widehat{I}_f -error = $\mathcal{O}\left(n^{-1} [\log n]^s\right)$. [121, 122] Hence, in practical applications, it is helpful to choose the number of Sobol sample elements to be a power of 2, as better discrepancy performance can be expected, and if initial sequence elements are to be skipped (e.g., to avoid performance degradation due to poor choice of direction numbers), it is advisable for the number of points to be skipped to be the largest power of 2 smaller than the number of sample elements. [124]

6.3.5.2 Introduction to scrambled Sobol sequences

One of the major drawbacks of low-discrepancy sequences, which are deterministic, is that sample elements may not be regarded as statistically independent; hence, in general, via application of low-discrepancy sequences to integration in the unit hypercube, unbiased integration cannot be guaranteed, and variance estimation cannot be undertaken. [73] The aim

of randomized quasi-Monte Carlo methods (RQMC) is to introduce randomness into low-discrepancy sequences so as to achieve a) unbiased integration, and variance estimation; and b) preserving low-discrepancy properties.[125]

The gold standard for RQMC methods is nested random scrambling, also referred to as Owen scrambling, which, when employing (t, m, s) -nets to integrate a function f , achieves \widehat{I}_f -RMSE = $\mathcal{O}(n^{-1/2})$ if f is square integrable (even if f is not of bounded variation), and which achieves \widehat{I}_f -RMSE = $\mathcal{O}\left(n^{-\frac{3}{2}} [\log n]^{\frac{(s-1)}{2}}\right)$ if f is continuously differentiable.[120, 125] For the case of square integrable functions, Owen scrambling RMSE performance is comparable to Monte Carlo, which suggests that, asymptotically, employing the former is no worse than the latter. However, for continuously differentiable functions, employing Owen scrambling results in considerable convergence improvements compared to Monte Carlo.

Nevertheless, Owen scrambling is computationally demanding; hence, approximations to Owen scrambling such as random linear scrambling have been developed. It has been shown that random linear scrambling achieves unbiased integration, and it retains Owen scrambling-like RMSE convergence rates for square integrable and continuously differentiable functions.[126] In this Chapter, random linear scrambling of Sobol (t, m, s) -nets is implemented in MATLAB R2020b as follows.[127] First, a `sobolset` object is created, and random linear scrambling is set via the `'MatousekAffineOwen'` setting of the `scramble` function. Then, scrambled Sobol sequence elements are generated via the `net` function (with appropriate exclusion of initial elements in the sequence) as described in Hong et al.'s work.[128]

6.3.5.3 Application of scrambled Sobol qrn's to MSS

Scrambled Sobol nets are employed to make MSS samples within $V_{d_{\max}}(\underline{X}) \subseteq \mathbb{R}^s$ in the following way. First, a single scrambled Sobol net is sampled in $[0, 1]^s$. Second, the original net is marginalized to the first $(s - 1)$ dimensions, which renders a scrambled Sobol net

in $[0, 1]^{(s-1)}$; via the Lambert equal-area transform, this set is mapped into a sample of the $(s - 1)$ -unit hypersphere, $\mathbb{S}^{(s-1)}$, which can then be regarded as statistically uniform on $\mathbb{S}^{(s-1)}$. Third, the s^{th} dimension of the original sample, which is statistically uncorrelated from the other $(s - 1)$ -dimensions of the original sample, is itself a statistically uniform sample on $[0, 1]$. The outcome of this process yields statistically uniform, uncorrelated samples in $[0, 1]$ and $\mathbb{S}^{(s-1)}$, which are then employed via Algorithm 1 to generate MSS samples.

6.4 Implementation – Test methodology for MSS stochastic convergence properties

This Chapter is a computational investigation of whether, for the MSS algorithm, the $\hat{\underline{\mu}}$ -MSE and $\hat{\underline{\Sigma}}$ -MSE asymptotic convergence rate in mean, covariance, and IPC may be modeled as

$$(\hat{\underline{\mu}}\text{-MSE})(n) = (C_{\underline{\mu}}) n^{-u} \quad (6.40)$$

$$(\hat{\underline{\Sigma}}\text{-MSE})(n) = (C_{\underline{\Sigma}}) n^{-u} \quad (6.41)$$

and whether $u > 1$. If both are true, then the MSS algorithm may be regarded as more computationally efficient, asymptotically, than Monte Carlo – in settings where MSS may be applicable. For further discussion on the stochastic convergence properties of the Monte Carlo method, the reader is referred to Appendix B.

6.4.1 Clohesy-Wiltshire (CW) vector and matrix norm

Appendix D introduces the Clohesy-Wiltshire (CW) vector and matrix norms for vectors in \mathbb{R}^6 and matrix norms $\mathbb{R}^{6 \times 6}$. These norms are developed in order to assign a magnitude to the first and second order statistics of the CW relative dynamic state via a normalization that allows for meaningful combinations of relative position and relative position rate in consistent, normalized unitless values. Additionally, Appendix D discusses the equivalence

of convergence criteria in terms of the CW vector and matrix norms as compared to the Euclidean vector and Frobenius matrix norms, respectively.

6.4.2 Estimating sample MSE

As mentioned in Section A.2, the mean and covariance of $\underline{\mathbf{R}}$, $\dot{\underline{\mathbf{R}}}$, and $\underline{\mathbf{X}}$ may be obtained analytically as per such Section; hence, it is assumed that the true values of these statistics are known for the purposes of MSE error analysis. For the rest of this chapter, the “ i, j ” subscript is omitted.

Let $B_C(t)$ be a Bernoulli random variable with value $B_C(t) = 1$ if the instantaneous collision event [i.e., $V_{i,j}(t)$, or $C_{i,j}(t)$] is satisfied. That is, $B_C(t)$ is defined as

$$B_C(t) = \begin{cases} 1 & \text{if } \|\underline{\mathbf{R}}(t)\|_2 < l_{i,j} \\ 0 & \text{otherwise} \end{cases} \quad (6.42)$$

Thus, the probability mass function of $B_C(t)$, $\text{pmf}_{B_C(t)} : \mathbb{R} \rightarrow \{0, 1\}$ is given by

$$\text{pmf}_{B_C(t)}(x) = \begin{cases} \text{IPC}(t) & \text{if } x = 1 \\ 1 - \text{IPC}(t) & \text{if } x = 0 \\ 0 & \text{otherwise} \end{cases} \quad (6.43)$$

Hence, the $\text{IPC}(t)$ can be thought of as the expected value of $B_C(t)$; that is,

$$\mathbb{E}[B_C(t)] = \text{IPC}(t) \quad (6.44)$$

The true $\text{IPC}(t)$ value is approximated as the outcome of a three-dimensional numerical quadrature scheme based on the instantaneous relative position statistics, implemented using the `integral3` function in MATLAB R2020b.[129] Because $B_C(t)$ is a Bernoulli

random variable, the variance of $B_C(t)$ is analytically given by

$$\text{Var}(B_C(t)) = [\text{IPC}(t)] [1 - \text{IPC}(t)] \quad (6.45)$$

Thus, the variance of B_C is not examined further in this Chapter.

For n in \mathbb{N} , for an i.i.d. sample $\{\underline{X}_k\}_{k \in S_n}$, the sample estimators of $\underline{\mu}$ and Σ may be obtained as

$$\hat{\underline{\mu}} = f_{\text{sample}}(\underline{X}_1, \dots, \underline{X}_n) \quad (6.46)$$

$$\hat{\Sigma} = g_{\text{sample}}(\underline{X}_1, \dots, \underline{X}_n) \quad (6.47)$$

Since the goal is to estimate the MSE, the drawing of a sample of \underline{X} is repeated N_{rep} times, where $N_{\text{rep}} \in \mathbb{N}$; that is, for all $j \in S_{N_{\text{rep}}}$, a sample $\{\underline{X}_k^j\}_{k \in S_n}$ is drawn. Sample estimates of the $\hat{\underline{\mu}}$ -MSE and $\hat{\Sigma}$ -MSE, denoted by $\hat{\underline{\mu}}-\widehat{\text{MSE}}$ and $\hat{\Sigma}-\widehat{\text{MSE}}$, are obtained as follows.

For all $j \in S_{N_{\text{rep}}}$,

$$\hat{\underline{\mu}}_j = f_{\text{sample}}(\underline{X}_1^j, \dots, \underline{X}_n^j) \quad (6.48)$$

$$\hat{\Sigma}_j = g_{\text{sample}}(\underline{X}_1^j, \dots, \underline{X}_n^j) \quad (6.49)$$

Then, for $\underline{\mathbf{R}}$, $\dot{\underline{\mathbf{R}}}$, and B_C ,

$$\hat{\underline{\mu}}-\widehat{\text{MSE}} = \frac{1}{N_{\text{rep}}} \sum_{j=1}^{N_{\text{rep}}} \|\hat{\underline{\mu}}_j - \underline{\mu}\|_2^2 \quad (6.50)$$

$$\hat{\Sigma}-\widehat{\text{MSE}} = \frac{1}{N_{\text{rep}}} \sum_{j=1}^{N_{\text{rep}}} \|\hat{\Sigma}_j - \Sigma\|_F^2 \quad (6.51)$$

and, for $\underline{\mathbf{X}}$,

$$\widehat{\underline{\mu}}-\widehat{\text{MSE}} = \frac{1}{N_{\text{rep}}} \sum_{j=1}^{N_{\text{rep}}} \left\| \widehat{\underline{\mu}}_j - \underline{\mu} \right\|_{\text{CW}}^2 \quad (6.52)$$

$$\widehat{\underline{\Sigma}}-\widehat{\text{MSE}} = \frac{1}{N_{\text{rep}}} \sum_{j=1}^{N_{\text{rep}}} \left\| \widehat{\underline{\Sigma}}_j - \underline{\Sigma} \right\|_{\text{CW},F}^2 \quad (6.53)$$

It can be verified that $\widehat{\underline{\mu}}-\widehat{\text{MSE}}$ and $\widehat{\underline{\Sigma}}-\widehat{\text{MSE}}$ are unbiased estimators for $\underline{\mu}-\text{MSE}$ and $\underline{\Sigma}-\text{MSE}$; that is,

$$\mathbb{E} \left[\widehat{\underline{\mu}}-\widehat{\text{MSE}} \right] = \underline{\mu}-\text{MSE} \quad (6.54)$$

$$\mathbb{E} \left[\widehat{\underline{\Sigma}}-\widehat{\text{MSE}} \right] = \underline{\Sigma}-\text{MSE} \quad (6.55)$$

In this Chapter, the approximation will be made that

$$\underline{\mu}-\text{MSE} \approx \widehat{\underline{\mu}}-\widehat{\text{MSE}} \quad (6.56)$$

$$\underline{\Sigma}-\text{MSE} \approx \widehat{\underline{\Sigma}}-\widehat{\text{MSE}} \quad (6.57)$$

and regression analysis on such MSE errors will be performed upon the basis of this approximation.

6.4.3 Regression analysis

6.4.3.1 Setting up regression analysis

The purpose of this Chapter is to study asymptotic MSE convergence for certain sampling methods. Since the Monte Carlo MSE can be modeled as a power function fit of the form

$$(\text{MSE})(n) = Cn^{-u} \quad (6.58)$$

then, multiple linear regression is performed using the following hypothesis model

$$y = \beta_0 - \beta_1 x + \varepsilon \quad (6.59)$$

In this context, x denotes the prediction variable, y denotes the response variable, ε denotes the error of the fit, and (β_0, β_1) represent the model parameters given by

$$x = \log_{10}(n) \quad (6.60)$$

$$y = \log_{10}(\text{MSE}) \quad (6.61)$$

$$\beta_0 = \log_{10}(C) \quad (6.62)$$

$$\beta_1 = u \quad (6.63)$$

Let $[\underline{x}]$, $[\underline{y}]$, and $[\underline{\varepsilon}]$ denote the collection of prediction and response variable and error observations, as given by

$$[\underline{x}]^T = \begin{bmatrix} 1 & \dots & 1 \\ x_1 & \dots & x_{N_n} \end{bmatrix} \quad (6.64)$$

$$[\underline{y}]^T = \begin{bmatrix} y_1 & \dots & y_{N_n} \end{bmatrix} \quad (6.65)$$

$$[\underline{\varepsilon}]^T = \begin{bmatrix} \varepsilon_1 & \dots & \varepsilon_{N_n} \end{bmatrix} \quad (6.66)$$

Thus, the relationship between prediction and response variables is given by

$$[\underline{y}] = [\underline{x}] \underline{\beta} + \underline{\varepsilon} \quad (6.67)$$

where $\underline{\beta}^T = [\beta_0, \beta_1]$. Then, the least squares error estimate of $\underline{\beta}$, $\hat{\underline{\beta}}$, is given by

$$\hat{\underline{\beta}} = \left([\underline{x}]^T [\underline{x}] \right)^{-1} [\underline{x}]^T [\underline{y}] \quad (6.68)$$

and the least squares model fit is given by

$$\hat{y} = \hat{\beta}_0 - \hat{\beta}_1 x \quad (6.69)$$

6.4.3.2 Goodness of fit

The goodness of fit of the model listed in Eq. 6.69 is characterized via the coefficient of determination, R_{fit}^2 , defined as

$$R_{fit}^2 = 1 - \frac{SSE_{fit}}{SST_{fit}} \quad (6.70)$$

$$SSE_{fit} = \sum_{i=1}^{N_n} (y_i - \hat{y}_i)^2 \quad (6.71)$$

$$SST_{fit} = \sum_{i=1}^{N_n} (y_i - \bar{y})^2 \quad (6.72)$$

$$\bar{y} = \frac{1}{N_n} \sum_{i=1}^{N_n} y_i \quad (6.73)$$

and by confidence intervals of the fit parameters. The covariance of $\underline{\beta}$, $\Sigma_{\underline{\beta}}$, is given by

$$\Sigma_{\underline{\beta}} = (\text{MSE}_{fit}) \left([\underline{x}]^T [\underline{x}] \right)^{-1} = \begin{bmatrix} \sigma_{\beta_0}^2 & \rho_{(\beta_0, \beta_1)} \sigma_{\beta_0} \sigma_{\beta_1} \\ \rho_{(\beta_0, \beta_1)} \sigma_{\beta_0} \sigma_{\beta_1} & \sigma_{\beta_1}^2 \end{bmatrix} \quad (6.74)$$

where the mean square error of the regression fit (denoted as MSE_{fit} in order to distinguish it from the sample statistic estimator MSE which is the subject of this Chapter) is given by

$$\text{MSE}_{fit} = \frac{1}{N_n - 2} \text{SSE}_{fit} \quad (6.75)$$

The denominator in the previous expression is $(N_n - 2)$ and not N_n because the model is constrained by two degrees of freedom (i.e., the model has two parameters in the regression).

Figure 6.5 shows an example of a $4\text{-}\sigma$ joint confidence region (CR) in (β_0, β_1) param-

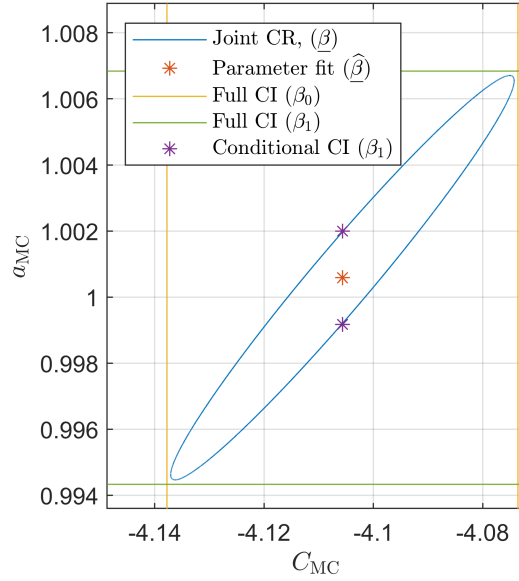


Figure 6.5: $4\text{-}\sigma$ confidence region on fit parameter space, regression on IPC at Time = 1.222 orbit periods, Monte Carlo sample from CW relative state, Example 3D.001.

parameter space (which is the region inside the $4\text{-}\sigma$ contour based on $\Sigma_{\underline{\beta}}$ and centered at $\hat{\underline{\beta}}$), specifically for the regression on the IPC at time $t_2 = 1.222$ orbit periods as obtained from Monte Carlo-sampling the entire relative state. Implicit in this construction is the assumption that the error distribution of $\underline{\beta}$ about $\hat{\underline{\beta}}$ is normal, i.e., that $\underline{\beta} \sim \mathcal{N}(\hat{\underline{\beta}}, \Sigma_{\underline{\beta}})$. As may be gleaned from Figure 6.5, there is a significant degree of linear correlation between the dispersions of β_0 and β_1 ; in particular, $\rho_{(\beta_0, \beta_1)} = 0.9741$ for this regression case. However, such high correlations are common for all regression cases observed. Hence, when marginalizing such a confidence region, the confidence intervals (CIs) obtained in β_0 and β_1 are conservative because of the high correlation observed.

6.5 Results and discussion

6.5.1 Test case and sample parameters for MSS stochastic convergence study

6.5.1.1 Test case for MSS stochastic convergence study

The test case chosen for study of MSS stochastic convergence properties is Example 3D.001, which is subject to CW dynamics, and whose IPC waveform is illustrated in Fig. 6.6. (Note: all test cases in this dissertation are described in Section A.2.)

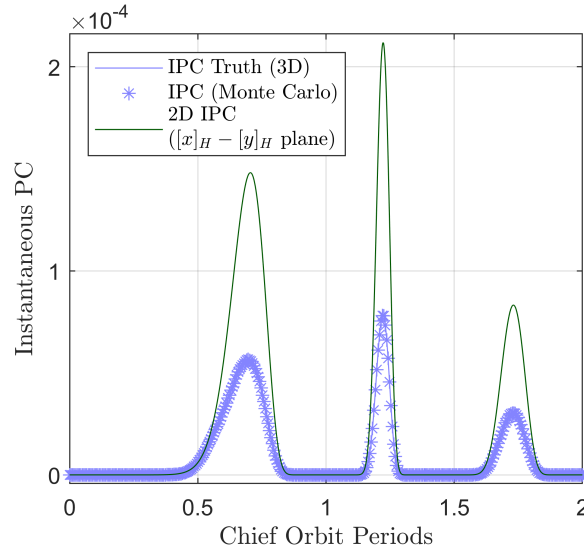


Figure 6.6: Sample, true, and $[x]_H - [y]_H$ projection IPC waveforms, Example 3D.001.

Example 3D.001 assumes a joint hard-body radii of $l_{i,j} = 32$ m. This figure is based on an estimate of Hubble Space Telescope’s hard body radius of $l_i = 16$ m.[130] For the purposes of this Chapter, having such a large joint hard-body radius allows obtaining higher (and thus, more significant) IPCs. Convergence properties are tested for the three timesteps in Example 3D.001 with IPC local maxima, listed in Table 6.2. Truth values for mean and covariance are propagated analytically, that is, using the analytically propagated relative state statistics listed in Eqns. A.22-A.23, while IPC values are obtained through multi-dimensional brute-force quadrature in MATLAB R2020b,[129] specifically, via the `integral3` function by integrating the instantaneous relative position pdf, which is ob-

tained through the marginalization listed in Eq. A.24. Stochastic convergence results in MSS sample mean and covariance would also directly apply to other MSS samples with the same covariance matrix because, per the assumption of normality of the relative state distribution, relative state sample points for all cases are statistically equal to within a constant shift (namely, the assumed expected value).

Table 6.2: Peak IPC times, Example 3D.001.

Peak time units	t_1	t_2	t_3
Hours	1.0797	1.8946	2.6805
Chief Orbit Periods	0.6965	1.2222	1.7292

6.5.1.2 Sample parameters for MSS stochastic convergence study

For a fixed d_{\max} , and for an underlying qrms sampling algorithm, the main tunable parameters in an MSS sample are the number of samples per shell N_{ss} , and the number of shells, N_{sh} . Choice of these parameters for MSS stochastic convergence analysis is motivated by insights into convergence rates in scrambled Sobol net-based unit hypercube integration, where, through computational experiments, it can be seen that beneficial convergence rates are only achieved with full nets (that is, with sample sizes equal to 2^{n_1} for some integer n_1), and that convergence rate degradation can be experienced without full nets.[125]

In this Chapter, N_{sh} is fixed, and regression analysis on stochastic MSS convergence properties is performed by increasing N_{ss} in $[2^{n_1}, 2^{n_2}]$ for integers n_1 and n_2 , and $n_1 < n_2$, distinguishing between ‘complete’ nets (i.e., those that only allow $N_{\text{ss}} = 2^{n_3}$ for integers n_3 such that $n_1 \leq n_3 \leq n_2$), and ‘incomplete’ nets (i.e., those that allow for any integer N_{ss} between 2^{n_1} and 2^{n_2}). (Details on n_1 , n_2 , and n_3 are given in Table 6.3.)

This process is repeated for $N_{\text{sh}} \in \{512, 700, 1024\}$, and for $d_{\max} = 7$. It is expected that N_{sh} and N_{ss} choices whose corresponding $N_{\text{samples}} = N_{\text{sh}}N_{\text{ss}}$ imply drawing full Sobol nets (namely, $N_{\text{sh}} \in \{512, 1024\}$ with ‘complete’ N_{ss}) would display better convergence rates compared to N_{sh} and N_{ss} choices without full Sobol nets (e.g., $N_{\text{sh}} = 700$

Table 6.3: Choice of N_{ss} sequence size for regression analysis.

N_{ss} type	n_1	n_2	Choice of n_3
'complete'	6	12	All integers between n_1 and n_2
'incomplete'	6	12	100 equally spaced points between n_1 and n_2 (with rounding)

with 'incomplete' N_{ss}). Additionally, the number of initial sample elements skipped is equal to the greatest integer power of 2 less than or equal to the number of samples.

6.5.2 Validation of Monte Carlo MSE convergence rate

A computational investigation on the Monte Carlo exponential rate of stochastic convergence in the MSE sense, u_{MC} , was undertaken. Samples were drawn in MATLAB R2020b, through the `mvnrnd` function,[127] and applying the Mersenne Twister pseudo-random number generator. Each sample had 3.2×10^8 elements; such sample sizes were chosen to ensure that samples are able to reproduce events with probabilities greater than 1×10^{-7} , which is considered a practical threshold for IPC significance, as discussed in Ref. [28]. The results of this analysis are shown in Fig. 6.7.

It was found that, when used to reproduce sample mean, covariance, and IPC via samples of \mathbf{R} , $\dot{\mathbf{R}}$, and \mathbf{X} (when applicable), for all timesteps chosen, the $4-\sigma$ CI on u_{MC} forms a tight bound around $u = 1$. This computational result validates the analytical conclusion that $u_{MC} = 1$ precisely. Therefore, $u_{MC} = 1$ becomes a baseline for sampling error performance comparison in the following way. In order to quantify improvements over the Monte Carlo method, if another sampling method also fits the hypothesis of an exponential rate of stochastic MSE convergence (see Eq. 6.59), then it is a legitimate approach to compare whether the proposed sampling method achieves $u > u_{MC} = 1$.

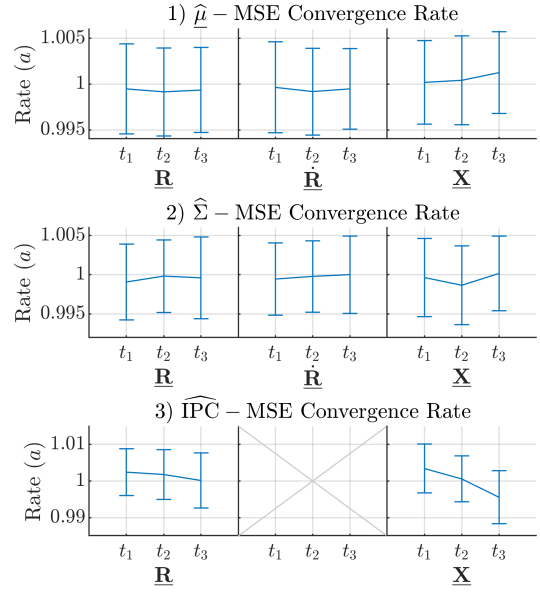


Figure 6.7: Monte Carlo asymptotic MSE-coefficient of determination results ($N_{\text{rep}} = 1000$), Example 3D.001.

6.5.3 MSS results, adequacy of error fit model

This Subsection addresses the adequacy of modeling MSS sample statistic error evolution (as a function of sample size) in the MSE sense as a power function fit, such as is listed in Eq. 6.59. This is measured via the coefficient of determination of the model fit, R_{fit}^2 , when considering sample mean, covariance, and IPC, and the results are shown in Fig. 6.8 for \mathbf{R} samples, in Fig. 6.9 for $\hat{\mathbf{R}}$ samples, in Fig. 6.10 for \mathbf{X} samples.

It is found that, except for the $\hat{\mu}$ -MSE in \mathbf{R} and $\hat{\mathbf{R}}$ MSS samples, all other MSS sample statistic model fits exhibit $R_{fit}^2 > 0.99$. It is also found that all MSS sample statistic model fits studied (namely, $\hat{\mu}$ -MSE, $\hat{\Sigma}$ -MSE, and $\widehat{\text{IPC}}$ -MSE) exhibit $R_{fit}^2 > 0.955$. These results suggest that it is adequate to approximate the MSS error evolution in the MSE sense (as a function of sample size) as a power function fit for different originating samples and statistics of interest, although this is an imperfect relationship. These results hold regardless of N_{sh} , peak IPC times, and N_{ss} types (see Table 6.3). In particular, in view of these results, it is meaningful to investigate whether the exponential rate of stochastic convergence in the

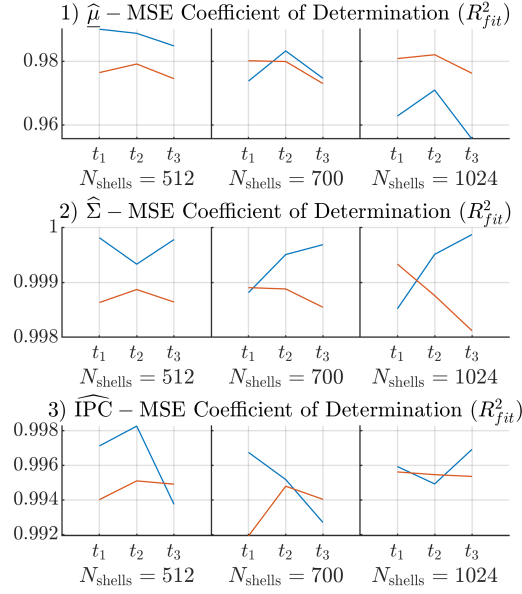


Figure 6.8: MSS asymptotic MSE-fit coefficient-of-determination (R_{fit}^2) results ($N_{rep} = 100$), $d_{max} = 7$, CW relative position, Example 3D.001: blue) 'complete' N_{ss} , and orange) 'incomplete' N_{ss} .

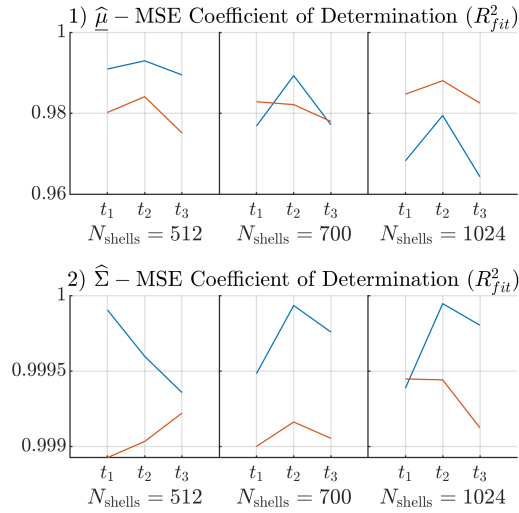


Figure 6.9: MSS asymptotic MSE-fit coefficient-of-determination (R_{fit}^2) results ($N_{rep} = 100$), $d_{max} = 7$, CW relative position rate, Example 3D.001: blue) 'complete' N_{ss} , and orange) 'incomplete' N_{ss} .

MSE sense, u_{MSS} , satisfies $u_{MSS} > u_{MC} = 1$, and to use these results to draw conclusions regarding MSS asymptotic convergence performance compared to Monte Carlo's.

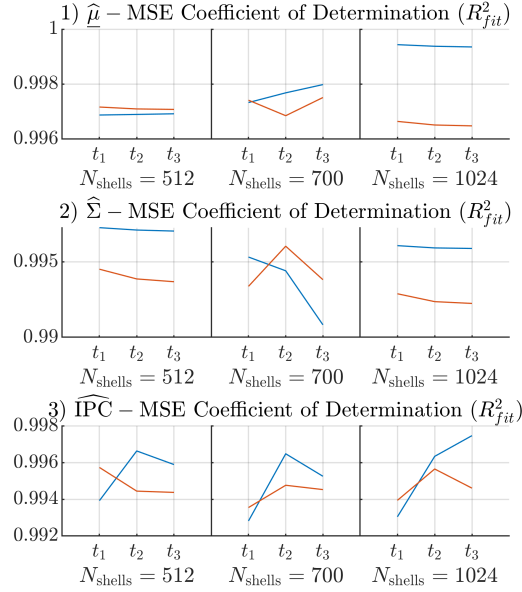


Figure 6.10: MSS asymptotic MSE-fit coefficient-of-determination (R_{fit}^2) results ($N_{rep} = 100$), $d_{max} = 7$, CW relative state, Example 3D.001: blue) ‘complete’ N_{ss} , and orange) ‘incomplete’ N_{ss} .

6.5.4 Computational results on MSS stochastic convergence properties

The MSS asymptotic convergence rate results are listed in Fig. 6.11 for \mathbf{R} samples, in Fig. 6.12 for $\hat{\mathbf{R}}$ samples, in Fig. 6.13 for \mathbf{X} samples, in terms of $4-\sigma$ confidence intervals on the MSS exponential rate of stochastic convergence, u_{MSS} .

6.5.4.1 MSS asymptotic convergence rate results, sample mean and covariance

For the $\hat{\mu}$ -MSE and $\hat{\Sigma}$ -MSE, all MSS samples displayed better convergence rates than Monte Carlo because, to within $4-\sigma$ confidence, all u_{MSS} values are greater than 1.

At face value, for the $\hat{\mu}_{\mathbf{R}}$ -MSE and $\hat{\mu}_{\hat{\mathbf{R}}}$ -MSE, ‘complete’ nets seem to have improved convergence performance compared to ‘incomplete’ nets, but when considering the full confidence intervals, it is not possible to ascertain whether this is true. For all other statistics considered in this subsection (namely, $\hat{\mu}_{\mathbf{X}}$ -MSE, $\Sigma_{\mathbf{R}}$ -MSE, $\Sigma_{\hat{\mathbf{R}}}$ -MSE, and $\Sigma_{\mathbf{X}}$ -MSE), there is similar expected performance between ‘complete’ and ‘incomplete’ nets, with the main difference concerning the variance of the MSS

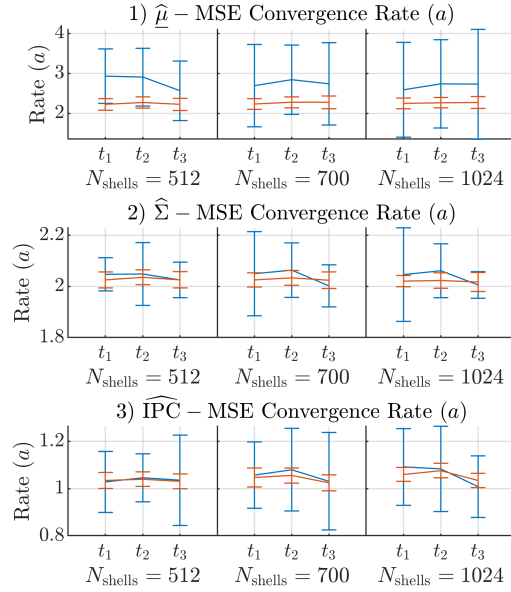


Figure 6.11: MSS asymptotic MSE-fit convergence rate (a) results ($N_{\text{rep}} = 100$), $d_{\text{max}} = 7$, CW relative position, Example 3D.001: blue) 'complete' N_{ss} , and orange) 'incomplete' N_{ss} .

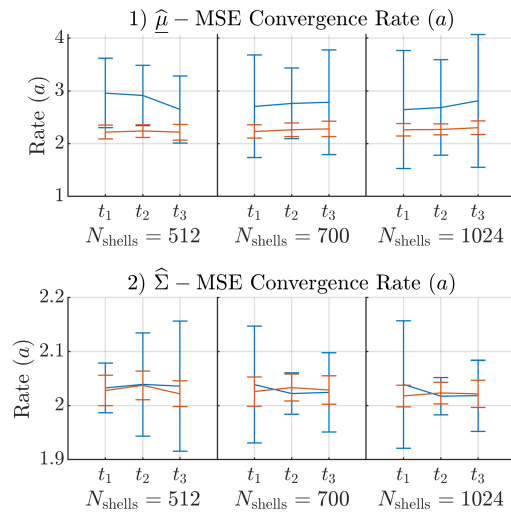


Figure 6.12: MSS asymptotic MSE-fit convergence rate (a) results ($N_{\text{rep}} = 100$), $d_{\text{max}} = 7$, CW relative position rate, Example 3D.001: blue) 'complete' N_{ss} , and orange) 'incomplete' N_{ss} .

convergence rate, u_{MSS} , which translates to differences in the size of the u_{MSS} confidence intervals.

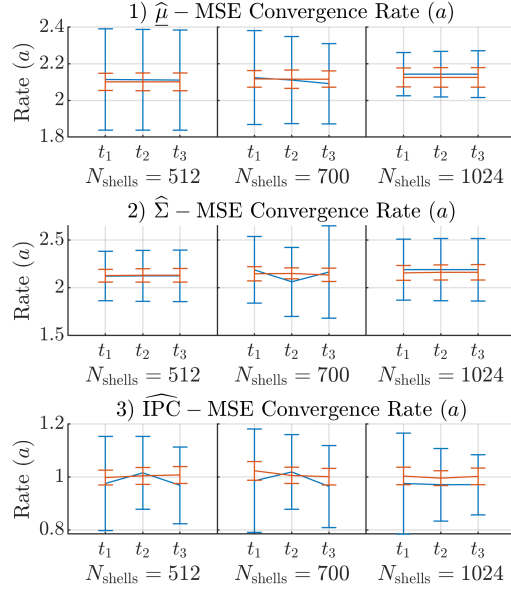


Figure 6.13: MSS asymptotic MSE-fit convergence rate (a) results ($N_{\text{rep}} = 100$), $d_{\text{max}} = 7$, CW relative state, Example 3D.001: blue) ‘complete’ N_{ss} , and orange) ‘incomplete’ N_{ss} .

The lower u_{MSS} variance observed in ‘incomplete’ nets implies that there is higher certainty of the u_{MSS} performance for ‘incomplete’ nets than for ‘complete’ nets; that is, for ‘incomplete’ nets, there is a higher degree of confidence in the convergence rate, whose performance stabilizes around $u_{\text{MSS}} = 2$ for samples in \mathbb{R}^3 reproducing 9-dimensional objects (namely, $\Sigma_{\mathbf{R}}\text{-MSE}$, and $\Sigma_{\mathbf{R}}\text{-MSE}$), and for samples in \mathbb{R}^6 reproducing 6- and 36-dimensional objects ($\widehat{\mu}_{\mathbf{X}}\text{-MSE}$, and $\Sigma_{\mathbf{X}}\text{-MSE}$, respectively).

One plausible interpretation for the higher variance observed in ‘complete’ nets is that the higher variance might be an indication that there is the potential for unrealized performance gains, which may not be detected within this study for one of the following reasons. First, as an issue of reproducibility, a higher N_{rep} might be needed for adequate convergence of MSE estimators, $\widehat{\text{MSE}}$, to the true MSE values. Second, MSS sample sizes employed in the regression may not be large enough to observe adequate performance improvements. One compelling reason for this interpretation is that, while expected u_{MSS} values for ‘complete’ nets are closer to 3 in $\widehat{\mu}_{\mathbf{R}}\text{-MSE}$ and $\widehat{\mu}_{\mathbf{R}}\text{-MSE}$, the true con-

vergence rate could be anywhere in [2, 4]; however, when employing ‘incomplete’ nets, the expected $\hat{\underline{\mu}}_{\mathbf{R}}-\text{MSE}$ and $\hat{\underline{\mu}}_{\mathbf{R}}-\text{MSE}$ performance is lower, yet there is lower variance. This behavior resembles the computational difference in performance between Sobol (t, m, s) -nets and Sobol (t, s) -sequences; in particular, analytically, Sobol (t, m, s) -nets have better performance than Sobol (t, s) -sequences, whereas computationally, the latter exhibit more consistent, yet lesser, performance. Hence, although this regression does indicate stochastic asymptotic convergence, more data points corresponding to larger sample sizes may be needed to ascertain the asymptotic rate of convergence more precisely.

On the other hand, it is possible that there may not be additional u_{MSS} performance gains in ‘complete’ sequences beyond what is exhibited by ‘incomplete’ nets because the uniformity properties of Sobol sequences may not be preserved under the mapping from the unit hypercube to the unit hypersphere, as well as with the scaling, rotation, and translation operations associated with transforming the standard normal distribution into the specific relative state distributions at hand. Hence, it would be helpful to explore the effects of different hypercube-to-hypersphere mapping algorithms on reproducing the standard normal distribution via an MSS sample, and then examining if any further changes need to be made in order to preserve Sobol uniformity and space filling properties as much as possible under scaling, rotation, and translation operations.

Although these results are inconclusive in terms of whether it is preferable to employ ‘complete’ or ‘incomplete’ N_{ss} sizes, these results nevertheless indicate that, when reproducing first and second order moments of a normal distribution, the MSS algorithm has an exponential rate of stochastic convergence (in the MSE sense) that improves by at least one order of magnitude on Monte Carlo. These results also indicate a statistical lack of bias, which has two powerful implications. First, because having statistically unbiased samples is necessary for trusting the meaning or interpretation of sample-based estimators for probability measures, these results validate the use of MSS estimators for probability measure approximation. Second, these results motivate future MSS applica-

tion as the underlying sampling algorithm in a particle-based filtering methodology with applications to spacecraft relative navigation.

6.5.4.2 MSS asymptotic convergence rate results, sample IPC

This subsection addresses the results on MSS convergence performance when reproducing the IPC, as obtained through regression on the $\widehat{\text{IPC}}\text{-MSE}$, which are shown in Fig. 6.11 for \mathbf{R} samples, and in Fig. 6.13 for \mathbf{X} samples.

Within $4\text{-}\sigma$ confidence, the MSS convergence rate is no better or worse than $u = 1$. Hence, it is appropriate to approximate the MSS rate of $\widehat{\text{IPC}}\text{-MSE}$ convergence as $u_{\text{MSS}} = 1$, which renders MSS performance in reproducing the IPC to be no worse than that of Monte Carlo.

There are multiple reasons why MSS $\widehat{\text{IPC}}\text{-MSE}$ convergence performance does not achieve the levels observed in MSS $\widehat{\underline{\mu}}\text{-MSE}$ and $\widehat{\Sigma}\text{-MSE}$ regression. First, even though $\widehat{\underline{\mu}}_{\text{MSS}}$, $\widehat{\Sigma}_{\text{MSS}}$, and $\widehat{p}_{E,\text{MSS}}$ are all constructed in the traditional form of weighted sample mean, covariance, and probability measure estimators, it can be shown that, without prior adjustment, the expected values of $\widehat{\underline{\mu}}_{\text{MSS}}$ and $\widehat{\Sigma}_{\text{MSS}}$ are scalar multiples of $\underline{\mu}$ and Σ , respectively, which can then be used to obtain the proper scaling factors needed to construct unbiased estimators within a finite number of shells, N_{sh} . However, this cannot be done for $\widehat{p}_{E,\text{MSS}}$. This can be explained in a couple of ways. For $\widehat{\underline{\mu}}_{\text{MSS}}$, through a symmetry argument, the sample mean $\widehat{\underline{\mu}}_l$ of points in the l^{th} Mahalanobis shell (i.e., $\{\tilde{\mathbf{x}}_{l,q}\}, q \in S_{N_{\text{ss}}}$) is an unbiased estimator for $\underline{\mu}$; the resulting lack of bias is maintained after aggregating the estimators, and the weights represent that estimators from shells with higher probability mass are trusted more highly. For $\widehat{\Sigma}_{\text{MSS}}$, unlike for $\widehat{\underline{\mu}}_{\text{MSS}}$, the sample estimator $\widehat{\Sigma}_l$ of the covariance of the points in the l^{th} Mahalanobis shell is not an unbiased estimator for Σ . However, $\mathbb{E}[\widehat{\Sigma}_l]$ is a scalar multiple of Σ , and the exact factor that relates $\mathbb{E}[\widehat{\Sigma}_l]$ and Σ may be found through the first and second order statistical properties of uniform distributions in $\mathbb{S}^{(s-1)}$ and $[0, 1]$, along with the assumption of independence between these distributions.

More abstractly, it is possible to do this because the form of the $\widehat{\underline{\mu}}_{\text{MSS}}$ and $\widehat{\underline{\Sigma}}_{\text{MSS}}$ estimators is suited to producing scalar multiples of the expected values of interest, and the domain of integration is fixed within each shell. In other words, a scale factor adjustment to $\widehat{\underline{\mu}}_{\text{MSS}}$ and $\widehat{\underline{\Sigma}}_{\text{MSS}}$ is available because, via the form of the estimators, the expectation to which the estimators should evaluate to is known.

On the other hand, such adjustments cannot be made for $\widehat{p}_{E,\text{MSS}}$ for several reasons. First, for an arbitrary measurable subset E , the true probability $p_E = p_{\underline{X}}(E)$ is unknown. Second, in general, E is not a union of Mahalanobis shells. Hence, even though for each l^{th} shell, the extent of the region of E inside the l^{th} shell ($E \cap V_{d_{l-1}}^{d_l}(\underline{X})$, for $\underline{X} \in \{\mathbf{R}, \mathbf{X}\}$) can be ascertained precisely, since the weights within each shell are averaged, there is inherent error between the true probability mass $p_{\underline{X}}(E \cap V_{d_{l-1}}^{d_l}(\underline{X}))$ and the fraction of the probability $p_{\underline{X}}(V_{d_{l-1}}^{d_l}(\underline{X}))$ corresponding to the number of points in the l^{th} shell that meet the definition of the E event. Therefore, even though $\widehat{p}_{E,\text{MSS}}$ correctly identifies (via sample points) which regions of the pdf of \underline{X} satisfy the E event, discrepancies in p_E approximations arising from the discretization of the weights within each shell can only be ameliorated through successive refinement of $V_{d_{\max}}(\underline{X})$ through increasing the number of shells.

These observations are consistent with previous MSS performance results in reproducing the IPC in lower-dimensional systems: for a fixed N_{sh} , increasing the number of samples per shell (N_{ss}) leads to probability measure convergence to within a fixed error threshold level that can only be reduced further with increasing N_{sh} . [46] Hence, in addition to error from IPC numerical estimates (assumed as truth values), the N_{sh} -dependent lower error threshold is another source of discrepancy when reproducing the IPC via MSS.

However, these results are consistent with the following interpretation of the convergence of sequences in some metric space. For a fixed $\varepsilon > 0$, and when choosing d_{\max} such that $p_{\text{exc}} < \varepsilon/2$, there exists an integer η_{sh} such that for every integer N_{sh} which satisfies

$\eta_{\text{sh}} \geq N_{\text{sh}}$, if $V_{i,j} \subseteq V_{d_{\max}}(\mathbf{R})$ or if $C_{i,j} \subseteq V_{d_{\max}}(\mathbf{X})$, it follows that

$$\widehat{\text{IPC}}_{\text{MSS-RMSE}} = \sqrt{\mathbb{E} \left[\left(\text{IPC} - \widehat{\text{IPC}}_{\text{MSS}} \right)^2 \right]} < \frac{\varepsilon}{2}$$

Via Jensen's inequality, and through properties of expected values, it follows that

$$\left| \text{IPC} - \mathbb{E} \left[\widehat{\text{IPC}}_{\text{MSS}} \right] \right| \leq \mathbb{E} \left[\left| \text{IPC} - \widehat{\text{IPC}}_{\text{MSS}} \right| \right] \leq \sqrt{\mathbb{E} \left[\left(\text{IPC} - \widehat{\text{IPC}}_{\text{MSS}} \right)^2 \right]} < \frac{\varepsilon}{2}$$

which implies, if $V_{i,j} \not\subseteq V_{d_{\max}}(\mathbf{R})$ or if $C_{i,j} \not\subseteq V_{d_{\max}}(\mathbf{X})$, that

$$\left| \text{IPC} - \mathbb{E} \left[\widehat{\text{IPC}}_{\text{MSS}} \right] \right| < \varepsilon$$

Hence, IPC convergence in the MSE sense, which has been demonstrated computationally in this subsection, is a much stronger result than convergence as stated in Proposition 22. Therefore, the results of this subsection on MSS IPC error properties, together with the results on $\widehat{\underline{\mu}}_{\text{MSS}}$ and $\widehat{\Sigma}_{\text{MSS}}$ convergence, are a computational validation of the MSS estimator properties asserted in Proposition 22, namely, that MSS IPC estimators can be made arbitrarily precise in a stochastic sense.

More generally, for an arbitrary measurable subset E , although the results in this subsection do not imply that true unbiased MSS probability measure estimators $\widehat{p}_{E,\text{MSS}}$ may be constructed, these results nevertheless validate the statement that such MSS probability measure estimators can be made arbitrarily precise in a stochastic sense, as asserted in Proposition 22. Although a computational investigation was not undertaken in this Chapter to study MSS estimators of the joint-time probability of collision, P_C , Proposition 22, (together with IPC MSS convergence results) justifies application of the MSS algorithm to estimate the P_C , as well as other probability measures. These conclusions validate use of the MSS algorithm in spacecraft collision risk assessment applications.

6.6 Conclusion

In this Chapter, a theoretical basis is presented for the Mahalanobis Shell Sampling (MSS) algorithm, which is designed to produce statistically random weighted samples of non-degenerate, multivariate normal distributions, in such a way that probabilistic outliers can be generated efficiently, i.e., without unduly penalizing sample size. This is achieved by employing uniformly distributed, independent samples in the $(s - 1)$ -unit hypersphere, $\mathbb{S}^{(s-1)}$, and the unit interval, $[0, 1]$, and then utilizing the first- and second-order statistics of normal distributions of interest in order to transform these point sets into probabilistically uniform sample points within Mahalanobis shells, which are regions bounded by hypersurfaces of constant Mahalanobis distance.

The first contribution of this Chapter is to present unbiased MSS estimators for the sample mean and covariance of a distribution of interest, as well as asymptotically unbiased MSS estimators for the probability measure of arbitrary measurable subsets in \mathbb{R}^s , including error bounds that are dependent of the truncation of the integration domain.

The second contribution of this Chapter is a methodology for application of randomized quasi-Monte Carlo (RQMC) techniques for the generation of uniformly distributed, independent samples in $\mathbb{S}^{(s-1)}$ and $[0, 1]$. Linearly scrambled Sobol nets in the unit hypercube, $[0, 1]^s$, are chosen because they retain the space-filling properties of deterministic Sobol nets, while introducing randomness into the samples in a way that allows for unbiased integral estimators, as well as integral variance estimation. Then, a technique is presented for transforming a single RQMC $[0, 1]^s$ sample into samples of $\mathbb{S}^{(s-1)}$ and $[0, 1]$.

The third contribution of this Chapter is a computational study on the quantification of MSS stochastic convergence properties; namely, the exponential rate of asymptotic convergence in the mean square error (MSE) sense, u_{MSS} . This contribution may be subdivided into four parts.

First, in order to produce a meaningful baseline for u_{MSS} comparison, the Monte Carlo

rate of convergence in the MSE sense, u_{MC} , was validated to within $4-\sigma$ confidence to be given by $u_{MC} = 1$ when reproducing the sample mean, covariance, and the IPC via Monte Carlo samples of the CW relative orbital dynamic state – specifically, the CW relative position, relative position rate, and relative state. This finding is in accordance with analytical properties of the Monte Carlo method.

Second, it is found that MSS error convergence in the MSE sense can be adequately modeled as a power function of the form $(\text{MSE})(n) = Cn^{-u_{MSS}}$ when reproducing the sample mean, covariance, and IPC via MSS samples based on the CW relative position, relative position rate, and relative state. This is necessary for meaningful comparisons between MSS and Monte Carlo stochastic convergence rates.

Third, it was found, when estimating sample mean and covariance, that the MSS algorithm achieves convergence in the order of $\mathcal{O}(n^{-2})$ in the MSE sense, which improves upon the corresponding Monte Carlo convergence rate by an order of magnitude.

Fourth, it was found, for a fixed number of shells, N_{sh} , that MSS estimators of the IPC achieve convergence in the order of $\mathcal{O}(n^{-1})$ in the MSE sense, which is comparable to Monte Carlo. Even though MSS IPC estimators are not unbiased due to sample weight averaging within each Mahalanobis shell, these results nevertheless validate the main theoretical result presented in this Chapter, namely, that MSS probability measure estimators can achieve arbitrary precision in a stochastic sense, which is consistent with prior work in IPC reproduction in lower-dimensional systems.

Therefore, through its geometric underpinnings, its theoretical guarantees of stochastic convergence, and its computational convergence rate performance, the MSS algorithm is an attractive sampling paradigm for a wide range of practical applications. First, the MSS method may be employed in a spacecraft relative navigation context as an underlying sampling algorithm within a particle-based filtering methodology. Second, the MSS method may be applied to spacecraft collision risk assessment, not just through MSS-based IPC computation, but also through computation of the joint-time probability of collision,

P_c ; even though MSS convergence properties when estimating the P_c have not been studied in this Chapter, the theoretical MSS convergence guarantees for arbitrary measurable subsets are applicable to the region of relative state space that defines the P_c . Third, more generally, through its geometric and probabilistic properties, the MSS algorithm would be a helpful computational tool in the field of rare event simulation.

CHAPTER 7
SPACECRAFT FORMATION COLLISION RISK QUANTIFICATION (PART 2) –
DISTANCE-BASED SFF COLLISION RISK INDICATORS

This Chapter describes the theoretical properties of the problem of finding extremal Euclidean distances from the origin of an reference frame in \mathbb{R}^s to the points in the d -Mahalanobis contour of a non-degenerate normal random variable in \mathbb{R}^s . These properties include a solution existence result, as well as bounds for such extremal Euclidean distances. Along with an area-preserving transformation from the unit 2-square to the unit 2-sphere, these theoretical properties are leveraged in order to pose an equivalent problem with reduced dimensionality and a simply connected search region, while also addressing singularities of the search regions which are caused by dimensionality-reducing transformations. The effectiveness of the modifications to this constrained optimization problem is examined in a pertinent relative orbital dynamic context.

7.1 Introduction

This Chapter addresses the minimum Euclidean distance from the origin to a “geometric” $3-\sigma$ contour, denoted by $\text{sep}_{\text{geo}|i,j}(t)$, as well as the minimum distance from the origin to an “equivalent” $3-\sigma$ contour, denoted by $\text{sep}_{\text{eq}|i,j}(t)$, which are formally defined in Subsection 2.6.2. This discussion includes a proof of the existence of the solution to the problems that define these indicators, upper and lower bounds on these solutions, as well as a unit square-based search methodology for the computation of these indicators, including mitigation

strategies for improving the search when it becomes ill-conditioned after long propagation horizons.

Although not included in this chapter, this dissertation also addresses several topics related to the computation of the 99.73% minimum distance, denoted by $\rho_{3\sigma}$. First, $\rho_{3\sigma}$ is formally defined in Definition 12, and $\rho_{3\sigma}$ is characterized in Subsubsection 9.3.4.1 as a quantile of the distribution the Euclidean norm of instantaneous relative position. Second, numerical and Monte Carlo sample computation methodologies for $\rho_{3\sigma}$ are presented in Subsections 9.4.1 and 9.4.2, respectively. Third, a hybrid numerical-sample based methodology is introduced in Subsection 9.4.3 for the computation of the probability density function (pdf) of the Euclidean norm of the relative position evaluated at the $\rho_{3\sigma}$ value, which is required for sensitivity studies of the $\rho_{3\sigma}$ collision risk indicator (cf. Subsubsection 9.3.4.2). Note: for implementation details on employing a large Monte Carlo sample framework for $\rho_{3\sigma}$ computation, the reader is encouraged to consult Appx. C.

7.2 Notation adjustments for this Chapter

Throughout this Chapter, balls and spheres are implicitly defined with respect to the Euclidean norm only. When the dimension of elements in $\mathbb{B}_r^s(\underline{x})$ is implicit, it is referred to as $\mathbb{B}_r(\underline{x})$ for simplicity. Additionally, the symbol “ $\mathbb{S}^{(s-1)}$ ” denotes $\mathbb{S}_1^{(s-1)}(\mathbf{0}_{s \times 1})$, i.e., the unit $(s - 1)$ -sphere (with respect to the Euclidean norm) centered at the origin of \mathbb{R}^s . Finally, the i, j subscripts are omitted from the notation of the instantaneous relative position $\mathbf{R}_{i,j}$.

7.3 Minimum Euclidean distance from origin to Mahalanobis contour – Theory

This section addresses the general problem of finding points on a d -Mahalanobis contour of a non-degenerate normal random variable \underline{X} in \mathbb{R}^s [denoted by $L_d(\underline{X})$] which are furthest and closest from the origin in \mathbb{R}^s as quantified by the Euclidean distance. The existence of such extremal points, as well as bounds for the Euclidean norms of their solution, are discussed.

Lemma 24 (Relating the unit sphere and Mahalanobis contour). Let $\underline{X} \sim \mathcal{N}(\underline{\mu}, \Sigma)$, where $\underline{\mu} \in \mathbb{R}^s$, and $\Sigma \in \mathbb{R}^{s \times s}$, $\Sigma > 0$. Let $d \in (0, \infty)$. Let the mapping $f_{d,\underline{X}} : \mathbb{S}^{(s-1)} \rightarrow \mathbb{R}^s$ be defined by the rule

$$f_{d,\underline{X}}(\underline{z}) = \underline{\mu} + d\Sigma^{1/2}\underline{z} \quad (7.1)$$

for \underline{z} in $\mathbb{S}^{(s-1)}$. Then,

$$L_d(\underline{X}) = f_{d,\underline{X}}(\mathbb{S}^{(s-1)}) \quad \diamond \quad (7.2)$$

Proof. Let the preceding assumptions and notation hold. Since $\Sigma > 0$, this implies that $\Sigma^{1/2} > 0$ and $\Sigma^{-1/2} > 0$ as well.[64] Thus, $f_{d,\underline{X}}$ is well defined. Let $g_{d,\underline{X}} : L_d(\underline{X}) \rightarrow \mathbb{R}^s$ be defined by the rule

$$g_{d,\underline{X}}(\underline{x}) = \frac{1}{d}\Sigma^{-1/2}(\underline{x} - \underline{\mu}) \quad (7.3)$$

Thus, $g_{d,\underline{X}}$ is also well defined. It will be proven that $f_{d,\underline{X}}(\mathbb{S}^{(s-1)}) = L_d(\underline{X})$.

1. $f_{d,\underline{X}}(\mathbb{S}^{(s-1)}) \subseteq L_d(\underline{X})$

Take $\underline{x} \in f_{d,\underline{X}}(\mathbb{S}^{(s-1)})$. Then, there exists $\underline{z} \in \mathbb{S}^{(s-1)}$ such that

$$\underline{x} = f_{d,\underline{X}}(\underline{z}) = \underline{\mu} + d\Sigma^{1/2}\underline{z}$$

Note: $\|\underline{z}\|_2 = 1$, so $\underline{z}^T \underline{z} = 1$. Thus,

$$\begin{aligned} D_{\underline{X}}^2(\underline{x}) &= (\underline{x} - \underline{\mu})^T \Sigma^{-1} (\underline{x} - \underline{\mu}) \\ &= (d\Sigma^{1/2}\underline{z})^T \Sigma^{-1} (d\Sigma^{1/2}\underline{z}) = d^2 \underline{z}^T \Sigma^{1/2} \Sigma^{-1} \Sigma^{1/2} \underline{z} \\ &= d^2 \underline{z}^T \underline{z} = d^2 \quad (7.4) \end{aligned}$$

Therefore, $\underline{x} \in L_d(\underline{X})$, which proves that $f_{d,\underline{X}}(\mathbb{S}^{(s-1)}) \subseteq L_d(\underline{X})$.

2. $L_d(\underline{X}) \subseteq f_{d,\underline{X}}(\mathbb{S}^{(s-1)})$

Take $\underline{x} \in L_d(\underline{X})$. Then,

$$(\underline{x} - \underline{\mu})^T \Sigma^{-1} (\underline{x} - \underline{\mu}) = d^2$$

Let $\underline{z} \doteq g_{d,\underline{X}}(\underline{x}) = \frac{1}{d} \Sigma^{-1/2} (\underline{x} - \underline{\mu})$. Then,

$$\underline{z}^T \underline{z} = \frac{1}{d^2} (\underline{x} - \underline{\mu})^T \Sigma^{-1} (\underline{x} - \underline{\mu}) = \frac{d^2}{d^2} = 1 \quad (7.5)$$

Thus, $\underline{z} \in \mathbb{S}^{(s-1)}$. Take $\underline{y} \doteq f_{d,\underline{X}}(\underline{z}) = \underline{\mu} + d \Sigma^{1/2} \underline{z}$. By definition, $\underline{y} \in f_{d,\underline{X}}(\mathbb{S}^{(s-1)})$. However, $\underline{z} = \frac{1}{d} \Sigma^{-1/2} (\underline{y} - \underline{\mu})$. It follows that $\underline{y} = \underline{x}$. Therefore, $\underline{x} \in f_{d,\underline{X}}(\mathbb{S}^{(s-1)})$, which proves that $L_d(\underline{X}) \subseteq f_{d,\underline{X}}(\mathbb{S}^{(s-1)})$.

It follows from statements 1 and 2 that $L_d(\underline{X}) = f_{d,\underline{X}}(\mathbb{S}^{(s-1)})$. □

Proposition 25. Let $\underline{X} \sim \mathcal{N}(\underline{\mu}, \Sigma)$, where $\underline{\mu} \in \mathbb{R}^s$, and $\Sigma \in \mathbb{R}^{s \times s}$, $\Sigma > 0$. Let $d \in (0, \infty)$. Then, a solution exists to the COP defined by Eqn. 7.6, i.e.

$$\begin{aligned} \min_{\underline{x} \in \mathbb{R}^s} \quad & \underline{x}^T \underline{x} \\ \text{s.t.} \quad & \underline{x} \in L_d(\underline{X}) \subsetneq \mathbb{R}^s \end{aligned} \quad (7.6)$$

Additionally, a solution exists to the COP defined by Eqn. 7.7, i.e.

$$\begin{aligned} \max_{\underline{x} \in \mathbb{R}^s} \quad & \underline{x}^T \underline{x} \\ \text{s.t.} \quad & \underline{x} \in L_d(\underline{X}) \subsetneq \mathbb{R}^s \quad \diamond \end{aligned} \quad (7.7)$$

Proof. The unit $(s - 1)$ -sphere, $\mathbb{S}^{(s-1)}$, is a closed set, and it is also bounded. Through the Heine-Borel Theorem, $\mathbb{S}^{(s-1)}$ is a compact set in \mathbb{R}^s . [34]

The function $f_{d,\underline{X}}$ is continuous. Via Lemma 24, $L_d(\underline{X}) = f_{d,\underline{X}}(\mathbb{S}^{(s-1)})$. Therefore,

$f_{d,\underline{X}}(\mathbb{S}^{(s-1)})$ is also compact. Let the function $h : \mathbb{R}^s \rightarrow [0, \infty)$ be defined by the rule

$$h(\underline{x}) = \underline{x}^T \underline{x} \quad (7.8)$$

for $\underline{x} \in \mathbb{R}^s$. Since h is a continuous function, it follows that $B \doteq h(L_d(\underline{X})) \subseteq \mathbb{R}$ is a compact set in \mathbb{R} . Because B is a compact set in \mathbb{R} , minimum and maximum values on B exist.[66] Let

$$a = \min(B) \quad (7.9)$$

$$b = \max(B) \quad (7.10)$$

Since there exist $\underline{x}^*, \underline{y}^* \in L_d(\underline{X})$ so that

$$a = h(\underline{x}^*) \quad (7.11)$$

$$b = h(\underline{y}^*) \quad (7.12)$$

it follows that \underline{x}^* and \underline{y}^* are solutions to the constrained optimization problems defined by Eqns. 7.6 and 7.7, respectively. \square

Proposition 26 (Solution bounds for distance extrema from origin to L_d). Let $\underline{X} \sim \mathcal{N}(\underline{\mu}, \Sigma)$, where $\underline{\mu} \in \mathbb{R}^s$, and $\Sigma \in \mathbb{R}^{s \times s}$, $\Sigma > 0$. Let $d \in (0, \infty)$. Let \underline{x}^* be a solution to the COP posed in Eq. 7.6. Let $\beta_U, \beta_L \in [0, \infty)$ be defined by

$$\beta_U \doteq \|\underline{\mu}\|_2 + d\sqrt{\max(\text{eig}(\Sigma))} \quad (7.13)$$

$$\beta_L \doteq \max\left\{0, d\sqrt{\min(\text{eig}(\Sigma))} - \|\underline{\mu}\|_2, \|\underline{\mu}\|_2 - d\sqrt{\max(\text{eig}(\Sigma))}\right\} \quad (7.14)$$

where $\text{eig}(\Sigma)$ is the set of eigenvalues of Σ . Then, β_U and β_L provide bounds for $\|\underline{x}^*\|_2$ as

given by Eq. 7.15.

$$0 \leq \beta_L \leq \inf_{\underline{x} \in L_d(\underline{X})} \|\underline{x}\|_2 \leq \|\underline{x}^*\|_2 \leq \sup_{\underline{x} \in L_d(\underline{X})} \|\underline{x}\|_2 \leq \beta_U < \infty \quad \diamond \quad (7.15)$$

Proof. Take $\underline{\mu} \in \mathbb{R}^s$, and $\Sigma \in \mathbb{R}^{s \times s}$, $\Sigma > 0$. Let $\underline{W} \sim \mathcal{N}(\underline{\mathbf{0}}_{s \times 1}, \Sigma)$. Via Proposition 25, there exist $\underline{q}, \underline{q}' \in L_d(\underline{W})$ so that

$$0 \leq \|\underline{q}\|_2 \leq \|\underline{w}\|_2 \leq \|\underline{q}'\|_2 < \infty \quad (7.16)$$

for all \underline{w} in $L_d(\underline{W})$. The first part of the proof will show that $\|\underline{q}\|_2 = d\sqrt{\min(\text{eig}(\Sigma))}$ and that $\|\underline{q}'\|_2 = d\sqrt{\max(\text{eig}(\Sigma))}$.

Let $\mathbf{U}, \mathbf{S}, \mathbf{V} \in \mathbb{R}^{s \times s}$ comprise the singular value decomposition (SVD) matrices of Σ . Since $\Sigma > 0$, $\mathbf{U} = \mathbf{V}$, \mathbf{U} is orthogonal, and $\mathbf{S} > 0$ also. Thus, $\Sigma = \mathbf{U}\mathbf{S}\mathbf{U}^T$, and

$$\Sigma^{1/2} = \mathbf{U}\mathbf{S}^{1/2}\mathbf{U}^T \quad (7.17)$$

Since $\mathbf{S} > 0$ is diagonal, the entries on its diagonal are its eigenvalues, so \mathbf{S} can be expressed without loss of generality as

$$\mathbf{S} = \begin{bmatrix} \xi_1 & & \\ & \ddots & \\ & & \xi_s \end{bmatrix} \quad (7.18)$$

where $0 < \xi_1 \leq \dots \leq \xi_s < \infty$. Let $\underline{\mathbf{v}}_j$ ($j \in \{1, \dots, s\}$) be the eigenvectors of Σ , i.e., the column vectors of \mathbf{U} . Thus,

$$\Sigma^{1/2}\underline{\mathbf{v}}_j = \xi_j^{1/2}\underline{\mathbf{v}}_j \quad (7.19)$$

for all $j \in \{1, \dots, s\}$. Let $\underline{\mathbf{a}}_1$ be the unit vector of Σ corresponding to the eigenvalue ξ_1 , i.e.,

$$\Sigma^{1/2}\underline{\mathbf{a}}_1 = \xi_1^{1/2}\underline{\mathbf{a}}_1 \quad (7.20)$$

Let $\underline{\mathbf{b}} \in \mathbb{S}^{(s-1)}$, i.e., $\underline{\mathbf{b}}$ is any unit vector in \mathbb{R}^s . It will be proven that

$$\xi_1^{1/2} = \|\Sigma^{1/2}\underline{\mathbf{a}}_1\|_2 \leq \|\Sigma^{1/2}\underline{\mathbf{b}}\|_2 \quad (7.21)$$

Since the columns of \mathbf{U} form an orthonormal basis for \mathbb{R}^s , there exist $b_1, \dots, b_s \in \mathbb{R}$ such that

$$\underline{\mathbf{b}} = \sum_{j=1}^s b_j \underline{\mathbf{v}}_j \quad (7.22)$$

and $\sum_j b_j^2 = 1$. Then,

$$\begin{aligned} \|\Sigma^{1/2}\underline{\mathbf{b}}\|_2^2 &= (\Sigma^{1/2}\underline{\mathbf{b}})^T (\Sigma^{1/2}\underline{\mathbf{b}}) = \left(\sum_{i=1}^s b_i \Sigma^{1/2} \underline{\mathbf{v}}_i \right)^T \left(\sum_{j=1}^s b_j \Sigma^{1/2} \underline{\mathbf{v}}_j \right) \\ &= \left(\sum_{i=1}^s b_i \sqrt{\xi_i} \underline{\mathbf{v}}_i \right)^T \left(\sum_{j=1}^s b_j \sqrt{\xi_j} \underline{\mathbf{v}}_j \right) = \sum_{i=1}^s \sum_{j=1}^s (b_i \sqrt{\xi_i}) (b_j \sqrt{\xi_j}) \underline{\mathbf{v}}_i^T \underline{\mathbf{v}}_j \quad (7.23) \end{aligned}$$

The $\underline{\mathbf{v}}_j$ vectors are orthonormal; i.e.,

$$\underline{\mathbf{v}}_i^T \underline{\mathbf{v}}_j = \begin{cases} 1, & \text{if } i = j \\ 0, & \text{otherwise} \end{cases} \quad (7.24)$$

Also, $0 < \xi_1 \leq \xi_i$ for all i in $\{1, \dots, s\}$. Therefore,

$$\begin{aligned} \|\Sigma^{1/2}\underline{\mathbf{b}}\|_2^2 &= \sum_{i=1}^s (b_i \sqrt{\xi_i}) (b_i \sqrt{\xi_i}) = \sum_{i=1}^s b_i^2 \xi_i \\ &\geq \sum_{i=1}^s b_i^2 \xi_1 = \xi_1 \sum_{i=1}^s b_i^2 = \xi_1 = \|\Sigma^{1/2}\underline{\mathbf{a}}_1\|_2^2 \quad (7.25) \end{aligned}$$

which proves that

$$\sqrt{\xi_1} = \|\Sigma^{1/2}\underline{\mathbf{a}}_1\|_2 \leq \|\Sigma^{1/2}\underline{\mathbf{b}}\|_2 \quad (7.26)$$

for every $\underline{\mathbf{b}} \in \mathbb{S}^{(s-1)}$, i.e., if $\underline{\mathbf{b}}$ is any unit vector in \mathbb{R}^s .

Take $\underline{w} \in L_d(\underline{W})$. Via Lemma 24, there exists $\underline{\mathbf{c}} \in \mathbb{S}^{(s-1)}$ so that $\underline{w} = d\Sigma^{1/2}\underline{\mathbf{c}}$. Also, via Lemma 24, there exists $\underline{w}_1 \in L_d(\underline{W})$ such that $\underline{w}_1 = d\Sigma^{1/2}\underline{\mathbf{a}}_1$. Therefore,

$$\sqrt{\xi_1} = \left\| \frac{1}{d}\underline{w}_1 \right\|_2 = \|\Sigma^{1/2}\underline{\mathbf{a}}_1\|_2 \leq \|\Sigma^{1/2}\underline{\mathbf{c}}\|_2 = \left\| \frac{1}{d}\underline{w} \right\|_2 \quad (7.27)$$

for all \underline{w} in $L_d(\underline{W})$. Since $q \in L_d(\underline{W})$, it follows from Eq. 7.27 that

$$\|\underline{w}_1\|_2 \leq \|q\|_2 \quad (7.28)$$

However, because of how q is characterized in Eq. 7.16, since $\underline{w}_1 \in L_d(\underline{W})$, then

$$\|q\|_2 \leq \|\underline{w}_1\|_2 \quad (7.29)$$

It follows that

$$\|q\|_2 = \|\underline{w}_1\|_2 = d\sqrt{\xi_1} \quad (7.30)$$

A similar argument can be construed for q' , employing ξ_s instead. Therefore,

$$\|q\|_2 = d\sqrt{\min(\text{eig}(\Sigma))} \quad (7.31)$$

$$\|q'\|_2 = d\sqrt{\max(\text{eig}(\Sigma))} \quad (7.32)$$

which concludes the first part of this proof.

The second part of this proof is to obtain an upper bound for $\|\underline{x}^*\|_2$. Take $\underline{x} \in L_d(\underline{X})$. Then, by definition, there exists $\underline{w} \in L_d(\underline{W})$ so that $\underline{x} = \underline{\mu} + \underline{w}$. Additionally, there exist $\underline{y}, \underline{y}' \in L_d(\underline{X})$ such that $\underline{y} = \underline{\mu} + q$ and $\underline{y}' = \underline{\mu} + q'$. Let \underline{y} and \underline{y}' satisfy these conditions. This observation allows restating the conditions posed in Eq. 7.16 as given by

$$0 \leq \|\underline{y} - \underline{\mu}\|_2 \leq \|\underline{x} - \underline{\mu}\|_2 \leq \|\underline{y}' - \underline{\mu}\|_2 < \infty \quad (7.33)$$

for all \underline{x} in $L_d(\underline{X})$, as illustrated in Fig. 7.1. It is helpful to note that

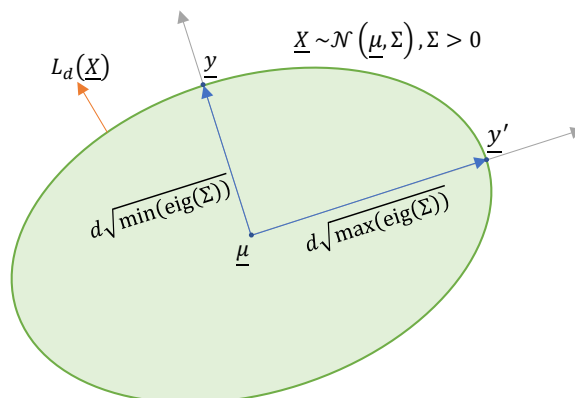


Figure 7.1: Illustration of bounds of $L_d(\underline{X})$ (in two-dimensional case) about its expected value.

$$\|\underline{y} - \underline{\mu}\|_2 = d\sqrt{\xi_1} \quad (7.34)$$

$$\|\underline{y}' - \underline{\mu}\|_2 = d\sqrt{\xi_s}. \quad (7.35)$$

Through the triangle inequality on the Euclidean norm in \mathbb{R}^s , it follows that

$$\begin{aligned} \|\underline{x}\|_2 &= \|(\underline{x} - \underline{\mu}) + \underline{\mu}\|_2 \leq \|\underline{x} - \underline{\mu}\|_2 + \|\underline{\mu}\|_2 \\ &\leq \|\underline{y}' - \underline{\mu}\|_2 + \|\underline{\mu}\|_2 = d\sqrt{\xi_s} + \|\underline{\mu}\|_2 =: \beta_U \end{aligned} \quad (7.36)$$

Hence, β_U is a real-valued, positive constant that only depends on the first- and second-order statistics of \underline{X} , i.e., on $\underline{\mu}$ and Σ . Thus, β_U is an upper bound on $\|\underline{x}\|_2$ for all \underline{x} in $L_d(\underline{X})$ – which, in particular, includes $\|\underline{x}^*\|_2$. Since β_U is a real number, it follows that

$$0 \leq \|\underline{x}\|_2 \leq \sup_{\underline{x} \in L_d(\underline{X})} \|\underline{x}\|_2 \leq \beta_U < \infty \quad (7.37)$$

for all \underline{x} in $L_d(\underline{X})$.

The third and final part of this proof is to obtain lower bounds for $\|\underline{x}^*\|_2$. First, it can be

seen again, through application of the triangle inequality on the Euclidean norm in \mathbb{R}^s , that

$$\|\underline{x} - \underline{\mu}\|_2 = \|\underline{x} + (-\underline{\mu})\|_2 \leq \|\underline{x}\|_2 + \|\underline{\mu}\|_2 \quad (7.38)$$

Thus

$$d\sqrt{\xi_1} - \|\underline{\mu}\|_2 = \|\underline{y} - \underline{\mu}\|_2 - \|\underline{\mu}\|_2 \leq \|\underline{x} - \underline{\mu}\|_2 - \|\underline{\mu}\|_2 \leq \|\underline{x}\|_2 \quad (7.39)$$

Let $\beta_{L,1} \doteq d\sqrt{\min(\text{eig}(\Sigma))} - \|\underline{\mu}\|_2$. Then, $\beta_{L,1} \leq \|\underline{x}\|_2$ for all \underline{x} in $L_d(\underline{X})$.

Next, through further application of the triangle inequality on the Euclidean norm in \mathbb{R}^s , it can be seen that

$$\|\underline{\mu}\|_2 = \|(\underline{\mu} - \underline{x}) + \underline{x}\|_2 \leq \|\underline{\mu} - \underline{x}\|_2 + \|\underline{x}\|_2 = \|\underline{x} - \underline{\mu}\|_2 + \|\underline{x}\|_2 \quad (7.40)$$

Thus,

$$\|\underline{\mu}\|_2 - d\sqrt{\xi_s} = \|\underline{\mu}\|_2 - \|\underline{y}' - \underline{\mu}\|_2 \leq \|\underline{\mu}\|_2 - \|\underline{x} - \underline{\mu}\|_2 \leq \|\underline{x}\|_2 \quad (7.41)$$

Let $\beta_{L,2} \doteq \|\underline{\mu}\|_2 - d\sqrt{\max(\text{eig}(\Sigma))}$. Then, $\beta_{L,2} \leq \|\underline{x}\|_2$ for all \underline{x} in $L_d(\underline{X})$.

Finally, $0 \leq \|\underline{x}\|_2$ for all \underline{x} in $L_d(\underline{X})$. This observation follows from the non-negativity of the Euclidean norm in \mathbb{R}^s .

Let $\beta_L \doteq \max\{0, \beta_{L,1}, \beta_{L,2}\}$. Hence, $\beta_L \leq \|\underline{x}\|_2$ for all \underline{x} in $L_d(\underline{X})$; i.e., β_L is a lower bound for $\|\underline{x}\|_2$. Therefore,

$$0 \leq \beta_L \leq \inf_{\underline{x} \in L_d(\underline{X})} \|\underline{x}\|_2 \leq \|\underline{x}\|_2 < \infty \quad (7.42)$$

for all \underline{x} in $L_d(\underline{X})$. Combining Eqns. 7.37 and 7.42, it follows that

$$0 \leq \beta_L \leq \inf_{\underline{x} \in L_d(\underline{X})} \|\underline{x}\|_2 \leq \|\underline{x}\|_2 \leq \sup_{\underline{x} \in L_d(\underline{X})} \|\underline{x}\|_2 \leq \beta_U < \infty \quad (7.43)$$

for all \underline{x} in $L_d(\underline{X})$. Since Eq. 7.43 applies to $\|\underline{x}^*\|_2$ in particular, the result follows. \square

Corollary 27. Let $a_{\min}, a_{\max} \in \mathbb{R}$. Let β_L and β_U be bounds for the COP defined in Eq. 7.6, as stated in Proposition 26. Then, the COP posed in Eq. 7.44, i.e.,

$$\begin{aligned} \min_{\underline{x} \in \mathbb{R}^s} \quad & f(\underline{x}) = a_{\min} + \frac{a_{\max} - a_{\min}}{\beta_U^2 - \beta_L^2} (\|\underline{x}\|_2^2 - \beta_L^2) \\ \text{s.t.} \quad & \underline{x} \in L_d(\underline{X}) \subsetneq \mathbb{R}^s \end{aligned} \tag{7.44}$$

is an equivalent, scaled version of the original COP, i.e., both COPs have equivalent solutions. \diamond

7.4 Minimum Euclidean distance from origin to Mahalanobis contour – Computational algorithm in \mathbb{R}^3

For a non-degenerate normal random variable \underline{X} in \mathbb{R}^s , Lemma 24 shows that $L_d(\underline{X}) \subsetneq \mathbb{R}^s$ and the unit $(s-1)$ -sphere are isomorphic. Additionally, it is known that the unit 2-square and the unit 2-sphere are also isomorphic to within boundary singularities. These facts, as well as the results found in the preceding subsection, are employed to develop a technique for obtaining the minimum Euclidean distance from the origin to $L_d(\underline{\mathbf{R}})$ for a non-degenerate normal random variable $\underline{\mathbf{R}}$ in \mathbb{R}^3 . That is, this section introduces a technique for obtaining a solution to the COP posed in Eq. 2.44, through which the distance-based SFF collision risk indicators represented by Methodologies 1 and 2 are defined. Specifically, the $L_d(\underline{\mathbf{R}})$ constraint and the aforementioned isomorphisms allow the search space to be the unit 2-square instead of $L_d(\underline{\mathbf{R}})$, which simplifies the search process, as illustrated in Fig. 7.2.

Conceptually, this process is similar to the generation of an MSS sample, with a few differences. First, an MSS sample may be generated in \mathbb{R}^s for any $s \in \mathbb{N}$, whereas the current computational algorithm is restricted for application in \mathbb{R}^3 . Second, an MSS sample is composed by the union of samples in $L_{d_l}(\underline{X})$ (for multiple d_l values), and each $L_{d_l}(\underline{X})$ is randomized so as to be more uniformly distributed in over its corresponding Mahalanobis

shell $V_{d_{l-1}}^{d_l}(\underline{X})$. On the other hand, the current computational algorithm focuses on a sample of $L_d(\mathbf{R})$ for a single d value.

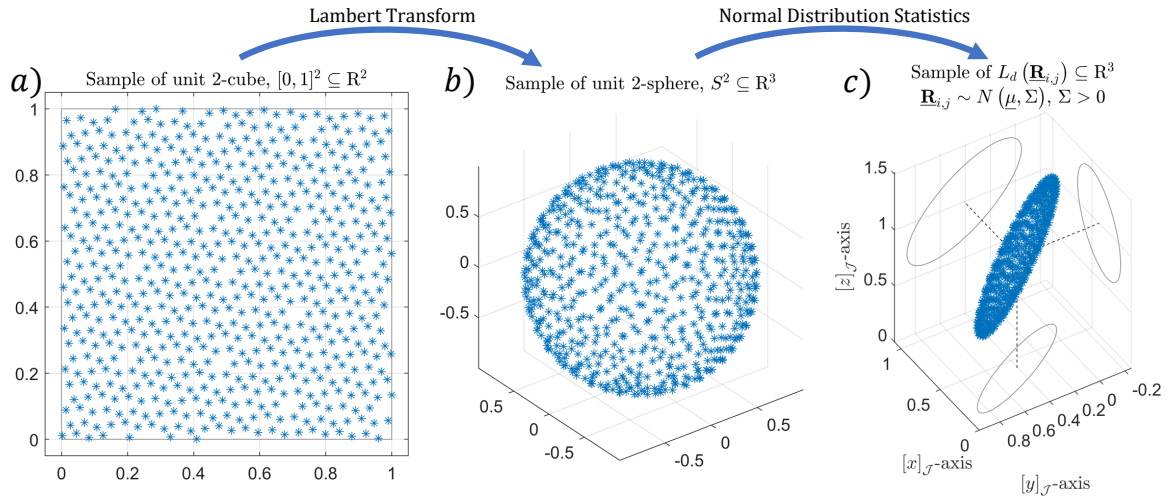


Figure 7.2: Process of finding initial conditions in Methodologies 1 & 2 in \mathbb{R}^3 : a) sample of unit 2-square, b) sample of unit 2-sphere, and c) sample of d -Mahalanobis contour, L_d .

1. Finding initial conditions:

First, a sample of evenly distributed points in the unit square is obtained through quasi-random number sequence (qrns) generation methods. Some widely employed qrns techniques for unit hypercube sampling include the Sobol, Niederreiter, Halton, Faure, and Hammersley sequences.[131, 132, 133, 121, 134] For more further background on specific qrns-based uniform unit-hypercube sampling constructions and computational implementations, the reader is encouraged to consult Ref. [135], Chaps. 2, 5; Ref. [120], Chaps. 5-6; Ref. [136], Chaps. 3-4; and Ref. [73], Ch. 2. In this dissertation (specifically, in Section 8.4), the Roberts method for unit hypercube sampling is employing to obtain a unit square sample for finding a suitable initial conditon for the search.[137]

Second, this uniform sample of the unit 2-square is mapped (or “lifted”) into a sample of the unit 2-sphere. In this dissertation, the area-preserving Lambert transform is used for this mapping, which ensures that the sample of the unit 2-sphere is also uniform, even in higher dimensions.[119]

Then, through inspection, the initial point in the unit 2-sphere, $\underline{\mathbf{z}}_0$ can be found as

$$\underline{\mathbf{z}}_0 = \underset{\underline{\mathbf{z}} \in \tilde{S}(N_{\text{small}})}{\operatorname{argmin}} \|\underline{\mathbf{r}}(\underline{\mathbf{z}})\|_2^2 \quad (7.45)$$

where $\tilde{S}(N_{\text{small}})$ is a sample of the unit 2-sphere with sample size N_{small} where

$$\underline{\mathbf{r}}(\underline{\mathbf{z}}) \doteq f_{d,\underline{\mathbf{R}}}(\underline{\mathbf{z}}) = \underline{\boldsymbol{\mu}} + d\Sigma^{1/2}\underline{\mathbf{z}} \quad (7.46)$$

where $\underline{\mathbf{R}} \sim \mathcal{N}(\underline{\boldsymbol{\mu}}, \Sigma)$, where $\underline{\boldsymbol{\mu}} \in \mathbb{R}^3$, $\Sigma \in \mathbb{R}^{3 \times 3}$, $\Sigma > 0$. Thus, $\underline{\mathbf{r}}(\underline{\mathbf{z}}_0)$ is the sample point in $L_d(\underline{\mathbf{R}})$ whose Euclidean norm is closest to the Euclidean norm of the optimal point(s), $\|\underline{\mathbf{r}}^*\|_2$. Because $\underline{\mathbf{r}}^*$ may not be unique, it is helpful to store several $\underline{\mathbf{z}}_0$ initial guesses.

It is recommended that N_{small} may satisfy $N_{\text{small}} \ll N_{\text{MC}}$, i.e., N_{small} should be significantly smaller than sample sizes required to accurately reproduce the probability of rare events; cf. Subsection 8.4.1. At this stage, only an initial guess is needed.

2. Reformulating search in $L_d(\underline{\mathbf{R}})$ as search in unit 2-square:

Since the sample of $L_d(\underline{\mathbf{R}})$ is nearly uniform, $\underline{\mathbf{z}}_0$ is expected to be close to $\underline{\mathbf{z}}^*$ under some metric. However, even with the isomorphism between $L_d(\underline{\mathbf{R}})$ and the unit 2-sphere posed in Lemma 24, modifying the objective function in Eq. 2.44 so that a solution is found on the unit 2-sphere still yields a three-dimensional search space with a nonlinear equality constraint (namely, unity inner product).

Nevertheless, the aforementioned equality constraint, along with a coordinate transformation, can be used to reformulate the search on the unit 2-sphere as a search in the unit 2-square. This technique is advantageous for the following reasons: a) it reduces the dimension of the search space from 3 to 2, b) it replaces equality constraints with inequality constraints, and c) it yields a search space that is simply connected.

The Lambert area-preserving transform in \mathbb{R}^3 , denoted by $T_{\mathbb{S}^2} : [0, 1] \times [0, 1] \rightarrow \mathbb{S}^2$, is

given by

$$T_{\mathbb{S}^2} \left(\begin{bmatrix} y_1 \\ y_2 \end{bmatrix} \right) = \begin{bmatrix} \sqrt{1 - (1 - 2y_2)^2} \cos(2\pi y_1) \\ \sqrt{1 - (1 - 2y_2)^2} \sin(2\pi y_1) \\ 1 - 2y_2 \end{bmatrix} \quad (7.47)$$

for all $[y_1, y_2]^T$ in $[0, 1) \times [0, 1]$. In this Chapter, the Lambert transform is used for the mapping from the unit 2-square to the unit 2-sphere. The Lambert transform is suitable for this purpose because it maps uniformly distributed samples in $[0, 1) \times [0, 1]$ to uniformly distributed samples in \mathbb{S}^2 . [119] The Lambert transform is further discussed in Subsubsection 9.3.1.2.

3. Addressing issues with search in unit 2-square space:

It is a known fact that dimension-reducing isomorphisms between the unit 2-square and the unit 2-sphere introduce singularities to the formulation. This remains the case when the Lambert transform in \mathbb{R}^3 is employed; specifically, the direct Lambert transform is not unique for $y_2 = \pm 1$. Therefore, the inverse Lambert transform is singular in the neighborhood of $\underline{z} = \pm[0, 0, 1]^T$. Figs. 7.3 and 7.4 summarize the conceptual issues that arise when applying the foregoing Lambert transform-based methodology to minimization problems subject to dimension-reducing constraints.

The first issue, shown in Fig. 7.3, is that small search regions in \mathbb{S}^2 near $\pm[0, 0, 1]^T$ do not correspond to small search regions in the unit square. More precisely, pre-images [through $(T_{\mathbb{S}^2})^{-1}$] of open neighborhoods (relative to \mathbb{S}^2) centered at $\pm[0, 0, 1]^T$, while converging to a single value of y_2 , can include elements with any value of $y_1 \in [0, 1)$. Thus, the search space in \mathbb{S}^2 in the neighborhood of $\pm[0, 0, 1]^T$ becomes artificially enlarged through the distortion introduced by the $(T_{\mathbb{S}^2})^{-1}$ mapping. This shows that Lambert transform-based unit 2-square optimization is unsuitable for initial conditions in \mathbb{S}^2 in the neighborhood of $\pm[0, 0, 1]^T$.

The second issue, shown in Fig. 7.4a, is that small, simply connected search regions in

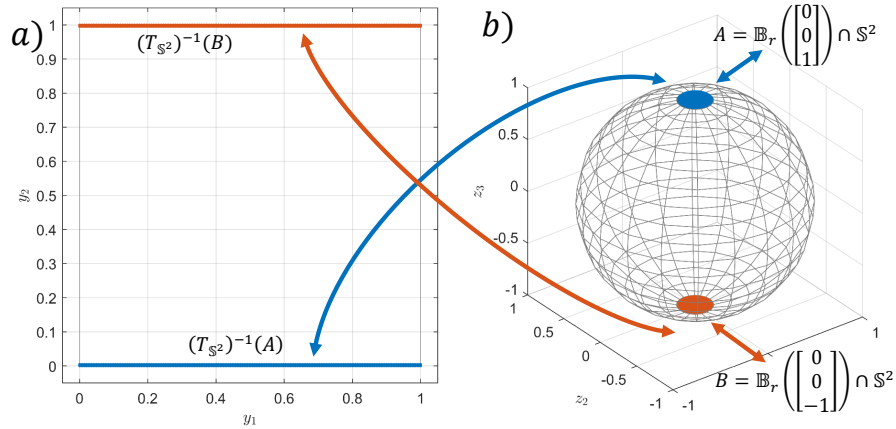


Figure 7.3: Distortions introduced by the Lambert transform to pre-images of open balls (relative to \mathbb{S}^2) centered at $\pm[0, 0, 1]^T$: a) unit 2-square space, b) unit 2-sphere space.

\mathbb{S}^2 near $[1, 0, 0]^T$ do not result in simply connected pre-images in the unit square [through $(T_{\mathbb{S}^2})^{-1}$]. On the contrary, such pre-images consist of two disjoint regions in the unit square whose y_1 values are at opposite ends of the interval $[0, 1]$. If the initial condition is in one of these regions while the optimal point is in the other region, it would be difficult to reach the optimal point with a search that is based on this initial condition. Thus, Lambert transform-based unit 2-square optimization is also unsuitable for initial conditions in \mathbb{S}^2 in the neighborhood of $[1, 0, 0]^T$.

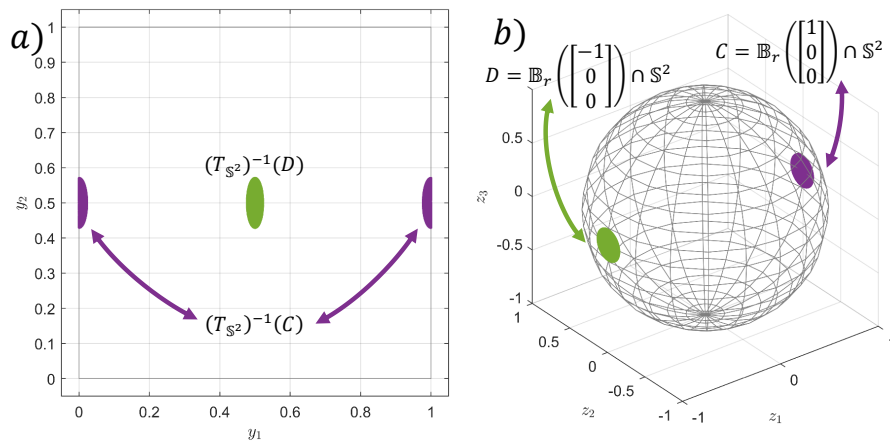


Figure 7.4: Distortions introduced by the Lambert transform to pre-images of open balls (relative to \mathbb{S}^2) centered at $\pm[1, 0, 0]^T$: a) unit 2-square space, b) unit 2-sphere space.

The aforementioned caveats may be avoided by defining a coordinate transformation $\Xi_{\mathcal{J}', \mathcal{J}}$ that allows representing \underline{z}_0 , which is implicitly represented in the coordinates of a

frame \mathcal{J} , in the coordinates of a frame \mathcal{J}' in which $\mathbf{z}'_0 = [-1, 0, 0]^T$. The unit 2-square representation of $\mathbf{z}'_0, \mathbf{y}'_0$, is given by $\mathbf{y}'_0 = [0.5, 0.5]^T$. The benefit of doing so is that small, simply connected search regions in \mathbb{S}^2 near $[-1, 0, 0]^T$ correspond to small, simply connected pre-images in the unit square near $\mathbf{y}'_0 = [0.5, 0.5]^T$, as shown in Fig. 7.4b. Thus, doing a search in \mathbf{y}' unit square coordinates would address the boundary distortions as desired. The $\Xi_{\mathcal{J}', \mathcal{J}}$ DCM is given by

$$\Xi_{\mathcal{J}', \mathcal{J}} \doteq A_{323}(\theta_0, -\lambda_0, \pi) = A_3(\pi) A_2(-\lambda_0) A_3(\theta_0) \quad (7.48)$$

where

$$\theta_0 = \text{atan2}([0, 1, 0] \mathbf{z}_0, [1, 0, 0] \mathbf{z}_0) \quad (7.49)$$

and

$$\lambda_0 = \arcsin([0, 0, 1] \mathbf{z}_0) \quad (7.50)$$

For the explicit forms of the A_2 and A_3 matrices, see Eqns. 2.4 and 2.5, respectively. It is clear that \mathbf{z}_0 and \mathbf{z}'_0 are related through $\Xi_{\mathcal{J}', \mathcal{J}}$ as

$$\Xi_{\mathcal{J}', \mathcal{J}} \mathbf{z}_0 = \begin{bmatrix} -1 \\ 0 \\ 0 \end{bmatrix} =: \mathbf{z}'_0 \quad (7.51)$$

4. Summary of search technique:

Let the functions $f_{L_d(\mathbf{R})} : [0, 1] \times [0, 1) \rightarrow [a_{\min}, a_{\max}]$ and $g_{L_d(\mathbf{R})} : [0, 1] \times [0, 1) \rightarrow \mathbb{R}^3$ be defined as

$$f_{L_d(\mathbf{R})}(\mathbf{y}') = a_{\min} + \frac{a_{\max} - a_{\min}}{\beta_U^2 - \beta_L^2} \left(\|g_{L_d(\mathbf{R})}(\mathbf{y}')\|_2^2 - \beta_L^2 \right) \quad (7.52)$$

$$g_{L_d(\mathbf{R})}(\mathbf{y}') = (\Xi_{\mathcal{J}', \mathcal{J}}) [f_{d, \mathbf{R}}(\Xi_{\mathcal{J}, \mathcal{J}'} [T_{\mathbb{S}^2}(\mathbf{y}')])] \quad (7.53)$$

for every $\mathbf{y}' \in [0, 1] \times [0, 1)$, where $\mathbf{R} \sim \mathcal{N}(\underline{\mu}, \Sigma)$, where $\underline{\mu} \in \mathbb{R}^3, \Sigma \in \mathbb{R}^{3 \times 3}, \Sigma > 0$; where

$\Xi_{\mathcal{J}',\mathcal{J}}$ is defined in terms of \mathbf{z}_0 as given by Eqns. 7.45, 7.48, 7.49, and 7.50; where β_L and β_U are defined in terms of d , $\underline{\mu}$, and Σ as stated in Proposition 26; and where a_{\min} and a_{\max} are scaling constants in \mathbb{R} . Via Eq. 7.1, $g_{L_d(\mathbf{R})}(\mathbf{y}')$ may be explicitly expressed as

$$g_{L_d(\mathbf{R})}(\mathbf{y}') = (\Xi_{\mathcal{J}',\mathcal{J}}) \underline{\mu} + d (\Xi_{\mathcal{J}',\mathcal{J}}) \Sigma^{1/2} (\Xi_{\mathcal{J},\mathcal{J}'} [T_{\mathbb{S}^2}(\mathbf{y}')] \quad (7.54)$$

Using the foregoing definitions, the problem of finding the minimum distance from the origin of 3D relative position space to the d -Mahalanobis contour $L_d(\mathbf{R})$, previously posed in Proposition 25, is equivalent to the scaled COP posed in Corollary 27 after modifications that account for the Lambert transform and the $\Xi_{\mathcal{J}',\mathcal{J}}$ coordinate transformation, as posed in Eq. 7.55:

$$\min_{\mathbf{y}' \in [0,1] \times [0,1]} f_{L_d(\mathbf{R})}(\mathbf{y}') \quad (7.55)$$

It is suggested to set $a_{\min} = -1$ and $a_{\max} = 1$.

7.5 Simulation Cases, Results and Discussion

The foregoing methodology for the computation of the minimum distance from the origin to points in $L_d(\mathbf{R})$ is employed in the context of Examples 3D.001–026, which are subject to CW dynamics, and which are listed in Section A.2. The outcome of this application is utilized in the computational study undertaken in Chapter 8, which compares the consistency of the correlation relationship between dissimilar types of collision risk indicators. Such results are expounded in Subsection 8.4.3.

7.6 Minimum Euclidean distance from origin to Mahalanobis contour – Effectiveness of \mathbb{R}^3 algorithm

As shown in Fig. 7.5, it is possible for the COP posed in Eq. 7.55 to have a strictly convex domain in the neighborhood of the initial condition and the optimal, which yields a

straightforward search for the unique global optimal. However, more generally, this COP does not have guarantees of convexity, and multiple, disjoint local minima regions can be observed in general, as seen in Fig. 7.6a. Furthermore, numerical ill-conditioning can be expected in the neighborhood of local optima, as seen in Fig. 7.6b.

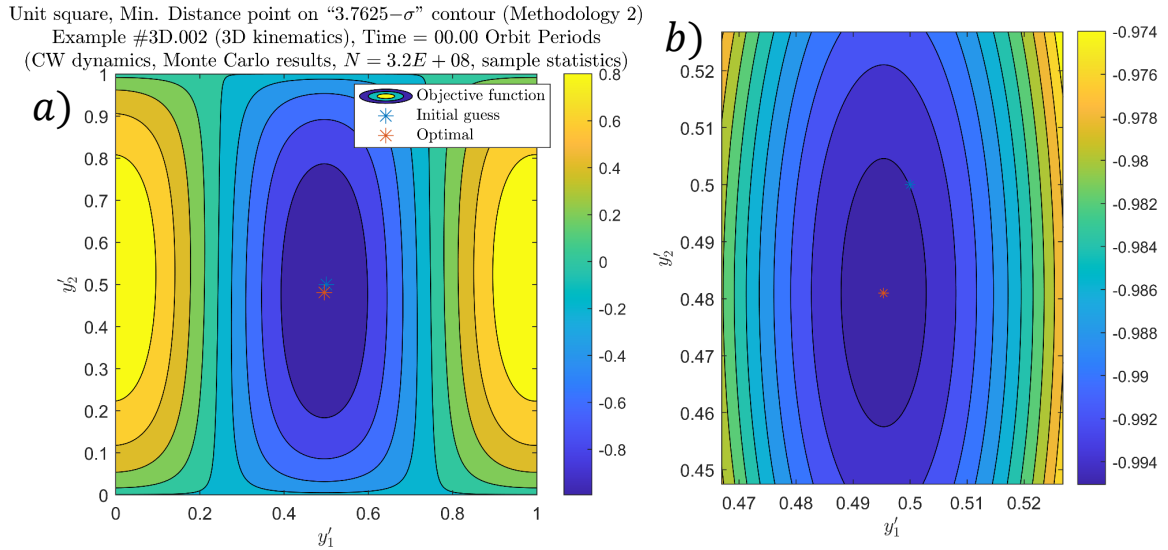


Figure 7.5: Objective function, min. distance from $L_d(\mathbf{R}_{i,j})$ to origin, unit 2-square space (Eq. 7.55), strictly convex neighborhood around unique global optimal: a) unit 2-square, and b) closeup.

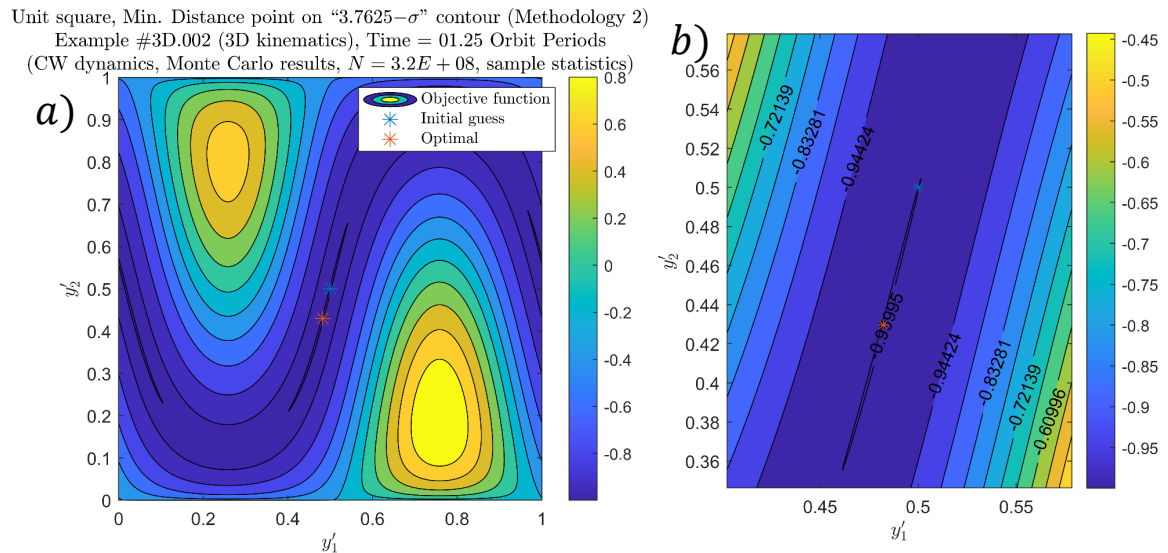


Figure 7.6: Objective function, min. distance from $L_d(\mathbf{R}_{i,j})$ to origin, unit 2-square space (Eq. 7.55), ill-conditioned neighborhood around global optimal: a) unit 2-square, and b) closeup.

The useful outcome of solving the COP posed in Eq. 7.55 is the Euclidan norm of the global optimal point, $\|\underline{\mathbf{r}}^*\|_2$, not the global optimal point $\underline{\mathbf{r}}^*$ itself. However, because two mappings must occur before $(\mathbf{y}')^*$ is translated to $\underline{\mathbf{r}}^*$ (through the Lambert transform $T_{\mathbb{S}^2}$ and the $f_{d,\mathbf{R}}$ function, respectively), small distortions to $(\mathbf{y}')^*$ may result in significant distortions to $\underline{\mathbf{r}}^*$. Thus, it is recommended to perform the search for the global optimal $(\mathbf{y}')^*$ with more than one initial guess \mathbf{z}_0 .

It is important to note that ill-conditioning in the unit 2-square search space after propagation is a consequence of the divergence of the covariance matrix in the $[y]_H$ -axis that is observed in open loop CW dynamics (i.e., CW dynamics without filtering), as illustrated in Fig. 7.7, which shows the same Monte Carlo sample prior distribution shown in Fig. 8.3 after propagating it for 0.67 orbits.

Thus, because relative state knowledge diverges in CW dynamics, it becomes meaningless after some time. This fact highlights an important philosophical nuance of collision risk assessments. Even though filtering would bound error divergence in a real-time application, collision risk assessments employ unfiltered dynamics because they are assessments, at the present time, of collision risk between the present and a specified future time. For further discussion, the reader is encouraged to consult Chapter 5.

Therefore, it is necessary to employ a receding horizon methodology for collision risk management in any relative orbital dynamic scenario (e.g., CW dynamics), including SFF implementations. First, instantaneously, SFF collision risk must be quantified within a future time window where relative state knowledge is meaningful based on present relative state statistics. Second, a rule must be implemented to decide whether remedial maneuvers must be undertaken based quantifiable SFF collision risk. Third, SFF collision risk reduction maneuvers must be planned and executed as needed. Lastly, the SFF COLRM process must be replicated in future timesteps. For further discussion, the reader is encouraged to consult Section 1.3.

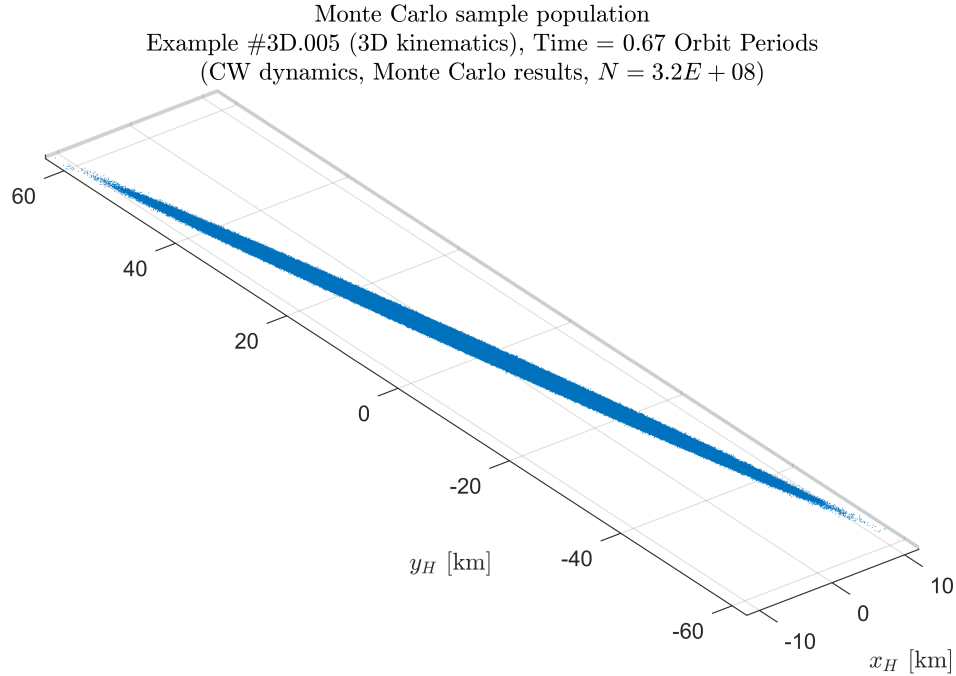


Figure 7.7: Monte Carlo sample relative position distribution (marginalization of sample relative state distribution) after 0.67 orbits.

7.7 Summary

The problem of finding the minimum Euclidean distance from the origin of \mathbb{R}^s to the d -Mahalanobis contour of a non-degenerate normal random variable \underline{X} in \mathbb{R}^s [$L_d(\underline{X})$] is discussed in this Chapter as follows. First, the $L_d(\underline{X})$ set and the unit $(s - 1)$ -sphere [$\mathbb{S}^{(s-1)}$] are shown to be isomorphic by demonstrating the existence of an invertible map $f_{d,\underline{X}}$ that characterizes the $L_d(\underline{X})$ set as the direct image of $\mathbb{S}^{(s-1)}$ under $f_{d,\underline{X}}$, and which also characterizes $\mathbb{S}^{(s-1)}$ as the inverse image of $L_d(\underline{X})$ under $f_{d,\underline{X}}$. Second, it is proven that there exist solutions to the problem of finding the minimum Euclidean distance from the origin in \mathbb{R}^s to points in $L_d(\underline{X})$. Third, theoretical upper and lower bounds for this problem are obtained in terms of scalar functions of the expected value and covariance of \underline{X} ; such bounds may be used to rescale the objective function that defines this problem to have predictable values.

The foregoing theoretical background is leveraged in order to develop a computa-

tional methodology to find the minimum Euclidean distance from the origin of \mathbb{R}^3 to the d -Mahalanobis contour of a non-degenerate normally distributed relative position $\underline{\mathbf{R}}_{i,j}(t)$ [$L_d(\underline{\mathbf{R}}_{i,j}(t))$]. Specifically, an isomorphism between the unit $(s - 1)$ -hypersphere and the unit $(s - 1)$ -hypercube (in particular, the Lambert area-preserving transform) is employed in order to reduce the search dimension from 3 to 2, and to perform an optimal search on a convex, simply-connected neighborhood of the unit-square representation of a best initial guess. Application of this computational methodology in the context of ill-conditioned search conditions (caused by relative orbital dynamic state covariance divergence over long propagation horizons) is shown to be sensible.

Hence, the methodology for the computation of the minimum Euclidean distance from $L_d(\underline{\mathbf{R}}_{i,j}(t))$ to the origin in \mathbb{R}^3 , which is described this Chapter, is utilized for distance-based SFF collision risk indicator computation in this dissertation – specifically, for the study of the correlation relationship between dissimilar types of collision risk indicators, as undertaken in Chapter 8.

CHAPTER 8
SPACECRAFT FORMATION COLLISION RISK INTERPRETATION AND
DECISION MAKING (PART 1) – RELATING COLLISION PROBABILITY AND
SEPARATION INDICATORS IN SPACECRAFT FORMATION COLLISION
RISK ANALYSIS

Active spacecraft formation flying collision avoidance schemes monitor collision risk through indicators such as miss distance and collision probability. This paper compares instantaneous collision probability measures based on planar projections to their three-dimensional counterparts. In this analysis, it is found that the former overestimate the latter. Additionally, this Chapter compares the consistency of risk assessments based on miss distance and instantaneous collision probability in closed Clohessy-Wiltshire (CW) trajectories. Certain statistics of relative position are well suited for collision risk assessments because their local minima and collision probability local maxima are anticorrelated. These results are a step toward connecting both types of indicators into a cohesive mathematical framework relating to collision risk.

8.1 Introduction

The existing literature in SFF collision avoidance (COLA) can be broadly divided into two categories: passive and active methods. Passive SFF COLA methods focus on passively safe formation designs. Using the terminology of Clohessy-Wiltshire (CW) relative orbital dynamics, [138, 139, 5] most of these passive SFF COLA methods account for the divergence of along-track uncertainty of the relative position of deputies with respect to chiefs by

causing sufficient separation in the radial/cross-track plane.[140, 60] These methodologies can be applied to spacecraft formation design, deployment, navigation and reconfiguration, without the need for COLA-dedicated maneuvers.[141, 142, 143, 144] Other passive SFF COLA methods include separation in the “sky-plane” (i.e., in the along-track/cross-track plane),[63] energy matching,[145] and minimum range variation safety ellipses.[146]

With active SFF COLA methods, collision risk is managed through predicting future motion of agents, determining whether the collision risk is acceptable, and if it is not, planning and executing COLA-dedicated maneuvers. Passive and active SFF COLA methods are not mutually exclusive, however, as active SFF COLA methods may presuppose passively safe formation orbits as baselines. However, the distinction is made because it is possible to have formations that only implement SFF COLA passively, i.e., only with regular, autonomous station-keeping maneuvers every few orbits, as demonstrated by the TanDEM-X and PRISMA missions, for example.[147, 141, 148, 142]

Active SFF COLA methods can be categorized by their collision risk indicators, i.e., by the measures or metrics used to conceptualize and mitigate risk. Once collision risk becomes unacceptable per such indicator, a correction signal is generally obtained by solving an optimal control problem, in which the risk is accounted for by setting appropriate constraints.

The first active SFF COLA method category comprises distance-based COLA methodologies, i.e., techniques that employ agent separation (e.g., the Euclidean distance between agents, or Cartesian components of relative position, etc.) to measure collision risk. Some miss distance-based COLA methods propose avoiding collision by setting appropriate inequality constraints directly in terms of the miss distance (or components of relative position).[39, 48, 149, 150, 151, 51, 152, 49, 50] Other miss distance-based COLA methods propose employing relative distance-based heuristics (e.g., artificial potential functions) to avoid collisions, applying the principles of swarm intelligence and distributed agent control theory.[25, 153, 26, 154, 53, 52] A subset of distance-based active SFF COLA techniques

account for state uncertainty directly in the formulation of the avoidance maneuvers by defining geometric collision regions (e.g., “covariance” contours, or reachable sets) that represent uncertainty envelopes.[49, 50, 53]

The second active SFF COLA method category comprises stochastic (or probabilistic) COLA methods, i.e., techniques whereby collision risk between pairs of agents is measured through the probability of the event that the relative position between agents is within a set that can be understood as a “collision region”. This presupposes that the relative position is described by a probability distribution, which can be obtained as the outcome of relative state estimation.[13, 54, 55] Then, collision is avoided by designing a control signal that brings the probability of collision below an acceptable threshold. Some miss distance-based active SFF COLA methods check collision probability,[51, 52] while most stochastic active SFF COLA methods also check for miss distance.[54]

This Chapter focuses on collision risk indicators for active SFF COLA methods. Specifically, the correlation relationship between miss distance and probability of collision is explored in order to understand whether these indicators provide consistent representations of collision risk. This contribution is beneficial for the following reasons. In collision monitoring schemes where both collision risk indicators are used, the interpretation of risk as portrayed by one indicator may be enhanced by consideration of the other indicator. In the more common case where only one collision risk indicator is used, this contribution may help understand the safety and performance tradeoffs of such a choice.

It is possible that the miss distance and collision probability indicators may provide conflicting information. In this case, understanding the relationship between these indicators can help evaluate which indicator may be a more accurate portrayal of collision risk, and based on the more suitable indicator, it can be decided whether the perceived risk should elicit a COLA maneuver. Additionally, if one type of indicator is a universally more accurate representation of collision risk than the other type of indicator, then the latter may be discarded or treated as a supplementary indicator. Overall, understanding the correlation

relationship between miss distance and probability of collision is a step toward unifying both types of active SFF COLA methods into a single, coherent mathematical framework relating to collision risk.

8.2 Background

8.2.1 Notation adjustments for this Chapter

The Notation and Nomenclature used in this Chapter, as well as the deterministic definition of collision events (derived from relative-attitude abstraction, and induced by arbitrary a -norm balls in relative position space), and the definition of stochastic collision risk measures (in both an instantaneous and joint-time sense), are addressed in Chapter 2.

Such general Notation and Nomenclature are made more specific for this Chapter as follows. First, the balls and spheres used are only those with respect to the Euclidean norm; additionally, only open balls are employed. (See Definition 1.) Hence, implicitly $a = 2$ or $a = \text{Eu}$; consequently, the a -norm symbol is omitted throughout this Chapter. (See Section 2.2.) From the aforementioned, it follows that collision sets and probabilities are induced from instantaneous collision conditions based on open balls with respect to the Euclidean norm in relative position space.

Second, the formulation for collision sets and stochastic collision risk measures, whether instantaneous or joint-time, are based on time-invariant joint-hard body radii. In other words, within this Chapter, formulations of instantaneous collision sets and the IPC, as well as JTC set and the PC measure, implicitly assume that the corresponding joint HBR is constant throughout the propagation horizon.

The foregoing assumptions are reflected in the notation adjustments concerning the following sets and probabilities:

- Instantaneous collision set in relative position space, denoted as $V_{i,j}$ (see Notation 5)
- Instantaneous probability of collision, $\text{IPC}_{i,j}(t)$ (see Definition 7)

- Joint-time probability of collision, $P_{c_{i,j}}[t_0, t_f]$ (see Definition 10)

8.2.2 Epistemic interpretation of collision probabilities

The question of whether it is adequate to employ probabilistic collision risk indicators that are based on stochastic distributions which reflect an epistemic representation of uncertainty has been previously addressed in the literature. A discussion of this topic is undertaken in Chapter 5, including remarks on the probability dilution phenomenon displayed by the probability of collision between spacecraft in a relative orbital dynamic context.[72]

8.2.3 Projection IPCs

The previous formulation of the instantaneous probability of collision (IPC) is general in the sense that it is applicable to dynamic systems where the relative position is defined in one-, two-, or three-dimensional Euclidean space. However, for the remainder of this Chapter, it is assumed that the true relative motion occurs in three-dimensional (3D) Euclidean space. Hence, the term “true IPC” is used to refer to IPCs in the sense of Definition 7, i.e., where the IPC is computed over a 3D collision region using the 3D relative position pdf.

Projecting 3D relative motion onto certain two-dimensional (2D) planes is a practice that arises naturally in spaceflight mechanics. For example, in CW dynamics, relative motion in the radial/along-track plane is decoupled from motion in the cross-track direction;[5] hence, it is common to W radial/along-track motion separately from cross-track motion in CW dynamics. Therefore, it is meaningful to also consider instantaneous projections of the relative motion onto arbitrary planes that cross the origin, and to examine whether a collision might be occurring as perceived in any such projection plane. This subsection introduces and formalizes the notions of collision events and probabilities of collision as perceived in projection planes.

Within this subsection, suppose that position RV \mathbf{R} and instances \mathbf{r} are expressed in the

coordinates of some reference frame \mathcal{J} , and that the DCM from frame \mathcal{J} to a projection frame W , $\Xi_{W,\mathcal{J}}$, is given.

Remark 28 (Projection position pdfs). Suppose a position random variable \mathbf{R} in \mathbb{R}^3 is absolutely continuous. Then, the pdf of the projection of the position onto the \widetilde{W} plane, $\text{pdf}_{[\tilde{\mathbf{r}}]_{\widetilde{W}}}$, is obtained through marginalization as

$$\text{pdf}_{[\tilde{\mathbf{r}}]_{\widetilde{W}}}([\tilde{\mathbf{r}}]_{\widetilde{W}}) = \int_{-\infty}^{+\infty} \text{pdf}_{[\mathbf{r}]_W}([\mathbf{r}]_W) d[y]_W \quad (8.1)$$

where $[\tilde{\mathbf{r}}]_{\widetilde{W}} = \mathbf{M}_p[\mathbf{r}]_W$, and

$$\text{pdf}_{[\mathbf{r}]_W}([\mathbf{r}]_W) = \text{pdf}_{[\mathbf{r}]_{\mathcal{J}}}(\Xi_{W,\mathcal{J}}^T[\mathbf{r}]_W) \quad (8.2)$$

When $[\mathbf{R}]_{\mathcal{J}} \sim \mathcal{N}([\underline{\mu}]_{\mathcal{J}}, \Sigma_{[\mathbf{R}]_{\mathcal{J}}})$ for some $[\underline{\mu}]_{\mathcal{J}} \in \mathbb{R}^3$ and $\Sigma_{[\mathbf{R}]_{\mathcal{J}}} \in \mathbb{R}^{3 \times 3}$, $\Sigma_{[\mathbf{R}]_{\mathcal{J}}} > 0$, it follows that[73]

$$[\tilde{\mathbf{R}}]_{\widetilde{W}} \sim \mathcal{N}(\mathbf{M}_p \Xi_{W,\mathcal{J}} [\underline{\mu}]_{\mathcal{J}}, \mathbf{M}_p \Xi_{W,\mathcal{J}} \Sigma_{[\mathbf{R}]_{\mathcal{J}}} \Xi_{W,\mathcal{J}}^T \mathbf{M}_p^T) \quad (8.3)$$

Note: because a relative position vector is a linear combination of two position vectors, this remark also applies to relative position pdfs. For more information on marginalizations of normal pdfs, see the work of Kroese et al.[73] \diamond

If $[\mathbf{r}]_{\mathcal{J}}$ is known deterministically, then $B_i^{\widetilde{W}}$ denotes the \widetilde{W} -projection of B_i , i.e., the set of all projections of points in B_i onto the \widetilde{W} -plane; that is,

$$B_i^{\widetilde{W}} \doteq \{[\tilde{\mathbf{r}}]_{\widetilde{W}} \in \mathbb{R}^2 : [\tilde{\mathbf{r}}]_{\widetilde{W}} = \mathbf{M}_p \Xi_{W,\mathcal{J}} [\mathbf{r}]_{\mathcal{J}}, [\mathbf{r}]_{\mathcal{J}} \in B_i\} \quad (8.4)$$

Since, for \mathbf{r} in \mathbb{R}^3 , $\|\mathbf{M}_p \mathbf{r}\|_2 \leq \|\mathbf{r}\|_2$, it follows from the definition of l_i that $B_i^{\widetilde{W}}$ is circumscribed within $\mathbb{B}_{l_i}^{2|\text{Eu}}([\tilde{\mathbf{r}}]_{\widetilde{W}})$, i.e., $B_i^{\widetilde{W}} \subseteq \mathbb{B}_{l_i}^{2|\text{Eu}}([\tilde{\mathbf{r}}]_{\widetilde{W}})$ in general.

Definition 29 (Projection HBR simplification). By assumption, $B_i^{\widetilde{W}} = \mathbb{B}_{l_i}^2([\tilde{\mathbf{r}}]_{\widetilde{W}})$. \diamond

In the rest of this Chapter, the projection HBR simplification, listed in Definition 29, is assumed to hold.

Definition 30 (Projection collision event). The \widetilde{W} -projection i - j collision event occurs whenever the disks spanned by agents i and j have a nonempty intersection in the \widetilde{W} -projection plane, i.e.,

$$\mathbb{B}_{l_i}^{2|\text{Eu}}([\tilde{\mathbf{r}}_i]_{\widetilde{W}}) \cap \mathbb{B}_{l_j}^{2|\text{Eu}}([\tilde{\mathbf{r}}_j]_{\widetilde{W}}) \neq \emptyset \quad \diamond \quad (8.5)$$

Definition 31 (Projection intersection sets). The \widetilde{W} -projection intersection disk $V_{i,j}^{\widetilde{W}}$ in \mathbb{R}^2 is defined as

$$V_{i,j}^{\widetilde{W}} \doteq \mathbb{B}_{l_{i,j}}^{2|\text{Eu}}(\mathbf{0}_{2 \times 1}) \quad (8.6)$$

and it is the region of \widetilde{W} -projected relative position space in which the \widetilde{W} -projection collision event occurs. Similarly, the \widetilde{W} -projection intersection cylinder $V_{i,j}^W$ in \mathbb{R}^3 is defined as

$$V_{i,j}^W \doteq \{[\mathbf{r}]_W \in \mathbb{R}^3 : \|\mathbf{M}_p[\mathbf{r}]_W\|_2 < l_{i,j}\} \quad (8.7)$$

i.e., it is the set of all points in \mathbb{R}^3 whose \widetilde{W} -projections in \mathbb{R}^2 satisfy the \widetilde{W} -projection collision event. \diamond

Proposition 32 (Projection collision condition equivalencies). Under the projection HBR simplification (see Definition 29), the following statements are equivalent:

1. $\mathbb{B}_{l_i}^{2|\text{Eu}}(\mathbf{M}_p[\mathbf{r}_i]_W) \cap \mathbb{B}_{l_j}^{2|\text{Eu}}(\mathbf{M}_p[\mathbf{r}_j]_W) \neq \emptyset$
2. $\|\mathbf{M}_p[\mathbf{r}_{i,j}]_W\|_2 < l_{i,j}$
3. $\mathbf{M}_p[\mathbf{r}_{i,j}]_W \in V_{i,j}^{\widetilde{W}}$
4. $[\mathbf{r}_{i,j}]_W \in V_{i,j}^W$ \diamond

Clearly, $V_{i,j}^W$ is a strict superset of $V_{i,j}$, i.e., $V_{i,j} \subsetneq V_{i,j}^W$. This entails that a true collision event implies a \widetilde{W} -projection collision event regardless of the \widetilde{W} -plane of choice, but the converse does not hold.

Definition 33 (Projection IPCs). The \widetilde{W} -projection instantaneous probability of collision between agents i and j at time t , denoted by $\text{IPC}_{i,j}^{\widetilde{W}}(t)$, is defined as the probability of “the event that the \widetilde{W} -projections of the bodies of agents i and j are intersecting at time t ”. Under the projection HBR simplification (see Def. 29), $\text{IPC}_{i,j}^{\widetilde{W}}(t)$ may be expressed as

$$\text{IPC}_{i,j}^{\widetilde{W}}(t) = p(\|\mathbf{M}_p[\mathbf{R}_{i,j}]_W(t)\|_2 < l_{i,j}) = p([\mathbf{R}_{i,j}]_W(t) \in V_{i,j}^W) \quad (8.8)$$

If $\mathbf{R}_{i,j}(t)$ is absolutely continuous and it is expressed in W -frame coordinates, via Proposition 32, $\text{IPC}_{i,j}^{\widetilde{W}}(t)$ may be equivalently expressed in terms of $V_{i,j}^{\widetilde{W}}$ and the pdf of $[\widetilde{\mathbf{R}}_{i,j}]_{\widetilde{W}}(t)$; then, $\text{IPC}_{i,j}^{\widetilde{W}}(t)$ may be computed as either of these integrals:

$$\text{IPC}_{i,j}^{\widetilde{W}}(t) = \int_{[\mathbf{r}]_W \in V_{i,j}^W} \text{pdf}_{[\mathbf{R}_{i,j}]_W(t)}([\mathbf{r}]_W) d[\mathbf{r}]_W = \int_{[\widetilde{\mathbf{r}}]_{\widetilde{W}} \in V_{i,j}^{\widetilde{W}}} \text{pdf}_{[\widetilde{\mathbf{R}}_{i,j}]_{\widetilde{W}}(t)}([\widetilde{\mathbf{r}}]_{\widetilde{W}}) d[\widetilde{\mathbf{r}}]_{\widetilde{W}} \quad \diamond \quad (8.9)$$

8.2.4 CW simulation cases

This Chapter focuses on Examples 3D.001–026, which are subject to CW dynamics, and are listed in Section A.2.

The initial relative state expectation parameters, along with the initial relative state covariance, are chosen so as to observe significant, nontrivial IPCs during a two-orbit propagation horizon, which is needed in order to meaningfully compare IPC signals to miss distance time-histories (or waveforms) during such a time window. Furthermore, the focus of the Results and Discussion section is on initial relative state expectations where the $[x]_H$ and $[z]_H$ motion are out of phase (cases 3D.003–026); this property corresponds to a specific passive SFF COLA methodology, namely, e-i vector separation.[60] Although

all cases have expected trajectories that are collision-free, the expected trajectories in Examples 3D.003–026 provide more separation between CW chief and CW deputy during closest approach than Examples 3D.001–002.

Finally, all cases assume joint hard-body radii of $l_{i,j} = 32$ m. This figure is based on an estimate of Hubble Space Telescope’s hard body radius of $l_i = 16$ m.[130] For the purposes of this Chapter, having such a large joint hard-body radius allows obtaining higher (and thus, more significant) IPCs. Additionally, conclusions are applicable to smaller spacecraft pairs that, by having additional buffer distance for increased safety, effectively have larger joint hard-body radii.

8.3 Theory

8.3.1 Theoretical results on projection IPCs

Since planar projections of relative motion are a valid analytical tool in spaceflight mechanics, their application to SFF COLA is plausible, as highlighted by the passive SFF COLA methodology of causing sufficient separation in the radial/cross-track plane.[60] Other SFF COLA methods neglect cross-track motion completely, i.e., only considering motion in the radial/along-track plane.[13, 53] Hence, it is meaningful to define IPCs on the projection of SFF relative motion onto planes that are useful in analysis. Thus, before comparing IPC and miss distance time-histories (or waveforms), it is worthwhile to understand the connection between true IPCs and projection IPCs on any plane.

Conceptually, true IPCs and projection IPCs are distinct, as illustrated in Figure 8.1. Thus, if “IPCs” are to be used as criteria for triggering COLA processes, choosing either true or projection IPCs for this purpose might produce different outcomes. In particular, it is helpful to understand what distortions in conjunction assessments might be introduced when “greater than or equal” COLA trigger thresholds are implemented; that is, if planning and/or execution of COLA maneuvers occurs whenever some IPC (true or projected) goes above a fixed constant. In this context, such a constant could be interpreted as a proxy for

the maximum collision risk that can be tolerated.

8.3.1.1 Projection IPCs overestimate true IPCs

Theorem 34 (Projection IPCs overestimate true IPCs). Suppose that $\mathbf{R}_{i,j}(t)$ is absolutely continuous. Let W describe a projection frame, i.e., a Cartesian reference frame in \mathbb{R}^3 in the sense of Remark 28. Then, every \widetilde{W} -projection IPC is an overestimate of the true IPC, i.e.,

$$0 \leq \text{IPC}_{i,j}(t) \leq \text{IPC}_{i,j}^{\widetilde{W}}(t) \leq 1 \quad (8.10)$$

for any choice of projection frame W . Additionally, if $\text{supp}(\text{pdf}_{\mathbf{R}_{i,j}(t)}) = \mathbb{R}^3$ (i.e., if, for \mathbf{r} in \mathbb{R}^3 , $\text{pdf}_{\mathbf{R}_{i,j}(t)}(\mathbf{r}) \neq 0$), then every \widetilde{W} -projection IPC is a strict overestimate of the true IPC, i.e.,

$$0 < \text{IPC}_{i,j}(t) < \text{IPC}_{i,j}^{\widetilde{W}}(t) \leq 1 \quad (8.11)$$

for any choice of projection frame W . Note: this second result applies, in particular, when the distribution of $\mathbf{R}_{i,j}(t)$ is nondegenerate normal. \diamond

Proof. In Subsection 8.2.3, it was noted that $V_{i,j} \subsetneq V_{i,j}^W$, so $V_{i,j} \subseteq V_{i,j}^W$. Hence, the first result follows from

$$0 \leq \text{IPC}_{i,j}(t) = p(\mathbf{R}_{i,j}(t) \in V_{i,j}) \leq p(\mathbf{R}_{i,j}(t) \in V_{i,j}^W) = \text{IPC}_{i,j}^{\widetilde{W}}(t) \leq 1 \quad (8.12)$$

Since $V_{i,j} \subseteq V_{i,j}^W$, for $B \doteq V_{i,j}^W \setminus V_{i,j}$, it follows from the proper difference rule that $\Delta \doteq p(\mathbf{R}_{i,j}(t) \in B)$ satisfies $\Delta = p(\mathbf{R}_{i,j}(t) \in V_{i,j}^W) - p(\mathbf{R}_{i,j}(t) \in V_{i,j}) \geq 0$. At this point, let $\text{supp}(\text{pdf}_{\mathbf{R}_{i,j}(t)}) = \mathbb{R}^3$; this implies that, for any $[\mathbf{r}]_W$ in \mathbb{R}^3 , $\text{pdf}_{[\mathbf{R}_{i,j}]_W(t)}([\mathbf{r}]_W) > 0$. Thus, it is enough to show that the set B has positive measure for Δ to be positive.

Let $\lambda(\cdot)$ denote the Lebesgue measure of sets in \mathbb{R}^3 . [34] Since both $V_{i,j}$ and $V_{i,j}^W$ are open sets, they are measurable. By expressing

$$V_{i,j}^W = \{[\mathbf{r}]_W \in \mathbb{R}^3 : ([x]_W)^2 + ([z]_W)^2 < l_{i,j}^2\}$$

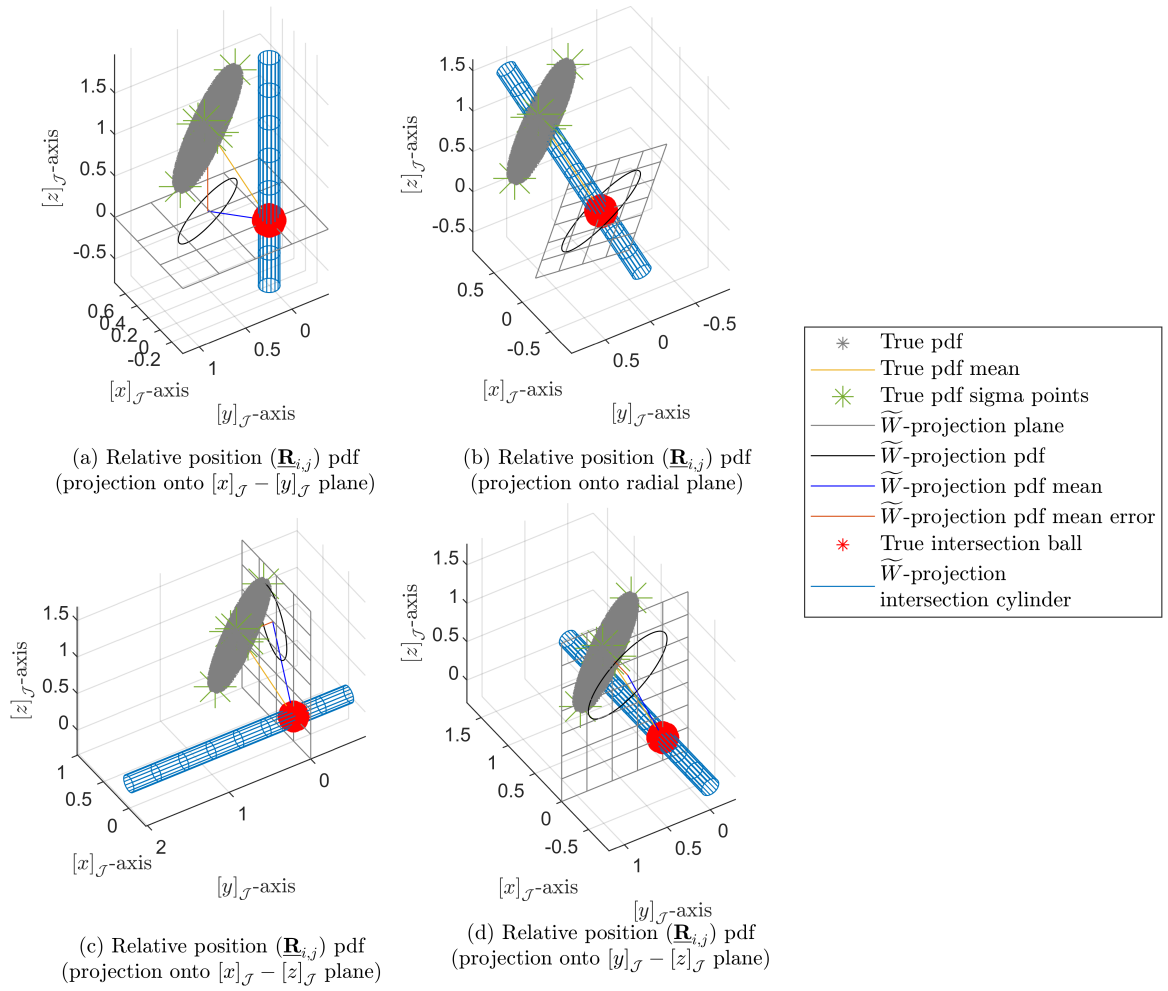


Figure 8.1: Conceptual distinction between true IPC and \widetilde{W} -projection IPC measures for a 3D relative position pdf (expressed in the coordinates of an arbitrary frame \mathcal{J}).

it is clear that $V_{i,j}^W$ has infinite measure, while the measure of

$$V_{i,j} = \{[\mathbf{r}]_W \in \mathbb{R}^3 : ([x]_W)^2 + ([y]_W)^2 + ([z]_W)^2 < l_{i,j}^2\}$$

is finite. By Caratheodory's criterion, it follows that

$$\lambda(B) = \lambda(V_{i,j}^W) - \lambda(V_{i,j}) = \infty - \frac{4}{3}\pi(l_{i,j})^3 = \infty > 0$$

Hence, both $V_{i,j}$ and B have positive measure. Therefore,

$$\Delta = \int_{[\mathbf{r}]_W \in B} \text{pdf}_{[\mathbf{r}_{i,j}]_W(t)}([\mathbf{r}]_W) d[\mathbf{r}]_W > 0 \quad (8.13)$$

which proves that $\text{IPC}_{i,j}^{\widetilde{W}}(t) = \text{IPC}_{i,j}(t) + \Delta > \text{IPC}_{i,j}(t)$. The last result follows from noting that any non-degenerate normal RV \underline{X} in \mathbb{R}^3 satisfies $\text{supp}(\text{pdf}_{\underline{X}}) = \mathbb{R}^3$. \square

Since projection IPCs are overestimates of true IPCs, using projection IPCs as COLA trigger criteria leads to considering collision risk greater than as would be indicated by true IPCs, which would be analogous to having probabilistic false positives. Customarily, a constraint after collision avoidance maneuvers is that the IPC be brought under a certain threshold (e.g., 1×10^{-7}) after a maneuver is conducted. Hence, using projection IPCs as post-maneuver constraint satisfaction criteria could lead to further correction efforts than warranted to sufficiently avoid collision risk. Accounting for scarce onboard resources, these observations show that using projection IPCs as collision safety criteria (i.e., either as COLA trigger criteria or as post-maneuver constraint satisfaction criteria) would result in additional COLA maneuvers and a shorter mission lifetime than would be warranted with the chosen risk threshold. This criticism applies only to projection IPCs and not to the P_c , as there are conjunction cases when it is valid to approximate the P_c in a way that is mathematically equivalent to a projection IPC, e.g., when the “short encounter” assumptions are met.[31]

Corollary 35. The \widetilde{W} -projection IPCs in the following \widetilde{W} -projection planes are overestimates of the true IPC:

- Every coordinate plane \widetilde{W} -projection IPC, i.e., for any arbitrary reference frame \mathcal{J} , the $[x]_{\mathcal{J}}\text{-}[y]_{\mathcal{J}}$, $[x]_{\mathcal{J}}\text{-}[z]_{\mathcal{J}}$, and $[y]_{\mathcal{J}}\text{-}[z]_{\mathcal{J}}$ coordinate planes.
- Any plane whose normal vector is:
 - The expected value of the relative position pdf (also called a radial projection).
 - The expected value of the relative position rate pdf.

Note: some of these projection IPCs are illustrated in Figure 8.1. ◇

8.3.1.2 Invariance of Euclidean norm-based projection IPCs

Under the assumption that instantaneous collision conditions in relative position are based on the Euclidean norm, it could be shown that \widetilde{W} -projection IPCs are unique functions of the \widetilde{W} -projection plane normal, which is clearly the $[y]_W$ axis.

Lemma 36 (Invariance of Euclidean norm-based \widetilde{W} -projection IPCs). Let W describe a projection frame in the sense of Remark 28, and suppose that the W is defined through a 3 – 1 – 2 Euler angle sequence with respect to an arbitrary reference frame I , [65] for example, as

$$\Xi_{W,\mathcal{J}} = A_{312}(-Az, El, \gamma) \quad (8.14)$$

as shown in Figure 8.2. Then, the \widetilde{W} -projection IPC is invariant under the last rotation of that sequence, i.e., it is invariant under arbitrary roll angles $\gamma \in [0, 2\pi]$. In other words, if any two projection frames W_1 and W_2 are defined through this sequence, and if these frames satisfy

$$Az_1 = Az_2 \quad (8.15)$$

$$El_1 = El_2 \quad (8.16)$$

then, it follows that

$$\text{IPC}_{i,j}^{\widetilde{W}_1}(t) = \text{IPC}_{i,j}^{\widetilde{W}_2}(t) \quad (8.17)$$

for all γ_1, γ_2 in $[0, 2\pi)$. Note: this result also applies to other $\Xi_{W,\mathcal{J}}$ direction cosine matrices defined through Euler angle sequences with a “2” as the last rotation of the sequence, i.e., with the 1 – 3 – 2, 2 – 1 – 2, and 2 – 3 – 2 Euler angle sequences. ◇

Proof. Suppose that the coordinate transformation matrices $\Xi_{W_k,\mathcal{J}}$, $k \in \{1, 2\}$ are constructed through 3 – 1 – 2 Euler angle sequences with respect to an arbitrary reference

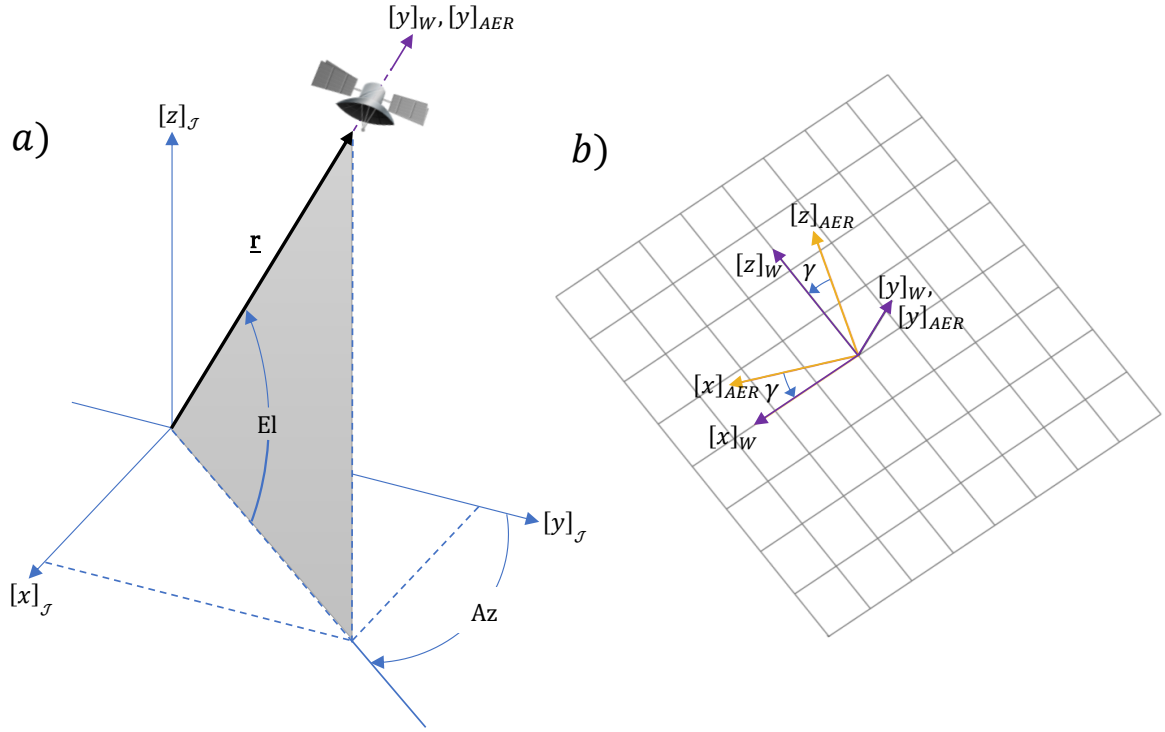


Figure 8.2: Geometry of W -projection frame with $\Xi_{W,\mathcal{J}} = A_{312}(-Az, El, \gamma)$ parametrization: a) Az, El geometry, b) γ geometry in \widetilde{W} -projection plane. Note: the AER frame is parametrized with $\gamma = 0$.

frame \mathcal{J} such that there exist angles (Az_k, El_k, γ_k) which satisfy

$$\Xi_{W_k,\mathcal{J}} = A_{312}(-Az_k, El_k, \gamma_k) \quad (8.18)$$

for $k \in \{1, 2\}$. Furthermore, assume that

$$Az_1 = Az_2 =: Az \quad (8.19)$$

$$El_1 = El_2 =: El \quad (8.20)$$

Consider \mathbf{r} in \mathbb{R}^3 . The goal is to show, under the current assumptions, that $\Xi_{W_1,W_2}[\mathbf{r}]_{W_2} \in V_{i,j}^{W_1}$ if and only if $[\mathbf{r}]_{W_2} \in V_{i,j}^{W_2}$.

In this case,

$$\begin{aligned}
\Xi_{W_1, W_2} &= \Xi_{W_1, \mathcal{J}} \Xi_{\mathcal{J}, W_2} = \Xi_{W_1, \mathcal{J}} \Xi_{W_2, \mathcal{J}}^T = \\
& [A_2(\gamma_1) A_1(\mathbf{E}l_1) A_3(-Az_1)] [A_2(\gamma_2) A_1(\mathbf{E}l_2) A_3(-Az_2)]^T \\
& = A_2(\gamma_1) A_1(\mathbf{E}l) A_3(-Az) A_3^{-1}(-Az) A_1^{-1}(\mathbf{E}l) A_2(-\gamma_2) \\
& = A_2(\gamma_1 - \gamma_2) \quad (8.21)
\end{aligned}$$

Thus,

$$\Xi_{W_1, W_2} = A_2(\gamma_1 - \gamma_2) = \begin{bmatrix} c & 0 & -s \\ 0 & 1 & 0 \\ s & 0 & c \end{bmatrix} \quad (8.22)$$

where

$$c \doteq \cos(\gamma_1 - \gamma_2) \quad (8.23)$$

$$s \doteq \sin(\gamma_1 - \gamma_2) \quad (8.24)$$

Therefore,

$$\Xi_{W_1, W_2}[\mathbf{r}]_{W_2} = \begin{bmatrix} c[x]_{W_2} - s[z]_{W_2} \\ [y]_{W_2} \\ s[x]_{W_2} + c[z]_{W_2} \end{bmatrix} \quad (8.25)$$

and

$$\mathbf{M}_p \Xi_{W_1, W_2}[\mathbf{r}]_{W_2} = \begin{bmatrix} c[x]_{W_2} - s[z]_{W_2} \\ s[x]_{W_2} + c[z]_{W_2} \end{bmatrix} \quad (8.26)$$

1. Let $\Xi_{W_1, W_2}[\mathbf{r}]_{W_2} \in V_{i,j}^{W_1}$. Then,

$$u \doteq \|\mathbf{M}_p \Xi_{W_1, W_2}[\mathbf{r}]_{W_2}\|_{\text{Eu}} < l_{i,j} \quad (8.27)$$

Hence,

$$\begin{aligned}
u^2 &= \\
c^2 ([x]_{W_2})^2 + s^2 ([z]_{W_2})^2 - 2cs [x]_{W_2} [z]_{W_2} + s^2 ([x]_{W_2})^2 + c^2 ([z]_{W_2})^2 + 2cs [x]_{W_2} [z]_{W_2} \\
&= ([x]_{W_2})^2 + ([z]_{W_2})^2 =: \|\mathbf{M}_p[\mathbf{r}]_{W_2}\|^2 \quad (8.28)
\end{aligned}$$

It follows that $\|\mathbf{M}_p[\mathbf{r}]_{W_2}\|_{\text{Eu}} < l_{i,j}$, which shows that $[\mathbf{r}]_{W_2} \in V_{i,j}^{W_2}$.

2. Let $[\mathbf{r}]_{W_2} \in V_{i,j}^{W_2}$. Thus, $\Xi_{W_2, W_1}[\mathbf{r}]_{W_1} \in V_{i,j}^{W_2}$. By reversing the order of the indices in the previous statement, Item 1, it follows that

$$[\mathbf{r}]_{W_1} \in V_{i,j}^{W_1} \quad (8.29)$$

Therefore, $\Xi_{W_1, W_2}[\mathbf{r}]_{W_2} \in V_{i,j}^{W_1}$.

The previous two statements, Items 1 and 2, show that $\Xi_{W_1, W_2}[\mathbf{r}]_{W_2} \in V_{i,j}^{W_1}$ if and only if $[\mathbf{r}]_{W_2} \in V_{i,j}^{W_2}$. Therefore,

$$\text{IPC}_{i,j}^{\widetilde{W}_1}(t) := p(\mathbf{R}_{i,j}(t) \in V_{i,j}^{W_1}) = p(\mathbf{R}_{i,j}(t) \in V_{i,j}^{W_2}) =: \text{IPC}_{i,j}^{\widetilde{W}_2}(t) \quad (8.30)$$

which was to be demonstrated. □

Lemma 36 is significant because it shows that Euclidean norm-based \widetilde{W} -projection IPCs are unique functions of the \widetilde{W} -projection plane normal, which is clearly the $[y]_W$ axis, as shown in Fig. 8.2. In other words, the orientation of the orthonormal basis vectors in the \widetilde{W} -projection plane (i.e., the $[x]_W$ and $[z]_W$ direction unit vectors) is immaterial to the value of Euclidean norm-based \widetilde{W} -projection IPCs.

8.3.2 Validation of projection IPC theoretical results

In this Chapter, general results are demonstrated regarding projection IPCs, one of which shows how projection IPCs always overestimate true IPCs regardless of projection plane choice, as illustrated in Figure 8.1, and as proven in Theorem 34. This theoretical finding is validated by Monte Carlo (MC) analysis. In this Chapter, such MC simulation assumes CW relative orbital dynamics in Low Earth Orbit (LEO). Numerical IPC waveforms (true and projected) are compared to the Monte Carlo-based IPC waveforms. Performing such a Monte Carlo simulation is challenging if the debris conjunction assessment and risk analysis (CARA) community requirement that P_c values above 1×10^{-7} are considered significant were to be adopted for SFF collision risk assessment based on IPC values.[29, 73] An example of Monte Carlo sample relative position distribution is illustrated in Figure 8.3. Several relevant spacecraft proximity cases are studied: without cross-track motion, and with cross-track motion (in- and out-of-phase with radial motion, and more general cases).

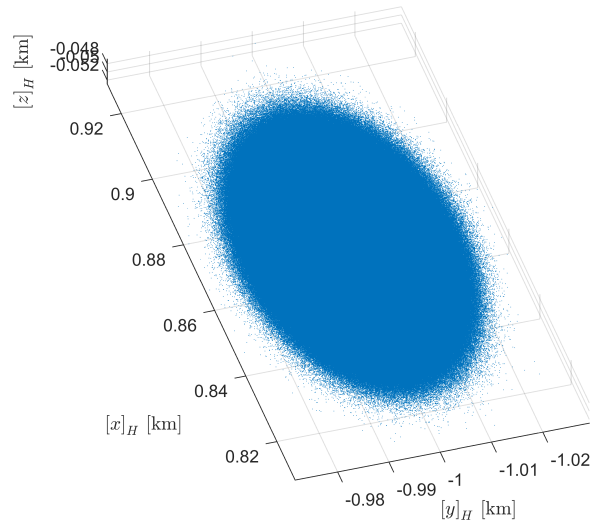


Figure 8.3: Relative position sample distribution (marginalization of relative state sample distribution), Example 3D.005, time = 0 orbits (3.2×10^8 particles in sample).

Through the preceding Monte Carlo analysis, it is found that not only does the Monte Carlo IPC waveform converge to the true IPC waveform (as computed through brute force quadrature), but that the true IPC is significantly different from every projection IPC con-

sidered, i.e., those with projection planes normal to relative position and relative position rate (see Figure 8.4), and CW coordinate planes (see Figure 8.5). Even though there is some meaningful correlation between the true IPC waveform and some of the projection IPCs (i.e., for projection planes normal to relative position rate, and for the radial/along-track plane), this correlation is not consistent across cases, and the difference in magnitude could lead to different risk assessment conclusions depending on IPC risk thresholds.[29] Furthermore, the projection IPC exceeds the true IPC in every case, regardless of the projection plane, as indicated by Theorem 34.

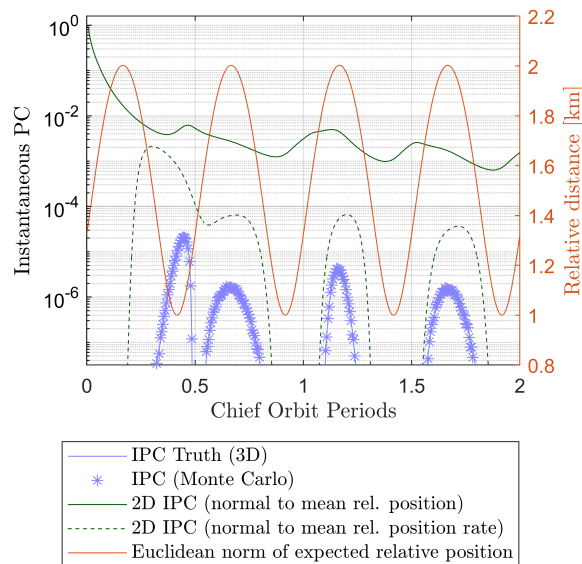


Figure 8.4: True IPC, projection IPCs, and Monte Carlo IPC, Example 3D.005 (projection IPCs are on planes normal to dynamics vectors).

8.3.3 Motivating distance measures for correlation with true IPC

The notion of consistency of collision risk assessments from dissimilar collision risk indicators requires exploring the correlation between such indicators. Specifically, with the collision risk indicators considered in this Chapter, consistency in collision risk assessments would ideally entail that local extrema of true IPC and local extrema of miss distance be anticorrelated. In other words, with consistent collision risk indicators, the true IPC

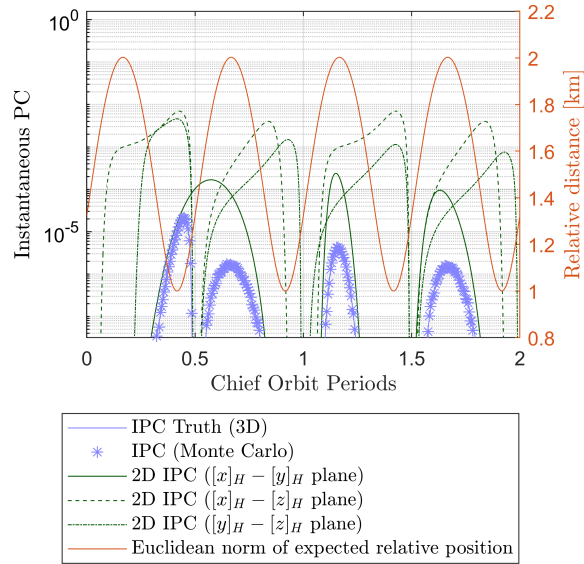


Figure 8.5: True IPC, projection IPCs, and Monte Carlo IPC, Example 3D.005 (projection IPCs are on coordinate planes).

waveform would ideally indicate greatest collision risk while the miss distance waveform indicates closest approach on the one hand; on the other hand, the former would ideally indicate lowest collision risk while the latter indicates furthest approach.

However, as shown by the example in Figures 8.4 and 8.5, the condition of collision risk indicator consistency is not generally met when comparing the Euclidean norm of expected relative position and true IPC waveforms. In this case, over a two-orbit horizon, these waveforms are mostly positively correlated. That is, primarily, the true IPC indicates lowest collision risk when the Euclidean norm of expected relative position indicates closest approach, and the true IPC indicates highest collision risk when the Euclidean norm of expected relative position indicates furthest approach. Evidently, these insights are inconsistent (as understood in this Chapter), and using one collision risk indicator over another would lead to diametrically opposite conclusions. Even though this inconsistent indicator waveform behavior does not always occur, it is common in many of the cases considered. Hence, the Euclidean norm of expected relative position is not a miss distance waveform that can be reliably used as a qualitative substitute for (or predictor of) true IPC extrema.

This finding prompts the search for other statistics of the relative position distribution that can be interpreted as miss distance and that, together with the true IPC, produce consistent collision risk assessments.

For $X \sim \mathcal{N}(\mu, \sigma^2)$ for some μ in \mathbb{R} and $\sigma > 0$, colloquially, a $3\text{-}\sigma$ set (in this case, the points $\{\mu \pm 3\sigma\}$) is considered a boundary between extreme events and non-extreme events. That is, events between $\mu - 3\sigma$ and $\mu + 3\sigma$ are typically not considered extreme, and events outside of that interval are colloquially considered extreme. Given that the IPCs considered in this Chapter have such low values, collisions can also be deemed as extreme events. Therefore, it is desirable for any proposed separation measures to represent extreme events in some sense as well.

Based on analogous extensions of the univariate normal $3\text{-}\sigma$ concept, the following methodologies define “miss distance”-like measures which are hypothesized to have the correct relationship to the true IPC:

1. Methodology 1: minimum distance to a “geometric” $3\text{-}\sigma$ contour, discussed in Subsubsection 2.6.2.1, and denoted by $\text{sep}_{\text{geo}|i,j}(t)$.
2. Methodology 2: minimum distance to an “equivalent” $3\text{-}\sigma$ contour, discussed in Subsubsection 2.6.2.2, and denoted by $\text{sep}_{\text{eq}|i,j}(t)$.
3. Methodology 3: 99.73% minimum distance, discussed in Subsubsection 2.7.1.1, and denoted by $\rho_{3\sigma}$.

Methodologies 1-2 and 3 are formally defined and discussed in Subsections 2.6.2 and 2.7.1, respectively. The “geometric” and “equivalent” $3\text{-}\sigma$ contours, as well as points in such contours that are closest to the origin, are illustrated in Figure 2.5. The 99.73% minimum distance measure (i.e., $\rho_{3\sigma}$) is illustrated in Figure 2.6.

Miss distance measures akin to Methodologies 1 and 2 have been proposed in the literature as collision risk indicators. Wang et al. propose a heuristic SFF COLA scheme whereby the relative position pdf is centered at the chief spacecraft instead of at the deputy

spacecraft; then, an artificial potential function (APF) is implemented to trigger COLA actions by the deputy when its position relative to the chief crosses below a safety MHD centered at the chief's location.[53] Conceptually, the contours proposed by Wang et al. differ from those defined by Methodologies 1 and 2 only by the specific MHD chosen to define those contours, and by defining the center of the relative position pdf differently.

Methodology 3 has two valid interpretations. First, $\rho_{3\sigma}$ can be interpreted as the solution of a root-finding problem, where a variable HBR is changed until its corresponding IPC matches $p_{3\sigma}$. Second, $\rho_{3\sigma}$ can be interpreted as a percentile in a cumulative distribution function (cdf), specifically, the cdf of the Euclidean norm of the instantaneous relative position.

8.3.4 Definition of collision correlation index

The conceptual notion of collision indicator waveform correlation used in this Chapter is formalized through the collision correlation index, introduced in Definition 37.

Definition 37 (Collision correlation index). The i - j collision correlation index over the $[t_0, t_0 + T]$ interval, $\Gamma_{i,j}$, is the normalized and unbiased \mathcal{L}^2 -inner product between $\text{IPC}_{i,j}(t)$ and some separation measure between agents i and j at time t , $\text{sep}_{i,j}(t)$, $t \in [t_0, t_0 + T]$. That is, $\Gamma_{i,j} : V \times V \rightarrow [-1, 1]$ is defined by the mapping

$$\Gamma_{i,j}(\text{IPC}_{i,j}, \text{sep}_{i,j}) = \frac{\langle y(\text{IPC}_{i,j}), y(\text{sep}_{i,j}) \rangle}{\|y(\text{IPC}_{i,j})\|_{\mathcal{L}^2} \|y(\text{sep}_{i,j})\|_{\mathcal{L}^2}} \quad (8.31)$$

where $\text{IPC}_{i,j} : [t_0, t_0 + T] \rightarrow [0, 1]$ is as presented in Definition 7, where $\text{sep}_{i,j} : [t_0, t_0 + T] \rightarrow [0, \infty)$ is some measure of separation between agents i and j at time t , $t \in [t_0, t_0 + T]$, and where $y : V \rightarrow V$ is given by

$$y(f) = f - \text{Av}(f), f \in V \quad (8.32)$$

where $V \doteq \mathcal{L}^2[t_0, t_0 + T]$ is the \mathcal{L}^2 -inner product space of Lebesgue measurable func-

tions in $[t_0, t_0 + T]$, [66] and where the \mathcal{L}^2 -norm, $\|\cdot\|_{\mathcal{L}^2}$, is defined in terms of the \mathcal{L}^2 -inner product, $\langle \cdot, \cdot \rangle$, as $\|\cdot\|_{\mathcal{L}^2} = \sqrt{\langle \cdot, \cdot \rangle}$, and where Av is the time-average function.

When V is restricted to the space of real-valued, bounded, continuous almost everywhere (a.e.) functions in $[t_0, t_0 + T]$, then the \mathcal{L}^2 -inner product $\langle \cdot, \cdot \rangle : V \times V \rightarrow \mathbb{R}$ can be computed in terms of the Riemann integral [66]

$$\langle x, z \rangle = \int_{t_0}^{t_0+T} x(t) z(t) dt; \quad x, z \in V \quad (8.33)$$

and $\text{Av} : V \rightarrow \mathbb{R}$ can be also be computed in terms of the Riemann integral as

$$\text{Av}(x) = \frac{1}{T} \int_{t_0}^{t_0+T} x(t) dt; \quad x \in V \quad (8.34)$$

Note: in the signal processing community, [155] the collision correlation index $\Gamma_{i,j}$ can be interpreted as the cross-correlation coefficient of $x_1(\cdot)$ and $x_2(\cdot)$, ρ_{x_1, x_2} , i.e.,

$$\Gamma_{i,j}(x_1, x_2) = \rho_{x_1, x_2} = \frac{\langle x_1(\cdot), x_2(\cdot) \rangle}{\sqrt{\mathcal{E}_{x_1} \mathcal{E}_{x_2}}} \quad (8.35)$$

where $x_1(\cdot)$ is the unbiased IPC $_{i,j}$ signal, $x_2(\cdot)$ is the unbiased sep $_{i,j}$ signal, and where the energy of the signal $x(\cdot)$, \mathcal{E}_x , is given by $\mathcal{E}_x \doteq \langle x(\cdot), x(\cdot) \rangle = \|x(\cdot)\|_E^2$. \diamond

The collision correlation index $\Gamma_{i,j}$ compares two waveforms directly and outputs a value between -1 and 1 that indicates the extent of linear correlation (or anti-correlation) between the waveforms (after bias removal). Thus, the notion of consistency entails that the IPC and miss distance waveforms, when passed through the $\Gamma_{i,j}$ operator, should give a value as close to -1 as possible.

8.4 Results and discussion

This section addresses findings in several areas of this Chapter. First, MC sample-based IPC convergence to the true IPC is discussed. Second, results on the correlation relationship

between the true IPC and several separation measures are examined. Third, the consistency between probabilistic indicators and the 99.73% minimum distance is explored.

8.4.1 Implementation notes

Numerical IPCs are computed through multi-dimensional brute-force quadrature in MATLAB R2020b,[129] using the analytically propagated relative state statistics listed in Eqns. A.22-A.23 The true IPC is computed via the `integral3` function by integrating the instantaneous relative position pdf, which is obtained through the marginalization listed in Eq. A.24 Similarly, projection IPCs are computed via the `integral2` function by integrating the instantaneous relative position pdf, as projected onto the respective planes of choice, obtained through the marginalization listed in Remark 28. (Normal pdfs are constructed through their associated statistics via Eq. 2.13.) In both cases, relative and absolute error tolerances are set to 1×10^{-6} and 1×10^{-10} , respectively, which achieve relative and absolute errors (approximately) to within 6 and 10 significant digits, respectively. (The `integral2/3` schemes may achieve either criteria, but they do not always meet both criteria.) Additionally, integration region limits are expressed in terms of Cartesian coordinates, namely, $z = \pm\sqrt{l_{i,j}^2 - x^2 - y^2}$, $y = \pm\sqrt{l_{i,j}^2 - x^2}$, and $x = \pm l_{i,j}$.

Conjecture 38. Suppose that a Monte Carlo (MC) sample is made of a non-degenerate multivariate normal distribution. Suppose that events with a probability of p_{req} or lower can be ignored. Then, it is expected that significant events (i.e., events with probability greater than or equal to p_{req}) can be captured with a sample size N_{MC} that satisfies

$$N_{\text{MC}} \geq 30 \left\lceil \frac{1}{p_{\text{req}}} \right\rceil \quad (8.36)$$

Note: the reasoning which grounds this Conjecture is discussed in Section C.3. ◇

Within NASA CARA practice,[29] potential conjunction events with P_C values of less than 1×10^{-7} are considered insignificant. For two agents in a potential conjunction event,

such P_c 's may often be approximated by an integral (over a disk region) of a 2D normal pdf, obtained by projecting a 3D normal relative position pdf (at the instant of closest approach between the agents) onto the plane perpendicular to the relative velocity vector. Hence, these P_c approximations are mathematically equivalent to a projection IPC. Thus, mirroring NASA CARA practice, it is assumed that potential conjunction events with IPCs less than 1×10^{-7} are insignificant. Under the assumption of Conjecture 38, it follows that $p_{\text{req}} = 1 \times 10^{-7}$, which implies that the MC sample size, N_{MC} , should satisfy $N_{\text{MC}} \geq 3.0 \times 10^8$. The sample size is chosen as $N_{\text{MC}} = 3.2 \times 10^8$, which is sufficiently large according to Conjecture 38.

The large MC sample size requirement is the main driving factor for the technique implemented for sample generation and data reduction. The MC sample handling technique has three broad steps: sample generation, intermediate data reduction, and aggregation of intermediate results into sample-level results. The specific MC sample management technique employed in this dissertation is described further in Section C.4.

Upper and lower bounds for the solution of the COP posed in Eq. 2.44 may be found in terms of the Euclidean norm of the expected relative position, the minimum and maximum eigenvalues of the relative position covariance, and the MHD d that defines the $L_d(\underline{\mathbf{R}}_{i,j})$ of choice. These bounds are listed in Proposition 26. Using these bounds, the COP can be normalized so as to have predictable objective function extrema bounds (cf. Corollary 27), e.g., -1 and 1 . Since $L_d(\underline{\mathbf{R}}_{i,j})$ and the unit 2-sphere are isomorphic, an initial guess for the COP may be found by making a uniform sample of the unit 2-sphere, then transforming it into a sample of $L_d(\underline{\mathbf{R}}_{i,j})$, and then starting the search using the best-performing sample element, as shown in Eq. 7.45. Similarly, as illustrated in Fig. 8.6, the nonlinear equality constraint in the COP can be used to reformulate the initial search (in \mathbb{R}^3) into a search in unit-square space, by implementing a mapping from the unit 2-square to the unit 2-sphere (e.g., the area-preserving Lambert Transform [119]), and from the unit 2-sphere into $L_d(\underline{\mathbf{R}}_{i,j})$ (through the relative position statistics), as posed in Eq. 7.55. In order to

avoid singularities, the coordinates in the unit 2-sphere are transformed so as to locate the initial search point in the center of the unit square, which gives regularity to the search and does not affect the final result (cf. Eq. 7.51). Using this parametrization, the outcome of Methodologies 1 and 2 is computed in MATLAB R2020b through the `fminsearch` function,[129] with both objective function and solution error tolerances set to 1×10^{-4} (where both tolerances are met before finishing the search).

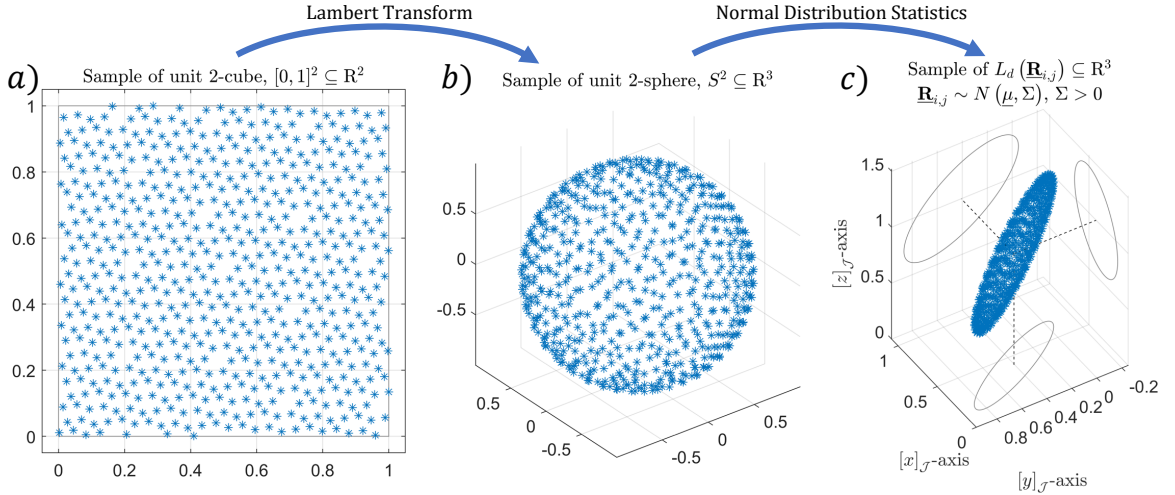


Figure 8.6: Relationship between a) unit square, b) unit 2-sphere, and c) $L_d(\mathbf{R}_{i,j})$.

8.4.2 Validation of MC sample and projection IPC theoretical results

Figure 8.7 shows that the cross-correlation coefficient (introduced in Definition 37) between sample and true IPC waveforms is approximately 1 for all dynamic cases listed in Table A.2. In the limit that this cross-correlation coefficient is 1, and in the limit of continuous timesteps, this result would imply that the sample and true IPC waveforms are equal almost everywhere — to within a scaling constant. It is therefore necessary to check whether the norms of the sample and true IPC waveforms are equal (or reasonably close) — if so, then the Monte Carlo samples at hand are able to faithfully reproduce IPC waveforms, and are therefore adequate for the purposes of this Chapter.

Figure 8.8 shows the sample-to-true IPC waveform norm ratio for all dynamic cases listed in Table A.2, which shows that, for all cases, the sample IPC waveform norm is

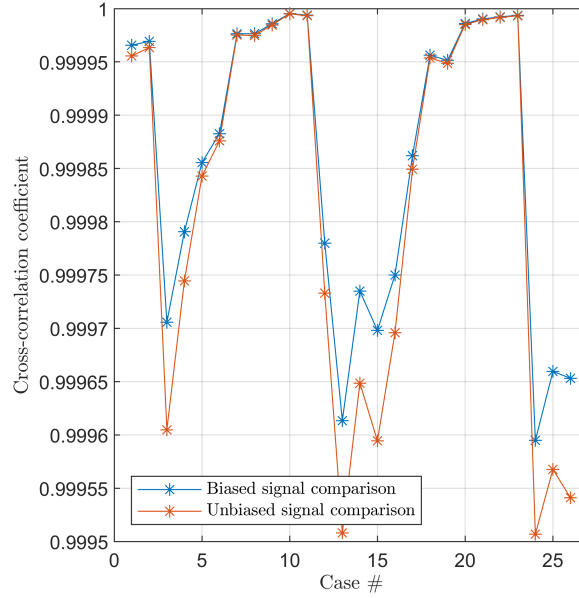


Figure 8.7: Cross-correlation coefficient between sample and true IPC waveforms (over 2 orbit periods), Monte Carlo results (all cases).

within 0.84% of the true IPC waveform norm. This fact, along with the cross-correlation coefficient between these waveforms, shows that the sample IPC approximates the true IPC adequately, i.e., such waveforms coincide with low discrepancy.

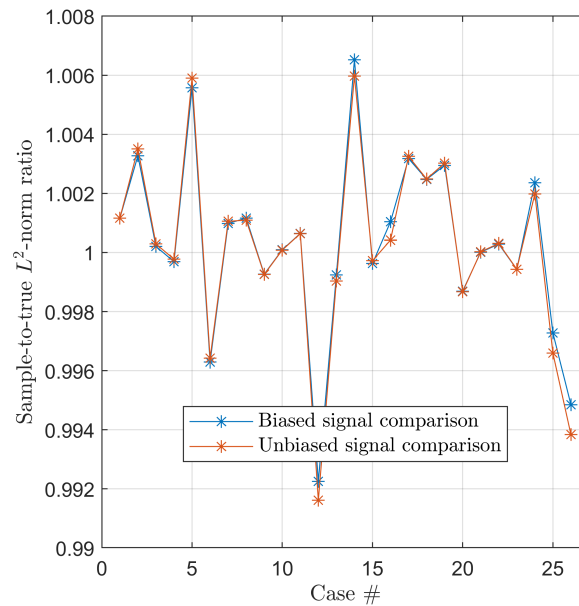


Figure 8.8: Sample-to-true IPC waveform \mathcal{L}^2 -norm ratios (over 2 orbit periods), Monte Carlo results (all cases).

Together, Figures 8.7 and 8.8 not only demonstrate the validity of the Monte Carlo

samples employed in this Chapter, but they also validate the theoretical results presented in Theorem 34 and Corollary 35 in the sense that sample IPCs coincide with true IPCs and not with projection IPCs. This notion is further reinforced with the cross-correlation coefficient between sample and projection IPCs, for both biased and unbiased waveforms, as shown in Figures 8.9 and 8.10, respectively. These figures demonstrate that, for a wide range of initial CW conditions, there is no consistent connection between sample and projection IPCs — unlike the connection between sample and true IPCs.

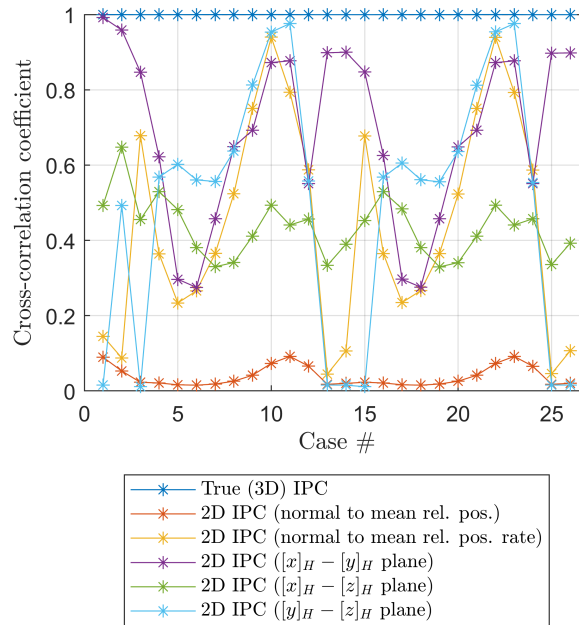


Figure 8.9: Cross-correlation coefficient between sample and projection IPC waveforms (over 2 orbit periods), Monte Carlo results (all cases, biased waveforms).

Out of all dynamic cases and projections considered, there is only near agreement (to within a constant) between the sample and $[x]_H, [y]_H$ -projection IPC waveforms in Case 3D.001, i.e., with no $[z]_H$ motion. However, there are two issues with the adequacy of this projection approximation. The first issue is that, as seen in Fig. 8.11, the $[x]_H, [y]_H$ -projection IPC overestimates the sample (and true) IPC — by a factor of 2.61. In this scenario, the expected relative trajectories are identical, and the origin of the respective collision regions is the same; the only distinction is that integrals for this projection IPC are taken over a 2D disk (as is the case for any projection IPC), whereas integrals for the

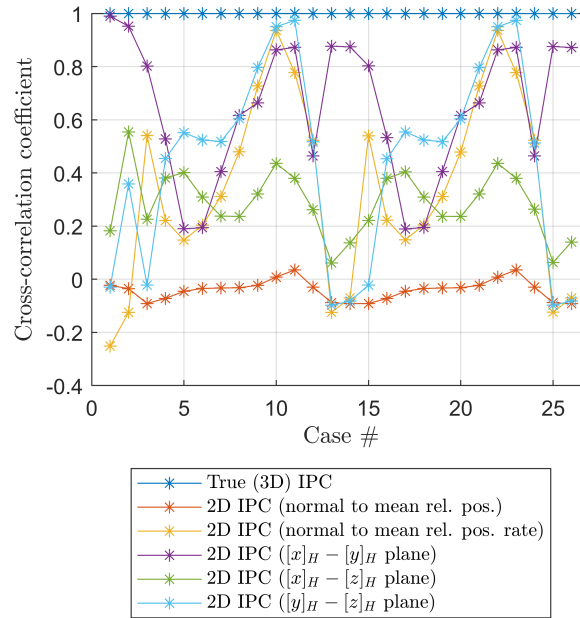


Figure 8.10: Cross-correlation coefficient between sample and true IPC waveforms (over 2 orbit periods), Monte Carlo results (all cases, unbiased waveforms).

sample IPC are taken over a 3D ball, as illustrated in Fig. 8.1. Since no other CW projection has relative motion that approximates the true relative motion better, it follows that every other CW projection case also fails to have projection IPCs that satisfactorily approximate the true IPC. The second issue is that, as discussed in the Introduction section, passive SFF COLA schemes that implement e-i vector separation are popular in applications; these schemes roughly correspond to $[x]_H$ and $[z]_H$ motion being out of phase, which implies nontrivial $[z]_H$ motion. Thus, even if $[x]_H, [y]_H$ -projection IPCs were adequate for the case of no $[z]_H$ motion, $[x]_H, [y]_H$ -projection IPCs would not be adequate when e-i vector separation is implemented. Therefore, Figures 8.7-8.10 and Figure 8.11 demonstrate that there are no general CW dynamics cases where any projection IPC waveform adequately approximates a true IPC waveform.

8.4.3 Correlating miss distance and true IPC

In this Chapter, true IPC and “miss distance”-like measures represented by Methodologies 1, 2 and 3 are compared in order to examine the consistency of collision risk assessments

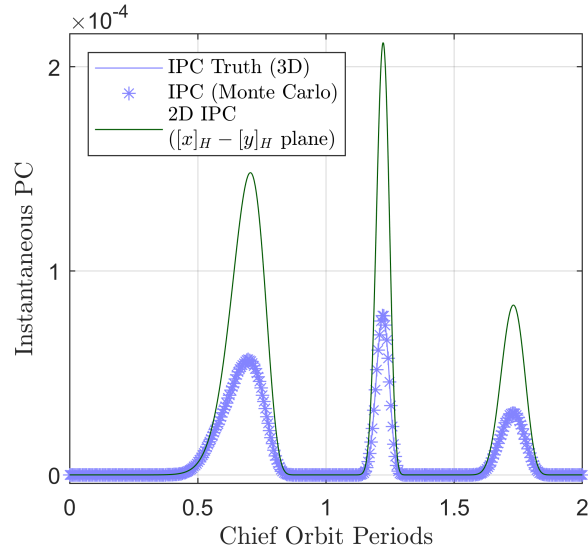


Figure 8.11: Sample, true, and $[x]_H - [y]_H$ projection IPC waveforms, Example 3D.001.

obtained by these comparisons. For the case of no $[z]_H$ motion (see Figure 8.12) and for the case of $[x]_H$ and $[z]_H$ motion in phase (see Figure 8.13), such comparisons are illustrated through the true IPC and miss distance waveforms themselves; for the case of $[x]_H$ and $[z]_H$ motion out of phase, the comparison is made through the collision correlation index introduced in Definition 37.

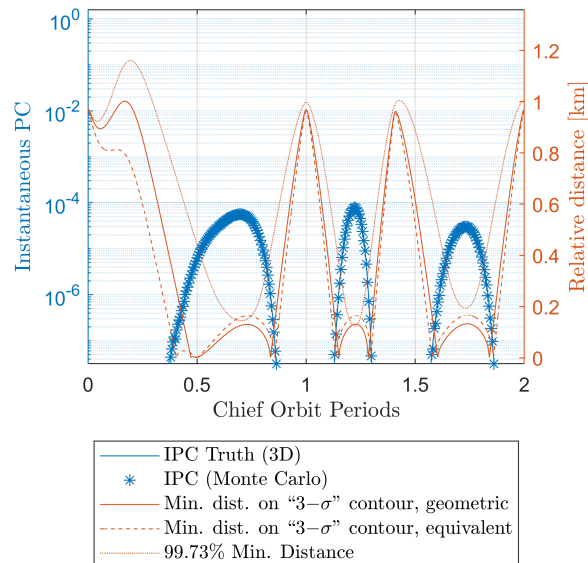


Figure 8.12: Comparison of IPC and “miss distance”-like waveforms, Methodologies 1, 2, and 3, Example 3D.001 (no $[z]_H$ motion).

It is found that there is no general correlation between the unbiased waveforms of the

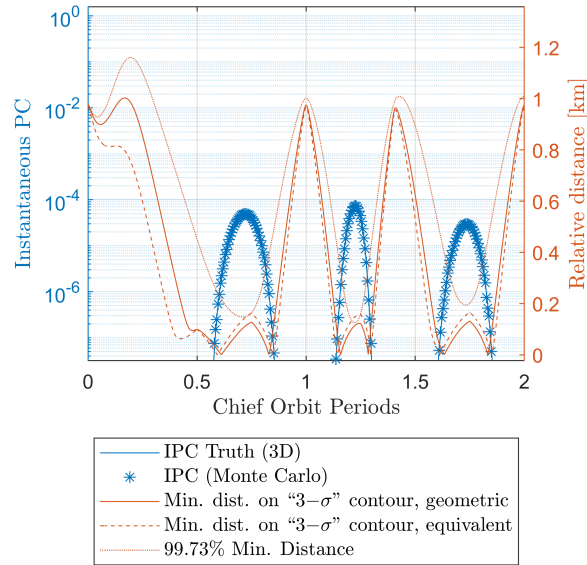


Figure 8.13: Comparison of IPC and “miss distance”-like waveforms, Methodologies 1, 2, and 3, Example 3D.002 ($[x]_H$ and $[z]_H$ motion in phase).

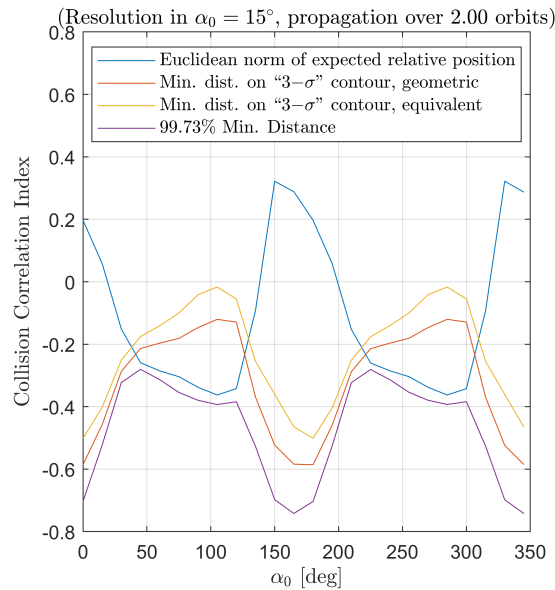


Figure 8.14: Collision correlation index between sample IPC and “miss distance” waveforms: Methodologies 1-3, and Euclidean norm of expected relative position ($[x]_H$, $[z]_H$ motion out of phase).

IPC and the Euclidean norm of expected relative position, since local extrema of the former and the latter are positively correlated as frequently as they are negatively correlated, and often, there is no correlation between the two waveforms. (It should be noted that, for a fixed time, the Euclidean norm of expected relative position is a constant, i.e., it is the Eu-

clidean norm of a constant, namely, the expected value of the relative position; on the other hand, because the relative position is a random variable, the Euclidean norm of the relative position is itself a random variable.) This result is significant because it renders collision risk assessments based on the Euclidean norm of expected relative position inconsistent when compared to the true IPC. This entails that employing the norm of expected relative position as a collision risk indicator may lead to conclusions that would contradict both intuition and probabilistic approaches to measure collision risk.

In contrast, Methodologies 1–3, together with the true IPC, exhibit either negative or null collision correlation indices over several cases of out-of-phase radial/cross-track motion, and this is observed more strongly for $\rho_{3\sigma}$ than for Methodologies 1 and 2. Thus, Methodology 3, together with the true IPC, produces the most consistent collision risk assessment under the collision correlation index criterion. This does not mean that Methodologies 1 or 2 provide incorrect or meaningless information. In fact, analogues of the $L_{d_{m_1}}(\underline{\mathbf{R}}_{i,j}(t))$ set and the $L_{d_{m_2}}(\underline{\mathbf{R}}_{i,j}(t))$ set have been proposed as confidence regions in absolute position space for each agent [specifically, $L_d(\underline{\mathbf{R}}_i(t))$ and $L_d(\underline{\mathbf{R}}_j(t))$ for some meaningful $d > 0$], where absence of intersection between such confidence ellipsoids may be interpreted as lack of plausibility of collision, with a certain degree of confidence, in light of the position statistics.[45] In relative position space, Methodologies 1 and 2, can be complementary to confidence ellipsoid information. For example, with a vanishingly small joint HBR, if $D_{\underline{\mathbf{R}}_{i,j}(t)}(\mathbf{0}_{3 \times 1}) > 3$ (i.e., if the MHD of the origin in relative position space is greater than 3), Methodology 1 would quantify the closeness (in km) of the relative position statistics to violation of the criteria for collision implausibility associated with $L_{d_{m_1}}(\underline{\mathbf{R}}_{i,j}(t))$, instead of just having a binary indicator of whether the criteria has been violated or not. Rather, Figures 8.12-8.14 indicate that the degree of correspondence between IPC and $\rho_{3\sigma}$ changes is greater than between IPC and Methodology 1 or 2 changes, which indicates that the IPC and $\rho_{3\sigma}$ are more qualitatively interchangeable than the IPC and Methodology 1 or 2. Hence, of all the statistical descriptions of agent separation con-

sidered, $\rho_{3\sigma}$ is the most intuitively related to the IPC as per the discussion in the Theory section.

Although $\rho_{3\sigma}$ (together with the true IPC) produces correlation indices that are consistently closer to -1 than any other distance measure, this relationship is distinct from—and does not closely approximate—linear dependence. In fact, the anti-correlation between the unbiased waveforms of the IPC and $\rho_{3\sigma}$ is much weaker than the correlation between certain projection IPCs and true IPCs. Yet, the conclusion is that projection IPCs are inadequate for approximating true IPCs, while $\rho_{3\sigma}$ is considered to be an adequate proxy for the true IPC. The reason for this interpretation is that, not only are distance measures and true IPCs conceptually and physically distinct, but employing one criterion over the other as an indicator of collision risk already leads to distinct active SFF COLA philosophies, as discussed in the Introduction section. Thus, the significant aspect of the relationship between $\rho_{3\sigma}$ and true IPCs is that, despite their conceptual distinction, they are still related to each other in a way that is consistent with intuition, and even though their anti-correlation is not as strong as it could be, their anti-correlation is still stronger for $\rho_{3\sigma}$ than for other distance measures over a wide range of CW dynamic cases and hard-body radii. Figure 8.15 shows the collision correlation index between the (brute force quadrature) IPC and Monte Carlo $\rho_{3\sigma}$ (or sample 99.73% min. distance), with variations of the underlying joint HBR that defines the IPC. (The reference signal is the yellow waveform, i.e., with a joint HBR of 32 m as previously assumed.) It is found that, even after varying the joint HBR, the relationship between the IPC and $\rho_{3\sigma}$ remains qualitatively the same – that is, local maxima of the unbiased IPC and local minima of the unbiased $\rho_{3\sigma}$ waveforms are correlated. Although the “consistency” between IPC and $\rho_{3\sigma}$ becomes stronger with a larger joint HBR, it is still observed for smaller joint hard-body radii, increasing the applicability of these conclusions for spacecraft classes ranging from small satellites to the International Space Station.

Therefore, it is deduced that $\rho_{3\sigma}$ (together with IPC) is more likely to produce consistent collision risk assessments (as understood in this Chapter) than other distance measures.

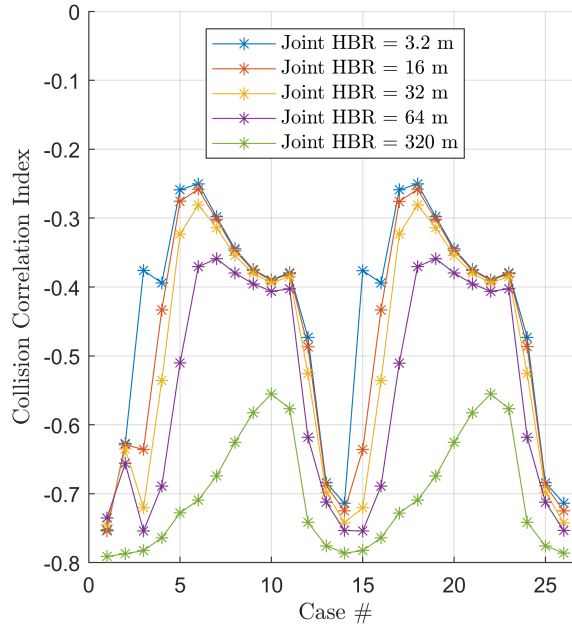


Figure 8.15: Collision correlation index between true IPC and sample $\rho_{3\sigma}$ waveforms (all cases).

Moreover, it can also be concluded that $\rho_{3\sigma}$ is a better predictor of true IPC (and vice versa) than the other distance measures considered, which is a helpful heuristic in applications where only one method of active SFF COLA is implemented. These conclusions align with previous work on use of fixed confidence intervals (in the space of the Euclidean norm of relative position) as collision risk indicators, where it has been proposed that employing lower linear distance interval estimates of confidence bounds with fixed confidence levels is no worse in terms of missed detection/false alarm rates than employing collision probabilities because of how the former and the latter coincide because of the probabilistic interpretation of the confidence bounds employed.[105]

8.4.4 Comparing the 99.73% minimum distance to the P_c

Since the true IPC and $\rho_{3\sigma}$ (i.e., the 99.73% minimum distance) produce consistent collision risk assessments, it is helpful to examine how these two collision risk indicators relate to the P_c , which is the focus of much of the literature in the field of spacecraft collision risk assessment. Unlike for the IPC, no comparison is made for the Monte Carlo P_c estimate

to a baseline numerical estimate based on an analytical formulation. Although such a formulation exists (as presented by Coppola[44]), it is not exact because it assumes that each region of the pdf that crosses into the collision region can only do so once, which cannot be guaranteed in general. When comparing these three indicators for the cases considered, it is found that these indicators are consistent and complementary, as they all indicate consistent aspects of the same collision assessment. That is, at the same time, the true IPC has local maxima, the P_c indicates increased risk of collision, and the 99.73% minimum distance indicates “closest approach” between the chief and deputy spacecraft, as depicted in Figure 8.16 for Example 3D.002. (Other examples exhibit similar behavior.)

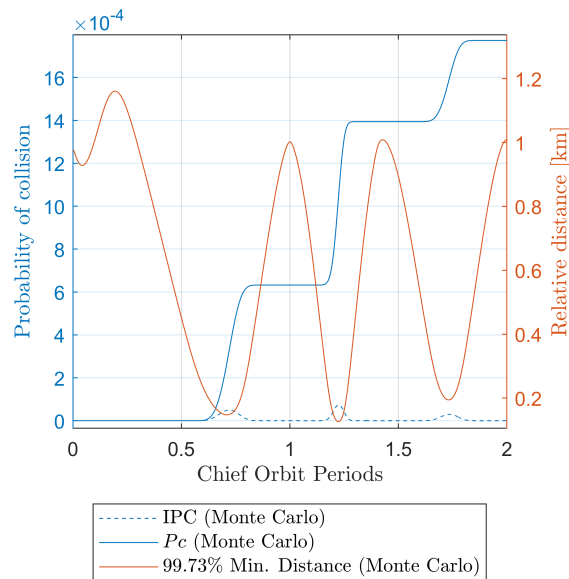


Figure 8.16: Comparison of IPC, P_c , and 99.73% minimum distance waveforms, Example 3D.002.

The extent of these insights is qualitatively only, since many effects have not been studied in detail. For instance, the effects of joint hard-body radius, orbit period, process noise, and propagation horizon have not been considered. Ultimately, it is not possible to draw general conclusions from these qualitative results because the P_c has a sub-additive relationship with the IPC, since a particle which indicates collisions at times t_1 and t_2 contributes to both $IPC(t_1)$ and $IPC(t_2)$, but will only contribute once to $P_c[t_1, t_2]$. However,

this also implies that whenever the IPC is null, the P_c does not change, which does contribute to the fact that significant peaks in IPC may contribute to sustained increases in P_c , as observed in these results. Since such a link may be established between IPC and P_c , and given the relationship exhibited by the IPC and $\rho_{3\sigma}$, the results presented herein indicate that the relationship between all three indicators warrants further examination.

If a more general consistency among the true IPC, P_c and 99.73% minimum distance waveforms were established, it would be a significant result for the SFF COLA community. Such a connection would imply that, by employing these collision risk indicators in unison, it might be possible to obtain consistent collision risk assessments, which would be valuable in the distinct yet complementary goals of SFF mission safety and operational performance. Additionally, by unifying the two main collision risk indicators found in the literature, a step toward bridging their corresponding SFF COLA philosophies into a unified framework may be achieved.

8.5 Conclusion

In this Chapter, several paradigms are addressed regarding collision risk assessment practices in the context of spacecraft formation flying (SFF) collision avoidance (COLA). The first contribution pertains to the true and projection instantaneous probabilities of collision (IPCs), which are defined using topological notions and employing the hard body radius assumption. It is proven that for continuous relative position probability density functions (pdfs), any choice of projection IPC always overestimates the true IPC. This result is validated through Monte Carlo (MC) simulation in an environment subject to Clohessy-Wiltshire (CW) dynamics for a wide range of initial conditions. This result implies that using projection IPCs instead of true IPCs in collision risk assessment results in probabilistic false positives in the detection of high collision risk events, which is detrimental to agents in spacecraft formations with limited, non-renewable onboard propellant. Therefore, it is concluded that employing projection IPCs for collision risk assessment in the

context of SFF COLA is an inefficient practice.

The second contribution examines the consistency of collision risk assessments based on separation measures and true IPCs. This analysis explores the question of whether or not separation measures and true IPC waveforms are related in accordance with intuition; namely, whether minimum separation is correlated with highest collision probability, and maximum separation is correlated with lowest collision probability. The notion of consistency is quantified through the collision correlation index introduced in Definition 37. Based on MC simulation results over a wide range of CW initial conditions, it is found that there are three separation measures (Euclidean norm of expected relative position, distance from the origin to a “geometric” $3\text{-}\sigma$ contour, and distance from the origin to an “equivalent” $3\text{-}\sigma$ contour) that, together with the true IPC, do not produce consistent collision risk assessments. In fact, it was found that using one waveform as a collision risk indicator over another could lead to opposite conclusions.

By comparison, it was found that a certain separation measure (namely, the 99.73% minimum distance, i.e., the $100(1 - 0.9973 \dots)$ -percentile in the distance distribution), together with the true IPC, produces consistent assessments over a wide range of CW initial conditions in the sense that the collision correlation index is always negative, although not to the point of indicating linear dependence. Therefore, waveforms of the separation measure defined by the 99.73% minimum distance are, in some sense, qualitative substitutes for true IPC waveforms. In principle, if the relative position has a pdf that, after propagation, can still be numerically integrated, then the 99.73% minimum distance could be computed numerically, which would prevent estimating it through a computationally costly sampling method. Thus, the 99.73% minimum distance could, in principle, be employed in real-time applications where collision risk assessments are based on separation measures. These results give insight into the tradeoffs of choosing one of the two main philosophies of high collision risk event detection (miss distance-based and IPC-based detection) over the other.

CHAPTER 9

SPACECRAFT FORMATION COLLISION RISK INTERPRETATION AND DECISION MAKING (PART 2) – SENSITIVITY OF SEPARATION INDICATORS IN SPACECRAFT FORMATION COLLISION RISK ANALYSIS

The 99.73% minimum distance, denoted as $\rho_{3\sigma}$, is the 0.27%-percentile in the distribution of the Euclidean norm of the instantaneous relative position between two agents. Previously, $\rho_{3\sigma}$ has been proposed as a probabilistic collision risk boundary for spacecraft formation flight under the assumption of Clohessy-Wiltshire (CW) relative orbital dynamics. In this case, agents with a isotropic keep-out-zone distance requirement greater than $\rho_{3\sigma}$ have an instantaneous probability of collision (IPC) of at least 0.27%. This Chapter of the doctoral dissertation validates the foregoing interpretation of $\rho_{3\sigma}$ by showing that small changes to the target probability of $\rho_{3\sigma}$ also result in small changes to $\rho_{3\sigma}$ itself.

9.1 Introduction

Approaches to SFF collision avoidance (COLA) can be broadly classified into two groups: passive and active.[27, 28] Passive SFF COLA methods focus on designing and keeping orbits that are passively safe (approximately), without directly addressing internal collision risk in an ongoing basis.[60, 145, 146] Conversely, active SFF COLA methods propose conducting internal collision risk quantification and assessment on a recurring basis, as well as planning and executing corrective actions when necessary.

Active SFF COLA methods are characterized by their collision risk indicators, which are used to quantify collision risk; these indicators are employed in developing threshold

criteria through which it can be decided whether collision risk warrants corrective maneuvers. The first indicator type, distance-based, employs some statistical description of the physical separation between two agents as measured by, for example, the Euclidean distance or Cartesian components of relative position.[39, 152, 25, 52] The second indicator type, probability-based, quantifies collision risk as the probability measure of the relative position over a region in which the collision event is understood to occur.[46, 27, 28, 13, 156, 55] Generally, collision risk is mitigated by setting constraints in an optimal control problem in terms of these indicators. Because distance-based and probability-based indicators have distinct physical interpretations, active SFF COLA methods are philosophically and practically distinct depending on the choice of collision risk indicator. For an extended discussion on distance-based and probability-based collision risk indicators and their relationship, the reader is encouraged to refer to the work of Núñez Garzón and Lightsey.[27, 28]

For an individual agent, its hard-body radius (HBR) is a safety parameter that describes the minimum safe isotropic distance from its center of mass to any objects outside itself. [27, 28, 38] Consequently, the joint hard-body radius for two agents, which is the sum of their individual hard-body radii, may be understood as a minimum safe isotropic separation distance between such agents. [32, 56, 24, 31] Hence, a collision between two agents may be defined to occur when the Euclidean distance between their centers of mass is less than their joint HBR. Then, the instantaneous probability of collision (IPC) between two agents is the probability of the instantaneous collision event; this measure is based on a stochastic description of the instantaneous relative geometry between such agents.[12]

If $p_{3\sigma}$ is defined as a constant with an approximate value of 0.27%, then the 99.73% minimum distance value, also known as $\rho_{3\sigma}$, is the Euclidean distance away from the origin of the frame describing the relative position between two agents such that $100(1 - p_{3\sigma})$ percent of randomly drawn points (according to the instantaneous relative position distribution) have a Euclidean distance from the origin greater than $\rho_{3\sigma}$. In the context of

Clohessey-Wiltshire (CW) relative orbital dynamics,[138, 139] $\rho_{3\sigma}$ has been proposed as an inter-agent Euclidean separation indicator with two benefits.[27, 28] First, through its definition, $\rho_{3\sigma}$ has the following probabilistic risk interpretation: [27, 28] $\rho_{3\sigma}$ is the joint HBR such that the corresponding IPC is equal to $p_{3\sigma}$. Second, with a fixed joint HBR, the corresponding IPC time-waveform has a correlation relationship with the $\rho_{3\sigma}$ time-waveform such that, roughly, local minima of IPC correspond with local maxima of $\rho_{3\sigma}$, and vice versa. That is, roughly, $\rho_{3\sigma}$ indicates closest inter-agent Euclidean distance in the same conditions that the IPC indicates highest collision risk, and $\rho_{3\sigma}$ indicates furthest inter-agent Euclidean distance while the IPC indicates lowest collision risk. Therefore, $\rho_{3\sigma}$ and the IPC are correlated to each other in a way that is consistent with intuition.

In the following way, $\rho_{3\sigma}$ can be interpreted as a probabilistic risk boundary: if the joint HBR for two agents were equal to $\rho_{3\sigma}$, then the instantaneous probability of collision between the agents would be equal to $p_{3\sigma}$. Hence, if the true joint HBR is less than $\rho_{3\sigma}$, the instantaneous collision probability is less than $p_{3\sigma}$; conversely, if the true joint HBR is greater than $\rho_{3\sigma}$, the instantaneous collision probability is greater than $p_{3\sigma}$. As a result, $\rho_{3\sigma}$ conceptually bridges the gap between probabilistic and distance-based approaches to collision risk quantification.

In order to validate the foregoing interpretation of $\rho_{3\sigma}$, it is important to understand the effects on $\rho_{3\sigma}$ caused by variations in its target probability, i.e., the value of the cumulative distribution function (associated with the Euclidean norm of the instantaneous relative position) which is obtained at the $\rho_{3\sigma}$ value, which should be equal to $p_{3\sigma}$ by definition. However, because of errors inherent to numerical methods, it is expected that there would be a discrepancy between the prescribed $p_{3\sigma}$ value and the computed radial probability measure of the relative position evaluated at the true $\rho_{3\sigma}$. Such discrepancies may affect both the meaning of $\rho_{3\sigma}$ and its computation. First, finding a $\rho_{3\sigma}$ candidate that achieves a target probability that approximates (but is not exactly equal to) $p_{3\sigma}$ is equivalent to solving for $\rho_{3\sigma}$ with a target probability different from $p_{3\sigma}$. Hence, if small variations in target

probability result in changes to $\rho_{3\sigma}$ that are small compared to the magnitude of $\rho_{3\sigma}$, then it makes sense to assert that a collision risk of approximately $p_{3\sigma}$ is incurred when the inter-agent keep-out Euclidean distance is approximately $\rho_{3\sigma}$. Second, if small changes in target probability cause small changes in $\rho_{3\sigma}$, the outcome of an estimator of $\rho_{3\sigma}$ could be trusted to hold the same interpretation as the exact $\rho_{3\sigma}$ value. Therefore, the goal of this Chapter is to examine the sensitivity of $\rho_{3\sigma}$ to small variations in its target probability. If such an investigation validates the foregoing interpretation of $\rho_{3\sigma}$, especially over extended propagation horizons, it would justify application of the $\rho_{3\sigma}$ construct in spacecraft formation collision risk analysis.

This Chapter is organized as follows. First, the Euclidean norm of the instantaneous relative position (which is a random variable) is itself characterized as a random variable. This allows for the computation of radial probability measures, as well as for the interpretation of $\rho_{3\sigma}$ as a quantile of the distribution of the Euclidean norm of instantaneous relative position. These theoretical findings lay the foundation for the sensitivity analysis of $\rho_{3\sigma}$, which is shown to depend on the probability density function (pdf) of the Euclidean norm of instantaneous relative position, as evaluated at the $\rho_{3\sigma}$ value. Second, this Chapter details the precise techniques employed for numerical and sample computation of $\rho_{3\sigma}$, which, in turn, are applied to computing the sensitivity of $\rho_{3\sigma}$ with respect to changes in $p_{3\sigma}$. Third, in the context of simulating pertinent relative orbital dynamic scenarios subject to CW dynamics, it is shown that small changes in the target probability $p_{3\sigma}$ induce proportionally small changes to the $\rho_{3\sigma}$ value. It follows that the percentile interpretation of $\rho_{3\sigma}$ holds under small variations to $p_{3\sigma}$. This fact implies that it is correct to interpret $\rho_{3\sigma}$ as encoding a collision risk boundary in relative position space with probabilistic interpretation; additionally, this interpretation holds under statistical estimator errors to within some acceptable user tolerance. Therefore, these results validate implementation of the $\rho_{3\sigma}$ construct in the practice of spacecraft formation flying as both a metric and measure in the quantification and management of collision risk.

9.2 Background

9.2.1 Notation adjustments for this Chapter

The Notation and Nomenclature used in this Chapter, as well as the deterministic definition of collision events (derived from relative-attitude abstraction, and induced by arbitrary a -norm balls in relative position space), and the definition of stochastic collision risk measures (in both an instantaneous and joint-time sense), are addressed in Chapter 2.

Such general Notation and Nomenclature are made more specific for this Chapter as follows. First, the balls and spheres used are only those with respect to the Euclidean norm; additionally, only open balls are employed. (See Definition 1.) Hence, implicitly $a = 2$ or $a = \text{Eu}$; consequently, the a -norm symbol is omitted throughout this Chapter. (See Section 2.2.) Additionally, the symbol “ $\mathbb{S}^{(s-1)}$ ” denotes $\mathbb{S}_1^{(s-1)}(\mathbf{0}_{s \times 1})$, i.e., the unit $(s - 1)$ -sphere centered at the origin. From the aforementioned, it follows that collision sets and probabilities are induced from instantaneous collision conditions based on open balls with respect to the Euclidean norm in relative position space.

Throughout the remainder of this Chapter, for simplicity, the instantaneous relative state $\underline{\mathbf{X}}_{i,j}(t)$ and relative position $\underline{\mathbf{R}}_{i,j}(t)$ are denoted as $\underline{\mathbf{X}}$ and $\underline{\mathbf{R}}$, respectively. Furthermore, only three-dimensional (3D) relative positions are considered.

9.3 Theory

9.3.1 Introducing radial probability measures

9.3.1.1 *Radial probability measures – definition.*

This Chapter draws heavily on the concept of radial probability measures of the relative position $\underline{\mathbf{R}}$; that is, in measures $h_{\underline{\mathbf{R}}} : [0, \infty) \rightarrow [0, 1]$ of the form

$$h_{\underline{\mathbf{R}}}(\rho) = p(\underline{\mathbf{R}} \in V_\rho) \tag{9.1}$$

where, for $\rho \geq 0$,

$$V_\rho \doteq \{\underline{\mathbf{r}} \in \mathbb{R}^3 : \|\underline{\mathbf{r}}\|_2 \leq \rho\} = \mathbb{B}_\rho^{3|\text{Eu}}(\underline{\mathbf{0}}_{3 \times 1}) \cup \mathbb{S}_\rho^{2|\text{Eu}}(\underline{\mathbf{0}}_{3 \times 1}) \quad (9.2)$$

Because the relative position random variable $\underline{\mathbf{R}}$ is assumed to be absolutely continuous, the measure $h_{\underline{\mathbf{R}}}$ can be computed as the integral

$$h_{\underline{\mathbf{R}}}(\rho) = \int_{\underline{\mathbf{r}} \in V_\rho} \text{pdf}_{\underline{\mathbf{R}}}(\underline{\mathbf{r}}) \, d\underline{\mathbf{r}} \quad (9.3)$$

where $\text{pdf}_{\underline{\mathbf{R}}}(\cdot)$ exists a.e. in \mathbb{R}^3 and is non-negative where defined; cf. Section 2.3.

Because the set $\mathbb{S}_\rho^{2|\text{Eu}}(\underline{\mathbf{0}}_{3 \times 1}) = \{\underline{\mathbf{r}} \in \mathbb{R}^3 : \|\underline{\mathbf{r}}\|_2 = \rho\}$ has zero measure in \mathbb{R}^3 , it follows that

$$h_{\underline{\mathbf{R}}}(\rho) = \int_{\|\underline{\mathbf{r}}\|_2 \leq \rho} \text{pdf}_{\underline{\mathbf{R}}}(\underline{\mathbf{r}}) \, d\underline{\mathbf{r}} = \int_{\|\underline{\mathbf{r}}\|_2 < \rho} \text{pdf}_{\underline{\mathbf{R}}}(\underline{\mathbf{r}}) \, d\underline{\mathbf{r}} \quad (9.4)$$

Therefore, by definition, $\text{IPC}_{i,j}(t)$ is simply the radial probability measure of $\underline{\mathbf{R}}$ evaluated at the joint hard-body radius $l_{i,j}$. That is,

$$h_{\underline{\mathbf{R}}}(l_{i,j}(t)) = \int_{\|\underline{\mathbf{r}}\|_2 < l_{i,j}} \text{pdf}_{\underline{\mathbf{R}}}(\underline{\mathbf{r}}) \, d\underline{\mathbf{r}} =: \text{IPC}_{i,j}(t) \quad (9.5)$$

9.3.1.2 Euclidean norm of the relative position – definition.

The Euclidean norm of the relative position, or R , is defined as $R \doteq \|\underline{\mathbf{R}}\|_2 = (\underline{\mathbf{R}}^T \underline{\mathbf{R}})^{1/2}$. Thus, R can be understood as the true isotropic inter-agent distance, which, due to uncertainty, cannot be known exactly.

Proposition 39. Let \underline{X} be an absolutely continuous random variable in \mathbb{R}^s . Define $X \doteq \|\underline{X}\|_2 = (\underline{X}^T \underline{X})^{1/2}$. Then, X is an absolutely continuous random variable as well. \diamond

Proof. See Corollary 16. \square

Because $\underline{\mathbf{R}}$ is assumed to be absolutely continuous, via Proposition 39, it follows that

R is absolutely continuous. Therefore, pdf_R exists a.e. in $[0, \infty)$, and cdf_R is an absolutely continuous function. Furthermore, $h_{\mathbf{R}}$ is an absolutely continuous function as well, which can be seen by noting that

$$h_{\mathbf{R}}(\rho) = p(\|\mathbf{R}\|_2 \leq \rho) = p(R \leq \rho) =: \text{cdf}_R(\rho) \quad (9.6)$$

If $\text{pdf}_{\mathbf{R}}$ is known, $h_{\mathbf{R}}(r)$ for $r \geq 0$ can be computed as

$$h_{\mathbf{R}}(r) = \int_0^r \int_0^{2\pi} \int_0^\pi \text{pdf}_{\mathbf{R}}(\mathbf{r}(\rho, \theta, \phi)) \rho^2 \sin \phi \, d\phi \, d\theta \, d\rho \quad (9.7)$$

where $\mathbf{r}(\rho, \theta, \phi)$ is a traditional spherical coordinate representation of \mathbf{r} as given by

$$\mathbf{r}^T(\rho, \theta, \phi) = \rho \begin{bmatrix} \cos \theta \sin \phi & \sin \theta \sin \phi & \cos \phi \end{bmatrix} \quad (9.8)$$

where $\rho \geq 0$, $0 \leq \theta < 2\pi$, and $0 \leq \phi \leq \pi$. It follows that $\text{pdf}_R(r)$ can be computed as an integral of $\text{pdf}_{\mathbf{R}}$ as given by

$$\text{pdf}_R(r) = \left. \frac{dh_{\mathbf{R}}(\rho)}{d\rho} \right|_{\rho=r} = r^2 \int_0^{2\pi} \int_0^\pi \text{pdf}_{\mathbf{R}}(\mathbf{r}(r, \theta, \phi)) \sin \phi \, d\phi \, d\theta \quad (9.9)$$

Alternatively, the Lambert area-preserving transform, previously introduced in Eq. 7.47, may be used to create a spherical coordinate representation of \mathbf{r} . [119] Although it may be generally employed as an area-preserving mapping between the unit hypercube the unit hypersphere in \mathbb{R}^s , the Lambert transform is specifically implemented in this Chapter as an area-preserving mapping between the unit 2-square and the (Euclidean) unit 2-sphere in \mathbb{R}^3 . Hence, the Lambert transform is denoted as $T_{\mathbb{S}^2} : [0, 1) \times [0, 1] \rightarrow \mathbb{S}^2$, and it is given by

$$T_{\mathbb{S}^2} \left(\begin{bmatrix} y_1 \\ y_2 \end{bmatrix} \right) = \begin{bmatrix} \sqrt{1 - (1 - 2y_2)^2} \cos(2\pi y_1) \\ \sqrt{1 - (1 - 2y_2)^2} \sin(2\pi y_1) \\ 1 - 2y_2 \end{bmatrix} \quad (9.10)$$

for all $[y_1, y_2]^T$ in $[0, 1] \times [0, 1]$. Using the Lambert transform, the computation of $h_{\underline{\mathbf{R}}}(r)$ becomes

$$h_{\underline{\mathbf{R}}}(r) = 4\pi \int_0^r \int_0^1 \int_0^1 \text{pdf}_{\underline{\mathbf{R}}}(\underline{\mathbf{r}}(\rho, y_1, y_2)) \rho^2 dy_2 dy_1 d\rho \quad (9.11)$$

and the computation of $\text{pdf}_R(r)$ becomes

$$\text{pdf}_R(r) = 4\pi r^2 \int_0^1 \int_0^1 \text{pdf}_{\underline{\mathbf{R}}}(\underline{\mathbf{r}}(r, y_1, y_2)) dy_2 dy_1 \quad (9.12)$$

where $\rho \geq 0$, $0 \leq y_1 < 1$, and $0 \leq y_2 \leq 1$, and where

$$\underline{\mathbf{r}}(\rho, y_1, y_2) = \rho T_{\mathbb{S}^2}([y_1, y_2]^T) \quad (9.13)$$

The spherical coordinate-based integral methods presented in this subsection for computing radial probability measures (in Eqns. 9.7 and 9.11) and the pdf of R (in Eqns. 9.9 and 9.12) are not only intuitive, but also general in the sense that they are applicable regardless of the distribution of $\underline{\mathbf{R}}$ – as long as its pdf is accessible and well-defined.

9.3.2 Radial probability measures for non-singular, normal relative position

Within this subsection, let $\underline{\mathbf{R}}$ have a non-singular, multivariate normal distribution (MVN), i.e., $\underline{\mathbf{R}} \sim \mathcal{N}(\underline{\boldsymbol{\mu}}, \Sigma)$, where $\underline{\boldsymbol{\mu}} \in \mathbb{R}^3$, $\Sigma \in \mathbb{R}^{3 \times 3}$, $\Sigma > 0$. Then, for $\underline{\mathbf{r}} \in \mathbb{R}^3$, $\text{pdf}_{\underline{\mathbf{R}}}(\underline{\mathbf{r}})$ is given by

$$\text{pdf}_{\underline{\mathbf{R}}}(\underline{\mathbf{r}}) = ((2\pi)^3 \det \Sigma)^{-1/2} \exp \left[-\frac{1}{2} (\underline{\mathbf{r}} - \underline{\boldsymbol{\mu}})^T \Sigma^{-1} (\underline{\mathbf{r}} - \underline{\boldsymbol{\mu}}) \right] \quad (9.14)$$

9.3.2.1 Euclidean norm of non-singular, normal relative position – integral computation.

When $\underline{\mathbf{R}}$ is non-singular normal, computing $h_{\underline{\mathbf{R}}}(r)$ and $\text{pdf}_R(r)$ in terms of traditional spherical coordinates can be accomplished by modifying Eqns. 9.7 and 9.9 into

$$h_{\underline{\mathbf{R}}}(r) = \int_0^r \int_0^{2\pi} \int_0^\pi g_1(\rho, \theta, \phi) d\phi d\theta d\rho \quad (9.15)$$

and

$$\text{pdf}_R(r) = \int_0^{2\pi} \int_0^\pi g_1(r, \theta, \phi) \, d\phi \, d\theta \quad (9.16)$$

where $\mathbf{r}(\rho, \theta, \phi)$ is as given by Eq. 9.8, and where

$$g_1(\rho, \theta, \phi) = \left[\frac{\det(\Sigma^{-1})}{(2\pi)^3} \right]^{1/2} \exp \left[-\frac{1}{2} (\mathbf{r}(\rho, \theta, \phi) - \boldsymbol{\mu})^T \Sigma^{-1} (\mathbf{r}(\rho, \theta, \phi) - \boldsymbol{\mu}) \right] \rho^2 \sin \phi \quad (9.17)$$

Similarly, $h_{\mathbf{R}}(r)$ and $\text{pdf}_R(r)$ can be computed in terms of Lambert equal-area spherical coordinates by adjusting Eqns. 9.11 and 9.12 as given by

$$h_{\mathbf{R}}(r) = \int_0^r \int_0^1 \int_0^1 g_2(\rho, y_1, y_2) \, dy_2 \, dy_1 \, d\rho \quad (9.18)$$

and

$$\text{pdf}_R(r) = \int_0^1 \int_0^1 g_2(r, y_1, y_2) \, dy_2 \, dy_1 \quad (9.19)$$

where $\mathbf{r}(\rho, y_1, y_2) = \rho T_{\mathbb{S}^2}([y_1, y_2]^T)$, and where

$$g_2(\rho, y_1, y_2) = \left[\frac{2}{\pi} \det(\Sigma^{-1}) \right]^{1/2} \exp \left[-\frac{1}{2} (\mathbf{r}(\rho, y_1, y_2) - \boldsymbol{\mu})^T \Sigma^{-1} (\mathbf{r}(\rho, y_1, y_2) - \boldsymbol{\mu}) \right] \rho^2 \quad (9.20)$$

9.3.3 Radial probability measures – approximations

9.3.3.1 Radial probability measures – Monte Carlo integration.

An integral I of a measurable function $g : \Omega \rightarrow \mathbb{R}$ of an absolutely continuous random variable \underline{X} over its sample space $\Omega \subseteq \mathbb{R}^s$ can be understood as the expectation of $g(\underline{X})$; that is,

$$I[g] = \int_{\underline{x} \in \Omega} g(\underline{x}) \, \text{pdf}_{\underline{X}}(\underline{x}) \, d\underline{x} =: \mathbb{E}[g(\underline{X})] \quad (9.21)$$

assuming that $\text{pdf}_{\underline{X}}(\cdot)$ exists. If $\{\underline{x}_k\}_{k \in \{1, \dots, N\}}$ is a statistically random sample of \underline{X} with sample size $N \in \mathbb{N}$ (that is, the elements of the sample are independent and identically distributed (i.i.d.), with the same distribution as \underline{X}), then $I[g]$ can be approximated through the expectation estimator given by[157]

$$\widehat{I}_N[g] = \frac{1}{N} \sum_{k=1}^N g(\underline{x}_k) \quad (9.22)$$

This technique is the most simple version of Monte Carlo-based integration, and it has the following advantages.[158] First, through application of the expectation operator to Eq. 9.22, and noting that $\mathbb{E}[g(\underline{x}_k)] = \mathbb{E}[g(\underline{X})]$ for all $k \in \{1, \dots, N\}$, it follows that $\mathbb{E}[\widehat{I}_N[g]] = I[g]$. Consequently, via the strong law of large numbers, $\widehat{I}_N[g]$ converges to $I[g]$ almost surely,[120] i.e., $p\left(\widehat{I}_N[g] \rightarrow I[g]\right) = 1$,[73] or

$$p\left(\lim_{N \rightarrow \infty} \widehat{I}_N[g] = I[g]\right) = 1 \quad (9.23)$$

Second, through the Central Limit Theorem (CLT), it can be shown that for large N , the approximation root-mean-square-error (RMSE) magnitude $\left|I[f] - \widehat{I}_N[f]\right|$ is proportional to $N^{-1/2}$ (assuming an unbiased estimator), so increasing sample size generally improves the accuracy of the approximated integral.[157] Although this convergence rate is very slow, it does remain as $\mathcal{O}(N^{-1/2})$ regardless of the dimension of elements in a Monte Carlo sample; hence, Monte Carlo integration is a consistently viable tool for approximating integrals in high-dimensional spaces. The Monte Carlo (MC) estimator presented in Eq. 9.22 is crude or naïve because it does not implement variance reduction techniques such as importance sampling, antithetic variates or control variates.[120, 159]

A crude MC estimator $\widehat{h}_{\underline{\mathbf{R}}, N}(\cdot)$ for the radial probability measure $h_{\underline{\mathbf{R}}}(\cdot)$ is given by

$$\widehat{h}_{\underline{\mathbf{R}}, N}(r) = \frac{1}{N} \sum_{k=1}^N f_{h_{\underline{\mathbf{R}}, r}}(\underline{\mathbf{r}}_k) \quad (9.24)$$

where $\{\mathbf{r}_k\}_{k \in \{1, \dots, N\}}$ is a Monte Carlo sample of \mathbf{R} , and where $f_{h_{\mathbf{R}}, r} : \mathbb{R}^3 \rightarrow \{0, 1\}$ is an indicator function,[73] which is based on the definition of radial probability measures, and thus satisfies

$$f_{h_{\mathbf{R}}, r}(\mathbf{r}) = \begin{cases} 1, & \|\mathbf{r}\|_2 \leq r \\ 0, & \text{otherwise} \end{cases} \quad (9.25)$$

for \mathbf{r} in \mathbb{R}^3 and $r > 0$.

9.3.4 Characterizing the 99.73% minimum distance ($\rho_{3\sigma}$)

9.3.4.1 99.73% minimum distance ($\rho_{3\sigma}$) – definition.

Let the constant $p_{3\sigma}$ be defined as

$$p_{3\sigma} \doteq 1 - \text{cdf}_{\chi_1^2}(3^2) \approx 1 - 0.9973 = 0.0027 \quad (9.26)$$

As previously noted, the 99.73% minimum distance, or $\rho_{3\sigma}$, is the distance away from the origin so that $100(1 - p_{3\sigma})$ percent of relative position cases have Euclidean distances from the origin that are greater than $\rho_{3\sigma}$. In other words, $\rho_{3\sigma}$ can be defined as

$$\rho_{3\sigma} \doteq \min \{r \in [0, \infty) : \text{cdf}_R(r) = p_{3\sigma}\} \quad (9.27)$$

It will be shown $\rho_{3\sigma}$ is a quantile of the distribution of R .

Definition 40 (Quantiles and quantile function [160, 161]). Take $q \in (0, 1)$. For a univariate, real-valued RV X with cdf denoted by F_X , a quantile $x \in \mathbb{R}$ of order q of the distribution of X satisfies $F_X(x) \geq q$ and

$$p(X < x) = \lim_{\varepsilon \rightarrow 0^+} F_X(x - \varepsilon) \leq q \quad (9.28)$$

The quantile function of X , $F_X^{-1} : (0, 1) \rightarrow \mathbb{R}$ is a generalized inverse of F_X , i.e.,

it satisfies $F_X^{-1}(q) \doteq \inf S_q$, where $S_q = \{x \in \mathbb{R} : F_X(x) \geq q\}$, where $\inf(\cdot)$ denotes the infimum operator. Since cdfs are right continuous, S_q is closed on the left, i.e., $\inf S_q \in S_q$. [35] Therefore, $F_X^{-1}(q)$ is given by

$$F_X^{-1}(q) = \min \{x \in \mathbb{R} : F_X(x) \geq q\} \quad (9.29)$$

and it exists for $q \in (0, 1)$. Therefore, $F_X^{-1}(q)$ is the minimum quantile of order q of the distribution of X .

If X is continuous, its cdf is continuous, so it has no jump discontinuities. In this case, $F_X^{-1}(q)$ is given by

$$F_X^{-1}(q) = \min \{x \in \mathbb{R} : F_X(x) = q\} \quad (9.30)$$

Finally, if F_X is strictly increasing, then F_X^{-1} is the true inverse of F_X . \diamond

In the context of real-valued random variables, absolutely continuous RVs (i.e., RVs that have pdfs) are also continuous RVs (i.e., RVs with continuous cdfs), although the converse is not true (see the Cantor function, a classical counterexample: it has a continuous cdf, as well as a zero a.e. derivative; hence, the cdf is not equal to the integral of its derivative). [35] Since R is absolutely continuous (per the assumption of absolute continuity of \mathbf{R} , and via Proposition 39), cdf_R is a continuous function by implication. Therefore, via Definition 40, $\rho_{3\sigma}$ is the minimum $p_{3\sigma}$ -quantile of R ; furthermore, $\rho_{3\sigma}$ exists and is unique.

It should be noted that there may be $p_{3\sigma}$ -quantiles of R other than $\rho_{3\sigma}$. For example, it is possible that $\text{pdf}_R(r) = 0$ a.e. for $r \in (\rho_{3\sigma}, \rho_{3\sigma} + \varepsilon)$ for some $\varepsilon > 0$; in that case, for any such r , $\text{cdf}_R(r) = p_{3\sigma}$. However, it is useful to define $\rho_{3\sigma} = \text{cdf}_R^{-1}(p_{3\sigma})$ because, as an output of the quantile function, $\rho_{3\sigma}$ is the smallest $p_{3\sigma}$ -quantile of R , which is consistent with its interpretation as a collision risk boundary. Additionally, if cdf_R is strictly increasing in the neighborhood of $p_{3\sigma}$, then $\rho_{3\sigma}$ is the unique $p_{3\sigma}$ -quantile of R .

9.3.4.2 99.73% minimum distance ($\rho_{3\sigma}$) – sensitivity analysis.

For a univariate random variable X , the derivative of the quantile function of X is given by

$$\left. \frac{d}{dy} \text{cdf}_X^{-1}(y) \right|_{y=u} = \lim_{\varepsilon \rightarrow 0} \frac{\text{cdf}_X^{-1}(u + \varepsilon) - \text{cdf}_X^{-1}(u)}{\varepsilon} \quad (9.31)$$

for $0 < u < 1$. When X is absolutely continuous (i.e., when its pdf exists; see the Notation subsection), Parzen has shown that the derivative of the quantile function of X satisfies the relation

$$\text{pdf}_X(\text{cdf}_X^{-1}(u)) \left[\left. \frac{d}{dy} \text{cdf}_X^{-1}(y) \right|_{y=u} \right] = 1 \quad (9.32)$$

for $0 < u < 1$. [161] When applied to R , and noting that $\rho_{3\sigma}$ satisfies $\text{cdf}_R^{-1}(p_{3\sigma}) = \rho_{3\sigma}$, it follows that

$$\left. \frac{d}{dy} \text{cdf}_R^{-1}(y) \right|_{y=p_{3\sigma}} = \frac{1}{\text{pdf}_R(\rho_{3\sigma})} \quad (9.33)$$

Since $\rho_{3\sigma} = \text{cdf}_R^{-1}(p_{3\sigma}) = \rho_{3\sigma}(p_{3\sigma})$, the derivative of quantile function of R evaluated at $p_{3\sigma}$ can be interpreted as the derivative of $\rho_{3\sigma}$ with respect to its target probability, $p_{3\sigma}$. Therefore,

$$\frac{d\rho_{3\sigma}}{dp_{3\sigma}} = \frac{1}{\text{pdf}_R(\rho_{3\sigma})} \quad (9.34)$$

Hence, the effects on $\rho_{3\sigma}$ caused by small changes in $p_{3\sigma}$ may be quantified via Eq. 9.34.

It should be noted that this sensitivity analysis could be extended to apply to cases where $\text{pdf}_R(\rho_{3\sigma})$ is undefined. One example of this is when $\text{pdf}_R(\rho_{3\sigma}^-)$ and $\text{pdf}_R(\rho_{3\sigma}^+)$ both exist and are finite, yet do not share the same value; in this case, the derivative of cdf_R evaluated at $\rho_{3\sigma}$ [i.e., $\text{pdf}_R(\rho_{3\sigma})$] does not exist. Another example is when $\text{pdf}_R(\rho_{3\sigma}^+) = 0$; in this case, there are multiple $p_{3\sigma}$ -quantiles of R , and $\rho_{3\sigma}$ is the smallest one. Since any $\rho < \rho_{3\sigma}$ satisfies $h_{\mathbf{R}}(\rho) < p_{3\sigma}$, it follows that $\text{cdf}_R(\rho)$ is strictly increasing for ρ that approaches $\rho_{3\sigma}$ from the left. Therefore, $\text{pdf}_R(\rho_{3\sigma}^-) > 0$, which also implies that $\text{pdf}_R(\rho_{3\sigma})$ does not exist.

In both of the aforementioned examples, the sensitivity analysis could be carried out by replacing $\text{pdf}_R(\rho_{3\sigma})$ in Eq. 9.34 with $\text{pdf}_R(\rho_{3\sigma}^-)$ instead, given that it is not only well

defined, but because it carries the same interpretation as $\text{pdf}_R(\rho_{3\sigma})$, i.e., how much $p_{3\sigma}$ would be reduced with a small reduction in $\rho_{3\sigma}$. Clearly, when $h_{\mathbf{R}}(\rho)$ is strictly increasing in the neighborhood of $\rho_{3\sigma}$, it follows that $\text{pdf}_R(\rho_{3\sigma})$ exists and is equal to $\text{pdf}_R(\rho_{3\sigma}^-)$, so $\text{pdf}_R(\rho_{3\sigma}^-)$ could be used without loss of generality.

9.4 Methodology

9.4.1 99.73% minimum distance ($\rho_{3\sigma}$) – numerical computation methodology

The approach undertaken here for the numerical computation of $\rho_{3\sigma}$ is through nested numerical solution of ordinary differential equations (ODEs), as seen through the combination of Figures 9.1 and 9.2. This is accomplished by using MATLAB's `ode113` function, which is an ODE solver best suited for high accuracy numerical solution of non-stiff ODEs.[162]

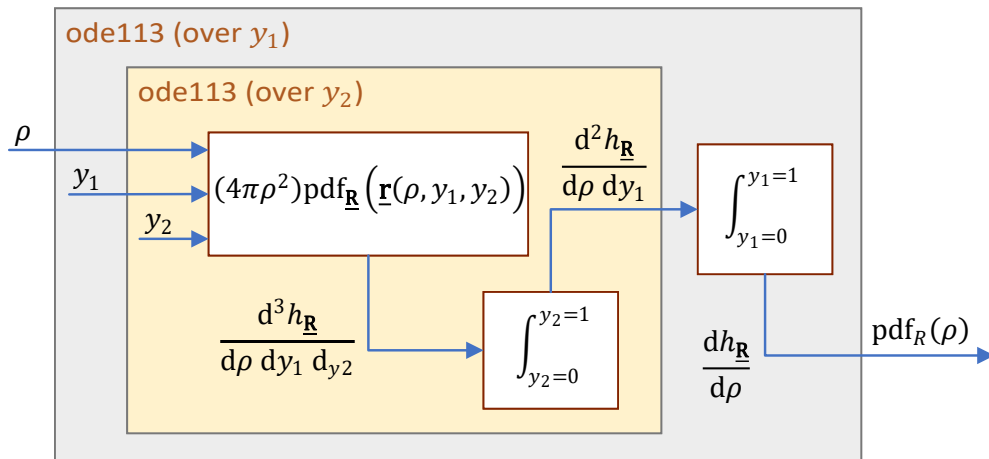


Figure 9.1: Numerical computation of the pdf of the Euclidean norm of the relative position using nested implementation of the `ode113` solver.

The notation of the `ode113` function, as well as for the other MATLAB ODE solvers, assumes that the variables to be integrated have computable time derivatives, and that it is the desire of the user to solve for the time histories of such variables over a closed interval of time. In the present paradigm, however, instead of integrating with respect to time, use of the `ode113` solver is adapted in order to integrate a function with respect to degrees of freedom that represent spatial coordinates.

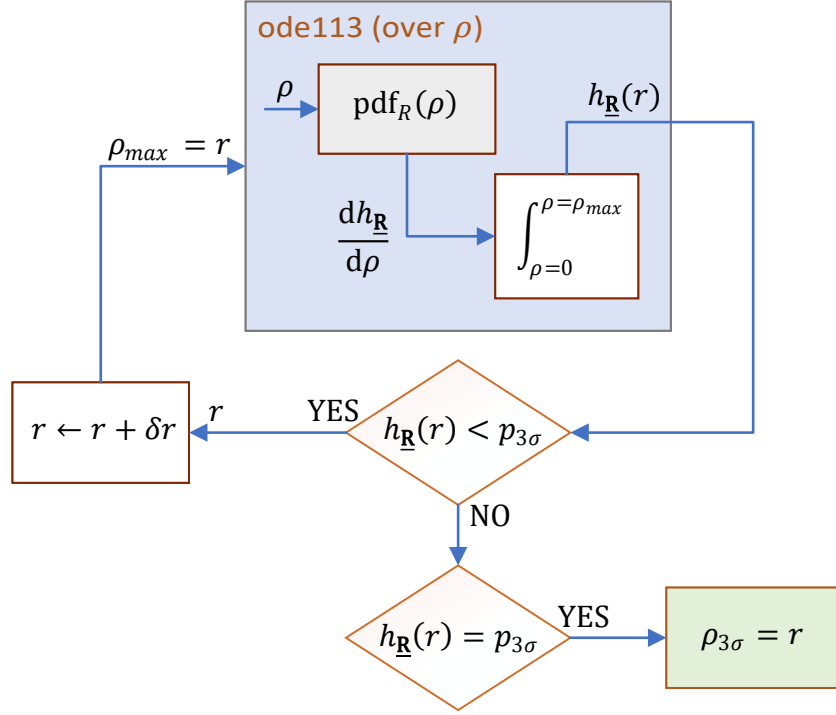


Figure 9.2: Numerical computation of radial probability measures and the 99.73% minimum distance ($\rho_{3\sigma}$) using nested implementation of the `ode113` solver.

It should be noted that y_1 and y_2 are the coordinates of the Lambert equal-area unit square parametrization of the unit 2-sphere. Then, as shown in Fig. 9.1, for a given $\rho \in (0, \infty)$, $\text{pdf}_R(\rho) = dh_{\mathbf{R}}/d\rho$ is computed through `ode113` as the integral of $d^2h_{\mathbf{R}}/d\rho dy_1$ over the sample space of Y_1 [i.e., $[0, 1]$], which, in turn, is computed through `ode113` as the integral of $d^3h_{\mathbf{R}}/d\rho dy_1 dy_2$ over the sample space of Y_2 (i.e., $[0, 1]$).

By definition, the definite integral of $\text{pdf}_R(\cdot)$ over the interval $[0, r]$ for $r \geq 0$ is the radial probability measure $h_{\mathbf{R}}(r)$. Hence, $\rho_{3\sigma}$ can be interpreted as the solution of the constrained optimization problem

$$\rho_{3\sigma} = \min_{r \in (0, \infty)} r \quad (9.35)$$

where $r \in (0, \infty)$ is subject to the integral equation constraint given by

$$p_{3\sigma} = \int_0^r \text{pdf}_R(\rho) d\rho =: h_{\mathbf{R}}(r) \quad (9.36)$$

However, because $h_{\mathbf{R}}(\cdot)$ is non-decreasing, numerical computation of $\rho_{3\sigma}$ can be accomplished as follows. First, a small value of $r \in (0, \infty)$ is chosen, and $h_{\mathbf{R}}(r)$ is computed. Second, if $h_{\mathbf{R}}(r) < p_{3\sigma}$, then r is increased until $h_{\mathbf{R}}(r^*) = p_{3\sigma}$, as posed in Eq. 9.36. When this condition is first met, the value of r^* will also satisfy the condition posed in Eq. 9.35; consequently, $\rho_{3\sigma} = r^*$ in this case. Hence, optimization is avoided by using the non-decreasing property of $h_{\mathbf{R}}(\cdot)$.

The foregoing methodology for the numerical computation of $\rho_{3\sigma}$ is implemented in the `ode113` solver (integrating over ρ coordinates, as seen in Fig. 9.2) through use of the `events` setting, which employs root-finding in order to check for one or multiple univariate equality constraints. In this case, the `events` setting is used to approximately identify the first r^* such that $h_{\mathbf{R}}(r^*) - p_{3\sigma} = 0$, and integration is stopped when this condition is first met. Overall, there are three levels of `ode113`-based numerical integration: the highest level (i.e., in ρ), the mid level (i.e., in y_1), and the lowest level (i.e., in y_2); additionally, the logic for solving for $\rho_{3\sigma}$ is implemented at the ρ -level.

9.4.2 99.73% minimum distance ($\rho_{3\sigma}$) – sample computation methodology

Given the statistical guarantees of crude MC estimators as previously discussed, such estimators may be used to construct approximations to univariate probability distributions via the empirical cdf; in turn, the empirical cdf may be used to formulate quantile estimators.[120] Therefore, Monte Carlo sampling is chosen for validating the foregoing `ode113`-based approach for numerical computation of $\rho_{3\sigma}$.

The methodology is illustrated in Fig. 9.3, and it begins by drawing a Monte Carlo of the relative position between two agents, \mathbf{R} , based on instantaneous statistics of the distribution. Subsequently, the Euclidean norm of each element in the sample is computed, which induces a MC sample of R ; this sample is then sorted, which yields the order statistics of the sample of R , i.e., $r_{(1)} \leq \dots \leq r_{(N)}$, where N is the sample size. Then, $\hat{\rho}_{3\sigma}$ is obtained through a linear interpolation estimator,[160] which is described as follows:

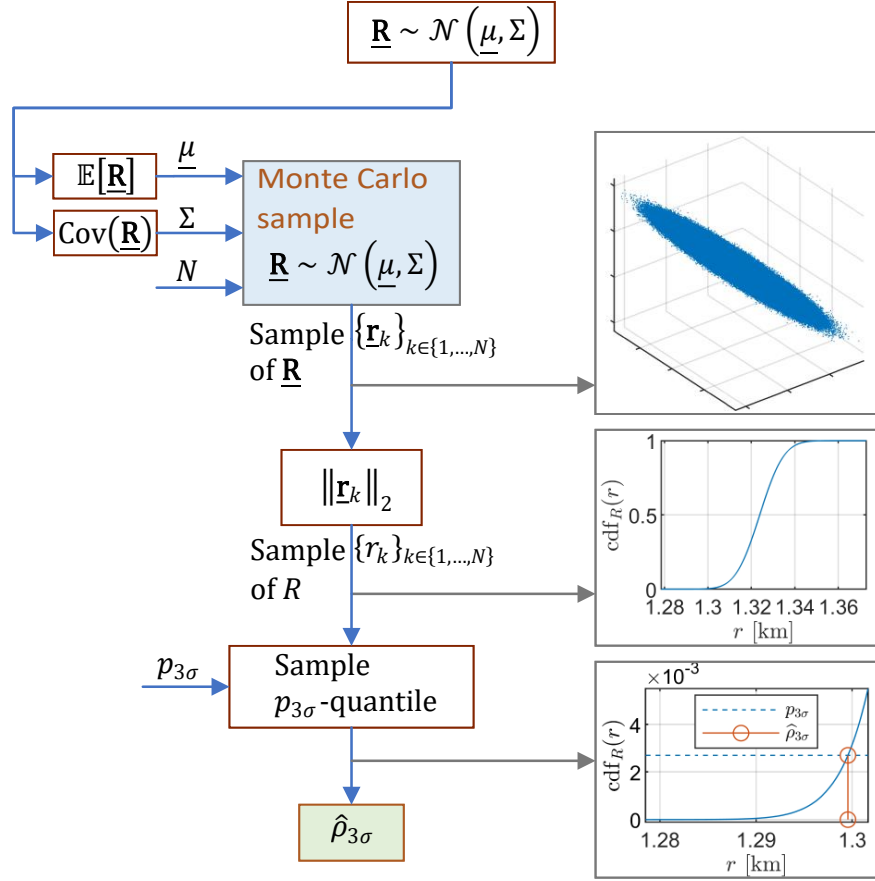


Figure 9.3: Sample computation of the 99.73% minimum distance ($\rho_{3\sigma}$) through Monte Carlo simulation based on instantaneous relative position statistics.

1. Compute $k = \lfloor (N - 1)p_{3\sigma} + 1 \rfloor$, where $\lfloor \cdot \rfloor$ is the floor operator.
2. Compute $\tau = ((N - 1)p_{3\sigma} + 1) - k$.
3. Obtain $\hat{\rho}_{3\sigma}$ as given by

$$\hat{\rho}_{3\sigma} = (1 - \tau)r_{(k)} + (\tau)r_{(k+1)} \quad (9.37)$$

In MATLAB, this sample quantile estimator is implemented through the `prctile` function.[163] It should be noted that, even though the notation of Fig. 9.3 assumes that the relative position has a multivariate normal distribution (whose samples can be drawn in MATLAB using the `mvnrnd` function [163]), the general process of quantile compu-

tation presented herein is applicable to Monte Carlo samples drawn from any absolutely continuous relative position distribution.

9.4.3 99.73% minimum distance ($\rho_{3\sigma}$) – derivative computation methodology

As previously stated, this Chapter aims to investigate the regularity of $\rho_{3\sigma}$, i.e., whether small changes of the defining parameter of $\rho_{3\sigma}$ (namely, $p_{3\sigma}$) result in commensurately small changes to $\rho_{3\sigma}$ itself. Such effective changes to $p_{3\sigma}$ would naturally arise from numerical errors in checking whether $h_{\mathbf{R}}(\rho_{3\sigma}) = p_{3\sigma}$. In particular, with some given initial uncertainty description, if such regularity were exhibited over extended time horizons, this would be helpful for the purposes of predicting the risk of future collisions via $\rho_{3\sigma}$, as it would give validity to $\rho_{3\sigma}$ over propagated horizons. Since the formulation of $\rho_{3\sigma}$ is instantaneous (i.e., it depends on the uncertainty at a single time t only), ascertaining $\rho_{3\sigma}(t)$ regularity over extended horizons entails the following basic steps: propagating relative state statistics to a given time, extracting relative position information, computing $\rho_{3\sigma}$, performing regularity calculations, and then repeating the process at a subsequent time.

The `ode113`-based $\rho_{3\sigma}$ computation methodology was developed so as to directly mimic the iterated integral formulation of $h_{\mathbf{R}}(\cdot)$ listed in Eq. 9.11, which itself follows directly from its definition through a coordinate transformation; hence, this methodology allows for estimates of $\rho_{3\sigma}$ that conceptually retain its interpretation. However, it is not feasible to implement this methodology accurately in practice over extended time horizons. For example, with a ρ -level step size of 1 m, and a $\rho_{3\sigma}$ of 1 km, the total spatial volume increase with each step size in the vicinity of $\rho_{3\sigma}$ is 1.26×10^7 times larger than 1 m^3 . Thus, unless the pdf of \mathbf{R} has zero mean and is spherically symmetric, capturing probability masses in such radial shells accurately requires increasingly small angular step sizes (in y_1 and y_2). The likelihood of round-off errors introduced to the computation, as well as the general computational expense, are exacerbated when increasingly small step sizes are needed for an acceptable resolution in $\rho_{3\sigma}$ itself – especially if, after extended

horizons, uncertainty diverges in some (but not all) directions (which does occur in CW dynamics with MVN prior distribution). However, in order to quantify the sensitivity of $\rho_{3\sigma}$ to small changes in $p_{3\sigma}$, which can be accomplished via $d\rho_{3\sigma}/dp_{3\sigma}$, Eq. 9.34 implies that $\rho_{3\sigma}$ must be first calculated, and then $\text{pdf}_R(\rho_{3\sigma})$ must be evaluated.

Therefore, in this Chapter, a hybrid approach is adopted for estimating $d\rho_{3\sigma}/dp_{3\sigma}$. First, $\rho_{3\sigma}$ is approximated through the crude MC estimator $\hat{\rho}_{3\sigma}$ as shown in Fig. 9.3; the validity of this assumption is explored in the Results and Discussion section. Second, the pdf of R is evaluated at $\hat{\rho}_{3\sigma}$ using the `ode113`-based approach shown in Fig. 9.1. Finally, $d\rho_{3\sigma}/dp_{3\sigma}$ is approximated as

$$\frac{d\rho_{3\sigma}}{dp_{3\sigma}} \approx \frac{1}{\text{pdf}_R(\hat{\rho}_{3\sigma})} \quad (9.38)$$

9.5 Results and discussion

9.5.1 Simulation parameters and CW dynamic cases

This Chapter focuses on Examples 3D.001–026, which are subject to CW dynamics, and which are described in Section A.2.

The choice of orbit altitude for these simulation cases ($\bar{a} = 6800$ km), and of initial relative state expectation and covariance parameters (see Tables A.2 and A.1, respectively), are driven by previous work, which suggests that, for those specific parameters, $\rho_{3\sigma}$ and the IPC (for a joint HBR $l_{i,j}$ of 32 m) are related to each other in a way that is consistent with intuition.[27, 28] That is, over a horizon of two orbit periods, $\rho_{3\sigma}$ indicates smallest separation while the IPC indicates highest collision risk, and the $\rho_{3\sigma}$ indicates largest separation while the IPC indicates lowest collision risk; this behavior is not consistently observed with other separation indicators studied. Hence, such parameters are used in order to validate the foregoing interpretation of $\rho_{3\sigma}$ as a true probabilistic risk boundary in relative position space.

Finally, the Monte Carlo sample size is chosen as 3.2×10^8 particles. For an MVN distribution, it is conjectured that such a sample size should be able to capture the probability of significant events where the significance threshold is set at 10^{-7} . [27, 28] Under this assumption, this sample size affords agreement of the $p_{3\sigma}$ -quantile of R to within approximately 4.4 significant digits in $p_{3\sigma}$.

9.5.2 99.73% minimum distance ($\rho_{3\sigma}$) – sample validation results

The first result in this Chapter, summarized in Figs. 9.4 and 9.5, demonstrates the agreement between numerical and sample approaches to the computation of $\rho_{3\sigma}$. Even though this is only corroborated for Example 3D.001, these results are representative of other examples as well because of their shared methodology.

For Example 3D.001, Fig. 9.4 shows that the numerical and sample $\rho_{3\sigma}$ waveforms agree to within 9.15 cm over 0.0729 chief orbit periods (or 6.78 minutes, which corresponds to 106 timesteps). At worst, the discrepancies observed represent no more than 0.0098% difference relative to the computed magnitude of $\rho_{3\sigma}$. Therefore, to within low discrepancy, the numerical and sample $\rho_{3\sigma}$ waveforms converge to each other over the restricted horizon $[0, t_c]$, where t_c denotes the cutoff propagation time for the numerical $\rho_{3\sigma}$ waveform. This kind of agreement is adequate for the computation of $\rho_{3\sigma}$ sensitivity, as effects on $d\rho_{3\sigma}/dp_{3\sigma}$ (from errors in $\rho_{3\sigma}$) are proportional to the derivative of pdf_R (i.e., a second derivative of probabilities in R , which is a higher order effect). It remains to be ascertained whether $\rho_{3\sigma}$ itself is estimated sufficiently accurately.

Definition 41 (Uniform norm (or sup-norm), and bounded continuous function spaces[34]).

Let X be a metric space. The uniform norm of a function $f : X \rightarrow \mathbb{R}$ is

$$\|f\|_u = \sup_{x \in X} |f(x)| \quad (9.39)$$

Let $C_b(X)$ denote the space of continuous, bounded, real-valued functions in X . That is,

$$C_b(X) = \{f : f : X \rightarrow \mathbb{R}, f \text{ is continuous, } \|f\|_{\text{u}} < \infty\} \quad \diamond \quad (9.40)$$

Let $C_b([0, 2P])$ denote the space of continuous and bounded functions (under the sup-norm) defined in the interval $[0, 2P]$, where P denotes the chief orbit period. Then, Figure 9.5 shows that $\hat{\rho}_{3\sigma} \in C_b([0, 2P])$. Since both numerical and sample approaches can be made arbitrarily accurate, it is possible to create sequences of $\rho_{3\sigma}$ waveform estimators that are Cauchy (i.e., sequences whose elements become arbitrarily close to one another). Since $C_b([0, 2P])$ is a complete function space (i.e., a space in which Cauchy sequences converge to an element of said space), [34, 66] the numerical and sample $\rho_{3\sigma}$ waveforms each converge to an element of $C_b([0, 2P])$, and since both methods converge to each other, it follows that both methods converge to the same function $f \in C_b([0, 2P])$ (which could be interpreted as the true $\rho_{3\sigma}$ waveform) — at least when limiting the domain to $[0, t_c]$. Within this restricted horizon, this establishes that the sample approach is representative of the numerical approach (so the former is an acceptable substitute for the latter), and that the sample approach converges to the true $\rho_{3\sigma}$. Given the general MC convergence guarantees aforementioned, it is concluded that the sample methodology is an acceptable estimator for $\rho_{3\sigma}$ over the full horizon $[0, 2P]$.

9.5.3 99.73% minimum distance ($\rho_{3\sigma}$) – sensitivity analysis results

For Example 3D.001, Figure 9.6 shows the time history of the derivative of $\rho_{3\sigma}$ with respect to its target probability $p_{3\sigma}$, $d\rho_{3\sigma}/dp_{3\sigma}$ (in units of [km/probability unit]), as approximated via Eq. 9.38, i.e., as computed via the hybrid numerical/sample approach described in the Methodology section. For this example, it is found that $d\rho_{3\sigma}/dp_{3\sigma}$ is continuous over time. Let $\delta p = 0.01\%$. If the target probability $p_{3\sigma}$ were to change by as much as δp (which would be a significant change since $\delta p/p_{3\sigma} \approx 3.7\%$), a first order estimate of the

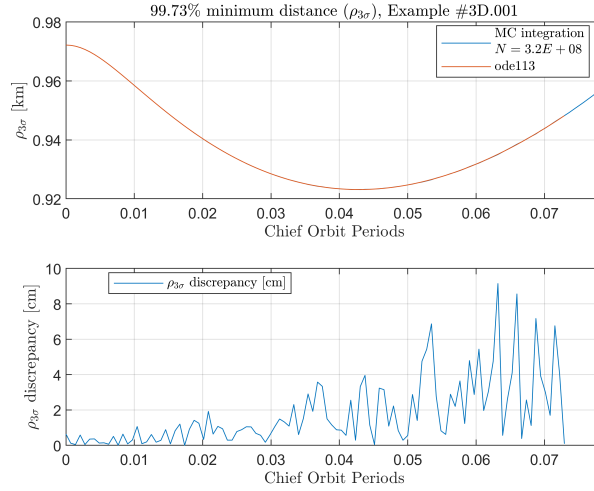


Figure 9.4: Example 3D.001, $\rho_{3\sigma}$ waveform results: (upper) numerical and sample results; (lower) absolute difference between numerical and sample results.

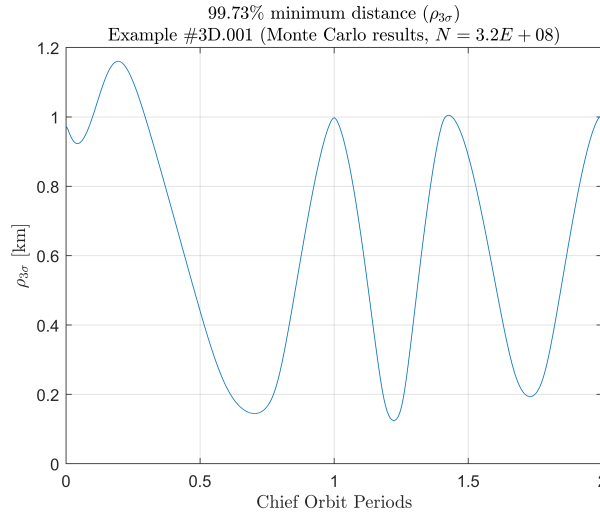


Figure 9.5: Example 3D.001, sample $\rho_{3\sigma}$ waveform results over full horizon.

corresponding change in $d\rho_{3\sigma}$, $\delta\rho_{3\sigma}$, would yield that $\delta\rho_{3\sigma} = 5.1$ m at worst over $[0, 2P]$. This is a small change compared to $\rho_{3\sigma}$, considering that $\rho_{3\sigma}$ is in the order of hundreds to thousands of meters over $[0, 2P]$.

For Example 3D.001, Figure 9.7 shows the first order approximation of the relative sensitivity of $\rho_{3\sigma}$ to a change δp in $p_{3\sigma}$; that is, it shows $\delta\rho_{3\sigma}/\rho_{3\sigma}$. For this example, it is found that a relative change in target probability of 3.7% causes, at worst, a change in $\rho_{3\sigma}$ of up to 1.88%. This shows that, within the confines of Example 3D.001, $\rho_{3\sigma}$ exhibits

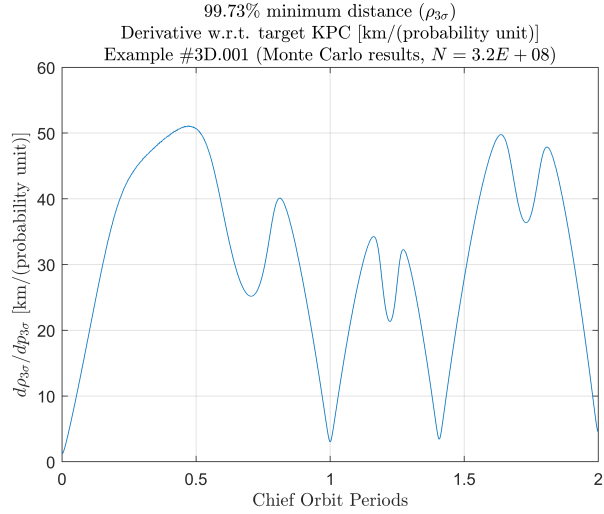


Figure 9.6: Example 3D.001, derivative of $\rho_{3\sigma}$ with respect to its target probability $p_{3\sigma}$, $d\rho_{3\sigma}/dp_{3\sigma}$, full horizon time-history.

regularity, i.e., small changes in $p_{3\sigma}$ also result in small changes to $\rho_{3\sigma}$.

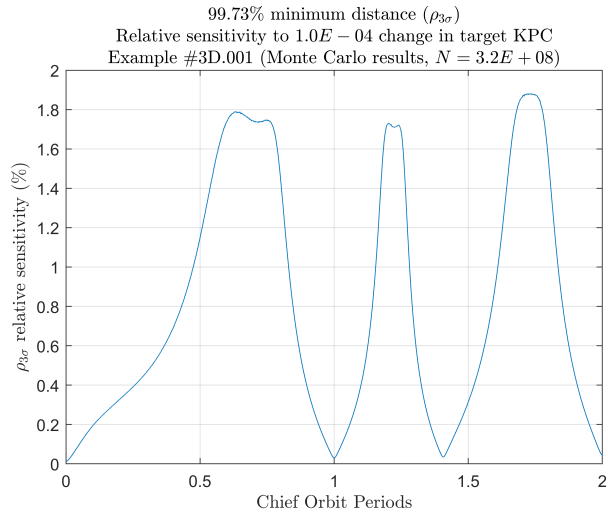


Figure 9.7: Example 3D.001, relative sensitivity of $\rho_{3\sigma}$ to a change $\delta p = 0.01\%$ in target probability $p_{3\sigma}$

The regularity of $\rho_{3\sigma}$ is observed more generally in other relative orbit regimes. As displayed in Figure 9.8, given a 3.7% variation in $p_{3\sigma}$, the maximum relative change in $\rho_{3\sigma}$ is less than 1.9% for relative orbits with no cross-track motion (Example 3D.001), with along-track and cross-track motion in phase (Example 3D.002), and with along-track and cross-track motion out of phase (Examples 3D.003–026).

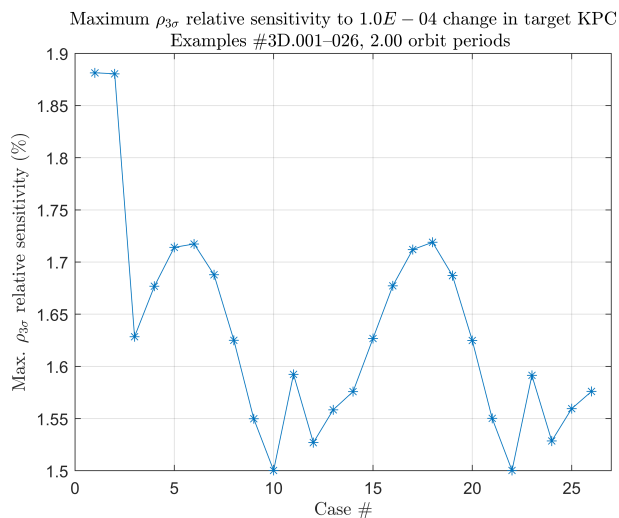


Figure 9.8: Examples 3D.001-026, maximum relative sensitivity of $\rho_{3\sigma}$ to a change $\delta p = 0.01\%$ in target probability $p_{3\sigma}$.

Whether these relative (and actual) sensitivities are acceptable depends on the specific operational scenario at hand. For example, for a minimum $\rho_{3\sigma}$ of 125 m, in a scenario where the tolerance for instantaneous collision risk is $p_{3\sigma}$ and the inter-spacecraft keep-out distance (i.e., joint HBR) is 50 m, a 5.1 m error in the $\rho_{3\sigma}$ estimate would not be problematic, but it would be for a keep-out distance of 120 m. Rather, these results imply that, to within commensurate tolerances, it is valid to interpret $\rho_{3\sigma}$ as a probabilistic risk boundary in the first place, with the understanding that errors in its computation must be accounted for in practice.

These results demonstrate that, for the dynamic examples considered in this Chapter, that $\rho_{3\sigma}$ is regular with respect to $p_{3\sigma}$, i.e., small changes in $p_{3\sigma}$ cause small changes in $\rho_{3\sigma}$. This validates the interpretation of $\rho_{3\sigma}$ as a probabilistic risk boundary in relative position space under the assumptions made (CW dynamics, and the specific relative state uncertainties chosen). Considering that the 1- σ error rms (in the relative position) grows to as much as over 25 km over the propagation horizon considered (for all cases, since they have the same relative state covariance), the regularity displayed by $\rho_{3\sigma}$ is especially noteworthy.

9.6 Conclusion

In this Chapter, when the relative position between two objects is a random variable, the Euclidean norm of the relative position is characterized as a univariate random variable in its own right. The 99.73% minimum distance, or $\rho_{3\sigma}$, is interpreted as the $p_{3\sigma}$ -quantile of the distribution of the Euclidean norm of relative position, where $p_{3\sigma}$ is a constant with approximate value of 0.27%. It has been proposed that $\rho_{3\sigma}$ should be interpreted as a probabilistic collision risk boundary in relative position space in the sense that, for actual, isotropic keep-out zones smaller than $\rho_{3\sigma}$, the instantaneous probability of collision (IPC) between two objects is less than $p_{3\sigma}$, and for isotropic keep-out zones larger than $\rho_{3\sigma}$, the IPC is less than $p_{3\sigma}$. Under the assumption of Clohessy-Wiltshire (CW) dynamics over several regimes of relative orbits in Low-Earth Orbit, it is found that $\rho_{3\sigma}$ exhibits regularity with respect to $p_{3\sigma}$. That is, small changes in $p_{3\sigma}$ produce changes in $\rho_{3\sigma}$ that are commensurately small as well. Therefore, under these assumptions, the regularity of $\rho_{3\sigma}$ validates the aforementioned interpretation of $\rho_{3\sigma}$ as a probabilistic collision risk boundary in relative position space.

These findings motivate further exploration of the $\rho_{3\sigma}$ construct. It would be helpful to establish whether $\rho_{3\sigma}$ exhibits similar regularity under different relative orbit representations (e.g., relative orbit elements), under different dynamic models (e.g., including higher order gravity effects, as well as atmospheric drag), and under different assumptions regarding the nature of the uncertainty (e.g., non-normality of relative state distributions). If $\rho_{3\sigma}$ exhibits regularity under more general conditions such as those listed, the foregoing interpretation of $\rho_{3\sigma}$ would also hold in such conditions, which would afford greater applicability to this construct. Additionally, utilizing $\rho_{3\sigma}$ as a constraint in chance-constrained optimal control problems should be explored in the context of applications to spacecraft formation station-keeping and collision avoidance.

CHAPTER 10
CYLINDRICAL ORTHOGONAL NORM-BASED STOCHASTIC COLLISION
RISK MEASURES IN SPACECRAFT FORMATION FLYING

The cylindrical orthogonal collision region (COCR) is introduced for the approximate satisfaction of spherical, three-dimensional avoidance constraints (S3ACs) used in spacecraft formation flying (SFF). The COCR construct affords safety sufficiency and reduced constraint satisfaction conservatism over other commonly employed regions, while it may allow for improved efficiency of collision-safe trajectory computation. The COCR is deterministically well-defined; instantaneous and joint-time stochastic measures of collision risk based on the COCR are well-defined and computable; probabilistic collision risk conservatism introduced by the COCR is characterized as consistent with volumetric conservatism. These results, which are validated computationally in pertinent relative orbital cases, demonstrate the feasibility of SFF collision risk management applications which perform COCR-based S3AC satisfaction.

10.1 Introduction

Because collision risk management (COLRM) relates to the survivability and continued operation of spacecraft formation missions, COLRM is a requirement for the success of any spacecraft formation flying (SFF) mission. The process of SFF COLRM consists of the following steps: collision risk quantification, collision risk interpretation and decision-

making, and collision risk reduction. This process depends on both the choice and efficient computation of suitable collision risk indicators.[12] The formulation of SFF collision risk indicators depends on two factors: the operational definition of collision events (ODCE), and state uncertainty. First, the choice of ODCE is reflective of: *i*) how collision events are physically understood, and *ii*) simplifying assumptions that help make tractable the task of determining whether a collision event takes place. Second, SFF collision risk indicators account for both the ODCE and state uncertainty in order to provide a picture of the risk of occurrence of collision events (as understood operationally).[38]

In this Chapter, collision events between any two agents within a spacecraft formation are defined as the violation of a minimum distance constraint with respect to the Euclidean norm. That is, each agent is approximated by a Euclidean ball [a solid spherical ball in three dimensions (3D); a solidly filled circular region in two dimensions (2D)] with radius set to the agent's hard-body radius (HBR), and collision events are defined as the non-empty intersection of such circumscribing balls.[27, 28, 38] The spherical-HBR collision event paradigm is commonly employed in the spaceflight mechanics community, both from the perspective of stochastic collision risk estimation,[32, 56, 24, 31] and in collision avoidance tasks – both directly,[57, 49, 151, 51, 146] and with adjustments pertaining to the in-plane 2:1 ellipse geometry which arises from linearizing spacecraft relative motion.[53, 152, 164] The spherical-HBR assumption is understood not only to allow for a formulation of collision events that is relative attitude- and relative geometry-abstract,[24] but also to provide a phenomenological justification for this abstraction – namely, by observing the isotropic (specifically, the rotation invariant) nature of the Euclidean norm.[65] In the context of relative attitude-abstract COLRM formulations, collision regions other than those induced by the spherical-HBR assumption are thus regarded as conservative approximations of (and hence, supersets of) “true”, spherical collision regions. Employing such alternate collision regions may be considered advantageous to the extent that they may simplify maneuver planning and constraint satisfaction verification.

In the context of the constrained spacecraft relative trajectory planning problem, complying with spherical-HBR 3D avoidance constraints (S3ACs) is challenging because the corresponding relative state constraints to be satisfied are nonlinear and nonconvex.[165, 152] Generally, indirect solutions to this kind of problem are highly sensitive to initial guesses, and direct solutions via nonlinear programming (NLP) are not guaranteed to exist, and even if they do, it is not possible to know a priori whether computing such solutions may be accomplished in finite time.[166] Approaches based on mixed-integer linear programming (MILP),[39] which satisfy linearizations of the original nonlinear constraints in an OR-logic manner (that is, satisfying at least one constraint a time) may be considered for the purpose of approximating the 3D spherical collision region.[152] However, 3D spherical collision regions are not amenable in principle to being avoided exactly via MILP because, for every point on the boundary of these regions, there exists a distinct constraint corresponding to a tangential plane which locally separates the safe region from the avoidance region, therefore resulting in an uncountable number of relative state-space hyperplane constraints to be satisfied for every timestep. Even when only a finite number of constraints is allowed for S3AC satisfaction via MILP, doing so while achieving any reasonable degree of accuracy requires a prohibitively large number of auxiliary decision variables,[164] rendering such an application impractical. Other approaches seek to reduce the number of constraints to exactly one linear constraint at a time;[152] such approaches rely on restrictive assumptions about the physics of the problem and of the solution itself, as well as on trial and error,[164] so approaches like this are often not practical or applicable in a general sense.

Hence, several methodologies for solving the relative trajectory planning problem aim to achieve S3AC satisfaction approximately for the purpose of reducing the dimensionality of the problem for computational efficiency while also retaining the sufficiency of safety conditions, which inherently introduces conservatism to the constraint satisfaction criteria. Such methodologies include, among others: methods based on direct linearization,

also known as sequential convexification;[167, 164, 168] model predictive control (MPC) frameworks, which may handle spherical constraints via rotating hyperplanes,[169, 170, 171] or dual hyperplanes;[172, 173] and artificial potential function-based control frameworks.[174, 175, 176, 177, 178] These methodologies are not mutually exclusive; for example, certain MPC frameworks are applied in tandem with direct linearization.[165, 179, 40, 180, 181] Therefore, the literature in spacecraft relative trajectory planning indicates, on the one hand, a goal to satisfy spherical collision avoidance constraints as closely as possible, and on the other hand, acceptance of approximate constraint satisfaction – as long as the safety of ensuing solutions is not compromised, and to the extent that the corresponding computational efficiency is enhanced.

This Chapter is motivated by the abundance of sources in the literature that advocate for achieving 3D collision safety by meeting a 2D circular collision constraint on a planar projection of 3D relative motion. Such methods entail avoiding a solidly filled circular region in the relative orbital coordinate planes – specifically, in the in-plane (i.e., the radial/along-track plane),[13, 182, 58, 53, 59] or in the cross-plane (i.e., the radial/cross-track plane),[140, 60, 61, 62] or in the sky-plane (i.e., the along-track/cross-track plane).[63] Parameterizations of relative orbital motion via geometric parameters, or via relative orbital elements, are often employed to derive initial solution guesses for correction maneuvers semi-analytically, and the resulting collision avoidance frameworks are attractive because: 1) if effective, these 2D methods ensure sufficient 3D collision safety; and 2) generally, to satisfy two-dimensional constraints only is a less computationally taxing task than satisfying constraints that are inherently three-dimensional. However, because 2D circular collision regions correspond to 3D infinite cylindrical regions, instantaneous probabilities of collision based on planar (2D) projections of relative motion are always overestimates over instantaneous probabilities of collision based on full 3D geometries.[27, 28] This fact on instantaneous stochastic collision risk analysis has consequential implications for the lifetime of spacecraft formation missions – namely, that implementing 2D collision risk

management frameworks based on the satisfaction of a single circular keep-out constraint may cause unnecessary maneuvers and a reduction in mission lifetime without resulting in additional overall safety guarantees (e.g., the minimum inter-agent distance is not guaranteed to improve).

The goal of this research is to motivate the relaxation of two-dimensional circular constraint satisfaction on coordinate planes of some reference frame (i.e., the XY, XZ, and YZ planes of such a frame), specifically, by putting these constraints together via an inclusive-OR logic – that is, by satisfying at least one of these three constraints at any one time. In other words, this Chapter seeks to incentivize achieving S3AC satisfaction by defining three cylinders in mutually orthogonal planes, and instead of choosing to avoid a specific cylinder, to evade at least one of them. The potential benefit of implementing such a cylindrical orthogonal collision region in the context of a SFF COLRM framework is twofold: first, the proposed practice may allow for taking advantage of existing methods of approximate S3AC satisfaction (specifically, those that flow from solutions that evade 2D circles) in order to ease computational cost; and second, the prospective method may enable combining these approximate, 2D circle-avoiding solutions in a way that would reduce S3AC satisfaction conservatism.

This Chapter encourages the implementation of a cylindrical orthogonal collision risk management framework by addressing concerns regarding the feasibility of such an application which immediately arise from the construction of the cylindrical orthogonal collision region (COCR). Such concerns may be grouped into three categories: basic region properties, well-definedness and computability of risk measures, and quantitative properties of risk measures. First, is the COCR well defined? What are the properties of COCR and cylindrical orthogonal-like spaces? Is there any quantitative advantage gained by encoding collision safety via the COCR? Second, from the perspective of collision risk management, are stochastic measures of collision risk defined, either instantaneously or over time periods? If defined, are these measures computable in a practical sense? Third, if these

measures are defined and computable, how do they quantitatively compare to other measures utilized in the literature, both theoretically and computationally? Favorable answers to these questions justify practical implementation of a collision risk management framework based on the COCR.

This Chapter is organized as follows. First, the cylindrical orthogonal norm (c.o.-norm) is defined in three-dimensional Euclidean space. The COCR is characterized as a ball with respect to the c.o.-norm, which demonstrates the measurability of the COCR. This fact, in turn, is used to establish that the COCR is well defined, and to compare the COCR volumetrically to other collision regions advocated in the literature, showing a close relationship to a spherical 3D collision region. Second, sufficient conditions are stated such that joint-time collision probabilities (defined with respect to the COCR) are: 1) well defined, and 2) practically computable. The applicability of the corresponding assumptions in the context of spaceflight mechanics is discussed. Third, quantitative results pertaining stochastic collision risk measures, such as event inclusion relationships and probability value inequalities, are presented. Fourth, the theoretical results asserted are validated through large sample Monte Carlo simulation. Together, these contributions demonstrate that the cylindrical orthogonal collision region is an effective building block in the development of SFF COLRM frameworks.

As a point of clarification, this Chapter of the dissertation does not advocate for replacing Euclidean balls as the primary method in spaceflight mechanics for encoding collision regions in relative position space. Rather, under the premise that it is computationally advantageous to compute collision safe trajectories that satisfy three mutually orthogonal planar circular collision constraints, this Chapter examines the region that is guaranteed to be avoided if such avoidance constraints are met (i.e., the COCR). Then, this Chapter motivates future collision avoidance work which may hinge on the avoidance of three mutually orthogonal planar circular collision constraints on the basis of the close volumetric agreement between Euclidean-ball-based collision regions and the COCR (and consequently,

the close agreement between the corresponding stochastic collision risk measures that arise from these collision regions).

10.2 Background

The Notation and Nomenclature used in this Chapter, as well as the deterministic definition of collision events (derived from relative-attitude abstraction, and induced by arbitrary a -norm balls in relative position space), and the definition of stochastic collision risk measures (in both joint-time and instantaneous senses), are addressed in Chapter 2.

10.3 Theory

The theoretical contributions of this Chapter to SFF COLRM include the following. First, general results concerning stochastic collision risk measures (where collision events are defined through balls with respect to some a -norm in $\mathbb{R}^{d_{\mathbb{R}}}$) are presented. First, conceptual results concerning the formulation, interpretation, and usability of cylindrical orthogonal collision regions in an SFF COLRM context are listed. General results concerning stochastic collision risk measures (where collision events are defined through balls with respect to some a -norm in $\mathbb{R}^{d_{\mathbb{R}}}$), which are found in Chapter 4, are leveraged in order to ascertain the well-definedness and usability of COCR-based stochastic collision risk measures. Second, quantitative results on the linear and volumetric conservatism of cylindrical orthogonal collision regions, including bounds for stochastic collision risk measures based on such regions, are reported.

10.3.1 Cylindrical Orthogonal (c.o.) collision safety – conceptual results

Here, the cylindrical orthogonal collision region is motivated and constructed. Subsequently, the cylindrical orthogonal vector norm is defined, and a connection is made between cylindrical orthogonal collision regions and open balls with respect to the cylindrical orthogonal vector norm; implications of this connection are also discussed. Note: the

remainder of this Chapter is concerned with collision events in three-dimensional relative position space only; that is, henceforth, $d_{\mathbf{R}} = 3$.

10.3.1.1 Cylindrical-orthogonal collision region (COCR) construction

Let $\widetilde{W} \in \{XY, XZ, YZ\}$. Consider the sets

$$A_{XY} = \left\{ [x, y, z]^T \in \mathbb{R}^3 : \sqrt{x^2 + y^2} \geq l_{i,j} \right\} \quad (10.1)$$

$$A_{XZ} = \left\{ [x, y, z]^T \in \mathbb{R}^3 : \sqrt{x^2 + z^2} \geq l_{i,j} \right\} \quad (10.2)$$

$$A_{YZ} = \left\{ [x, y, z]^T \in \mathbb{R}^3 : \sqrt{y^2 + z^2} \geq l_{i,j} \right\} \quad (10.3)$$

Then, the $A_{\widetilde{W}}$ set encodes the collision safe and marginally-safe regions in \mathbb{R}^3 that correspond to a 2D circular constraint on the \widetilde{W} -plane projection of points in \mathbb{R}^3 . It follows that any point $\mathbf{r} = [x, y, z]^T$ belonging to any of these three sets automatically satisfies an S3AC at least marginally, because meeting any of the conditions i) $\sqrt{x^2 + y^2} \geq l_{i,j}(t)$, ii) $\sqrt{x^2 + z^2} \geq l_{i,j}(t)$, or iii) $\sqrt{y^2 + z^2} \geq l_{i,j}(t)$, implies that $\|\mathbf{r}\|_2 = \sqrt{x^2 + y^2 + z^2} \geq l_{i,j}(t)$. Consider the set

$$A_{\text{co}} = [A_{XY} \cup A_{XZ} \cup A_{YZ}]^C \quad (10.4)$$

Therefore, the A_{co} set is the region (in relative position space) which is avoided when at least one of the three sufficient collision safety conditions encoded by $A_{\widetilde{W}}$ is met. Conversely, noting that

$$A_{\text{co}} = [A_{XY}]^C \cap [A_{XZ}]^C \cap [A_{YZ}]^C \quad (10.5)$$

it follows that A_{co} is the region in \mathbb{R}^3 where there is a simultaneous violation of all three safety criteria encoded by $A_{\widetilde{W}}$. Therefore, the A_{co} may be interpreted as a cylindrical orthogonal collision region (COCR).

Let $\mathbf{r} \in 2\text{-UNSAFE}_{i,j}(t) = \mathbb{B}_{l_{i,j}(t)}^{3|2}(\mathbf{0}_{3 \times 1})$. Hence, $\|\mathbf{r}\|_2 = \sqrt{x^2 + y^2 + z^2} < l_{i,j}(t)$. It

follows that

$$\sqrt{x^2 + y^2} < l_{i,j}(t) \quad \wedge \quad \sqrt{x^2 + z^2} < l_{i,j}(t) \quad \wedge \quad \sqrt{y^2 + z^2} < l_{i,j}(t) \quad (10.6)$$

which, in turn, implies that $\mathbf{r} \in A_{\text{co}}$. Hence, A_{co} encodes a conservative approximation to S3AC violation. Figure 10.1 shows the construction of the A_{co} set.

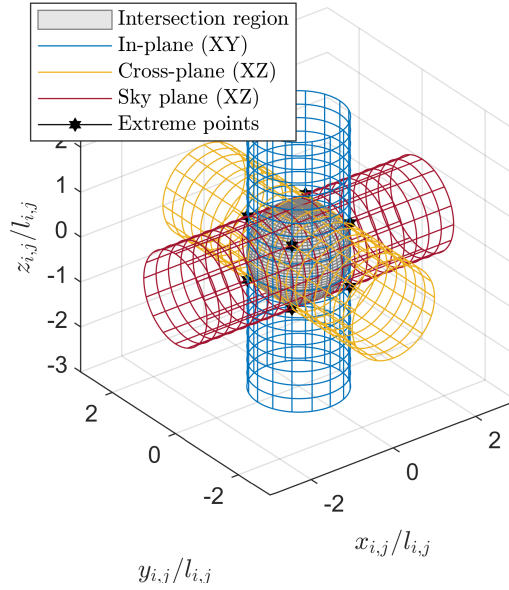


Figure 10.1: Construction of the cylindrical orthogonal collision region (COCR; i.e., the A_{co} set) in \mathbb{R}^3 .

10.3.1.2 Cylindrical-orthogonal (c.o.) vector norm – definition and basic properties

Definition 42 introduces the cylindrical orthogonal norm (c.o.-norm) in \mathbb{R}^3 , which may be understood as the maximum two-dimensional Euclidean vector norm as perceived in any of the coordinate planes in whatever implicit, underlying reference frame is assumed. Proposition 43 establishes the norm properties of the c.o.-norm. Note: the symbol for the c.o.-norm is $a = \text{co}$.

Definition 42 (Cylindrical orthogonal norm). For $\mathbf{r} = [x, y, z]^T \in \mathbb{R}^3$, the cylindrical

orthogonal vector norm, denoted by $\|\cdot\|_{\text{co}}$, is defined as

$$\|\underline{\mathbf{r}}\|_{\text{co}} = \max \left\{ \sqrt{x^2 + y^2}, \sqrt{x^2 + z^2}, \sqrt{y^2 + z^2} \right\} \quad \diamond \quad (10.7)$$

Proposition 43 (Norm properties of cylindrical orthogonal norm). The cylindrical orthogonal norm, $\|\cdot\|_{\text{co}}$, is a norm in \mathbb{R}^3 . That is, for all $\underline{\mathbf{x}}, \underline{\mathbf{y}}$ in \mathbb{R}^3 and for all scalars c , the following properties hold:

1. Nonnegativity: $0 \leq \|\underline{\mathbf{x}}\|_{\text{co}} < \infty$
2. Homogeneity: $\|c\underline{\mathbf{x}}\|_{\text{co}} = |c| \|\underline{\mathbf{x}}\|_{\text{co}}$
3. The Triangle Inequality: $\|\underline{\mathbf{x}} + \underline{\mathbf{y}}\|_{\text{co}} \leq \|\underline{\mathbf{x}}\|_{\text{co}} + \|\underline{\mathbf{y}}\|_{\text{co}}$
4. Uniqueness: $\|\underline{\mathbf{x}}\|_{\text{co}} = 0$ if and only if $\underline{\mathbf{x}} = \underline{\mathbf{0}}_{3 \times 1}$ ◇

Proof. Omitted. □

Fact 44 reflects a helpful observation: that the COCR has an underlying norm structure with respect to the c.o.-norm, as illustrated in Figure 10.2.

Fact 44. The cylindrical orthogonal collision region (COCR), denoted by A_{co} , is an open ball with respect to the cylindrical orthogonal vector norm, specifically, as given by

$$A_{\text{co}} = \mathbb{B}_{l_{i,j}(t)}^{3|\text{co}}(\underline{\mathbf{0}}_{3 \times 1}) \quad \diamond \quad (10.8)$$

Proof. Let $\underline{\mathbf{r}} = [x, y, z]^T \in A_{\text{co}}$. Then,

$$\sqrt{x^2 + y^2} < l_{i,j}(t) \quad \bigwedge \quad \sqrt{x^2 + z^2} < l_{i,j}(t) \quad \bigwedge \quad \sqrt{y^2 + z^2} < l_{i,j}(t) \quad (10.9)$$

By properties of the supremum operator, $\|\underline{\mathbf{r}}\|_{\text{co}}$ satisfies

$$\|\underline{\mathbf{r}}\|_{\text{co}} = \max \left\{ \sqrt{x^2 + y^2}, \sqrt{x^2 + z^2}, \sqrt{y^2 + z^2} \right\} < l_{i,j}(t) \quad (10.10)$$

Hence, $A_{\text{co}} \subseteq \mathbb{B}_{l_{i,j}(t)}^{3|\text{co}}(\mathbf{0}_{3 \times 1})$. To show the converse, assume $\mathbf{r} = [x, y, z]^T \in \mathbb{B}_{l_{i,j}(t)}^{3|\text{co}}(\mathbf{0}_{3 \times 1})$. Then, Eq. 10.10 holds, which implies Eq. 10.9. Therefore, $\mathbb{B}_{l_{i,j}(t)}^{3|\text{co}}(\mathbf{0}_{3 \times 1}) \subseteq A_{\text{co}}$. \square

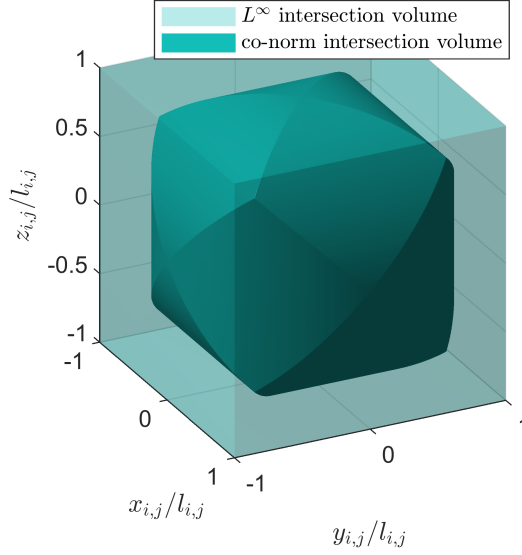


Figure 10.2: Comparison between instantaneous collision regions based on cylindrical-orthogonal and L^∞ norms.

Fact 44 also implies that the following instantaneous collision set entities refer to the one and the same region:

$$A_{\text{co}} = \text{co-UNSAFE}_{i,j}(t) = V_{i,j}(t; l_{i,j}(t), \text{co}) = \mathbb{B}_{l_{i,j}(t)}^{3|\text{co}}(\mathbf{0}_{3 \times 1}) \quad (10.11)$$

Proposition 45 establishes the topological properties of three-dimensional Euclidean space via sets that are open with respect to the c.o.-norm.

Proposition 45 (Openness of c.o.-open sets). A set $A \subseteq \mathbb{R}^3$ is open (with respect to the c.o.-norm) if and only if A is open. In particular, let $\mathbf{r} \in \mathbb{R}^3$, $c > 0$. Then, the open ball (with respect to the c.o.-norm) centered at \mathbf{r} with radius c , denoted by $\mathbb{B}_c^{3|\text{co}}(\mathbf{r})$, is an open set in \mathbb{R}^3 . \diamond

Proof. The $\|\cdot\|_{\text{co}}$ and $\|\cdot\|_2$ norms are both norms in \mathbb{R}^3 ; therefore, they are equivalent.[66] Hence, a set $A \subseteq \mathbb{R}^3$ is open with respect to the $\|\cdot\|_{\text{co}}$ norm if and only if A is open with

respect to the $\|\cdot\|_2$ norm,[66] upon which the underlying topology of \mathbb{R}^3 is assumed to be constructed. In particular, by definition, $\mathbb{B}_c^{3|\text{co}}(\mathbf{r})$ is an open set with respect to the $\|\cdot\|_{\text{co}}$ norm. □

The norm structure of the COCR (specifically, its equivalence to an open ball with respect to some norm) is significant because of what it indicates about its suitability in an SFF COLRM context.

Remark 46 (Practical implications of COCR openness). As per Proposition 45 and Eq. 10.11, the COCR is an open set. This fact has many implications, some of which are:

(1) Basic implications

(1.a) The COCR is a measurable subset in \mathbb{R}^3 . That is, $A_{\text{co}} \in \mathcal{L}(\mathbb{R}^3)$ – see Subsection 2.3.

(1.b) Because the COCR is measurable, a volume can be assigned to it – specifically, via its Lebesgue measure in \mathbb{R}^3 .

(2) Deterministic SFF COLRM

(2.a) Because the COCR is an open ball (with respect to some norm in \mathbb{R}^3), it follows that the COCR is a convex set in \mathbb{R}^3 .

(2.b) Because the COCR is convex, avoiding it poses a non-convex constraint in \mathbb{R}^3 . Hence, the avoidance constraint induced by the COCR is, in principle, no different than avoiding any region defined through other norms advocated in the literature, such as the box or spherical collision regions.

(3) Stochastic SFF COLRM

(3.a) Because the COCR is measurable, IPC measures in \mathbb{R}^3 based on the COCR are automatically defined.

(3.b) Because the c.o.-norm is a norm in \mathbb{R}^3 , Propositions 17 and 18 imply, under some reasonable assumptions, that P_c measures (in initial relative state space) based on the COCR are well-defined and computable. \diamond

Hence, per Remark 46, the c.o.-norm construct is, in principle, a helpful candidate for SFF COLRM applications because it may be employed to describe three-dimensional regions which correspond to sufficient conditions for collision safety. Additionally, with respect to c.o.-norm-based regions, it is meaningful: a) to compute trajectories that are collision-safe, and b) to quantify stochastic measures of collision risk.

10.3.2 Cylindrical Orthogonal (c.o.) collision safety – quantitative results

This Chapter presents the following quantitative results pertaining to COCR-based set and measure entities. First, norm equivalence between the c.o.-norm and the Euclidean and box norms is used to ascertain of linear and volumetric conservatism that the COCR introduces. Second, upper and lower bounds for probability measures based on c.o.-balls are listed with application to IPC values based on the COCR. Third, set inclusion relationships for the COCR-based JTC set, as well as upper and lower bounds for the COCR-based P_c measure, are presented.

10.3.2.1 Spherical and box collision regions vs. COCR – linear and volumetric comparison

This subsection compares, linearly and volumetrically, the COCR to spherical and box collision regions which are commonly employed in the literature in the context of SFF COLRM applications.

Proposition 47 quantifies equivalence constants between the c.o.-norm and the L^2 and L^∞ norms in the sense of Eq. 2.11. Hence, for points in \mathbb{R}^3 , this result indicates lower and upper bounds for their c.o.-norm values in terms of their L^2 and L^∞ norms.

Proposition 47 (Equivalence between c.o.-norm and the L^2 and L^∞ norms). Since the $\|\cdot\|_{\text{co}}$, $\|\cdot\|_2$, and $\|\cdot\|_\infty$ norms are norms in \mathbb{R}^3 , they are equivalent.[66] In particular, for every $\underline{\mathbf{r}}$ in \mathbb{R}^3 ,

1. $0 \leq \left(\sqrt{\frac{2}{3}}\right) \|\underline{\mathbf{r}}\|_2 \leq \|\underline{\mathbf{r}}\|_{\text{co}} \leq \|\underline{\mathbf{r}}\|_2 < \infty$
2. $0 \leq \|\underline{\mathbf{r}}\|_\infty \leq \|\underline{\mathbf{r}}\|_{\text{co}} \leq (\sqrt{2}) \|\underline{\mathbf{r}}\|_\infty < \infty$

These equivalence constants are optimal. That is, for every $\varepsilon > 0$,

3. There exists $\underline{\mathbf{r}}$ in \mathbb{R}^3 such that $\left(\sqrt{\frac{2}{3}} + \varepsilon\right) \|\underline{\mathbf{r}}\|_2 > \|\underline{\mathbf{r}}\|_{\text{co}}$
4. There exists $\underline{\mathbf{r}}$ in \mathbb{R}^3 such that $(1 + \varepsilon) \|\underline{\mathbf{r}}\|_{\text{co}} > \|\underline{\mathbf{r}}\|_2$
5. There exists $\underline{\mathbf{r}}$ in \mathbb{R}^3 such that $(1 + \varepsilon) \|\underline{\mathbf{r}}\|_\infty > \|\underline{\mathbf{r}}\|_{\text{co}}$
6. There exists $\underline{\mathbf{r}}$ in \mathbb{R}^3 such that $(1 + \varepsilon) \|\underline{\mathbf{r}}\|_{\text{co}} > (\sqrt{2}) \|\underline{\mathbf{r}}\|_\infty$ ◇

Proof. 1.-2. Omitted.

3. Consider $\underline{\mathbf{r}} = \left[\frac{1}{\sqrt{2}}, \frac{1}{\sqrt{2}}, \frac{1}{\sqrt{2}}\right]^T$
4. Consider $\underline{\mathbf{r}} = \left[\frac{1}{\sqrt{2}}, \frac{1}{\sqrt{2}}, 0\right]^T$
5. Consider $\underline{\mathbf{r}} = [1, 0, 0]^T$
6. Consider $\underline{\mathbf{r}} = \left[\frac{1}{\sqrt{2}}, \frac{1}{\sqrt{2}}, \frac{1}{\sqrt{2}}\right]^T$ □

Next, Lemma 48 lists an intermediate result which employs norm equivalence relationships in order to simplify proving inclusion/exclusion relationships between balls defined through any two different norms in \mathbb{R}^s .

Lemma 48 (*a-b ball exclusion*). Let $\|\cdot\|_a$ and $\|\cdot\|_b$ be norms in \mathbb{R}^s . Assume there exists some $A > 0$ such that

$$A \|\underline{\mathbf{x}}\|_a \leq \|\underline{\mathbf{x}}\|_b \tag{10.12}$$

for every \underline{x} in \mathbb{R}^s . Assume there exist $c > 0$, $\underline{y}_c \in \mathbb{R}^s$ (i.e., a vector in \mathbb{R}^s which may change if c changes) such that

$$A \|\underline{y}_c\|_a < c \quad (10.13)$$

$$\|\underline{y}_c\|_b \geq c \quad (10.14)$$

Then, for every $c' > 0$ and $\underline{x} \in \mathbb{R}^n$,

$$\mathbb{B}_{c'}^{s|b}(\underline{x}) \subsetneq \mathbb{B}_{c'/A}^{s|a}(\underline{x}) \quad \diamond \quad (10.15)$$

Proof. Omitted. □

Then, Proposition 49 builds on Lemma 48 to show how cylindrical orthogonal norm-based balls (c.o.-balls) compare to L^2 - and L^∞ -balls from an inclusion/exclusion perspective.

Proposition 49 (c.o.-ball inclusion/exclusion w.r.t. L^2 - and L^∞ -balls). For every $\underline{\mathbf{r}} \in \mathbb{R}^3$, $c > 0$,

$$1. \mathbb{B}_c^{3|\text{Eu}}(\underline{\mathbf{r}}) \subsetneq \mathbb{B}_c^{3|\text{co}}(\underline{\mathbf{r}}) \subsetneq \mathbb{B}_{c\sqrt{3/2}}^{3|\text{Eu}}(\underline{\mathbf{r}})$$

$$2. \mathbb{B}_{c/\sqrt{2}}^{3|\infty}(\underline{\mathbf{r}}) \subsetneq \mathbb{B}_c^{3|\text{co}}(\underline{\mathbf{r}}) \subsetneq \mathbb{B}_c^{3|\infty}(\underline{\mathbf{r}}) \quad \diamond$$

Proof. Let $d = 0.9999999$. Via Proposition 47 and Lemma 48, consider:

$$1.\text{a) } c = 1, \underline{\mathbf{r}} = \left[\frac{d}{\sqrt{2}}, \frac{d}{\sqrt{2}}, \frac{d}{\sqrt{2}} \right]^T$$

$$1.\text{b) } c = 1, \underline{\mathbf{r}} = [1, 0, 0]^T$$

$$2.\text{a) } c = 1, \underline{\mathbf{r}} = [d, 0, 0]^T$$

$$2.\text{b) } c = 1, \underline{\mathbf{r}} = [d, d, d]^T \quad \square$$

Corollary 50. For $t \in \mathbb{R}$, $l_{i,j}(t) > 0$,

$$V_{i,j}(t; l_{i,j}(t), \text{Eu}) \subsetneq V_{i,j}(t; l_{i,j}(t), \text{co}) \subsetneq V_{i,j}\left(t; \sqrt{\frac{3}{2}}l_{i,j}(t), \text{Eu}\right) \quad (10.16)$$

$$V_{i,j}\left(t; \frac{1}{\sqrt{2}}l_{i,j}(t), \infty\right) \subsetneq V_{i,j}(t; l_{i,j}(t), \text{co}) \subsetneq V_{i,j}(t; l_{i,j}(t), \infty) \quad (10.17)$$

In particular,

$$V_{i,j}(t; l_{i,j}(t), \text{Eu}) \subsetneq V_{i,j}(t; l_{i,j}(t), \text{co}) \subsetneq V_{i,j}(t; l_{i,j}(t), \infty) \quad \diamond \quad (10.18)$$

Proof. In Proposition 49, let $\mathbf{r} = \mathbf{0}_{3 \times 1}$, and let $c = l_{i,j}(t)$. □

Corollary 50 has implications for the relationship between the COCR and spherical and box collision regions. First, spatially, via Eq. 10.18, the COCR strictly overestimates a spherical collision region, yet such an overestimate is strictly better than how the box collision region overestimates the spherical collision region. Second, Corollary 50 allows for interpreting Proposition 47 as follows. As projected onto lines through the origin along any unit direction, Item 1 of Proposition 47 implies that the COCR has, at worst, 22.47% more points than a spherical collision region – in particular, along the $(1/\sqrt{3}) \cdot [\pm 1, \pm 1, \pm 1]^T$ directions. For reference, linearly along any unit direction, Eq. 2.29 implies that the box collision region has, at worst, 73.21% more points than the spherical collision region.

Fact 51 quantifies the Lebesgue measure (in \mathbb{R}^3) of c.o.-balls, which may be used to precisely obtain the relative volume of the COCR compared to the spherical and box collision regions.

Fact 51 (c.o.-ball measure inequalities). For every $\mathbf{r} \in \mathbb{R}^3$, $c > 0$,

1. $\lambda\left(\mathbb{B}_c^{3\text{Eu}}(\mathbf{r})\right) = \frac{4}{3}\pi c^3 \approx 4.1888c^3$
2. $\lambda\left(\mathbb{B}_c^{3\text{co}}(\mathbf{r})\right) = 8(2 - \sqrt{2})c^3 \approx 4.6863c^3$
3. $\lambda\left(\mathbb{B}_c^{3\infty}(\mathbf{r})\right) = 8c^3$

Therefore,

$$0 < \lambda (\mathbb{B}_c^{3|\text{Eu}}(\mathbf{r})) < \lambda (\mathbb{B}_c^{3|\text{co}}(\mathbf{r})) < \lambda (\mathbb{B}_c^{3|\infty}(\mathbf{r})) < \infty \quad \diamond \quad (10.19)$$

Letting $\mathbf{r} = \mathbf{0}_{3 \times 1}$ and $c = l_{i,j}(t)$, Fact 51 implies that the COCR volumetrically overestimates the spherical collision region by 11.88%. For reference, the box collision region volumetrically overestimates the spherical collision region by 90.99%.

The close volumetric agreement between the COCR and the spherical collision region, which is visualized in Figure 10.3, is one of the chief advantages of employing a COCR in an SFF COLRM context. By considering three planar circular constraints and by seeking to fulfill at least one of them at a time, and under the premise that doing so is computationally less expensive than trying to satisfy S3ACs exactly (cf. Section 10.1), an approximate collision region is avoided whose extent closely resembles the original spherical collision region of interest. This property results in reduced collision constraint satisfaction conservatism in a way that does not compromise phenomenological collision safety, and in a way which may produce computational efficiency gains. Hence, feasibility and benefits for employing the COCR (in a deterministic SFF COLRM context) are understood.

10.3.2.2 *Spherical and box collision regions vs. COCR – IPC measure comparison*

This subsection compares the instantaneous probabilities of collision induced by the COCR to those induced by the spherical and box collision regions.

As discussed in Remark 46, Proposition 45 implies that probability measures (implicitly defined over the Lebesgue measurable subsets in \mathbb{R}^3) are well-defined over c.o.-balls. Proposition 52 employs the set inclusion/exclusion relationships listed in Proposition 49, as well as the ball measure differences that may be inferred from Fact 51, in order to obtain inequalities that relate probability measures based on c.o.-balls to their spherical- and box-ball counterparts.

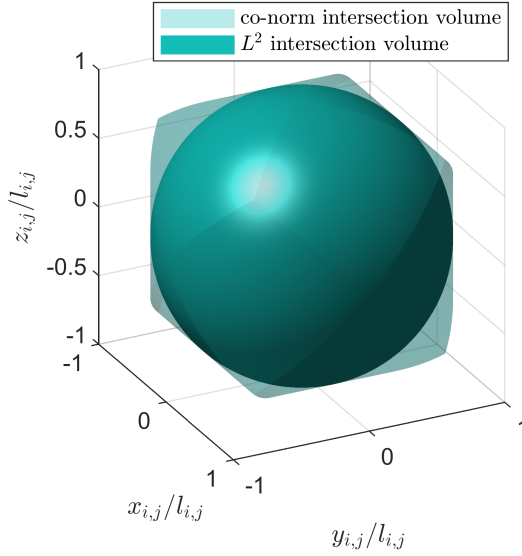


Figure 10.3: Comparison between instantaneous collision regions based on cylindrical-orthogonal and L^2 norms.

Proposition 52 (c.o.-ball-based probability measures). Let $(\mathbb{R}^3, \mathcal{L}(\mathbb{R}^3), \mathbb{P})$ be a probability space in \mathbb{R}^3 . Then, for every $\mathbf{r} \in \mathbb{R}^3$, $c > 0$,

1. $0 \leq \mathbb{P} \left(\mathbb{B}_c^{3|\text{Eu}}(\mathbf{r}) \right) \leq \mathbb{P} \left(\mathbb{B}_c^{3|\text{co}}(\mathbf{r}) \right) \leq \mathbb{P} \left(\mathbb{B}_{c\sqrt{3/2}}^{3|\text{Eu}}(\mathbf{r}) \right) \leq 1$
2. $0 \leq \mathbb{P} \left(\mathbb{B}_{c/\sqrt{2}}^{3|\infty}(\mathbf{r}) \right) \leq \mathbb{P} \left(\mathbb{B}_c^{3|\text{co}}(\mathbf{r}) \right) \leq \mathbb{P} \left(\mathbb{B}_c^{3|\infty}(\mathbf{r}) \right) \leq 1$

Let \mathbb{P} be an absolutely continuous probability measure, and let g denote the pdf of \mathbb{P} . If $\text{supp}(g) = \mathbb{R}^3$ (i.e., if for \mathbf{r} in \mathbb{R}^3 , $g(\mathbf{r}) \neq 0$), then

3. $0 < \mathbb{P} \left(\mathbb{B}_c^{3|\text{Eu}}(\mathbf{r}) \right) < \mathbb{P} \left(\mathbb{B}_c^{3|\text{co}}(\mathbf{r}) \right) < \mathbb{P} \left(\mathbb{B}_{c\sqrt{3/2}}^{3|\text{Eu}}(\mathbf{r}) \right) < 1$
4. $0 < \mathbb{P} \left(\mathbb{B}_{c/\sqrt{2}}^{3|\infty}(\mathbf{r}) \right) < \mathbb{P} \left(\mathbb{B}_c^{3|\text{co}}(\mathbf{r}) \right) < \mathbb{P} \left(\mathbb{B}_c^{3|\infty}(\mathbf{r}) \right) < 1$ ◇

Proof. Omitted. □

By applying Proposition 52 to the probability measure associated with the instantaneous relative position, upper and lower bounds for c.o.-IPC values (in terms of Euclidean-IPC and box-IPC values) may be gleaned.

Corollary 53 (c.o.-IPC inequalities). Let $\mathbf{R}_{i,j}(t)$ be a random variable defined in $\mathcal{L}(\mathbb{R}^3)$. Then,

$$0 \leq \text{IPC}_{i,j}(t; l_{i,j}(t)) \leq \text{IPC}_{i,j}(t; l_{i,j}(t), \text{co}) \leq \text{IPC}_{i,j}\left(t; \sqrt{\frac{3}{2}}l_{i,j}(t)\right) \leq 1 \quad (10.20)$$

$$0 \leq \text{IPC}_{i,j}\left(t; \frac{1}{\sqrt{2}}l_{i,j}(t), \infty\right) \leq \text{IPC}_{i,j}(t; l_{i,j}(t), \text{co}) \leq \text{IPC}_{i,j}(t; l_{i,j}(t), \infty) \leq 1 \quad (10.21)$$

Furthermore, if $\mathbf{R}_{i,j}(t)$ is an absolutely continuous random variable, and if $\text{supp}(\text{pdf}_{\mathbf{R}_{i,j}(t)}) = \mathbb{R}^3$, it follows that

$$0 < \text{IPC}_{i,j}(t; l_{i,j}(t)) < \text{IPC}_{i,j}(t; l_{i,j}(t), \text{co}) < \text{IPC}_{i,j}\left(t; \sqrt{\frac{3}{2}}l_{i,j}(t)\right) < 1 \quad (10.22)$$

$$0 < \text{IPC}_{i,j}\left(t; \frac{1}{\sqrt{2}}l_{i,j}(t), \infty\right) < \text{IPC}_{i,j}(t; l_{i,j}(t), \text{co}) < \text{IPC}_{i,j}(t; l_{i,j}(t), \infty) < 1 \quad \diamond \quad (10.23)$$

Proof. Via Proposition 52, consider the probability space $(\mathbb{R}^3, \mathcal{L}(\mathbb{R}^3), \mathbb{P})$ where $\mathbb{P} : \mathcal{L}(\mathbb{R}^3) \rightarrow [0, 1]$ is the probability measure associated with the random variable $\mathbf{R}_{i,j}(t)$. The result follows by noting that

$$\text{IPC}_{i,j}(t; l_{i,j}(t), a) = \mathbb{P}\left(\mathbb{B}_{l_{i,j}(t)}^{3|a}(\mathbf{0}_{3 \times 1})\right) \quad \square \quad (10.24)$$

Corollary 53 is significant for validating use of the COCR construct in an SFF COLRM context, because such a result has immediate applications for the computation and interpretation of instantaneous collision probability measures based on the COCR. For example, the c.o.-IPC is at most equal to the Euclidean-IPC with the HBR increased by a safety factor of 22.47%, and at least equal to the Euclidean-IPC without a safety factor on the HBR. Similarly, the c.o.-IPC is at most equal to the box-IPC without a safety factor on the HBR, and at least equal to the box-IPC with the HBR decreased by a factor of 29.29%. These inequalities may be understood as the direct consequence of the volumetric relation-

ships between the spherical and box collision regions, illustrated in Figures 10.3 and 10.2, respectively.

10.3.2.3 Spherical and box collision regions vs. COCR – JTC set and P_c measure comparison

This subsection compares the joint-time collision sets and joint-time probabilities of collision induced by the COCR to their counterparts induced by the spherical and box collision regions.

Under certain assumptions (such as continuity and surjectivity of g_P , as well as continuity of the flow function F_{t,t_0}), Propositions 17 and 18 show that as long as the instantaneous collision condition is defined as a ball with respect to some a -norm in $\mathbb{R}^{d_{\mathbf{R}}}$, it follows that the corresponding a -JTC set in $\mathbb{R}^{n_{\mathbf{x}}}$ is measurable (and hence, the a - P_c measure is well-defined). Furthermore, if the joint HBR time-history has continuous variation (including no variation), then these Propositions imply that the a -JTC set and the a - P_c measure may be obtained through successive discretization – and hence, they may be approximated arbitrarily precisely in a probabilistic sense in the limit. Thus, Propositions 17 and 18 imply that P_c measures in $\mathbb{R}^{n_{\mathbf{x}}}$ – whose underlying collision conditions in relative position space are based on the COCR – are well-defined and computable under certain non-restrictive conditions.

Proposition 54 is an intermediate result which employs norm equivalence relationships between any two norms in $\mathbb{R}^{d_{\mathbf{R}}}$ in order to establish JTC set inclusion relationships in $\mathbb{R}^{n_{\mathbf{x}}}$ (and hence, P_c inequalities) concerning the underlying collision regions induced by balls with respect to these norms.

Proposition 54 (JTC inclusion/ P_c inequalities). Let $\|\cdot\|_a, \|\cdot\|_b$ be norms in $\mathbb{R}^{d_{\mathbf{R}}}$. Let $C_1, C_2 > 0$ be equivalence constants for the a, b -norms; that is, for every $\mathbf{r} \in \mathbb{R}^{d_{\mathbf{R}}}$,

$$C_1 \|\mathbf{r}\|_a \leq \|\mathbf{r}\|_b \leq C_2 \|\mathbf{r}\|_a \quad (10.25)$$

Let Remark 8 hold. Assume the function $F_{t_0}(t, \mathbf{x})$ (see Eq. 2.38) is continuous in t and \mathbf{x} . Let $l_{i,j} : [t_0, t_f] \rightarrow (0, \infty)$. Then,

$$\begin{aligned} \text{JTC}_{i,j} \left([t_0, t_f]; \frac{1}{C_2} l_{i,j}(\cdot), a \right) &\subseteq \text{JTC}_{i,j} ([t_0, t_f]; l_{i,j}(\cdot), b) \\ &\subseteq \text{JTC}_{i,j} \left([t_0, t_f]; \frac{1}{C_1} l_{i,j}(\cdot), a \right) \end{aligned} \quad (10.26)$$

Consequently,

$$\begin{aligned} 0 \leq Pc_{i,j} \left([t_0, t_f]; \frac{1}{C_2} l_{i,j}(\cdot), a \right) &\leq Pc_{i,j} ([t_0, t_f]; l_{i,j}(\cdot), b) \\ &\leq Pc_{i,j} \left([t_0, t_f]; \frac{1}{C_1} l_{i,j}(\cdot), a \right) \leq 1 \quad \diamond \end{aligned} \quad (10.27)$$

Proof. This result follows from: 1) inclusion relationships among balls defined via equivalent norms; 2) the preservation of inclusion relationships after pre-images, specifically, those of $g_P : \mathbb{R}^{n\mathbf{x}} \rightarrow \mathbb{R}^{d\mathbf{R}}$ and $F_{t,t_0} : \mathbb{R}^{n\mathbf{x}} \rightarrow \mathbb{R}^{n\mathbf{x}}$; and 3) Definition 9 and Proposition 17. □

Corollary 55 builds on Proposition 54, as well as on the c.o.-norm equivalence constants listed in Proposition 47, in order to establish inequalities that relate the COCR-based Pc to the Pc measures based on the spherical and box collision regions.

Corollary 55 (c.o.-JTC inclusion/c.o.- Pc inequalities). Let Remark 8 hold. Assume the function $F_{t_0}(t, \mathbf{x})$ (see Eq. 2.38) is continuous in t and \mathbf{x} . Let $l_{i,j} : [t_0, t_f] \rightarrow (0, \infty)$. Consider the $\|\cdot\|_{\text{Eu}}$, $\|\cdot\|_{\text{co}}$, $\|\cdot\|_{\infty}$ norms in \mathbb{R}^3 . Then,

$$\begin{aligned} \text{JTC}_{i,j} ([t_0, t_f]; l_{i,j}(\cdot), \text{Eu}) &\subseteq \text{JTC}_{i,j} ([t_0, t_f]; l_{i,j}(\cdot), \text{co}) \\ &\subseteq \text{JTC}_{i,j} \left([t_0, t_f]; \sqrt{\frac{3}{2}} l_{i,j}(\cdot), \text{Eu} \right) \end{aligned} \quad (10.28)$$

$$\begin{aligned} \text{JTC}_{i,j} \left([t_0, t_f]; \frac{1}{\sqrt{2}} l_{i,j}(\cdot), \infty \right) &\subseteq \text{JTC}_{i,j} ([t_0, t_f]; l_{i,j}(\cdot), \text{co}) \\ &\subseteq \text{JTC}_{i,j} ([t_0, t_f]; l_{i,j}(\cdot), \infty) \end{aligned} \quad (10.29)$$

Consequently,

$$\begin{aligned} 0 \leq P_{C_{i,j}} ([t_0, t_f]; l_{i,j}(\cdot), \text{Eu}) &\leq P_{C_{i,j}} ([t_0, t_f]; l_{i,j}(\cdot), \text{co}) \\ &\leq P_{C_{i,j}} \left([t_0, t_f]; \sqrt{\frac{3}{2}} l_{i,j}(\cdot), \text{Eu} \right) \leq 1 \end{aligned} \quad (10.30)$$

$$\begin{aligned} 0 \leq P_{C_{i,j}} \left([t_0, t_f]; \frac{1}{\sqrt{2}} l_{i,j}(\cdot), \infty \right) &\leq P_{C_{i,j}} ([t_0, t_f]; l_{i,j}(\cdot), \text{co}) \\ &\leq P_{C_{i,j}} ([t_0, t_f]; l_{i,j}(\cdot), \infty) \leq 1 \quad \diamond \end{aligned} \quad (10.31)$$

Proof. This result follows from Proposition 47 and Proposition 54. □

Corollary 55 is significant for validating use of the COCR construct in an SFF COLRM context, because such a result indicates bounds for joint-time collision probability measures based on the COCR in terms of P_C measures based on other collision regions advocated for in the literature. For instance, the c.o.- P_C is at most equal to the Euclidean- P_C with the HBR increased by a safety factor of 22.47%, and at least equal to the Euclidean- P_C without a safety factor on the HBR. Likewise, the c.o.- P_C is at most equal to the box- P_C without a safety factor on the HBR, and at least equal to the box- P_C with the HBR decreased by a factor of 29.29%. These c.o.- P_C bounds are analogous to those obtained for the c.o.-IPC in Corollary 53.

Although quite similar, there is a significant difference between Corollary 53 (where c.o.-IPC bounds are listed) and Corollary 55 (where c.o.- P_C bounds are listed): while the former result does indicate a sufficient condition for such inequalities to be strict (namely, if the instantaneous relative position has a pdf, and if this pdf is non-zero in \mathbb{R}^3), the latter

result does not indicate a sufficient condition for the corresponding inequalities to be strict (which would require imposing additional restrictions on the flow function F_{t,t_0}).

10.4 Results and discussion

This section has two goals, both of which pertain to the theoretical results presented in Corollaries 53 and 55: first, to test whether the COCR-based IPC/ P_c inequalities (with respect to the bounds listed in Table 10.1) are satisfied; and second, to quantify the extent of probabilistic collision risk conservatism induced by employing a COCR versus other collision regions (specifically, those listed in Table 10.1). Such inquiries are studied through numerical and Monte Carlo sample simulation over a variety of SFF geometric regime cases subject to CW relative orbital dynamics. The COCR-based m -bounds listed in Table 10.1 include set membership and probabilistic collision risk bounds – from both instantaneous and joint-time perspectives.

Table 10.1: COCR-based set membership and probabilistic collision risk m -bounds.

m	Norm (a_m)	Bound Type	$l_{i,j}$ multiplier (c_m)	Set membership Eqns.		IPC Eqns.		P_c Eqns.
				Inst.	Joint-Time	Non-Strict	Strict	Non-Strict
1	Euclidean	Lower	1	10.16	10.28	10.20	10.22	10.30
2	Euclidean	Upper	$\sqrt{3/2}$	10.16	10.28	10.20	10.22	10.30
3	L^∞ (or box)	Lower	$\sqrt{1/2}$	10.17	10.29	10.21	10.23	10.31
4	L^∞ (or box)	Upper	1	10.17	10.29	10.21	10.23	10.31

10.4.1 Simulation cases and computational methodology

10.4.1.1 CW simulation cases

This Chapter focuses on Examples 3D.001–026, which are subject to CW dynamics, and which are described in Section A.2.

10.4.1.2 Description of computational methodology

All simulation cases assume time-invariant joint hard-body radii of $l_{i,j} = 32$ m. This figure is based on an estimate of Hubble Space Telescope's HBR of $l_i = 16$ m.[130] For the purposes of this Chapter, having such a large joint HBR allows obtaining higher and thus, more significant IPC values during a two-orbit propagation horizon, which is needed in order to meaningfully compare numerically-computed IPC signals to sample-computed IPC time-histories (or waveforms) during such a time window.

Probabilistic collision risk indicators are computed via numerical integration for IPC values only, and through Monte Carlo (MC) simulation for IPC and P_c values. For numerical IPC integration, truth values for mean and covariance are propagated analytically (i.e., using the analytically propagated relative state statistics listed in Eqns. A.22-A.23), while IPC values are obtained through multi-dimensional brute-force quadrature in MATLAB R2020b,[129] specifically, via the `integral3` function by integrating the instantaneous relative position pdf, which is obtained through the marginalization listed in Eq. A.24. In particular, the integration region limits for the COCR are expressed in terms of Cartesian coordinates, namely, as

$$x = \pm l_{i,j} \quad (10.32)$$

$$y = \pm \sqrt{l_{i,j}^2 - x^2} \quad (10.33)$$

$$z = \begin{cases} \pm \sqrt{l_{i,j}^2 - y^2} & \text{if } \theta \in \left[\frac{\pi}{4}, \frac{3\pi}{4} \right) \cup \left[\frac{5\pi}{4}, \frac{7\pi}{4} \right) \\ \pm \sqrt{l_{i,j}^2 - x^2} & \text{otherwise} \end{cases} \quad (10.34)$$

where $\theta = \text{atan2}(y, x)$. The absolute and relative error tolerances are set to 10^{-10} and 10^{-6} , respectively.

Monte Carlo samples of initial CW relative states are drawn in MATLAB R2020b, through the `mvnrnd` function,[127] and applying the Mersenne Twister pseudo-random

number generator. Each sample has 3.2×10^8 elements; such sample sizes are chosen to ensure that samples are able to reproduce events with probabilities greater than 1×10^{-7} , which is considered a practical threshold for IPC significance, as discussed in Ref. [28].

10.4.1.3 Validation of computational methodology

The cross-correlation coefficient between two real-valued signals is defined as the inner product between both signals (that is, the integral of the product of both signals) normalized by the \mathcal{L}^2 -norm of each signal (that is, the square root of the self-inner product of each signal).[155] For the c.o.- and m -bound-based collision regions, Figure 10.4 shows that the cross-correlation coefficient between sample and numerical IPC time-histories is approximately equal to 1 for all dynamic cases listed in Table A.2. In the limit that this cross-correlation coefficient is equal to 1, and in the limit of continuous timesteps, this result would imply that the sample and numerical IPC waveforms are equal almost everywhere to within a scaling constant. It is therefore necessary to check whether the \mathcal{L}^2 -norm values of the sample and numerical IPC time-history signals are equal (or reasonably close) – if so, this would imply that both IPC computation methods produce essentially the same outcomes.

Figure 10.5 shows the sample-to-numerical IPC waveform \mathcal{L}^2 -norm ratio for all dynamic cases listed in Table A.2, which shows that, for all cases, the sample IPC waveform \mathcal{L}^2 -norm is within 0.78% of the numerical IPC waveform \mathcal{L}^2 -norm. This fact, along with the cross-correlation coefficient between these waveforms, shows that the sample IPC approximates the numerical IPC adequately, i.e., such waveforms coincide with low discrepancy. Together, Figures 10.4 and 10.5 entail, for c.o.- and m -bound-based collision regions, that sample and numerical IPC results are mutually consistent (even if not exactly equal), and therefore, information gleaned from both computational methods is assumed to be reflective of the same underlying phenomena.

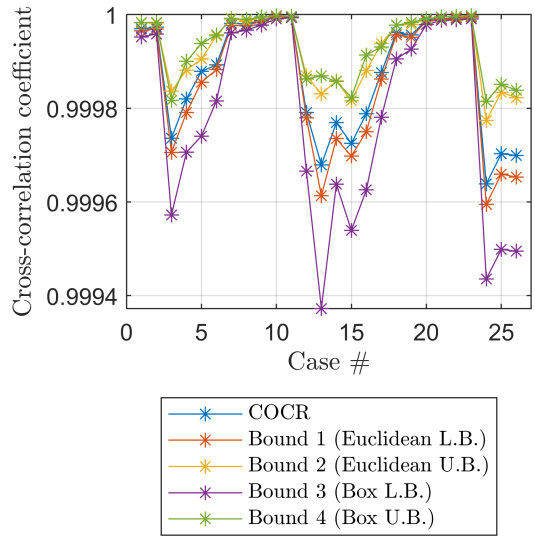


Figure 10.4: Cross-correlation coefficient between sample and numerical IPC waveforms (over 2 orbit periods), c.o.- and m -bound-based collision regions.

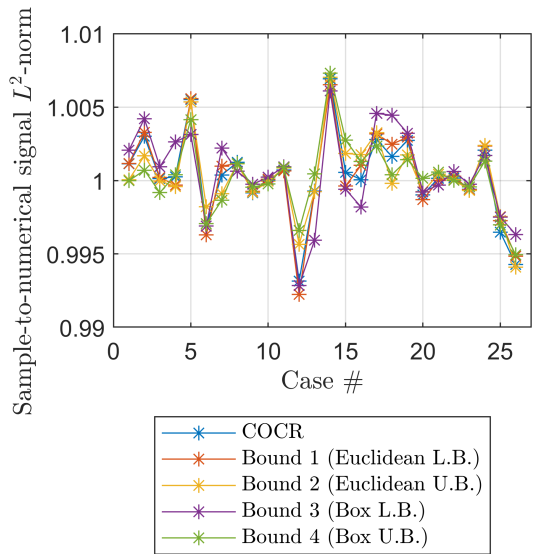


Figure 10.5: Sample-to-numerical IPC waveform \mathcal{L}^2 -norm ratios (over 2 orbit periods), c.o.- and m -bound-based collision regions.

10.4.2 Validation of COCR-based probabilistic collision risk inequalities

The computational validation of inequalities concerning probabilistic collision risk indicators based on the COCR and their corresponding bounds presented in Corollaries 53 and

55 is addressed in this subsection.

10.4.2.1 Validation of c.o.-IPC inequalities

Strict c.o.-IPC inequality satisfaction is expected because, for all dynamic cases and for any time in the propagation horizon, the instantaneous relative position distribution is non-degenerate normal, and therefore, the corresponding pdf has support in \mathbb{R}^3 . Figures 10.6 and 10.7 illustrate numerical c.o.-IPC and sample c.o.- Pc waveforms, as compared to their Euclidean and L^∞ /box bounds (respectively), for one of the CW dynamic cases considered. Note: throughout the Results and Discussion section, the “ m -bound” and “Bound m ” objects are equivalent, $m \in \{1, 2, 3, 4\}$; properties of each Bound m have been previously detailed in Table 10.1.

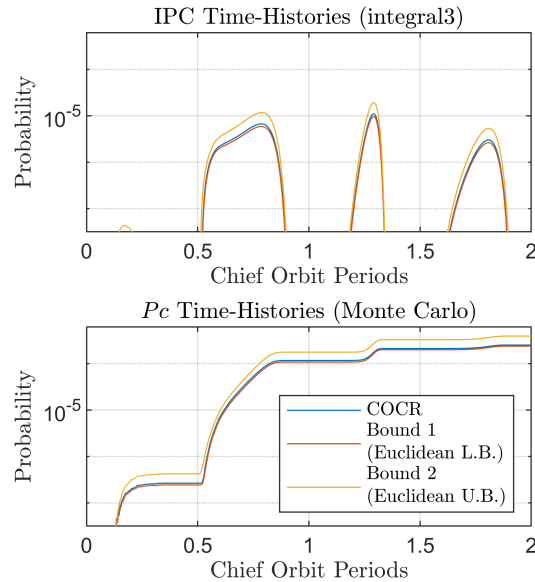


Figure 10.6: Comparison of IPC and Pc waveforms, c.o.- and Euclidean-bound-based collision regions, Example 3D.013.

Numerically-computed c.o.-IPC measures and their m -bounds are compared so as to establish whether the inequalities listed in Corollary 53 hold for numerically computed c.o.-IPCs. First, the `integral3` c.o.-IPC waveforms do not always meet the non-strict IPC inequalities listed in Eqns. 10.20 and 10.21; specifically, the non-strict Euclidean

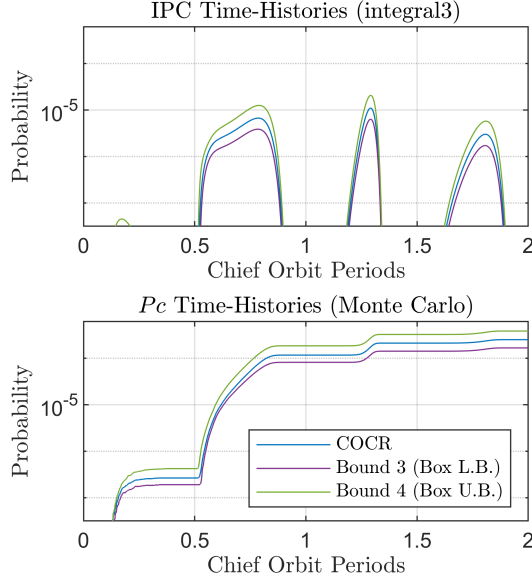


Figure 10.7: Comparison of IPC and Pc waveforms, c.o.- and box-bound-based collision regions, Example 3D.013.

bounds (Eq. 10.20) hold in 24/26 cases, and the non-strict L^∞ /box bounds (Eq. 10.21) hold in 22/26 cases. However, when examining IPC values above the significance threshold $p_{\text{threshold}} = 10^{-7}$, the c.o.-IPC inequalities are met strictly for all cases considered, for both Euclidean bounds (Eq. 10.22, which implies non-strict satisfaction, cf. Eq. 10.20) and L^∞ /box bounds (Eq. 10.23, which implies non-strict satisfaction, cf. Eq. 10.21). Interpreting the aforementioned discrepancies as arising from errors inherent to numerical integration, it follows that numerically computed c.o.-IPC values behave in accordance with the inequalities laid out in Corollary 53.

Similarly, MC c.o.-IPC measures and their m -bounds are compared in order to ascertain whether the inequalities listed in Corollary 53 are met for MC-computed c.o.-IPCs. First, the MC c.o.-IPC waveforms always meet the non-strict IPC inequalities, listed in Eqns. 10.20 and 10.21, regardless of significance threshold. This is expected because collision event logic, which is applied to each individual particle in the sample, precisely enforces non-strict subset relationships corresponding to different collision regions – in this case, those implied by the strict subset relationships listed in Eqns. 10.16 and 10.17. However,

although MC c.o.-IPC waveforms (above the significance threshold) always meet the strict IPC inequalities for Bounds 2-4 (that is, for the Euclidean upper bound and the L^∞ /box bounds), the strict Bound 1 c.o.-IPC inequalities are not always satisfied; specifically, the strict Euclidean lower bound only holds in 12/26 of cases. Such sample c.o.-IPC strict inequality discrepancies with respect to Bound 1 are henceforth discussed:

- Averaging over all 26 cases, the MC c.o.-IPC does not meet the strict Bound 1 inequality in 1.23/2881 timesteps (or in 0.043% of the complete propagation horizon) – which is a small fraction of the simulation time-window.
- Averaging over the 14 violating cases, the MC c.o.-IPC does not meet the strict Bound 1 inequality during 0.29% of the propagation horizon for which both MC c.o.- and Bound 1-IPC values are above $p_{\text{threshold}}$.
- Throughout the 14 violating cases, whenever the MC c.o.-IPC does not indicate a strict Bound 1 inequality (that is, when the MC c.o.- and Bound 1-IPC values are equal), in those precise timesteps, the corresponding numerically computed IPC values indicate on average a positive difference (between MC c.o.- and Bound 1-IPC values) of $\Delta = 1.08 \times 10^{-8}$ – or about 3.46 particles in a sample of $N_{\text{MC}} = 3.2 \times 10^8$ points.
- The difference Δ is below the threshold of significance $p_{\text{threshold}} = 10^{-7}$, and thus, it is not expected that the chosen MC sample size is capable of reproducing such a difference accurately. In other words, even though the violating timesteps should indicate a positive difference between c.o.- and Bound 1-IPC values, such a difference is too small to be captured by the probabilistic event resolution that the chosen MC sample size is able to provide.

Hence, over a vanishingly small fraction of the propagation horizon, the MC-based IPC is not able to discern an insignificant, yet positive difference between the c.o.-IPC and its

Euclidean lower bound. Therefore, it is concluded, to within the accuracy afforded by the numerical integration and MC sampling methods implemented in this Chapter, that the non-strict and strict c.o.-IPC inequalities presented in Corollary 53 are validated by simulation results in an SFF COLRM context.

10.4.2.2 Validation of c.o.- P_c inequalities

In turn, for MC c.o.- P_c waveforms, the non-strict inequalities listed in Eqns. 10.30 and 10.31 are always met, for all dynamic cases and for any choice of m -bound, irrespective of significance threshold. This result is expected for the same reasons that MC c.o.-IPC values always meet their corresponding non-strict inequalities – namely, that non-strict subset relationships (specifically, those listed in Eqns. 10.28 and 10.29) are enforced precisely through application of the corresponding logic to each particle in the sample. Hence, Monte Carlo simulations validate the c.o.- P_c inequalities listed in Corollary 55.

Furthermore, the MC c.o.- P_c waveforms (above the significance threshold) meet strict versions of the non-strict inequalities listed in 10.30 and 10.31 for all m -bounds considered. As previously discussed, although the fact that c.o.- P_c meets strict m -bound inequalities is consistent with the finding that c.o.-IPC meets strict m -bound inequalities, the former outcome is not necessarily guaranteed by the latter.

Because the probability distribution of the initial relative state $\underline{\mathbf{X}}_{i,j}(t_0)$ is non-degenerate normal, its associated probability measure 1) is absolutely continuous with respect to the Lebesgue measure in \mathbb{R}^{n_x} , and 2) its pdf has support in \mathbb{R}^{n_x} . Hence, these strict c.o.- P_c inequalities imply that the symmetric set-difference between the c.o.-JTC and its corresponding m -bound JTC sets has positive Lebesgue measure in \mathbb{R}^{n_x} . In other words, the following set has positive Lebesgue measure and therefore, non-zero probability: the set of initial conditions in relative state space for which a) the c.o.-collision condition is met during the propagation horizon, and also b) a lower bound (Euclidean or L^∞ /box) collision condition is not met. Similarly, the following set has positive Lebesgue measure and there-

fore, non-zero probability: the set of initial conditions in relative state space for which a) the c.o.-collision condition is not met during the propagation horizon, and also b) an upper bound (Euclidean or L^∞ /box) collision condition is met. Therefore, these findings motivate future research that would help ascertain conditions to be imposed on the flow function F_{t,t_0} and the propagation horizon such that the set difference between JTC sets (whose underlying collision conditions are defined via distinct a -norms) has positive Lebesgue measure in \mathbb{R}^{n_x} . Identifying these conditions would be a first step toward ascertaining more generally (e.g., for more families of relative state distributions) whether non-trivial differences may be expected among P_c measures based on distinct a -norm collision conditions.

10.4.3 Conservatism of COCR-based probabilistic collision risk inequalities

The aims of the current subsection are as follows: first, to compare c.o.-IPC/ P_c waveforms to their corresponding m -bounds in order to ascertain which m -bound the c.o.-IPC/ P_c might generally be in closest agreement with; and second, to quantify the degree of volumetric, IPC, and P_c conservatism that is introduced by employing a COCR instead of other collision regions utilized in the literature. Within this subsection, numerical IPC and sample P_c values are employed for these comparisons.

10.4.3.1 Agreement between c.o.- and m -bound-based IPC/ P_c values

In this Chapter, the waveform \mathcal{L}^2 -metric (between two signals) refers to the the \mathcal{L}^2 -norm (as previously discussed) of the difference between such two signals. Although not shown here, the waveform \mathcal{L}^2 -metric between the c.o.-IPC and the Bound 1-IPC time-histories is always strictly less than the waveform \mathcal{L}^2 -metric between the c.o.-IPC and the Bound m' -IPC time-histories, $m' \in \{2, 3, 4\}$. Similarly, the waveform \mathcal{L}^2 -metric between the c.o.- P_c and the Bound 1- P_c time-histories is always strictly less than the waveform \mathcal{L}^2 -metric between the c.o.- P_c and the Bound m' - P_c time-histories, $m' \in \{2, 3, 4\}$. Therefore, as quantified by the waveform \mathcal{L}^2 -metric, the c.o.-IPC is closer to its Euclidean lower

bound than to its other bounds, and the c.o.- P_c is closer to its Euclidean lower bound than to its other m -bounds. Such results hold for all dynamic cases considered. It follows that, from an SFF probabilistic collision risk perspective, the COCR is most similar to the original spherical collision risk region than to any other Euclidean or L^∞ /box tight set-theoretic bound.

The nature of the observed probabilistic close agreement between the COCR and its Euclidean lower bound is apparent from Figures 10.8 and 10.9. First, for all dynamic cases, the cross-correlation coefficient between the c.o.-IPC waveform and its Euclidean lower bound is greater than or equal to the cross-correlation coefficient between the c.o.-IPC and its other m -bounds. Interpreting such IPC waveforms as points in an abstract vector space (specifically, the space of square-integrable functions defined over the propagation horizon) which is endowed with an inner product and hence, where the notion of an angle between vectors is meaningful, such a cross-correlation coefficient result implies that the c.o.-IPC is more similar to its Euclidean lower bound over the propagation horizon than to its other m -bounds in the sense that the former pair of signals is more closely correlated (i.e., such signals have greater agreement in the timing and relative extent of waveform local extrema) than the latter pair – in the same way that, for vectors in \mathbb{R}^s , to have a greater normalized inner product implies having a lower angular (or directional) difference. The same result holds for c.o.- P_c signals, with a caveat: in 2/26 cases, the cross-correlation coefficient between the c.o.- P_c and Bound 2- P_c signals is numerically greater than the cross-correlation coefficient between the c.o.- P_c and Bound 1- P_c signals; and in 2/26 cases, the cross-correlation coefficient between the c.o.- P_c and Bound 3- P_c signals is numerically greater than the cross-correlation coefficient between the c.o.- P_c and Bound 1- P_c signals. In all discrepant c.o.- P_c cases, the cross-correlation coefficients at hand differ from 1 by $\epsilon = 1.13 \times 10^{-6}$ on average; in other words, the c.o.- P_c waveforms and their corresponding bounds in these discrepant instances are, essentially, equal almost everywhere – to within a scaling constant. Hence, practically, for all dynamic cases, the correlation between the

c.o.- Pc and its Euclidean lower bound is at least as strong (if not more) than the correlation between the c.o.- Pc and its other m -bounds.

Second, for all dynamic cases, for both c.o.-IPC and c.o.- Pc waveforms, their corresponding waveform \mathcal{L}^2 -norms are strictly closer in magnitude to their Euclidean lower bounds than to their other m -bounds. Hence, in an abstract vector sense, the c.o.-IPC and c.o.- Pc are closer in “direction” (as quantified by the cross-correlation coefficient) and “magnitude” (as quantified by the waveform \mathcal{L}^2 -norm) to their Euclidean lower bounds than to their other m -bounds. This result explains the previously observed close c.o.-IPC/ Pc agreement with their Euclidean lower bounds as observed through the comparison based on the waveform \mathcal{L}^2 -metric.

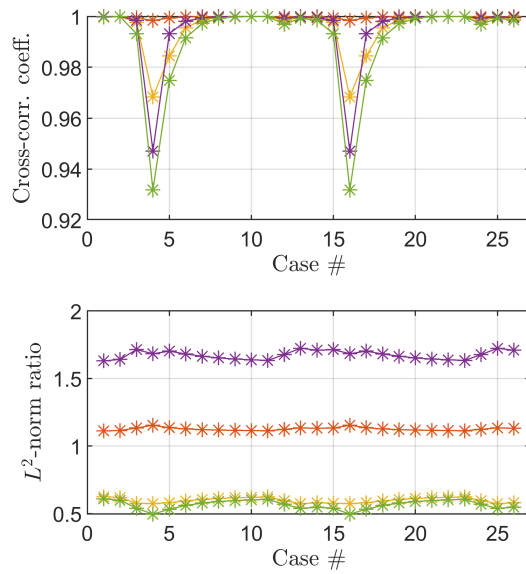


Figure 10.8: Numerical c.o.-to- m -bound IPC waveform \mathcal{L}^2 -based comparison (over 2 orbit periods): (orange) Bound 1, (yellow) Bound 2, (purple) Bound 3, (green) Bound 4.

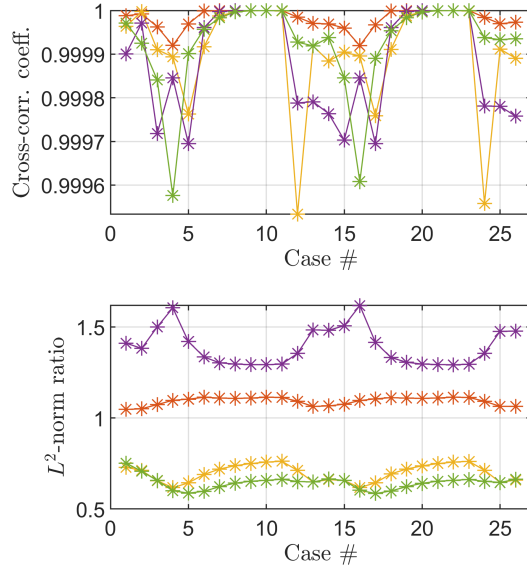


Figure 10.9: Sample c.o.-to- m -bound P_c waveform \mathcal{L}^2 -based comparison (over 2 orbit periods): (orange) Bound 1, (yellow) Bound 2, (purple) Bound 3, (green) Bound 4.

10.4.3.2 Relative averaged difference between c.o.- and m -bound-based IPC/ P_c values

The extent of c.o.-IPC conservatism with respect to its m -bounds is quantified through the c.o.-IPC m -comparison index, denoted as $\text{comp}_m\text{-IPC}_{i,j}$, defined as

$$\text{comp}_m\text{-IPC}_{i,j} = \frac{1}{\lambda(D_m)} \int_{t \in [t_0, t_f]} [\text{IPC}_{i,j}\text{-ratio}_m(t)] f_{D_m}(t) dt \quad (10.35)$$

$$\text{IPC}_{i,j}\text{-ratio}_m(t) = \frac{\text{IPC}_{i,j}(t; l_{i,j}, \text{co}) - \text{IPC}_{i,j}(t; c_m l_{i,j}, a_m)}{\text{IPC}_{i,j}(t; c_m l_{i,j}, a_m)} \quad (10.36)$$

where $f_{D_m} : [t_0, t_f] \rightarrow \{0, 1\}$ is the characteristic (or indicator function) of the D_m set, defined as

$$D_m = \{t \in [t_0, t_f] : \text{IPC}_{i,j}(t; l_{i,j}, \text{co}) \geq p_{\text{comp}}\} \\ \cap \{t \in [t_0, t_f] : \text{IPC}_{i,j}(t; c_m l_{i,j}, a_m) \geq p_{\text{comp}}\} \quad (10.37)$$

Hence, the $\text{comp}_m\text{-IPC}_{i,j}$ index may be understood as the relative difference between the c.o.-IPC and its m -bound, as averaged over the portion of the propagation horizon where both the c.o.-IPC and its m -bound are above some limit, which is denoted as p_{comp} (set here as $p_{\text{comp}} = 5 \times 10^{-7}$). The c.o.- PC m -comparison index, denoted as $\text{comp}_m\text{-}PC_{i,j}$, is defined and interpreted similarly, as given by

$$\text{comp}_m\text{-}PC_{i,j} = \frac{1}{\lambda(E_m)} \int_{t \in [t_0, t_f]} [PC_{i,j}\text{-ratio}_m(t)] f_{E_m}(t) dt \quad (10.38)$$

$$PC_{i,j}\text{-ratio}_m(t) = \frac{PC_{i,j}([t_0, t]; l_{i,j}, \text{co}) - PC_{i,j}([t_0, t]; c_m l_{i,j}, a_m)}{PC_{i,j}([t_0, t]; c_m l_{i,j}, a_m)} \quad (10.39)$$

$$E_m = \{t \in [t_0, t_f] : PC_{i,j}([t_0, t]; l_{i,j}, \text{co}) \geq p_{\text{comp}}\} \\ \cap \{t \in [t_0, t_f] : PC_{i,j}([t_0, t]; c_m l_{i,j}, a_m) \geq p_{\text{comp}}\} \quad (10.40)$$

Results for the $\text{comp}_m\text{-IPC}_{i,j}$ and $\text{comp}_m\text{-}PC_{i,j}$ indices for Bound 1 comparison (i.e., $m = 1$) are shown in Figure 10.10. These results are compared to reference values, denoted by $\text{comp}_m\text{-vol}_{i,j}$, which represent the volumetric difference between the COCR and its m -bounds. The $\text{comp}_m\text{-vol}_{i,j}$ values may be also interpreted as the instantaneous m -IPC ratio, $\text{IPC}_{i,j}\text{-ratio}_m(t)$, which would result from imposing an underlying instantaneous relative position distribution that is uniform over the Cartesian product $B_\rho = [-\rho, \rho]^3$ in \mathbb{R}^3 , for $\rho > 0$ large enough to include all m -bound collision regions. Note:

$$B_\rho = [-\rho, \rho]^3 = \{[x, y, z]^T \in \mathbb{R}^3 : b \in \{x, y, z\}, -\rho \leq b \leq \rho\} \quad (10.41)$$

The m -reference values $\text{comp}_m\text{-vol}_{i,j}$ are listed in Table 10.2.

Although not shown, it is found that, for all dynamic cases, the $\text{comp}_1\text{-IPC}_{i,j}$ index is strictly lesser in magnitude than those of the $\text{comp}_{m'}\text{-IPC}_{i,j}$ indices ($m' \in \{2, 3, 4\}$), and the $\text{comp}_1\text{-}PC_{i,j}$ index is strictly lesser in magnitude than those of the $\text{comp}_{m'}\text{-}PC_{i,j}$

Table 10.2: COCR volumetric (and uniform $\underline{\mathbf{R}}_{i,j}(t)$ distribution-based IPC) m -reference comparison values.

m	1	2	3	4
$\text{comp}_m\text{-vol}_{i,j}$	11.88%	-39.10%	65.69%	-41.42%

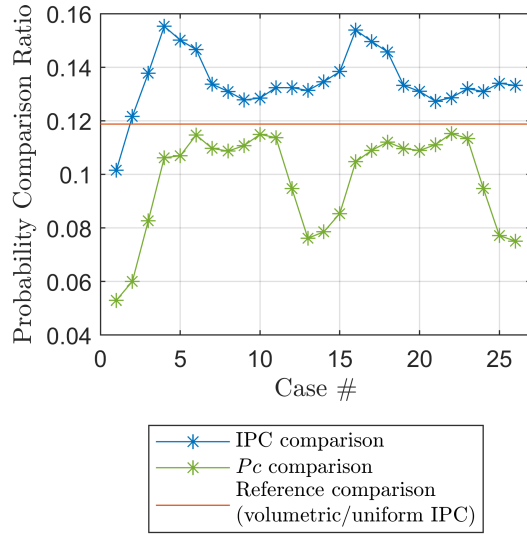


Figure 10.10: Cylindrical orthogonal IPC and Pc m -comparison indices (over 2 orbit periods), Bound 1 (i.e., Euclidean lower bound, $m = 1$).

indices ($m' \in \{2, 3, 4\}$). In other words, for every dynamic case considered, from a significant under/overestimate perspective, the c.o.-IPC and c.o.- Pc are closer in magnitude (over the propagation horizon) than to their other m -bounds. This result is consistent with the outcome of waveform \mathcal{L}^2 -norm analysis of Subsubsection 10.4.3.1. Hence, the remainder of this discussion focuses on comparing the c.o.-IPC and c.o.- Pc to their respective Euclidean lower bounds.

Except for Example 3D.001, for all other dynamic cases, the $\text{comp}_1\text{-IPC}_{i,j}$ index is strictly above the $\text{comp}_1\text{-vol}_{i,j} = 11.88\%$ reference value; averaging over all cases, the $\text{comp}_1\text{-IPC}_{i,j}$ index is only 1.59% above the $\text{comp}_1\text{-vol}_{i,j}$ reference. In principle, it is not expected that $\text{comp}_m\text{-IPC}_{i,j}$ indices would closely resemble $\text{comp}_m\text{-vol}_{i,j}$ values, since the instantaneous relative position distribution is not uniform over a sufficient large com-

pact set in \mathbb{R}^3 , but it is non-degenerate normal for all dynamic cases. Nonetheless, the close agreement observed between the $\text{comp}_1\text{-IPC}_{i,j}$ index and the $\text{comp}_1\text{-vol}_{i,j}$ reference suggests that, from a c.o.-IPC and Bound 1-IPC perspective, when such IPC values are significant (i.e., above p_{comp}), the instantaneous relative position behaves on average as if it were uniformly distributed in the neighborhood of the COCR and the original spherical collision region. These findings motivate future work which aims to ascertain conditions under which instantaneous relative position distributions may be adequately approximated by locally uniform distributions in a SFF COLRM context.

The foregoing discussion is further validated by $\text{comp}_1\text{-}P_{C_{i,j}}$ results. First, for all dynamic cases, $\text{comp}_1\text{-}P_{C_{i,j}}$ values are strictly lesser in magnitude than $\text{comp}_1\text{-IPC}_{i,j}$ values. This outcome implies, after averaging over portions of the propagation horizon where probabilistic collision risk indicators are significant, that the c.o.-IPC overestimates the Bound 1-IPC to a greater extent than the c.o.- P_C overestimates the Bound 1- P_C . This fact indicates that there is a greater degree of temporal overlap in terms of collision conditions after propagation as defined via the COCR than as defined via the original spherical collision region. In other words, the event that collisions occur at multiple timesteps comprises a larger probabilistic proportion of IPC values for collisions defined via the COCR than for collisions defined via the original spherical collision region. In turn, this result is consistent with the temporal and spatial continuity of the flow function of the dynamic cases at hand. Since the COCR is a superset of the original spherical collision region, by continuity of the flow function, relative position trajectories that enter the COCR remain in it for at least as long (and often, longer) than how long relative position trajectories remain in the original spherical collision region after entering it. Second, although lower than the $\text{comp}_1\text{-vol}_{i,j}$ for all dynamic cases, the $\text{comp}_1\text{-}P_{C_{i,j}}$ index is only 2.08% below the $\text{comp}_1\text{-vol}_{i,j}$ reference after averaging over all cases. This outcome is consistent with the c.o.-IPC overestimate and the c.o.- P_C overlap behaviors previously discussed.

10.5 Conclusion

In the context of spacecraft formation flying (SFF) collision risk management (COLRM), this Chapter motivates the implementation of a cylindrical orthogonal collision region (COCR) in \mathbb{R}^3 , which is constructed through the intersection of three mutually orthogonal cylinders, each of which represents a two-dimensional avoidance constraint. Since it is computationally expensive to satisfy spherical, three-dimensional avoidance constraints (S3ACs) directly, the purpose of the COCR construct is to provide a means for approximate S3AC satisfaction that allows for both safety sufficiency and reduced constraint satisfaction conservatism as compared to cubic collision regions and to the three-dimensional counterparts of single circular collision conditions on planar projections of spacecraft relative motion.

Application of the COCR for approximate S3AC satisfaction in an SFF COLRM context is validated theoretically and computationally. First, it is shown that the COCR is a ball with respect to a norm in \mathbb{R}^3 – specifically, the cylindrical orthogonal norm in \mathbb{R}^3 , hereby introduced. This outcome implies that the COCR is a well-defined region, and that stochastic measures of collision risk in both an instantaneous and joint-time sense based on the COCR are well-defined and computable. Second, relationships between the COCR and its tight upper and lower bounds in terms of Euclidean- and L^∞ /box-norms are presented from the following perspectives: volumetric, instantaneous set inclusion/exclusion, and joint-time set inclusion. Third, the aforementioned set-theoretic relationships between COCR-based collision sets and their bounds are used to infer upper and lower bound inequalities for instantaneous and joint-time probabilities of collision in terms of their Euclidean- and L^∞ /box-norm counterparts. Fourth, a computational methodology is presented and validated for the estimation of the instantaneous probability of collision (IPC) and the joint-time probability of collision (P_c) based on numerical integration and Monte Carlo sampling, respectively. Fifth, the preceding tight upper and lower bound inequalities for the

COCR-based IPC and P_c in terms of their Euclidean and L^∞ /box bounds are validated over a wide range of SFF geometric cases subject to Clohessy-Wiltshire (CW) relative orbital dynamics. Sixth, it is found that from volumetric as well as IPC and P_c time-history perspectives, the COCR is in closest agreement with its Euclidean lower bound, which is the original spherical collision region. Finally, the averaged overestimate of the COCR-based IPC and P_c (relative to the original spherical collision region-based IPC and P_c) is quantified, and it is found to be in close agreement with the volumetric COCR overestimate (relative to the original spherical collision region) of 11.88%. The significance and applicability of these findings is addressed.

Together, these theoretical and computational contributions constitute substantial support for employing the COCR construct in practical SFF COLRM applications. Specifically, these contributions motivate investigating whether there may be efficiency gains in the computation and verification of SFF relative trajectories that are safe with respect to the COCR (as opposed to the original spherical collision region).

CHAPTER 11

STATUS OF INVESTIGATION AND FUTURE WORK

An overview of the benefits of spacecraft formation flying (SFF), the sources of collision risk in spacecraft formations, and the process of collision risk management (COLRM) in SFF, is provided in Chapter 1.

Chapter 2 addresses the notation used in this work, a deterministic formulation of collision events, as well as definitions of probabilistic, distance-based, and hybrid collision risk indicators.

Contribution 1, addressed in Chapters 3 and 4, is concerned with foundational work in SFF COLRM. First, for a finite dimensional random vector with a probability density function (pdf), its Euclidean norm also has a pdf.[12] This substantiates sensitivity studies of the direct- and inverse-IPC problem. Second, well-definedness and computability is shown for joint-time probabilities of collision whose instantaneous collision condition is defined as a ball with respect to an arbitrary norm in relative position space.[183] The extent of this contribution will be completed after submitting a proof of the well-definedness and computability of the aforementioned joint-time collision probabilities as a peer-reviewed journal article, as listed in Table 11.1.

Contribution 2, addressed in Chapters 6 and 7, is concerned with SFF collision risk quantification, and it encompasses the development of the Mahalanobis Shell Sampling (MSS) algorithm for collision probability computation,[38] as well as computation techniques for distance-based collision risk indicators. While the MSS stochastic convergence contribution has been published as a journal article,[38] the distance-based SFF collision risk contribution will not be published beyond this dissertation. Contribution 2 is therefore complete, as shown in Table 11.1.

Contribution 3, addressed in Chapters 8 and Chapters 9, is concerned with SFF collision

risk interpretation and decision-making; it comprises the relationships between probabilistic and distance-based SFF collision risk indicators,[27, 28] and it characterizes the interpretation of hybrid SFF collision risk indicators.[33] While contribution of establishing the correlation relationship between probabilistic and distance-based SFF collision risk indicators has been published as a journal article,[28] the characterizing the interpretation of hybrid SFF collision risk indicators has been (and will only be) published as a conference paper.[33] Contribution 3 is hence complete, as shown in Table 11.1.

Contribution 4, addressed in Chapter 10, contributes to foundational SFF COLRM work and to SFF collision risk interpretation and decision-making. The cylindrical orthogonal collision risk (COCR), which is a new collision region in three-dimensional relative position space, and which arises from the violation of three mutually orthogonal two-dimensional collision constraints, is recommended in Contribution 4 for application to approximate spherical collision constraint satisfaction. Contribution 4 shows that the COCR is deterministically well-defined, it shows that instantaneous and joint-time stochastic SFF collision risk measures based on the COCR are well-defined and computable, it presents theoretical inequalities that relate these measures to upper and lower bounds based on the violation of the Euclidean and L^∞ /box norms (which are computationally validated), and it quantifies the extent of the overestimate of COCR-based stochastic SFF collision risk measures as compared to their Euclidean L^∞ /box upper and lower bounds. These developments have been submitted as a peer-reviewed journal article.[41] Contribution 4 is thus complete, as shown in Table 11.1.

Additionally, Appendix A lists initial conditions for test cases subject to CW dynamics used throughout the work; Appendix B discusses the analytical convergence properties of the Monte Carlo method in the mean square error (MSE) sense when estimating the sample mean, covariance, and probability measures; Appendix C describes the specific Monte Carlo simulation framework utilized for SFF collision risk indicator computation throughout this dissertation; and Appendix D discusses the definition of the CW vector and

matrix norms, which are used to directly compare CW relative state expected values and covariances for the purpose of testing asymptotic convergence rates in various sampling methods.

Table 11.1: Publication list for this investigation.

Contribution area to SFF COLRM	Publication title	Publication type	Status	Est. Date of Completion
Foundational (Contribution 1)	Existence of Probability Density Function for Norm of Finite-Dimensional Random Vector[12]	Journal Article	Complete	Feb. 2022
	Arbitrary relative position norm effects on spacecraft formation flying joint-time collision probability well-definedness[183]	Journal Article	In Progress	Jun. 2023
Quantification (Contribution 2)	Mahalanobis Shell Sampling (MSS) Method for Collision Probability Computation[47]	Master's Report	Complete	Feb. 2020
	Mahalanobis Shell Sampling (MSS) Method for Collision Probability Computation[46]	Conference Paper	Complete	Jan. 2021
	Stochastic Convergence of Sobol-Based Mahalanobis Shell Sampling (MSS) Collision Probability Computation[38]	Journal Article	Complete	Sep. 2022
Interpretation (Contribution 3)	Relating Collision Probability and Miss Distance Indicators in Spacecraft Formation Collision Risk Analysis[27]	Conference Paper	Complete	Aug. 2020
	Relating Collision Probability and Separation Indicators in Spacecraft Formation Collision Risk Analysis[28]	Journal Article	Complete	Nov. 2021
	Sensitivity of Separation Indicators in Spacecraft Formation Collision Risk Analysis[33]	Conference Paper	Complete	Aug. 2021
Foundational/ Interpretation (Contribution 4)	Cylindrical orthogonal norm-based stochastic collision risk measures in spacecraft formation flying[41]	Journal Article	Submitted	Apr. 2023

CHAPTER 12

CONCLUDING REMARKS

12.1 Dissertation problem statement

In view of the advantages to space mission capabilities and performance that may be provided by operational implementations of the spacecraft formation flying (SFF) mission design paradigm, considering the prevalence of collision risk to SFF missions from sources external and internal to such formations, and in light of the drastic consequences to spacecraft formations that would ensue from the occurrence of collision events, this dissertation seeks to conceptually frame the problem of collision risk management (COLRM) in SFF, and to provide relevant contributions towards the solution of this problem.

In a practical space mission implementation, operational SFF COLRM tasks comprise the following: computing indicators of SFF collision risk in a way that accounts for relative state uncertainty (i.e., SFF collision risk quantification), employing computed SFF collision risk indicators in order to ascertain whether corrective maneuvers are warranted (i.e., SFF collision risk interpretation and decision-making), and, if needed, planning and executing of collision avoidance maneuvers in a manner that ensures collision safety and the efficient use of onboard resources (i.e., SFF collision risk reduction). Operational SFF COLRM tasks implicitly rely on the formal definition of SFF collision risk indicators, as well as the characterization of their basic properties and guarantees; such items are the subject of foundational SFF COLRM work. From an ontological perspective, any practical SFF mission implementation must address the ongoing threat of SFF-related collision risk by adhering to the basic SFF COLRM framework hereby posed.

With the exception of SFF collision risk reduction (also known as SFF collision avoidance), the goal of this dissertation is to contribute to each aspect of the SFF COLRM prob-

lem, specifically, as related to the long-term risk of collisions among agents in spacecraft formations. Together, the contributions comprised by this dissertation may appeal to members of the spaceflight and astronautics communities interested in a resource which systematically (albeit not comprehensively) addresses the definition, usability, computation, and interpretation of indicators of collision risk among agents in spacecraft formations.

12.2 Overview of findings and implications of this investigation

Throughout this Chapter, the instantaneous probability of collision (IPC) and the joint-time probability of collision (P_c) between two agents in a spacecraft formation are specifically based on instantaneous collision regions defined as open balls (in relative position space) with respect to the Euclidean norm.

12.2.1 Foundational SFF COLRM work

12.2.1.1 Existence of probability density function (pdf) for Euclidean norm of finite-dimensional random vector

As per Chapter 3, for a finite-dimensional random vector whose probability distribution is absolutely continuous [i.e., if this random vector has a probability density function (pdf)], its Euclidean norm is also an absolutely continuous random variable. For the direct and inverse Euclidean norm-based instantaneous probability of collision (IPC) problems [i.e., respectively, for computing the IPC value corresponding to a fixed joint hard-body radius (HBR), and for obtaining the joint HBR corresponding to a fixed IPC value], this contribution substantiates studies of the sensitivity of such problems with respect to their defining parameters (i.e., joint HBR and IPC values, respectively), which can be shown to depend on the pdf of the Euclidean norm of the instantaneous relative position. Since the instantaneous relative position is often modeled as random vector with a pdf in the spaceflight mechanics community, this result has wide applicability for SFF practice.

12.2.1.2 *Well-Definedness and Computability of Joint-Time Stochastic Collision Risk Measures*

In the context of probability measures (including absolutely continuous probability measures), the probability of an event is well-defined if the event (which is represented as a subset of some reference space) is a measurable subset of the corresponding probability measure space.

Let a - Pc measures refer to joint-time probabilities of collision whose underlying collision conditions in relative position space are defined as origin-centered open balls with respect to some a -norm in relative position space. Then, Chapter 4 indicates sufficient conditions for a - Pc measures to be well-defined, namely: 1) if the flow function (corresponding to the relative dynamic process employed to propagate initial relative state space points) is invertible and continuous, and 2) if the function that projects points in relative state space into points in relative position space is a continuous surjection. Specifically, Conditions 1)-2) ensure that the joint-time collision set with respect to the a -norm (denoted by a -JTC) is a Lebesgue measurable subset of initial relative state space. Since the initial relative state (between two agents in a spacecraft formation) is often modeled as an absolutely continuous random vector, Conditions 1)-2) imply that an a - Pc measure in this context may be computed as an integral of the initial relative state pdf over the a -JTC set, and that this integral exists and is finite.

The notion of a - Pc computability refers to the property by which finite-timestep a - Pc approximations are able to approximate a - Pc measures arbitrarily well in the limit of vanishingly small timesteps. Then, Chapter 4 shows that a - Pc measures are computable under the following sufficient conditions: if Conditions 1)-2) are met, and 3) if the time-history of the joint HBR (which parameterizes the instantaneous collision region) has continuous variation over the propagation horizon.

Since Conditions 1)-3) are weak conditions that are met with high generality in space-flight mechanics applications, the results comprised by this contribution have a powerful

implication: if any relative position space a -norm is employed (via open balls) to encode the operational definition of instantaneous collision events, the corresponding a - Pc measures are automatically known to be well-defined and computable – and hence, such a - Pc measures may be employed for operational SFF COLRM tasks. Therefore, this contribution justifies the customization of collision regions in relative position space (specifically, as enabled by a -norms) in order to better suit operational needs in a wide range of SFF COLRM contexts.

12.2.2 Algorithms and methods for SFF collision risk indicator quantification

12.2.2.1 Stochastic Convergence of Sobol-based Mahalanobis Shell Sampling (MSS) Collision Probability Computation

Chapter 6 describes the Mahalanobis Shell Sampling (MSS) algorithm, which is a method for making samples of a finite-dimensional, non-degenerate normal random vector \underline{X} . The MSS algorithm employs uniform unit hypersphere samples (derived from uniform hypercube samples), which are then geometrically mapped into arbitrary Mahalanobis shells (i.e., regions whose boundaries are hypersurfaces of constant Mahalanobis distance).

The MSS algorithm produces samples of \underline{X} which have a user-defined number of points within each Mahalanobis shell. Hence, the MSS algorithm allows for obtaining an arbitrarily large number of probabilistically extreme sample points (as quantified by Mahalanobis distance) in an MSS sample, which enables the inclusion of points that represent rare events with more ease and predictability than would be allowed by Monte Carlo samples.

Theoretically, MSS-based estimators of sample mean and covariance are unbiased under invertible linear transformations, and MSS-based sample estimators of probability measures are asymptotically unbiased (with a pre-determined upper error bound) in the limit of increasing the number of sample shells.

The asymptotic rate of stochastic convergence [in the mean-square-error (MSE) sense] is quantified for MSS samples [of the Clohessy-Wiltshire (CW) relative orbital dynamic

state] whose underlying method of unit hypercube generation is the randomized Sobol sequence. It is found that, when reproducing the distribution mean and covariance for the CW relative position, relative position rate, and relative state, MSS-based MSE convergence improves upon Monte Carlo-based MSE convergence by an order of magnitude. Additionally, MSS-based IPC computation achieves similar error properties as Monte Carlo-based IPC computation.

Therefore, through its theoretical and computational properties, the MSS algorithm constitutes an implementable collision risk quantification tool for SFF practitioners seeking to realize SFF mission concepts that rely on IPC/ P_c -based SFF COLRM. Employing the MSS algorithm for this purpose would have the added benefit of creating the potential for guidance, navigation, and control (GN&C) synergies in the case that the MSS algorithm is also utilized as a building block in the development of particle filter-based SFF relative navigation architectures.

12.2.2.2 *Quantification of distance-based SFF collision risk indicators*

Let $D_{i,j;d}$ denote the minimum Euclidean distance from the origin of relative position space to the d -Mahalanobis contour of the instantaneous relative position random vector, which is assumed to be non-degenerate normal. For certain d -values, the $D_{i,j;d}$ quantity has been proposed as an SFF collision risk indicator representing critical points in boundaries between probabilistically extreme and non-extreme events.

Chapter 7 introduces a methodology in three dimensions for $D_{i,j;d}$ computation as follows. First, in the context of the more general problem of finding the minimum Euclidean distance from the origin of a finite-dimensional real vector space to the d -Mahalanobis contour of some non-degenerate random vector \underline{X} , the following theoretical properties are ascertained: the existence of solutions to this problem is proven, and upper and lower bounds for these solutions are obtained in terms of scalar functions of the first- and second-order statistical moments of \underline{X} . Second, such general finite-dimensional results are applied

to $D_{i,j;d}$ for the purposes of: 1) establishing the well-definedness of $D_{i,j;d}$, and 2) to aid the computation of $D_{i,j;d}$ – specifically, by rescaling the objective function that defines $D_{i,j;d}$ so that it has predictable upper and lower bounds. Third, a dimension-reducing isomorphism between the unit 2-sphere and the unit square, in addition to a coordinate basis transformation, enable reframing the problem of finding $D_{i,j;d}$ as a search in a convex, simply-connected subset of the unit square.

The aforementioned $D_{i,j;d}$ computation methodology is validated in the context of relative position distributions which have become ill-conditioned after propagation through CW dynamics. In this dissertation, this methodology is utilized for $D_{i,j;d}$ computation in the context of a study of the correlation relationship between miss-distance and probabilistic SFF collision risk indicators (see Ch. 8).

Therefore, the $D_{i,j;d}$ computation methodology introduced in Chapter 7 represents a starting point for SFF practitioners who wish to employ the $D_{i,j;d}$ quantity as a collision risk indicator for the purposes of developing an SFF COLRM concept.

12.2.3 Spacecraft formation collision risk interpretation and decision-making

12.2.3.1 Relating collision probability and separation indicators in spacecraft formation collision risk analysis

Active methods of SFF collision avoidance (COLA) may be broadly classified in terms of which SFF collision risk indicator type is employed as a decision variable on the basis of which to develop thresholds which encode sufficient conditions for SFF collision safety. While miss distance-based SFF collision risk indicators refer to statistical descriptions of inter-agent separation, probabilistic SFF collision risk indicators refer to probability measures associated with the instantaneous or joint-time risk of inter-agent collisions.

Recognizing the foregoing active SFF COLA decision variable dichotomy prompts examining whether both types of SFF collision risk indicators provide consistent information regarding the risk of inter-agent collisions. In Ch. 8, the degree of such consistency is

assessed via the collision correlation index, which quantifies the extent of the correlation relationship between miss distance and IPC time-history peaks.

As per the collision correlation index, the Euclidean norm of expected relative position has no consistent relationship with IPC/P_c measures, while the 99.73% minimum distance ($\rho_{3\sigma}$; this is the 0.27%-quantile of the distribution of the Euclidean norm of relative position) exhibited the highest extent of SFF collision risk information consistency with IPC/P_c measures.

This contribution is valuable to SFF practitioners because it identifies pitfalls of certain miss distance-based SFF collision risk indicators, while it also substantiates application of other miss distance-based indicators (in particular, $\rho_{3\sigma}$). Additionally, via the collision correlation index, this contribution provides a coherent mechanism for quantifying whether miss distance and probabilistic SFF collision risk indicators are related to each other in a way that accords with intuition.

12.2.3.2 Sensitivity of separation indicators in spacecraft formation collision risk analysis

The 99.73% minimum distance ($\rho_{3\sigma}$), which is the 0.27%-quantile in the distribution of the Euclidean norm of the relative position, is a quantity which has been recommended for application as a miss distance-based SFF collision risk indicator because it exhibits a high degree of SFF collision risk information consistency with respect to IPC/P_c measure-based SFF collision risk information.

The $\rho_{3\sigma}$ quantity may be understood as a hybrid SFF collision risk indicator in the following way: if the isotropic keep-out-zone distance requirement between two agents is greater than $\rho_{3\sigma}$, their corresponding IPC has a value of at least 0.27%. This probabilistic $\rho_{3\sigma}$ interpretation is validated in Chapter 9 by showing that small changes in the IPC value that defines $\rho_{3\sigma}$ (i.e., 0.27%.) induce proportionally small changes to the value of $\rho_{3\sigma}$ itself. This $\rho_{3\sigma}$ behavior is observed over a wide range of relative orbital dynamic regimes.

These results validate the interpretation of $\rho_{3\sigma}$ as encoding an SFF collision risk boundary in relative position space with a specific interpretation pertaining to probabilistic SFF collision risk. Therefore, this contribution is valuable to SFF practitioners because it shows that the foregoing interpretation of $\rho_{3\sigma}$ holds under numerical and statistical estimator errors to within acceptable user tolerances, which is a property that SFF collision risk indicators must display before being employed in any SFF hardware implementation.

12.2.4 Cylindrical orthogonal norm-based stochastic collision risk measures in spacecraft formation flying

Every SFF COLRM framework depends on the operational definition of collision events; such a definition reflects: 1) how SFF collision events are physically understood, and 2) any assumptions imposed so that collision event occurrences are practically determinable.

A common practice in the spaceflight mechanics community is to define spacecraft collisions in terms of the violation of minimum distance constraints with respect to the Euclidean norm; doing so allows for a formulation of collision events that is independent of relative attitude and the coordinate basis of relative position space. However, satisfying spherical three-dimensional avoidance constraints (S3ACs) precisely is computationally expensive (sometimes prohibitively so); hence much of the spacecraft relative trajectory planning literature focuses on approximate S3AC satisfaction.

Chapter 10 is concerned with the cylindrical orthogonal collision region (COCR), which arises from the simultaneous violation of two-dimensional (2D) circular collision constraints as perceived in three mutually orthogonal planar projections of three-dimensional (3D) spacecraft relative motion. The COCR is the relative position region guaranteed to be avoided if at least of one out of three mutually orthogonal planar circular constraints (e.g., in the in-plane, cross-plane, and sky-plane) is satisfied at any one time.

Chapter 10 motivates application of the COCR as encoding the operational definition of collision events in an SFF COLRM context by addressing concerns which arise from

the construction of the COCR. First, the COCR is a well-defined convex region of 3D relative position space; hence, avoiding this region is conceptually no different than satisfying an S3AC. Any COCR is volumetrically 11.88% larger than the largest Euclidean collision region circumscribed within the COCR. Hence, by satisfying three circular planar constraints instead of uncountably many hyperplane constraints, the COCR affords collision safety sufficiency while also reducing collision safety conservatism as compared to other regions employed in the literature (such as cubic box regions). Second, based on the well-definedness of a -norm based IPC/P_c measures listed in Chapter 4, COCR-based IPC/P_c measures are known to be well-defined and computable as well. Third, upper and lower bounds for COCR-based IPC/P_c measures are derived in terms of Euclidean norm- and box norm-based IPC/P_c measures. These bounds are validated numerically for IPC values and through Monte Carlo simulation for IPC/P_c values in the context of a wide range of pertinent relative orbital dynamic regimes. Fourth, the extent of COCR-based IPC/P_c measure overestimate over the original Euclidean norm-based IPC/P_c measures is quantified, showing that the former measures are more closely related to the latter measures than how the former measures are related to other upper and lower bounds.

Together, these results are a valuable contribution to SFF practitioners because they substantiate the validity of deterministic and stochastic applications of the COCR in an operational SFF COLRM context, specifically, by identifying the potential benefits of their use and by characterizing the corresponding deterministic and stochastic drawbacks of applying the COCR in this way.

12.3 Final remarks

This dissertation utilizes the notion of spacecraft formation flying (SFF) collision risk indicators as quantities whose computed values may be employed to make informed decisions concerning the necessity of performing correction maneuvers in order to preserve inter-agent collision safety in an operational SFF context. This investigation makes con-

tributions to the following subfields within the SFF collision risk management (COLRM) discipline: SFF collision risk quantification, SFF collision risk interpretation and decision-making, and foundational SFF collision risk management (COLRM) work. As discussed in this Chapter, these contributions are relevant to members of the spaceflight and astronautics communities who might be interested in practical, hardware-based implementations of the SFF mission design paradigm.

Appendices

APPENDIX A

CLOHESSY-WILTSHIRE (CW) DYNAMICS, GEOMETRY, AND TEST CASES

A.1 Clohessy-Wiltshire (CW) dynamics and geometry

Simulation cases in this dissertation are subject to Clohessy Wiltshire (CW) relative orbital dynamics,[5] which are linearizations of the restricted two-body problem around a reference Keplerian, circular orbit. The position of the deputy agent k about the chief agent j_0 ($[\mathbf{r}_{k,j_0}]_H \in \mathbb{R}^3$, or simply $[\mathbf{r}_k]_H$) is expressed in the coordinates of the Hill frame,[138] which is a rotating reference frame, and which is also designated as the RIC,[184] RTN,[90] and LVLH frame.[5] The CW relative dynamic state $[\mathbf{x}_{k,j_0}]_H$ is completed by the relative position rate, i.e., $[\mathbf{x}_{k,j_0}]_H^T = [[\mathbf{r}_{k,j_0}]_H^T, [\dot{\mathbf{r}}_{k,j_0}]_H^T]$, where $[\dot{\mathbf{r}}_{k,j_0}]_H$ is not a true, inertial velocity because Hill frames are rotating reference frames. CW motion exhibits linear, time-invariant (LTI) dynamics; thus, a deterministic CW relative state $[\mathbf{x}_{k,j_0}]_H(t)$ is related to its initial conditions at time t_0 as given by

$$[\mathbf{x}_{k,j_0}]_H(t) = \Phi_{j_0}(t, t_0) [\mathbf{x}_{k,j_0}]_H(t_0) \quad (\text{A.1})$$

where the j_0 state transition matrix, Φ_{j_0} , is given by

$$\Phi_{j_0}(t, t_0) = \begin{bmatrix} 4 - 3c & 0 & 0 & \frac{s}{n_{j_0}} & \frac{2}{n_{j_0}} - \frac{2c}{n_{j_0}} & 0 \\ -6n_{j_0}(t - t_0) + 6s & 1 & 0 & -\frac{2}{n_{j_0}} + \frac{2c}{n_{j_0}} & \frac{4s}{n_{j_0}} - 3(t - t_0) & 0 \\ 0 & 0 & c & 0 & 0 & \frac{s}{n_{j_0}} \\ 3n_{j_0}s & 0 & 0 & c & 2s & 0 \\ -6n_{j_0} + 6n_{j_0}c & 0 & 0 & -2s & -3 + 4c & 0 \\ 0 & 0 & -n_{j_0}s & 0 & 0 & c \end{bmatrix} \quad (\text{A.2})$$

where n_{j_0} denotes the mean orbital motion of chief agent j_0 , and where

$$c \doteq \cos(n_{j_0}(t - t_0)) \quad (\text{A.3})$$

$$s \doteq \sin(n_{j_0}(t - t_0)) \quad (\text{A.4})$$

General CW relative trajectories may be described in terms of the geometric parameters $(A_0, B_0, x_{\text{off}}, y_{\text{off}}, \alpha_0, \beta_0)$ as given by Equations A.5, A.6 and A.7, as listed in the Nomenclature, and in accordance with the notation of Schaub.[5]

$$[x_{k,j_0}]_H(t) = A_0 \cos(n_{j_0}(t - t_0) + \alpha_0) + x_{\text{off}} \quad (\text{A.5})$$

$$[y_{k,j_0}]_H(t) = -2A_0 \sin(n_{j_0}(t - t_0) + \alpha_0) - \frac{3}{2}n_{j_0}(t - t_0)x_{\text{off}} + y_{\text{off}} \quad (\text{A.6})$$

$$[z_{k,j_0}]_H(t) = B_0 \cos(n_{j_0}(t - t_0) + \beta_0) \quad (\text{A.7})$$

If the CW trajectory of agent k about agent j_0 is closed, then the initial relative CW state $[\mathbf{x}_{k,j_0}]_H(t_0)$ is constrained such that $x_{\text{off}} = 0$ (i.e., when trajectories have no constant radial offset; cf. Eq. A.6). This condition is the CW counterpart to Keplerian orbits having equal energy (and hence, having the same orbital period). Equivalently, closed CW trajectories satisfy

$$[\dot{y}_{k,j_0}]_H(t_0) = -2n_{j_0} [x_{k,j_0}]_H(t_0) \quad (\text{A.8})$$

Proposition 56 (Duality of relative CW trajectories). Suppose two agents i and j are in closed CW trajectories about the same arbitrary chief agent, denoted by j_0 . Then, the motion of agent i relative to agent j is a virtual, closed CW trajectory with agent j as the chief. \diamond

Proof. Suppose agent k is in a closed CW trajectory about j_0 . Then,

$$[\dot{y}_{k,j_0}]_H(t_0) = -2n_{j_0} [x_{k,j_0}]_H(t_0) \quad (\text{A.9})$$

Since, for $t \geq t_0$, $[\mathbf{x}_k]_H(t) = \Phi_{j_0}(t, t_0) [\mathbf{x}_k]_H(t_0)$, it follows that

$$[x_{k,j_0}]_H(t) = c [x_{k,j_0}]_H(t_0) + \frac{s}{n_{j_0}} [\dot{x}_{k,j_0}]_H(t_0) \quad (\text{A.10})$$

$$\begin{aligned} [\dot{y}_{k,j_0}]_H(t) &= -2n_{j_0} c [x_{k,j_0}]_H(t_0) - 2s [\dot{x}_k]_H(t_0) \\ &= -2n_{j_0} \left[c [x_{k,j_0}]_H(t_0) + \frac{s}{n_{j_0}} [\dot{x}_{k,j_0}]_H(t_0) \right] \end{aligned} \quad (\text{A.11})$$

Therefore, when k has a closed CW trajectory about j_0 , it follows that, for $t \geq t_0$,

$$[\dot{y}_{k,j_0}]_H(t) = -2n_{j_0} [x_{k,j_0}]_H(t) \quad (\text{A.12})$$

Suppose agents i and j are both in closed CW trajectories about j_0 . Then,

$$[\mathbf{x}_{i,j_0}]_H(t) = \Phi_{j_0}(t, t_0) [\mathbf{x}_{i,j_0}]_H(t_0) \quad (\text{A.13})$$

$$[\mathbf{x}_{j,j_0}]_H(t) = \Phi_{j_0}(t, t_0) [\mathbf{x}_{j,j_0}]_H(t_0) \quad (\text{A.14})$$

Since agent j is in a closed trajectory about agent j_0 , and since the j motion is an oscillator in any H -coordinate direction with period $2\pi/n_{j_0}$, it follows that the motion of agent j occurs with the same periodicity as that of agent j_0 , i.e., $n_j = n_{j_0}$, and $\Phi_j(t, t_0) = \Phi_{j_0}(t, t_0)$.

Thus, because of linearity,

$$\begin{aligned} [\mathbf{x}_{i,j}]_H(t) &\doteq [\mathbf{x}_i]_H(t) - [\mathbf{x}_j]_H(t) \\ &= \Phi_{j_0}(t, t_0) ([\mathbf{x}_i]_H(t_0) - [\mathbf{x}_j]_H(t_0)) = \Phi_j(t, t_0) [\mathbf{x}_{i,j}]_H(t_0) \end{aligned} \quad (\text{A.15})$$

By inspecting Eq. A.15 and applying the general closed orbit condition for $t \geq t_0$, it

follows that

$$\begin{aligned}
[\mathbf{x}_{i,j}]_H^T(t) &= [\mathbf{x}_i]_H^T(t) - [\mathbf{x}_j]_H^T(t) \\
&= \begin{bmatrix} x_i(t) & y_i(t) & z_i(t) & \dot{x}_i(t) & -2n_{j_0}x_i(t) & \dot{z}_i(t) \end{bmatrix}_H \\
&\quad - \begin{bmatrix} x_j(t) & y_j(t) & z_j(t) & \dot{x}_j(t) & -2n_{j_0}x_j(t) & \dot{z}_j(t) \end{bmatrix}_H \\
&= \begin{bmatrix} x_{i,j}(t) & y_{i,j}(t) & z_{i,j}(t) & \dot{x}_{i,j}(t) & -2n_j x_{i,j}(t) & \dot{z}_{i,j}(t) \end{bmatrix}_H \quad (\text{A.16})
\end{aligned}$$

In particular, for $t = t_0$, $[y_{i,j}]_H(t_0) = -2n_j [x_{i,j}]_H(t_0)$, which satisfies the closed orbit condition from Eq. A.8. Therefore, the trajectory of agent i relative to j is a closed CW trajectory with agent j as a virtual chief. \square

Via Proposition 56, if a pair of agents have closed CW orbits about a common chief, it is possible to reformulate the trajectory of one agent of such pair as a virtual CW trajectory about the other agent in the pair, thereby obviating the need to consider this case as a separate problem. Although this would only hold under major practical assumptions (i.e., closed relative orbits about the same agent), these assumptions help generalize the analysis. Therefore, in the rest of this Appendix, the i - j subscripts in the relative state of CW agents are omitted with the understanding that agent i is any agent that orbits relative to an arbitrary chief agent j , whether real (in the sense of Eqns. A.2-A.8) or virtual (in the sense of Proposition 56, if applicable). Additionally, the mean motion of agent j , n_j , is simply denoted by n .

Closed CW relative trajectories can be described in terms of the geometric parameters $(A_0, B_0, y_{\text{off}}, \alpha_0, \beta_0)$ as given by Equations A.17, A.18, and A.19.

$$[x_{k,j_0}]_H(t) = A_0 \cos(n_{j_0}(t - t_0) + \alpha_0) \quad (\text{A.17})$$

$$[y_{k,j_0}]_H(t) = -2A_0 \sin(n_{j_0}(t - t_0) + \alpha_0) + y_{\text{off}} \quad (\text{A.18})$$

$$[z_{k,j_0}]_H(t) = B_0 \cos(n_{j_0}(t - t_0) + \beta_0) \quad (\text{A.19})$$

These are five, not six, geometric parameters, owing to the closed CW trajectory constraint, given by Eq. A.8. Also, $[z]_H$ motion is that of a simple harmonic oscillator, independent of $[x]_H$ - $[y]_H$ motion. Figure A.1 illustrates the geometry of closed CW orbits.[140, 5] The foregoing closed CW geometric parameters are illustrated in Fig. A.1, and they may be interpreted as follows:

- A_0 : amplitude of $[x]_H$ motion.
- y_{off} : steady-state offset of $[y]_H$ motion. Note: the amplitude of $[y]_H$ motion about y_{off} is $2A_0$.
- B_0 : amplitude of $[z]_H$ motion.
- α_0 : phase angle of $[x]_H$ motion. Note: the $[y]_H$ motion leads the $[x]_H$ motion by a phase difference of $\pi/2$, i.e., by 0.25 chief orbit periods, regardless of the value of α_0 . Thus, the $[x]_H$ - $[y]_H$ motion is always a 1:2 ellipse (i.e., a “football”-shaped relative orbit) centered at $(0, y_{\text{off}})$.
- β_0 : phase angle of $[z]_H$ motion.

It should be noted that the α_0 and β_0 angles are only meaningful if the A_0 and B_0 amplitudes, respectively, are nontrivial. If defined, the $\beta_0 - \alpha_0$ geometric parameter creates the greatest variability in the shape of closed CW trajectories. In particular, the following cases are noteworthy:

- $\text{mod}(\beta_0 - \alpha_0, 2\pi) \in \{0, \pi\}$. Here, the $[x]_H$ and $[z]_H$ motions are in phase and are either correlated or anti-correlated straight lines, whereas the $[y]_H$ and $[z]_H$ motions are out of phase, creating a $2:(B_0/A_0)$ ellipse. For example, in this $\beta_0 - \alpha_0$ case, if $B_0 = 2A_0$, then the relative trajectory as perceived in the $[y]_H$ - $[z]_H$ plane is a 1:1 ellipse (i.e., a circle) centered at $(y_{\text{off}}, 0)$.

- $\text{mod}(\beta_0 - \alpha_0, 2\pi) \in \{\pi/2, 3\pi/2\}$. Here, the $[y]_H$ and $[z]_H$ motions are in phase and are either correlated or anti-correlated straight lines, whereas the $[x]_H$ and $[z]_H$ motions are out of phase, creating a $1:(B_0/A_0)$ ellipse.
- $\text{mod}(\beta_0 - \alpha_0, \pi/2) \neq 0$. Here, the $[z]_H$ motion is neither in phase nor out of phase with either the $[x]_H$ or $[y]_H$ motions, creating either correlated or anti-correlated ellipses in the $[x]_H$ - $[z]_H$ and $[y]_H$ - $[z]_H$ planes.

A.2 CW simulation cases

Dynamic scenarios in this dissertation follow CW dynamics. Additionally, the initial relative state distribution is multivariate, non-degenerate normal; i.e.,

$$\underline{\mathbf{X}}(t_0) \sim \mathcal{N}(\underline{\mu}_{\underline{\mathbf{X}}}(t_0), \Sigma_{\underline{\mathbf{X}}}(t_0)) \quad (\text{A.20})$$

Because CW dynamics are linear, the distribution of the relative state remains multivariate, non-degenerate normal; that is,

$$\underline{\mathbf{X}}(t) \sim \mathcal{N}(\underline{\mu}_{\underline{\mathbf{X}}}(t), \Sigma_{\underline{\mathbf{X}}}(t)) \quad (\text{A.21})$$

where $\underline{\mu}_{\underline{\mathbf{X}}}(t)$ and $\Sigma_{\underline{\mathbf{X}}}(t)$ are given by

$$\underline{\mu}_{\underline{\mathbf{X}}}(t) = \Phi_{j_0}(t, t_0) \underline{\mu}_{\underline{\mathbf{X}}}(t_0) \quad (\text{A.22})$$

$$\Sigma_{\underline{\mathbf{X}}}(t) = \Phi_{j_0}(t, t_0) [\Sigma_{\underline{\mathbf{X}}}(t_0)] \Phi_{j_0}^T(t, t_0) \quad (\text{A.23})$$

where $\Phi_{j_0}(t, t_0)$ is the CW STM listed in Eq. A.2. In particular, the instantaneous relative position distribution is obtained through marginalization as

$$\underline{\mathbf{R}}(t) \sim \mathcal{N}\left(\left[\mathbb{I}_3, \mathbf{0}_{3 \times 3}\right] \underline{\mu}_{\underline{\mathbf{X}}}(t), \left[\mathbb{I}_3, \mathbf{0}_{3 \times 3}\right] \Sigma_{\underline{\mathbf{X}}}(t) \left[\mathbb{I}_3, \mathbf{0}_{3 \times 3}\right]^T\right) \quad (\text{A.24})$$

Simulation cases are assumed to have a chief agent j_0 whose orbit's semimajor axis is $\bar{a}_{j_0} = 6800$ km. Then, the mean motion \bar{n}_{j_0} (in [rad/s] units) can be computed in terms of Earth's standard gravitational parameter μ_E as

$$\bar{n}_{j_0} \doteq \sqrt{\mu_E / (\bar{a}_{j_0})^3} \quad (\text{A.25})$$

where $\mu_E = 3.986004418 \times 10^5 \text{ km}^3/\text{s}^2$. The simulation horizon is two orbit periods of the chief agent, and the timestep resolution is 3.8754 seconds, which corresponds to 1/1440th of one orbit period, or 1/4th of one degree (of mean anomaly) of one revolution of the orbit of the chief spacecraft.

For simplicity, all cases have the same initial state covariance matrix $\Sigma_{\underline{\mathbf{x}}}(t_0)$, which assumed to be diagonal, as given by

$$\Sigma_{\underline{\mathbf{x}}}(t_0) = \text{diag} \left(\left[\sigma_{[x]_H}^2(t_0) \quad \sigma_{[y]_H}^2(t_0) \quad \sigma_{[z]_H}^2(t_0) \quad \sigma_{[x]_H}^2(t_0) \quad \sigma_{[y]_H}^2(t_0) \quad \sigma_{[z]_H}^2(t_0) \right] \right) \quad (\text{A.26})$$

The diagonal components of $\Sigma_{\underline{\mathbf{x}}}(t_0)$ are listed in Table A.1. The initial expected relative state $\underline{\mu}_{\underline{\mathbf{x}}}(t_0)$ is prescribed in terms of the geometric parametrization of a closed CW relative orbit as depicted in Section A.1, and these parameters are listed in Table A.2. In other words, $\underline{\mu}_{\underline{\mathbf{x}}}(t_0)$ is given by $\underline{\mu}_{\underline{\mathbf{x}}}(t_0) = \left[\underline{\mu}_{\underline{\mathbf{R}}}(t_0), \underline{\mu}_{\underline{\mathbf{R}}}(t_0) \right]$, where

$$\underline{\mu}_{\underline{\mathbf{R}}}(t_0) = \left[\bar{A}_0 \cos(\bar{\alpha}_0) \quad -2\bar{A}_0 \sin(\bar{\alpha}_0) + \bar{y}_{\text{off}} \quad \bar{B}_0 \cos(\bar{\beta}_0) \right] \quad (\text{A.27})$$

$$\underline{\mu}_{\underline{\mathbf{R}}}(t_0) = \left[-\bar{n}_{j_0} \bar{A}_0 \sin(\bar{\alpha}_0) \quad -2\bar{n}_{j_0} \bar{A}_0 \cos(\bar{\alpha}_0) \quad -\bar{n}_{j_0} \bar{B}_0 \sin(\bar{\beta}_0) \right] \quad (\text{A.28})$$

Hence, it follows from Equations A.17, A.18, and A.19 that the expected value of the distribution follows a closed CW trajectory – even though the covariance matrix may grow without bound over time.

Table A.1: Initial relative state covariance parameters

Standard deviation at t_0	Relative pos. [m]	Rel. pos. rate [m/s]
Radial direction ($[x]_H$)	10	0.25
Along-track direction ($[y]_H$)	5	0.75
Cross-track direction ($[z]_H$)	0.5	0.05

Table A.2: Initial relative state expectation parameters

Cases	Comments	A_0	B_0	\bar{y}_{off}	$\bar{\alpha}_0$	$\beta_0 - \bar{\alpha}_0$
		[km]			[deg]	
3D.001	No $[z]_H$ motion	1	0	0	0	N/A
3D.002	With $[z]_H$ motion ($[x]_H$ and $[z]_H$ motion in phase)	1	0.1	0	0	0
3D. c ($c \in \{003, 004, \dots, 026\}$)	With $[z]_H$ motion ($[x]_H$ and $[z]_H$ motion out of phase)	1	0.1	0	$15(c - 3)$ ($\bar{\alpha}_0 \in \{0, 15, \dots, 345\}$)	90

A.3 Effects of two-body relative orbital dynamics on SFF probabilistic collision risk indicators

The effects of employing CW relative orbital dynamics as the underlying dynamic model for SFF scenario simulation in this dissertation are examined as follows. An overview is provided for the process of adjusting initial relative dynamic state statistics for propagation in an inertial frame (via relative Keplerian two-body dynamics) instead of the Hill frame (via CW dynamics). Then, IPC and P_c measures based on Keplerian dynamics are computed as arising from the collision regions described in Section 10.4 (specifically, Table 10.1). Subsequently, IPC/ P_c measures based on relative Keplerian orbital dynamics are compared to those based on CW dynamics. Ensuing results are briefly discussed.

A.3.1 Setting up relative two-body propagation of a prior Hill-frame relative state sample

Let $N \in \mathbb{N}$. Let $H_j(t)$ denote the Hill frame (at time t) centered at some agent j whose inertial trajectory is a circular Keplerian orbit. This Subsection is concerned with an i.i.d. finite sample $\left\{ \left[\widehat{\mathbf{x}}_{i,j;k}(t_0) \right]_{H_j(t_0)} \right\}$ ($k \in S_N$) of $\mathbf{X}_{i,j}(t_0)$. In particular, a deterministic no-

tation of sample points is employed here (i.e., lowercase; cf. Section 2.3) because the following methodology may utilize any specific realization of a finite random sample of $\mathbf{X}_{i,j}(t_0)$. Furthermore, since the process is the same for all $k \in S_N$, $[\widehat{\mathbf{x}}_{i,j;k}(t_0)]_{H_j(t_0)}$ is referred to as $[\widehat{\mathbf{x}}_{i,j}(t_0)]_{H_j(t_0)}$ throughout the rest of this Subsection for conciseness.

Let \mathcal{I} denote an implicit inertial frame, and let PQW_i denote the i^{th} implicit perifocal frame. This Subsection describes how to obtain the i^{th} inertial position and velocity $[\widehat{\mathbf{r}}_i(t_0)]_{\mathcal{I}}$ and $[\widehat{\dot{\mathbf{r}}}_i(t_0)]_{\mathcal{I}}$ in terms of $[\widehat{\mathbf{x}}_{i,j;k}(t_0)]_{H_j(t_0)}$.

Let the initial classical orbital element set describing the \mathcal{I} -inertial two-body trajectory of agent j be given by

$$\begin{bmatrix} a_j \\ e_j \\ \text{inc}_j \\ \Omega_j \\ \omega_j \\ M_j(t_0) \end{bmatrix} = \begin{bmatrix} j^{\text{th}} \text{ semimajor axis} \\ j^{\text{th}} \text{ eccentricity} \\ j^{\text{th}} \text{ inclination} \\ j^{\text{th}} \text{ RAAN} \\ j^{\text{th}} \text{ argument of periapsis} \\ j^{\text{th}} \text{ mean anomaly at } t_0 \end{bmatrix} = \begin{bmatrix} 6800 \text{ km} \\ 0 \\ 45^\circ \\ 20^\circ \\ 10^\circ \\ 0^\circ \end{bmatrix} \quad (\text{A.29})$$

Note: the classical orbital elements $\{\text{inc}_j, \Omega_j, \omega_j, M_j(t_0)\}$ are chosen arbitrarily, whereas the $\{a_j, e_j\}$ elements are chosen for consistency with the simulation cases listed in Section A.2. Within this scenario, the central planetary mass is Earth; cf. Section A.2. The j^{th} classical orbital element set is transformed into the j^{th} inertial position and velocity $[\mathbf{r}_j]_{\mathcal{I}}$ and $[\dot{\mathbf{r}}_j]_{\mathcal{I}}$ via the process described in Ref. [185], Ch 2.

The coordinate transformation matrix from frame \mathcal{I} to the j^{th} perifocal frame, $\Xi_{\text{PQW}_j, \mathcal{I}}$, is given by[186]

$$\Xi_{\text{PQW}_j, \mathcal{I}} = A_3(\omega_j) A_1(\text{inc}_j) A_3(\Omega_j) \quad (\text{A.30})$$

whereas the coordinate transformation matrix from the j^{th} perifocal frame to the j^{th} Hill

frame at t_0 , $\Xi_{H_j(t_0),\text{PQW}_j}$, is given by[5]

$$\Xi_{H_j(t_0),\text{PQW}_j} = A_3(\theta_j(t_0)) \quad (\text{A.31})$$

where $\theta_j(t_0)$ is the j^{th} true anomaly at time t_0 ; this value is obtained by transforming the outcome of solving Kepler's equation (see Ref. [185], Ch. 4). Then, the coordinate transformation matrix from frame \mathcal{I} to the j^{th} Hill frame at t_0 , $\Xi_{H_j(t_0),\mathcal{I}}$, is given by

$$\Xi_{H_j(t_0),\mathcal{I}} = \Xi_{H_j(t_0),\text{PQW}_j} \Xi_{\text{PQW}_j,\mathcal{I}} = A_3(\omega_j + \theta_j(t_0)) A_1(\text{inc}_j) A_3(\Omega_j) \quad (\text{A.32})$$

Therefore, the i^{th} \mathcal{I} -inertial position at time t_0 , $[\hat{\mathbf{r}}_i(t_0)]_{\mathcal{I}}$, is given by

$$[\hat{\mathbf{r}}_i(t_0)]_{\mathcal{I}} = [\mathbf{r}_j(t_0)]_{\mathcal{I}} + [\Xi_{H_j(t_0),\mathcal{I}}]^T [\hat{\mathbf{r}}_{i,j}(t_0)]_{H_j(t_0)} \quad (\text{A.33})$$

and, based on the transport theorem for \mathbb{R}^3 -vector time derivatives in rotating frames, the i^{th} \mathcal{I} -inertial velocity, $[\hat{\dot{\mathbf{r}}}_i(t_0)]_{\mathcal{I}}$, is given by

$$\begin{aligned} [\hat{\dot{\mathbf{r}}}_i(t_0)]_{\mathcal{I}} &= [\dot{\mathbf{r}}_j(t_0)]_{\mathcal{I}} + [\Xi_{H_j(t_0),\mathcal{I}}]^T [\hat{\dot{\mathbf{r}}}_{i,j}(t_0)]_{H_j(t_0)} \\ &\quad + \left(\dot{\theta}_j(t_0)\right) [\Xi_{H_j(t_0),\mathcal{I}}]^T \begin{bmatrix} 0 & -1 & 0 \\ 1 & 0 & 0 \\ 0 & 0 & 0 \end{bmatrix} [\hat{\mathbf{r}}_{i,j}(t_0)]_{H_j(t_0)} \end{aligned} \quad (\text{A.34})$$

where the j^{th} true anomaly time derivative, $\dot{\theta}_j(t_0)$, may be computed as

$$\dot{\theta}_j(t_0) = \frac{\|[\mathbf{r}_j(t_0)]_{\mathcal{I}} \times [\dot{\mathbf{r}}_j(t_0)]_{\mathcal{I}}\|_2}{\|[\mathbf{r}_j(t_0)]_{\mathcal{I}}\|_2^2} \quad (\text{A.35})$$

Note: for $e_j = 0$, $\dot{\theta}_j(t_0)$ is equal to the j^{th} mean motion, n_j .

Once $[\hat{\mathbf{r}}_i(t_0)]_{\mathcal{I}}$ and $[\hat{\dot{\mathbf{r}}}_i(t_0)]_{\mathcal{I}}$ are obtained, they are mapped into the i^{th} classical orbital

element set at time t_0 (i.e., $\{\widehat{a}_i, \widehat{e}_i, \widehat{\text{inc}}_i, \widehat{\Omega}_i, \widehat{\omega}_i, \widehat{M}_i(t_0)\}$) via the process described in Ref. [185], Ch 2. Finally, by solving Kepler’s problem and by mapping propagated classical orbital elements back into inertial Cartesian elements, the i^{th} and j^{th} inertial positions at time t ($[\widehat{\mathbf{r}}_i(t)]_{\mathcal{I}}$ and $[\mathbf{r}_j(t)]_{\mathcal{I}}$, respectively) are obtained.

Consequently, instantaneous a -norm collision events in \mathbb{R}^3 are defined whenever the i^{th} position relative to agent j meets the condition

$$\|\Xi_{\mathcal{A}(t), \mathcal{I}}([\widehat{\mathbf{r}}_i(t)]_{\mathcal{I}} - [\mathbf{r}_j(t)]_{\mathcal{I}})\|_a < l_{i,j}(t) \quad (\text{A.36})$$

where $\mathcal{A}(t)$ describes the orthonormal coordinate basis of \mathbb{R}^3 at time t under which the instantaneous relative position is implicitly expressed in for the purposes of a -norm computation. For consistency of the comparison of the effects of two-body relative orbital dynamics on probabilistic SFF collision risk indicators with respect to previous CW-based indicators, the $\mathcal{A}(t)$ frame should be set to $H_j(t)$; cf. Section 10.4, where computational results are computed assuming the instantaneous relative position is always expressed in chief agent-centered Hill-frame coordinates. Note: for Euclidean norm-based collision events (i.e., where $a = 2$, or Eu), the rotation-invariant nature of the Euclidean norm renders the definition of the instantaneous a -norm collision event independent of the choice of $\mathcal{A}(t)$, e.g., the same deterministic collision condition on the i^{th} particle is obtained whether $\mathcal{A}(t) = \mathcal{I}$ or $\mathcal{A}(t) = H_j(t)$.

A.3.2 Probabilistic SFF collision risk indicators based on two-body relative orbital dynamics: simulation results

Probabilistic SFF collision risk indicators based on two-body propagation of relative orbital dynamic motion are computed in MATLAB R2020b for Examples 3D.001-026, specifically, for IPC/ P_c measures based on the Euclidean lower and upper bounds to the cylindrical orthogonal collision region (COCR) used in Section 10.4 – i.e., for collision regions

defined by origin-centered Euclidean balls in relative position space whose radii are set to joint HBR values that are scaled by factors of 1 and $\sqrt{3/2}$ (cf. Table 10.1) of the original joint HBR of 32 m employed throughout this dissertation. (For further information on this joint HBR choice, see Subsections 6.5.1, 8.2.4, 9.5.1, 10.4.1.)

Such results are summarized in Fig. A.2, which shows the relative change of the maximum P_c value based on relative two-body motion (over the propagation horizon) with respect to the maximum P_c value based on CW motion. In particular, changing the relative orbital dynamic model from CW dynamics to relative two-body dynamics results in changes to the maximum P_c value of 1.21% at most throughout all simulation cases considered.

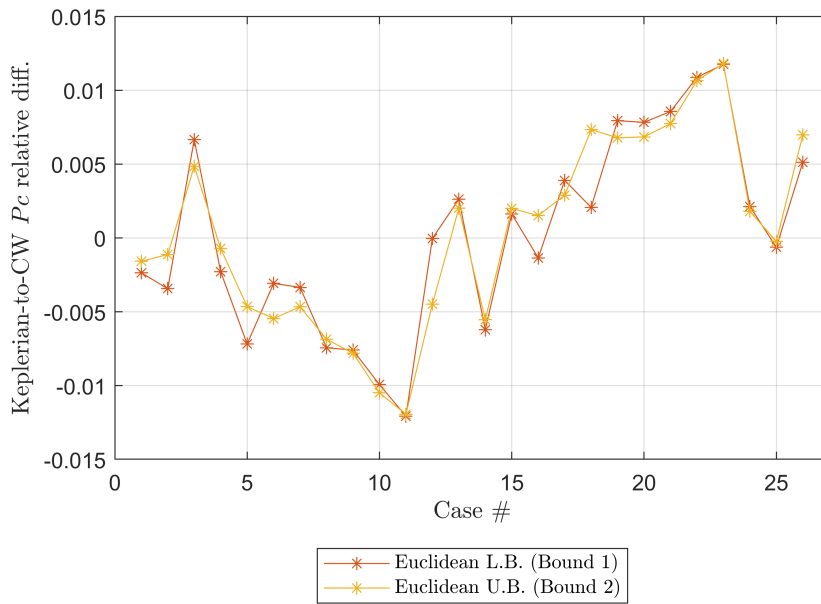


Figure A.2: Relative change of maximum P_c based on two-body relative orbital dynamics with respect to maximum P_c based on CW dynamics (Euclidean norm-based relative position space collision regions).

The close agreement observed between CW-based and two-body-based maximum P_c values suggests that, from an IPC/ P_c measure perspective, CW dynamics are an accurate representation of true SFF relative motion for the duration of the current propagation

horizon. Although this notion is validated by close agreement between CW-based and two-body-based IPC/P_c time-histories, as illustrated in Figure A.3 for Example 3D.012 (similar behavior is observed for all simulation cases), performing precise waveform analysis in order to confirm these qualitative insights is beyond the scope of this dissertation. Similarly, although similar agreement is expected for IPC/P_c arising from collision regions defined via balls (in relative position space) with respect to the L^∞ /box and cylindrical orthogonal norms, such computations are beyond the scope of this work.

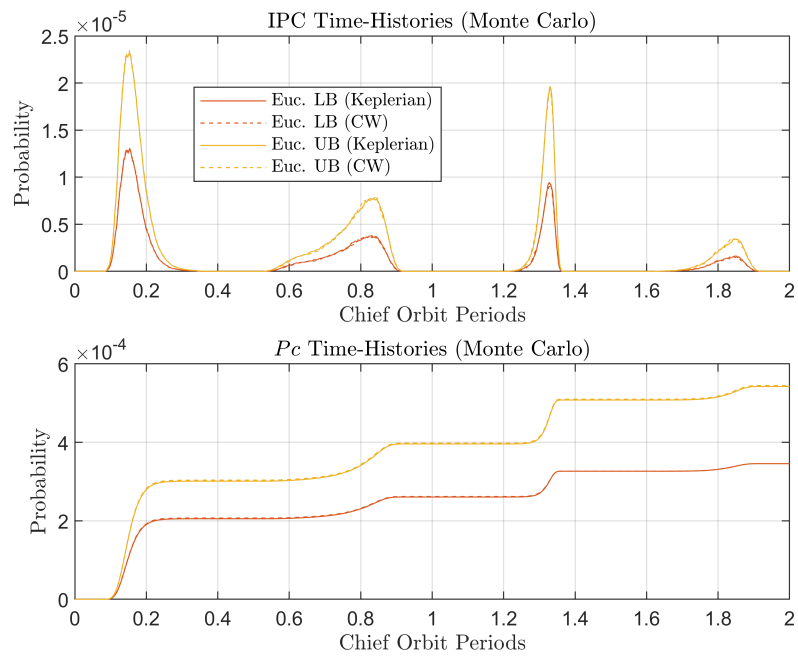


Figure A.3: Comparison of IPC and P_c waveforms, two-body- and CW-based dynamics, Euclidean-norm-based collision regions, Example 3D.012.

APPENDIX B

MONTE CARLO STOCHASTIC CONVERGENCE PROPERTIES

B.1 Monte Carlo sample estimators of mean and covariance

Let \underline{X} be a finite-dimensional random variable in \mathbb{R}^s , where $s \in \mathbb{N}$. Let $\underline{\mu} \in \mathbb{R}^s$ and $\Sigma \in \mathbb{R}^{s \times s}$ be constants such that

$$\underline{\mu} = \mathbb{E}[\underline{X}] \quad (\text{B.1})$$

$$\Sigma = \text{Cov}(\underline{X}) = \mathbb{E} \left[(\underline{X} - \mathbb{E}[\underline{X}]) (\underline{X} - \mathbb{E}[\underline{X}])^T \right] = \mathbb{E} \left[(\underline{X} - \underline{\mu}) (\underline{X} - \underline{\mu})^T \right] \quad (\text{B.2})$$

Hence, $\underline{\mu}$ and Σ are the mean and covariance of \underline{X} . By definition, $\Sigma \geq 0$, i.e., Σ is a symmetric, positive semi-definite matrix.[64]

Take $n \in \mathbb{N}$. Let $S_n = \{1, \dots, n\}$. Let $\{\underline{X}_k\}_{k \in S_n}$ be a finite collection of random variables that are mutually independent and have identical distribution (denoted as i.i.d.) as \underline{X} . Let the sample mean of \underline{X} , $\hat{\underline{\mu}}$, and the sample covariance of \underline{X} , $\hat{\Sigma}$, be defined as

$$\hat{\underline{\mu}} = \frac{1}{n} \sum_{k=1}^n \underline{X}_k \quad (\text{B.3})$$

$$\hat{\Sigma} = \frac{1}{n-1} \sum_{k=1}^n (\underline{X}_k - \hat{\underline{\mu}}) (\underline{X}_k - \hat{\underline{\mu}})^T \quad (\text{B.4})$$

For a finite sequence of i.i.d. random variables, it is a known fact that the sample mean and covariance are unbiased estimators for the actual mean and covariance; that is,

$$\mathbb{E}[\hat{\underline{\mu}}] = \underline{\mu} \quad (\text{B.5})$$

$$\mathbb{E}[\hat{\Sigma}] = \Sigma \quad (\text{B.6})$$

B.2 Monte Carlo errors in sample mean and covariance

Let $\|\cdot\|_2$ and $\|\cdot\|_F$ denote the Euclidean vector norm and the Frobenius matrix norm, respectively. (See Section 2.3.) Let the $\hat{\mu}$ -error and $\hat{\Sigma}$ -error be defined as

$$\hat{\mu}\text{-error} = \|\hat{\mu} - \mu\|_2 \quad (\text{B.7})$$

$$\hat{\Sigma}\text{-error} = \left\| \hat{\Sigma} - \Sigma \right\|_F \quad (\text{B.8})$$

Although μ and Σ are constants, $\hat{\mu}$ and $\hat{\Sigma}$ are typically not, so the $\hat{\mu}$ -error and $\hat{\Sigma}$ -error cannot be quantified precisely under this framework. However, it is possible to examine statistical properties of these errors, specifically, via moments of the distribution of these errors.

The $\hat{\mu}$ -mean error ($\hat{\mu}$ -ME) and $\hat{\Sigma}$ -mean error ($\hat{\Sigma}$ -ME) are defined as

$$\hat{\mu}\text{-ME} = \mathbb{E} [\|\hat{\mu} - \mu\|_2] \quad (\text{B.9})$$

$$\hat{\Sigma}\text{-ME} = \mathbb{E} \left[\left\| \hat{\Sigma} - \Sigma \right\|_F \right] \quad (\text{B.10})$$

Similarly, the $\hat{\mu}$ -mean square error ($\hat{\mu}$ -MSE) and $\hat{\Sigma}$ -mean square error ($\hat{\Sigma}$ -MSE) are defined as

$$\hat{\mu}\text{-MSE} = \mathbb{E} [\|\hat{\mu} - \mu\|_2^2] \quad (\text{B.11})$$

$$\hat{\Sigma}\text{-MSE} = \mathbb{E} \left[\left\| \hat{\Sigma} - \Sigma \right\|_F^2 \right] \quad (\text{B.12})$$

Finally, the $\hat{\mu}$ -root mean square error ($\hat{\mu}$ -RMSE) and $\hat{\Sigma}$ -root mean square error ($\hat{\Sigma}$ -RMSE)

are defined as

$$\hat{\underline{\mu}}\text{-RMSE} = \sqrt{\mathbb{E} [\|\hat{\underline{\mu}} - \underline{\mu}\|_2^2]} = \sqrt{\hat{\underline{\mu}}\text{-MSE}} \quad (\text{B.13})$$

$$\hat{\underline{\Sigma}}\text{-RMSE} = \sqrt{\mathbb{E} [\|\hat{\underline{\Sigma}} - \underline{\Sigma}\|_F^2]} = \sqrt{\hat{\underline{\Sigma}}\text{-MSE}} \quad (\text{B.14})$$

Since the RMSE is the square root of the MSE, convergence in the RMSE sense and the MSE sense are addressed interchangeably. It must also be noted that, although the definition of these errors is motivated by the Monte Carlo sample mean and covariance estimators, these error definitions hold for mean and covariance estimators for any sampling method.

B.3 Expressions for Monte Carlo mean-square error (MSE) in sample mean

The $\hat{\underline{\mu}}$ -error can be expressed as

$$\begin{aligned} \|\hat{\underline{\mu}} - \underline{\mu}\|_2 &= \sqrt{(\hat{\underline{\mu}} - \underline{\mu})^T (\hat{\underline{\mu}} - \underline{\mu})} \\ &= \sqrt{\text{trace} \left((\hat{\underline{\mu}} - \underline{\mu})^T (\hat{\underline{\mu}} - \underline{\mu}) \right)} \end{aligned} \quad (\text{B.15})$$

since the original expression inside the square root is a scalar. By trace properties, it follows that

$$\|\hat{\underline{\mu}} - \underline{\mu}\|_2 = \sqrt{\text{trace} \left((\hat{\underline{\mu}} - \underline{\mu}) (\hat{\underline{\mu}} - \underline{\mu})^T \right)} \quad (\text{B.16})$$

Because of the linearity of both the trace and expectation operators, it follows that the $\hat{\underline{\mu}}$ -MSE can be expressed as

$$\begin{aligned} \hat{\underline{\mu}}\text{-MSE} &= \mathbb{E} [\|\hat{\underline{\mu}} - \underline{\mu}\|_2^2] = \mathbb{E} \left[\text{trace} \left((\hat{\underline{\mu}} - \underline{\mu}) (\hat{\underline{\mu}} - \underline{\mu})^T \right) \right] \\ &= \text{trace} \left(\mathbb{E} \left[(\hat{\underline{\mu}} - \underline{\mu}) (\hat{\underline{\mu}} - \underline{\mu})^T \right] \right) \end{aligned} \quad (\text{B.17})$$

In a Monte Carlo sampling framework, it can be shown that

$$\mathbb{E} \left[(\hat{\underline{\mu}} - \underline{\mu}) (\hat{\underline{\mu}} - \underline{\mu})^T \right] = \frac{1}{n} \Sigma \quad (\text{B.18})$$

Therefore, via trace properties, the Monte Carlo $\hat{\underline{\mu}}$ -MSE can be expressed as

$$\hat{\underline{\mu}}\text{-MSE} = \mathbb{E} \left[\|\hat{\underline{\mu}} - \underline{\mu}\|_2^2 \right] = \frac{1}{n} \text{trace}(\Sigma) \quad (\text{B.19})$$

From Eq. B.19, a limiting expression for the rate of convergence of $\hat{\underline{\mu}}$ to $\underline{\mu}$ in the MSE sense may be obtained, namely,

$$\lim_{n \rightarrow \infty} n (\hat{\underline{\mu}}\text{-MSE}) = \lim_{n \rightarrow \infty} n \left(\mathbb{E} \left[\|\hat{\underline{\mu}} - \underline{\mu}\|_2^2 \right] \right) = \text{trace}(\Sigma) = \text{constant} \quad (\text{B.20})$$

In other words, asymptotically, the Monte Carlo $\hat{\underline{\mu}}$ -MSE may be modeled as being described by a power function fit of the form

$$(\hat{\underline{\mu}}\text{-MSE})(n) = (C_{\underline{\mu}}) n^{-u} \quad (\text{B.21})$$

where $C_{\underline{\mu}} = \text{trace}(\Sigma)$ and $u = 1$.

B.4 Expressions for Monte Carlo mean-square error (MSE) in sample covariance

By definition, the $\hat{\Sigma}$ -error can be expressed as

$$\left\| \hat{\Sigma} - \Sigma \right\|_F = \sqrt{\text{trace} \left(\left(\hat{\Sigma} - \Sigma \right) \left(\hat{\Sigma} - \Sigma \right)^T \right)} \quad (\text{B.22})$$

Because of the linearity of both the trace and expectation operators, it follows that the $\widehat{\Sigma}$ -MSE can be expressed as

$$\begin{aligned}\widehat{\Sigma}\text{-MSE} &= \mathbb{E} \left[\left\| \widehat{\Sigma} - \Sigma \right\|_F^2 \right] = \mathbb{E} \left[\text{trace} \left(\left(\widehat{\Sigma} - \Sigma \right) \left(\widehat{\Sigma} - \Sigma \right)^T \right) \right] \\ &= \text{trace} \left(\mathbb{E} \left[\left(\widehat{\Sigma} - \Sigma \right) \left(\widehat{\Sigma} - \Sigma \right)^T \right] \right)\end{aligned}\quad (\text{B.23})$$

Employing the expression Eq. B.23, the definition of the sample mean and covariance estimators in Eqns. B.3 and B.4, and the i.i.d. property of the elements in the sample, it can be shown that the $\widehat{\Sigma}$ -MSE in the Monte Carlo framework is given by

$$\widehat{\Sigma}\text{-MSE} = \mathbb{E} \left[\left\| \widehat{\Sigma} - \Sigma \right\|_F^2 \right] = \frac{1}{n} \text{trace} (\Delta_n) \quad (\text{B.24})$$

where the matrix $\Delta_n \in \mathbb{R}^{s \times s}$ is given by

$$\begin{aligned}\Delta_n &= \mathbb{E} [\underline{X}\underline{X}^T \underline{X}\underline{X}^T] - 4 \cdot \mathbb{E} [\underline{X}\underline{X}^T \underline{X}] \underline{\mu}^T + 4 \cdot \Sigma \underline{\mu} \underline{\mu}^T \\ &+ \frac{1}{n-1} [\text{trace} (\Sigma + \underline{\mu} \underline{\mu}^T)] (\Sigma + \underline{\mu} \underline{\mu}^T) + \frac{2(n-2)}{n-1} [\text{trace} (\underline{\mu} \underline{\mu}^T)] (\Sigma + \underline{\mu} \underline{\mu}^T) \\ &+ \frac{n}{n-1} \underline{\mu} \underline{\mu}^T \underline{\mu} \underline{\mu}^T - \frac{n-2}{n-1} \Sigma \Sigma\end{aligned}\quad (\text{B.25})$$

The expression in Eq. B.25 is given without proof. However, it may be verified through inspection that, when \underline{X} is one-dimensional, and by denoting \underline{X} as X , $\underline{\mu}$ as μ , and Σ as σ^2 , that

$$\Delta_n = \mathbb{E} [(X - \mu)^4] - \frac{(n-3)}{(n-1)} \sigma^4 \quad (\text{B.26})$$

and therefore, the expression for the $\widehat{\Sigma}$ -MSE (for this unidimensional case) coincides with the variance of the sample variance of X , which is given by [187]

$$\text{Var}(\widehat{\sigma}^2) = \frac{1}{n} \left(\mathbb{E} [(X - \mu)^4] - \frac{(n-3)}{(n-1)} \sigma^4 \right) = \frac{1}{n} \Delta_n \quad (\text{B.27})$$

From Eq. B.24, a limiting expression for the rate of convergence of $\widehat{\Sigma}$ to Σ in the MSE sense may be obtained, namely,

$$\lim_{n \rightarrow \infty} n \left(\widehat{\Sigma}\text{-MSE} \right) = \lim_{n \rightarrow \infty} n \left(\mathbb{E} \left[\left\| \widehat{\Sigma} - \Sigma \right\|_F^2 \right] \right) = \text{trace}(\Delta) = \text{constant} \quad (\text{B.28})$$

where $\Delta \in \mathbb{R}^{s \times s}$ is given by

$$\begin{aligned} \Delta &= \lim_{n \rightarrow \infty} \Delta_n \\ &= \mathbb{E} [\underline{X}\underline{X}^T \underline{X}\underline{X}^T] - 4 \cdot \mathbb{E} [\underline{X}\underline{X}^T \underline{X}] \underline{\mu}^T + 4 \cdot \Sigma \underline{\mu} \underline{\mu}^T + 2 \cdot [\text{trace}(\underline{\mu} \underline{\mu}^T)] (\Sigma + \underline{\mu} \underline{\mu}^T) \\ &\quad + \underline{\mu} \underline{\mu}^T \underline{\mu} \underline{\mu}^T - \Sigma \Sigma \quad (\text{B.29}) \end{aligned}$$

In other words, asymptotically, the Monte Carlo $\widehat{\Sigma}$ -MSE may be modeled as being described by a power function fit of the form

$$\left(\widehat{\Sigma}\text{-MSE} \right) (n) = (C_\Sigma) n^{-u} \quad (\text{B.30})$$

where $C_\Sigma = \text{trace}(\Delta)$ and $u = 1$.

B.5 Why study in Monte Carlo convergence in the RMSE sense

Theorem 57 (Jensen's inequality[85]). Let Y be a random variable with $p(a < Y < b)$ for $-\infty \leq a < b \leq \infty$. Let the function $\phi : (a, b) \rightarrow \mathbb{R}$ be convex on (a, b) . Then,

$$\mathbb{E} [\phi(Y)] \geq \phi(\mathbb{E}[Y]) \quad (\text{B.31})$$

provided $\mathbb{E}[|Y|] < \infty$ and $\mathbb{E}[|\phi(Y)|] < \infty$. Furthermore, if ϕ is a strictly convex function, then the inequality in Eq. B.31 is strict unless Y is a constant almost surely (a.s.). (Note: for any random variable, a property holds a.s. if it holds with probability 1, i.e., if it holds everywhere except maybe within a set of zero probability. The a.s. notion is analogous

to the a.e. notion, i.e., properties that hold everywhere except maybe within a set of zero measure.) \diamond

This dissertation only considers random variables that are not a.s. constants and that do not have infinite absolute moments. Letting $Y = \|\hat{\underline{\mu}} - \underline{\mu}\|_2$, and letting $\phi : \mathbb{R} \rightarrow \mathbb{R}$ satisfy

$$\phi(x) = x^2 \tag{B.32}$$

for $x \in \mathbb{R}$. Hence, ϕ is strictly convex in \mathbb{R} ; thus, Jensen's inequality implies that

$$(\hat{\underline{\mu}}\text{-ME})^2 = (\mathbb{E} [\|\hat{\underline{\mu}} - \underline{\mu}\|_2])^2 < \mathbb{E} [\|\hat{\underline{\mu}} - \underline{\mu}\|_2^2] = \hat{\underline{\mu}}\text{-MSE} < \infty \tag{B.33}$$

Similarly, letting $Y = \|\hat{\Sigma} - \Sigma\|_F$, Jensen's inequality implies that

$$(\hat{\Sigma}\text{-ME})^2 = \left(\mathbb{E} [\|\hat{\Sigma} - \Sigma\|_F]\right)^2 < \mathbb{E} [\|\hat{\Sigma} - \Sigma\|_F^2] = \hat{\Sigma}\text{-MSE} < \infty \tag{B.34}$$

Therefore, the previously obtained expressions for the precise Monte Carlo convergence rate in the MSE sense cannot be used to obtain a similarly precise rate of convergence in the ME sense. It should be noted, however, that Eqns. B.33 and B.34 do imply that

$$\lim_{n \rightarrow \infty} n (\hat{\underline{\mu}}\text{-ME})^2 \leq \lim_{n \rightarrow \infty} n (\hat{\underline{\mu}}\text{-MSE}) = \text{tr}(\Sigma) \tag{B.35}$$

$$\lim_{n \rightarrow \infty} n (\hat{\Sigma}\text{-ME})^2 \leq \lim_{n \rightarrow \infty} n (\hat{\Sigma}\text{-MSE}) = \text{tr}(\Delta) \tag{B.36}$$

which shows that $\hat{\underline{\mu}}\text{-ME} = \mathcal{O}(n^{-1/2})$ and $\hat{\Sigma}\text{-ME} = \mathcal{O}(n^{-1/2})$, i.e., that the convergence rates for the sample mean and covariance in the ME sense are no worse than decrease at a $n^{-1/2}$ rate.

For an arbitrary real-valued measurable function ϕ with real domain, Jensen's gap is

defined as

$$J(\phi, Y) = \mathbb{E}[\phi(Y)] - \phi(\mathbb{E}[Y]) \quad (\text{B.37})$$

Typically, ascertaining the value of $J(\phi, Y)$ is just as difficult as establishing the value of $\phi(\mathbb{E}[Y])$ itself; hence, research related to Jensen's gap focuses on finding upper and lower bounds for it, and such bounds are dependent on the specific distribution of Y . [188]

Since the precise Monte Carlo convergence rate in the MSE sense is not distribution-dependent, it is ideal to use this MSE convergence rate as a theoretical benchmark against which the statistical convergence properties of other sampling methods may be compared.

B.6 Probability measure estimators in the Monte Carlo sense

Let $E \subseteq \mathbb{R}^s$ be a measurable subset of \mathbb{R}^s . Let $f_E : \mathbb{R}^s \rightarrow \{0, 1\}$ satisfy

$$f_E(\underline{x}) = \begin{cases} 1 & \text{if } \underline{x} \in E \\ 0 & \text{otherwise} \end{cases} \quad (\text{B.38})$$

for $\underline{x} \in \mathbb{R}^s$. Hence, f_E is the characteristic function of E . Let $B_E = f_E(\underline{X})$. Then, B_E is a Bernoulli random variable, and $\text{pmf}_{B_E} : \mathbb{R} \rightarrow [0, 1]$ satisfies

$$\text{pmf}_{B_E}(b) = \begin{cases} p_E & \text{if } b = 1 \\ 1 - p_E & \text{if } b = 0 \\ 0 & \text{otherwise} \end{cases} \quad (\text{B.39})$$

where $p_E \in [0, 1]$ is defined as

$$p_E = p_{\underline{X}}(E) = p(\underline{X} \in E) \quad (\text{B.40})$$

It should be noted that

$$\mathbb{E} [B_E] = p_E \quad (\text{B.41})$$

$$\text{Var} (B_E) = p_E (1 - p_E) \quad (\text{B.42})$$

For an i.i.d. sample of \underline{X} , $\{\underline{X}_k\}_{k \in S_n}$, the i.i.d. property is retained under transformations of elements in the collection. Hence, $\{f_E(\underline{X}_k)\}_{k \in S_n}$ is an i.i.d. sample of B_E . Therefore, MC estimators of the mean and variance of B_E are the same as listed in Subsubsection B.1, and error definitions (that is, ME, MSE, and RMSE) for MC estimators are the same as listed in Subsubsection B.2. The expressions for the $\hat{\underline{\mu}}$ -MSE and $\hat{\underline{\Sigma}}$ -MSE rate of convergence may be further simplified as given by

$$(\hat{\underline{\mu}}\text{-MSE}) (n) = [p_E (1 - p_E)] n^{-u} \quad (\text{B.43})$$

$$(\hat{\underline{\Sigma}}\text{-MSE}) (n) = [p_E (1 - 5p_E + 8p_E^2 - 4p_E^3)] n^{-u} \quad (\text{B.44})$$

where $a = 1$, as before. As implied by Eq. B.42, if $p_E \in \{0, 1\}$, then $B_E = 0$ or 1 a.s., which would imply, in this case, that

$$\hat{\underline{\mu}}\text{-ME} = \hat{\underline{\mu}}\text{-MSE} = \hat{\underline{\mu}}\text{-RMSE} = 0 \quad (\text{B.45})$$

$$\hat{\underline{\Sigma}}\text{-ME} = \hat{\underline{\Sigma}}\text{-MSE} = \hat{\underline{\Sigma}}\text{-RMSE} = 0 \quad (\text{B.46})$$

B.7 Monte Carlo estimators for the instantaneous probability of collision (IPC)

Let $\underline{\mathbf{X}}$ and $\underline{\mathbf{R}}$ denote random vectors in \mathbb{R}^3 and \mathbb{R}^6 , respectively, that represent the CW relative position and the CW relative state, respectively. Let $\{\underline{\mathbf{R}}_k\}_{k \in S_n}$ and $\{\underline{\mathbf{X}}_k\}_{k \in S_n}$ be collections of random vectors that are i.i.d. as $\underline{\mathbf{R}}$ and $\underline{\mathbf{X}}$, respectively. Let $E_{C, \underline{\mathbf{R}}} \subseteq \mathbb{R}^3$ and

$E_{C, \underline{\mathbf{x}}} \subseteq \mathbb{R}^6$ be the sets defined as

$$E_{C, \underline{\mathbf{R}}} = \mathbb{B}_{l_{i,j}}^{3|\text{Eu}}(\mathbf{0}_{3 \times 1}) = \{\underline{\mathbf{x}} \in \mathbb{R}^3 : \|\underline{\mathbf{x}}\|_2 < l_{i,j}\} \quad (\text{B.47})$$

$$E_{C, \underline{\mathbf{x}}} = \left\{ \underline{\mathbf{x}} \in \mathbb{R}^6 : \left\| \begin{bmatrix} \mathbb{I}_3 & \mathbf{0}_{3 \times 3} \end{bmatrix} \underline{\mathbf{x}} \right\|_2 < l_{i,j} \right\} \quad (\text{B.48})$$

Then, the MC sample estimators of the IPC based on $\underline{\mathbf{R}}$ and $\underline{\mathbf{x}}$, $\widehat{\text{IPC}}_{\underline{\mathbf{R}}}$ and $\widehat{\text{IPC}}_{\underline{\mathbf{x}}}$, respectively, are given by

$$\widehat{\text{IPC}}_{\underline{\mathbf{R}}} = \frac{1}{n} \sum_{k=1}^n f_{E_{C, \underline{\mathbf{R}}}}(\underline{\mathbf{R}}_k) \quad (\text{B.49})$$

$$\widehat{\text{IPC}}_{\underline{\mathbf{x}}} = \frac{1}{n} \sum_{k=1}^n f_{E_{C, \underline{\mathbf{x}}}}(\underline{\mathbf{x}}_k) \quad (\text{B.50})$$

where $f_{E_{C, \underline{\mathbf{R}}}} : \mathbb{R}^3 \rightarrow \{0, 1\}$ and $f_{E_{C, \underline{\mathbf{x}}}} : \mathbb{R}^6 \rightarrow \{0, 1\}$ are the characteristic functions of $E_{C, \underline{\mathbf{R}}}$ and $E_{C, \underline{\mathbf{x}}}$, respectively. It can be verified that both $\widehat{\text{IPC}}_{\underline{\mathbf{R}}}$ and $\widehat{\text{IPC}}_{\underline{\mathbf{x}}}$ are unbiased estimators for the IPC; that is,

$$\mathbb{E} \left[\widehat{\text{IPC}}_{\underline{\mathbf{R}}} \right] = \mathbb{E} \left[\widehat{\text{IPC}}_{\underline{\mathbf{x}}} \right] = \text{IPC} \quad (\text{B.51})$$

APPENDIX C

MONTE CARLO STOCHASTIC LARGE SAMPLE MANAGEMENT

C.1 Introduction

This Chapter describes the computational aspects of Monte Carlo simulation as implemented in this dissertation for the purpose of estimating SFF distance, probabilistic, and hybrid collision risk indicators. Monte Carlo sample size requirements are explored with the goal of adequately reproducing the probability of low-likelihood events. Second, given that large sample sizes are employed, a technique for partitioning and parallelizing the propagation and processing of such samples is presented.

C.2 Notation adjustments for this Chapter

Throughout this Chapter, unless otherwise noted, SFF collision risk indicators, whether instantaneous or joint-time, are based on underlying collision conditions in relative position space expressed in terms of the violation of minimum norm conditions with respect to the Euclidean norm only, specifically, with respect to time-invariant joint-hard body radii $l_{i,j}$ (cf. Subsections 6.2.1, 8.2.1, and 9.2.1, and Section 7.2). While the i, j subscripts are omitted from the notation of relative state and relative position vectors (whether deterministic or random), it is implied that such vectors are i, j -relative in the sense of Section 2.2. Additionally, agent subscripts are omitted from the CW relative state transition matrix, which is listed in Eq. A.2.

C.3 Monte Carlo (MC) sample requirements

The goal of Conjecture 58 is to introduce and justify a practical requirement for Monte Carlo sample size as a function of the probabilistic threshold of event significance.

Note: Conjecture 58 is not rigorously proven; therefore, it is only motivated. Nonetheless, application of Conjecture 58 has been resulted in sufficiently large MC samples for the purposes of this work.

Conjecture 58. Suppose that a Monte Carlo (MC) sample is made of a non-degenerate multivariate normal distribution. Suppose that events with a probability of p_{req} or lower can be ignored. Then, it is expected that significant events (i.e., events with probability greater or equal to than p_{req}) can be captured with a sample size N_{MC} that satisfies

$$N_{\text{MC}} \geq 30 \left\lceil \frac{1}{p_{\text{req}}} \right\rceil \quad (\text{C.1})$$

Motivation. This conjecture has the following working assumptions:

1. Any particle in the empirical MC distribution is equally likely to be drawn. For further background on empirical distributions, the reader is encouraged to consult Ref. [73], Ch. 8. Note: since elements of an MC sample are i.i.d., this assumption is justified.
2. The empirical MC distribution represents the underlying distributions adequately; that is, the empirical MC distribution is multivariate non-degenerate normal in initial relative state space (cf. Eq. A.20), and χ_s^2 on the space of the Mahalanobis distance of the initial relative state (cf. Eqns. 6.9 and 6.13), where s denotes the dimension of elements in the sample. Note: this assumption holds when averaging over all possible MC samples of fixed size. However, this might not be (and is generally not) true for a specific fixed-size Monte Carlo sample realization.
3. At least one more significant digit for the probability resolution of single particle events is needed beyond the probabilistic significance requirement. This assumption is made in order to ensure that any events that are insignificant can be disregarded correctly. For example, if $p_{\text{req}} = 1 \times 10^{-7}$, then any events with probability between

5×10^{-8} and 15×10^{-8} would satisfy such a criterion, even though some events would be significant and others would not.

First, this analysis begins by obtaining a worst case estimate of the most extreme events that would need to be captured by a MC sample, as measured by the Mahalanobis distance (MHD). This analysis employs the notion of sample leftover particles, denoted by N_{Leftover} , which are the particles in MC sample that can be expected to have an MHD value beyond some d in $(0, \infty)$. The number of sample leftover particles can be computed as

$$N_{\text{Leftover}}(N_{\text{sample}}, d) = \lfloor N_{\text{sample}} (1 - \text{cdf}_{\chi_s^2}(d^2)) \rfloor \quad (\text{C.2})$$

The notion of sample leftover particles is illustrated in Fig. C.1. In accordance with intuition, more extreme cases (as measured by MHD) can be found in MC samples with larger sample sizes.

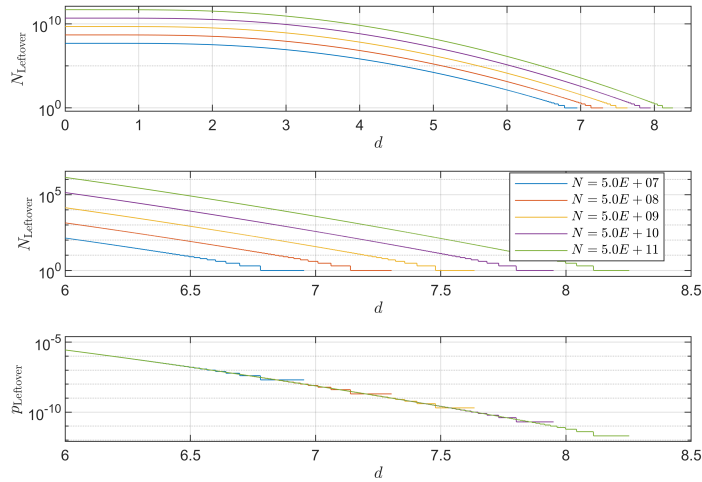


Figure C.1: Notion of sample leftover points, N_{Leftover} (see Eq. C.2) for multivariate normal distributions (in six dimensions): (top) N_{Leftover} , $d \in [0, 8.5]$; (middle) N_{Leftover} , closeup; (bottom) probability of sample points at MHD greater than or equal to d .

Additionally, it is clear that the most extreme expected event in a MC sample (i.e., the event that occurs before a MC sample can no longer be expected to describe any events)

occurs at $N_{\text{Leftover}} = 1$, which implies that

$$N_{\text{sample}} (1 - \text{cdf}_{\chi_s^2}(d^2)) \in [0.5, 1.5] \quad (\text{C.3})$$

which, in turn, implies that $d \in [d_{\text{LB}}, d_{\text{UB}}]$, where d_{LB} and d_{UB} satisfy

$$\text{cdf}_{\chi_s^2}(d_{\text{LB}}^2) = 1 - \frac{1.5}{N_{\text{sample}}} \quad (\text{C.4})$$

$$\text{cdf}_{\chi_s^2}(d_{\text{UB}}^2) = 1 - \frac{0.5}{N_{\text{sample}}} \quad (\text{C.5})$$

Given that elements of an MC sample are i.i.d., all elements of the sample are equally likely to have been drawn. Hence, the probability of the most extreme event in an MC sample (i.e., the sample point with largest MHD value) is the same as that of any other element of the sample. Thus, a naïve estimate of N_{sample} , $N_{\text{sample}}^{\text{naïve}}$, would be

$$N_{\text{sample}}^{\text{naïve}} = \left\lceil \frac{1}{p_{\text{req}}} \right\rceil \quad (\text{C.6})$$

However, because another significant digit of resolution is needed beyond the p_{req} requirement (cf. Assumption 3), a better first estimate of the sample size, N_{sample}^- , is defined as

$$N_{\text{sample}}^- = 10 \left\lceil \frac{1}{p_{\text{req}}} \right\rceil \quad (\text{C.7})$$

Hence, the worst-case MHD requirement (i.e., the MHD of the most extreme event that must be included in the MC sample) is d_{UB}^- , which is implicitly defined by

$$\text{cdf}_{\chi_s^2}((d_{\text{UB}}^-)^2) = 1 - \frac{0.5}{N_{\text{sample}}^-} \quad (\text{C.8})$$

Let d^+ denote the largest MHD value that an MC sample is able to provide; i.e., d^+ is the

largest MHD of any point in an MC sample. Then, d^+ must be at least as large as d_{UB}^- , i.e.,

$$d^+ \geq d_{\text{UB}}^- \quad (\text{C.9})$$

Therefore, because of rounding (cf. Eqns. C.2 and C.3), the minimum value of d^+ that an MC sample is able to provide is given by $d^+ = d_{\text{LB}}^+$, which satisfies

$$\text{cdf}_{\chi_s^2} \left((d_{\text{LB}}^+)^2 \right) = 1 - \frac{1.5}{N_{\text{sample}}^+} \quad (\text{C.10})$$

Thus,

$$\text{cdf}_{\chi_s^2} \left((d^+)^2 \right) \geq \text{cdf}_{\chi_n^2} \left((d_{\text{LB}}^+)^2 \right) = 1 - \frac{1.5}{N_{\text{sample}}^+} \geq 1 - \frac{0.5}{N_{\text{sample}}^-} \quad (\text{C.11})$$

which in turn implies that

$$N_{\text{sample}}^+ \geq 3N_{\text{sample}}^- = 30 \left\lceil \frac{1}{p_{\text{req}}} \right\rceil \quad (\text{C.12})$$

At this stage, suppose that the sample size, N_{MC} , satisfies

$$N_{\text{MC}} \geq N_{\text{sample}}^+ \geq 30 \left\lceil \frac{1}{p_{\text{req}}} \right\rceil \quad (\text{C.13})$$

As shown previously (cf. Eqns. C.4 and C.5), under the current assumptions,

$$d^{\text{MC}} \in [d_{\text{LB}}^{\text{MC}}, d_{\text{UB}}^{\text{MC}}] \quad (\text{C.14})$$

where $d_{\text{LB}}^{\text{MC}}$ and $d_{\text{UB}}^{\text{MC}}$ satisfy

$$\text{cdf}_{\chi_s^2} \left((d_{\text{LB}}^{\text{MC}})^2 \right) = 1 - \frac{1.5}{N_{\text{MC}}} \quad (\text{C.15})$$

$$\text{cdf}_{\chi_s^2} \left((d_{\text{UB}}^{\text{MC}})^2 \right) = 1 - \frac{0.5}{N_{\text{MC}}} \quad (\text{C.16})$$

Thus, it is expected that

$$d^{\text{MC}} \geq d_{\text{LB}}^{\text{MC}} \geq d_{\text{LB}}^+ \geq d_{\text{UB}}^- \geq d^- \quad (\text{C.17})$$

which shows that, in a probabilistic sense, the MC sample is able to capture as many extreme cases as needed. From this statement, it also follows that

$$\text{cdf}_{\chi_s^2} \left((d^{\text{MC}})^2 \right) \geq \text{cdf}_{\chi_s^2} \left((d_{\text{LB}}^{\text{MC}})^2 \right) \geq \text{cdf}_{\chi_s^2} \left((d_{\text{UB}}^-)^2 \right) \geq \text{cdf}_{\chi_s^2} \left((d^-)^2 \right) \quad (\text{C.18})$$

Thus, via Eqns. C.7 and C.11, Eq. C.18 implies that

$$1 - \frac{1}{N_{\text{MC}}} \geq 1 - \frac{1.5}{N_{\text{MC}}} \geq 1 - \frac{0.5}{N_{\text{sample}}} \geq 1 - \frac{1}{N_{\text{sample}}} = 1 - 10 \left[\frac{1}{p_{\text{req}}} \right] \geq 1 - \frac{10}{p_{\text{req}}} \quad (\text{C.19})$$

Let p_{MC} denote the empirical probability of any individual particle in an MC sample with size N_{MC} . That is, p_{MC} is given by

$$p_{\text{MC}} = \frac{1}{N_{\text{MC}}} \quad (\text{C.20})$$

Therefore, it follows that

$$p_{\text{MC}} \leq \frac{1}{10} p_{\text{req}} \quad (\text{C.21})$$

as desired. ■

In this dissertation, it is assumed that Conjecture 58 holds. An argument based on NASA CARA practice,[29] detailed in Subsection 8.4.1, is used to establish that IPC and Pc values less than 1×10^{-7} may be regarded as operationally insignificant for the purposes of this dissertation. Thus, $p_{\text{req}} = 1 \times 10^{-7}$, which implies that the MC sample size, N_{MC} , should satisfy $N_{\text{MC}} \geq 3.0 \times 10^8$. The sample size N_{MC} is chosen as $N_{\text{MC}} = 3.2 \times 10^8$, which is sufficiently large according to Conjecture 58.

C.4 MC sample propagation and data reduction process

The large MC sample size requirement is the main driving factor for the technique implemented for sample generation and data reduction. The MC sample management framework employed in this dissertation has three broad steps: sample generation, intermediate data reduction, and aggregation of intermediate results into sample-level results.

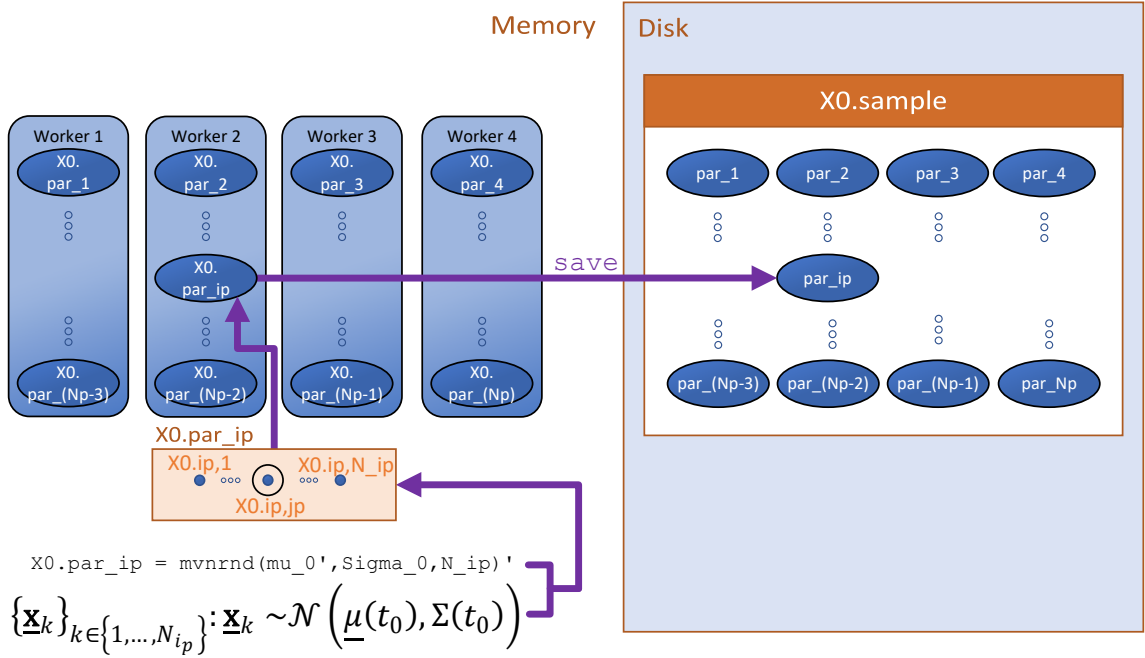


Figure C.2: MC sample processing Step 1 (sample generation).

C.4.1 Step 1: MC sample generation

Step 1, MC sample generation, is illustrated in Fig. C.2. For each relative orbital dynamic case considered (see Section A.2), Monte Carlo samples of the initial relative state are made in MATLAB R2020b through the `mvnrnd` function,[127] by employing the Mersenne Twister pseudo-random number generator. Each element in the sample is a 6×1 double array. Since variables with double precision occupy 8 bytes in memory, 14.3 GiB of memory are required to store the generated sample; much more memory usage is required to generate or process the sample. Taking advantage of the fact that the underlying dynamic

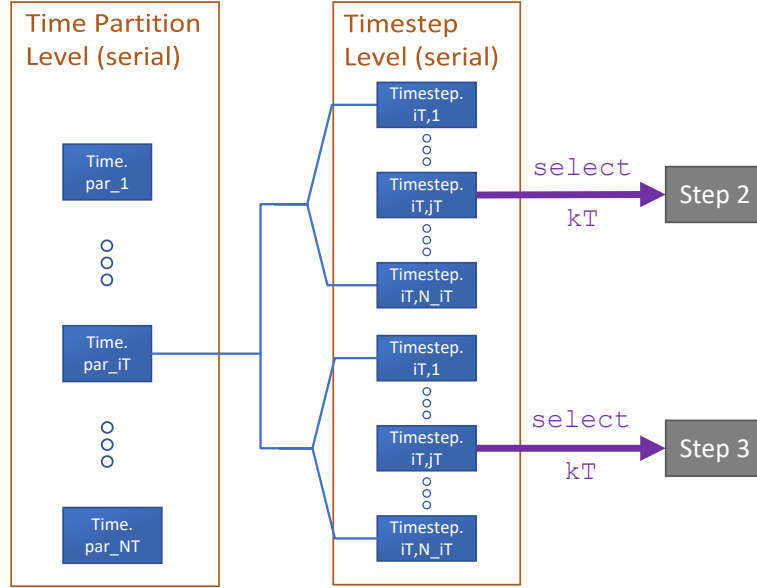


Figure C.3: MC sample processing Steps 2 and 3 (high level logic).

process is linear, time-invariant (LTI), the sample is generated once and stored into sample partitions (as shown in Fig. C.2), and each partition is loaded and propagated in accordance with the current timestep. For this specific implementation, it is assumed that each sample partition has 8×10^6 elements, which yields 40 sample partitions. After compression, each $\times 0$ sample partition occupies 347 MiB in disk, with 13.5 GiB disk space for the entire $\times 0$ sample.

Even though linear, time-invariant (LTI) dynamics could allow for parallelization of code execution in sample elements time as well as in time, sample estimation of the joint-time probability of collision (P_c) indicator does not allow for parallelization in time. In this framework, the sample P_c estimator at timestep t_c is the fraction of sample particles which have collided at any time between the initial and current timesteps t_0 and t_c , respectively; cf. Definition 9. Thus, given that particles at any timestep are dynamically coupled with themselves at the immediately preceding timestep, sample management execution must be serial in time.

Nevertheless, time partitions are also implemented in order to be enable sample estimate of $\rho_{3\sigma}$, i.e., the hybrid SFF collision risk indicator defined as Methodology 3. In particular,

the Euclidean norm of the relative position (i.e., inter-agent Euclidean distances) of every element in the entire MC sample must be processed together at once in order to compute sample percentiles. Time partitions are meaningful sets of timesteps within which sample distances are stored to disk, and after which the required sample percentiles can be computed. Then, sample inter-agent Euclidean distances may be deleted in order to free space in disk for further saving to disk in the next time partition. Fig. C.3 illustrates how Steps 2 and 3 are called within serial execution in time partitions and timesteps.

C.4.2 Step 2: intermediate data reduction

In Step 2, illustrated in Fig. C.4, after sample generation, X_0 sample partitions are processed in parallel using the MATLAB Parallel Computing Toolbox, mainly through usage of `parfor` (“parallel for”) loops. Through these loops, MATLAB processing engines called “workers” take advantage of multi-core processors by having such workers execute individual loop iterations simultaneously.[129] Thus, processing of sample partitions is done in parallel, with the allocation and monitoring of worker execution being automatically handled in the background. In this specific implementation (i.e., with the specific processor and MATLAB version utilized), MATLAB is able to task 4 workers through the Parallel Computing Toolbox.

C.4.2.1 Step 2: conceptual description

For each sample element, the Euclidean norm of the relative position is computed. Instantaneous collision indicators are computed by checking whether the Euclidean norm of relative position exceeds the joint hard-body radius specified, where the outcome of this check is a Boolean variable. Cumulative collision indicators are computed by applying an OR operation to both instantaneous collision indicators and the cumulative collision indicators from the previous timestep. (Cumulative collision indicators are initialized as logical `false` values, and since they are needed at the next timestep, they are stored to disk,

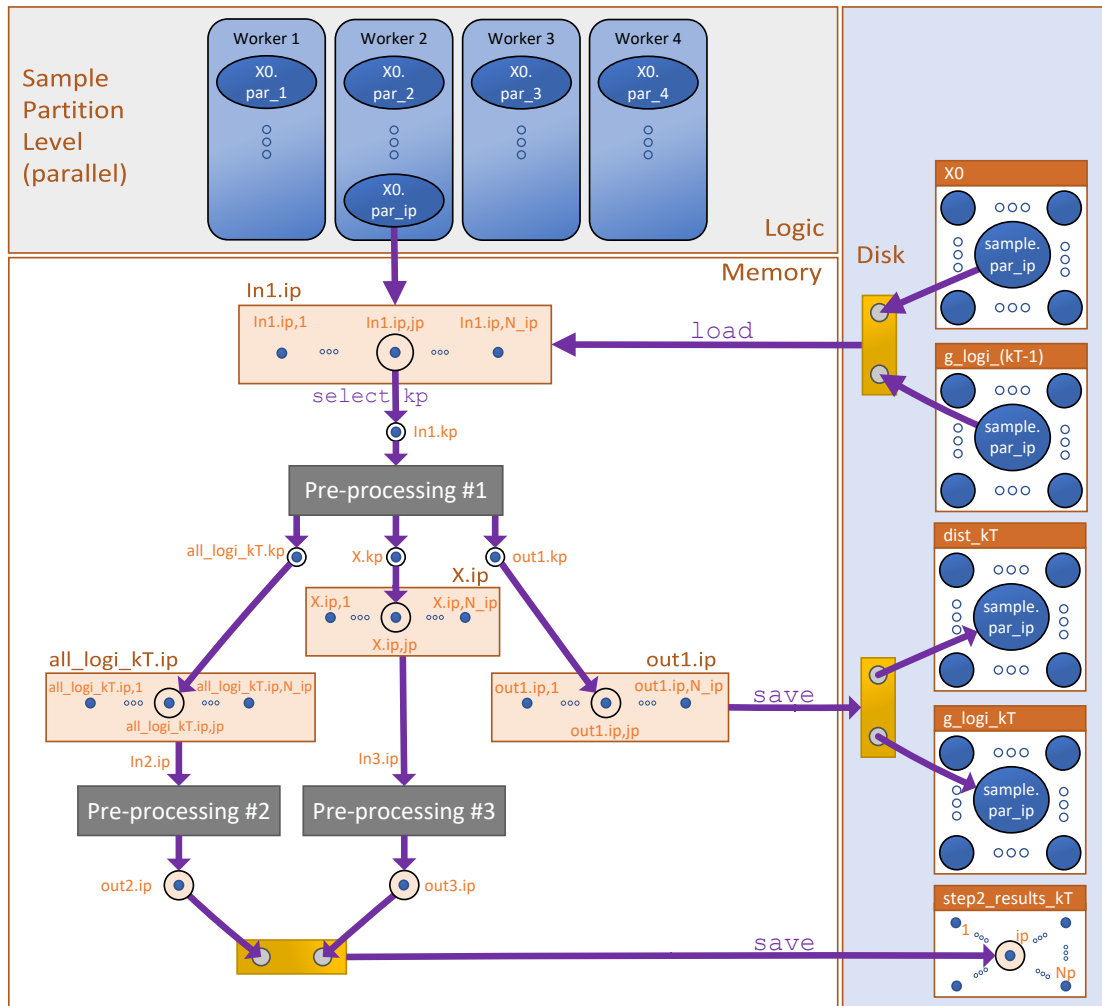


Figure C.4: MC sample processing Step 2.

retrieved, and deleted when appropriate.)

The Euclidean norm of the relative position for every particle in the relative state sample (i.e., the entire sample of the Euclidean norm of the relative position) is stored to disk for each timestep because, in order to compute sample percentiles, the entire sample (2.25 GiB per timestep) must be processed at once.

C.4.2.2 Step 2: algorithmic implementation

Let g_logi denote the cumulative collision indicator of a particle in the MC sample as described in Subsubsection C.4.2.1; hence, g_logi denotes a time-“global” collision “log-

ical” or boolean indicator. In Step 2, when a specific partition is tasked to a worker, the corresponding partition X_0 sample and partition cumulative g_{logi} sample are loaded into the workspace of such worker. Then, each particle in the partition sample is passed through the Pre-processing #1 subroutine illustrated in Fig. C.5, which consists of the following tasks: relative state propagation, computation of the Euclidean distance from the particle to the origin, instantaneous determination of collision in the sense of Proposition 6 (denoted by c_{logi} , which encodes a “current” collision “logical” or boolean indicator), and ongoing determination of collision in the sense of the g_{logi}/Pc indicator. After the Pre-processing #1 subroutine, the partition g_{logi} sample and the partition inter-agent Euclidean distance sample are stored to disk.

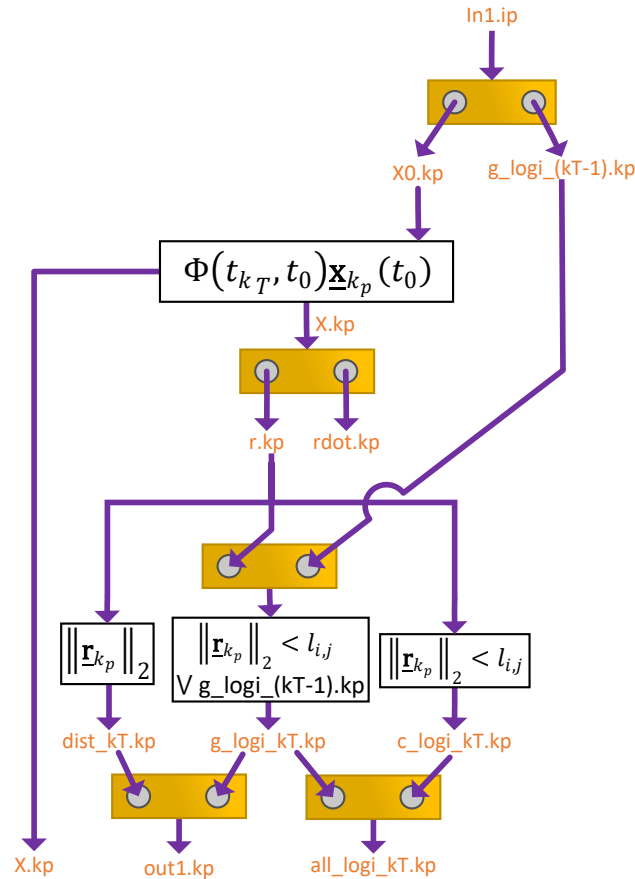


Figure C.5: MC sample processing, Step 2, Pre-processing #1 subroutine.

Before Step 2 is finished, two more intermediate processing tasks are needed. First, in the Pre-processing #2 subroutine, the current and ongoing collision indicators are simply

aggregated into final tallies, as shown in Fig. C.6. Second, in the Pre-processing #3 subroutine, X partition sample moments (mean and covariance) are computed and then slightly modified in order to more easily compute the moments (mean and covariance) of the overall sample, as shown in Fig. C.7. Third, the outcomes of the Pre-processing #2 and #3 subroutines are stored to disk, as illustrated in Fig. C.4.

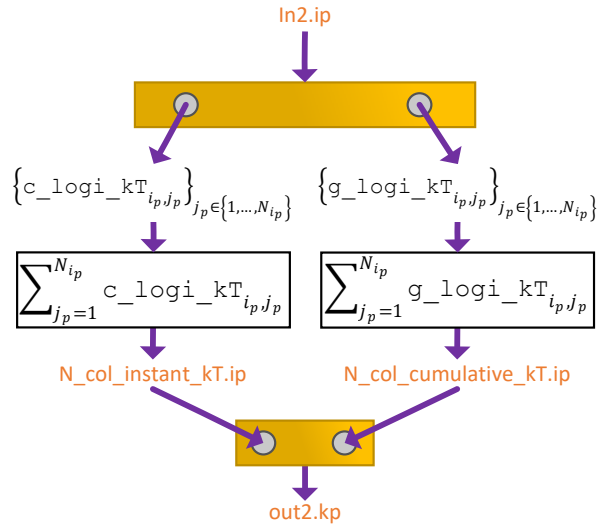


Figure C.6: MC sample processing, Step 2, Pre-processing #2 subroutine.

C.4.3 Step 3: aggregation of final results

Finally, in Step 3, intermediate, partition-level MC sample results are aggregated into overall results for SFF collision risk indicators based on MC sample estimates.

C.4.3.1 Step 3: conceptual description

Using the instantaneous and cumulative collision indicators previously stored in Step 2, sample IPC and P_c estimates are computed as the number of particles colliding (instantaneously and cumulatively, respectively) divided by the number of sample particles.

In order to quantify MC sample $\rho_{3\sigma}$ estimates, the entire inter-agent Euclidean distance sample (stored to disk in Step 2) is loaded into memory; subsequently, the sample $\rho_{3\sigma}$ is estimated as the $100p_{3\sigma}\%$ -percentile of this sample, as computed through the `prctile`

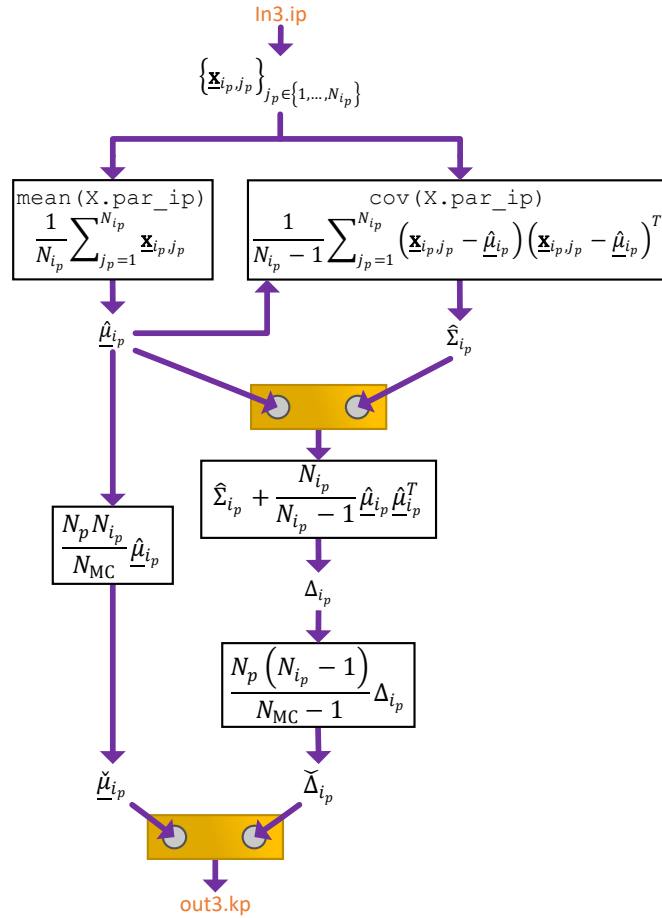


Figure C.7: MC sample processing, Step 2, Pre-processing #3 subroutine.

function.[127]

C.4.3.2 Step 3: algorithmic implementation

- Step 3.1: Compute IPC.

- Input: all_N_col_instant_kT

Vector of size N_p whose entries represent the number of particles within each sample partition that are colliding at timestep.kT (see Fig. C.3).

- Output: $\widehat{\text{IPC}}_{i,j}(t_{k_T})$ (sample $\text{IPC}_{i,j}$ at timestep.kT)

– Process:

$$\widehat{\text{IPC}}_{i,j}(t_{k_T}) = \frac{1}{N_{\text{MC}}} \sum_{i_p=1}^{N_p} \text{all_N_col_instant_kT_ip} \quad (\text{C.22})$$

• Step 3.2: Compute Pc .

– Input: `all_N_col_cumulative_kT`

Vector of size N_p whose entries represent the number of particles within each sample partition that have collided at any timestep between t_0 and `timestep.kT`.

– Output: $\widehat{P}c_{i,j}[t_0, t_{k_T}]$ (sample $Pc_{i,j}$ over $[t_0, t_{k_T}]$ time interval)

Sample estimate of the i - j joint-time probability of collision over the time interval $[t_0, t_{k_T}]$, i.e, the probability that agents i and j have collided at any time in the time interval $[t_0, t_{k_T}]$.

– Process:

$$\widehat{P}c_{i,j}[t_0, t_{k_T}] = \frac{1}{N_{\text{MC}}} \sum_{i_p=1}^{N_p} \text{all_N_col_cumulative_kT_ip} \quad (\text{C.23})$$

• Step 3.3: Compute MC sample statistics.

– Input: $\{\check{\mu}_{i_p}\}_{i_p \in \{1, \dots, N_p\}}$ and $\{\check{\Delta}_{i_p}\}_{i_p \in \{1, \dots, N_p\}}$

Collections of MC sample-based \mathbf{X} pseudo-mean and pseudo-covariance values, respectively, taken over each sample partition (see Fig. C.7) at `timestep.kT`.

– Output: \mathbf{X} sample mean $\hat{\mu}_{\mathbf{X}}$ and sample covariance $\hat{\Sigma}_{\mathbf{X}}$

– Process:

$$\hat{\mu}_{\mathbf{X}} = \frac{1}{N_p} \sum_{i_p=1}^{N_p} \check{\mu}_{i_p} \quad (\text{C.24})$$

$$\hat{\Sigma}_{\mathbf{X}} = -\frac{N_{\text{MC}}}{N_{\text{MC}} - 1} \hat{\mu}_{\mathbf{X}} \hat{\mu}_{\mathbf{X}}^T + \frac{1}{N_p} \sum_{i_p=1}^{N_p} \check{\Delta}_{i_p} \quad (\text{C.25})$$

- Step 3.4: Compute distance-based SFF collision risk indicators (i.e., Methodologies 1 & 2).

- Input: \mathbb{R} sample mean $\hat{\underline{\mu}}_{\mathbf{R}}$ and sample covariance $\hat{\underline{\Sigma}}_{\mathbf{R}}$, and corresponding MHDs (d_{m_1} and d_{m_2}) at `timestep.kT`. (Note: $\hat{\underline{\mu}}_{\mathbf{R}}$ and $\hat{\underline{\Sigma}}_{\mathbf{R}}$ are obtained by inspection from $\hat{\underline{\mu}}_{\mathbf{X}}$ and $\hat{\underline{\Sigma}}_{\mathbf{X}}$, respectively.)
- Output: $\widehat{\text{sep}}_{i,j}^{m_1}(t_{k_T})$ and $\widehat{\text{sep}}_{i,j}^{m_2}(t_{k_T})$
- Process: The function `dist_to_Ld_R3` refers to the algorithm described in Section 7.4 for computing the minimum inter-agent Euclidean distance from the origin of relative position space in \mathbb{R}^3 to $L_d(\mathbf{R})$, computed using MC sample statistics of relative position. Thus,

$$\widehat{\text{sep}}_{i,j}^{m_1}(t_{k_T}) = \text{dist_to_Ld_R3}(\hat{\underline{\mu}}_{\mathbf{R}}, \hat{\underline{\Sigma}}_{\mathbf{R}}, d_{m_1}) \quad (\text{C.26})$$

$$\widehat{\text{sep}}_{i,j}^{m_2}(t_{k_T}) = \text{dist_to_Ld_R3}(\hat{\underline{\mu}}_{\mathbf{R}}, \hat{\underline{\Sigma}}_{\mathbf{R}}, d_{m_2}) \quad (\text{C.27})$$

- Step 3.5: Compute hybrid SFF collision risk indicators (i.e., Methodology 3).

- Input: $\{\|\mathbf{r}_q\|_2\}_{q \in \{1, \dots, N_{\text{MC}}\}}$ (`all_dist_kT`)
Euclidean distance from origin of relative position space (i.e., Euclidean norm of inter-agent relative position) of every particle in the Monte Carlo sample at `timestep.kT`.
- Output: $\widehat{\text{sep}}_{i,j}^{m_3}(t_{k_T}) = \widehat{\rho}_{3\sigma}(t_{k_T})$
- Process: Thus far, every other substep in Step 3 has been straightforward, given that the computation of their inputs is embarrassingly parallel, and aggregating such inputs is trivial. However, computing the output of Methodology 3 (i.e., $\widehat{\rho}_{3\sigma}$) is nontrivial because of the large size MC sample (of the instantaneous inter-agent Euclidean distance) employed, which must be processed in its entirety at once in order to compute sample quantiles. Hence, the MATLAB

Parallel Computing Toolbox and the MATLAB Statistics and Machine Learning Toolbox are employed as follows:[129, 127]

- * Virtually loading the inter-agent Euclidean distance sample through a `table` array
- * Virtually computing the quantile c as

$$c = \text{prctile}(\text{all_dist_kT}, 1 - 0.9973\dots) \quad (\text{C.28})$$

- * Calling the `gather` function to evaluate c as

$$\widehat{\text{sep}}_{i,j}^{m_3}(t_{k_T}) = \text{gather}(c) \quad (\text{C.29})$$

Note: this subsubstep loads the inter-agent Euclidean distance sample and computes the result in parallel in the background.

C.5 Extensions of the current MC sample management framework methodology

One of the advantages of implementing a Monte Carlo sample framework for SFF collision risk indicator computation is that, for certain indicator types, logical conditions which signal the violation of collision constraints may be easily modified in response to changes in the definition of collision constraints.

Specifically, instantaneous and joint-time probabilistic collision risk indicators (such as the IPC and Pc) and quantile-based collision risk indicators (such as the $\rho_{3\sigma}$) may be customized by updating Step 2, Pre-processing #1 subroutine (illustrated in Fig. C.5) as follows. First, the a -norm collision event that underlies the definition of these indicators may be changed from the Euclidean norm (i.e., if $a = \text{Eu}$) to an arbitrary a -norm in relative position space. This change is undertaken in the computational studies carried out in Chapter 10.

Second, the joint HBR may be allowed to vary over the simulation horizon, subject to the continuity constraints necessary for a - Pc computability and well-definedness, as evidenced in Propositions 17 and 18.

Third, the dynamic process through which each sample particle is propagated may be changed from LTI to arbitrary non-linear dynamics. For example, such a customization is employed in Section A.3, which examines the effects on probabilistic SFF collision risk indicators caused by changing the underlying relative orbital dynamic model from CW dynamics to relative 2-body orbital dynamics.

C.6 Discussion of MC sample methodology application

In particular, the following studies carried out in this dissertation have been enabled by the Monte Carlo (MC) implementation listed in this Chapter. For these studies, Monte Carlo samples are generated from non-degenerate normal initial relative state distributions, whose expectations follow closed, collision-free CW trajectories, in accordance with the cases described in Section A.2.

First, the analytical MC rate convergence (in the RMSE sense) of sample estimators of random variable mean and covariance (listed in Eqns. B.21 and B.30) is validated in Subsection 6.5.2. This result establishes a baseline for MSS convergence rate comparison.

Second, the statement that certain \widetilde{W} -projection IPCs are overestimates of true IPCs, listed in Corollary 35 (cf. Theorem 34), is validated via MC simulation in Subsection 8.4.2.

Third, in Subsection 8.4.4 the $\rho_{3\sigma}$ collision risk indicator is found to have a relationship with the IPC and Pc that is consistent with intuition. The $\rho_{3\sigma}$ indicator, which is the $p_{3\sigma}$ -quantile of the distribution of the Euclidean norm of the instantaneous, three-dimensional relative position between agents in an SFF context (see Subsection 9.3.4), is computed via MC simulation in accordance with the method described in Subsection 9.4.2.

Fourth, in Subsection 9.5.3, it is concluded that the $\rho_{3\sigma}$ can be interpreted as a collision region in three-dimensional relative position space with a specific probabilistic SFF colli-

sion risk interpretation. This result is enabled by numerically computing the probability density function of the Euclidean norm of the relative position, as evaluated at a $\rho_{3\sigma}$ value estimated via MC simulation.

Finally, COCR-based stochastic SFF collision risk measures are characterized in 10.4. The theoretical c.o.-IPC and c.o.- Pc inequalities which relate these measures to their Euclidean and box/ L^∞ upper and lower bound counterparts, as posed in Corollaries 53 and 55 (respectively), are validated via MC simulation in Subsection 10.4.2. Finally, c.o.- Pc overestimate quantification (as compared to Euclidean and box/ L^∞ upper and lower bound counterparts) is enabled by MC simulation in Subsection 10.4.3.

Consequently, the MC simulation methodology laid out in this Chapter has been instrumental in this dissertation, having been utilized in every major result presented in this work.

APPENDIX D

CLOHESSY-WILTSHIRE (CW) VECTOR AND MATRIX NORM

D.1 Introduction

When assigning magnitude to statistics of $\underline{\mathbf{R}}$ or $\dot{\underline{\mathbf{R}}}$, individually, it is meaningful to employ Euclidean (or Euclidean-like) norm operators for two reasons. First, such operators are rotation-invariant in two and three dimensions. Second, each component of a statistic of $\underline{\mathbf{R}}$ and $\dot{\underline{\mathbf{R}}}$, individually, has the same physical interpretation, whether it might be position (in [m]) or position rate (in [m/s]). However, when considering statistics of $\underline{\mathbf{X}}$, assigning magnitude via such a norm, without any normalization, would involve operations (specifically, sums and products of position and position rate) whose result has no meaningful physical interpretation. Hence, vector and matrix norms are developed in \mathbb{R}^6 and $\mathbb{R}^{6 \times 6}$, respectively, that allow for meaningful assignment of magnitude to statistics of $\underline{\mathbf{X}}$ through a suitable normalization.

D.2 Clohessy-Wiltshire (CW) vector and matrix norm – definition

Fix t in \mathbb{R} . Let $\bar{\underline{\mathbf{X}}}(t)$ denote the expected CW relative state, and assume that $\bar{\underline{\mathbf{X}}}(t)$ is representative of a closed CW trajectory in the sense of Section A.1. Then, the expected amplitude of relative position in the Hill-radial direction, \bar{A}_t , is given by

$$\bar{A}_t = \left\| \begin{bmatrix} [\bar{x}]_H & (\bar{n})^{-1} [\dot{\bar{x}}]_H \end{bmatrix}^T \right\|_2 = \sqrt{[\bar{x}]_H^2 + \frac{[\dot{\bar{x}}]_H^2}{\bar{n}^2}} \quad (\text{D.1})$$

If $\bar{A}_t > 0$, the matrix M_t in $\mathbb{R}^{6 \times 6}$ is defined as

$$M_t = \begin{bmatrix} \mathbb{I}_3 (\bar{A}_t) & \mathbf{0}_{3 \times 3} \\ \mathbf{0}_{3 \times 3} & \mathbb{I}_3 (\bar{n} \bar{A}_t) \end{bmatrix} = M_t^T \quad (\text{D.2})$$

The inverse of M_t , M_t^{-1} , may be readily computed as

$$(M_t)^{-1} = \begin{bmatrix} \mathbb{I}_3 (\bar{A}_t)^{-1} & \mathbf{0}_{3 \times 3} \\ \mathbf{0}_{3 \times 3} & \mathbb{I}_3 (\bar{n} \bar{A}_t)^{-1} \end{bmatrix} = (M_t^T)^{-1} \quad (\text{D.3})$$

For \underline{x} in \mathbb{R}^6 , the transformation $\text{Can} : \mathbb{R}^6 \rightarrow \mathbb{R}^6$ is given by

$$\text{Can}(\underline{x}) = (M_t^{-1}) \underline{x} \quad (\text{D.4})$$

can be conceptualized as a transformation between dimensional Hill-frame coordinates onto a set of non-dimensional, “canonical” Hill-frame coordinates.

Definition 59 (CW vector and matrix norms). Fix t in \mathbb{R} . Assume $\bar{A}_t > 0$. Then, for \underline{x} in \mathbb{R}^6 , the CW vector norm, denoted by $\|\cdot\|_{\text{CW}}$, is defined as

$$\|\underline{x}\|_{\text{CW}} = \|(M_t^{-1}) \underline{x}\|_2 \quad (\text{D.5})$$

Similarly, for P in $\mathbb{R}^{6 \times 6}$, the CW matrix norm, denoted by $\|\cdot\|_{\text{CW},F}$, is defined as

$$\|P\|_{\text{CW},F} = \left\| (M_t^{-1}) P (M_t^T)^{-1} \right\|_F \quad \diamond \quad (\text{D.6})$$

Theorem 60 (Norm properties of CW vector and matrix norms). Fix t in \mathbb{R} . Let $\bar{A}_t > 0$. Then, $\|\cdot\|_{\text{CW}}$ is a norm in \mathbb{R}^6 . That is, for all $\underline{x}, \underline{y}$ in \mathbb{R}^6 and for all scalars c , the following properties hold:

1. Nonnegativity: $0 \leq \|\underline{x}\|_{\text{CW}} < \infty$

2. Homogeneity: $\|c\underline{x}\|_{CW} = |c| \|\underline{x}\|_{CW}$
3. The Triangle Inequality: $\|\underline{x} + \underline{y}\|_{CW} \leq \|\underline{x}\|_{CW} + \|\underline{y}\|_{CW}$
4. Uniqueness: $\|\underline{x}\|_{CW} = 0$ if and only $\underline{x} = \mathbf{0}_{6 \times 1}$

Similarly, $\|\cdot\|_{CW,F}$ is a norm in $\mathbb{R}^{6 \times 6}$. That is, for all M, P in $\mathbb{R}^{6 \times 6}$ and for all scalars c , the following properties hold:

1. Nonnegativity: $0 \leq \|M\|_{CW,F} < \infty$
2. Homogeneity: $\|cM\|_{CW,F} = |c| \|M\|_{CW,F}$
3. The Triangle Inequality: $\|M + P\|_{CW,F} \leq \|M\|_{CW,F} + \|P\|_{CW,F}$
4. Uniqueness: $\|M\|_{CW,F} = 0$ if and only $M = \mathbf{0}_{6 \times 6}$ ◇

Proof. Omitted. □

It must be noted that the CW matrix norm, $\|\cdot\|_{CW,F}$, is not a submultiplicative matrix norm because (M_t^{-1}) is not an orthogonal matrix (i.e., a matrix whose transpose is equal to its inverse).

D.3 Clohessy-Wiltshire (CW) vector and matrix norm – deterministic and MSE convergence rates

Since $\|\cdot\|_2$ and $\|\cdot\|_{CW}$ are both norms in \mathbb{R}^6 , which is a finite-dimensional space, it follows that both norms are equivalent.[34] That is, there exist constants $C_1, C_2 > 0$ such that for every \underline{x} in \mathbb{R}^6 ,

$$C_1 \|\underline{x}\|_2 \leq \|\underline{x}\|_{CW} \leq C_2 \|\underline{x}\|_2 \tag{D.7}$$

It is a known fact that equivalent norms determine the same convergence criterion.[34] For the case of the $\|\cdot\|_2$ and $\|\cdot\|_{CW}$ norms in \mathbb{R}^6 , this means that a sequence $\{\underline{x}_k\}_{k \in \mathbb{N}}$ of points

in \mathbb{R}^6 converges to a point \underline{x} in \mathbb{R}^6 with respect to the $\|\cdot\|_2$ norm if and only if the sequence converges to \underline{x} with respect to the $\|\cdot\|_{CW}$ norm. That is,

$$\lim_{k \rightarrow \infty} \|\underline{x} - \underline{x}_k\|_{CW} = 0 \iff \lim_{k \rightarrow \infty} \|\underline{x} - \underline{x}_k\|_2 = 0 \quad (\text{D.8})$$

Similarly, $\|\cdot\|_F$ and $\|\cdot\|_{CW,F}$ are both matrix norms in $\mathbb{R}^{6 \times 6}$. Since all matrix norms in finite-dimensional spaces are equivalent, it follows that both of these norms determine the same convergence criterion. That is, a sequence $\{M_k\}_{k \in \mathbb{N}}$ of matrices in $\mathbb{R}^{6 \times 6}$ and a constant matrix M in $\mathbb{R}^{6 \times 6}$ satisfy

$$\lim_{k \rightarrow \infty} \|M - M_k\|_{CW,F} = 0 \iff \lim_{k \rightarrow \infty} \|M - M_k\|_F = 0 \quad (\text{D.9})$$

Letting $\underline{\mu}$ and Σ denote the covariance of \underline{X} in \mathbb{R}^6 , it can be shown that the Monte Carlo $\widehat{\underline{\mu}}$ -MSE and $\widehat{\Sigma}$ -MSE asymptotic convergence rates are not affected by employing the CW vector and matrix norms instead of the regular Euclidean and Frobenius norms. Specifically, these rates may be modeled as

$$(\widehat{\underline{\mu}}\text{-MSE})(n) = \left(\tilde{C}_{\underline{\mu}}\right) n^{-u} \quad (\text{D.10})$$

$$\left(\widehat{\Sigma}\text{-MSE}\right)(n) = \left(\tilde{C}_{\Sigma}\right) n^{-u} \quad (\text{D.11})$$

where $u = 1$, $\tilde{C}_{\underline{\mu}} = \text{trace}\left(\Sigma (M_t^{-1})^2\right)$, and

$$\tilde{C}_{\Sigma} = \text{trace}\left(\tilde{\Delta}\right) \quad (\text{D.12})$$

where the matrix $\tilde{\Delta} \in \mathbb{R}^{6 \times 6}$ satisfies

$$\begin{aligned} \tilde{\Delta} (M_t)^4 &= \mathbb{E} [\underline{X}\underline{X}^T \underline{X}\underline{X}^T] - 4 \cdot \mathbb{E} [\underline{X}\underline{X}^T \underline{X}] \underline{\mu}^T + 4 \cdot \Sigma \underline{\mu} \underline{\mu}^T \\ &\quad + 2 \cdot \left[\text{trace}\left(\underline{\mu} \underline{\mu}^T (M_t^{-1})^2\right) \right] (\Sigma + \underline{\mu} \underline{\mu}^T) (M_t)^2 + \underline{\mu} \underline{\mu}^T \underline{\mu} \underline{\mu}^T - \Sigma \Sigma \end{aligned} \quad (\text{D.13})$$

These expressions arise from the way the CW vector and matrix norms are formulated in Definition 59 in terms of the Euclidean vector and Frobenius matrix norms (respectively), and from the Monte Carlo asymptotic rates of mean-square-error convergence for the sample mean (in terms of the Euclidean vector norm; cf. B.21) and the sample covariance (in terms of the Frobenius matrix norm; cf. B.30), respectively.

D.4 Discussion on application of the CW vector and matrix norms

In Chapter 6, the CW vector and matrix norms are employed in the assignment of magnitude to first and second order statistics to the uncertain CW relative orbital state vector, the deterministic version of which has been introduced in Section A.1. The CW state encodes relative position and relative position rate information; since these physical quantities are dimensionally inconsistent, the normalization embedded in the CW vector and matrix norms allows for direct comparison among CW relative state sample points (as well as estimates of the CW expected value), and between estimates of CW relative state covariance.

The ability to perform these direct comparisons is leveraged in order to quantify the stochastic rate of mean-square-error convergence for sample estimators of CW relative state mean, covariance, and instantaneous probability of collision, with samples based on the Monte Carlo (MC; see Subsection 6.5.2) and Mahalanobis Shell Sampling (MSS; see Subsection 6.5.4) methods.

APPENDIX E

**PROOFS RELATED TO FOUNDATIONAL WORK IN SPACECRAFT
FORMATION COLLISION RISK**

E.1 Measurability of a -JTC sets

Proposition 61 (Measurability of a -JTC). Let Remark 8 hold. Let $l_{i,j} : [t_0, t_f] \rightarrow (0, \infty)$. Let $\|\cdot\|_a$ be any norm in $\mathbb{R}^{d_{\mathbf{R}}}$. Assume the function $F_{t_0}(t, \mathbf{x})$ (see Eq. 2.38) is continuous in t and \mathbf{x} . Then, the $\text{JTC}_{i,j}([t_0, t_f]; l_{i,j}(\cdot), a)$ set (see Definition 9) is an open set (and hence, it is a measurable subset of $\mathbb{R}^{n_{\mathbf{x}}}$). Consequently, the $P_{C_{i,j}}([t_0, t_f]; l_{i,j}(\cdot), a)$ measure is well-defined.

Assume the joint-HBR time history, $l_{i,j} : [t_0, t_f] \rightarrow (0, \infty)$, is continuous. Then, the $\text{JTC}_{i,j}([t_0, t_f]; l_{i,j}(\cdot), a)$ set can be computed as a countable union of sets; specifically, as given by

$$\text{JTC}_{i,j}([t_0, t_f]; l_{i,j}(\cdot), a) = \widetilde{\text{JTC}}_{i,j}([t_0, t_f]; l_{i,j}(\cdot), a) \quad (\text{E.1})$$

Consequently, under these assumptions, the a - P_C and the countable a - P_C are equivalent; that is,

$$P_{C_{i,j}}([t_0, t_f]; l_{i,j}(\cdot), a) = \widetilde{P}_{C_{i,j}}([t_0, t_f]; l_{i,j}(\cdot), a) \quad \diamond \quad (\text{E.2})$$

Proof. Fix $t \in [t_0, t_f]$, and let $\|\cdot\|_a$ denote any norm in $\mathbb{R}^{d_{\mathbf{R}}}$. Since the $V_{i,j}(t; l_{i,j}(t), a)$ set is an open ball with respect to $\|\cdot\|_a$ – specifically, as given by

$$V_{i,j}(t; l_{i,j}(t), a) = \mathbb{B}_{l_{i,j}(t)}^{d_{\mathbf{R}}|a} \left(\mathbf{0}_{d_{\mathbf{R}} \times 1} \right) \quad (\text{E.3})$$

it follows that $V_{i,j}(t; l_{i,j}(t), a)$ set is an open set in $\mathbb{R}^{d_{\mathbf{R}}}$. [66]

Let $g_P : \mathbb{R}^{n_{\mathbf{x}}} \rightarrow \mathbb{R}^{d_{\mathbf{R}}}$ be a continuous surjection (i.e., g_P is a continuous and onto function), as discussed in Subsection 2.5.1. Since g_P is continuous, and since $C_{i,j}(t; l_{i,j}(t), a)$

is the pre-image of $V_{i,j}(t; l_{i,j}(t), a)$ under g_P , i.e.,

$$C_{i,j}(t; l_{i,j}(t), a) = g_P^{-1}(V_{i,j}(t; l_{i,j}(t), a)) \quad (\text{E.4})$$

it follows that $C_{i,j}(t; l_{i,j}(t), a)$ is an open set in $\mathbb{R}^{n_{\mathbf{x}}}$. [66]

Let Remark 8 hold. Assume the function $F_{t_0}(t, \underline{\mathbf{x}})$ (see Eq. 2.38) is continuous in t and $\underline{\mathbf{x}}$. Then, $F_{t,t_0} : \mathbb{R}^{n_{\mathbf{x}}} \rightarrow \mathbb{R}^{n_{\mathbf{x}}}$ (see Definition 9) is continuous and invertible. Since F_{t,t_0} is continuous, the set $[F_{t,t_0}]^{-1}[C_{i,j}(t; l_{i,j}(t), a)]$ is also an open set in $\mathbb{R}^{n_{\mathbf{x}}}$.

It is a property of topological spaces (i.e., spaces where the notion of set openness is defined) that an arbitrary (even uncountable) union of open sets is also an open set. [66] Since the a -JTC set is defined as an uncountable union of open sets in $\mathbb{R}^{n_{\mathbf{x}}}$, specifically, as given by

$$\text{JTC}_{i,j}([t_0, t_f]; l_{i,j}(\cdot), a) = \bigcup_{t \in [t_0, t_f]} [F_{t,t_0}]^{-1}[C_{i,j}(t; l_{i,j}(t), a)] \quad (\text{E.5})$$

it follows that the a -JTC set is open. Furthermore, since all open sets are Lebesgue measurable, [34], the a -JTC set is a measurable subset in $\mathbb{R}^{n_{\mathbf{x}}}$.

The initial relative state $\underline{\mathbf{X}}_{i,j}(t_0)$ is modeled as an absolutely continuous random variable, which implies that the a - Pc measure is a Lebesgue integral – specifically, of the pdf of $\underline{\mathbf{X}}_{i,j}(t_0)$ over the a -JTC set, as given by

$$Pc_{i,j}([t_0, t_f]; l_{i,j}(\cdot), a) = \int_{\underline{\mathbf{x}} \in \text{JTC}_{i,j}([t_0, t_f]; l_{i,j}(\cdot), a)} \text{pdf}_{\underline{\mathbf{X}}_{i,j}(t_0)}(\underline{\mathbf{x}}) d\underline{\mathbf{x}} \quad (\text{E.6})$$

Therefore, the a - Pc measure is well-defined.

This proof will show that the a -JTC and the countable a -JTC sets are equivalent under the current assumptions, i.e.,

$$\text{JTC}_{i,j}([t_0, t_f]; l_{i,j}(\cdot), a) = \widetilde{\text{JTC}}_{i,j}([t_0, t_f]; l_{i,j}(\cdot), a) \quad (\text{E.7})$$

Within this proof, let h_T be denoted as h ; i.e., $h : [0, 1] \rightarrow [t_0, t_f]$ satisfies

$$h(c) = t_0 + (t_f - t_0)c \quad (\text{E.8})$$

for $c \in [0, 1]$. Let the \mathcal{T} set be defined as

$$\mathcal{T} \doteq \{t_0 + (t_f - t_0)c : c \in \mathbb{Q} \cap [0, 1]\} = h(\mathbb{Q} \cap [0, 1]) \quad (\text{E.9})$$

Since $\mathbb{Q} \cap [0, 1] \subseteq [0, 1]$, $\mathcal{T} \subseteq [t_0, t_f]$. Therefore,

$$\begin{aligned} & \widetilde{\text{JTC}}_{i,j}([t_0, t_f]; l_{i,j}(\cdot), a) \\ &= \bigcup_{t \in \mathcal{T}} [F_{t,t_0}]^{-1} [C_{i,j}(t; l_{i,j}(t), a)] \subseteq \bigcup_{t \in [t_0, t_f]} [F_{t,t_0}]^{-1} [C_{i,j}(t; l_{i,j}(t), a)] \\ &= \text{JTC}_{i,j}([t_0, t_f]; l_{i,j}(\cdot), a) \quad (\text{E.10}) \end{aligned}$$

The remainder of this proof is concerned with whether the reverse subset relationship to the one listed in Eq. E.10 also holds; i.e., if the countable a -JTC set is a superset of the a -JTC set.

Let $c \in \{0, 1\} \subseteq \mathbb{Q}$. Then, $h(c) \in \mathcal{T}$. Thus,

$$[F_{h(c),t_0}]^{-1} [C_{i,j}(h(c); l_{i,j}(h(c)), a)] \subseteq \widetilde{\text{JTC}}_{i,j}([t_0, t_f]; l_{i,j}(\cdot), a) \quad (\text{E.11})$$

The a -JTC set may be expressed as

$$\begin{aligned}
& \text{JTC}_{i,j}([t_0, t_f]; l_{i,j}(\cdot), a) \\
&= \left([F_{h(0), t_0}]^{-1} [C_{i,j}(h(0); l_{i,j}(h(0)), a)] \right) \\
&\cup \left([F_{h(1), t_0}]^{-1} [C_{i,j}(h(1); l_{i,j}(h(1)), a)] \right) \\
&\cup \left(\bigcup_{0 < c < 1} [F_{h(c), t_0}]^{-1} [C_{i,j}(h(c); l_{i,j}(h(c)), a)] \right) \quad (\text{E.12})
\end{aligned}$$

Hence, without loss of generality, assume $0 < c < 1$.

Let $t_c = h(c)$. Take $\underline{y}_c \in C_{i,j}(t_c; l_{i,j}(t_c), a) \subseteq \mathbb{R}^s$. It will be shown that there exists some $\delta > 0$ such that:

1. $(t_c - \delta, t_c + \delta) \subsetneq (t_0, t_f)$
2. For all $t_d \in (t_c - \delta, t_c + \delta)$,

$$\underline{y}_d = [F_{t_d, t_c}] [\underline{y}_c] \in C_{i,j}(t_d; l_{i,j}(t_d), a) \quad (\text{E.13})$$

3. There exists some $d' \in \mathbb{Q} \cap [0, 1]$ such that, for $t_{d'} = h(d')$,

$$\underline{y}_{d'} = [F_{t_{d'}, t_c}] [\underline{y}_c] \in C_{i,j}(t_{d'}; l_{i,j}(t_{d'}), a) \quad (\text{E.14})$$

Furthermore, d' may be constrained such that $t_{d'} \in (t_c - \delta, t_c + \delta)$.

Subproof. Let $0 < c < 1$. Let $t_c \doteq h(c)$. Let $A_c \doteq C_{i,j}(t_c; l_{i,j}(t_c), a)$.

Let $\underline{y}_c \in A_c$. Let $\underline{\mathbf{r}}_c = g_P(\underline{y}_c)$. Let $f_c : [t_0, t_f] \rightarrow \mathbb{R}^s$ be defined as

$$f_c(t) = F_{t_c}(t, \underline{y}_c) \quad (\text{E.15})$$

for $t \in [t_0, t_f]$. From Remark 8, f_c is a continuous function. Note: $f_c(t_c) = \underline{y}_c$.

Since A_c is an open set in \mathbb{R}^s , there exists some $\varepsilon > 0$ such that

$$\mathbb{B}_\varepsilon^{s|\text{Eu}}(\underline{y}_c) \subseteq A_c \quad (\text{E.16})$$

Take $\varepsilon' = \frac{2}{3}\varepsilon > 0$. Then,

$$\overline{\mathbb{B}}_{\varepsilon'}^{s|\text{Eu}}(\underline{y}_c) = \left\{ \underline{y}' \in \mathbb{R}^s : \|\underline{y}' - \underline{y}_c\|_2 \leq \varepsilon' \right\} \subseteq \mathbb{B}_\varepsilon^{s|\text{Eu}}(\underline{y}_c) \quad (\text{E.17})$$

Let the sets B_1 , B_2 , and B_3 be defined as

$$B_1 = g_P \left(\overline{\mathbb{B}}_{\varepsilon'}^{s|\text{Eu}}(\underline{y}_c) \right) \quad (\text{E.18})$$

$$B_2 = g_P \left(\mathbb{B}_\varepsilon^{s|\text{Eu}}(\underline{y}_c) \right) \quad (\text{E.19})$$

$$B_3 = g_P(A_c) =: V_{i,j}(t_c; l_{i,j}(t_c), a) \quad (\text{E.20})$$

Since the following subset relationships hold

$$\overline{\mathbb{B}}_{\varepsilon'}^{s|\text{Eu}}(\underline{y}_c) \subseteq \mathbb{B}_\varepsilon^{s|\text{Eu}}(\underline{y}_c) \subseteq A_c \quad (\text{E.21})$$

and since subset relationships are preserved under direct images, it follows that

$$B_1 \subseteq B_2 \subseteq B_3 \quad (\text{E.22})$$

The closed ball $\overline{\mathbb{B}}_{\varepsilon'}^{s|\text{Eu}}(\underline{y}_c)$ is a closed and bounded set; hence, by the Heine-Borel Theorem, $\overline{\mathbb{B}}_{\varepsilon'}^{s|\text{Eu}}(\underline{y}_c)$ is a compact set in $\mathbb{R}^{n_{\mathbf{x}}}$. [34] Since g_P is a continuous function, and since B_1 is the direct image of a compact set under g_P (see Eq. E.18), it follows that B_1 is a compact set in $\mathbb{R}^{d_{\mathbf{x}}}$. [34]

All compact sets are bounded; hence,

$$M_{\varepsilon'} = \sup_{\underline{\mathbf{r}} \in B_1} (\|\underline{\mathbf{r}}\|_a) < \infty \quad (\text{E.23})$$

All compact sets are closed; in particular, since B_1 is compact, there exists some $\underline{\mathbf{r}}_{\varepsilon'}$ in B_1 such that

$$\|\underline{\mathbf{r}}_{\varepsilon'}\|_a = M_{\varepsilon'} \quad (\text{E.24})$$

However, $B_1 \subseteq B_3$, which implies that $\|\underline{\mathbf{r}}_{\varepsilon'}\|_a < l_{i,j}(t_c)$. Therefore,

$$M_{\varepsilon'} < l_{i,j}(t_c) \quad (\text{E.25})$$

In particular, since $\underline{\mathbf{r}}_c \in B_1$, $\|\underline{\mathbf{r}}_c\|_a \leq M_{\varepsilon'}$; hence,

$$\|\underline{\mathbf{r}}_c\|_a \leq M_{\varepsilon'} < l_{i,j}(t_c) \quad (\text{E.26})$$

Let $\varepsilon'' = \frac{1}{3}\varepsilon > 0$. Since f_c is continuous, it follows that there exists some $\delta_1 > 0$ such that, for all $t_{d_1} \in (t_c - \delta_1, t_c + \delta_1)$,

$$\|f_c(t_{d_1}) - f_c(t_c)\|_2 < \varepsilon'' \quad (\text{E.27})$$

Let $t_{d_1} \in (t_c - \delta_1, t_c + \delta_1)$. Let $\underline{y}_{d_1} = f_c(t_{d_1})$. Let $\underline{\mathbf{r}}_{d_1} = g_P(\underline{y}_{d_1})$. Note: $f_c(t_c) = y_c$. Then,

$$\|\underline{y}_{d_1} - \underline{y}_c\|_2 < \varepsilon'' \quad (\text{E.28})$$

which implies that

$$\underline{y}_{d_1} \in \left\{ \underline{y}_{d'} \in \mathbb{R}^s : \|\underline{y}_{d'} - \underline{y}_c\|_2 < \varepsilon'' \right\} = \mathbb{B}_{\varepsilon''}^{s|\text{Eu}}(\underline{y}_c) \subseteq \mathbb{B}_{\varepsilon'}^{s|\text{Eu}}(\underline{y}_c) \subseteq \overline{\mathbb{B}_{\varepsilon'}^{s|\text{Eu}}}(\underline{y}_c) \quad (\text{E.29})$$

Therefore, $\mathbf{r}_{d_1} \in B_1$ (see Eq. E.18). Hence,

$$\|\mathbf{r}_{d_1}\|_a \leq M_{\varepsilon'} \quad (\text{E.30})$$

Let $\varepsilon''' > 0$ be defined as

$$\varepsilon''' = \frac{l_{i,j}(t_c) - M_{\varepsilon'}}{2} > 0 \quad (\text{E.31})$$

Let the joint-HBR time-history $l_{i,j} : [t_0, t_f] \rightarrow (0, \infty)$ be a continuous function. Then, there exists some $\delta_2 > 0$ such that for all $t_{d_2} \in (t_c - \delta_2, t_c + \delta_2)$,

$$|l_{i,j}(t_{d_2}) - l_{i,j}(t_c)| < \varepsilon''' \quad (\text{E.32})$$

Let $t_{d_2} \in (t_c - \delta_2, t_c + \delta_2)$. Then,

$$|l_{i,j}(t_{d_2}) - l_{i,j}(t_c)| < \varepsilon''' \quad (\text{E.33})$$

which implies that

$$l_{i,j}(t_c) - \varepsilon''' < l_{i,j}(t_{d_2}) \quad (\text{E.34})$$

Let $\delta = \min(\delta_1, \delta_2) > 0$. Let $t_d \in (t_c - \delta, t_c + \delta)$. Let $y_d = f_c(t_d)$, and let the point \mathbf{r}_d in $\mathbb{R}^{d_{\mathbf{r}}}$ be defined such that

$$\mathbf{r}_d = g_P(\underline{y}_d) = g_P(f_c(t_d)) \quad (\text{E.35})$$

Hence, \mathbf{r}_d satisfies

$$\|\mathbf{r}_d\|_a \leq M_{\varepsilon'} \quad (\text{E.36})$$

$$l_{i,j}(t_c) - \varepsilon''' < l_{i,j}(t_d) \quad (\text{E.37})$$

Via algebraic manipulation, it can be shown that

$$M_{\varepsilon'} + \varepsilon''' = l_{i,j}(t_c) - \varepsilon''' \quad (\text{E.38})$$

Hence,

$$\|\underline{\mathbf{r}}_d\|_a \leq M_{\varepsilon'} < M_{\varepsilon'} + \varepsilon''' = l_{i,j}(t_c) - \varepsilon''' < l_{i,j}(t_d) \quad (\text{E.39})$$

Thus, $\underline{\mathbf{r}}_d \in V_{i,j}(t_d; l_{i,j}(t_d), a)$. Since $\underline{\mathbf{r}}_d = g_P(\underline{y}_d)$, it follows that $\underline{y}_d \in C_{i,j}(t_d; l_{i,j}(t_d), a) = A_d$.

Therefore, for every $y_c \in A_c$, there exists some $\delta > 0$ such that for every $t_d \in (t_c - \delta, t_c + \delta)$, $y_d = f_c(t_d) \in A_d$. Without loss of generality, δ may be restricted such that $(t_c - \delta, t_c + \delta) \subsetneq (t_0, t_f)$ – for example, by setting $\delta' = \frac{1}{2} \min(\delta, t_c - t_0, t_f - t_c) > 0$.

In particular, since $t_c < t_c + \delta$, it follows from the properties of real numbers that there exists some $d' \in \mathbb{Q}$ such that

$$\frac{t_c - t_0}{t_f - t_0} < d' < \frac{(t_c + \delta) - t_0}{t_f - t_0} \quad (\text{E.40})$$

which implies that

$$t_c < h(d') = t_0 + (t_f - t_0)d' < t_c + \delta \quad (\text{E.41})$$

It follows that, for every $y_c \in A_c$, there exists some $\delta' > 0$ such that:

1. $(t_c - \delta', t_c + \delta') \subsetneq (t_0, t_f)$
2. For all $t_d \in (t_c - \delta', t_c + \delta')$,

$$\underline{y}_d = f_c(t_d) \in C_{i,j}(t_d; l_{i,j}(t_d), a) \quad (\text{E.42})$$

3. There exists some $d' \in \mathbb{Q} \cap [0, 1]$ such that, for $t_{d'} = h(d')$,

$$\underline{y}_{d'} = f_c(t_{d'}) \in C_{i,j}(t_{d'}; l_{i,j}(t_{d'}), a) \quad (\text{E.43})$$

Furthermore, d' may be constrained such that $t_{d'} \in (t_c - \delta', t_c + \delta')$.

■

Let $0 < c < 1$. Let $t_c = h(c)$. Take $\underline{y}_c \in A_c = C_{i,j}(t_c; l_{i,j}(t_c), a)$. Choose $d' \in \mathbb{Q} \cap [0, 1]$ such that

$$\underline{y}_{d'} = [F_{t_{d'}, t_c}] [\underline{y}_c] \quad (\text{E.44})$$

$$\underline{y}_{d'} \in A_{d'} = C_{i,j}(t_{d'}; l_{i,j}(t_{d'}), a) \quad (\text{E.45})$$

where $t_{d'} = h(d')$.

Let the sets B_4, B_5 be defined as

$$B_4 = \{\underline{y}_0 \in \mathbb{R}^s : [F_{t_c, t_0}](\underline{y}_0) \in \{\underline{y}_c\}\} = [F_{t_c, t_0}]^{-1}(\{\underline{y}_c\}) \quad (\text{E.46})$$

$$B_5 = \{\underline{y}_0 \in \mathbb{R}^s : [F_{t_{d'}, t_0}](\underline{y}_0) \in A_{d'}\} = [F_{t_{d'}, t_0}]^{-1}(A_{d'}) \quad (\text{E.47})$$

It will be shown that $B_4 \subseteq B_5$.

Take $\underline{y}_0 \in B_4$. Then, $[F_{t_c, t_0}](\underline{y}_0) = \underline{y}_c$. Additionally, $\underline{y}_{d'} = [F_{t_{d'}, t_c}] [\underline{y}_c] \in A_{d'}$. By properties of flow functions,[86] it follows that

$$\underline{y}_{d'} = [F_{t_{d'}, t_c}] ([F_{t_c, t_0}](\underline{y}_0)) = [F_{t_{d'}, t_0}](\underline{y}_0) \quad (\text{E.48})$$

which implies that

$$\underline{y}_0 \in [F_{t_{d'}, t_0}]^{-1}(A_{d'}) = B_5 \quad (\text{E.49})$$

Hence, $B_4 \subseteq B_5$, which proves that, for every $\underline{y}_c \in C_{i,j}(h(c); l_{i,j}(h(c)), a)$, there exists some $d' \in \mathbb{Q} \cap [0, 1]$ such that

$$[F_{h(c), t_0}]^{-1}(\{\underline{y}_c\}) \subseteq [F_{h(d'), t_0}]^{-1}(C_{i,j}(h(d'); l_{i,j}(h(d')), a)) \quad (\text{E.50})$$

which implies that

$$\begin{aligned}
& \bigcup_{\underline{y}_c \in C_{i,j}(h(c); l_{i,j}(h(c)), a)} [F_{h(c), t_0}]^{-1} (\{\underline{y}_c\}) \\
& \subseteq \bigcup_{d' \in \mathbb{Q} \cap [0,1]} [F_{h(d'), t_0}]^{-1} [C_{i,j}(h(d'); l_{i,j}(h(d')), a)] \\
& = \widetilde{\text{JTC}}_{i,j}([t_0, t_f]; l_{i,j}(\cdot), a) \quad (\text{E.51})
\end{aligned}$$

However, by properties of pre-images under unions,[66] it follows that

$$\begin{aligned}
& \bigcup_{\underline{y}_c \in C_{i,j}(h(c); l_{i,j}(h(c)), a)} [F_{h(c), t_0}]^{-1} (\{\underline{y}_c\}) \\
& = [F_{h(c), t_0}]^{-1} \left[\bigcup_{\underline{y}_c \in C_{i,j}(h(c); l_{i,j}(h(c)), a)} \{\underline{y}_c\} \right] \\
& = [F_{h(c), t_0}]^{-1} [C_{i,j}(h(c); l_{i,j}(h(c)), a)] \quad (\text{E.52})
\end{aligned}$$

Then,

$$[F_{h(c), t_0}]^{-1} [C_{i,j}(h(c); l_{i,j}(h(c)), a)] \subseteq \widetilde{\text{JTC}}_{i,j}([t_0, t_f]; l_{i,j}(\cdot), a) \quad (\text{E.53})$$

Since c was assumed to satisfy $0 < c < 1$, Eq. E.53 holds for $0 < c < 1$. Furthermore, Eq. E.53 has already been shown to hold for $c \in \{0, 1\}$ (see Eq. E.11). Thus, Eq. E.53 holds for $0 \leq c \leq 1$, which implies that

$$\begin{aligned}
& \text{JTC}_{i,j}([t_0, t_f]; l_{i,j}(\cdot), a) \\
& = \bigcup_{c \in [0,1]} [F_{h(c), t_0}]^{-1} [C_{i,j}(h(c); l_{i,j}(h(c)), a)] \\
& \subseteq \widetilde{\text{JTC}}_{i,j}([t_0, t_f]; l_{i,j}(\cdot), a) \quad (\text{E.54})
\end{aligned}$$

Therefore, under the current assumptions, the a -JTC and the countable a -JTC sets are equivalent; that is,

$$\text{JTC}_{i,j}([t_0, t_f]; l_{i,j}(\cdot), a) = \widetilde{\text{JTC}}_{i,j}([t_0, t_f]; l_{i,j}(\cdot), a) \quad (\text{E.55})$$

which was to be shown. \square

E.2 Computability of a - Pc measures

Proposition 62 (Convergence of discrete-timestep a -JTC/ a - Pc approximations). Let Remark 8 hold. Let $\|\cdot\|_a$ be any norm in $\mathbb{R}^{d_{\mathbf{x}}}$. Assume the function $F_{t_0}(t, \mathbf{x})$ (see Eq. 2.38) is continuous in t and \mathbf{x} . Assume the joint HBR time history, $l_{i,j} : [t_0, t_f] \rightarrow (0, \infty)$, is continuous. Let A, D_N denote the sets

$$A = \text{JTC}_{i,j}([t_0, t_f]; l_{i,j}(\cdot), a) \quad (\text{E.56})$$

$$D_N = \text{JTC}_{i,j}^N([t_0, t_f]; l_{i,j}(\cdot), a) \quad (\text{E.57})$$

for $N \in \mathbb{N}$. Let \mathbb{P} denote the probability measure associated with $\underline{\mathbf{X}}_{i,j}(t_0)$. Then,

$$\lim_{N \rightarrow \infty} \mathbb{P}(A \setminus D_N) = 0 \quad (\text{E.58})$$

$$\lim_{N \rightarrow \infty} \mathbb{P}(D_N) = \mathbb{P}(A) \quad (\text{E.59})$$

In terms of the current notation, the preceding equations may be expressed as

$$\lim_{N \rightarrow \infty} p(\underline{\mathbf{X}}_{i,j}(t_0) \in [\text{JTC}_{i,j}([t_0, t_f]; l_{i,j}(\cdot), a)] \setminus [\text{JTC}_{i,j}^N([t_0, t_f]; l_{i,j}(\cdot), a)]) = 0 \quad (\text{E.60})$$

$$\lim_{N \rightarrow \infty} Pc_{i,j}^N([t_0, t_f]; l_{i,j}(\cdot), a) = Pc_{i,j}([t_0, t_f]; l_{i,j}(\cdot), a) \quad \diamond \quad (\text{E.61})$$

Proof. Let $\mathbb{P} : \mathcal{L}(\mathbb{R}^{n_{\mathbf{x}}}) \rightarrow [0, 1]$ denote the probability measure associated with $\underline{\mathbf{X}}_{i,j}(t_0)$. In

other words, for a set $E \in \mathcal{L}(\mathbb{R}^{n_{\mathbf{x}}})$ (i.e., E is Lebesgue measurable in relative state space),

$$\mathbb{P}(E) = p(\underline{\mathbf{X}}_{i,j}(t_0) \in E) \quad (\text{E.62})$$

Let $\|\cdot\|_a$ be any norm in $\mathbb{R}^{d_{\mathbf{B}}}$. Let the set $A \subseteq \mathbb{R}^{n_{\mathbf{x}}}$ denote the a -JTC set; i.e.,

$$A = \text{JTC}_{i,j}([t_0, t_f]; l_{i,j}(\cdot), a) \quad (\text{E.63})$$

Let $c \in [0, 1]$. Let $t_c = h_T(c)$. Then, let the set $A_c \subseteq \mathbb{R}^{n_{\mathbf{x}}}$ be defined as

$$A_c = [F_{t_c, t_0}]^{-1} [C_{i,j}(t_c; l_{i,j}(t_c), a)] \quad (\text{E.64})$$

Hence,

$$A = \bigcup_{c \in [0,1]} A_c \quad (\text{E.65})$$

Consider $N \in \mathbb{N}$. Let $k \in \{0, \dots, N\}$. Then, let the set $B_{N,k} \subseteq \mathbb{R}^{n_{\mathbf{x}}}$ be defined as

$$B_{N,k} = A_{k/N} \quad (\text{E.66})$$

Let the D_N set in $\mathbb{R}^{n_{\mathbf{x}}}$ be defined as

$$D_N = \bigcup_{k=0}^N B_{N,k} = \bigcup_{k=0}^N A_{k/N} \quad (\text{E.67})$$

Under the current assumptions, the A , D_N , and A_c sets are related to each other as given by

$$A = \bigcup_{N \in \mathbb{N}} D_N = \bigcup_{c \in \mathbb{Q} \cap [0,1]} A_c \quad (\text{E.68})$$

It should be noted that the finite-timestep a -JTC set and the finite-timestep a -PC measure

are a function of the D_N set, as given by

$$\text{JTC}_{i,j}^N([t_0, t_f]; l_{i,j}(\cdot), a) = D_N \quad (\text{E.69})$$

$$Pc_{i,j}^N([t_0, t_f]; l_{i,j}(\cdot), a) = p(\underline{\mathbf{x}}_{i,j}(t_0) \in \text{JTC}_{i,j}^N([t_0, t_f]; l_{i,j}(\cdot), a)) = \mathbb{P}(D_N) \quad (\text{E.70})$$

Similarly, the a - Pc measure is defined via A ; i.e.,

$$Pc_{i,j}([t_0, t_f]; l_{i,j}(\cdot), a) = \mathbb{P}(A) \quad (\text{E.71})$$

Let Remark 8 hold. Assume the function $F_{t_0}(t, \underline{\mathbf{x}})$ (see Eq. 2.38) is continuous in t and $\underline{\mathbf{x}}$. Via Proposition 17, the A , A_c , D_N , and $B_{N,k}$ sets are Lebesgue measurable in relative state space.

Let $\chi_A : A \rightarrow \{0, 1\}$, $\chi_{D_N} : D_N \rightarrow \{0, 1\}$ denote the characteristic functions of the A and D_N sets; that is, for $\underline{\mathbf{x}} \in \mathbb{R}^{n\underline{\mathbf{x}}}$,

$$\chi_A(\underline{\mathbf{x}}) = \begin{cases} 1 & \text{if } \underline{\mathbf{x}} \in A \\ 0 & \text{if } \underline{\mathbf{x}} \notin A \end{cases} \quad (\text{E.72})$$

$$\chi_{D_N}(\underline{\mathbf{x}}) = \begin{cases} 1 & \text{if } \underline{\mathbf{x}} \in D_N \\ 0 & \text{if } \underline{\mathbf{x}} \notin D_N \end{cases} \quad (\text{E.73})$$

Assume the joint HBR time history, $l_{i,j} : [t_0, t_f] \rightarrow (0, \infty)$, is continuous. It will be shown, under the current assumptions, that $\chi_A \rightarrow \chi_{D_N}$ pointwise, i.e., for every $\underline{\mathbf{x}} \in \mathbb{R}^{n\underline{\mathbf{x}}}$,

$$\lim_{N \rightarrow \infty} \chi_{D_N}(\underline{\mathbf{x}}) = \chi_A(\underline{\mathbf{x}}) \quad (\text{E.74})$$

Subproof. Let the preceding notation and assumptions hold.

First, let $x \notin A$. Since $D_N \subseteq A$, by properties of set complements,

$$(A)^C \subseteq (D_N)^C \quad (\text{E.75})$$

Hence, $\underline{x} \notin D_N$. Therefore,

$$\chi_{D_N}(\underline{x}) = 0 = \chi_A(\underline{x}) \quad (\text{E.76})$$

Since this is true for all $N \in \mathbb{N}$, it follows that

$$\lim_{N \rightarrow \infty} \chi_{D_N}(\underline{x}) = \chi_A(\underline{x}) = 0 \quad (\text{E.77})$$

Take $\underline{x} \in A$. Then, as per Eq. E.65, there exists some $c \in [0, 1]$ such that $\underline{x} \in A_c$. If $c \in \{0, 1\}$, then $\underline{x} \in D_N$ for all $N \in \mathbb{N}$. Hence, in the case that $c \in \{0, 1\}$,

$$|\chi_A(\underline{x}) - \chi_{D_N}(\underline{x})| = |1 - 1| = 0 \quad (\text{E.78})$$

which implies that

$$\lim_{N \rightarrow \infty} \chi_{D_N}(\underline{x}) = \chi_A(\underline{x}) \quad (\text{E.79})$$

Hence, without loss of generality, $c \in (0, 1)$.

Additionally, in the context of the current subproof, since $[0, 1]$ and $[t_0, t_f]$ are related through a linear mapping, t_0 and t_f are set to $t_0 = 0$ and $t_f = 1$ without loss of generality.

As per the subproof included in the proof of Proposition 17, there exists some $\delta > 0$ such that, for every $d \in (c - \delta, c + \delta) \subsetneq (0, 1)$

$$\underline{x} \in A_d = C_{i,j}(t_d; l_{i,j}(t_d), a) \quad (\text{E.80})$$

for $t_d = h_T(d)$.

The goal is to show that $\lim_{N \rightarrow \infty} \chi_{D_N}(\underline{x}) = \chi_A(\underline{x})$; i.e., that for every $\varepsilon > 0$, there exists some $N \in \mathbb{N}$ such that, for all $n \geq N$,

$$|\chi_{D_n}(\underline{x}) - \chi_A(\underline{x})| < \varepsilon \quad (\text{E.81})$$

Since $\underline{x} \in A$, then $\chi_A(\underline{x}) = 1$. Hence,

$$|\chi_{D_n}(\underline{x}) - 1| < \varepsilon \quad (\text{E.82})$$

Since Eq. E.82 holds for every $\varepsilon > 0$ if $\chi_{D_N}(\underline{x}) \rightarrow \chi_A(\underline{x})$, and since $\chi_{D_N}(\underline{x}) \in \{0, 1\}$, Eq. E.82 implies that demonstrating Eq. E.81 is equivalent to showing that there exists some $N \in \mathbb{N}$ such that, for every $n \geq N$, $\underline{x} \in D_n$, i.e.,

$$\chi_{D_n}(\underline{x}) = 1 \quad (\text{E.83})$$

Eq. E.83 will be demonstrated through an argument by induction; specifically, by showing that there exists some $N_{L_1} \in \mathbb{N}$ that is large enough to meet the following two criteria:

1. There exists some $K_{L_1} \in \{1, \dots, N_{L_1} - 1\}$ such that

$$\frac{K_{L_1}}{N_{L_1}} \in \left(c - \frac{\delta}{2}, c + \frac{\delta}{2} \right) \quad (\text{E.84})$$

2. For $N_{L_2} = N_{L_1} + 1$, there exists some $K_{L_2} \in \{1, \dots, N_{L_2} - 1\}$ such that

$$\frac{K_{L_2}}{N_{L_2}} \in \left(c - \frac{\delta}{2}, c + \frac{\delta}{2} \right) \quad (\text{E.85})$$

Observe that

$$0 < c - \frac{\delta}{2} < c + \frac{\delta}{2} < 1 \quad (\text{E.86})$$

By properties of real numbers, there exists some $d_1 \in \mathbb{Q}$ such that

$$0 < c - \frac{\delta}{2} < d_1 < c + \frac{\delta}{2} < 1 \quad (\text{E.87})$$

Since $d_1 \in \mathbb{Q}$, there exists some $N_1, K_1 \in \mathbb{N}$ such that

$$d_1 = \frac{K_1}{N_1} \tag{E.88}$$

However,

$$0 < d_1 = \frac{K_1}{N_1} < 1 \tag{E.89}$$

which implies that

$$0 < K_1 < N_1 \tag{E.90}$$

Therefore, there exists a $N_1 \in \mathbb{N}$, $K_1 \in \{1, \dots, N_1 - 1\}$ such that

$$\frac{K_1}{N_1} \in \left(c - \frac{\delta}{2}, c + \frac{\delta}{2} \right) \tag{E.91}$$

Let the integer N_2 be defined as

$$N_2 = \left\lceil \frac{8}{\delta} + 1 \right\rceil \tag{E.92}$$

Then,

$$N_2 \geq \frac{8}{\delta} + 1 > \frac{8}{\delta} \tag{E.93}$$

which implies that

$$\frac{1}{N_2} < \frac{\delta}{8} \tag{E.94}$$

Observe that d_1 satisfies

$$d_1 = \frac{K_1}{N_1} = \frac{K_1 N_2}{N_1 N_2} \tag{E.95}$$

Let the integers N_{L_1}, K_{L_1} be defined as

$$N_{L_1} = N_1 N_2 \tag{E.96}$$

$$K_{L_1} = K_1 N_2 \tag{E.97}$$

Since $0 < K_1 < N_1$, it follows that

$$0 < K_{L_1} = K_1 N_2 < N_1 N_2 = N_{L_1} \quad (\text{E.98})$$

However $N_1 > 1$; hence,

$$N_{L_1} = N_1 N_2 > N_2 \quad (\text{E.99})$$

which shows that

$$\frac{1}{N_{L_1}} < \frac{1}{N_2} < \frac{\delta}{8} \quad (\text{E.100})$$

Note: $N_{L_1} \in \mathbb{N}$, $K_{L_1} \in \{1, \dots, N_{L_1} - 1\}$, and

$$d_1 = \frac{K_{L_1}}{N_{L_1}} \in \left(c - \frac{\delta}{2}, c + \frac{\delta}{2} \right) \quad (\text{E.101})$$

Let x and x' be defined as

$$x = \frac{K_{L_1} + 1}{N_{L_1} + 1} \quad (\text{E.102})$$

$$x' = \frac{K_{L_1} - 1}{N_{L_1} + 1} \quad (\text{E.103})$$

Let Δ and Δ' be defined as

$$\begin{aligned} \Delta = x - d_1 &= \frac{K_{L_1} + 1}{N_{L_1} + 1} - \frac{K_{L_1}}{N_{L_1}} \\ &= \frac{(K_{L_1} + 1)N_{L_1} - K_{L_1}(N_{L_1} + 1)}{(N_{L_1} + 1)N_{L_1}} \\ &= \frac{N_{L_1} - K_{L_1}}{(N_{L_1} + 1)N_{L_1}} \quad (\text{E.104}) \end{aligned}$$

$$\begin{aligned}\Delta' = d_1 - x' &= \frac{K_{L_1}}{N_{L_1}} - \frac{K_{L_1} - 1}{N_{L_1} + 1} \\ &= \frac{(N_{L_1} + 1)K_{L_1} - (K_{L_1} - 1)N_{L_1}}{N_{L_1}(N_{L_1} + 1)} \\ &= \frac{K_{L_1} + N_{L_1}}{N_{L_1}(N_{L_1} + 1)}\end{aligned}\quad (\text{E.105})$$

1. Case 1: $d_1 = c$

Since $N_{L_1} - K_{L_1} > 0$, $\Delta > 0$, which shows that $d_1 < x$.

Note: $0 < N_{L_1} - K_{L_1} < N_{L_1} < N_{L_1} + 1$. Therefore,

$$\Delta = \frac{N_{L_1} - K_{L_1}}{(N_{L_1} + 1)N_{L_1}} < \frac{N_{L_1}}{(N_{L_1} + 1)N_{L_1}} = \frac{1}{N_{L_1} + 1} < \frac{1}{N_{L_1}} < \frac{\delta}{8}\quad (\text{E.106})$$

However,

$$c - \frac{\delta}{2} < c = d_1 < x = c + \Delta < c + \frac{\delta}{8} < c + \frac{\delta}{2}\quad (\text{E.107})$$

Hence,

$$x = \frac{K_{L_1} + 1}{N_{L_1} + 1} \in \left(c - \frac{\delta}{2}, c + \frac{\delta}{2}\right)\quad (\text{E.108})$$

2. Case 2: $d_1 < c$

Since $d_1 \in (c - \frac{\delta}{2}, c + \frac{\delta}{2})$ still, and since $\Delta = x - d_1 < \frac{\delta}{8}$, it follows that

$$c - \frac{\delta}{2} < d_1 < x = d_1 + \Delta < c + \Delta < c + \frac{\delta}{8} < c + \frac{\delta}{2}\quad (\text{E.109})$$

Therefore,

$$x = \frac{K_{L_1} + 1}{N_{L_1} + 1} \in \left(c - \frac{\delta}{2}, c + \frac{\delta}{2}\right)\quad (\text{E.110})$$

3. Case 3: $d_1 > c$

Since $0 < K_{L_1} < N_{L_1} < K_{L_1} + N_{L_1} < 2N_{L_1}$, it follows that

$$\Delta' = \frac{K_{L_1} + N_{L_1}}{N_{L_1}(N_{L_1} + 1)} < \frac{2N_{L_1}}{N_{L_1}(N_{L_1} + 1)} = \frac{2}{N_{L_1} + 1} < \frac{2}{N_{L_1}} < \frac{\delta}{4}\quad (\text{E.111})$$

Therefore,

$$c - \frac{\delta}{2} < c - \frac{\delta}{4} < c - \Delta' < d_1 - \Delta' = x' < d_1 < c + \frac{\delta}{2} \quad (\text{E.112})$$

which implies that

$$x' = \frac{K_{L_1} - 1}{N_{L_1} + 1} \in \left(c - \frac{\delta}{2}, c + \frac{\delta}{2} \right) \quad (\text{E.113})$$

By induction, it follows that, for all $n \geq N_{L_1}$, there exists some $k \in \{1, \dots, n-1\}$ such that

$$d = \frac{k}{n} \in \left(c - \frac{\delta}{2}, c + \frac{\delta}{2} \right) \quad (\text{E.114})$$

Hence, via Eq. E.80, for $t_d = h_T(d)$,

$$\underline{x} \in C_{i,j}(t_d; l_{i,j}(t_d), a) = A_d = A_{k/n} = B_{k,n} \subseteq \bigcup_{k=0}^n B_{k,n} = D_n \quad (\text{E.115})$$

which implies that $\chi_{D_n}(\underline{x}) = 1$. Therefore, via Eq. E.83,

$$\lim_{N \rightarrow \infty} \chi_{D_N}(\underline{x}) = \chi_A(\underline{x}) \quad (\text{E.116})$$

which was to be shown. ■

Fix $N \in \mathbb{N}$. Let $g_N = \chi_{D_N}$. Then, $g_N \rightarrow \chi_A$ pointwise, which implies that $g_N \rightarrow \chi_A$ pointwise a.e. [with respect to (w.r.t.) \mathbb{P}]; i.e., there exists a set $Z \subseteq \mathbb{R}^{n_{\mathbf{x}}}$ (namely, $Z = \emptyset$) such that

$$\mathbb{P}(Z) = 0 \quad (\text{E.117})$$

$$g_N(\underline{x}) \rightarrow \chi_A(\underline{x}) \quad (\text{E.118})$$

for all $\underline{x} \in \mathbb{R}^{n_{\mathbf{x}}} \setminus Z$.

The g_N function has the following properties:

1. g_N is a simple function

This means that the co-domain of g_N is a finite set; i.e., g_N only has a finite number of possible values – specifically, values in $\{0, 1\}$.

2. g_N is non-negative

3. g_N is integrable with respect to \mathbb{P}

Treating \mathbb{P} as an abstract measure with respect to which integration may be performed, it follows that

$$\begin{aligned} \int_{\underline{x} \in \mathbb{R}^{n_{\mathbf{X}}}} |g_N(\underline{x})| d\mathbb{P}(\underline{x}) &= \int_{\underline{x} \in \mathbb{R}^{n_{\mathbf{X}}}} g_N(\underline{x}) d\mathbb{P}(\underline{x}) \\ &= \int_{\underline{x} \in \mathbb{R}^{n_{\mathbf{X}}}} \chi_{D_N}(\underline{x}) d\mathbb{P}(\underline{x}) = \mathbb{P}(D_N) < \infty \end{aligned} \quad (\text{E.119})$$

Let the function $f : \mathbb{R}^{n_{\mathbf{X}}} \rightarrow \mathbb{R}$ be defined as

$$f(\underline{x}) = 1 \quad (\text{E.120})$$

for $\underline{x} \in \mathbb{R}^{n_{\mathbf{X}}}$. Since $|g_N| \leq |f|$ [that is, for $\underline{x} \in \mathbb{R}^{n_{\mathbf{X}}}$, $|g_N(\underline{x})| \leq |f(\underline{x})|$], it follows that $|g_N| \leq |f|$ a.e. (w.r.t. \mathbb{P}); that is, there's a set $Z \subseteq \mathbb{R}^{n_{\mathbf{X}}}$ (namely $Z = \emptyset$) such that

$$\mathbb{P}(Z) = 0 \quad (\text{E.121})$$

$$|g_N(\underline{x})| \leq |f(\underline{x})| \quad (\text{E.122})$$

for all $\underline{x} \in \mathbb{R}^{n_{\mathbf{X}}} \setminus Z$.

Additionally, f is integrable (w.r.t. \mathbb{P}), i.e.,

$$\int_{\underline{x} \in \mathbb{R}^{n_{\mathbf{X}}}} |f(\underline{x})| d\mathbb{P}(\underline{x}) = \int_{\underline{x} \in \mathbb{R}^{n_{\mathbf{X}}}} d\mathbb{P}(\underline{x}) = \mathbb{P}(\mathbb{R}^{n_{\mathbf{X}}}) = 1 < \infty \quad (\text{E.123})$$

Summarizing,

- a. For all $N \in \mathbb{N}$, $|g_N| \leq |f|$ a.e. (w.r.t. \mathbb{P})
- b. f is integrable (w.r.t. \mathbb{P})
- c. $g_N \rightarrow \chi_A$ pointwise a.e. (w.r.t. \mathbb{P})

Therefore, by the Lebesgue Dominated Convergence Theorem (DCT),[85] the following statements hold:

- i.* χ_A is an integrable function (w.r.t. \mathbb{P}) on the measure space $(\mathbb{R}^s, \mathcal{L}(\mathbb{R}^s), \mathbb{P})$

Note: this was already known, since $\mathbb{P}(A) \leq 1 < \infty$.

- ii.* χ_A, g_N satisfy

$$\lim_{N \rightarrow \infty} \int_{\underline{x} \in \mathbb{R}^{n\mathbf{X}}} |\chi_A(\underline{x}) - g_N(\underline{x})| d\mathbb{P}(\underline{x}) \quad (\text{E.124})$$

- iii.* χ_A, g_N satisfy

$$\lim_{N \rightarrow \infty} \int_{\underline{x} \in \mathbb{R}^{n\mathbf{X}}} g_N(\underline{x}) d\mathbb{P}(\underline{x}) = \int_{\underline{x} \in \mathbb{R}^{n\mathbf{X}}} \chi_A(\underline{x}) d\mathbb{P}(\underline{x}) \quad (\text{E.125})$$

However,

$$\int_{\underline{x} \in \mathbb{R}^{n\mathbf{X}}} g_N(\underline{x}) d\mathbb{P}(\underline{x}) = \mathbb{P}(D_N) \quad (\text{E.126})$$

$$\int_{\underline{x} \in \mathbb{R}^{n\mathbf{X}}} \chi_A(\underline{x}) d\mathbb{P}(\underline{x}) = \mathbb{P}(A) \quad (\text{E.127})$$

Therefore, Eq. E.125 implies that

$$\lim_{N \rightarrow \infty} \mathbb{P}(D_N) = \mathbb{P}(A) \quad (\text{E.128})$$

It should be noted that $\chi_A - \chi_{D_N} = \chi_{A \setminus D_N}$, shown as follows:

1. Case 1: $\underline{x} \in D_N \subseteq A$

First,

$$\chi_A(\underline{x}) = \chi_{D_N}(\underline{x}) = 1 \quad (\text{E.129})$$

which implies that

$$\chi_A(\underline{x}) - \chi_{D_N}(\underline{x}) = 0 \quad (\text{E.130})$$

Second, since $A \setminus D_N = A \cap (D_N)^C$, the fact that $\underline{x} \in D_N$ implies that $\underline{x} \notin (D_N)^C \supseteq A \cap (D_N)^C = A \setminus D_N$. Therefore,

$$\chi_{A \setminus D_N}(\underline{x}) = 0 \quad (\text{E.131})$$

2. Case 2: $\underline{x} \in A \setminus D_N$

Since $\underline{x} \in A$ and $\underline{x} \notin D_N$,

$$\chi_A(\underline{x}) - \chi_{D_N}(\underline{x}) = 1 - 0 = 1 = \chi_{A \setminus D_N}(\underline{x}) \quad (\text{E.132})$$

3. Case 3: $\underline{x} \in (A)^C$

Since $D_N \subseteq A$, $(A)^C \subseteq (D_N)^C$, it follows that $\underline{x} \in (D_N)^C$, so $\underline{x} \notin D_N$. Since $A \supseteq A \setminus D_N$, it follows that $\underline{x} \notin A \setminus D_N$, which implies,

$$\chi_A(\underline{x}) - \chi_{D_N}(\underline{x}) = 0 - 0 = 0 = \chi_{A \setminus D_N}(\underline{x}) \quad (\text{E.133})$$

Hence,

$$|\chi_A - \chi_{D_N}| = |\chi_{A \setminus D_N}| = \chi_{A \setminus D_N} \quad (\text{E.134})$$

Therefore,

$$\int_{\underline{x} \in \mathbb{R}^{n_{\mathbf{X}}}} |\chi_A(\underline{x}) - \chi_{D_N}(\underline{x})| \, d\mathbb{P}(\underline{x}) = \int_{\underline{x} \in \mathbb{R}^{n_{\mathbf{X}}}} \chi_{A \setminus D_N}(\underline{x}) \, d\mathbb{P}(\underline{x}) = \mathbb{P}(A \setminus D_N) \quad (\text{E.135})$$

Consequently, Eq. E.124 implies that

$$\lim_{N \rightarrow \infty} \mathbb{P}(A \setminus D_N) = 0 \quad (\text{E.136})$$

In terms of the original notation, Eqns. E.128 and E.136 equations may be expressed as

$$\lim_{N \rightarrow \infty} p(\underline{\mathbf{X}}_{i,j}(t_0) \in [\text{JTC}_{i,j}([t_0, t_f]; l_{i,j}(\cdot), a)] \setminus [\text{JTC}_{i,j}^N([t_0, t_f]; l_{i,j}(\cdot), a)]) = 0 \quad (\text{E.137})$$

$$\lim_{N \rightarrow \infty} P_{i,j}^N([t_0, t_f]; l_{i,j}(\cdot), a) = P_{i,j}([t_0, t_f]; l_{i,j}(\cdot), a) \quad (\text{E.138})$$

which was to be shown.

In summary, this Proposition is a consequence of the continuity of $l_{i,j}(\cdot)$ and F_{t,t_0} , of Proposition 17, and of the Lebesgue Dominated Convergence Theorem (DCT) (as applied to integrals with respect to the abstract measure \mathbb{P}).[85] □

APPENDIX F
PROOFS OF MAHALANOBIS SHELL SAMPLING (MSS) THEORETICAL
RESULTS

F.1 Preliminaries

Throughout this Chapter, unless otherwise noted, Lebesgue-measurable and Lebesgue-integrable functions are simply referred to measurable and integrable functions.

Definition 63 (\mathcal{L}^1 -norm[34]). Let $g : \mathbb{R}^s \rightarrow \mathbb{R}$ be a measurable, real-valued function. Then, the \mathcal{L}^1 -norm of g is defined as

$$\|g\|_{\mathcal{L}^1} = \int_{\underline{x} \in \mathbb{R}^s} |g(\underline{x})| \, d\underline{x} \quad (\text{F.1})$$

Note: $\|g\|_{\mathcal{L}^1}$ always exists in the extended-real sense; i.e., $\|g\|_{\mathcal{L}^1} \leq \infty$. The statement “ g is integrable” implies that $\|g\|_{\mathcal{L}^1} < \infty$. ◇

Definition 64 (\mathcal{L}^∞ -norm[34]). Let $g : \mathbb{R}^s \rightarrow \mathbb{R}$ be a measurable, real-valued function. Then, the \mathcal{L}^∞ -norm of g is defined as

$$\|g\|_{\mathcal{L}^\infty} = \operatorname{ess\,sup}_{\underline{x} \in \mathbb{R}^s} |g(\underline{x})| \quad (\text{F.2})$$

where the essentially supremum of a measurable function $f : \mathbb{R}^s \rightarrow \mathbb{R}$ is given by

$$\operatorname{ess\,sup}_{\underline{x} \in \mathbb{R}^s} f(\underline{x}) = \inf\{M \in [-\infty, \infty] : f(\underline{x}) \leq M \text{ for a.e. } \underline{x} \in \mathbb{R}^s\} \quad (\text{F.3})$$

Note: $\|g\|_{\mathcal{L}^\infty}$ always exists in the extended-real sense; i.e., $\|g\|_{\mathcal{L}^\infty} \leq \infty$. The statements “ g is essentially bounded” or (equivalently) “ g is bounded a.e.” imply that $\|g\|_{\mathcal{L}^\infty} < \infty$. ◇

The space denoted by $\mathcal{L}^1(\mathbb{R}^s)$ is the set of integrable, measurable real-valued functions $g : \mathbb{R}^s \rightarrow \mathbb{R}$. Similarly, the space denoted by $\mathcal{L}^\infty(\mathbb{R}^s)$ is the set of essentially bounded, measurable real-valued functions $g : \mathbb{R}^s \rightarrow \mathbb{R}$. For further background on measurable functions, as well as on the spaces $\mathcal{L}^1(\mathbb{R}^s)$ and $\mathcal{L}^\infty(\mathbb{R}^s)$, the reader is encouraged to consult Ref. [34], Chaps. 3-4.

It can be shown that D^2 is chi-square distributed if and only if D is chi-distributed; i.e.,

$$D^2 \sim \chi_s^2 \iff D \sim \chi_s \quad (\text{F.4})$$

F.2 Mahalanobis Shell Sampling (MSS) – Asymptotically Unbiased Theoretical Results

Lemma 65 (Existence of expected value of real-valued function of non-degenerate normal random variable). Let $\underline{\mu} \in \mathbb{R}^s$, $\Sigma \in \mathbb{R}^{s \times s}$, $\Sigma > 0$. Let $\underline{X} \sim \mathcal{N}(\underline{\mu}, \Sigma)$. Let $g : \mathbb{R}^s \rightarrow \mathbb{R}$ be a measurable, integrable real-valued function. Then, $\mathbb{E}[g(\underline{X})]$ exists and is finite. Additionally, $g \text{ pdf}_{\underline{X}}$ is an integrable function. \diamond

Proof. The pdf of \underline{X} is bounded on \mathbb{R}^s . In particular,

$$0 < M_{\underline{X}} = \sup_{\underline{x} \in \mathbb{R}^s} \text{pdf}_{\underline{X}}(\underline{x}) = [(2\pi)^s \det(\Sigma)]^{-1/2} < \infty \quad (\text{F.5})$$

Hence, $\text{pdf}_{\underline{X}}$ is essentially bounded on \mathbb{R}^s [i.e., $\text{pdf}_{\underline{X}} \in \mathcal{L}^\infty(\mathbb{R}^s)$]. By assumption, $g \in \mathcal{L}^1(\mathbb{R}^s)$. Therefore, via Ref. [34] (Problem 4.4.21.a), $(g \text{ pdf}_{\underline{X}}) \in \mathcal{L}^1(\mathbb{R}^s)$. That is,

$$\|g \text{ pdf}_{\underline{X}}\|_{\mathcal{L}^1} = \int_{\underline{x} \in \mathbb{R}^s} |g(\underline{x}) \text{pdf}_{\underline{X}}(\underline{x})| \, d\underline{x} < \infty \quad (\text{F.6})$$

Therefore,

$$I = \int_{\underline{x} \in \mathbb{R}^s} g(\underline{x}) \text{pdf}_{\underline{X}}(\underline{x}) \, d\underline{x} \quad (\text{F.7})$$

exists and is finite. However, whenever $\mathbb{E}[g(\underline{X})]$ exists, it is given by

$$\mathbb{E}[g(\underline{X})] = \int_{\underline{x} \in \mathbb{R}^s} g(\underline{x}) \text{pdf}_{\underline{X}}(\underline{x}) d\underline{x} \quad (\text{F.8})$$

Therefore, $\mathbb{E}[g(\underline{X})]$ exists and is finite. \square

Fact 66 (Relationship between non-degenerate normal, uniform spherical, and chi-square distributions). Let $\underline{\mu} \in \mathbb{R}^s$, $\Sigma \in \mathbb{R}^{s \times s}$, $\Sigma > 0$. Let \underline{X} , \underline{Z} be random variables in \mathbb{R}^s , and let D be a random variable in $[0, \infty)$. Then, the following statements are equivalent:

1. $\underline{X} \sim \mathcal{N}(\underline{\mu}, \Sigma)$
2. $\underline{X} = \underline{\mu} + \Sigma^{1/2}(D\underline{Z})$, D and \underline{Z} are independent, and

$$D^2 \sim \chi_s^2 \quad (\text{F.9})$$

$$\underline{Z} \sim \mathbb{U}(\mathbb{S}^{(s-1)}) \quad \diamond \quad (\text{F.10})$$

Proof. See Ref. [189], Theorem 4.1.1. \square

Lemma 67. Fix $N \in \mathbb{N}$. Let $l \in \{1, \dots, N\}$. Let the B_l interval be defined as

$$B_l = \begin{cases} \left[\frac{l-1}{N}, \frac{l}{N} \right) & \text{if } l \in \{1, \dots, N\} \\ \left[\frac{N-1}{N}, \frac{N}{N} \right] & \text{if } l = N \end{cases} \quad (\text{F.11})$$

Fix $v \in [0, 1]$. Then, there exists some $j \in \{1, \dots, N\}$ such that

$$v \in B_j \quad (\text{F.12})$$

$$v \notin \bigcup_{\substack{l \in \{1, \dots, N\} \\ l \neq j}} B_l \quad \diamond \quad (\text{F.13})$$

Proof. Since v must belong to B_l for some $l \in \{1, \dots, N\}$, and since the $\{B_l\}_{l \in \{1, \dots, N\}}$ sets are disjoint, the result follows. \square

Proposition 68. Let $g : \mathbb{R}^s \rightarrow \mathbb{R}$ be a measurable, integrable real-valued function. Let $d_{\max} > 0$. Let $\underline{\mu} \in \mathbb{R}^s$, $\Sigma \in \mathbb{R}^{s \times s}$, $\Sigma > 0$. Let $\underline{X} \sim \mathcal{N}(\underline{\mu}, \Sigma)$. Let the support of g , $\text{supp}(g)$, satisfy $\text{supp}(g) \subseteq V_{d_{\max}}(\underline{X})$.

Let $\{\tilde{\underline{x}}_{l,q}\}$, $l \in S_{N_{\text{sh}}}$, $q \in S_{N_{\text{ss}}}$ be an MSS sample drawn in accordance with Algorithm 1, with sample weights $\{w_{l,q}\}$ and $\{W_l\}$. Let the MSS asymptotic estimator of $\mathbb{E}[g(\underline{X})]$, $\hat{\mu}_{g(\underline{X}),\text{MSS}}$, be defined as

$$\hat{\mu}_{g(\underline{X}),\text{MSS}} = \sum_{l=1}^{N_{\text{sh}}} \left(\frac{W_l}{N_{\text{ss}}} \right) \sum_{q=1}^{N_{\text{ss}}} g(\tilde{\underline{x}}_{l,q}) \quad (\text{F.14})$$

Then,

$$\lim_{N_{\text{sh}} \rightarrow \infty} \mathbb{E}[\hat{\mu}_{g(\underline{X}),\text{MSS}}] = \mathbb{E}[g(\underline{X})] \quad \diamond \quad (\text{F.15})$$

Proof. Let $g : \mathbb{R}^s \rightarrow \mathbb{R}$ be integrable. Let $\text{supp}(g) \subseteq V_{d_{\max}}(\underline{X})$. Since the quantity $I = \mathbb{E}[g(\underline{X})]$ satisfies

$$I = \int_{\underline{x} \in \mathbb{R}^s} g(\underline{x}) \text{pdf}_{\underline{X}}(\underline{x}) d\underline{x} = \int_{\underline{x} \in V_{d_{\max}}(\underline{X})} g(\underline{x}) \text{pdf}_{\underline{X}}(\underline{x}) d\underline{x} \quad (\text{F.16})$$

it follows that I exists and is finite (see Lemma 65).

Let $\gamma : \mathbb{R}^s \rightarrow \mathbb{R}^s$ be the invertible function defined by

$$\gamma(\underline{y}) = \underline{\mu} + \Sigma^{1/2} \underline{y} \quad (\text{F.17})$$

for $\underline{y} \in \mathbb{R}^s$. Let the random variable \underline{Y} in \mathbb{R}^s be defined as $\underline{Y} = \gamma^{-1}(\underline{X})$. Then, $\underline{Y} \sim \mathcal{N}(\mathbf{0}_{s \times 1}, \mathbb{I}_s)$.

Throughout the rest of this proof, let $\underline{z} \in \mathbb{S}^{(s-1)}$, $d \in [0, \infty)$.

Let \underline{Z} and D be random variables defined as

$$\underline{Z} = \frac{\underline{Y}}{\|\underline{Y}\|_2} \quad (\text{F.18})$$

$$D = \|\underline{Y}\|_2 \quad (\text{F.19})$$

Then, via Fact 66, \underline{Z} and D are independent random variables.

For $s = 1$, $\mathbb{S}^{(s-1)} = \{\pm 1\}$; hence, the random variable \underline{Z} can only take on values in $\{\pm 1\}$. Since \underline{Z} is a discrete random variable with a finite set of possible values, \underline{Z} is an absolutely continuous random variable with respect to the counting measure in $\mathbb{S}^{(s-1)}$. Hence, for $s = 1$, integrals with respect to the Lebesgue measure in $\mathbb{S}^{(s-1)}$ may be replaced with integrals with respect to the counting measure in $\mathbb{S}^{(s-1)}$. Similarly, for $s = 1$, integrals with respect to the Lebesgue measure in $\mathbb{S}^{(s-1)} \times [0, d_{\max}]$ may be replaced by integrals with respect to the product measure in $\mathbb{S}^{(s-1)} \times [0, d_{\max}]$ induced by the counting measure in $\mathbb{S}^{(s-1)}$ and the Lebesgue measure in $[0, d_{\max}]$ (referred to as the the “prod” measure for the rest of this proof). With this abuse of notation in mind, for $s = 1$, the pdf of \underline{Z} with respect to the counting measure in $\mathbb{S}^{(s-1)}$ is given by

$$\text{pdf}_{\underline{Z}}(\underline{z}) = \frac{1}{2} \quad (\text{F.20})$$

for $\underline{z} \in \mathbb{S}^{(s-1)}$. Hence, for $s = 1$, the pdf of \underline{Z} with respect to the counting measure in $\mathbb{S}^{(s-1)}$ is a bounded function in $\mathbb{S}^{(s-1)}$.

For integers $s \geq 2$, the pdf of \underline{Z} [implicitly, with respect to the Lebesgue measure in $\mathbb{S}^{(s-1)}$] is given by

$$\text{pdf}_{\underline{Z}}(\underline{z}) = \frac{1}{\text{Area}(\mathbb{S}^{(s-1)})} \quad (\text{F.21})$$

for $\underline{z} \in \mathbb{S}^{(s-1)}$, where $\text{Area}(\mathbb{S}^{(s-1)})$ denotes the surface area of $\mathbb{S}^{(s-1)}$, which satisfies

$$0 < \text{Area}(\mathbb{S}^{(s-1)}) = \frac{2(\pi)^{(s/2)}}{\Gamma(s/2)} < \infty \quad (\text{F.22})$$

where $\Gamma(x)$ denotes the complete gamma function evaluated at $x > 0$. [190] Hence,

$$0 < \text{pdf}_{\underline{Z}}(\underline{z}) = \frac{1}{\text{Area}(\mathbb{S}^{(s-1)})} < \infty \quad (\text{F.23})$$

Thus, for integers $s \geq 2$, the pdf of \underline{Z} with respect to the Lebesgue measure in $\mathbb{S}^{(s-1)}$ is a bounded function in $\mathbb{S}^{(s-1)}$.

Therefore, because \underline{Z} and D are independent, their joint pdf satisfies

$$\text{pdf}_{\underline{Z}, D}(\underline{z}, d) = \text{pdf}_{\underline{Z}}(\underline{z}) \text{pdf}_D(d) \quad (\text{F.24})$$

Let $h : \mathbb{S}^{(s-1)} \times [0, \infty) \rightarrow \mathbb{R}^s$ satisfy

$$h(\underline{z}, d) = d\underline{z} \quad (\text{F.25})$$

Hence,

$$\mathbb{E}[g(\underline{X})] = \mathbb{E}[g(\gamma[\underline{Y}])] = \mathbb{E}[g(\gamma[h(\underline{Z}, D))]] \quad (\text{F.26})$$

Then,

$$I = \iint_{\mathbb{S}^{(s-1)} \times [0, d_{\max}]} g(\gamma[h(\underline{z}, d)]) \text{pdf}_{\underline{Z}}(\underline{z}) \text{pdf}_D(d) \, d\underline{z} \, dd \quad (\text{F.27})$$

Let the function $f : \mathbb{S}^{(s-1)} \times [0, d_{\max}] \rightarrow \mathbb{R}$ satisfy

$$f\left(\begin{bmatrix} \underline{z} \\ d \end{bmatrix}\right) = g(\gamma[h(\underline{z}, d)]) \text{pdf}_{\underline{Z}}(\underline{z}) \text{pdf}_D(d) \quad (\text{F.28})$$

for $[\underline{z}^T, d]^T \in \mathbb{S}^{(s-1)} \times [0, d_{\max}]$. Then, the \mathcal{L}^1 -norm of f , $\|f\|_{\mathcal{L}^1}$, satisfies

$$\begin{aligned} \|f\|_{\mathcal{L}^1} &= \iint_{\mathbb{S}^{(s-1)} \times [0, d_{\max}]} \left| f\left(\begin{bmatrix} \underline{z} \\ d \end{bmatrix}\right) \right| \, d\underline{z} \, dd \\ &= \iint_{\mathbb{S}^{(s-1)} \times [0, d_{\max}]} |g(\gamma[h(\underline{z}, d)]) \text{pdf}_{\underline{Z}}(\underline{z}) \text{pdf}_D(d)| \, d\underline{z} \, dd \\ &= \iint_{\mathbb{S}^{(s-1)} \times [0, d_{\max}]} |g(\gamma[h(\underline{z}, d)])| \text{pdf}_{\underline{Z}}(\underline{z}) \text{pdf}_D(d) \, d\underline{z} \, dd \\ &= \mathbb{E}[|g(\gamma[h(\underline{Z}, D))|] = \mathbb{E}[|g(\gamma[\underline{Y}])|] = \mathbb{E}[|g(\underline{X})|] \quad (\text{F.29}) \end{aligned}$$

Since $g \text{ pdf}_{\underline{X}}$ is an integrable function in \mathbb{R}^s [i.e., $g \text{ pdf}_{\underline{X}} \in \mathcal{L}^1(\mathbb{R}^s)$], Eq. F.29 implies that

$$\begin{aligned} \|f\|_{\mathcal{L}^1} &= \mathbb{E} [|g(\underline{X})|] = \int_{\underline{x} \in \mathbb{R}^s} |g(\underline{x})| \text{ pdf}_{\underline{X}}(\underline{x}) \, d\underline{x} \\ &= \int_{\underline{x} \in \mathbb{R}^s} |g(\underline{x}) \text{ pdf}_{\underline{X}}(\underline{x})| \, d\underline{x} = \|g \text{ pdf}_{\underline{X}}\|_{\mathcal{L}^1} < \infty \end{aligned} \quad (\text{F.30})$$

which shows that f is an integrable function in $\mathbb{S}^{(s-1)} \times [0, d_{\max}]$. Specifically, for $s = 1$, $f \in \text{prod}^1(\mathbb{S}^{(s-1)} \times [0, d_{\max}])$ – that is, f belongs to the set of functions in $\mathbb{S}^{(s-1)} \times [0, d_{\max}]$ that are integrable with respect to the prod measure; for integers $s \geq 2$, $f \in \mathcal{L}^1(\mathbb{S}^{(s-1)} \times [0, d_{\max}])$.

It also follows from Eqns. F.27 and F.28 that

$$I = \iint_{\mathbb{S}^{(s-1)} \times [0, d_{\max}]} f \left(\begin{bmatrix} z \\ d \end{bmatrix} \right) \, dz \, dd = \mathbb{E} [g(\underline{X})] \quad (\text{F.31})$$

Note: since f is integrable, the integral of f over its domain exists and is finite.

Let $l \in \{0, \dots, N_{\text{sh}}\}$. Let d_l be defined as

$$d_l = \frac{d_{\max}}{N_{\text{sh}}} l \quad (\text{F.32})$$

For $l \in \{1, \dots, N_{\text{sh}} - 1\}$, let the sets A_l and $A_{N_{\text{sh}}}$ be defined as

$$A_l = [d_{l-1}, d_l) \quad (\text{F.33})$$

$$A_{N_{\text{sh}}} = [d_{(N_{\text{sh}}-1)}, d_{N_{\text{sh}}}] \quad (\text{F.34})$$

Fix $l \in \{1, \dots, N_{\text{sh}}\}$. Then,

$$d_l - d_{l-1} = \frac{d_{\max}}{N_{\text{sh}}} \quad (\text{F.35})$$

Let the random variable U_l be uniformly distributed on A_l – i.e., $U_l \sim \mathbb{U}(A_l)$. There-

fore,

$$\text{pdf}_{U_l}(d) = \begin{cases} \frac{1}{d_{\max}/N_{\text{sh}}} & d \in A_l \\ 0 & d \notin A_l \end{cases} \quad (\text{F.36})$$

Fix $q \in N_{\text{ss}}$. From Algorithm 1, it follows that the $(l, q)^{\text{th}}$ MSS sample point, $\tilde{x}_{l,q}$, satisfies

$$\tilde{x}_{l,q} = \underline{\mu} + u_{l,q} [\Sigma^{1/2}] \underline{z}_{l,q} \quad (\text{F.37})$$

where $u_{l,q} \sim \mathbb{U}(A_l)$, $\underline{z}_{l,q} \sim \mathbb{U}(\mathbb{S}^{(s-1)})$, and where $u_{l,q}$ and $\underline{z}_{l,q}$ are independent. In other words, $u_{l,q} \sim \mathbb{U}(U_l)$, $\underline{z}_{l,q} \sim Z$, where U_l and Z are independent. Note: $\tilde{x}_{l,q}$ satisfies

$$\tilde{x}_{l,q} = \gamma[u_{l,q} \underline{z}_{l,q}] = \gamma[h(\underline{z}_{l,q}, u_{l,q})] \quad (\text{F.38})$$

Let $I_{N_{\text{sh}}}$ be defined as

$$I_{N_{\text{sh}}} = \mathbb{E}[\hat{\mu}_{g(\underline{X}), \text{MSS}}] \quad (\text{F.39})$$

Then, by linearity of the expectation operator,

$$\begin{aligned} I_{N_{\text{sh}}} &= \sum_{l=1}^{N_{\text{sh}}} \left(\frac{W_l}{N_{\text{ss}}} \right) \sum_{q=1}^{N_{\text{ss}}} \mathbb{E}[g(\tilde{x}_{l,q})] \\ &= \sum_{l=1}^{N_{\text{sh}}} \left(\frac{W_l}{N_{\text{ss}}} \right) \sum_{q=1}^{N_{\text{ss}}} \mathbb{E}[g(\gamma[h(\underline{Z}, U_l)])] = \sum_{l=1}^{N_{\text{sh}}} (W_l) \mathbb{E}[g(\gamma[h(\underline{Z}, U_l)])] \\ &= \sum_{l=1}^{N_{\text{sh}}} (W_l) \iint_{\mathbb{S}^{(s-1)} \times A_l} g(\gamma[h(\underline{z}, u)]) \text{pdf}_{\underline{Z}}(\underline{z}) \text{pdf}_{U_l}(u) \, d\underline{z} \, du \quad (\text{F.40}) \end{aligned}$$

From Algorithm 1, it follows that

$$W_l = \text{cdf}_{\chi_s} \left(\left[\frac{d_{\max}}{N_{\text{sh}}} \right] l \right) - \text{cdf}_{\chi_s} \left(\left[\frac{d_{\max}}{N_{\text{sh}}} \right] (l-1) \right) \quad (\text{F.41})$$

Let $\delta = d_{\max}/N_{\text{sh}}$. Let the function $a_{N_{\text{sh}}} : [0, d_{\max}] \rightarrow [0, \infty)$ be defined as

$$a_{N_{\text{sh}}}(u) = \begin{cases} \frac{1}{\delta} [\text{cdf}_{\chi_s}(u + \delta) - \text{cdf}_{\chi_s}(u)] & \text{if } \frac{u}{\delta} \in \{0, \dots, N_{\text{sh}} - 1\} \\ \frac{1}{\delta} [\text{cdf}_{\chi_s}(d_{\max}) - \text{cdf}_{\chi_s}(d_{\max} - \delta)] & \text{if } u = d_{\max} \\ \frac{1}{\delta} \left[\text{cdf}_{\chi_s}\left(\delta \left\lceil \frac{u}{\delta} \right\rceil\right) - \text{cdf}_{\chi_s}\left(\delta \left\lfloor \frac{u}{\delta} \right\rfloor\right) \right] & \text{otherwise} \end{cases} \quad (\text{F.42})$$

Let $l \in \{1, \dots, N_{\text{sh}} - 1\}$. Consider $u \in \left[\frac{d_{\max}}{N_{\text{sh}}}(l - 1), \frac{d_{\max}}{N_{\text{sh}}}l \right)$. Then, $\frac{uN_{\text{sh}}}{d_{\max}} \in [l - 1, l)$, which implies that, for such u ,

$$a_{N_{\text{sh}}}(u) = \frac{\text{cdf}_{\chi_s}\left(\frac{d_{\max}}{N_{\text{sh}}}[l]\right) - \text{cdf}_{\chi_s}\left(\frac{d_{\max}}{N_{\text{sh}}}[l - 1]\right)}{d_{\max}/N_{\text{sh}}} = (W_l) \text{pdf}_{U_l}(u) \quad (\text{F.43})$$

Let $l = N_{\text{sh}}$. Consider $u \in \left[\frac{d_{\max}}{N_{\text{sh}}}(l - 1), \frac{d_{\max}}{N_{\text{sh}}}l \right)$. Then, $\frac{uN_{\text{sh}}}{d_{\max}} \in [l - 1, l]$, which implies that, for such u ,

$$a_{N_{\text{sh}}}(u) = \frac{\text{cdf}_{\chi_s}\left(\frac{d_{\max}}{N_{\text{sh}}}[l]\right) - \text{cdf}_{\chi_s}\left(\frac{d_{\max}}{N_{\text{sh}}}[l - 1]\right)}{d_{\max}/N_{\text{sh}}} = (W_l) \text{pdf}_{U_l}(u) \quad (\text{F.44})$$

Therefore, for $u \in A_l$, for $l \in \{1, \dots, N_{\text{sh}}\}$, the value of $a_{N_{\text{sh}}}(u)$ is given by

$$a_{N_{\text{sh}}}(u) = \frac{\text{cdf}_{\chi_s}\left(\frac{d_{\max}}{N_{\text{sh}}}[l]\right) - \text{cdf}_{\chi_s}\left(\frac{d_{\max}}{N_{\text{sh}}}[l - 1]\right)}{d_{\max}/N_{\text{sh}}} = (W_l) \text{pdf}_{U_l}(u) \quad (\text{F.45})$$

Then,

$$\begin{aligned} I_{N_{\text{sh}}} &= \sum_{l=1}^{N_{\text{sh}}} \iint_{\mathbb{S}^{(s-1)} \times A_l} g(\gamma[h(\underline{z}, u)]) \text{pdf}_{\underline{Z}}(\underline{z}) [(W_l) \text{pdf}_{U_l}(u)] d\underline{z} du \\ &= \sum_{l=1}^{N_{\text{sh}}} \iint_{\mathbb{S}^{(s-1)} \times A_l} g(\gamma[h(\underline{z}, u)]) \text{pdf}_{\underline{Z}}(\underline{z}) a_{N_{\text{sh}}}(u) d\underline{z} du \quad (\text{F.46}) \end{aligned}$$

Note: the A_l sets are disjoint; hence, the Cartesian products $\mathbb{S}^{(s-1)} \times A_l$ are also disjoint.

Hence, the fact that

$$\bigcup_{l=1}^{N_{\text{sh}}} A_l = [0, d_{\text{max}}] \quad (\text{F.47})$$

implies that

$$\bigcup_{l=1}^{N_{\text{sh}}} [\mathbb{S}^{(s-1)} \times A_l] = \mathbb{S}^{(s-1)} \times \bigcup_{l=1}^{N_{\text{sh}}} A_l = \mathbb{S}^{(s-1)} \times [0, d_{\text{max}}] \quad (\text{F.48})$$

By countable additivity of integrals with respect to abstract measures, it follows that

$$I_{N_{\text{sh}}} = \iint_{\mathbb{S}^{(s-1)} \times [0, d_{\text{max}}]} g(\gamma[h(\underline{z}, u)]) \text{pdf}_{\underline{z}}(\underline{z}) a_{N_{\text{sh}}}(u) \, d\underline{z} \, du \quad (\text{F.49})$$

Let the function $f_{N_{\text{sh}}} : \mathbb{S}^{(s-1)} \times [0, d_{\text{max}}] \rightarrow \mathbb{R}$ be defined such that

$$f_{N_{\text{sh}}} \left(\begin{bmatrix} \underline{z} \\ u \end{bmatrix} \right) = g(\gamma[h(\underline{z}, u)]) \text{pdf}_{\underline{z}}(\underline{z}) a_{N_{\text{sh}}}(u) \quad (\text{F.50})$$

for $[\underline{z}^T, u]^T \in \mathbb{S}^{(s-1)} \times [0, d_{\text{max}}]$. Note:

$$I_{N_{\text{sh}}} = \iint_{\mathbb{S}^{(s-1)} \times [0, d_{\text{max}}]} f_{N_{\text{sh}}} \left(\begin{bmatrix} \underline{z} \\ u \end{bmatrix} \right) \, d\underline{z} \, du \quad (\text{F.51})$$

It will be shown that $f_{N_{\text{sh}}} \rightarrow f$ pointwise a.e.; that is, it will be demonstrated that, for a.e. $[\underline{z}^T, u]^T \in \mathbb{S}^{(s-1)} \times [0, d_{\text{max}}]$,

$$\lim_{N_{\text{sh}} \rightarrow \infty} f_{N_{\text{sh}}} \left(\begin{bmatrix} \underline{z} \\ u \end{bmatrix} \right) = f \left(\begin{bmatrix} \underline{z} \\ u \end{bmatrix} \right) \quad (\text{F.52})$$

where such a.e. property holds w.r.t. to the prod measure in $\mathbb{S}^{(s-1)} \times [0, d_{\text{max}}]$ (for $s = 1$) w.r.t. to the Lebesgue measure in $\mathbb{S}^{(s-1)} \times [0, d_{\text{max}}]$ (for integers $s \geq 2$).

Subproof. Let the preceding notation and assumptions hold.

Fix $[\underline{z}^T, u]^T \in \mathbb{S}^{(s-1)} \times [0, d_{\max}]$. Then,

$$\begin{aligned} \lim_{N_{\text{sh}} \rightarrow \infty} f_{N_{\text{sh}}} \left(\begin{bmatrix} \underline{z} \\ u \end{bmatrix} \right) &= \lim_{N_{\text{sh}} \rightarrow \infty} g(\gamma[h(\underline{z}, u)]) \text{pdf}_{\underline{z}}(\underline{z}) a_{N_{\text{sh}}}(u) \\ &= g(\gamma[h(\underline{z}, u)]) \text{pdf}_{\underline{z}}(\underline{z}) \lim_{N_{\text{sh}} \rightarrow \infty} a_{N_{\text{sh}}}(u) \end{aligned} \quad (\text{F.53})$$

Hence, the main goal in this subproof is to show that, for a.e. $u \in [0, d_{\max}]$,

$$\lim_{N_{\text{sh}} \rightarrow \infty} a_{N_{\text{sh}}}(u) = \text{pdf}_{\chi_s}(u) \quad (\text{F.54})$$

Fix $u \in (0, d_{\max})$. Let $h \in \mathbb{R}$ satisfy $u + h \in (0, d_{\max})$, which implies that $h \in (-u, -u + d_{\max})$. Let the function $F : (-u, -u + d_{\max}) \rightarrow \mathbb{R}$ be defined as

$$F(h) = \frac{\text{cdf}_{\chi_s}(u + h) - \text{cdf}_{\chi_s}(u)}{h} \quad (\text{F.55})$$

for $h \in (-u, -u + d_{\max})$. Then, the variable L_u satisfies

$$L_u = \lim_{h \rightarrow 0} F(h) = \lim_{h \rightarrow 0} \frac{\text{cdf}_{\chi_s}(u + h) - \text{cdf}_{\chi_s}(u)}{h} = \text{pdf}_{\chi_s}(u) \quad (\text{F.56})$$

Note: the cdf of χ_s is continuously differentiable in $[0, \infty)$; i.e., the pdf of χ_s exists and is continuous in $[0, \infty)$. [191] However, for the purposes of this subproof, only the existence of the pdf of χ_s on $(0, d_{\max})$ is needed.

Take $\varepsilon > 0$. Then, there exists some $\delta > 0$ such that, for every h such that $0 < |h| < \delta$,

$$\left| \frac{\text{cdf}_{\chi_s}(u + h) - \text{cdf}_{\chi_s}(u)}{h} - \text{pdf}_{\chi_s}(u) \right| < \varepsilon \quad (\text{F.57})$$

without loss of generality, δ may be restricted such that $(u - \delta, u + \delta) \subsetneq (0, d_{\max})$.

Let $N \in \mathbb{N}$. For $l \in \{1, \dots, N-1\}$, let the sets B_l and B_N be defined as

$$B_l = \left[\frac{l-1}{N}, \frac{l}{N} \right) \quad (\text{F.58})$$

$$B_N = \left[\frac{N-1}{N}, \frac{N}{N} \right] \quad (\text{F.59})$$

It will be demonstrated that there exists some $M \in \mathbb{N}$ such that, for all integers $N \geq M$, there exists some $l \in \{1, \dots, N\}$ such that

$$\frac{u}{d_{\max}} \in B_l \subseteq \left(\frac{u-\delta}{d_{\max}}, \frac{u+\delta}{d_{\max}} \right) \quad (\text{F.60})$$

Let $M \in \mathbb{N}$ be defined such that

$$\frac{1}{M} < \frac{1}{4} \frac{\delta}{d_{\max}}. \quad (\text{F.61})$$

Then,

$$M < \frac{4d_{\max}}{\delta}. \quad (\text{F.62})$$

Let $N \in \mathbb{N}$ be defined such that $N \geq M$, which implies that

$$\frac{1}{N} \leq \frac{1}{M} < \frac{1}{4} \frac{\delta}{d_{\max}}. \quad (\text{F.63})$$

Then, by Lemma 67, there exists some $l \in \{1, \dots, N\}$ such that

$$\frac{u}{d_{\max}} \in B_l \quad (\text{F.64})$$

$$\frac{u}{d_{\max}} \notin \bigcup_{\substack{j \in \{1, \dots, N\} \\ j \neq l}} B_j \quad (\text{F.65})$$

Let $l \in \{1, \dots, N\}$ satisfy Eqns. F.64 and F.65. Then,

$$\frac{l-1}{N} \leq \frac{u}{d_{\max}} \leq \frac{l}{N} \quad (\text{F.66})$$

which implies that

$$\frac{l-1}{N} + \frac{1}{N} = \frac{l}{N} \leq \frac{u}{d_{\max}} + \frac{1}{N} \quad (\text{F.67})$$

$$\frac{u}{d_{\max}} - \frac{1}{N} \leq \frac{l}{N} - \frac{1}{N} = \frac{l-1}{N} \quad (\text{F.68})$$

Therefore,

$$\frac{u}{d_{\max}} - \frac{1}{N} \leq \frac{l-1}{N} \leq \frac{u}{d_{\max}} \leq \frac{l}{N} \leq \frac{u}{d_{\max}} + \frac{1}{N} \quad (\text{F.69})$$

Then,

$$\frac{u}{d_{\max}} \in B_l \subseteq \left[\frac{l-1}{N}, \frac{l}{N} \right] \subseteq \left[\frac{u}{d_{\max}} - \frac{1}{N}, \frac{u}{d_{\max}} + \frac{1}{N} \right] \quad (\text{F.70})$$

Since $N \geq M$,

$$\frac{1}{N} < \frac{1}{4} \frac{\delta}{d_{\max}} < \frac{\delta}{d_{\max}} \quad (\text{F.71})$$

$$-\frac{1}{N} > -\frac{1}{4} \frac{\delta}{d_{\max}} > -\frac{\delta}{d_{\max}} \quad (\text{F.72})$$

Then,

$$\frac{u}{d_{\max}} + \frac{1}{N} < \frac{u}{d_{\max}} + \frac{1}{4} \frac{\delta}{d_{\max}} < \frac{u}{d_{\max}} + \frac{\delta}{d_{\max}} \quad (\text{F.73})$$

$$\frac{u}{d_{\max}} - \frac{1}{N} > \frac{u}{d_{\max}} - \frac{1}{4} \frac{\delta}{d_{\max}} > \frac{u}{d_{\max}} - \frac{\delta}{d_{\max}} \quad (\text{F.74})$$

Aggregating these results, it follows that

$$\frac{u-\delta}{d_{\max}} < \frac{u}{d_{\max}} - \frac{1}{N} \leq \frac{l-1}{N} \leq \frac{u}{d_{\max}} \leq \frac{l}{N} \leq \frac{u}{d_{\max}} + \frac{1}{N} < \frac{u+\delta}{d_{\max}} \quad (\text{F.75})$$

Therefore,

$$\frac{u}{d_{\max}} \in B_l \subseteq \left[\frac{l-1}{N}, \frac{l}{N} \right] \subseteq \left[\frac{u}{d_{\max}} - \frac{1}{N}, \frac{u}{d_{\max}} + \frac{1}{N} \right] \not\subseteq \left(\frac{u-\delta}{d_{\max}}, \frac{u+\delta}{d_{\max}} \right) \quad (\text{F.76})$$

Let $\eta_{\text{sh}} \in \mathbb{N}$ be given by

$$\eta_{\text{sh}} = \left\lceil \frac{4d_{\max}}{\delta} \right\rceil + 1 \quad (\text{F.77})$$

Then,

$$\eta_{\text{sh}} > \left\lceil \frac{4d_{\max}}{\delta} \right\rceil \geq \frac{4d_{\max}}{\delta} \quad (\text{F.78})$$

Let $N_{\text{sh}} \geq \eta_{\text{sh}}$. Then, $N_{\text{sh}} > \frac{4d_{\max}}{\delta}$, so

$$\delta > \frac{4d_{\max}}{N_{\text{sh}}} > \frac{d_{\max}}{N_{\text{sh}}} \quad (\text{F.79})$$

Then, via Eqns. F.64, F.65, and F.76, there exists some $l \in \{1, \dots, N_{\text{sh}}\}$ such that

$$\frac{u}{d_{\max}} \in B_l \subseteq \left[\frac{l-1}{N_{\text{sh}}}, \frac{l}{N_{\text{sh}}} \right] \subseteq \left[\frac{u}{d_{\max}} - \frac{1}{N_{\text{sh}}}, \frac{u}{d_{\max}} + \frac{1}{N_{\text{sh}}} \right] \not\subseteq \left(\frac{u-\delta}{d_{\max}}, \frac{u+\delta}{d_{\max}} \right) \quad (\text{F.80})$$

$$\frac{u}{d_{\max}} \notin \bigcup_{\substack{j \in \{1, \dots, N_{\text{sh}}\} \\ j \neq l}} B_j \quad (\text{F.81})$$

Let $l \in \{1, \dots, N_{\text{sh}}\}$. Let u/d_{\max} satisfy Eqns. F.80 and F.81. Then, as per Eq. F.45,

$$a_{N_{\text{sh}}}(u) = \frac{\text{cdf}_{\chi_s} \left(\left[l \right] \frac{d_{\max}}{N_{\text{sh}}} \right) - \text{cdf}_{\chi_s} \left(\left[l-1 \right] \frac{d_{\max}}{N_{\text{sh}}} \right)}{d_{\max}/N_{\text{sh}}} = (W_l) \text{pdf}_{U_l}(u) \quad (\text{F.82})$$

Let u/d_{\max} be restricted so that $u/d_{\max} \in (0, 1)$. It will be shown whether all such u/d_{\max} satisfy

$$|a_{N_{\text{sh}}}(u) - \text{pdf}_{\chi_s}(u)| < \varepsilon \quad (\text{F.83})$$

1. Case I: $u = \frac{d_{\max}}{N_{\text{sh}}} [l]$

Let $h = \frac{d_{\max}}{N_{\text{sh}}}$. Then, $h < \delta$. Let $h' = -h$. Note that $|h'| = |h| < \delta$. Therefore,

$$\begin{aligned} a_{N_{\text{sh}}}(u) &= \frac{\text{cdf}_{\chi_s}(u) - \text{cdf}_{\chi_s}(u - h)}{h} \\ &= \frac{\text{cdf}_{\chi_s}(u) - \text{cdf}_{\chi_s}(u + h')}{-h'} \\ &= \frac{\text{cdf}_{\chi_s}(u + h') - \text{cdf}_{\chi_s}(u)}{h'} \end{aligned} \quad (\text{F.84})$$

It follows from Eq. F.57 that

$$|a_{N_{\text{sh}}}(u) - \text{pdf}_{\chi_s}(u)| < \varepsilon \quad (\text{F.85})$$

Note: this case is listed for informational purposes only, since this case would only occur if $l = N_{\text{sh}}$, which is not being considered since $u/d_{\max} \in (0, 1)$.

2. Case 2: $u = \frac{d_{\max}}{N_{\text{sh}}}[l - 1]$

Let $h = \frac{d_{\max}}{N_{\text{sh}}}$. Then, $h < \delta$. Therefore,

$$a_{N_{\text{sh}}}(u) = \frac{\text{cdf}_{\chi_s}(u + h) - \text{cdf}_{\chi_s}(u)}{h} \quad (\text{F.86})$$

Hence, from Eq. F.57, it follows that

$$|a_{N_{\text{sh}}}(u) - \text{pdf}_{\chi_s}(u)| < \varepsilon \quad (\text{F.87})$$

3. Case 3: $\frac{d_{\max}}{N_{\text{sh}}}[l - 1] < u < \frac{d_{\max}}{N_{\text{sh}}}[l]$.

Let the variables d_L , d_U , and d'_L be defined as

$$d_L = u - [l - 1] \frac{d_{\max}}{N_{\text{sh}}} > 0 \quad (\text{F.88})$$

$$d_U = \frac{[l]d_{\max}}{N_{\text{sh}}} - u > 0 \quad (\text{F.89})$$

$$d'_L = -d_L \quad (\text{F.90})$$

Then, the following properties concerning d_L , d_U , and d'_L hold on.

$$d_L + d_U = \frac{d_{\max}}{N_{\text{sh}}} < \delta \quad (\text{F.91})$$

$$d_L = |d'_L| < \frac{d_{\max}}{N_{\text{sh}}} < \delta \quad (\text{F.92})$$

$$d_U < \frac{d_{\max}}{N_{\text{sh}}} < \delta \quad (\text{F.93})$$

Then,

$$a_{N_{\text{sh}}}(u) = \frac{\text{cdf}_{\chi_s} \left(\frac{[l]d_{\max}}{N_{\text{sh}}} \right) - \text{cdf}_{\chi_s} \left([l-1] \frac{d_{\max}}{N_{\text{sh}}} \right)}{d_{\max}/N_{\text{sh}}} = \frac{\text{cdf}_{\chi_s}(u + d_U) - \text{cdf}_{\chi_s}(u - d_L)}{d_{\max}/N_{\text{sh}}} \quad (\text{F.94})$$

which implies that

$$a_{N_{\text{sh}}}(u) = \frac{\text{cdf}_{\chi_s}(u + d_U) - \text{cdf}_{\chi_s}(u) + \text{cdf}_{\chi_s}(u) - \text{cdf}_{\chi_s}(u - d_L)}{d_{\max}/N_{\text{sh}}} \quad (\text{F.95})$$

which, in turn, implies that

$$a_{N_{\text{sh}}}(u) = \frac{d_U}{d_{\max}/N_{\text{sh}}} \frac{\text{cdf}_{\chi_s}(u + d_U) - \text{cdf}_{\chi_s}(u)}{d_U} + \frac{d_L}{d_{\max}/N_{\text{sh}}} \frac{\text{cdf}_{\chi_s}(u) - \text{cdf}_{\chi_s}(u - d_L)}{d_L} \quad (\text{F.96})$$

It should be noted that

$$\text{pdf}_{\chi_s}(u) = \text{pdf}_{\chi_s}(u) \left[\frac{d_U}{d_{\max}/N_{\text{sh}}} + \frac{d_L}{d_{\max}/N_{\text{sh}}} \right] \quad (\text{F.97})$$

Hence,

$$\begin{aligned} |a_{N_{\text{sh}}}(u) - \text{pdf}_{\chi_s}(u)| &\leq \left| \frac{d_U}{d_{\text{max}}/N_{\text{sh}}} \left[\frac{\text{cdf}_{\chi_s}(u + d_U) - \text{cdf}_{\chi_s}(u)}{d_U} - \text{pdf}_{\chi_s}(u) \right] \right| \\ &+ \left| \frac{d_L}{d_{\text{max}}/N_{\text{sh}}} \left[\frac{\text{cdf}_{\chi_s}(u) - \text{cdf}_{\chi_s}(u - d_L)}{d_L} - \text{pdf}_{\chi_s}(u) \right] \right| \end{aligned} \quad (\text{F.98})$$

which implies that

$$\begin{aligned} |a_{N_{\text{sh}}}(u) - \text{pdf}_{\chi_s}(u)| &\leq \frac{d_U}{d_{\text{max}}/N_{\text{sh}}} \left| \frac{\text{cdf}_{\chi_s}(u + d_U) - \text{cdf}_{\chi_s}(u)}{d_U} - \text{pdf}_{\chi_s}(u) \right| \\ &+ \frac{d_L}{d_{\text{max}}/N_{\text{sh}}} \left| \frac{\text{cdf}_{\chi_s}(u + d'_L) - \text{cdf}_{\chi_s}(u)}{d'_L} - \text{pdf}_{\chi_s}(u) \right| \end{aligned} \quad (\text{F.99})$$

Thus,

$$\begin{aligned} |a_{N_{\text{sh}}}(u) - \text{pdf}_{\chi_s}(u)| &< \frac{d_U}{d_{\text{max}}/N_{\text{sh}}} \varepsilon + \frac{d_L}{d_{\text{max}}/N_{\text{sh}}} \varepsilon \\ &= \varepsilon \left[\frac{d_U}{d_{\text{max}}/N_{\text{sh}}} + \frac{d_L}{d_{\text{max}}/N_{\text{sh}}} \right] = \varepsilon \end{aligned} \quad (\text{F.100})$$

Therefore, Eqns. F.87 and F.100 imply that, for every $u/d_{\text{max}} \in (0, 1)$, for every $\varepsilon > 0$, there exists some integer η_{sh} such that, for every integer $N_{\text{sh}} \geq \eta_{\text{sh}}$,

$$|a_{N_{\text{sh}}}(u) - \text{pdf}_{\chi_s}(u)| < \varepsilon \quad (\text{F.101})$$

Thus, $a_{N_{\text{sh}}} \rightarrow \text{pdf}_{\chi_s}$ pointwise on $(0, d_{\text{max}})$.

Since the set $\{0, d_{\text{max}}\}$ has zero Lebesgue measure, it follows that $a_{N_{\text{sh}}} \rightarrow \text{pdf}_{\chi_s}$ pointwise a.e. on $[0, d_{\text{max}}]$.

Let $u \in (0, d_{\text{max}})$. Hence,

$$\lim_{N_{\text{sh}} \rightarrow \infty} a_{N_{\text{sh}}}(u) = \text{pdf}_{\chi_s}(u) = \text{pdf}_D(u) \quad (\text{F.102})$$

Consider $[\underline{z}^T, u]^T \in \mathbb{S}^{(s-1)} \times (0, d_{\max})$. Then, via Eqns. F.28, F.53, and F.102, it follows that

$$\begin{aligned} \lim_{N_{\text{sh}} \rightarrow \infty} f_{N_{\text{sh}}} \left(\begin{bmatrix} \underline{z} \\ u \end{bmatrix} \right) &= g(\gamma[h(\underline{z}, u)]) \text{pdf}_{\underline{z}}(\underline{z}) \lim_{N_{\text{sh}} \rightarrow \infty} a_{N_{\text{sh}}}(u) \\ &= g(\gamma[h(\underline{z}, u)]) \text{pdf}_{\underline{z}}(\underline{z}) \text{pdf}_D(u) = f \left(\begin{bmatrix} \underline{z} \\ u \end{bmatrix} \right) \end{aligned} \quad (\text{F.103})$$

Hence, $f_{N_{\text{sh}}} \rightarrow f$ pointwise on $\mathbb{S}^{(s-1)} \times (0, d_{\max})$.

However, since the set $\{0, d_{\max}\}$ has zero Lebesgue measure on $[0, d_{\max}]$, it follows that:

1. For $s = 1$, the set $\mathbb{S}^{(s-1)} \times \{0, d_{\max}\}$ has zero prod measure in $\mathbb{S}^{(s-1)} \times [0, d_{\max}]$.
2. For integers $s \geq 2$, the set $\mathbb{S}^{(s-1)} \times \{0, d_{\max}\}$ has zero Lebesgue measure in $\mathbb{S}^{(s-1)} \times [0, d_{\max}]$. [34]

Therefore,

$$f_{N_{\text{sh}}} \rightarrow f \text{ pointwise a.e. } \begin{cases} \text{w.r.t. prod measure on } \mathbb{S}^{(s-1)} \times [0, d_{\max}] & \text{if } s = 1 \\ \text{w.r.t. Lebesgue measure on } \mathbb{S}^{(s-1)} \times [0, d_{\max}] & \text{if } s \geq 2 \end{cases} \quad (\text{F.104})$$

which was to be shown. ■

Let $N_{\text{sh}} \in \mathbb{N}$. Let $l \in \{1, \dots, N_{\text{sh}}\}$. Let $P_{N_{\text{sh}}}$ be the set defined as

$$P_{N_{\text{sh}}} = \left\{ x \in [0, 1] : x = \frac{l}{N_{\text{sh}}}, l \in \{0, \dots, N_{\text{sh}}\} \right\} \quad (\text{F.105})$$

Let $u \in [0, d_{\max}]$ be restricted to

$$u \in \left(\frac{[l-1]d_{\max}}{N_{\text{sh}}}, \frac{[l]d_{\max}}{N_{\text{sh}}} \right) \subseteq A_l \quad (\text{F.106})$$

Then, via Lemma 67,

$$\frac{u}{d_{\max}} \notin \bigcup_{\substack{j \in \{1, \dots, N_{\text{sh}}\} \\ j \neq l}} B_j \quad (\text{F.107})$$

Note: for such an u , $a_{N_{\text{sh}}}(u)$ is given by

$$a_{N_{\text{sh}}}(u) = \frac{\text{cdf}_{\chi_s} \left(\frac{\lfloor l \rfloor d_{\max}}{N_{\text{sh}}} \right) - \text{cdf}_{\chi_s} \left(\frac{\lfloor l-1 \rfloor d_{\max}}{N_{\text{sh}}} \right)}{d_{\max}/N_{\text{sh}}} \quad (\text{F.108})$$

Let the variables c_1 and c_2 ,

$$c_1 = \frac{\lfloor l-1 \rfloor d_{\max}}{N_{\text{sh}}} \quad (\text{F.109})$$

$$c_2 = \frac{\lfloor l \rfloor d_{\max}}{N_{\text{sh}}} \quad (\text{F.110})$$

Then,

$$a_{N_{\text{sh}}}(u) = \frac{\text{cdf}_{\chi_s}(c_2) - \text{cdf}_{\chi_s}(c_1)}{c_2 - c_1} \quad (\text{F.111})$$

Since cdf_{χ_s} is differentiable in $(0, \infty) \supseteq (c_1, c_2)$, by the Mean Value Theorem (MVT), [66] there exists some $c \in (c_1, c_2)$ such that

$$a_{N_{\text{sh}}}(u) = \frac{d}{dx} \text{cdf}_{\chi_s}(x) \Big|_{x=c} = \text{pdf}_{\chi_s}(c) \quad (\text{F.112})$$

Hence, for all $u \in [0, d_{\max}] \setminus P_{N_{\text{sh}}}$, there exists some $c \in [0, d_{\max}] \setminus P_{N_{\text{sh}}}$ such that

$$a_{N_{\text{sh}}}(u) = \text{pdf}_{\chi_s}(c) \quad (\text{F.113})$$

Note: for $s \in \mathbb{N}$, pdf_{χ_s} is a bounded function. Hence,

$$M_{\chi_s} = \sup_{u \in [0, \infty)} |\text{pdf}_{\chi_s}(u)| < \infty \quad (\text{F.114})$$

Hence, for all $u \in [0, d_{\max}] \setminus P_{N_{\text{sh}}}$, there exist some $c \in [0, d_{\max}] \setminus P_{N_{\text{sh}}}$,

$$a_{N_{\text{sh}}}(u) = \text{pdf}_{\chi_s}(c) \leq M_{\chi_s} \quad (\text{F.115})$$

Therefore, the function $a_{N_{\text{sh}}}$ is bounded on $[0, d_{\max}] \setminus P_{N_{\text{sh}}}$. Since $P_{N_{\text{sh}}}$ is a set of zero Lebesgue measure in $[0, d_{\max}]$, it follows that the function $a_{N_{\text{sh}}}$ is bounded a.e. in $[0, d_{\max}]$.

Let the function $V : \mathbb{S}^{(s-1)} \times [0, d_{\max}] \rightarrow \mathbb{R}$ satisfy

$$V \left(\begin{bmatrix} \underline{z} \\ u \end{bmatrix} \right) = g(\gamma[h(\underline{z}, u)]) \quad (\text{F.116})$$

for $[\underline{z}^T, u]^T \in \mathbb{S}^{(s-1)} \times [0, d_{\max}]$. Then, because of the integrability of g [and since $\text{supp}(g) \subseteq V_{d_{\max}}(\underline{X})$], it follows that

$$\begin{aligned} \int_{\mathbb{S}^{(s-1)} \times [0, d_{\max}]} |V([\underline{z}^T, u]^T)| \, d\underline{z} \, du &= \int_{\mathbb{S}^{(s-1)} \times [0, d_{\max}]} |g(\gamma[h(\underline{z}, u)])| \, d\underline{z} \, du \\ &= \int_{V_{d_{\max}}(\underline{X})} |g(\underline{x})| \, d\underline{x} = \int_{\mathbb{R}^s} |g(\underline{x})| \, d\underline{x} < \infty \end{aligned} \quad (\text{F.117})$$

Therefore, V is an integrable function in $\mathbb{S}^{(s-1)} \times [0, d_{\max}]$. Specifically, for $s = 1$, $V \in \text{prod}^1(\mathbb{S}^{(s-1)} \times [0, d_{\max}])$; for integers $s \geq 2$, $V \in \mathcal{L}^1(\mathbb{S}^{(s-1)} \times [0, d_{\max}])$.

Let the functions $W_{N_{\text{sh}}} : \mathbb{S}^{(s-1)} \times [0, d_{\max}] \rightarrow [0, \infty)$ and $W : \mathbb{S}^{(s-1)} \times [0, d_{\max}] \rightarrow [0, \infty)$ be defined as

$$W_{N_{\text{sh}}} \left(\begin{bmatrix} \underline{z} \\ u \end{bmatrix} \right) = \text{pdf}_{\underline{z}}(\underline{z}) a_{N_{\text{sh}}}(u) \quad (\text{F.118})$$

$$W \left(\begin{bmatrix} \underline{z} \\ u \end{bmatrix} \right) = \frac{\Gamma(s/2)}{2(\pi)^{(s/2)}} M_{\chi_s} =: C_{\chi_s} \quad (\text{F.119})$$

for $[\underline{z}^T, u]^T \in \mathbb{S}^{(s-1)} \times [0, d_{\max}]$. Note: for $[\underline{z}^T, u]^T \in \mathbb{S}^{(s-1)} \times [0, d_{\max}] \setminus P_{N_{\text{sh}}}$,

$$\left| W_{N_{\text{sh}}} \left(\begin{bmatrix} \underline{z} \\ u \end{bmatrix} \right) \right| = |\text{pdf}_{\underline{z}}(\underline{z}) a_{N_{\text{sh}}}(u)| = \left| \frac{\Gamma(s/2)}{2(\pi)^{(s/2)}} a_{N_{\text{sh}}}(u) \right| \quad (\text{F.120})$$

which implies that

$$\left| W_{N_{\text{sh}}} \left(\begin{bmatrix} \underline{z} \\ u \end{bmatrix} \right) \right| = \frac{\Gamma(s/2)}{2(\pi)^{(s/2)}} |a_{N_{\text{sh}}}(u)| \leq \frac{\Gamma(s/2)}{2(\pi)^{(s/2)}} M_{\chi_s} = W \left(\begin{bmatrix} \underline{z} \\ u \end{bmatrix} \right) \quad (\text{F.121})$$

Thus, $|W_{N_{\text{sh}}}| \leq W$ in $\mathbb{S}^{(s-1)} \times [0, d_{\max}] \setminus P_{N_{\text{sh}}}$. Since the set $P_{N_{\text{sh}}}$ has zero Lebesgue measure in $[0, d_{\max}]$, it follows that:

1. For $s = 1$, the set $\mathbb{S}^{(s-1)} \times P_{N_{\text{sh}}}$ has zero prod measure in $\mathbb{S}^{(s-1)} \times [0, d_{\max}]$. Therefore, $|W_{N_{\text{sh}}}| \leq W$ a.e. (w.r.t. to the prod measure in $\mathbb{S}^{(s-1)} \times [0, d_{\max}]$).
2. For integers $s \geq 2$, the set $\mathbb{S}^{(s-1)} \times P_{N_{\text{sh}}}$ has zero Lebesgue measure in $\mathbb{S}^{(s-1)} \times [0, d_{\max}]$. Therefore, $|W_{N_{\text{sh}}}| \leq W$ a.e. (w.r.t. to the Lebesgue measure in $\mathbb{S}^{(s-1)} \times [0, d_{\max}]$).

Since W is a function with a single, finite constant value throughout its domain (specifically, C_{χ_s}), W is a bounded function in $\mathbb{S}^{(s-1)} \times [0, d_{\max}]$. Therefore, W is an essentially bounded function in $\mathbb{S}^{(s-1)} \times [0, d_{\max}]$. Specifically, for $s = 1$, it follows that $W \in \text{prod}^\infty(\mathbb{S}^{(s-1)} \times [0, d_{\max}])$ – that is, W belongs to the set of functions in $\mathbb{S}^{(s-1)} \times [0, d_{\max}]$ that are essentially bounded with respect to the prod measure; for integers $s \geq 2$, $W \in \mathcal{L}^\infty(\mathbb{S}^{(s-1)} \times [0, d_{\max}])$.

Since the product of an integrable function and an essentially bounded function is an integrable function,[34] it follows that VW is an integrable function in $\mathbb{S}^{(s-1)} \times [0, d_{\max}]$. Specifically, for $s = 1$, $VW \in \text{prod}^1(\mathbb{S}^{(s-1)} \times [0, d_{\max}])$; for integers $s \geq 2$, $VW \in \mathcal{L}^1(\mathbb{S}^{(s-1)} \times [0, d_{\max}])$.

Consider $[z^T, u]^T \in \mathbb{S}^{(s-1)} \times [0, d_{\max}] \setminus P_{N_{\text{sh}}}$. Then,

$$\left| f_{N_{\text{sh}}} \left(\begin{bmatrix} z \\ u \end{bmatrix} \right) \right| = |g(\gamma[h(z, u)]) \text{pdf}_{\underline{z}}(z) a_{N_{\text{sh}}}(u)| = |g(\gamma[h(z, u)])| |\text{pdf}_{\underline{z}}(z) a_{N_{\text{sh}}}(u)| \quad (\text{F.122})$$

which implies that

$$\left| f_{N_{\text{sh}}} \left(\begin{bmatrix} z \\ u \end{bmatrix} \right) \right| = \left| V \left(\begin{bmatrix} z \\ u \end{bmatrix} \right) \right| \left| W_{N_{\text{sh}}} \left(\begin{bmatrix} z \\ u \end{bmatrix} \right) \right| \leq \left| V \left(\begin{bmatrix} z \\ u \end{bmatrix} \right) \right| \left| W \left(\begin{bmatrix} z \\ u \end{bmatrix} \right) \right| \quad (\text{F.123})$$

Hence, $|f_{N_{\text{sh}}}| \leq |VW|$ in $\mathbb{S}^{(s-1)} \times [0, d_{\max}] \setminus P_{N_{\text{sh}}}$. Hence,

1. Since for $s = 1$, the set $\mathbb{S}^{(s-1)} \times P_{N_{\text{sh}}}$ has zero prod measure in $\mathbb{S}^{(s-1)} \times [0, d_{\max}]$, it follows that $|f_{N_{\text{sh}}}| \leq |VW|$ a.e. (w.r.t. to the prod measure in $\mathbb{S}^{(s-1)} \times [0, d_{\max}]$).
2. Since for integers $s \geq 2$, the set $\mathbb{S}^{(s-1)} \times P_{N_{\text{sh}}}$ has zero Lebesgue measure in $\mathbb{S}^{(s-1)} \times [0, d_{\max}]$, it follows that $|f_{N_{\text{sh}}}| \leq |VW|$ a.e. (w.r.t. to the Lebesgue measure in $\mathbb{S}^{(s-1)} \times [0, d_{\max}]$).

Therefore, there exists an integrable function $f_{\text{dom}} : \mathbb{S}^{(s-1)} \times [0, d_{\max}] \rightarrow [0, \infty]$ [namely, $f_{\text{dom}} \doteq |VW|$; for $s = 1$, $f_{\text{dom}} \in \text{prod}^1(\mathbb{S}^{(s-1)} \times [0, d_{\max}])$, and for integers $s \geq 2$, $f_{\text{dom}} \in \mathcal{L}^1(\mathbb{S}^{(s-1)} \times [0, d_{\max}])$] such that, for every integer N_{sh} ,

$$|f_{N_{\text{sh}}}| \leq f_{\text{dom}} \text{ a.e. } \begin{cases} \text{w.r.t. prod measure on } \mathbb{S}^{(s-1)} \times [0, d_{\max}] & \text{if } s = 1 \\ \text{w.r.t. Lebesgue measure on } \mathbb{S}^{(s-1)} \times [0, d_{\max}] & \text{if } s \geq 2 \end{cases} \quad (\text{F.124})$$

In summary, via Eqns. F.104 and F.124, the following statements hold [noting that a.e. statements and integrability hold w.r.t. the prod measure on $\mathbb{S}^{(s-1)} \times [0, d_{\max}]$ (if $s = 1$) and w.r.t. the Lebesgue measure on $\mathbb{S}^{(s-1)} \times [0, d_{\max}]$ (for integers $s \geq 2$):

- a. For all $N_{\text{sh}} \in \mathbb{N}$, $|f_{N_{\text{sh}}}| \leq f_{\text{dom}}$ a.e.

- b. f_{dom} is integrable
- c. $|f_{N_{\text{sh}}}| \rightarrow f$ pointwise a.e.

Therefore, one of the consequences of the Dominated Convergence Theorem (DCT) is the following:[85, 34]

$$\begin{aligned} \lim_{N_{\text{sh}} \rightarrow \infty} \iint_{\mathbb{S}^{(s-1)} \times [0, d_{\text{max}}]} f_{N_{\text{sh}}} \left(\begin{bmatrix} z \\ u \end{bmatrix} \right) d\underline{z} du \\ = \iint_{\mathbb{S}^{(s-1)} \times [0, d_{\text{max}}]} f \left(\begin{bmatrix} z \\ u \end{bmatrix} \right) d\underline{z} du \end{aligned} \quad (\text{F.125})$$

It follows from Eqns. F.31, F.39, F.51, and F.125 that

$$\lim_{N_{\text{sh}} \rightarrow \infty} \mathbb{E} [\hat{\mu}_{g(\underline{X}), \text{MSS}}] = \mathbb{E} [g(\underline{X})] \quad (\text{F.126})$$

which was to be shown. □

Proposition 69. Let $g : \mathbb{R}^s \rightarrow \mathbb{R}$ be a measurable, integrable real-valued function. Let $d_{\text{max}} > 0$. Let $\underline{\mu} \in \mathbb{R}^s$, $\Sigma \in \mathbb{R}^{s \times s}$, $\Sigma > 0$. Let $\underline{X} \sim \mathcal{N}(\underline{\mu}, \Sigma)$.

Let g be bounded a.e. in \mathbb{R}^s ; i.e., let $g \in \mathcal{L}^\infty(\mathbb{R}^s)$. Let $M \geq 0$, $\mu_{g(\underline{X})} \in \mathbb{R}$ satisfy

$$\mu_{g(\underline{X})} = \mathbb{E} [g(\underline{X})] \quad (\text{F.127})$$

$$M = \text{esssup}_{\underline{x} \in [V_{d_{\text{max}}}(\underline{X})]^c} |g(\underline{x})| \quad (\text{F.128})$$

Let $\{\tilde{\underline{x}}_{l,q}\}$, $l \in S_{N_{\text{sh}}}$, $q \in S_{N_{\text{ss}}}$ be an MSS sample drawn in accordance with Algorithm 1, with sample weights $\{w_{l,q}\}$ and $\{W_l\}$. Let the MSS asymptotic estimator of $\mathbb{E} [g(\underline{X})]$, $\hat{\mu}_{g(\underline{X}), \text{MSS}}$, be defined as

$$\hat{\mu}_{g(\underline{X}), \text{MSS}} = \sum_{l=1}^{N_{\text{sh}}} \left(\frac{W_l}{N_{\text{ss}}} \right) \sum_{q=1}^{N_{\text{ss}}} g(\tilde{\underline{x}}_{l,q}) \quad (\text{F.129})$$

Then,

$$\left| \mu_{g(\underline{X})} - \lim_{N_{\text{sh}} \rightarrow \infty} \mathbb{E} [\widehat{\mu}_{g(\underline{X}), \text{MSS}}] \right| \leq M p_{\text{exc}} \quad (\text{F.130})$$

where p_{exc} satisfies Eq. 6.18. \diamond

Proof. Let the preceding assumptions and notation hold.

Let the functions $g_1 : \mathbb{R}^s \rightarrow \mathbb{R}$, $g_2 : \mathbb{R}^s \rightarrow \mathbb{R}$ be defined as

$$g_1(\underline{x}) = g(\underline{x}) \chi_{V_{d_{\max}}(\underline{X})}(\underline{x}) \quad (\text{F.131})$$

$$g_2(\underline{x}) = g(\underline{x}) \chi_{[V_{d_{\max}}(\underline{X})]^c}(\underline{x}) \quad (\text{F.132})$$

Then,

$$\begin{aligned} \mu_{g(\underline{X})} &= \mathbb{E} [g(\underline{X})] = \int_{\underline{x} \in \mathbb{R}^s} g(\underline{x}) \text{pdf}_{\underline{X}}(\underline{x}) \, d\underline{x} \\ &= \int_{\underline{x} \in V_{d_{\max}}(\underline{X})} g(\underline{x}) \text{pdf}_{\underline{X}}(\underline{x}) \, d\underline{x} + \int_{\underline{x} \in [V_{d_{\max}}(\underline{X})]^c} g(\underline{x}) \text{pdf}_{\underline{X}}(\underline{x}) \, d\underline{x} \\ &= \int_{\underline{x} \in \mathbb{R}^s} g(\underline{x}) \chi_{V_{d_{\max}}(\underline{X})}(\underline{x}) \text{pdf}_{\underline{X}}(\underline{x}) \, d\underline{x} + \int_{\underline{x} \in \mathbb{R}^s} g(\underline{x}) \chi_{[V_{d_{\max}}(\underline{X})]^c}(\underline{x}) \text{pdf}_{\underline{X}}(\underline{x}) \, d\underline{x} \end{aligned} \quad (\text{F.133})$$

Since $g \in \mathcal{L}^1(\mathbb{R}^s)$, and since $\chi_{V_{d_{\max}}(\underline{X})}$, $\chi_{[V_{d_{\max}}(\underline{X})]^c} \in \mathcal{L}^\infty(\mathbb{R}^s)$, it follows that g_1 and g_2 are integrable functions; that is, $g_1, g_2 \in \mathcal{L}^1(\mathbb{R}^s)$. Therefore, $\mu_{g_1(\underline{X})}$ and $\mu_{g_2(\underline{X})}$ exist and are finite, where these variables are defined as

$$\mu_{g_1(\underline{X})} = \mathbb{E} [g_1(\underline{X})] = \int_{\underline{x} \in \mathbb{R}^s} g(\underline{x}) \chi_{V_{d_{\max}}(\underline{X})}(\underline{x}) \text{pdf}_{\underline{X}}(\underline{x}) \, d\underline{x} \quad (\text{F.134})$$

$$\mu_{g_2(\underline{X})} = \mathbb{E} [g_2(\underline{X})] = \int_{\underline{x} \in \mathbb{R}^s} g(\underline{x}) \chi_{[V_{d_{\max}}(\underline{X})]^c}(\underline{x}) \text{pdf}_{\underline{X}}(\underline{x}) \, d\underline{x} \quad (\text{F.135})$$

Note:

$$\mu_{g(\underline{X})} = \mu_{g_1(\underline{X})} + \mu_{g_2(\underline{X})} \quad (\text{F.136})$$

Since $g_1 = g \chi_{V_{d_{\max}}(\underline{X})}$, it follows that $\text{supp}(g_1) \subseteq V_{d_{\max}}(\underline{X})$ and $g_1 = g$ on $V_{d_{\max}}(\underline{X})$.

Therefore,

$$\widehat{\mu}_{g_1(\underline{X}),\text{MSS}} = \sum_{l=1}^{N_{\text{sh}}} \left(\frac{W_l}{N_{\text{ss}}} \right) \sum_{q=1}^{N_{\text{ss}}} g_1(\tilde{\underline{x}}_{l,q}) = \sum_{l=1}^{N_{\text{sh}}} \left(\frac{W_l}{N_{\text{ss}}} \right) \sum_{q=1}^{N_{\text{ss}}} g(\tilde{\underline{x}}_{l,q}) = \widehat{\mu}_{g(\underline{X}),\text{MSS}} \quad (\text{F.137})$$

It follows from Proposition 68 and from Eqns. F.129 and F.134 that

$$\mu_{g_1(\underline{X})} = \lim_{N_{\text{sh}} \rightarrow \infty} \mathbb{E} [\widehat{\mu}_{g_1(\underline{X}),\text{MSS}}] = \lim_{N_{\text{sh}} \rightarrow \infty} \mathbb{E} [\widehat{\mu}_{g(\underline{X}),\text{MSS}}] \quad (\text{F.138})$$

which, based on Lebesgue integral properties and Eq. F.135, implies that

$$\begin{aligned} \left| \mu_{g(\underline{X})} - \lim_{N_{\text{sh}} \rightarrow \infty} \mathbb{E} [\widehat{\mu}_{g(\underline{X}),\text{MSS}}] \right| &= \left| \int_{\underline{x} \in [V_{d_{\max}}(\underline{X})]^c} g(\underline{x}) \text{pdf}_{\underline{X}}(\underline{x}) \, d\underline{x} \right| \\ &\leq \int_{\underline{x} \in [V_{d_{\max}}(\underline{X})]^c} |g(\underline{x}) \text{pdf}_{\underline{X}}(\underline{x})| \, d\underline{x} = \int_{\underline{x} \in [V_{d_{\max}}(\underline{X})]^c} |g(\underline{x})| \text{pdf}_{\underline{X}}(\underline{x}) \, d\underline{x} \quad (\text{F.139}) \end{aligned}$$

Assume $g \in \mathcal{L}^\infty(\mathbb{R}^s)$. Since $|g_2| \leq |g|$, $g_2 \in \mathcal{L}^\infty(\mathbb{R}^s)$. Therefore,

$$M = \text{esssup}_{\underline{x} \in [V_{d_{\max}}(\underline{X})]^c} |g(\underline{x})| < \infty \quad (\text{F.140})$$

Thus,

$$|g(\underline{x})| \leq M \text{ for a.e. } \underline{x} \in [V_{d_{\max}}(\underline{X})]^c \quad (\text{F.141})$$

It follows from Eq. 6.18 that

$$\begin{aligned} \int_{\underline{x} \in [V_{d_{\max}}(\underline{X})]^c} |g(\underline{x})| \text{pdf}_{\underline{X}}(\underline{x}) \, d\underline{x} &\leq \int_{\underline{x} \in [V_{d_{\max}}(\underline{X})]^c} M \text{pdf}_{\underline{X}}(\underline{x}) \, d\underline{x} \\ &= M \int_{\underline{x} \in [V_{d_{\max}}(\underline{X})]^c} \text{pdf}_{\underline{X}}(\underline{x}) \, d\underline{x} = M \int_{\underline{x} \in \mathbb{R}^s} \chi_{[V_{d_{\max}}(\underline{X})]^c}(\underline{x}) \text{pdf}_{\underline{X}}(\underline{x}) \, d\underline{x} \\ &= M \mathbb{E} [\chi_{[V_{d_{\max}}(\underline{X})]^c}(\underline{X})] = M p_{\underline{X}}([V_{d_{\max}}(\underline{X})]^c) = M p_{\text{exc}} \quad (\text{F.142}) \end{aligned}$$

Therefore, from Eqns. F.139 and F.142, it follows that

$$\left| \mu_{g(\underline{X})} - \lim_{N_{\text{sh}} \rightarrow \infty} \mathbb{E} [\widehat{\mu}_{g(\underline{X}), \text{MSS}}] \right| \leq M p_{\text{exc}} \quad (\text{F.143})$$

which was to be shown. \square

Proposition 70 (Asymptotic MSS estimators of probability measures). Let $E \subseteq \mathbb{R}^s$ be a measurable subset of \mathbb{R}^s . Let $p_E = p_{\underline{X}}(E) = p(\underline{X} \in E)$.

Let $d_{\text{max}} > 0$. Let $\underline{\mu} \in \mathbb{R}^s$, $\Sigma \in \mathbb{R}^{s \times s}$, $\Sigma > 0$. Let $\underline{X} \sim \mathcal{N}(\underline{\mu}, \Sigma)$.

Let $\{\tilde{\underline{x}}_{l,q}\}$, $l \in S_{N_{\text{sh}}}$, $q \in S_{N_{\text{ss}}}$ be an MSS sample drawn in accordance with Algorithm 1, with sample weights $\{w_{l,q}\}$ and $\{W_l\}$.

Let the MSS asymptotic estimator of p_E , denoted by $\widehat{p}_{E, \text{MSS}}$, be defined as

$$\widehat{p}_{E, \text{MSS}} = \sum_{l=1}^{N_{\text{sh}}} \left(\frac{W_l}{N_{\text{ss}}} \right) \sum_{q=1}^{N_{\text{ss}}} \chi_E(\tilde{\underline{x}}_{l,q}) \quad (\text{F.144})$$

where $\chi_E : \mathbb{R}^s \rightarrow \{0, 1\}$. Then, if $E \subseteq V_{d_{\text{max}}}(\underline{X})$,

$$\lim_{N_{\text{sh}} \rightarrow \infty} \mathbb{E} [\widehat{p}_{E, \text{MSS}}] = p_E \quad (\text{F.145})$$

Alternatively, if $E \not\subseteq V_{d_{\text{max}}}(\underline{X})$,

$$\left| p_E - \lim_{N_{\text{sh}} \rightarrow \infty} \mathbb{E} [\widehat{p}_{E, \text{MSS}}] \right| \leq p_{\text{exc}} \quad (\text{F.146})$$

where p_{exc} satisfies Eq. 6.18. \diamond

Proof. Let the preceding notation and assumptions hold.

Subproof, Case 1: $E \subseteq V_{d_{\text{max}}}(\underline{X})$. Since the $V_{d_{\text{max}}}(\underline{X})$ set is bounded, it follows that the Lebesgue measure of $V_{d_{\text{max}}}(\underline{X})$ is finite; i.e.,

$$\lambda(V_{d_{\text{max}}}(\underline{X})) < \infty \quad (\text{F.147})$$

Letting $\chi_E : \mathbb{R}^s \rightarrow \{0, 1\}$ denote the characteristic function of $E \subseteq V_{d_{\max}}(\underline{X})$, the integral of $|\chi_E|$ satisfies

$$\begin{aligned} \int_{\underline{x} \in \mathbb{R}^s} |\chi_E(\underline{x})| \, d\underline{x} &= \int_{\underline{x} \in \mathbb{R}^s} \chi_E(\underline{x}) \, d\underline{x} = \int_{\underline{x} \in E} 1 \, d\underline{x} \\ &\leq \int_{\underline{x} \in V_{d_{\max}}(\underline{X})} 1 \, d\underline{x} = \lambda(V_{d_{\max}}(\underline{X})) < \infty \end{aligned} \quad (\text{F.148})$$

Hence, χ_E is integrable; i.e., $\chi_E \in \mathcal{L}^1(\mathbb{R}^s)$. Note: since $E \subseteq V_{d_{\max}}(\underline{X})$, it follows that $\text{supp}(\chi_E) \subseteq \text{supp}(\chi_{V_{d_{\max}}(\underline{X})}) = V_{d_{\max}}(\underline{X})$.

Therefore, by Proposition 68,

$$\lim_{N_{\text{sh}} \rightarrow \infty} \mathbb{E}[\widehat{p}_{E, \text{MSS}}] = p_E \quad (\text{F.149})$$

which was to be shown. ■

Subproof, Case 2: $E \not\subseteq V_{d_{\max}}(\underline{X})$. Let the sets A, B in \mathbb{R}^s be defined as

$$A = E \cap V_{d_{\max}}(\underline{X}) \quad (\text{F.150})$$

$$B = E \cap [V_{d_{\max}}(\underline{X})]^C \quad (\text{F.151})$$

Let the p_A, p_B variables be given by

$$p_A = p_{\underline{X}}(A) = p(\underline{X} \in A) \quad (\text{F.152})$$

$$p_B = p_{\underline{X}}(B) = p(\underline{X} \in B) \quad (\text{F.153})$$

Note: since A and B are disjoint sets, the fact that $E = A \cup B$ implies that

$$p_E = p(\underline{X} \in E) = p(\underline{X} \in A) + p(\underline{X} \in B) = p_A + p_B \quad (\text{F.154})$$

Since $\chi_A = \chi_E$ on A , it follows that

$$\widehat{p}_{E,\text{MSS}} = \sum_{l=1}^{N_{\text{sh}}} \left(\frac{W_l}{N_{\text{ss}}} \right) \sum_{q=1}^{N_{\text{ss}}} \chi_E(\tilde{\mathbf{x}}_{l,q}) = \sum_{l=1}^{N_{\text{sh}}} \left(\frac{W_l}{N_{\text{ss}}} \right) \sum_{q=1}^{N_{\text{ss}}} \chi_A(\tilde{\mathbf{x}}_{l,q}) = \widehat{p}_{A,\text{MSS}} \quad (\text{F.155})$$

Since $A \subseteq V_{d_{\max}}(\underline{X})$, it follows from Subproof, Case 1 and Eq. F.155 that

$$p_A = \lim_{N_{\text{sh}} \rightarrow \infty} \mathbb{E}[\widehat{p}_{A,\text{MSS}}] = \lim_{N_{\text{sh}} \rightarrow \infty} \mathbb{E}[\widehat{p}_{E,\text{MSS}}] \quad (\text{F.156})$$

It should be noted that

$$\begin{aligned} p_A &= \int_{\mathbf{x} \in \mathbb{R}^s} \chi_A(\mathbf{x}) \text{pdf}_{\underline{X}}(\mathbf{x}) \, d\mathbf{x} = \int_{\mathbf{x} \in V_{d_{\max}}(\underline{X})} \chi_A(\mathbf{x}) \text{pdf}_{\underline{X}}(\mathbf{x}) \, d\mathbf{x} \\ &= \int_{\mathbf{x} \in V_{d_{\max}}(\underline{X})} \chi_E(\mathbf{x}) \text{pdf}_{\underline{X}}(\mathbf{x}) \, d\mathbf{x} \quad (\text{F.157}) \end{aligned}$$

It should also be noted that

$$\begin{aligned} p_E &= \int_{\mathbf{x} \in \mathbb{R}^s} \chi_E(\mathbf{x}) \text{pdf}_{\underline{X}}(\mathbf{x}) \, d\mathbf{x} \\ &= \int_{\mathbf{x} \in V_{d_{\max}}(\underline{X})} \chi_E(\mathbf{x}) \text{pdf}_{\underline{X}}(\mathbf{x}) \, d\mathbf{x} + \int_{\mathbf{x} \in [V_{d_{\max}}(\underline{X})]^C} \chi_E(\mathbf{x}) \text{pdf}_{\underline{X}}(\mathbf{x}) \, d\mathbf{x} \quad (\text{F.158}) \end{aligned}$$

Therefore, Eq. F.156 implies that

$$p_E - p_A = \int_{\mathbf{x} \in [V_{d_{\max}}(\underline{X})]^C} \chi_E(\mathbf{x}) \text{pdf}_{\underline{X}}(\mathbf{x}) \, d\mathbf{x} = p_E - \lim_{N_{\text{sh}} \rightarrow \infty} \mathbb{E}[\widehat{p}_{E,\text{MSS}}] \quad (\text{F.159})$$

Hence, the quantity Δ satisfies

$$\Delta = \left| p_E - \lim_{N_{\text{sh}} \rightarrow \infty} \mathbb{E}[\widehat{p}_{E,\text{MSS}}] \right| = \left| \int_{\mathbf{x} \in [V_{d_{\max}}(\underline{X})]^C} \chi_E(\mathbf{x}) \text{pdf}_{\underline{X}}(\mathbf{x}) \, d\mathbf{x} \right| \quad (\text{F.160})$$

Since $B = E \cap [V_{d_{\max}}(\underline{X})]^C$, it follows that $\chi_E = \chi_B$ on $[V_{d_{\max}}(\underline{X})]^C$, which implies

(via Lebesgue integral properties) that

$$\Delta = \left| \int_{\underline{x} \in [V_{d_{\max}}(\underline{X})]^C} \chi_B(\underline{x}) \text{pdf}_{\underline{X}}(\underline{x}) \, d\underline{x} \right| \leq \int_{\underline{x} \in [V_{d_{\max}}(\underline{X})]^C} |\chi_B(\underline{x}) \text{pdf}_{\underline{X}}(\underline{x})| \, d\underline{x} \quad (\text{F.161})$$

Since $B \subseteq [V_{d_{\max}}(\underline{X})]^C$, $\chi_B \leq \chi_{[V_{d_{\max}}(\underline{X})]^C}$ in \mathbb{R}^s . Because the χ_B and $\text{pdf}_{\underline{X}}$ functions are non-negative, it follows from Eq. 6.18 that

$$\begin{aligned} \Delta &\leq \int_{\underline{x} \in [V_{d_{\max}}(\underline{X})]^C} \chi_B(\underline{x}) \text{pdf}_{\underline{X}}(\underline{x}) \, d\underline{x} \leq \int_{\underline{x} \in [V_{d_{\max}}(\underline{X})]^C} \chi_{[V_{d_{\max}}(\underline{X})]^C}(\underline{x}) \text{pdf}_{\underline{X}}(\underline{x}) \, d\underline{x} \\ &= \int_{\underline{x} \in \mathbb{R}^s} \chi_{[V_{d_{\max}}(\underline{X})]^C}(\underline{x}) \text{pdf}_{\underline{X}}(\underline{x}) \, d\underline{x} = \mathbb{E} \left[[V_{d_{\max}}(\underline{X})]^C \right] \\ &= p_{\underline{X}} \left([V_{d_{\max}}(\underline{X})]^C \right) = p_{\text{exc}} \quad (\text{F.162}) \end{aligned}$$

Therefore,

$$\left| p_E - \lim_{N_{\text{sh}} \rightarrow \infty} \mathbb{E} [\hat{p}_{E, \text{MSS}}] \right| \leq p_{\text{exc}} \quad (\text{F.163})$$

which was to be shown. ■

Through the results for Subproof, Case 1 and Subproof, Case 2, the result follows. □

F.3 Mahalanobis Shell Sampling (MSS) – Unbiased Theoretical Results

The unbiased MSS sample estimators presented in this section rely on the definition of the following constants:

$$S_1 = \sum_{l=1}^{N_{\text{sh}}} W_l = \text{cdf}_{\chi_s^2} \left((d_{\max})^2 \right) \quad (\text{F.164})$$

$$S_2 = \sum_{l=1}^{N_{\text{sh}}} W_l^2 \quad (\text{F.165})$$

$$S_3 = \frac{1}{s} \left(\frac{d_{\max}}{N_{\text{sh}}} \right)^2 \sum_{l=1}^{N_{\text{sh}}} W_l \left(l - \frac{1}{2} \right)^2 \quad (\text{F.166})$$

$$S_4 = \frac{1}{s} \left(\frac{d_{\max}}{N_{\text{sh}}} \right)^2 \sum_{l=1}^{N_{\text{sh}}} W_l^2 \left(l - \frac{1}{2} \right)^2 \quad (\text{F.167})$$

$$D_1 = \frac{1}{12s} \left(\frac{d_{\max}}{N_{\text{sh}}} \right)^2 \quad (\text{F.168})$$

Proposition 71 (Unbiased MSS estimators in sample mean). Let $s, N_{\text{sh}}, N_{\text{ss}} \in \mathbb{N}$, and let $0 < d_{\max} < \infty$. Let $\underline{X} \sim \mathcal{N}(\underline{\mu}, \Sigma)$, where $\underline{\mu} \in \mathbb{R}^s, \Sigma \in \mathbb{R}^{s \times s}, \Sigma > 0$.

Let $\{\tilde{\underline{x}}_{l,q}\}, l \in \{1, \dots, N_{\text{sh}}\}, q \in \{1, \dots, N_{\text{ss}}\}$ be an MSS sample drawn in accordance with Algorithm 1, with sample weights $\{w_{l,q}\}$ and $\{W_l\}$. Let the constant H be defined as

$$H = \frac{1}{S_1} = \frac{1}{\text{cdf}_{\chi_s^2}((d_{\max})^2)} \quad (\text{F.169})$$

Let $\hat{\underline{\mu}}_{\text{MSS}}$ be defined as

$$\hat{\underline{\mu}}_{\text{MSS}} = H \sum_{l=1}^{N_{\text{sh}}} \left(\frac{W_l}{N_{\text{ss}}} \right) \sum_{q=1}^{N_{\text{ss}}} \tilde{\underline{x}}_{l,q} \quad (\text{F.170})$$

Then, $\hat{\underline{\mu}}_{\text{MSS}}$ is an unbiased estimator of $\underline{\mu}$; that is,

$$\mathbb{E}[\hat{\underline{\mu}}_{\text{MSS}}] = \underline{\mu} \quad \diamond \quad (\text{F.171})$$

Proof. Let the preceding notation and assumptions hold.

Let $l \in \{1, \dots, N_{\text{sh}}\}, q \in \{1, \dots, N_{\text{ss}}\}$. Then, by Algorithm 1, there exist some $\underline{z}_{l,q} \sim \mathbb{U}(\mathbb{S}^{(s-1)}), u_{l,q} \sim \mathbb{U}([0, 1])$ such that $\underline{z}_{l,q}$ and $u_{l,q}$ are independent, and

$$\tilde{\underline{x}}_{l,q} = \underline{\mu} + (d_l + u_{l,q} \delta_d) [\Sigma^{1/2}] \underline{z}_{l,q} \quad (\text{F.172})$$

where δ_d and d_l satisfy

$$\delta_d = \frac{d_{\max}}{N_{\text{sh}}} \quad (\text{F.173})$$

$$d_l = [l - 1] \delta_d \quad (\text{F.174})$$

Let the constant d'_l and the random variable $v_{l,q}$ be defined as

$$d'_l \doteq d_l + \frac{1}{2}\delta_d \quad (\text{F.175})$$

$$v_{l,q} \doteq u_{l,q} - \frac{1}{2} \quad (\text{F.176})$$

Note: $v_{l,q} \sim \mathbb{U}\left(\left[-\frac{1}{2}, \frac{1}{2}\right]\right)$, and

$$d_l + u_{l,q} \delta_d = \left[d_l + \frac{1}{2}\delta_d \right] + \left[u_{l,q} \delta_d - \frac{1}{2}\delta_d \right] = d'_l + v_{l,q} \delta_d \quad (\text{F.177})$$

Let the expression B be defined as

$$\begin{aligned} B &\doteq \sum_{l=1}^{N_{\text{sh}}} \left(\frac{W_l}{N_{\text{ss}}} \right) \sum_{q=1}^{N_{\text{ss}}} \tilde{x}_{l,q} = \sum_{l=1}^{N_{\text{sh}}} \left(\frac{W_l}{N_{\text{ss}}} \right) \sum_{q=1}^{N_{\text{ss}}} [\mu + (d_l + u_{l,q} \delta_d) [\Sigma^{1/2}] z_{l,q}] \\ &= \sum_{l=1}^{N_{\text{sh}}} \left(\frac{W_l}{N_{\text{ss}}} \right) \sum_{q=1}^{N_{\text{ss}}} [\mu + (d'_l + v_{l,q} \delta_d) [\Sigma^{1/2}] z_{l,q}] \quad (\text{F.178}) \end{aligned}$$

Let the expressions B_1, B_2, B_3 be defined as

$$B_1 \doteq \sum_{l=1}^{N_{\text{sh}}} \left(\frac{W_l}{N_{\text{ss}}} \right) \sum_{q=1}^{N_{\text{ss}}} \mu \quad (\text{F.179})$$

$$B_2 \doteq \sum_{l=1}^{N_{\text{sh}}} \left(\frac{W_l}{N_{\text{ss}}} \right) \sum_{q=1}^{N_{\text{ss}}} d'_l [\Sigma^{1/2}] z_{l,q} \quad (\text{F.180})$$

$$B_3 \doteq \sum_{l=1}^{N_{\text{sh}}} \left(\frac{W_l}{N_{\text{ss}}} \right) \sum_{q=1}^{N_{\text{ss}}} (v_{l,q} \delta_d) [\Sigma^{1/2}] z_{l,q} \quad (\text{F.181})$$

Therefore,

$$B = B_1 + B_2 + B_3 \quad (\text{F.182})$$

The expression B_1 satisfies

$$B_1 \doteq \sum_{l=1}^{N_{\text{sh}}} W_l \underline{\mu} = (\underline{\mu}) \sum_{l=1}^{N_{\text{sh}}} W_l \quad (\text{F.183})$$

However,

$$d_l + \delta_d = [l - 1]\delta_d + \delta_d = l \delta_d \quad (\text{F.184})$$

which implies that

$$\begin{aligned} \sum_{l=1}^{N_{\text{sh}}} W_l &= \sum_{l=1}^{N_{\text{sh}}} \text{cdf}_{\chi_s^2}([l\delta_d]^2) - \text{cdf}_{\chi_s^2}([(l-1)\delta_d]^2) \\ &= \text{cdf}_{\chi_s^2}([N_{\text{sh}}\delta_d]^2) - \text{cdf}_{\chi_s^2}(0) = \text{cdf}_{\chi_s^2}([d_{\text{max}}]^2) =: S_1 \end{aligned} \quad (\text{F.185})$$

Hence,

$$B_1 = S_1 \underline{\mu} \quad (\text{F.186})$$

Since B_1 is a constant, it follows that

$$\mathbb{E}[B_1] = B_1 = S_1 \underline{\mu} \quad (\text{F.187})$$

The expression B_2 satisfies

$$B_2 = \sum_{l=1}^{N_{\text{sh}}} \left(\frac{W_l}{N_{\text{ss}}} \right) d'_l \sum_{q=1}^{N_{\text{ss}}} [\Sigma^{1/2}] \tilde{z}_{l,q} = \sum_{l=1}^{N_{\text{sh}}} \left(\frac{W_l}{N_{\text{ss}}} \right) d'_l [\Sigma^{1/2}] \left(\sum_{q=1}^{N_{\text{ss}}} \tilde{z}_{l,q} \right) \quad (\text{F.188})$$

By the linearity of the expectation operator, $\mathbb{E}[B_2]$ satisfies

$$\mathbb{E}[B_2] = \sum_{l=1}^{N_{\text{sh}}} \left(\frac{W_l}{N_{\text{ss}}} \right) d'_l [\Sigma^{1/2}] \sum_{q=1}^{N_{\text{ss}}} \mathbb{E}[\tilde{z}_{l,q}] \quad (\text{F.189})$$

Since $\underline{z}_{l,q} \sim \mathbb{U}(\mathbb{S}^{(s-1)})$, $\mathbb{E}[\underline{z}_{l,q}] = \mathbf{0}_{s \times 1}$, which implies that

$$\mathbb{E}[B_2] = \mathbf{0}_{s \times 1} \quad (\text{F.190})$$

Similarly, the expression B_3 satisfies

$$B_3 = \sum_{l=1}^{N_{\text{sh}}} \left(\frac{W_l}{N_{\text{ss}}} \right) \delta_d \sum_{q=1}^{N_{\text{ss}}} v_{l,q} [\Sigma^{1/2}] \underline{z}_{l,q} \quad (\text{F.191})$$

By scalar multiplication,

$$B_3 = \sum_{l=1}^{N_{\text{sh}}} \left(\frac{W_l}{N_{\text{ss}}} \right) \delta_d \sum_{q=1}^{N_{\text{ss}}} [\Sigma^{1/2}] (v_{l,q} \underline{z}_{l,q}) \quad (\text{F.192})$$

By linearity of matrix multiplication,

$$B_3 = \sum_{l=1}^{N_{\text{sh}}} \left(\frac{W_l}{N_{\text{ss}}} \right) \delta_d [\Sigma^{1/2}] \left(\sum_{q=1}^{N_{\text{ss}}} v_{l,q} \underline{z}_{l,q} \right) \quad (\text{F.193})$$

By linearity of the expectation operator, $\mathbb{E}[B_3]$ satisfies

$$\mathbb{E}[B_3] = \sum_{l=1}^{N_{\text{sh}}} \left(\frac{W_l}{N_{\text{ss}}} \right) \delta_d [\Sigma^{1/2}] \sum_{q=1}^{N_{\text{ss}}} \mathbb{E}[v_{l,q} \underline{z}_{l,q}] \quad (\text{F.194})$$

Since $\underline{z}_{l,q}$ and $v_{l,q}$ are independent, it follows from Eq. F.176 that $\underline{z}_{l,q}$ and $v_{l,q}$ are also independent. Hence, $\underline{z}_{l,q}$ and $v_{l,q}$ are uncorrelated; i.e.,

$$\mathbb{E}[v_{l,q} \underline{z}_{l,q}] = \mathbb{E}[v_{l,q}] \mathbb{E}[\underline{z}_{l,q}] \quad (\text{F.195})$$

Since $\mathbb{E}[v_{l,q}] = \frac{1}{2}$, Eq. F.176 implies that $\mathbb{E}[v_{l,q}] = 0$. (Also: $\mathbb{E}[\underline{z}_{l,q}] = \mathbf{0}_{s \times 1}$, as noted previously). Hence,

$$\mathbb{E}[B_3] = \mathbf{0}_{s \times 1} \quad (\text{F.196})$$

Collecting terms, it follows that

$$\mathbb{E}[\widehat{\underline{\mu}}_{\text{MSS}}] = \mathbb{E}[HB] = \frac{1}{S_1} \mathbb{E}[B_1 + B_2 + B_3] = \frac{1}{S_1} (\mathbb{E}[B_1] + \mathbb{E}[B_2] + \mathbb{E}[B_3]) \quad (\text{F.197})$$

Therefore,

$$\mathbb{E}[\widehat{\underline{\mu}}_{\text{MSS}}] = \frac{1}{S_1} B_1 = \frac{1}{S_1} S_1 \underline{\mu} = \underline{\mu} \quad (\text{F.198})$$

which was to be shown. \square

Proposition 72 (Unbiased MSS estimators in sample covariance). Let $s, N_{\text{sh}}, N_{\text{ss}} \in \mathbb{N}$, and let $0 < d_{\text{max}} < \infty$. Let $\underline{X} \sim \mathcal{N}(\underline{\mu}, \Sigma)$, where $\underline{\mu} \in \mathbb{R}^s$, $\Sigma \in \mathbb{R}^{s \times s}$, $\Sigma > 0$.

Let $\{\tilde{\underline{x}}_{l,q}\}$, $l \in \{1, \dots, N_{\text{sh}}\}$, $q \in \{1, \dots, N_{\text{ss}}\}$ be an MSS sample drawn in accordance with Algorithm 1, with sample weights $\{w_{l,q}\}$ and $\{W_l\}$.

Let the constants H and G be defined as

$$H = \frac{1}{S_1} = \frac{1}{\text{cdf}_{\chi_s^2}((d_{\text{max}})^2)} \quad (\text{F.199})$$

$$G = \left[1 + \frac{H^2 S_2}{N_{\text{ss}}}\right] S_3 - \frac{2(HS_4)}{N_{\text{ss}}} + D_1 \left(S_1 - \frac{HS_2}{N_{\text{ss}}}\right) \quad (\text{F.200})$$

Let $\widehat{\underline{\mu}}_{\text{MSS}}$ and $\widehat{\Sigma}_{\text{MSS}}$ be defined as

$$\widehat{\underline{\mu}}_{\text{MSS}} = H \sum_{l=1}^{N_{\text{sh}}} \left(\frac{W_l}{N_{\text{ss}}}\right) \sum_{q=1}^{N_{\text{ss}}} \tilde{\underline{x}}_{l,q} \quad (\text{F.201})$$

$$\widehat{\Sigma}_{\text{MSS}} = \frac{1}{G} \sum_{l=1}^{N_{\text{sh}}} \left(\frac{W_l}{N_{\text{ss}}}\right) \sum_{q=1}^{N_{\text{ss}}} (\tilde{\underline{x}}_{l,q} - \widehat{\underline{\mu}}_{\text{MSS}}) (\tilde{\underline{x}}_{l,q} - \widehat{\underline{\mu}}_{\text{MSS}})^T \quad (\text{F.202})$$

Then, $\widehat{\Sigma}_{\text{MSS}}$ is an unbiased estimator of Σ ; that is,

$$\mathbb{E}[\widehat{\Sigma}_{\text{MSS}}] = \Sigma \quad \diamond \quad (\text{F.203})$$

Proof. Let the preceding notation and assumptions hold.

Let $l \in \{1, \dots, N_{\text{sh}}\}$, $q \in \{1, \dots, N_{\text{ss}}\}$. Then, by Algorithm 1, there exist some $\underline{z}_{l,q} \sim \mathbb{U}(\mathbb{S}^{(s-1)})$, $u_{l,q} \sim \mathbb{U}([0, 1])$ such that $\underline{z}_{l,q}$ and $u_{l,q}$ are independent, and

$$\tilde{\underline{x}}_{l,q} = \underline{\mu} + (d_l + u_{l,q} \delta_d) [\Sigma^{1/2}] \underline{z}_{l,q} \quad (\text{F.204})$$

where δ_d and d_l satisfy

$$\delta_d = \frac{d_{\text{max}}}{N_{\text{sh}}} \quad (\text{F.205})$$

$$d_l = [l - 1] \delta_d \quad (\text{F.206})$$

Let the constant d'_l and the random variable $v_{l,q}$ be defined as

$$d'_l \doteq d_l + \frac{1}{2} \delta_d = \left[l - \frac{1}{2} \right] \delta_d \quad (\text{F.207})$$

$$v_{l,q} \doteq u_{l,q} - \frac{1}{2} \quad (\text{F.208})$$

Note: $v_{l,q} \sim \mathbb{U}\left(-\frac{1}{2}, \frac{1}{2}\right)$, and

$$d_l + u_{l,q} \delta_d = \left[d_l + \frac{1}{2} \delta_d \right] + \left[u_{l,q} \delta_d - \frac{1}{2} \delta_d \right] = d'_l + v_{l,q} \delta_d \quad (\text{F.209})$$

Consequently,

$$\tilde{\underline{x}}_{l,q} = \underline{\mu} + (d'_l + v_{l,q} \delta_d) [\Sigma^{1/2}] \underline{z}_{l,q} \quad (\text{F.210})$$

Additionally, the first and second order moment statistics of $v_{l,q}$ and $\underline{z}_{l,q}$ are given by

$$\mathbb{E} [v_{l,q}] = 0 \quad (\text{F.211})$$

$$\text{Var} (v_{l,q}) = \mathbb{E} [(v_{l,q} - \mathbb{E} [v_{l,q}])^2] = \mathbb{E} [(v_{l,q})^2] = \frac{1}{12} \quad (\text{F.212})$$

$$\mathbb{E} [\underline{z}_{l,q}] = \mathbf{0}_{s \times 1} \quad (\text{F.213})$$

$$\text{Cov} (\underline{z}_{l,q}) = \mathbb{E} [(\underline{z}_{l,q} - \mathbb{E} [\underline{z}_{l,q}]) (\underline{z}_{l,q} - \mathbb{E} [\underline{z}_{l,q}])^T] = \mathbb{E} [(\underline{z}_{l,q}) (\underline{z}_{l,q})^T] = \frac{1}{s} \mathbb{I}_s \quad (\text{F.214})$$

Since $\underline{z}_{l,q}$ and $u_{l,q}$ are independent, it follows from Eq. F.208 that $\underline{z}_{l,q}$ and $v_{l,q}$ are also independent.

Within this proof, let $\hat{\underline{\mu}}_{\text{MSS}}$ be denoted as $\hat{\underline{\mu}}$ for simplicity.

Let the expression B be defined as

$$\begin{aligned} B &\doteq \sum_{l=1}^{N_{\text{sh}}} \left(\frac{W_l}{N_{\text{ss}}} \right) \sum_{q=1}^{N_{\text{ss}}} (\tilde{\underline{x}}_{l,q} - \hat{\underline{\mu}}) (\tilde{\underline{x}}_{l,q} - \hat{\underline{\mu}})^T \\ &= \sum_{l=1}^{N_{\text{sh}}} \left(\frac{W_l}{N_{\text{ss}}} \right) \sum_{q=1}^{N_{\text{ss}}} [\tilde{\underline{x}}_{l,q} \tilde{\underline{x}}_{l,q}^T - \tilde{\underline{x}}_{l,q} \hat{\underline{\mu}}^T - \hat{\underline{\mu}} \tilde{\underline{x}}_{l,q}^T + \hat{\underline{\mu}} \hat{\underline{\mu}}^T] \quad (\text{F.215}) \end{aligned}$$

Let the expressions B_1 , B_2 , and B_3 be defined as

$$B_1 \doteq \tilde{\underline{x}}_{l,q} \tilde{\underline{x}}_{l,q}^T \quad (\text{F.216})$$

$$B_2 \doteq \tilde{\underline{x}}_{l,q} \hat{\underline{\mu}}^T \quad (\text{F.217})$$

$$B_3 \doteq \hat{\underline{\mu}} \hat{\underline{\mu}}^T \quad (\text{F.218})$$

Let the expressions T_1 , T_2 and T_3 be defined as

$$T_1 \doteq \sum_{l=1}^{N_{\text{sh}}} \left(\frac{W_l}{N_{\text{ss}}} \right) \sum_{q=1}^{N_{\text{ss}}} \tilde{\underline{x}}_{l,q} \tilde{\underline{x}}_{l,q}^T = \sum_{l=1}^{N_{\text{sh}}} \left(\frac{W_l}{N_{\text{ss}}} \right) \sum_{q=1}^{N_{\text{ss}}} B_1 \quad (\text{F.219})$$

$$T_2 \doteq \sum_{l=1}^{N_{\text{sh}}} \left(\frac{W_l}{N_{\text{ss}}} \right) \sum_{q=1}^{N_{\text{ss}}} \tilde{\underline{x}}_{l,q} \hat{\underline{\mu}}^T = \sum_{l=1}^{N_{\text{sh}}} \left(\frac{W_l}{N_{\text{ss}}} \right) \sum_{q=1}^{N_{\text{ss}}} B_2 \quad (\text{F.220})$$

$$T_3 \doteq \sum_{l=1}^{N_{\text{sh}}} \left(\frac{W_l}{N_{\text{ss}}} \right) \sum_{q=1}^{N_{\text{ss}}} \hat{\underline{\mu}} \hat{\underline{\mu}}^T = \sum_{l=1}^{N_{\text{sh}}} \left(\frac{W_l}{N_{\text{ss}}} \right) \sum_{q=1}^{N_{\text{ss}}} B_3 \quad (\text{F.221})$$

Therefore,

$$B = T_1 - T_2 - T_2^T + T_3 \quad (\text{F.222})$$

Subproof: Examining the B_1 expression. Let the preceding assumptions and notation hold.

The expression B_1 may be expanded as follows:

$$\begin{aligned}
B_1 &= \tilde{x}_{l,q} \tilde{x}_{l,q}^T = [\underline{\mu} + (d'_l + v_{l,q} \delta_d) [\Sigma^{1/2}] \underline{z}_{l,q}] [\underline{\mu} + (d'_l + v_{l,q} \delta_d) [\Sigma^{1/2}] \underline{z}_{l,q}]^T \\
&= [\underline{\mu} + (d'_l + v_{l,q} \delta_d) [\Sigma^{1/2}] \underline{z}_{l,q}] [\underline{\mu}^T + (d'_l + v_{l,q} \delta_d) \underline{z}_{l,q}^T [\Sigma^{1/2}]] \\
&= \underline{\mu} \underline{\mu}^T + (d'_l + v_{l,q} \delta_d) \underline{\mu} \underline{z}_{l,q}^T [\Sigma^{1/2}] + (d'_l + v_{l,q} \delta_d) [\Sigma^{1/2}] \underline{z}_{l,q} \underline{\mu}^T \\
&\quad + (d'_l + v_{l,q} \delta_d)^2 [\Sigma^{1/2}] \underline{z}_{l,q} \underline{z}_{l,q}^T [\Sigma^{1/2}] \quad (\text{F.223})
\end{aligned}$$

Let the expressions C_1 through C_6 be defined as

$$C_1 = \underline{\mu} \underline{\mu}^T \quad (\text{F.224})$$

$$C_2 = d'_l \underline{\mu} \underline{z}_{l,q}^T [\Sigma^{1/2}] \quad (\text{F.225})$$

$$C_3 = \delta_d \underline{\mu} (v_{l,q} \underline{z}_{l,q}^T) [\Sigma^{1/2}] \quad (\text{F.226})$$

$$C_4 = (d'_l)^2 [\Sigma^{1/2}] \underline{z}_{l,q} \underline{z}_{l,q}^T [\Sigma^{1/2}] \quad (\text{F.227})$$

$$C_5 = 2 (d'_l \delta_d) [\Sigma^{1/2}] (\underline{z}_{l,q} \underline{z}_{l,q}^T v_{l,q}) [\Sigma^{1/2}] \quad (\text{F.228})$$

$$C_6 = (\delta_d)^2 [\Sigma^{1/2}] (\underline{z}_{l,q} \underline{z}_{l,q}^T [v_{l,q}]^2) [\Sigma^{1/2}] \quad (\text{F.229})$$

Therefore,

$$B_1 = C_1 + C_2 + C_3 + C_2^T + C_3^T + C_4 + C_5 + C_6 \quad (\text{F.230})$$

Since C_1 is a constant, it follows that $\mathbb{E}[C_1]$ satisfies

$$\mathbb{E}[C_1] = C_1 \quad (\text{F.231})$$

By the linearity of the expectation operator, it follows that $\mathbb{E}[C_2]$ satisfies

$$\mathbb{E}[C_2] = \mathbb{E}[d'_l \underline{\mu} \underline{z}_{l,q}^T [\Sigma^{1/2}]] = d'_l \underline{\mu} (\mathbb{E}[\underline{z}_{l,q}])^T [\Sigma^{1/2}] \quad (\text{F.232})$$

Since $\underline{z}_{l,q} \sim \mathbb{U}(\mathbb{S}^{(s-1)})$, Eq. F.213 implies that

$$\mathbb{E}[C_2] = \mathbf{0}_{s \times s} \quad (\text{F.233})$$

By the linearity of the expectation operator, it follows that $\mathbb{E}[C_3]$ satisfies

$$\mathbb{E}[C_3] = \mathbb{E}[\delta_d \underline{\mu}(v_{l,q} \underline{z}_{l,q}^T) [\Sigma^{1/2}]] = (\delta_d \underline{\mu}) (\mathbb{E}[v_{l,q} \underline{z}_{l,q}])^T [\Sigma^{1/2}] \quad (\text{F.234})$$

Since $v_{l,q}$ and $\underline{z}_{l,q}$ are independent, they are uncorrelated; i.e.,

$$\mathbb{E}[v_{l,q} \underline{z}_{l,q}] = \mathbb{E}[v_{l,q}] \mathbb{E}[\underline{z}_{l,q}] \quad (\text{F.235})$$

which, via Eqns. F.211 and F.213, implies that

$$\mathbb{E}[C_3] = \mathbf{0}_{s \times s} \quad (\text{F.236})$$

By the linearity of the expectation operator, via Eq. F.214, it follows that $\mathbb{E}[C_4]$ satisfies

$$\begin{aligned} \mathbb{E}[C_4] &= \mathbb{E}[(d'_l)^2 [\Sigma^{1/2}] \underline{z}_{l,q} \underline{z}_{l,q}^T [\Sigma^{1/2}]] = (d'_l)^2 [\Sigma^{1/2}] \mathbb{E}[\underline{z}_{l,q} \underline{z}_{l,q}^T] [\Sigma^{1/2}] \\ &= \frac{(d'_l)^2}{s} [\Sigma^{1/2}] \mathbb{I}_s [\Sigma^{1/2}] = \frac{(d'_l)^2}{s} \Sigma \quad (\text{F.237}) \end{aligned}$$

By the linearity of the expectation operator, it follows that $\mathbb{E}[C_5]$ satisfies

$$\begin{aligned} \mathbb{E}[C_5] &= \mathbb{E}[2 (d'_l \delta_d) [\Sigma^{1/2}] (\underline{z}_{l,q} \underline{z}_{l,q}^T v_{l,q}) [\Sigma^{1/2}]] \\ &= 2 (d'_l \delta_d) [\Sigma^{1/2}] (\mathbb{E}[\underline{z}_{l,q} \underline{z}_{l,q}^T v_{l,q}]) [\Sigma^{1/2}] \quad (\text{F.238}) \end{aligned}$$

Since $v_{l,q}$ and $\underline{z}_{l,q}$ are independent, it follows that $v_{l,q}$ and $\underline{z}_{l,q} \underline{z}_{l,q}^T$ are independent, which

implies that $v_{l,q}$ and $\underline{z}_{l,q} \underline{z}_{l,q}^T$ are uncorrelated; i.e.,

$$\mathbb{E} [v_{l,q} \underline{z}_{l,q} \underline{z}_{l,q}^T] = \mathbb{E} [v_{l,q}] \mathbb{E} [\underline{z}_{l,q} \underline{z}_{l,q}^T] \quad (\text{F.239})$$

Thus, via Eq. F.211,

$$\mathbb{E} [C_5] = \mathbf{0}_{s \times s} \quad (\text{F.240})$$

By the linearity of the expectation operator, it follows that $\mathbb{E} [C_6]$ satisfies

$$\begin{aligned} \mathbb{E} [C_6] &= \mathbb{E} [(\delta_d)^2 [\Sigma^{1/2}] (\underline{z}_{l,q} \underline{z}_{l,q}^T [v_{l,q}]^2) [\Sigma^{1/2}]] \\ &= (\delta_d)^2 [\Sigma^{1/2}] \mathbb{E} [\underline{z}_{l,q} \underline{z}_{l,q}^T [v_{l,q}]^2] [\Sigma^{1/2}] \quad (\text{F.241}) \end{aligned}$$

Since $v_{l,q}$ and $\underline{z}_{l,q}$ are independent, it follows that $(v_{l,q})^2$ and $\underline{z}_{l,q} \underline{z}_{l,q}^T$ are independent, which implies that $(v_{l,q})^2$ and $\underline{z}_{l,q} \underline{z}_{l,q}^T$ are uncorrelated; i.e.,

$$\mathbb{E} [(v_{l,q})^2 \underline{z}_{l,q} \underline{z}_{l,q}^T] = \mathbb{E} [(v_{l,q})^2] \mathbb{E} [\underline{z}_{l,q} \underline{z}_{l,q}^T] \quad (\text{F.242})$$

which, via Eqns. F.212 and F.214, implies that

$$\mathbb{E} [C_6] = (\delta_d)^2 [\Sigma^{1/2}] \left(\frac{1}{12} \right) \left(\frac{1}{s} \mathbb{I}_s \right) [\Sigma^{1/2}] = \frac{(\delta_d)^2}{12s} \Sigma \quad (\text{F.243})$$

Let the expressions C_7 , C_8 , C_9 , and C_{10} be defined as

$$C_7 = \left[\frac{(d'_l)^2}{s} + \frac{(\delta_d)^2}{12s} \right] \Sigma \quad (\text{F.244})$$

$$C_8 = \frac{(d'_l)^2}{s} + \frac{(\delta_d)^2}{12s} \quad (\text{F.245})$$

$$C_9 = \frac{(d'_l)^2}{s} \quad (\text{F.246})$$

$$C_{10} = \frac{(\delta_d)^2}{12s} \quad (\text{F.247})$$

Note: $C_7 = C_8 \Sigma$, and $C_8 = C_9 + C_{10}$.

Collecting terms, $\mathbb{E}[B_1]$ satisfies

$$\begin{aligned} \mathbb{E}[B_1] &= \mathbb{E}[C_1] + \mathbb{E}[C_2] + \mathbb{E}[C_3] + \mathbb{E}[C_2^T] + \mathbb{E}[C_3^T] + \mathbb{E}[C_4] + \mathbb{E}[C_5] + \mathbb{E}[C_6] \\ &= \mathbb{E}[C_1] + \mathbb{E}[C_4] + \mathbb{E}[C_6] = C_1 + \left[\frac{(d'_l)^2}{s} \right] \Sigma + \left[\frac{(\delta_d)^2}{12s} \right] \Sigma \\ &= C_1 + C_7 =: \mathbb{E}[\tilde{\mathbf{x}}_{l,q} \tilde{\mathbf{x}}_{l,q}^T] \quad (\text{F.248}) \end{aligned}$$

which concludes examination of the B_1 expression. ■

Subproof: Examining the B_2 expression. Let the preceding assumptions and notation hold (including those of the preceding subproof).

The quantity $\hat{\underline{\mu}}$ may be expressed as

$$\hat{\underline{\mu}} = H \sum_{l'=1}^{N_{\text{sh}}} \left(\frac{W_{l'}}{N_{\text{ss}}} \right) \sum_{q'=1}^{N_{\text{ss}}} \tilde{\mathbf{x}}_{l',q'} \quad (\text{F.249})$$

Hence, the expression B_2^T may be expanded as follows:

$$B_2^T = H \sum_{l'=1}^{N_{\text{sh}}} \left(\frac{W_{l'}}{N_{\text{ss}}} \right) \sum_{q'=1}^{N_{\text{ss}}} \tilde{\mathbf{x}}_{l',q'} \tilde{\mathbf{x}}_{l,q}^T \quad (\text{F.250})$$

which implies that the expression $\mathbb{E}[B_2^T]$ is given by

$$\mathbb{E}[B_2^T] = H \sum_{l'=1}^{N_{\text{sh}}} \left(\frac{W_{l'}}{N_{\text{ss}}} \right) \sum_{q'=1}^{N_{\text{ss}}} \mathbb{E}[\tilde{\mathbf{x}}_{l',q'} \tilde{\mathbf{x}}_{l,q}^T] \quad (\text{F.251})$$

First, the expression $\mathbb{E}[\tilde{\mathbf{x}}_{l',q'} \tilde{\mathbf{x}}_{l,q}^T]$ will be calculated for the case that $(l', q') = (l, q)$.

For this case, Eq. F.248 implies that

$$\mathbb{E} [\tilde{\mathbf{x}}_{l',q'} \tilde{\mathbf{x}}_{l,q}^T] = \mathbb{E} [\tilde{\mathbf{x}}_{l,q} \tilde{\mathbf{x}}_{l,q}^T] = \mathbb{E} [B_1] = C_1 + C_7 \quad (\text{F.252})$$

Second, the expression $\mathbb{E} [\tilde{\mathbf{x}}_{l',q'} \tilde{\mathbf{x}}_{l,q}^T]$ will be calculated for the case that $(l', q') \neq (l, q)$.

For this case, the expression $\tilde{\mathbf{x}}_{l',q'} \tilde{\mathbf{x}}_{l,q}^T$ may be expanded as follows:

$$\begin{aligned} \tilde{\mathbf{x}}_{l',q'} \tilde{\mathbf{x}}_{l,q}^T &= [\underline{\boldsymbol{\mu}} + (d'_{l'} + v_{l',q'} \delta_d) [\Sigma^{1/2}] \mathbf{z}_{l',q'}] [\underline{\boldsymbol{\mu}} + (d'_l + v_{l,q} \delta_d) [\Sigma^{1/2}] \mathbf{z}_{l,q}]^T \\ &= [\underline{\boldsymbol{\mu}} + (d'_{l'} + v_{l',q'} \delta_d) [\Sigma^{1/2}] \mathbf{z}_{l',q'}] [\underline{\boldsymbol{\mu}}^T + (d'_l + v_{l,q} \delta_d) \mathbf{z}_{l,q}^T [\Sigma^{1/2}]] \end{aligned} \quad (\text{F.253})$$

Let the expressions D_0 and D_1 be defined as

$$D_0 = (d'_{l'} + v_{l',q'} \delta_d) \underline{\boldsymbol{\mu}} \mathbf{z}_{l,q}^T [\Sigma^{1/2}] =: C_2 + C_3 \quad (\text{F.254})$$

$$D_1 = (d'_{l'} + v_{l',q'} \delta_d) \underline{\boldsymbol{\mu}} \mathbf{z}_{l',q'}^T [\Sigma^{1/2}] =: ([D_0]^T) \Big|_{(l',q')=(l,q)} \quad (\text{F.255})$$

In other words, Eq. F.255 implies that expression D_1 is equal to expression $[D_0]^T$ when the (l, q) indices in $[D_0]^T$ are replaced by the (l', q') indices.

Let the expression D_2 be defined as

$$D_2 = (d'_{l'} + v_{l',q'} \delta_d) (d'_l + v_{l,q} \delta_d) [\Sigma^{1/2}] \mathbf{z}_{l',q'} \mathbf{z}_{l,q}^T [\Sigma^{1/2}] \quad (\text{F.256})$$

Hence,

$$\tilde{\mathbf{x}}_{l',q'} \tilde{\mathbf{x}}_{l,q}^T = C_1 + D_0 + D_1 + D_2 \quad (\text{F.257})$$

By Eqns. F.233 and F.236, the expression $\mathbb{E} [D_0]$ satisfies

$$\mathbb{E} [D_0] = \mathbb{E} [C_2 + C_3] = \mathbb{E} [C_2] + \mathbb{E} [C_3] = \mathbf{0}_{s \times s} \quad (\text{F.258})$$

Since Eq. F.258 holds for an arbitrary index pair (l, q) , it also holds for an arbitrary index

pair (l', q') . It follows from Eq. F.258 that

$$\mathbb{E} [D_1] = \mathbb{E} [(D_0)^T] = \mathbf{0}_{s \times s} \quad (\text{F.259})$$

The expression D_2 may be expanded further as follows:

$$\begin{aligned} D_2 &= (d'_{l'} d'_l + d'_{l'} v_{l,q} \delta_d + d'_l v_{l',q'} \delta_d + \delta_d^2 v_{l',q'} v_{l,q}) [\Sigma^{1/2}] \underline{z}_{l',q'} \underline{z}_{l,q}^T [\Sigma^{1/2}] \\ &= (d'_{l'} d'_l) [\Sigma^{1/2}] \underline{z}_{l',q'} \underline{z}_{l,q}^T [\Sigma^{1/2}] + (d'_{l'} v_{l,q} \delta_d) [\Sigma^{1/2}] \underline{z}_{l',q'} \underline{z}_{l,q}^T [\Sigma^{1/2}] \\ &\quad + (d'_l v_{l',q'} \delta_d) [\Sigma^{1/2}] \underline{z}_{l',q'} \underline{z}_{l,q}^T [\Sigma^{1/2}] \\ &\quad + (\delta_d^2 v_{l',q'} v_{l,q}) [\Sigma^{1/2}] \underline{z}_{l',q'} \underline{z}_{l,q}^T [\Sigma^{1/2}] \quad (\text{F.260}) \end{aligned}$$

which, in turn, implies that

$$\begin{aligned} D_2 &= (d'_{l'} d'_l) [\Sigma^{1/2}] \left[(\underline{z}_{l',q'}) (\underline{z}_{l,q})^T \right] [\Sigma^{1/2}] \\ &+ (d'_{l'} \delta_d) [\Sigma^{1/2}] \left[(\underline{z}_{l',q'}) (v_{l,q} \underline{z}_{l,q})^T \right] [\Sigma^{1/2}] + (d'_l \delta_d) [\Sigma^{1/2}] \left[(v_{l',q'} \underline{z}_{l',q'}) (\underline{z}_{l,q})^T \right] [\Sigma^{1/2}] \\ &\quad + (\delta_d^2) [\Sigma^{1/2}] \left[(v_{l',q'} \underline{z}_{l',q'}) (v_{l,q} \underline{z}_{l,q})^T \right] [\Sigma^{1/2}] \quad (\text{F.261}) \end{aligned}$$

The $[0, 1]$ and $\mathbb{S}^{(s-1)}$ and samples [from which $\{v_{l',q'}, v_{l,q}\}$ and $\{\underline{z}_{l',q'}, \underline{z}_{l,q}\}$ are selected] are i.i.d. as per Algorithm 1. Since $(l', q') \neq (l, q)$, it follows that $(v_{l',q'}, \underline{z}_{l',q'})$ and $(v_{l,q}, \underline{z}_{l,q})$ are independent. This fact has the following implications:

1. $\underline{z}_{l',q'}$ and $\underline{z}_{l,q}$ are independent $\implies \underline{z}_{l',q'}$ and $\underline{z}_{l,q}^T$ are uncorrelated; i.e.,

$$\mathbb{E} [\underline{z}_{l',q'} \underline{z}_{l,q}^T] = \mathbb{E} [\underline{z}_{l',q'}] \mathbb{E} [\underline{z}_{l,q}^T] \quad (\text{F.262})$$

2. $\underline{z}_{l',q'}$ and $v_{l,q} \underline{z}_{l,q}$ are independent $\implies \underline{z}_{l',q'}$ and $v_{l,q} \underline{z}_{l,q}^T$ are uncorrelated; i.e.,

$$\mathbb{E} [\underline{z}_{l',q'} v_{l,q} \underline{z}_{l,q}^T] = \mathbb{E} [\underline{z}_{l',q'}] \mathbb{E} [v_{l,q} \underline{z}_{l,q}^T] \quad (\text{F.263})$$

3. $v_{l',q'}$, $\underline{z}_{l',q'}$ and $\underline{z}_{l,q}$ are independent $\implies v_{l',q'}$, $\underline{z}_{l',q'}$ and $\underline{z}_{l,q}^T$ are uncorrelated; i.e.,

$$\mathbb{E} [v_{l',q'} \underline{z}_{l',q'} \underline{z}_{l,q}^T] = \mathbb{E} [v_{l',q'} \underline{z}_{l',q'}] \mathbb{E} [\underline{z}_{l,q}^T] \quad (\text{F.264})$$

4. $v_{l',q'}$, $\underline{z}_{l',q'}$ and $v_{l,q}$, $\underline{z}_{l,q}$ are independent $\implies v_{l',q'}$, $\underline{z}_{l',q'}$ and $v_{l,q}$, $\underline{z}_{l,q}^T$ are uncorrelated; i.e.,

$$\mathbb{E} [v_{l',q'} \underline{z}_{l',q'} v_{l,q} \underline{z}_{l,q}^T] = \mathbb{E} [v_{l',q'} \underline{z}_{l',q'}] \mathbb{E} [v_{l,q} \underline{z}_{l,q}^T] \quad (\text{F.265})$$

Since the expression $\mathbb{E} [D_2]$ is given by

$$\begin{aligned} \mathbb{E} [D_2] &= (d_{l'}' d_l') [\Sigma^{1/2}] \mathbb{E} [(\underline{z}_{l',q'}) (\underline{z}_{l,q})^T] [\Sigma^{1/2}] \\ &+ (d_{l'}' \delta_d) [\Sigma^{1/2}] \mathbb{E} [(\underline{z}_{l',q'}) (v_{l,q} \underline{z}_{l,q})^T] [\Sigma^{1/2}] + (d_l' \delta_d) [\Sigma^{1/2}] \mathbb{E} [(v_{l',q'} \underline{z}_{l',q'}) (\underline{z}_{l,q})^T] [\Sigma^{1/2}] \\ &\quad + (\delta_d^2) [\Sigma^{1/2}] \mathbb{E} [(v_{l',q'} \underline{z}_{l',q'}) (v_{l,q} \underline{z}_{l,q})^T] [\Sigma^{1/2}] \quad (\text{F.266}) \end{aligned}$$

Hence, from from Eqns. F.262, F.263, F.264, and F.265, it follows that

$$\begin{aligned} \mathbb{E} [D_2] &= (d_{l'}' d_l') [\Sigma^{1/2}] \mathbb{E} [\underline{z}_{l',q'}] \mathbb{E} [\underline{z}_{l,q}^T] [\Sigma^{1/2}] \\ &\quad + (d_{l'}' \delta_d) [\Sigma^{1/2}] \mathbb{E} [\underline{z}_{l',q'}] \mathbb{E} [v_{l,q} \underline{z}_{l,q}^T] [\Sigma^{1/2}] \\ &\quad + (d_l' \delta_d) [\Sigma^{1/2}] \mathbb{E} [v_{l',q'} \underline{z}_{l',q'}] \mathbb{E} [\underline{z}_{l,q}^T] [\Sigma^{1/2}] \\ &\quad + (\delta_d^2) [\Sigma^{1/2}] \mathbb{E} [v_{l',q'} \underline{z}_{l',q'}] \mathbb{E} [v_{l,q} \underline{z}_{l,q}^T] [\Sigma^{1/2}] \quad (\text{F.267}) \end{aligned}$$

Therefore, via Eqns. F.211, F.213, and F.235, the expression $\mathbb{E} [D_2]$ satisfies

$$\mathbb{E} [D_2] = \mathbf{0}_{s \times s} \quad (\text{F.268})$$

Hence, from Eqns. F.257, F.258, F.259, and F.268, it follows that for the case where

$(l', q') \neq (l, q)$, the expression $\mathbb{E} [\tilde{\mathbf{x}}_{l',q'} \tilde{\mathbf{x}}_{l,q}^T]$ is given by

$$\mathbb{E} [\tilde{\mathbf{x}}_{l',q'} \tilde{\mathbf{x}}_{l,q}^T] = C_1 \quad (\text{F.269})$$

Therefore, Eqns. F.252 and F.269 imply that the expression $\mathbb{E} [\tilde{\mathbf{x}}_{l',q'} \tilde{\mathbf{x}}_{l,q}^T]$ is given generally by

$$\mathbb{E} [\tilde{\mathbf{x}}_{l',q'} \tilde{\mathbf{x}}_{l,q}^T] = C_1 + \begin{cases} C_7 & \text{if } (l', q') = (l, q) \\ \mathbf{0}_{s \times s} & \text{otherwise} \end{cases} \quad (\text{F.270})$$

Since $(l', q') = (l, q)$ only once for (l', q') in $\{1, \dots, N_{\text{sh}}\} \times \{1, \dots, N_{\text{ss}}\}$, and since it can be shown that

$$\sum_{l=1}^{N_{\text{sh}}} W_l = \text{cdf}_{\chi_s^2} ([d_{\text{max}}]^2) =: S_1 = \frac{1}{H} \quad (\text{F.271})$$

(cf. Eqns. F.199 and F.185), it follows from Eq. F.251 that the expression $\mathbb{E} [B_2^T]$ satisfies

$$\begin{aligned} \mathbb{E} [B_2^T] &= H \left[\frac{W_l}{N_{\text{ss}}} C_7 + \sum_{l'=1}^{N_{\text{sh}}} \left(\frac{W_{l'}}{N_{\text{ss}}} \right) \sum_{q'=1}^{N_{\text{ss}}} C_1 \right] \\ &= H \left[\frac{W_l}{N_{\text{ss}}} C_7 + \left(\sum_{l'=1}^{N_{\text{sh}}} \left(\frac{W_{l'}}{N_{\text{ss}}} \right) \sum_{q'=1}^{N_{\text{ss}}} 1 \right) C_1 \right] = \frac{H W_l}{N_{\text{ss}}} C_7 + C_1 \quad (\text{F.272}) \end{aligned}$$

Since the C_1 and C_7 matrices are symmetric (as see in Eqns. F.224 and F.244, while noting Σ is a symmetric matrix), it follows that the expression $\mathbb{E} [B_2]$ is given by

$$\mathbb{E} [B_2] = \mathbb{E} [(B_2)^T] = \frac{H W_l}{N_{\text{ss}}} C_7^T + C_1^T = \frac{H W_l}{N_{\text{ss}}} C_7 + C_1 =: \mathbb{E} [B_2^T] \quad (\text{F.273})$$

which concludes examination of the B_2 expression. ■

Let the preceding assumptions and notation hold (including those of the preceding sub-proofs).

Let the expressions E_1 and Q_1 be defined as

$$E_1 \doteq B_1 - B_2 - B_2^T \quad (\text{F.274})$$

$$Q_1 \doteq T_1 - T_2 - T_2^T = \sum_{l=1}^{N_{\text{sh}}} \left(\frac{W_l}{N_{\text{ss}}} \right) \sum_{q=1}^{N_{\text{ss}}} (B_1 - B_2 - B_2^T) = \sum_{l=1}^{N_{\text{sh}}} \left(\frac{W_l}{N_{\text{ss}}} \right) \sum_{q=1}^{N_{\text{ss}}} E_1 \quad (\text{F.275})$$

Hence, via Eqns. F.248 and F.273, the expression $\mathbb{E}[E_1]$ is given by

$$\begin{aligned} \mathbb{E}[E_1] &= \mathbb{E}[B_1] - \mathbb{E}[B_2] - \mathbb{E}[B_2^T] = \mathbb{E}[B_1] - 2\mathbb{E}[B_2] \\ &= (C_1 + C_7) - 2 \left(C_1 + \frac{H W_l}{N_{\text{ss}}} C_7 \right) = C_7 \left(1 - \frac{2H W_l}{N_{\text{ss}}} \right) - C_1 \quad (\text{F.276}) \end{aligned}$$

The expression B_3 is given by

$$\begin{aligned} B_3 \doteq \hat{\underline{\mu}} \hat{\underline{\mu}}^T &= H \left[\sum_{l'=1}^{N_{\text{sh}}} \left(\frac{W_{l'}}{N_{\text{ss}}} \right) \sum_{q'=1}^{N_{\text{ss}}} \tilde{\underline{x}}_{l',q'} \right] H \left[\sum_{l=1}^{N_{\text{sh}}} \left(\frac{W_l}{N_{\text{ss}}} \right) \sum_{q=1}^{N_{\text{ss}}} \tilde{\underline{x}}_{l,q}^T \right] \\ &= H^2 \sum_{l'=1}^{N_{\text{sh}}} \sum_{q'=1}^{N_{\text{ss}}} \sum_{l=1}^{N_{\text{sh}}} \sum_{q=1}^{N_{\text{ss}}} \left(\frac{W_{l'}}{N_{\text{ss}}} \right) \left(\frac{W_l}{N_{\text{ss}}} \right) \tilde{\underline{x}}_{l',q'} \tilde{\underline{x}}_{l,q}^T \\ &= H^2 \sum_{l=1}^{N_{\text{sh}}} \sum_{q=1}^{N_{\text{ss}}} \sum_{l'=1}^{N_{\text{sh}}} \sum_{q'=1}^{N_{\text{ss}}} \left(\frac{W_{l'}}{N_{\text{ss}}} \right) \left(\frac{W_l}{N_{\text{ss}}} \right) \tilde{\underline{x}}_{l',q'} \tilde{\underline{x}}_{l,q}^T \quad (\text{F.277}) \end{aligned}$$

Based on Eq. F.270, it follows that the expression $\mathbb{E}[B_3]$ satisfies

$$\begin{aligned} \mathbb{E}[B_3] &= H^2 \sum_{l=1}^{N_{\text{sh}}} \sum_{q=1}^{N_{\text{ss}}} \sum_{l'=1}^{N_{\text{sh}}} \sum_{q'=1}^{N_{\text{ss}}} \left[\left(\frac{W_{l'}}{N_{\text{ss}}} \right) \left(\frac{W_l}{N_{\text{ss}}} \right) C_1 \right] + H^2 \sum_{l=1}^{N_{\text{sh}}} \sum_{q=1}^{N_{\text{ss}}} \left[\left(\frac{W_l}{N_{\text{ss}}} \right)^2 C_7 \right] \\ &= H^2 \left[\sum_{l=1}^{N_{\text{sh}}} \sum_{q=1}^{N_{\text{ss}}} \sum_{l'=1}^{N_{\text{sh}}} \sum_{q'=1}^{N_{\text{ss}}} \left(\frac{W_{l'}}{N_{\text{ss}}} \right) \left(\frac{W_l}{N_{\text{ss}}} \right) \right] C_1 + H^2 \left[\sum_{l=1}^{N_{\text{sh}}} \sum_{q=1}^{N_{\text{ss}}} \left(\frac{W_l}{N_{\text{ss}}} \right)^2 \right] C_7 \quad (\text{F.278}) \end{aligned}$$

Let the expressions F_1 and F_2 be defined as

$$F_1 = H^2 \sum_{l=1}^{N_{\text{sh}}} \sum_{q=1}^{N_{\text{ss}}} \sum_{l'=1}^{N_{\text{sh}}} \sum_{q'=1}^{N_{\text{ss}}} \left(\frac{W_{l'}}{N_{\text{ss}}} \right) \left(\frac{W_l}{N_{\text{ss}}} \right) \quad (\text{F.279})$$

$$F_2 = H^2 \sum_{l=1}^{N_{\text{sh}}} \sum_{q=1}^{N_{\text{ss}}} \left(\frac{W_l}{N_{\text{ss}}} \right)^2 \quad (\text{F.280})$$

Via Eq. F.271, the expression F_1 satisfies

$$\begin{aligned} F_1 &= H^2 \left[\sum_{l=1}^{N_{\text{sh}}} \sum_{q=1}^{N_{\text{ss}}} \left(\frac{W_l}{N_{\text{ss}}} \right) \right] \left[\sum_{l'=1}^{N_{\text{sh}}} \sum_{q'=1}^{N_{\text{ss}}} \left(\frac{W_{l'}}{N_{\text{ss}}} \right) \right] \\ &= H^2 \left[\sum_{l=1}^{N_{\text{sh}}} W_l \right] \left[\sum_{l'=1}^{N_{\text{sh}}} W_{l'} \right] = H^2 \frac{1}{H^2} = 1 \quad (\text{F.281}) \end{aligned}$$

It follows that the expression $\mathbb{E}[B_3]$ is given by

$$\mathbb{E}[B_3] = C_1 + F_2 C_7 \quad (\text{F.282})$$

Via Eqns. F.222 and F.275, it follows that the expression B satisfies

$$B = Q_1 + T_3 = \sum_{l=1}^{N_{\text{sh}}} \left(\frac{W_l}{N_{\text{ss}}} \right) \sum_{q=1}^{N_{\text{ss}}} (E_1 + B_3) \quad (\text{F.283})$$

which, in turn, implies (via Eqns. F.276 and F.282) that the expression $\mathbb{E}[B]$ is given by

$$\begin{aligned} \mathbb{E}[B] &= \sum_{l=1}^{N_{\text{sh}}} \left(\frac{W_l}{N_{\text{ss}}} \right) \sum_{q=1}^{N_{\text{ss}}} (\mathbb{E}[E_1] + \mathbb{E}[B_3]) \\ &= \sum_{l=1}^{N_{\text{sh}}} \left(\frac{W_l}{N_{\text{ss}}} \right) \sum_{q=1}^{N_{\text{ss}}} \left[C_7 \left(1 - \frac{2H W_l}{N_{\text{ss}}} \right) - C_1 + C_1 + F_2 C_7 \right] \\ &= \sum_{l=1}^{N_{\text{sh}}} \left(\frac{W_l}{N_{\text{ss}}} \right) \sum_{q=1}^{N_{\text{ss}}} \left[\left(1 - \frac{2H W_l}{N_{\text{ss}}} \right) + F_2 \right] [C_7] \quad (\text{F.284}) \end{aligned}$$

Consequently, it follows that from Eqns. F.244 and F.245 that $\mathbb{E}[B]$ is proportional to Σ ,

specifically, as given by

$$\begin{aligned}\mathbb{E}[B] &= \sum_{l=1}^{N_{\text{sh}}} \left(\frac{W_l}{N_{\text{ss}}} \right) \sum_{q=1}^{N_{\text{ss}}} \left[1 - \frac{2H W_l}{N_{\text{ss}}} + F_2 \right] [C_8 \Sigma] \\ &= \left(\sum_{l=1}^{N_{\text{sh}}} \left(\frac{W_l}{N_{\text{ss}}} \right) \sum_{q=1}^{N_{\text{ss}}} \left[1 - \frac{2H W_l}{N_{\text{ss}}} + F_2 \right] [C_8] \right) [\Sigma] \quad (\text{F.285})\end{aligned}$$

Let the constant G be defined as

$$G \doteq \sum_{l=1}^{N_{\text{sh}}} \left(\frac{W_l}{N_{\text{ss}}} \right) \sum_{q=1}^{N_{\text{ss}}} \left[1 - \frac{2H W_l}{N_{\text{ss}}} + F_2 \right] [C_8] \quad (\text{F.286})$$

It follows that the expression B/G is an unbiased estimator of Σ ; i.e.,

$$\mathbb{E} \left[\frac{B}{G} \right] = \frac{1}{G} \mathbb{E}[B] = \frac{1}{G} G \Sigma = \Sigma \quad (\text{F.287})$$

Therefore, the remainder of this proof is concerned with simplifying the expression G .

Subproof: Simplifying the G expression. Let the preceding assumptions and notation hold (including those of the preceding subproofs).

Note:

$$\sum_{q=1}^{N_{\text{ss}}} \left(\frac{W_l}{N_{\text{ss}}} \right)^2 = \frac{(W_l)^2}{N_{\text{ss}}} \quad (\text{F.288})$$

which, via Eq. F.165, implies that

$$\sum_{l=1}^{N_{\text{sh}}} \sum_{q=1}^{N_{\text{ss}}} \left(\frac{W_l}{N_{\text{ss}}} \right)^2 = \frac{1}{N_{\text{ss}}} \sum_{l=1}^{N_{\text{sh}}} (W_l)^2 = \frac{S_2}{N_{\text{ss}}} \quad (\text{F.289})$$

Therefore, via Eq. F.280, the expression F_2 is given by

$$F_2 = H^2 \sum_{l=1}^{N_{\text{sh}}} \sum_{q=1}^{N_{\text{ss}}} \left(\frac{W_l}{N_{\text{ss}}} \right)^2 = \frac{H^2 S_2}{N_{\text{ss}}} \quad (\text{F.290})$$

Hence, F_2 is a constant.

In order to highlight the dependence of the expression C_9 on l (see Eq. F.246), it will be denoted as $C_9(l)$. Additionally, C_{10} is a constant (see Eq. F.247).

Hence, the expression G may be expanded as follows:

$$\begin{aligned}
G &\doteq \sum_{l=1}^{N_{\text{sh}}} \left(\frac{W_l}{N_{\text{ss}}} \right) \sum_{q=1}^{N_{\text{ss}}} \left[1 - \frac{2H W_l}{N_{\text{ss}}} + F_2 \right] [C_8] \\
&= \sum_{l=1}^{N_{\text{sh}}} \left(\frac{W_l}{N_{\text{ss}}} \right) \sum_{q=1}^{N_{\text{ss}}} \left[1 - \frac{2H W_l}{N_{\text{ss}}} + F_2 \right] [C_9(l) + C_{10}] \\
&= \sum_{l=1}^{N_{\text{sh}}} W_l \left[1 - \frac{2H W_l}{N_{\text{ss}}} + F_2 \right] [C_9(l) + C_{10}] \quad (\text{F.291})
\end{aligned}$$

which implies that the expression G may be expanded further, as given by

$$\begin{aligned}
G &= \sum_{l=1}^{N_{\text{sh}}} [W_l (1 + F_2) C_{10}] + \sum_{l=1}^{N_{\text{sh}}} [W_l C_9(l) (1 + F_2)] \\
&\quad + \sum_{l=1}^{N_{\text{sh}}} \left[W_l^2 \left(-\frac{2H C_{10}}{N_{\text{ss}}} \right) \right] + \sum_{l=1}^{N_{\text{sh}}} \left[W_l^2 C_9(l) \left(-\frac{2H}{N_{\text{ss}}} \right) \right] \quad (\text{F.292})
\end{aligned}$$

Note: Eqns. F.166, F.167, F.168, F.205, F.207, F.246 and F.247 imply that

$$\begin{aligned}
\sum_{l=1}^{N_{\text{sh}}} W_l C_9(l) &= \sum_{l=1}^{N_{\text{sh}}} W_l \frac{(d'_l)^2}{s} = \frac{1}{s} \sum_{l=1}^{N_{\text{sh}}} W_l \left(\left[l - \frac{1}{2} \right] \delta_d \right)^2 \\
&= \frac{1}{s} \left(\frac{d_{\text{max}}}{N_{\text{sh}}} \right)^2 \sum_{l=1}^{N_{\text{sh}}} W_l \left(l - \frac{1}{2} \right)^2 =: S_3 \quad (\text{F.293})
\end{aligned}$$

$$\begin{aligned}
\sum_{l=1}^{N_{\text{sh}}} W_l^2 C_9(l) &= \sum_{l=1}^{N_{\text{sh}}} W_l^2 \frac{(d'_l)^2}{s} = \frac{1}{s} \sum_{l=1}^{N_{\text{sh}}} W_l^2 \left(\left[l - \frac{1}{2} \right] \delta_d \right)^2 \\
&= \frac{1}{s} \left(\frac{d_{\text{max}}}{N_{\text{sh}}} \right)^2 \sum_{l=1}^{N_{\text{sh}}} W_l^2 \left(l - \frac{1}{2} \right)^2 =: S_4 \quad (\text{F.294})
\end{aligned}$$

$$C_{10} = \frac{(\delta_d)^2}{12s} = \frac{1}{12s} \left(\frac{d_{\text{max}}}{N_{\text{sh}}} \right)^2 =: D_1 \quad (\text{F.295})$$

Therefore, via Eqns. F.164, F.165, and F.291, the expression G is given by

$$\begin{aligned}
G &= (1 + F_2) C_{10} \sum_{l=1}^{N_{\text{sh}}} [W_l] + (1 + F_2) \sum_{l=1}^{N_{\text{sh}}} [W_l C_9(l)] \\
&\quad + \left(-\frac{2H C_{10}}{N_{\text{ss}}} \right) \sum_{l=1}^{N_{\text{sh}}} [W_l^2] + \left(-\frac{2H}{N_{\text{ss}}} \right) \sum_{l=1}^{N_{\text{sh}}} [W_l^2 C_9(l)] \\
&= (1 + F_2) C_{10} S_1 + (1 + F_2) S_3 + \left(-\frac{2H C_{10}}{N_{\text{ss}}} \right) S_2 + \left(-\frac{2H}{N_{\text{ss}}} \right) S_4 \quad (\text{F.296})
\end{aligned}$$

Hence, the expression G is given by

$$G = (1 + F_2) (C_{10} S_1 + S_3) + \left(-\frac{2H}{N_{\text{ss}}} \right) (C_{10} S_2 + S_4) \quad (\text{F.297})$$

Via Eqns. F.290 and F.295, the expression G is given by

$$\begin{aligned}
G &= \left(1 + \frac{H^2 S_2}{N_{\text{ss}}} \right) (C_{10} S_1 + S_3) + \left(-\frac{2H}{N_{\text{ss}}} \right) (C_{10} S_2 + S_4) \\
&= \left(1 + \frac{H^2 S_2}{N_{\text{ss}}} \right) S_3 + (C_{10} S_1) + \frac{H S_2}{N_{\text{ss}}} C_{10} + -\frac{2H S_2}{N_{\text{ss}}} C_{10} - \frac{2H}{N_{\text{ss}}} S_4 \\
&= \left(1 + \frac{H^2 S_2}{N_{\text{ss}}} \right) S_3 - \frac{2H}{N_{\text{ss}}} S_4 + D_1 \left(S_1 - \frac{H S_2}{N_{\text{ss}}} \right) \quad (\text{F.298})
\end{aligned}$$

which concludes simplification of the G expression. ■

Since the G expressions listed in Eqns. F.200 and F.298 are in agreement, the result follows from Eq. F.202 and F.287. □

As can be seen in Figure F.1, the value of the G expression is close to 1, as calculated numerically through direct application of Eq. F.200 (as well as its corresponding intermediate constants).

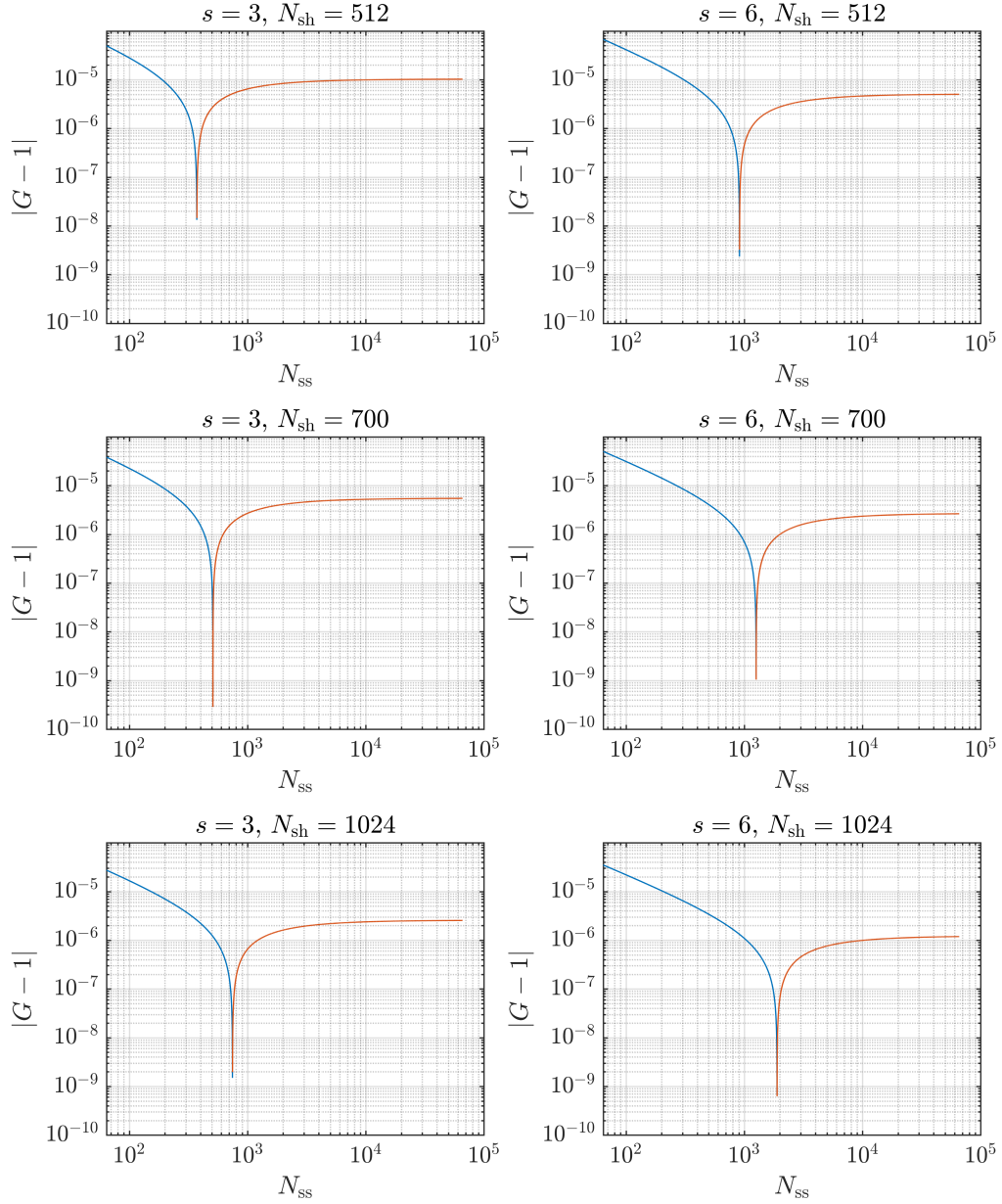


Figure F.1: Values of $|G - 1|$ as a function of MSS sample dimension (s) and number of MSS sample shells (N_{sh}): (blue) $G < 1$, (red) $G > 1$.

REFERENCES

- [1] D. P. Scharf, F. Y. Hadaegh, and S. R. Ploen, “A survey of spacecraft formation flying guidance and control (part I): guidance,” in *Proceedings of the 2003 American Control Conference*, vol. 2, Denver, CO: IEEE, Jun. 2003, pp. 1733–1739.
- [2] K. Alfriend, S. R. Vadali, P. Gurfil, J. How, and L. Breger, “Spacecraft formation flying: Dynamics, control and navigation,” in (Elsevier Astrodynamics Series), 1st ed., Elsevier Astrodynamics Series. Oxford, UK: Butterworth–Heinemann (Elsevier Science), 2010, ch. 1, 14, pp. 1–11, 329–330.
- [3] S. -.-J. Chung, S. Bandyopadhyay, R. Foust, G. P. Subramanian, and F. Hadaegh, “Review of formation flying and constellation missions using nanosatellites,” *Journal of Spacecraft and Rockets*, vol. 53, no. 3, pp. 567–578, 2016.
- [4] J. R. Wertz, “Mission concept definition and exploration,” in *Space Mission Engineering: The New SMAD*, ser. Space Technology Library, J. R. Wertz, D. F. Everett, and J. J. Puschell, Eds., Hawthorne, CA: Microcosm Press, 2011, ch. 4, pp. 61–82.
- [5] H. Schaub and J. L. Junkins, “Spacecraft formation flying,” in *Analytical Mechanics of Space Systems*, ser. AIAA Education Series, 2nd ed., Reston, VA: American Institute of Aeronautics and Astronautics, 2009, ch. 14, pp. 593–673.
- [6] B. D. Tapley, S. Bettadpur, M. Watkins, and C. Reigber, “The gravity recovery and climate experiment: Mission overview and early results,” *Geophysical Research Letters*, vol. 31, no. 9, 2004.
- [7] B. Tapley *et al.*, “GGM02 – An improved Earth gravity field model from GRACE,” *Journal of Geodesy*, vol. 79, no. 8, pp. 467–478, Nov. 2005.
- [8] A. K. Sugihara El Maghraby, A. Grubisic, C. Colombo, and A. Tatnall, “A novel approach to microwave interferometric radiometry in the geostationary orbit using formation flight,” in *67th International Astronautical Congress of the International Astronautical Federation*, ser. IAC-16,B1,2,8,x33950, Guadalajara, Mexico, Sep. 2016, pp. 1–14.
- [9] A. W. Koenig, B. Macintosh, and S. D’Amico, “Formation design of distributed telescopes in Earth orbit for astrophysics applications,” *Journal of Spacecraft and Rockets*, vol. 56, no. 5, pp. 1462–1477, 2019.
- [10] G. Wang and W. T. Ni, “Numerical simulation of time delay interferometry for eLISA/NGO,” *Classical and Quantum Gravity*, vol. 30, no. 6, p. 065 011, Feb. 2013.

- [11] G. Wang and W. T. Ni, “Orbit optimization and time delay interferometry for inclined ASTROD–GW formation with half-year precession–period,” *Chinese Physics B*, vol. 24, no. 5, p. 059 501, 2015.
- [12] U. E. Núñez Garzón and E. G. Lightsey, “Existence of probability density function for norm of finite-dimensional random vector,” *Journal of Guidance, Control, and Dynamics*, vol. 45, no. 6, pp. 1137–1142, 2022.
- [13] G. L. Slater, S. M. Byram, and T. W. Williams, “Collision avoidance for satellites in formation flight,” *Journal of Guidance, Control, and Dynamics*, vol. 29, no. 5, pp. 1140–1146, 2006.
- [14] H. Klinkrad, “Space debris: Models and risk analysis,” in (Springer-Praxis Books in Astronautical Engineering), Springer-Praxis Books in Astronautical Engineering. Chichester, UK: Springer-Verlag Berlin Heidelberg, 2006, ch. 1–2, pp. 1–58.
- [15] D. B. Spencer and R. A. Madler, “Orbital debris—a space hazard,” in *Space Mission Engineering: The New SMAD*, ser. Space Technology Library, J. R. Wertz, D. F. Everett, and J. J. Puschell, Eds., Hawthorne, CA: Microcosm Press, 2011, ch. 7.5, pp. 139–147.
- [16] D. J. Kessler, “Collisional cascading: The limits of population growth in low Earth orbit,” *Advances in Space Research*, vol. 11, no. 12, pp. 63–66, 1991.
- [17] J. N. Pelton, “Space debris and other threats from outer space,” in (SpringerBriefs in Space Development), SpringerBriefs in Space Development. New York, NY: Springer-Verlag New York, 2013, ch. 1–2, pp. 1–23.
- [18] V. A. Chobotov *et al.*, “Space debris,” in *Orbital Mechanics*, ser. AIAA Education Series, V. A. Chobotov, Ed., 3rd ed., Reston, VA: American Institute of Aeronautics and Astronautics, 2011, ch. 13, pp. 301–334.
- [19] F. Letizia, C. Colombo, and H. G. Lewis, “Collision probability due to space debris clouds through a continuum approach,” *Journal of Guidance, Control, and Dynamics*, vol. 39, no. 10, pp. 2240–2249, 2016.
- [20] M. Shan, J. Guo, and E. Gill, “Review and comparison of active space debris capturing and removal methods,” *Progress in Aerospace Sciences*, vol. 80, pp. 18–32, Jan. 2016.
- [21] A. Wander, K. Konstantinidis, R. Förstner, and P. Voigt, “Autonomy and operational concept for self-removal of spacecraft: Status detection, removal triggering and passivation,” *Acta Astronautica*, vol. 164, pp. 92–105, Nov. 2019.

- [22] S. Hilton, R. Sabatini, A. Gardi, H. Ogawa, and P. Teofilatto, "Space traffic management: Towards safe and unsegregated space transport operations," *Progress in Aerospace Sciences*, vol. 105, pp. 98–125, Feb. 2019.
- [23] M. R. Akella and K. T. Alfriend, "Probability of collision between space objects," *Journal of Guidance, Control, and Dynamics*, vol. 23, no. 5, pp. 769–772, 2000.
- [24] R. P. Patera, "General method for calculating satellite collision probability," *Journal of Guidance, Control, and Dynamics*, vol. 24, no. 4, pp. 716–722, 2001.
- [25] R. Bevilacqua, T. Lehmann, and M. Romano, "Development and experimentation of LQR/APF guidance and control for autonomous proximity maneuvers of multiple spacecraft," *Acta Astronautica*, vol. 68, no. 7, pp. 1260–1275, 2011.
- [26] S. Nag and L. Summerer, "Behaviour based, autonomous and distributed scatter manoeuvres for satellite swarms," *Acta Astronautica*, 6th International Workshop on Satellite Constellation and Formation Flying, vol. 82, no. 1, pp. 95–109, 2013.
- [27] U. E. Núñez Garzón and E. G. Lightsey, "Relating collision probability and miss distance indicators in spacecraft formation collision risk analysis," in *2020 AAS/AIAA Astrodynamics Specialist Conference*, ser. AAS 20-528, San Diego, CA: Univelt, Inc., Aug. 2020, pp. 3853–3872.
- [28] U. E. Núñez Garzón and E. G. Lightsey, "Relating collision probability and separation indicators in spacecraft formation collision risk analysis," *Journal of Guidance, Control, and Dynamics*, vol. 45, no. 3, pp. 517–532, 2022.
- [29] L. K. Newman, R. C. Frigm, M. G. Duncan, and M. D. Hejduk, "Evolution and implementation of the NASA robotic conjunction assessment risk analysis concept of operations," in *2014 Advanced Maui Optical and Space Surveillance Technologies Conference Proceedings*, ser. GSFC-E-DAA-TN17386, Red Hook, NY: Curran Associates, Inc., Sep. 2014, pp. 1–14.
- [30] A. Weiss, C. Petersen, M. Baldwin, R. S. Erwin, and I. Kolmanovsky, "Safe positively invariant sets for spacecraft obstacle avoidance," *Journal of Guidance, Control, and Dynamics*, vol. 38, no. 4, pp. 720–732, 2015.
- [31] F. K. Chan, "Spacecraft collision probability," in El Segundo, CA and Reston, VA: Aerospace Press and American Institute of Aeronautics and Astronautics, 2008, ch. 1–5, 13–14, pp. 1–97, 237–271.
- [32] S. Alfano, "A numerical implementation of spherical object collision probability," *The Journal of the Astronautical Sciences*, vol. 53, no. 1, pp. 103–109, Mar. 2005.

- [33] U. E. Núñez Garzón and E. G. Lightsey, “Sensitivity of separation indicators in spacecraft formation collision risk analysis,” in *2021 AAS/AIAA Astrodynamics Specialist Conference*, ser. AAS 21-562, San Diego, CA: Univelt, Inc., Aug. 2021, pp. 1179–1198.
- [34] C. Heil, “Introduction to real analysis,” in (Graduate Texts in Mathematics), Graduate Texts in Mathematics. Cham, Switzerland: Springer International Publishing, 2019, ch. 1–8, pp. 15–326.
- [35] P. Billingsley, “Probability and measure,” in (Wiley Series in Probability and Mathematical Statistics), 3rd ed., Wiley Series in Probability and Mathematical Statistics. New York, NY: John Wiley & Sons, Ltd., 1995, ch. 1-4, 6, pp. 1–326, 400–481.
- [36] A. M. Mathai and S. B. Provost, “Quadratic forms in random variables: Theory and applications,” in (Statistics: Textbooks and Monographs), 1st ed., Statistics: Textbooks and Monographs. New York, NY: Statistics: Textbooks and Monographs, Marcel Dekker, Inc., 1992, ch. 3–5, pp. 25–242.
- [37] K. J. DeMars, R. H. Bishop, and M. K. Jah, “Entropy-based approach for uncertainty propagation of nonlinear dynamical systems,” *Journal of Guidance, Control, and Dynamics*, vol. 36, no. 4, pp. 1047–1057, 2013.
- [38] U. E. Núñez Garzón and E. G. Lightsey, “Stochastic Convergence of Sobol-Based Mahalanobis Shell Sampling Collision Probability Computation,” *Journal of Guidance, Control, and Dynamics*, vol. 46, no. 5, pp. 796–814, 2023.
- [39] A. Richards, T. Schouwenaars, J. P. How, and E. Feron, “Spacecraft trajectory planning with avoidance constraints using mixed-integer linear programming,” *Journal of Guidance, Control, and Dynamics*, vol. 25, no. 4, pp. 755–764, 2002.
- [40] X. Wang, Z. Wang, and Y. Zhang, “Model predictive control to autonomously approach a failed spacecraft,” *International Journal of Aerospace Engineering*, vol. 2018, p. 7428535, Dec. 2018.
- [41] U. E. Núñez Garzón and E. G. Lightsey, “Cylindrical orthogonal norm-based stochastic collision risk measures in spacecraft formation flying,” *Acta Astronautica*, Apr. 2023, Submitted for publication Apr. 2023.
- [42] K. J. DeMars, Y. Cheng, and M. K. Jah, “Collision probability with Gaussian mixture orbit uncertainty,” *Journal of Guidance, Control, and Dynamics*, vol. 37, no. 3, pp. 979–985, 2014.

- [43] S. Alfano, “Satellite Conjunction Monte Carlo Analysis,” in *2009 AAS/AIAA Space Flight Mechanics Meeting*, ser. AAS 09-233, Savannah, GA: AAS/AIAA, Feb. 2009, pp. 2007–2024.
- [44] V. T. Coppola, “Including velocity uncertainty in the probability of collision between space objects,” in *2012 AAS/AIAA Space Flight Mechanics Meeting*, ser. AAS 12-247, Charleston, SC: AAS/AIAA, Jan. 2012, pp. 2159–2178.
- [45] M. S. Balch, R. Martin, and S. Ferson, “Satellite conjunction analysis and the false confidence theorem,” *Proceedings of the Royal Society A: Mathematical, Physical and Engineering Sciences*, vol. 475, no. 2227, p. 20 180 565, 2019.
- [46] U. E. Núñez Garzón and E. G. Lightsey, “Mahalanobis Shell Sampling (MSS) Method for Collision Probability Computation,” in *AIAA SciTech 2021 Forum*, ser. AIAA 2021-1855, Reston, VA: AIAA, Jan. 2021, pp. 1–25.
- [47] U. E. Núñez Garzón and E. G. Lightsey, “Mahalanobis Shell Sampling (MSS) Method for Collision Probability Computation,” Georgia Institute of Technology, Space Systems Design Lab, Atlanta, GA, Tech. Rep., Feb. 2020, pp. 1–44.
- [48] Y. Kim, M. Mesbahi, and F. Y. Hadaegh, “Multiple-spacecraft reconfiguration through collision avoidance, bouncing, and stalemate,” *Journal of Optimization Theory and Applications*, vol. 122, no. 2, pp. 323–343, 2004.
- [49] X. Chu, J. Zhang, S. Lu, Y. Zhang, and Y. Sun, “Optimised collision avoidance for an ultra-close rendezvous with a failed satellite based on the Gauss pseudospectral method,” *Acta Astronautica*, vol. 128, pp. 363–376, 2016.
- [50] Z. Xu, X. Chen, Y. Huang, Y. Bai, and Q. Chen, “Collision prediction and avoidance for satellite ultra-close relative motion with zonotope-based reachable sets,” *Proceedings of the Institution of Mechanical Engineers, Part G: Journal of Aerospace Engineering*, vol. 233, no. 11, pp. 3920–3937, 2019.
- [51] Z. Guoqiang, H. Min, and S. Junling, “Collision monitoring and optimal collision avoidance manoeuvre for formation flying satellites,” *Aircraft Engineering and Aerospace Technology*, vol. 84, no. 6, pp. 413–422, Jan. 2012.
- [52] Y. Wang, X. Chen, D. Ran, Y. Zhao, Y. Chen, and Y. Bai, “Spacecraft formation reconfiguration with multi-obstacle avoidance under navigation and control uncertainties using adaptive artificial potential function method,” *Astrodynamics*, vol. 4, no. 1, pp. 41–56, Mar. 2020.
- [53] Y. Wang, Y. Bai, J. Xing, G. Radice, Q. Ni, and X. Chen, “Equal-collision-probability-curve method for safe spacecraft close-range proximity maneuvers,” *Advances in Space Research*, vol. 62, no. 9, pp. 2599–2619, 2018.

- [54] R. Serra, D. Arzelier, M. Joldes, and A. Rondepierre, “Probabilistic collision avoidance for long-term space encounters via risk selection,” in *CEAS Specialist Conference on Guidance, Navigation and Control*, Cham, Switzerland: Springer International Publishing, Apr. 2015, pp. 679–698.
- [55] J.-B. Caillau, M. Cerf, A. Sassi, E. Trélat, and H. Zidani, “Solving chance constrained optimal control problems in aerospace via kernel density estimation,” *Optimal Control Applications and Methods*, vol. 39, no. 5, pp. 1833–1858, 2018.
- [56] S. Alfano and D. Oltrogge, “Probability of collision: Valuation, variability, visualization, and validity,” *Acta Astronautica*, vol. 148, pp. 301–316, 2018.
- [57] B. Wan *et al.*, “Collision avoidance engineering design for satellite formation flying,” in *2018 IEEE CSAA Guidance, Navigation and Control Conference (CGNCC)*, Red Hook, NY: Curran Associates, Inc., Aug. 2018, pp. 1–6.
- [58] H. Park, S. Di Cairano, and I. Kolmanovsky, “Model predictive control of spacecraft docking with a non-rotating platform,” *IFAC Proceedings Volumes*, vol. 44, no. 1, pp. 8485–8490, 2011, 18th IFAC World Congress.
- [59] Q. Chen, Y. Meng, Y. Liao, and C. Wei, “Intersatellite distance-keeping control based on relative motion geometry,” *Journal of Guidance, Control, and Dynamics*, vol. 46, no. 1, pp. 177–185, 2023.
- [60] S. D’Amico and O. Montenbruck, “Proximity operations of formation-flying spacecraft using an eccentricity/inclination vector separation,” *Journal of Guidance, Control, and Dynamics*, vol. 29, no. 3, pp. 554–563, 2006.
- [61] J. Wang, C. Zhang, and J. Zhang, “Analytical solution of satellite formation impulsive reconfiguration considering passive safety constraints,” *Aerospace Science and Technology*, vol. 119, p. 107 108, 2021.
- [62] T. Sasaki, M. Hidaka, R. Nakamura, and T. Yamamoto, “Robust relative trajectory design considering passive abort safety under sensor failure situation,” in *2022 IEEE Aerospace Conference (AERO)*, Red Hook, NY: Curran Associates, Inc., 2022, pp. 1–10.
- [63] P. Palmer and M. Halsall, “Designing natural formations of low-Earth-orbiting satellites,” *Journal of Guidance, Control, and Dynamics*, vol. 32, no. 3, pp. 860–868, 2009.
- [64] D. S. Bernstein, “Matrix mathematics: Theory, facts, and formulas,” in 2nd ed. Princeton, NJ: Princeton University Press, 2009, ch. 3, 8, pp. 179–252, 417–542.

- [65] F. L. Markley and J. L. Crassidis, “Matrices, vectors, frames, transforms,” in *Fundamentals of Spacecraft Attitude Determination and Control*, ser. Space Technology Library, New York, NY: Springer New York, 2014, ch. 2, pp. 17–65.
- [66] C. Heil, “Metrics, norms, inner products, and operator theory,” in (Applied and Numerical Harmonic Analysis), *Applied and Numerical Harmonic Analysis*. Cham, Switzerland: Springer International Publishing, 2018, ch. 1–3, 5, pp. 1–139, 191–241.
- [67] H. Schwarzlender, “Part 4: Transformationsathreya and multiple random variables,” in *Probability Concepts and Theory for Engineers*, 1st ed., Chichester, UK: John Wiley & Sons, Ltd., 2011, ch. 4, pp. 227–304.
- [68] P. C. Mahalanobis, “On the generalised distance in statistics,” *Proceedings of the National Institute of Sciences of India*, vol. 2, no. 1, pp. 49–55, Apr. 1936.
- [69] J. G. Hocking and G. S. Young, “Topological spaces and functions,” in *Topology*, 1st ed., Reading, MA: Addison-Wesley, Inc., 1961, ch. 1, pp. 1–36.
- [70] K. H. Khalil, “Fundamental Properties,” in *Nonlinear Systems*, 3rd ed., Upper Saddle River, NJ: Prentice-Hall, 2002, ch. 3, pp. 87–110.
- [71] B. Øksendal, “Stochastic Differential Equations,” in *Stochastic Differential Equations: An Introduction with Applications*, ser. Universitext, 5th ed., New York, NY: Springer-Verlag Berlin Heidelberg New York, 1998, ch. 5, pp. 61–78.
- [72] S. Alfano, “Relating position uncertainty to maximum conjunction probability,” *The Journal of the Astronautical Sciences*, vol. 53, no. 2, pp. 193–205, Jun. 2005.
- [73] D. P. Kroese, T. Taimre, and Z. I. Botev, “Handbook of Monte Carlo methods,” in (Wiley Series in Probability and Statistics), *Wiley Series in Probability and Statistics*. New York, NY: John Wiley & Sons, Ltd., 2011, ch. 2, 4, 8, Appx. A, pp. 25–41, 85–151, 301–345, 605–651.
- [74] R. P. Patera, “Satellite collision probability for nonlinear relative motion,” *Journal of Guidance, Control, and Dynamics*, vol. 26, no. 5, pp. 728–733, 2003.
- [75] S. Zhang, T. Fu, D. Chen, and H. Cao, “Satellite instantaneous collision probability computation using equivalent volume cuboids,” *Journal of Guidance, Control, and Dynamics*, vol. 43, no. 9, pp. 1757–1763, 2020.
- [76] O. Dovgoshey, O. Martio, V. Ryazanov, and M. Vuorinen, “The Cantor function,” *Expositiones Mathematicae*, vol. 24, no. 1, pp. 1–37, 2006.

- [77] M. Valli, R. Armellin, P. Di Lizia, and M. R. Lavagna, “Nonlinear mapping of uncertainties in celestial mechanics,” *Journal of Guidance, Control, and Dynamics*, vol. 36, no. 1, pp. 48–63, 2013.
- [78] K. Vishwajeet, P. Singla, and M. Jah, “Nonlinear uncertainty propagation for perturbed two-body orbits,” *Journal of Guidance, Control, and Dynamics*, vol. 37, no. 5, pp. 1415–1425, 2014.
- [79] J. T. Horwood, N. D. Aragon, and A. B. Poore, “Gaussian sum filters for space surveillance: Theory and simulations,” *Journal of Guidance, Control, and Dynamics*, vol. 34, no. 6, pp. 1839–1851, 2011.
- [80] K. J. DeMars and M. K. Jah, “Probabilistic initial orbit determination using Gaussian mixture models,” *Journal of Guidance, Control, and Dynamics*, vol. 36, no. 5, pp. 1324–1335, 2013.
- [81] V. Vittaldev and R. P. Russell, “Space object collision probability using multidirectional Gaussian mixture models,” *Journal of Guidance, Control, and Dynamics*, vol. 39, no. 9, pp. 2163–2169, 2016.
- [82] B. A. Jones and A. Doostan, “Satellite collision probability estimation using polynomial chaos expansions,” *Advances in Space Research*, vol. 52, no. 11, pp. 1860–1875, 2013.
- [83] T. Nguyen, “N-dimensional quasipolar coordinates - Theory and application,” M.S. thesis, University of Nevada, Las Vegas, Las Vegas, NV, May 2014, ch. 2, pp. 11–22.
- [84] R. G. Hubbard and B. B. Hubbard, “Solving equations,” in *Vector Calculus, Linear Algebra, and Differential Forms: A Unified Approach*, 5th ed., Ithaca, NY: Matrix Editions, 2015, ch. 2, pp. 159–282.
- [85] K. B. Athreya and S. N. Lahiri, “Measure theory and probability theory,” in (Springer Texts in Statistics), Springer Texts in Statistics. New York, NY: Springer New York, 2006, ch. 2-3, pp. 39–111.
- [86] M. W. Hirsch, S. Smale, and R. L. Devaney, “Nonlinear systems,” in *Differential Equations, Dynamical Systems, and an Introduction to Chaos*, 3rd ed., Boston, MA: Academic Press, 2013, ch. 7, pp. 139–157.
- [87] Z. Dang, “Solutions of Tschauner–Hempel equations,” *Journal of Guidance, Control, and Dynamics*, vol. 40, no. 11, pp. 2956–2960, 2017.

- [88] G. Inalhan, M. Tillerson, and J. P. How, “Relative dynamics and control of spacecraft formations in eccentric orbits,” *Journal of Guidance, Control, and Dynamics*, vol. 25, no. 1, pp. 48–59, 2002.
- [89] D.-W. Gim and K. T. Alfriend, “Satellite relative motion using differential equinoctial elements,” *Celestial Mechanics and Dynamical Astronomy*, vol. 92, no. 4, pp. 295–336, Aug. 2005.
- [90] J. Sullivan, S. Grimberg, and S. D’Amico, “Comprehensive survey and assessment of spacecraft relative motion dynamics models,” *Journal of Guidance, Control, and Dynamics*, vol. 40, no. 8, pp. 1837–1859, 2017.
- [91] M. Searcóid, “Uniform continuity,” in *Metric Spaces*, ser. Springer Undergraduate Mathematics Series, London, UK: Springer-Verlag London, 2007, ch. 9, pp. 147–163.
- [92] J. K. Hale, “General Properties of Differential Equations,” in *Ordinary Differential Equations*, 2nd ed., Malabar, FL: Robert E. Krieger Publishing Company, Inc., 1980, ch. 1, pp. 12–50.
- [93] N. Baresi, Z. P. Olikara, and D. J. Scheeres, “Fully numerical methods for continuing families of quasi-periodic invariant tori in astrodynamics,” *The Journal of the Astronautical Sciences*, vol. 65, no. 2, pp. 157–182, Jun. 2018.
- [94] J.-M. Mondelo, “Computing invariant manifolds for libration point missions,” in *Satellite Dynamics and Space Missions*, G. Baù, A. Celletti, C. B. Galeş, and G. F. Gronchi, Eds., Cham, Switzerland: Springer International Publishing, 2019, pp. 159–223.
- [95] K. K. Boudad, K. C. Howell, and D. C. Davis, “Dynamics of synodic resonant near rectilinear halo orbits in the bicircular four-body problem,” *Advances in Space Research*, vol. 66, no. 9, pp. 2194–2214, 2020.
- [96] K. C. Howell, B. T. Barden, and M. W. Lo, “Application of dynamical systems theory to trajectory design for a libration point mission,” *The Journal of the Astronautical Sciences*, vol. 45, no. 2, pp. 161–178, Jun. 1997.
- [97] K. C. Howell, D. C. Davis, and A. F. Haapala, “Application of periapse maps for the design of trajectories near the smaller primary in multi-body regimes,” *Mathematical Problems in Engineering*, vol. 2012, p. 351 759, Dec. 2011.
- [98] A. F. Haapala and K. C. Howell, “Representations of higher-dimensional Poincaré maps with applications to spacecraft trajectory design,” *Acta Astronautica*, vol. 96, pp. 23–41, 2014.

- [99] X. Tricoche, W. Schlei, and K. C. Howell, “Extraction and visualization of Poincare map topology for spacecraft trajectory design,” *IEEE Transactions on Visualization and Computer Graphics*, vol. 27, no. 2, pp. 765–774, 2021.
- [100] B. Kumar, R. L. Anderson, and R. de la Llave, “Rapid and accurate methods for computing whiskered tori and their manifolds in periodically perturbed planar circular restricted 3-body problems,” *Celestial Mechanics and Dynamical Astronomy*, vol. 134, no. 1, p. 3, Jan. 2022.
- [101] M. S. Balch, “A corrector for probability dilution in satellite conjunction analysis,” in *18th AIAA Non-Deterministic Approaches Conference*, ser. AIAA 2016-1445, San Diego, CA: AIAA, Jan. 2016, pp. 1–12.
- [102] R. C. Frigm, “A single conjunction risk assessment metric: The f-value,” in *2009 AAS/AIAA Astrodynamics Specialist Conference*, ser. AAS 09-373, San Diego, CA: Univelt, Inc., Aug. 2009, pp. 1175–1192.
- [103] M. D. Hejduk, “Satellite conjunction assessment risk analysis for “Dilution Region” events: Issues and operational approaches,” in *5th Annual Space Traffic Management Conference “Progress through Collaboration”*, Daytona Beach, FL: Embry Riddle Scholarly Commons, Feb. 2019, pp. 1–15.
- [104] J. R. Carpenter *et al.*, “Relevance of the American Statistical Society’s warning on p -values for conjunction assessment,” in *2017 AAS/AIAA Astrodynamics Specialist Conference*, ser. AAS 17-614, San Diego, CA: Univelt, Inc., Aug. 2017, pp. 921–939.
- [105] J. R. Carpenter, “Covariance realism is not enough,” in *2019 AAS/AIAA Astrodynamics Specialist Conference*, ser. AAS 19-605, Portland, ME: AAS/AIAA, Aug. 2019, pp. 1–19.
- [106] S. Elkantassi and A. C. Davison, “Space Oddity? A statistical formulation of conjunction assessment,” *Journal of Guidance, Control, and Dynamics*, vol. 45, no. 12, pp. 2258–2274, 2022.
- [107] The MathWorks, Inc., “MATLAB[®] Function Reference,” in MATLAB R2018b. Natick, MA: The MathWorks, Inc., Sep. 2018, ch. 1, pp. 1-7003 –1-7009.
- [108] J. R. Carpenter, F. L. Markley, and D. Gold, “Sequential Probability Ratio Test for collision avoidance maneuver decisions,” *The Journal of the Astronautical Sciences*, vol. 59, no. 1, pp. 267–280, Jun. 2012.
- [109] J. R. Carpenter, F. L. Markley, and D. Gold, “Wald Sequential Probability Ratio Test for analysis of orbital conjunction data,” in *AIAA Guidance, Navigation, and*

Control (GNC) Conference, ser. AIAA 2013-5187, Boston, MA: AIAA, Aug. 2013, pp. 1–13.

- [110] J. R. Carpenter and F. L. Markley, “Wald Sequential Probability Ratio Test for space object conjunction assessment,” *Journal of Guidance, Control, and Dynamics*, vol. 37, no. 5, pp. 1385–1396, 2014.
- [111] A. K. Mashiku and J. R. Carpenter, “A collision avoidance strategy for a potential natural satellite around the asteroid Bennu for the OSIRIS-REx mission,” in *2016 AAS/AIAA Astrodynamics Specialist Conference*, ser. AIAA 2016-5655, Long Beach, CA: AAS/AIAA, Sep. 2016, pp. 1–10.
- [112] B. Schilling, Y. Taleb, J. R. Carpenter, M. Balducci, and T. W. Williams, “Operational experience with the Wald Sequential Probability Ratio Test for conjunction assessment from the Magnetospheric MultiScale mission,” in *2016 AAS/AIAA Astrodynamics Specialist Conference*, ser. AIAA 2016-5424, Long Beach, CA: AAS/AIAA, Sep. 2016, pp. 1–13.
- [113] T. Williams, J. R. Carpenter, M. Farahmand, N. Ottenstein, M. Demoret, and D. Godine, “Conjunction assessment techniques and operational results from the Magnetospheric Multiscale Mission,” in *2017 International Workshop on Satellite Constellations and Formation Flying (IWSCFF)*, ser. IWSCFF 17-01, Boulder, CO: International Astronautical Federation (IAF) Astrodynamics Committee, Jun. 2017, pp. 1–16.
- [114] J. R. Carpenter and F. L. Markley, “Sequential Wald Test employing a constrained filter bank: Application to spacecraft conjunctions,” *Journal of Optimization Theory and Applications*, vol. 191, no. 2, pp. 440–458, Dec. 2021.
- [115] G. J. McLachlan, “Mahalanobis distance,” *Resonance*, vol. 4, no. 6, pp. 20–26, Jun. 1999.
- [116] P. Bhattacharya and P. Burman, “12 - Multivariate Analysis,” in *Theory and Methods of Statistics*, London, UK: Academic Press, 2016, pp. 383–429.
- [117] R. De Maesschalck, D. Jouan-Rimbaud, and D. L. Massart, “The Mahalanobis distance,” *Chemometrics and Intelligent Laboratory Systems*, vol. 50, no. 1, pp. 1–18, 2000.
- [118] M. Hubert, P. J. Rousseeuw, and S. Van Aelst, “Multivariate outlier detection and robustness,” in *Handbook of Statistics, Vol. 24: Data Mining and Data Visualization*, C. Rao, E. Wegman, and J. Solka, Eds., Amsterdam, Netherlands: Elsevier, 2005, ch. 10, pp. 263–302.

- [119] J. S. Brauchart, J. Dick, and L. Fang, “Spatial low-discrepancy sequences, spherical cone discrepancy, and applications in financial modeling,” *Journal of Computational and Applied Mathematics*, vol. 286, pp. 28–53, Oct. 2015.
- [120] C. Lemieux, “Monte Carlo and quasi-Monte Carlo sampling,” in (Springer Series in Statistics), Springer Series in Statistics. New York, NY: Springer-Verlag New York, 2009, ch. 1, 5–6, pp. 1–39, 139–199.
- [121] B. L. Fox, “Algorithm 647: Implementation and relative efficiency of quasirandom sequence generators,” *ACM Transactions on Mathematical Software*, vol. 12, no. 4, pp. 362–376, Dec. 1986.
- [122] H. Niederreiter, “Random number generation and quasi-Monte Carlo methods,” in Philadelphia, PA: Society for Industrial and Applied Mathematics (SIAM), 1992, ch. 2, 4, pp. 13–22, 47–99.
- [123] P. Bratley and B. L. Fox, “Algorithm 659: Implementing Sobol’s quasirandom sequence generator,” *ACM Transactions on Mathematical Software*, vol. 14, no. 1, pp. 88–100, Mar. 1988.
- [124] S. Joe and F. Y. Kuo, “Remark on algorithm 659: Implementing Sobol’s quasirandom sequence generator,” *ACM Transactions on Mathematical Software*, vol. 29, no. 1, pp. 49–57, Mar. 2003.
- [125] B. Burley, “Practical hash-based Owen scrambling,” *Journal of Computer Graphics Techniques (JCGT)*, vol. 10, no. 4, pp. 1–20, Dec. 2020.
- [126] A. B. Owen, “Variance with alternative scramblings of digital nets,” *ACM Transactions on Mathematical Software*, vol. 13, no. 4, pp. 363–378, Oct. 2003.
- [127] The MathWorks, Inc., “Statistics and Machine Learning Toolbox™ User’s Guide,” in MATLAB R2020b. Natick, MA: The MathWorks, Inc., Sep. 2020, ch. 3, 5, pp. 3-1 –3-17, 5-1 –5-239.
- [128] H. S. Hong and F. J. Hickernell, “Algorithm 823: Implementing scrambled digital sequences,” *ACM Transactions on Mathematical Software*, vol. 29, no. 2, pp. 95–109, Jun. 2003.
- [129] The MathWorks, Inc., “MATLAB® Function Reference,” in MATLAB R2020b. Natick, MA: The MathWorks, Inc., Sep. 2020, ch. 1, pp. 1-3955 –1-3965, 1-4184 –1-4187, 1-6514 –1-6524, 1-8793 –1-8804, 1-9037 –1-9038.
- [130] Lockheed Martin Missiles and Space, “Introduction,” in *Hubble Space Telescope Servicing Mission 3B: Media Reference Guide*, B. Nelson, Ed., ser. NP-2001-12-412-GSFC, NASA Goddard Space Flight Center, Sep. 2002, ch. 1, pp. 1–7.

- [131] I. M. Sobol, “On the distribution of points in a cube and the approximate evaluation of integrals,” *USSR Computational Mathematics and Mathematical Physics*, vol. 7, no. 4, pp. 86–112, 1967.
- [132] H. Niederreiter, “Point sets and sequences with small discrepancy,” *Monatshefte für Mathematik*, vol. 104, no. 4, pp. 273–337, Dec. 1987.
- [133] J. H. Halton, “On the efficiency of certain quasi-random sequences of points in evaluating multi-dimensional integrals,” *Numerische Mathematik*, vol. 2, no. 1, pp. 84–90, Dec. 1960.
- [134] J. M. Hammersley, “Monte Carlo methods for solving multivariable problems,” *Annals of the New York Academy of Sciences*, vol. 86, no. 3, pp. 844–874, 1960.
- [135] G. Leobacher and F. Pillichshammer, “Introduction to quasi-Monte Carlo integration and applications,” in (Compact Textbooks in Mathematics), *Compact Textbooks in Mathematics*. Cham, Switzerland: Birkhäuser Cham, 2014, ch. 2, 5, pp. 11–53, 107–142.
- [136] H. Niederreiter, “Random number generation and quasi-Monte Carlo methods,” in Philadelphia, PA: Society for Industrial and Applied Mathematics (SIAM), 1992, ch. 2-4, pp. 13–99.
- [137] M. Roberts, *The unreasonable effectiveness of quasirandom sequences*, extremelearning.com.au/unreasonable-effectiveness-of-quasirandom-sequences/, Online; accessed 19 November 2019, Aug. 2018.
- [138] G. W. Hill, “Researches in the lunar theory,” *American Journal of Mathematics*, vol. 1, no. 1, pp. 5–26, 1878.
- [139] W. H. Clohessy and R. S. Wiltshire, “Terminal guidance system for satellite rendezvous,” *Journal of Aerospace Sciences*, vol. 27, no. 9, pp. 653–658, 1960.
- [140] B. Naasz, “Safety ellipse motion with coarse sun angle optimization,” in *595 Flight Mechanics Symposium*, Greenbelt, MD: NASA Goddard Space Flight Center, Oct. 2005, pp. 1–13.
- [141] O. Montenbruck, R. Kahle, S. D’Amico, and J.-S. Ardaens, “Navigation and control of the TanDEM-X formation,” *The Journal of the Astronautical Sciences*, vol. 56, no. 3, pp. 341–357, Sep. 2008.
- [142] S. D’Amico, J.-S. Ardaens, and R. Larsson, “Spaceborne autonomous formation-flying experiment on the prisma mission,” *Journal of Guidance, Control, and Dynamics*, vol. 35, no. 3, pp. 834–850, 2012.

- [143] A. W. Koenig and S. D’Amico, “Safe spacecraft swarm deployment and acquisition in perturbed near-circular orbits subject to operational constraints,” *Acta Astronautica*, vol. 153, pp. 297–310, Dec. 2018.
- [144] P. Liu, X. Chen, and Y. Zhao, “Safe deployment of cluster-flying nano-satellites using relative E/I vector separation,” *Advances in Space Research*, vol. 64, no. 4, pp. 964–981, 2019.
- [145] D. Morgan, S.-J. Chung, L. Blackmore, B. Acikmese, D. Bayard, and F. Y. Hadaegh, “Swarm-keeping strategies for spacecraft under J2 and atmospheric drag perturbations,” *Journal of Guidance, Control, and Dynamics*, vol. 35, no. 5, pp. 1492–1506, 2012.
- [146] R. Opromolla, G. Fasano, G. Rufino, and M. Grassi, “Design of relative trajectories for in orbit proximity operations,” *Acta Astronautica*, vol. 145, pp. 342–356, Apr. 2018.
- [147] E. Gill, S. D’Amico, and O. Montenbruck, “Autonomous formation flying for the PRISMA mission,” *Journal of Spacecraft and Rockets*, vol. 44, no. 3, pp. 671–681, 2007.
- [148] J.-S. Ardaens and D. Fischer, “TanDEM-X autonomous formation flying system: Flight results,” *IFAC Proceedings Volumes*, 18th IFAC World Congress, vol. 44, no. 1, pp. 709–714, 2011.
- [149] J. B. Mueller and R. Larsson, “Collision avoidance maneuver planning with robust optimization,” in *7th International ESA Conference on Guidance, Navigation & Control Systems*, Tralee, Ireland: European Space Agency, Jun. 2008, pp. 1–16.
- [150] J. Mueller, “Onboard planning of collision avoidance maneuvers using robust optimization,” in *AIAA Infotech@Aerospace Conference*, Seattle, WA: AIAA, Apr. 2009, pp. 1–17.
- [151] H. Min, Z. Guoqiang, and S. Junling, “Collision avoidance control for formation flying satellites,” in *AIAA Guidance, Navigation, and Control Conference*, Toronto, Canada: AIAA, Aug. 2010, pp. 1–9.
- [152] J. B. Mueller, P. R. Griesemer, and S. J. Thomas, “Avoidance maneuver planning incorporating station-keeping constraints and automatic relaxation,” *Journal of Aerospace Information Systems*, vol. 10, no. 6, pp. 306–322, 2013.
- [153] I. Okoloko, “Path planning for multiple spacecraft using consensus with LMI avoidance constraints,” in *2012 IEEE Aerospace Conference*, Mar. 2012, pp. 1–8.

- [154] X. Lin, X. Shi, and S. Li, “Optimal cooperative control for formation flying spacecraft with collision avoidance,” *Science Progress*, vol. 103, no. 1, pp. 1–19, 2020.
- [155] J. Proakis and M. Salehi, “Deterministic and random signal analysis,” in *Digital Communications*, 5th ed., New York, NY: McGraw-Hill, 2008, ch. 2, pp. 17–94.
- [156] R. Serra, D. Arzelier, M. Joldes, and A. Rondepierre, “Probabilistic collision avoidance for long-term space encounters via risk selection,” in *Advances in Aerospace Guidance, Navigation and Control: Third CEAS Specialist Conference on Guidance, Navigation and Control*, J. Bordeneuve-Guibé, A. Drouin, and C. Roos, Eds., Cham, Switzerland: Springer International Publishing, Apr. 2015, pp. 679–698.
- [157] R. E. Caflisch, “Monte Carlo and quasi-Monte Carlo methods,” *Acta Numerica*, vol. 7, pp. 1–49, 1998.
- [158] J. Dick, F. Y. Kuo, and I. H. Sloan, “High-dimensional integration: The quasi-Monte Carlo way,” *Acta Numerica*, vol. 22, pp. 133–288, 2013.
- [159] A. Genz and F. Bretz, “Methods that approximate the integral,” in *Computation of Multivariate Normal and t Probabilities*, Berlin, Heidelberg: Springer Berlin Heidelberg, 2009, ch. 4, pp. 29–54.
- [160] R. V. Hogg, J. W. McKean, and A. T. Craig, “Introduction to mathematical statistics,” in 8th ed. Boston, MA: Pearson, 2019, ch. 1, 4, pp. 1–84, 255–320.
- [161] E. Parzen, “Nonparametric statistical data modeling,” *Journal of the American Statistical Association*, vol. 74, no. 365, pp. 105–121, 1979.
- [162] The MathWorks, Inc., “Ordinary differential equations (ODEs),” in *MATLAB® Mathematics*, MATLAB R2019b, Natick, MA: The MathWorks, Inc., Sep. 2019, ch. 11, pp. 11-1 –11-74.
- [163] The MathWorks, Inc., “Statistics and Machine Learning Toolbox™ User’s Guide,” in *MATLAB R2019b*. Natick, MA: The MathWorks, Inc., Sep. 2019, ch. 3, 5, pp. 3-1 –3-22, 5-1 –5-196.
- [164] X. Liu and P. Lu, “Solving nonconvex optimal control problems by convex optimization,” *Journal of Guidance, Control, and Dynamics*, vol. 37, no. 3, pp. 750–765, 2014.
- [165] D. Morgan, S.-J. Chung, and F. Y. Hadaegh, “Model predictive control of swarms of spacecraft using sequential convex programming,” *Journal of Guidance, Control, and Dynamics*, vol. 37, no. 6, pp. 1725–1740, 2014.

- [166] X. Liu, P. Lu, and B. Pan, “Survey of convex optimization for aerospace applications,” *Astrodynamics*, vol. 1, no. 1, pp. 23–40, Sep. 2017.
- [167] P. Lu and X. Liu, “Autonomous trajectory planning for rendezvous and proximity operations by conic optimization,” *Journal of Guidance, Control, and Dynamics*, vol. 36, no. 2, pp. 375–389, 2013.
- [168] J. Virgili-Llop, C. Zagaris, R. Zappulla II, A. Bradstreet, and M. Romano, “Convex optimization for proximity maneuvering of a spacecraft with a robotic manipulator,” in *2017 AAS/AIAA Spaceflight Mechanics Meeting*, ser. AAS 17-418, San Diego, CA: Univelt, Inc., Feb. 2017, pp. 1059–1078.
- [169] H. Park, S. Di Cairano, and I. Kolmanovsky, “Linear quadratic model predictive control approach to spacecraft rendezvous and docking,” in *2011 AAS/AIAA Spaceflight Mechanics Meeting*, ser. AAS 11-412, San Diego, CA: Univelt, Inc., Jan. 2011, pp. 565–584.
- [170] S. Di Cairano, H. Park, and I. Kolmanovsky, “Model predictive control approach for guidance of spacecraft rendezvous and proximity maneuvering,” *International Journal of Robust and Nonlinear Control*, vol. 22, no. 12, pp. 1398–1427, 2012.
- [171] A. Weiss, M. Baldwin, R. S. Erwin, and I. Kolmanovsky, “Model predictive control for spacecraft rendezvous and docking: Strategies for handling constraints and case studies,” *IEEE Transactions on Control Systems Technology*, vol. 23, no. 4, pp. 1638–1647, 2015.
- [172] H. Park, C. Zagaris, J. Virgili-Llop, R. Zappulla, I. Kolmanovsky, and M. Romano, “Analysis and experimentation of model predictive control for spacecraft rendezvous and proximity operations with multiple obstacle avoidance,” in *2016 AIAA/AAS Astrodynamics Specialist Conference*, Reston, VA: American Institute of Aeronautics and Astronautics, Sep. 2016, pp. 1–17.
- [173] C. Zagaris, H. Park, J. Virgili-Llop, R. Zappulla II, M. Romano, and I. Kolmanovsky, “Model predictive control of spacecraft relative motion with convexified keep-out-zone constraints,” *Journal of Guidance, Control, and Dynamics*, vol. 41, no. 9, pp. 2054–2062, 2018.
- [174] J. Munoz, G. Boyarko, and N. Fitz-Coy, “Rapid path-planning options for autonomous proximity operations of spacecraft,” in *2010 AIAA/AAS Astrodynamics Specialist Conference*, Reston, VA: American Institute of Aeronautics and Astronautics, Aug. 2010, pp. 1–24.
- [175] Q. Hu, H. Dong, Y. Zhang, and G. Ma, “Tracking control of spacecraft formation flying with collision avoidance,” *Aerospace Science and Technology*, vol. 42, pp. 353–364, 2015.

- [176] H. Dong, Q. Hu, and M. R. Akella, “Safety control for spacecraft autonomous rendezvous and docking under motion constraints,” *Journal of Guidance, Control, and Dynamics*, vol. 40, no. 7, pp. 1680–1692, 2017.
- [177] X. Huang, Y. Yan, and Y. Zhou, “Underactuated spacecraft formation reconfiguration with collision avoidance,” *Acta Astronautica*, vol. 131, pp. 166–181, 2017.
- [178] L. Cao, D. Qiao, and J. Xu, “Suboptimal artificial potential function sliding mode control for spacecraft rendezvous with obstacle avoidance,” *Acta Astronautica*, vol. 143, pp. 133–146, 2018.
- [179] Q. Li, J. Yuan, B. Zhang, and C. Gao, “Model predictive control for autonomous rendezvous and docking with a tumbling target,” *Aerospace Science and Technology*, vol. 69, pp. 700–711, 2017.
- [180] K. Dong, J. Luo, Z. Dang, and L. Wei, “Tube-based robust output feedback model predictive control for autonomous rendezvous and docking with a tumbling target,” *Advances in Space Research*, vol. 65, no. 4, pp. 1158–1181, 2020.
- [181] X. Wang, Y. Li, X. Zhang, R. Zhang, and D. Yang, “Model predictive control for close-proximity maneuvering of spacecraft with adaptive convexification of collision avoidance constraints,” *Advances in Space Research*, vol. 71, no. 1, 2023.
- [182] H. Park, S. Di Cairano, and I. Kolmanovsky, “Model predictive control for spacecraft rendezvous and docking with a rotating/tumbling platform and for debris avoidance,” in *Proceedings of the 2011 American Control Conference*, Red Hook, NY: Curran Associates, Inc., Jun. 2011, pp. 1922–1927.
- [183] U. E. Núñez Garzón and E. G. Lightsey, “Arbitrary relative position norm effects on spacecraft formation flying joint-time collision probability well-definedness,” *Journal of Guidance, Control, and Dynamics*, Jun. 2023, Submitted for publication Jun. 2023.
- [184] A. Dietrich and J. W. McMahon, “Orbit determination using flash lidar around small bodies,” *Journal of Guidance, Control, and Dynamics*, vol. 40, no. 3, pp. 650–665, 2017.
- [185] R. R. Bate, D. D. Mueller, and J. E. White, “Orbit determination from observations,” in *Fundamentals of Astrodynamics*. New York, NY: Dover Publications, 1971, ch. 2, 4, pp. 51–150, 177–226.
- [186] H. D. Curtis, “Orbits in three dimensions,” in *Orbital Mechanics for Engineering Students*, 3rd ed. Oxford, UK: Butterworth-Heinemann, 2013, ch. 4, pp. 187–237.

- [187] A. M. Mood, F. A. Graybill, and D. C. Boes, “Parametric point estimation,” in *Introduction to the Theory of Statistics*, 3rd ed., New York, NY: McGraw-Hill New York, 1974, ch. 7, pp. 271–371.
- [188] X. Gao, M. Sitharam, and A. Roitberg, “Bounds on the Jensen gap, and implications for mean-concentrated distributions,” *Australian Journal of Mathematical Analysis and Applications*, vol. 16, no. 2, pp. 1–16, 2019.
- [189] Y. L. Tong, “Other related properties,” in *The Multivariate Normal Distribution*, ser. Springer Series in Statistics, New York, NY: Springer-Verlag New York, 1990, ch. 4, pp. 62–90.
- [190] P. J. Davis, “Gamma function and related functions,” in *Handbook of Mathematical Functions with Formulas, Graphs, and Mathematical Tables*, ser. Applied Mathematics Series, M. Abramowitz and I. A. Stegun, Eds., 9th ed., U.S. Department of Commerce, Washington, D.C.: National Bureau of Standards, 1970, ch. 6, pp. 253–294.
- [191] N. Johnson, S. Kotz, and N. Balakrishnan, “Chi-square distributions, including chi and Rayleigh,” in *Continuous Univariate Distributions, Vol. 1*, 2nd ed., Boston, MA: Houghton Mifflin, 1994, ch. 18, pp. 415–493.

VITA

Ulises Eduardo Núñez Garzón was born in 1995 in Santiago, Veraguas Province, Republic of Panama. Ulises attended the Colegio San Vicente de Paúl school in Santiago, Panama from grades Pre-K through 12th (1999-2012), where he was high school valedictorian in Dec. 2012, and where he received awards in the Panamanian Physics Olympics competition (Gold Medal, 2010; Silver Medal, 2012).

Ulises attended the Georgia Institute of Technology (Georgia Tech) for his undergraduate degree (2013-2017) with a full scholarship as the personal scholar of Mr. Juan Carlos Varela, Vice-President of Panama (2009-2014) and President of Panama (2014-2019). Ulises received his B.S. (2017; Highest Honors) and M.S. (2020) degrees in aerospace engineering from Georgia Tech. Ulises' industry experience includes aeronautics (Copa Airlines, and Boeing Commercial Airplanes) and space (Odyssey Space Research, LLC) work experience.

While at Georgia Tech, Ulises has been a member of the Dr. E. Glenn Lightsey Research Group within the Georgia Tech Space Systems Design Lab (SSDL). Ulises' research interests are in the areas of astrodynamics and spacecraft guidance, navigation, and control (GN&C). His current work encompasses applications of measure and probability theory and quasi-random number sequence generation to spaceflight mechanics, specifically, in the context of the dynamics of spacecraft relative motion. These techniques are applied to the process of collision risk management in spacecraft formations – specifically, in the areas of collision risk quantification, collision risk interpretation and decision-making, and in the ascertaining of well-definedness and computability of new collision risk indicators.

During his time at the SSDL (2015-2023), Ulises has also participated in the following activities outside of his doctoral thesis work: mission operations for the Bevo-2/AggieSat-4 missions, satellite range scheduling optimization research, early mission concept for-

mulation for the Virtual Super Optics Reconfigurable Swarm (VISORS) mission, mission concept formulation for the Formation Flying Radio Astronomy group within the Precision Aggregated Space Systems (PASS) initiative of the Georgia Tech Research Institute (GTRI), and lab instruction for the Space Systems undergraduate design capstone course within the Daniel Guggenheim School of Aerospace Engineering.

Ulises has been married to Amanda (née Remus) since Aug. 3, 2019, and they currently reside in Atlanta, GA, where they are members of Christ Covenant Church. Ulises and Amanda enjoy serving in the children's ministry at Christ Covenant and participating in the Brooks' Community Group, of which they are active members.